THE INFLUENCE OF SURFACE STRUCTURE AND ADLAYER COMPOSITION ON THE KINETICS AND MECHANISMS OF GAS-SURFACE REACTIONS

Thesis by

James Robert Engstrom

In Partial Fulfillment of the Requirements

for the Degree of

Doctor of Philosophy

California Institute of Technology

Pasadena, California

1987

(Submitted December 12, 1986)

This thesis is dedicated to my parents,

George and Helen Engstrom

ACKNOWLEDGEMENTS

During the course of my work at Caltech leading to my final degree, I have benefited from the support, encouragement and camradarie of a number of people. Although some have become but distant memories, I am indebted to all of you.

My advisor, Henry Weinberg, allowed me considerable freedom in the direction I chose for my research, yet still provided support and encouragement when needed. He taught me a great deal about the proper approach to scientific reasearch; it gave me great pleasure working with him these past few years. Brad Anton provided valuable insights into research in general on many occasions (in ways unique to his personality), and was, and remains, a good friend. Malina Hills was most understanding and cooperative in not only sharing lab space, but also her lab computer. Wilman Tsai was invaluable for his technical assistance in the obtaining of the data that are detailed in Chapter 4. Phil Szuromi helped guide my first experimental encounters with UHV surface science. I have also had the pleasure of working with a number of outstanding individuals who have been associated with Henry's research group over the years; in no particular order: Neal, Lynn, Greg, Pat, Steve, Eric, Chuan, Art, Buddy, John, Udo, Charles, Yongkui, Mike, Brian, John and Jenna. Finally, the staff personnel that I had the chance to interact with were always friendly and helpful and included: Betty Benjamin, Pat Bullard, Tom Dunn, Guy Duremberg, George Griffith, Floyd Litreal, Mike Nagy, Chic Nakawatase, Henry Smith, Sig Jenner, Kathy Lewis, Tony Stark and John Yehle.

Wayne Goodman was most accomodating during the four months I spent working in his lab at Sandia in Albuquerque. His unbridled enthusiasm for science made my brief stay one of the most pleasurable and rewarding experiences of my life as a graduate student. I shall always be grateful for the opportunity he afforded me. In addition, it was also my pleasure to be associated with a number of people in the Surface Science Division at Sandia: Jack Houston, Gary Kellogg, Chuck Peden, Bill Rodgers and Bob Rye.

Roxy and Strawberry have probably been my closest friends during my brief stay in southern California. Most of my pleasant memories are directly attributable to them. I would especially like to thank Roxy for putting up with me for over three years. I have also enjoyed the friendship of Ken Reardon, Miles Gehm, Jim Stoos, Howard Stone, Mike & Mike, and George Yates and the Caltech Hockey Club. I would also like to thank those friends across the miles who have made a concerted effort to stay in touch: John Kitt, Gene Martinez, Susan Howitz, Liz Thurman, Jim Naslund, Ceal Sorrentino, Dan Thorpe, Grant Benjamin and Dave Kinning.

As a PhD represents the culmination of one's formal education, I would like to acknowledge those teachers who have made the long journey bearable and even enjoyable. My 5th and 6th grade teacher, Barbara Dow, made a remarkable and lasting impact on my life. My confimation pastor, George Weinmann, aided my spiritual development considerably. My high school math and science teachers, Larry Luck and William Marcoullier, made science enjoyable. Thomas Geankoplis taught me the importance of taking the detailed, thorough approach in any endeavor. In regard to my undergraduate education at the University of Minnesota, there is a high probability that I would not have attended graduate school if it were not for the personal encouragement of Profs. George Stephanopoulos and, especially, Matt Tirrell. Although I've had my doubts, postgraduate education was well worth the effort.

Last, but certainly not least, I would like to thank my family for their unwavering support over these past five years: my brothers Dave and Glenn and their families, and my father and mother, George and Helen. I love you all very much.

ABSTRACT

The theoretical formulation of a frequency response technique, based on surface temperature modulation, for the study of the kinetics of elementary gas-surface reactions is described in detail. The formalism is developed for analyzing adsorption, desorption, and both unimolecular and bimolecular surface reactions. The technique possesses a distinct advantage over competitive techniques, such as modulated molecular beam reactive scattering, since the evaluation of activation barriers for elementary surface reactions is straightforward *even in the presence of strong nonlinearities* and requires no knowledge of the composition and/or configuration of the adlayer. The technique has been employed successfully to investigate the adsorption, desorption and oxidation of CO on the Pt(110)-(1x2) surface. The oxidation of CO has been studied with emphasis on examining the kinetics of the elementary bimolecular surface reaction $CO(a) + O(a) \rightarrow CO_2(g)$. The activation energy is found to correlate well with the oxygen adatom concentration, the variation being quite nonlinear. This nonlinear variation is interpreted as a manifestation of the dominant role that the *local* configuration of the reactants play in determining the reaction dynamics. It is suggested that the power of the technique can be increased significantly by either coupling it with time-resolved, surface-sensitive spectroscopies or employing localized (*e.g.*, laser) heating techniques to provide the modulation in surface temperature. The chemisorption of hydrogen on both the Ir(111) and Pt(110)-(1x2) surfaces has been examined by employing primarily thermal desorption mass spectrometry. Comparisons of the results obtained on the (111) and (110)-(1x2) surfaces of both iridium and platinum suggest strongly that *local* surface structure has a profound influence on the kinetics of adsorption of hydrogen on these surfaces. Surface structure also influences greatly the desorption kinetics of hydrogen via the mediation of "through-metal" adatom-adatom interactions. In particular, both attractive and repulsive interactions are clearly manifest within the higher binding energy β_2-adstates on the (110)-(1x2) surfaces,

these β_2 states associated with adsorption into one-dimensional channels which are composed of high-coordination "trough" sites. However, only repulsive interactions were apparent on the (111) surfaces or for the lower binding energy β_1-adstates on the (110)-(1x2) surfaces, these β_1 states associated with adsorption on the (111) microfacets. The hydrogenolysis of several alkanes and cycloalkanes has been examined on both the (111) and (110)-(1x2) single crystalline surfaces of iridium for hydrocarbon partial pressures near 1 Torr, hydrogen partial pressures near 100 Torr, and surface temperatures between 400 and 700 K. The choice of these two surfaces has proven to be decisive for the unambiguous assessment of the effects of surface geometry on both catalytic activity and selectivity. Concerning the hydrogenolysis of alkanes, excepting the special case of *n*-butane on Ir(110)-(1x2), a mechanism involving a rate-limiting unimolecular C-C bond cleavage in an adsorbed, dehydrogenated hydrocarbon fragment describes well the variations in both the specific activity and selectivity of hydrogenolysis with variations in the reactant partial pressures. In cases where similar activities and selectivities are observed over the two surfaces, essentially identical reaction intermediates (mechanisms) are implicated. On the other hand, in cases where different activities and/or selectivities are observed over the two surfaces, distinct reaction intermediates (mechanisms) are implicated. In the particular case of the reaction of *n*-butane, the selectivity for ethane was identified explicitly with the participation (concentration) of low-coordination-number metal surface atoms. It is suggested that the intermediate that leads to the high selectivity for ethane is a mononuclear *metallacycle pentane*; the formation of this intermediate is sterically forbidden on (111) surfaces. Concerning the hydrogenolysis and hydrogenation of cycloalkanes, the Ir(110)-(1x2) surface possesses a greater specific activity (per metal surface atom basis) with respect to the Ir(111) surface for both the hydrogenation (to propane) and the hydrogenolysis (to methane and ethane) of cyclopropane. This result is interpreted by invoking a greater intrinsic activity (for these reactions) for the low-coordination-number metal surface atoms that are present in higher concentrations on Ir(110)-(1x2).

Unlike the reactions of alkanes, for cyclopropane under "severe" reaction conditions (*i.e.*, large hydrocarbon-to-hydrogen partial pressure ratios and/or high temperatures), a transformation in the composition of the adlayer occurs, with the coverage of the carbonaceous residue increasing from one-half of a monolayer to nearly a full monolayer. Concomitant with the adlayer transformation, the selectivity of the reaction of cyclopropane and hydrogen shifts dramatically from methane (hydrogenolysis) to propylene (isomerization). The dominance of the (relatively facile) isomerization channel on the "carburized" surface is interpreted as a manifestation of a weakened interaction between the metal surface and the relevant adsorbed reaction intermediates.

TABLE OF CONTENTS

ACKNOWLEDGEMENTS		iii
ABSTRACT		v
INTRODUCTION		1
CHAPTER 1	Surface Reaction Dynamics via Temperature Modulation: Applications to the Oxidation of Carbon Monoxide on the Pt(110)-(1x2) Surface	12
	References	16
CHAPTER 2	Analysis of Gas-Surface Reactions by Surface Temperature Modulation: I. Theoretical Formulation	17
	References	41
	Table	45
	Figures	46
CHAPTER 3	Analysis of Gas-Surface Reactions by Surface Temperature Modulation: II. Experimental Applications to the Adsorption and Oxidation of Carbon Monoxide on the Pt(110)-(1x2) Surface	53
	References	75
	Figures	80
CHAPTER 4	The Chemisorption of Hydrogen on the (111) and (110)-(1x2) Surfaces of Iridium and Platinum	91
	References	124
	Table	129
	Figures	130
CHAPTER 5	Hydrogenolysis of *n*-Butane over the (111) and (110)-(1x2) Surfaces of Iridium: A Direct Correlation between Catalytic Selectivity and Surface Structure	151
	References	

CHAPTER 6	The Hydrogenolysis of Ethane, Propane, *n*-Butane and Neopentane over the (111) and (110)-(1x2) Surfaces of Iridium	155
	References	200
	Tables	206
	Figures	212
CHAPTER 7	The Reaction of Cyclopropane, Methylcyclopropane and Propylene with Hydrogen on the (111) and (110)-(1x2) Surfaces of Iridium	232
	References	267
	Tables	270
	Figures	273
CONCLUSIONS		295
APPENDIX A	Design and Construction of a Digital Temperature Controller for Use in Surface Studies	298
	References	304
APPENDIX B	Spatial Temperature Distribution of the Crystal Surface	305
	Figure	311
APPENDIX C	Numerical Model Describing the Oxidation of CO on Pt(110)-(1x2)	312
	References	317
	Figure	318
APPENDIX D	The Reaction of Saturated and Unsaturated Hydrocarbons with the (110)-(1x2) and (111) Surfaces of Iridium	319
	References	329
APPENDIX E	Adsorption and Reaction of *n*-Alkanes on the Pt(110)-(1x2) Surface	330
	References	

INTRODUCTION

The study of the kinetics and mechanisms of chemical reactions occurring on solid surfaces is of tremendous scientific and technological importance, most notably in connection with heterogeneous catalysis. The importance of the structure of the surface in determining the activity and selectivity of various classes of heterogeneous catalyzed reactions has been long recognized **(1)**. For example, in regard to supported metal catalysts, the *specific* activity (per metal surface atom) of many reactions has been found to be sensitive to the average metallic particle size, prompting Boudart to introduce the term "structure sensitivity" to describe the phenomenon **(2)**. On the other hand, the composition of the adlayer can profoundly affect both the activity and selectivity of a particular catalyst. In particular, examinations of both the deleterious and beneficial effects of "foreign" species adsorbed on the catalytic surface, *e.g.*, the so-called "poisons" or "inhibitors" and "promotors," have attracted considerable attention **(3)**. Of course, the reactants *themselves* can also lead to variations in the catalytic properties (*i.e.*, in addition to the intrinsic concentration dependence of the particular reaction) via, for example, a "self-poisoning" of the surface or a phase transition in the adlayer **(4)**.

Modern ultrahigh vacuum (UHV) surface science has proven itself to be invaluable for a complete understanding of the mechanisms, and the associated adsorbed intermediates, of *elementary* gas-surface reactions **(5)**. However, the conditions for which the experiments are typically carried out (*e.g.*, pressures below 10^{-6} Torr, temperatures below 300 K, and relatively low adsorbate concentrations) make subsequent extrapolation to "realistic" catalytic conditions (*e.g.*, pressures above 10^{2} Torr, temperatures above 500 K, and relatively high adsorbate concentrations) difficult. Nevertheless, in a few simple cases, correlations have been made between UHV measurements and the specific rates of the corresponding reactions at elevated pressures **(6)**. One major difficulty yet to be resolved is the proper assessment of the importance of various adsorbed reaction intermediates that have been observed un-

der UHV conditions. A recent review has suggested that more restraint (*i.e.*, with respect to the proposition of reaction intermediates) is warranted in this area (**7**). It is hoped that, with the development of high resolution *in situ* spectroscopic techniques that are compatible with high pressures (**8**), a better understanding of the catalytically important reaction intermediates will emerge.

An alternate approach to obtaining a more microscopic understanding of heterogeneous catalysis has been developed by Goodman and co-workers (**9**). In particular, this approach involves the combination of both modern UHV analytical techniques and the use of oriented metal single crystals with classical high-pressure kinetic measurements. With this method, all experiments are conducted in the same apparatus by utilizing an *in situ* sample (*i.e.*, the single crystalline catalyst) transfer system, as shown schematically in Fig. 1. Although *in situ* spectroscopic techniques are precluded by adopting this approach, the effects of surface structure and adlayer compostion on a particular reaction can be assessed in a straightforward manner. The unambiguous evaluation of the various factors controlling catalytic activity and selectivity afforded by this method gives it a decided advantage over more classical high-pressure techniques employing metal films and/or supported metal catalysts. In particular, since single crystalline catalysts are essentially not affected by the heat and mass transfer limitations associated with supported metal catalysts, the reaction conditions (*i.e.*, reactant partial pressures and surface temperature) can be varied over a wide range, permitting a rigorous test of any reaction mechanism that is proposed. In addition, if variations in the catalytic properties with varying reaction conditions occur due to a transformation in the composition of the adlayer (*e.g.*, "self-poisoning"), the causes for these changes can be identified explicitly via post-reaction surface characterization.

The work detailed in the following chapters can be conveniently divided into two sections, based on the particular experimental method that was adopted in each case. Chapters 1–4 deal with the application of (UHV) temperature programming techniques to the analysis of the kinetics and mechanisms of elementary chemical

reactions occurring on metal surfaces. Specifically, emphasis is placed on examining the coverage (adsorbate concentration) dependence of the integral kinetic rate parameters— the activation energy and the preexponential factor. Chapters 5–7 deal with employing the coupled high-pressure reactor/UHV analysis chamber to the examination of several prototypical reactions of small hydrocarbon molecules over oriented single crystalline surfaces of iridium. In particular, emphasis is placed on the evaluation of the effects of surface geometry on both the activity and selectivity of these reactions.

Temperature programming techniques have been utilized extensively in UHV surface science for the investigation of gas-surface kinetics, the primary example being thermal desorption mass spectrometry (TDMS) **(10)**. In a thermal desorption experiment, molecules are adsorbed at a sufficiently low temperature (*i.e.*, such that adsorption is irreversible), the surface is heated at an approximately constant rate (*e.g.*, a linear temperature ramp), and the partial pressure of the molecules desorbed is monitored with a mass spectrometer. If the UHV analysis chamber is pumped sufficiently fast, the partial pressure is proportional to the the instantaneous *rate* of desorption of the adsorbed molecules. The resulting desorption spectrum can be utilized to obtain fundamental information concerning the desorption reaction: *(i)* the peak temperature gives a qualitative estimate of the activation energy of desorption; *(ii)* the integrated spectrum (versus time) is proportional to the initial coverage; and *(iii)* the variations of the spectra with a varying initial coverage suggest an "order" for the desorption reaction **(11)**.

Quantitative analysis is best achieved by varying the (linear) rate at which the surface is heated **(12)**. Precise temperature control of the substrate is *very* desirable in this case (see Appendix A). In particular, by varying the heating rate, the rate of desorption can be measured at different temperatures and at a *fixed coverage*, permitting an evaluation of the *coverage-dependence* of the rate parameters that describe the desorption reaction. Previous work has demonstrated explicitly that the rate parameters can depend *strongly* on coverage **(13)**. These variations in the rate

parameters, excluding the simple cases where it can be attributed to multiple, distinct (*e.g.*, geometrically) adsorption sites, have usually been rationalized in terms of interactions between the adsorbed molecules or atoms. In particular, the strength of these interactions cannot be rationalized in terms of "through-space" interactions (*e.g.*, dipole-dipole); rather, a "through-metal" interaction must be invoked. This, of course, is not suprising for strongly bound (*i.e.*, chemisorbed) adsorbates, which are expected to perturb the local electronic density of states near the Fermi level of the metallic substrate, and, consequently, change the nature of further adsorbate chemisorption. Chapter 4 is concerned with the desorption (and adsorption) kinetics of hydrogen on the (111) and (110)-(1x2) surfaces of both iridium and platinum. It is demonstrated on these surfaces that hydrogen adatom-adatom interactions are present, and, furthermore, the nature (*i.e.*, repulsive or attractive) and strength of these interactions are dictated by the structure of the surface.

Unfortunately, linear temperature programming techniques are not well suited for more complex systems such as bimolecular reactions (excluding the simple case of molecular desorption via adatom-adatom recombination). For example, serious problems arise in the construction of an Arrhenius plot, since the coverages of *both* reactants must be fixed **(14)**. On the other hand, effects due to temperature-dependent reactant phase segregation (or dissolution) occurring during the linear temperature ramp, if present, will virtually invalidate any attempted quantitative analysis. Alternate techniques such as modulated molecular beam reactive scattering (MMBRS) are also fraught with limitations. For example, quantitative analysis by MMBRS is essentially restricted to *linear* systems (*e.g.*, first-order reactions), and, in most cases, to the limit of low coverages **(15)**.

Virtually all of the above difficulties with examining nonlinear systems such as bimolecular reactions can be circumvented by employing surface temperature modulation **(16)**. This technique, detailed in Chapters 1–3, permits the direct determination of the activation energies of elementary surface reactions even in the presence of strong nonlinearities. Furthermore, knowledge of the adlayer composi-

tion or configuration (*i.e.*, structure) of the adlayer is not required for an evaluation of the activation energy. The surface temperature modulation technique may be summarized as follows:

(i) Impose a small sinusoidal temperature profile on a solid surface during a steady-state gas-surface reaction

(ii) Monitor simultaneously the surface temperature and the reaction product(s) partial pressures(s)

(iii) Analyze the input (surface temperature) and output (product partial pressure) waveforms to evaluate the activation energy of a ***single*** elementary surface reaction

Although the surface temperature modulation technique possesses conceptual similarities to other frequency response techniques such as MMBRS, activation energies are not evaluated by constructing Arrhenius plots of apparent rate coefficients. (Note that these apparent rate coefficients are often simply related to the modulation frequency and the phase difference between input and output waveforms.) Rather, the absolute magnitude of the amplitude ratio of the input and output waveforms AR reflects directly the activation energy E_r of a single elementary reaction; *e.g.*,

$$AR(\omega) = \frac{(E_r/k_B T_s)}{\sqrt{(\nu/\omega)^2 + 1}} ,$$

where ν is an apparent rate coefficient, ω is the modulation frequency, and T_s is the steady-state surface temperature. Thus, unlike most frequency response techniques, the frequency is varied in order to "select" (in frequency space) a particular reaction such that the amplitude ratio is characteristic of the selected reaction only.

The technique is applied successfully to an examination of the elementary reaction between CO admolecules and oxygen adatoms to form CO_2, $CO(a) + O(a) \rightarrow CO_2$, on the Pt(110)-(1x2) surface. These results, detailed in Chapter 3, especially

those concerning the variation of the activation energy with the steady-state oxygen adatom concentration, represent an important contribution to a more complete understanding of the surface reaction dynamics of the oxidation of CO on platinum.

Finally, it must be noted that the kinetic parameters obtained via the surface temperature modulation technique represent those at the *steady-state*, which are often difficult to obtain. In addition, the technique is not inherently limited to a particular range of coverages; most importantly, the kinetics representative of the limit of high coverages may be evaluated in a straightforward manner. Since the high coverage regime is often the one most representative of the state of the catalytic surface under "realistic" reaction conditions, it is hoped that this technique will lead to a better understanding of gas-surface reactions at elevated pressures.

The hydrogenolysis of several alkanes and cycloalkanes has been examined on both the (111) and (110)-(1x2) single crystalline surfaces of iridium, and the results are discussed in Chapters 5–7. These two surfaces were chosen primarily in order to investigate the relationship between surface structure and both catalytic activity and selectivity. For example, the (110)-(1x2) surface contains a large fraction of low-coordination-number (C_7) edge atoms, whereas a perfect (111) surface contains no such atoms (*cf.* Fig. 2). Consequently, if the mechanism and/or rate of a particular reaction is influenced by the relative concentration of these low-coordination-number surface atoms, then these two surfaces should be decisive in quantifying their connnection to catalytic activity and selectivity.

A number of results were obtained concerning these hydrocarbon reactions over the two model Ir catalysts. The results for the hydrogenolysis of *n*-butane (*i.e.*, "cracking" to methane, ethane and propane) are most provocative. In connection with these results, recent work by Rooney and co-workers **(17)** has led to the suggestion that mechanisms common to transition metal homogeneous complexes are also important to heterogeneous catalysis. For example, the cyclization of five-carbon chain alkanes over a number of transition metal films (including Ir, Rh, Pd, and Pt) can be explained by the heterogeneous counterpart of reductive

elimination of alkyls in organometallic chemistry, *i.e.*, in this case, the production of cyclopentane from a mononuclear metallacycle hexane. The results presented here in Chapters 5 and 6 for the hydrogenolysis of *n*-butane over the two Ir single crystalline catalysts can be reconciled by invoking the participation of a mononuclear metallacycle pentane on the Ir(110)-(1x2) surface. Most importantly, the mechanism (*i.e.*, the reaction intermediate) is different over the (111) surface. Comparison to results obtained over supported Ir catalysts of varying metallic particle size leads to the identification of the low-coordination-number (C_7) atoms as the "active site" on the Ir(110)-(1x2) surface.

These results can be interpreted if one considers the stereochemistry of the two surfaces— significant repulsion between the α-hydrogens of a metallacycle pentane and the nearest neighbor Ir atoms is predicted on the Ir(111) surface, whereas no steric repulsion is apparent if one coordinates the ligand to the low-coordination-number C_7 atoms on the Ir(110)-(1x2) surface (*cf.* Fig. 1). The immediate implication is that mononuclear metallacycle (certainly pentane and probably hexane) formation is favored on low-coordination-number metal surface atoms. Furthermore, whereas mechanisms involving a single metal atom are unquestionably important on extended metal surfaces, all surface atoms are *obviously* not equivalent in regard to their catalytic properties. In particular, the work described here suggests strongly that a "coordination requirement" exists for the formation of mononuclear metallacycle complexes.

References

1. H. S. Taylor, Proc. Roy. Soc. London Ser. A **108**, 105 (1925).
2. M. Boudart, Adv. Catal. **20**, 153 (1969).
3. D. W. Goodman, Appl. Surface Sci. **19**, 1 (1984).
4. M. P. Cox, G. Ertl and R. Imbihl, Phys. Rev. Letters **54**, 1725 (1985).
5. See, *e.g.*, W. H. Weinberg in: *Survey of Progress in Chemistry* **10**, 1 (1983).
6. See, *e.g.*, G. Ertl in : *Critical Reviews of Solid State and Materials Science*, CRC Press, Boca Raton, 1982, p. 349.
7. J. J. Rooney, J. Molec. Catal. **31**, 147 (1985).
8. F. M. Hoffmann, J. Vac. Sci. Technol. A, to be published.
9. D. W. Goodman, R. D. Kelley, T. E. Madey and J. T. Yates, Jr., J. Catal. **63**, 226 (1980); D. W. Goodman, Ann. Rev. Phys. Chem. **37**, 425 (1986).
10. D. Menzel, in: *Chemistry and Physics of Solid Surfaces IV*, R. Vanselow and R. Howe Eds., Springer-Verlag, Heidelberg-New York, 1982, p. 389.
11. C.-M. Chan, R. Aris and W. H. Weinberg, Appl. Surface Sci. **1**, 360 (1978);C.-M. Chan, and W. H. Weinberg, Appl. Surface Sci. **1**, 378 (1978).
12. J. L. Taylor and W. H. Weinberg, Surface Sci. **78**, 259 (1978).
13. H. Pfnür, P. Feulner, H. A. Engelhardt and D. Menzel, Chem. Phys. Lett. **59**, 481 (1978).
14. J. L. Taylor, D. E. Ibbotson and W. H. Weinberg, Surface Sci. **90**, 37 (1979).
15. M. P. D'Evelyn and R. J. Madix, Surf. Sci. Reports **3**, 413 (1984).
16. J. R. Engstrom and W. H. Weinberg, Phys. Rev. Letters **55**, 2017 (1985).
17. O. E. Finlayson, J. K. A. Clarke and J. J. Rooney, J. C. S. Faraday Trans. I **80**, 191 (1984).
18. J. R. Engstrom, D. W. Goodman and W. H. Weinberg, J. Am. Chem. Soc. **108**, 4653 (1986).

Figure Captions

Figure 1. A schematic of the coupled high-pressure reactor/UHV analysis chamber that was employed for the experiments that are described in Chapters 5–7.

Figure 2. Structural models for the (110)-(1x2) and (111) surfaces of iridium. The z-axis is perpendicular to the plane of the surface. The C_n designate the coordination numbers of the metal surface atoms.

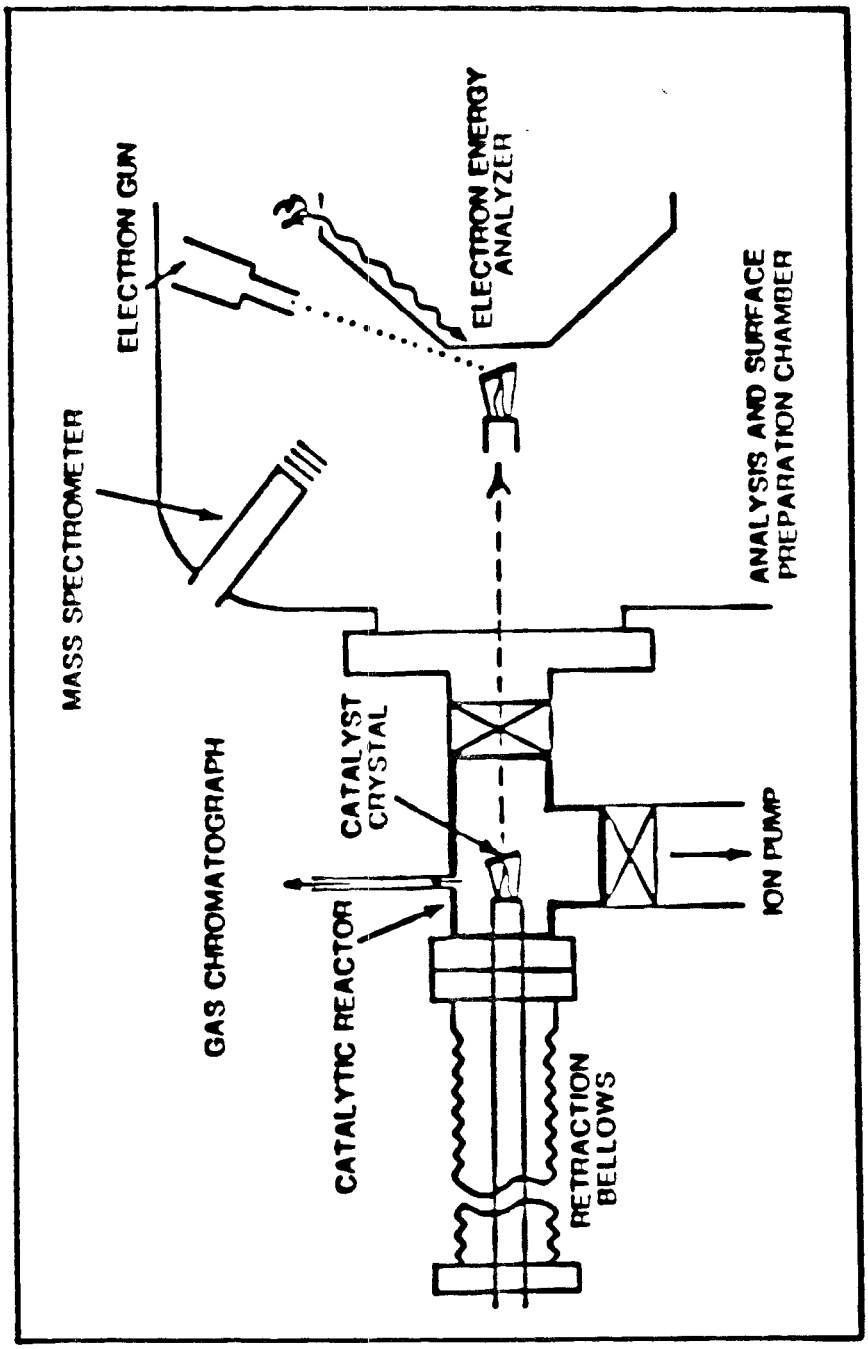
ELECTRON GUN
ELECTRON ENERGY ANALYZER
MASS SPECTROMETER
ANALYSIS AND SURFACE PREPARATION CHAMBER
GAS CHROMATOGRAPH
CATALYST CRYSTAL
ION PUMP
CATALYTIC REACTOR
RETRACTION BELLOWS

Figure 1

Ir(110)-(1×2)

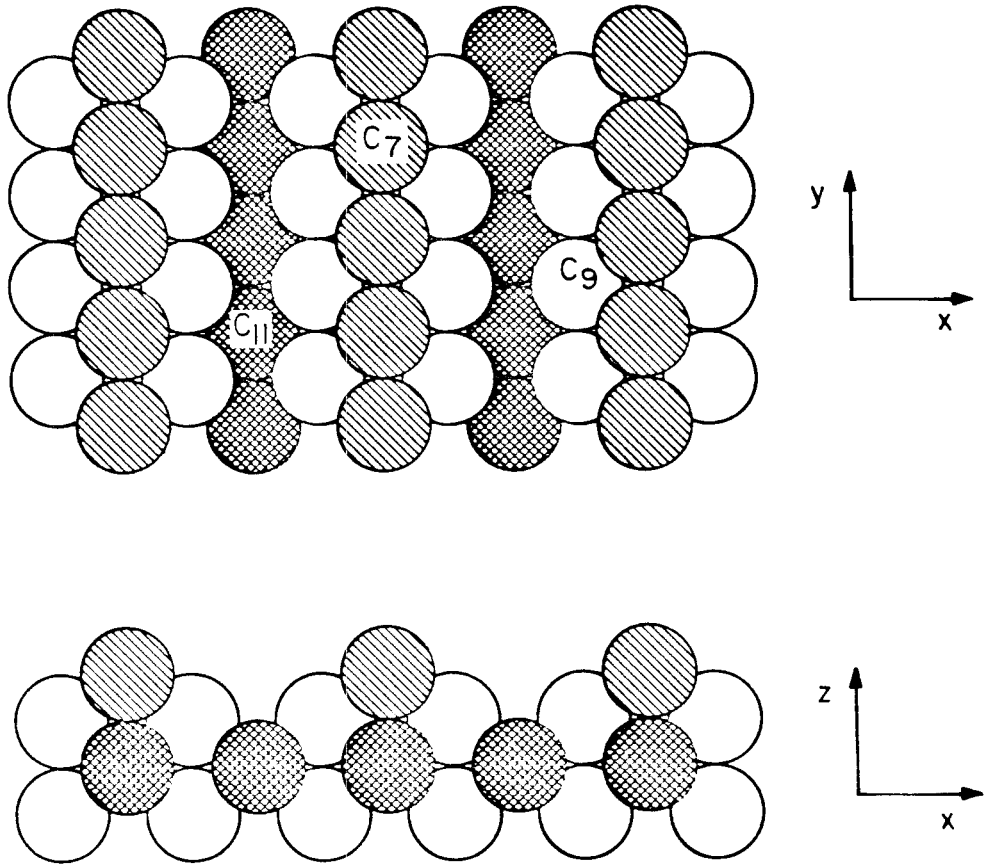

Ir(111)

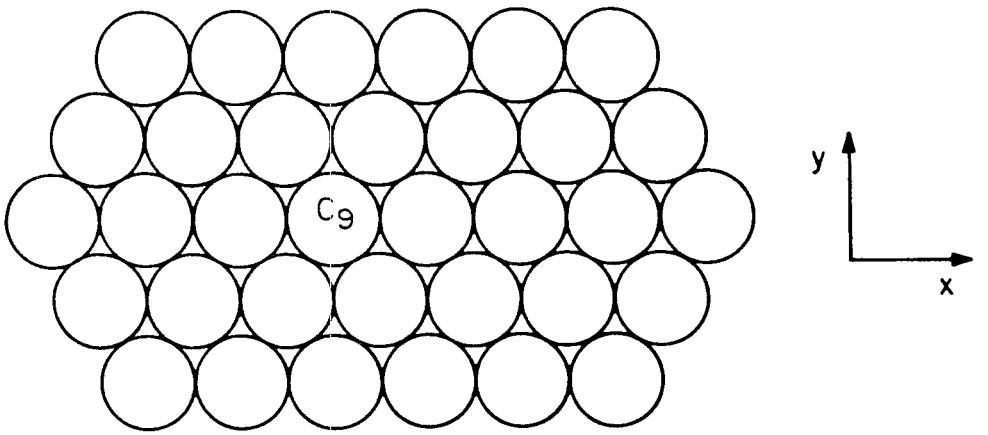

Figure 2

CHAPTER 1

Surface Reaction Dynamics via Temperature Modulation: Applications to the Oxidation of Carbon Monoxide on the Pt(110)-(1x2) Surface

[The text of Chapter 1 consists of an article coauthored with W. H. Weinberg, which has appeared in *Physical Review Letters* **55**, 2017 (1985).]

Surface Reaction Dynamics via Temperature Modulation: Applications to the Oxidation of Carbon Monoxide on the Pt(110)-(1×2) Surface

J. R. Engstrom and W. H. Weinberg

Division of Chemistry and Chemical Engineering, California Institute of Technology, Pasadena, California 91125

(Received 11 June 1985)

The novel application of a surface-temperature-modulation technique to the important class of bimolecular surface reactions is shown to lead to detailed dynamical information in a direct fashion. Knowledge of the adlayer composition or structure is not required for an evaluation of the activation energy. The activation barrier for the reaction $CO(a)+O(a)\rightarrow CO_2(g)$ on the Pt(110) surface is found to decrease precipitously from a value of 22 kcal-mol^{-1} at low coverages to a value of approximately 8 kcal-mol^{-1} in the presence of high coverages of oxygen adatoms.

PACS numbers: 68.40.+e, 82.65.Jv

The study of chemical reaction dynamics on solid surfaces is of fundamental scientific and technological importance. Modulated molecular-beam reactive scattering (MMBRS) has proven to be a powerful technique for the investigation of linear surface processes, e.g., unimolecular reactions.[1,2] However, substantial difficulties arise in the study of nonlinear processes such as bimolecular reactions and/or surface reactions described by coverage-dependent rate coefficients. It is demonstrated here that the use of a surface-temperature-modulation technique leads to detailed energetic information in a direct fashion, independent of the presence of nonlinear effects.

With MMBRS, an analysis of the measured phase response, $\phi(\omega)$, as a function of the modulation frequency, ω, is utilized to obtain reaction rate coefficients.[1] For example, consider the simple case of adsorption and desorption described by the mass balance, $d\theta(t)/dt = SF(t) - k_d(\theta)\theta(t)$, where $\theta(t)$ is the fractional coverage, S is the (constant) probability of adsorption, $F(t)$ is the incident flux of reactant molecules, and $k_d(\theta)$ is the coverage-dependent desorption rate coefficient. The generally nonlinear response of this system can be linearized experimentally about the steady state,[3] and an analysis shows that the phase response is given by $\phi(\omega) = -\tan^{-1}(\omega/k_d')$, where $k_d' = k_{d,s} + \theta_s(\partial k_d/\partial\theta)_s$, the subscript s referring to the values occurring at the steady state. Clearly, the *apparent* rate coefficient (k_d') is equivalent to the *true* rate coefficient ($k_{d,s}$) *only* at very low coverages ($\theta_s \ll 1$) or in the absence of coverage-dependent rate parameters [$(\partial k_d/\partial\theta)_s \cong 0$]. Furthermore, if the activation energy is to be evaluated, these restrictions must be satisfied for a range of temperatures sufficient for the construction of an Arrhenius plot (typically $\gtrsim 50$ K). Alternatively, the reactant pressure and surface temperature can be varied to maintain the coverage constant, but this requires *independent* knowledge of the coverage, often difficult to obtain at the steady state. Obviously, these ideas apply also to bimolecular reactions with the *additional* complications that the pseudo-first-order reaction rate coefficient will contain the implicit coverage dependence (i.e., reaction "order") of the other reactant in addition to any coverage-dependent effects of the other reactant on the rate coefficient itself.

These nonlinear effects can be circumvented by the use of surface-temperature modulation. Whereas similar difficulties exist in the interpretation of *phase* response data obtained via surface-temperature modulation, analysis of the *amplitude* response is direct and results in information unique to this technique. In particular, we shall demonstrate below that under appropriate reaction conditions and by varying the modulation frequency, the magnitude of the amplitude response will reflect the energetics of a *single elementary reaction*.

In general, linearization methods are required for temperature perturbation techniques,[4,5] e.g., due to nonlinear rate expressions of the form $k(\theta(t), T(t))\theta(t)$. Our technique employs the use of linearized mass-balance equations for the relevant adsorbed species, coupled with the use of transform techniques. The linearized mass-balance equations may be written as

$$d\boldsymbol{\theta}'(t)/dt = -\mathbf{A}\boldsymbol{\theta}'(t) - \mathbf{B}T'(t), \tag{1}$$

where $\boldsymbol{\theta}'(t)$ is a column vector of which the component $\theta_i'(t) = \theta_i(t) - \theta_{i,s}$ is the deviation of the fractional surface coverage of species "i" from the steady-state value (subscript s), and $T'(t) = T(t) - T_s$ is the corresponding deviation of the surface temperature. The componets of the square matrix $\mathbf{A}$ (column vector $\mathbf{B}$), with the coefficients a_{ij} (b_i), represent combinations of the appropriate partial derivatives of the rate expressions (i.e., adsorption, desorption, and surface reaction) which define the surface mass balances. These partial derivatives are taken with respect to coverage (temperature) and evaluated at the steady state. Taking the Laplace transform of Eq. (1), we have

$$\boldsymbol{\theta}'(p) = -(\mathbf{A}+p\mathbf{I})^{-1}\mathbf{B}T'(p) = \mathbf{H}(p)T'(p), \tag{2}$$

where p is the (complex) transform variable, I is the identity matrix, and $\mathbf{H}(p) = -(\mathbf{A}+p\mathbf{I})^{-1}\mathbf{B}$. For a

© 1985 The American Physical Society

system involving only two adsorbed species, we find $H_i(p) = -b_i(p-z_i)/[(p-P_1)(p-P_2)]$, where $P_{1,2} = [-\mathrm{tr}\mathbf{A} \pm (\mathrm{tr}\mathbf{A}^2 - 4|\mathbf{A}|)^{1/2}]/2$ [poles of $H_i(p)$], and $z_i = (a_{ij}b_j - a_{jj}b_i)/b_i$ [zero of $H_i(p)$] where $(i,j) = (1,2)$ and $(2,1)$.

We now consider an explicit mass balance on the gas-phase-product species that is formed by a surface reaction between two different adsorbed reactants and which desorbs "immediately," i.e., reaction-limited desorption. Effects due to momentary trapping of the product, not important here, are considered elsewhere.[6] For a continuously pumped system,

$$dN_3/dt = N_s x(\theta_1,\theta_2) k_r(\theta_1,\theta_2,T) - (N_3/\tau), \quad (3)$$

where

$$k_r(\theta_1,\theta_2,T) = n_s k_r^{(2)}(\theta_1,\theta_2)\exp[-E_r(\theta_1,\theta_2)/k_B T]$$

is a coverage-dependent reaction rate coefficient describing the elementary bimolecular surface reaction, $x(\theta_1,\theta_2)$ represents the implicit coverage dependence of the surface reaction [a simple case being $x(\theta_1,\theta_2) = \theta_1\theta_2$], N_s (n_s) is the number (concentration) of surface sites, τ is the pumping time constant of the reactor, and N_3 is the number of reaction-product molecules in the gas phase. If we linearize Eq. (3) about $\theta_{i,s}$ and T_s, take the Laplace transform, and combine the result with Eq. (2), we find

$$(\tau p + 1)N_3^*(p) = \epsilon_r G(p) T^*(p), \quad (4)$$

where

$$G(p) = 1 + \boldsymbol{\chi}\cdot\mathbf{H}(p)/b_r, \quad N_3^*(p) = [N_3(p)/N_{3,s}] - 1,$$

$\epsilon_r = (E_r/k_B T)_s$ is the dimensionless activation energy of the surface reaction, $\boldsymbol{\chi}$ is a column vector with components $\chi_j = [\partial(k_r x)/\partial\theta_j]_s$, $T^*(p) = T'(p)/T_s$, and $b_r = (\epsilon_r k_r x/T)_s$.

The limiting forms of the system transfer function, $\epsilon_r G(p)$, in the low- and high-frequency ($p = i\omega$) limits are of special importance. [Refer to the expression for $H_i(p)$ below Eq. (2).] In the limit of low frequencies, the transfer function will approach a constant value that represents the dimensionless *apparent* activation energy of the overall reaction, i.e., the value that is obtained by plotting the overall rate of reaction versus the reciprocal temperature. In the limit of high frequencies, the transfer function will also approach a constant value that is given by the dimensionless activation energy of the *elementary surface reaction* between the two adsorbed species (i.e., ϵ_r). In general, the approach to this high-frequency limit is governed (scaled) by the magnitude of the poles of the adsorbate transfer functions, $H_i(p)$ [i.e., P_1 and P_2].

A useful approximate form for the system transfer function can be obtained if we consider a reaction system in which the reaction probability upon adsorption of both reactants is high (i.e., desorption rates much smaller than reaction rate). If the adsorption reactions are essentially unactivated, the components of the vector $\mathbf{B}$ are approximated well by the corresponding surface reaction term, i.e., $b_i \cong b_r$. This also implies that contributions to the components of the matrix $\mathbf{A}$ due to the desorption rate expressions will be small with respect to those due to the surface reaction rate expression (by definition χ_j). Consequently, we separate the matrix $\mathbf{A}$ into two parts given by $\mathbf{A} = \mathbf{U}\boldsymbol{\chi} + \alpha$ where $\mathbf{U}$ is a unit matrix (all $u_{ij} = 1$), and the components of the matrix α, α_{ij}, embody combinations of partial derivative terms of the adsorption and desorption rate expressions. If either (i) $\chi_k, \chi_l >> $ all α_{ij} or (ii) $\chi_k >> \chi_l$, all α_{ij} where $k \neq l$, it can be shown[7] that the system transfer function, $\epsilon_r G(p)$, is well approximated by

$$\epsilon_r G(p) \cong \epsilon_r/[1 + (\nu_r'/p)], \quad (5)$$

where $\nu_r' = \mathrm{tr}\mathbf{A} \cong \chi_1 + \chi_2$. In general, this approximation is excellent for $p \gtrsim \nu_r'$. In addition, if $x(\theta_1,\theta_2) = \theta_1\theta_2$, and if $k_r(\theta_1,\theta_2,T)$ is only weakly coverage dependent [or if the rate parameters $(k_r^{(2)}, E_r)$ exhibit compensatory behavior], ν_r' contains information concerning the elementary surface reaction, viz. $\nu_r' \cong [(\theta_1+\theta_2)k_r]_s$. Finally, if the approximations inherent in the derivation of Eq. (5) are satisfied, the observed apparent activation energy, $E_r G(0)$, will be nearly zero with respect to the actual activation energy of the surface reaction, E_r [i.e., $|G(0)| << 1$]. Thus, experimental observations of both high reaction probabilities and low apparent activation energies (relative to E_r) virtually assure the applicability of Eq. (5).

The experimental measurements concerning the CO oxidation reaction on the Pt(110) surface were performed in an ion-pumped, stainless-steel, ultrahigh-vacuum bell jar equipped with a multicapillary directional beam doser which permits careful control of reactant partial pressures. The reaction product is detected mass spectrometrically, and the temperature is measured by a thermocouple spot welded on the back of the crystal. Accurate temperature control is maintained by the use of an optimal control scheme, described elsewhere,[8] which utilizes a laboratory microcomputer as the control element. For each frequency of oscillation, data are collected and summed into a periodic array, increasing the signal-to-noise ratio. Once collected, the data are analyzed utilizing standard digital Fourier-transform techniques. The pumping time constant can be obtained by imposing a step-function change in the rate of reaction.[6] Distortion of the input (temperature) or output (mass spectrometer ion current) wave forms by the measurement electronics was found to be negligible for the frequency range of interest (0.01–1.0 Hz).

In an analysis of the experimental data, it is useful to examine the conditions for which the simple approximate form of $G(p)$, given by Eq. (5), can be employed. For the experimental conditions studied here the desorption rate of oxygen is negligible,[9] and a

minimum value of the probability of reaction of CO can be calculated by utilizing the probability of adsorption on the clean surface[10] and the measured rate of reaction. For the data that appear below, the reaction probability of adsorbed CO was calculated to be $\gtrsim 0.9$. Thus, the approximation $b_i \cong b_r$ is excellent. Regarding the components of the matrix α, it can be shown easily that the surface reaction terms (χ_{CO}, χ_O) will dominate adsorption (and desorption as discussed above) terms for low coverages of both species [i.e., case (i) above]. Alternatively, if the oxygen coverage is relatively high and the CO coverage is low, the surface reaction term with respect to CO (χ_{CO}) will dominate all terms [i.e., case (ii) above], since the probability of adsorption of CO is only weakly dependent on oxygen coverage.[9] Finally, we note that high coverages of *both* reactants are not observed at *steady state* under similar experimental conditions,[11] whereas high coverages of CO result in large positive apparent activation energies ($\gtrsim 20$ kcal-mol^{-1}).[9] Thus, the observation of low apparent activation energies can be used to confirm the approximations inherent in the derivation of Eq. (5). For the data that appear below, the observed *apparent* activation energies are such that $|G(0)| \lesssim 0.05$.

Amplitude and phase response data representing the system transfer function, $\epsilon_r G(p)$, for a particular set of reaction conditions are shown in Fig. 1. The linearity of the response was verified by varying the amplitude of the temperature forcing function from less than one-half to twice the "standard" amplitude used, namely 0.3–2.0 K, depending on the frequency.[6] As a result of the limited frequency bandwidth (0.01–1.0 Hz) of the temperature forcing functions used, reaction conditions (P_{O_2}, P_{CO}, and T_s) were chosen such that the restrictions placed on the use of Eq. (5) were met. Curves representing Eq. (5) with the parameters ϵ_r and ν_r' determined by a least-squares functional minimization routine are also displayed in Fig. 1. The functional agreement of both the amplitude and phase is excellent, supporting the use of Eq. (5) for these reaction conditions. An analysis of the data shown in Fig. 1 leads to a *direct determination* of the activation energy of the elementary surface reaction via the parameter ϵ_r (i.e., $E_r = k_B T_s \epsilon_r$). These activation energies are approximately 21 and 17.5 kcal-mol^{-1} at 375 and 400 K. With use of the parameter ν_r' and calculated values for the adsorbate concentrations (see below), we evaluate corresponding preexponential factors ($k_r^{(2)}$) of 3×10^{-3} and 3×10^{-5} cm^2-s^{-1}.

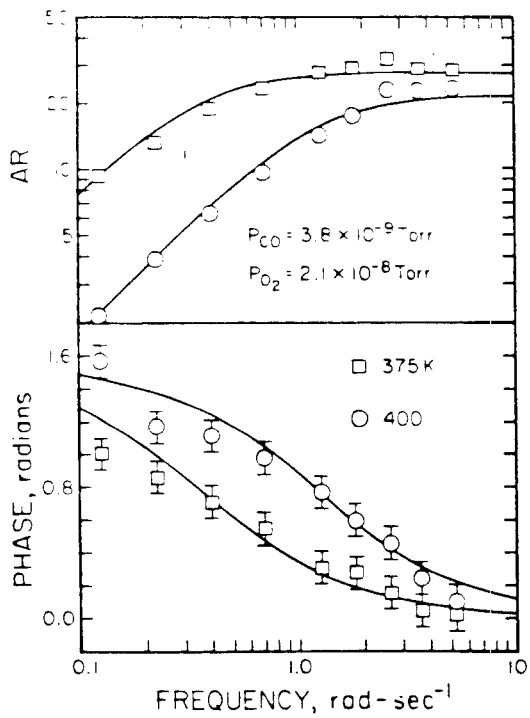

FIG. 1. Experimental data representing the system transfer function, $(\tau p + 1)N_3^+(p)/T^+(p) = \epsilon_r G(p)$, shown as a function of frequency in terms of the amplitude ratio (AR) and phase response. The solid lines represent least-squares fits to Eq. (5), i.e., $AR(\omega) = \epsilon_r/[(\nu_r'/\omega)^2 + 1]^{1/2}$ and $\phi(\omega) = \tan^{-1}(\nu_r'/\omega)$.

To determine the effect of the composition of the adlayer on the dynamics of the surface reaction, experiments were carried out at a constant CO partial pressure and a varying oxygen partial pressure. The activation energy of the surface reaction was evaluated for a variety of conditions, and the results are displayed in Fig. 2(a).[12] For small values of $P_{O_2}/P_{CO} \lesssim 3$, the activation energy is virtually independent of the adlayer composition, of which the latter is dictated by the surface temperature. The measured value of approximately 22 kcal-mol^{-1} is in excellent agreement with

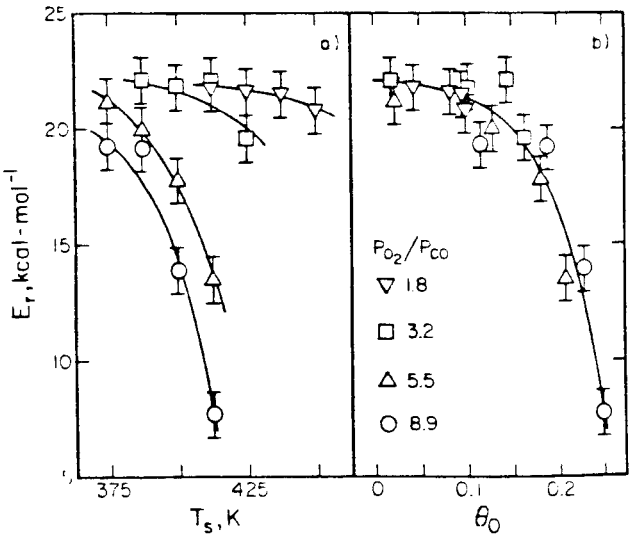

FIG. 2. Activation energy for the surface reaction, CO(a) + O(a) — CO_2(g), as a function of (a) the surface temperature, and (b) the calculated fractional coverage of oxygen adatoms, θ_O. $P_{CO} = 3.8\times10^{-9}$ Torr.

previous results in the low-coverage limit on other platinum surfaces.[13,14] [Note that the *difference* between the activation energies for the desorption and the oxidation of CO was measured in this previous work to obtain the low-coverage value.[13,14]] However, for larger values of P_{O_2}/P_{CO}, > 3, the activation energy decreases markedly as the surface temperature is increased.

The most reasonable explanation for the observed variation in the activation energy is the following. High coverages of oxygen adatoms have been observed to have a profound effect on the activation barrier for this reaction. Values between 10 and 12 kcal mol^{-1} have been observed in the presence of high coverages of oxygen adatoms.[13,15] With use of our reaction rate measurements and previously measured rates of adsorption and desorption, the details of which are given elsewhere,[6] the adsorbate concentrations were calculated for the reaction conditions of Fig. 2(a). There is a decrease in CO coverage and a concomitant increase in oxygen coverage as the temperature increases, in agreement with experimental measurements.[11,16] As may be seen in Fig. 2(b), the variation of the activation energy of the surface reaction correlates well with the coverage of oxygen adatoms. Furthermore, the variation of the activation energy with oxygen coverage is obviously quite nonlinear. Previous work with MMBRS[13] could not have investigated this behavior. Because of the difficulties discussed above, MMBRS measurements are restricted to extremes in the composition of the adlayer (either low coverages of both reactants or high oxygen adatom coverages).[13] The precipitous drop in the activation energy above $\theta_O \cong 0.15$ suggests that configurational effects (e.g., *locally* higher oxygen adatom concentrations) are important. In this picture, for low coverages of oxygen, $\theta_O \lesssim 0.15$, the adsorbed CO reacts with nearly independent (isolated) oxygen adatoms. However, for $\theta_O > 0.15$ the adsorbed CO reacts in regions of higher local oxygen adatom concentration (incipient island nucleation). In these regions of the surface, the binding energy of the CO is decreased, which leads directly to a decrease in the activation energy for the production of CO_2.

To summarize, the formalism underlying a novel, relatively simple, and experimentally inexpensive temperature-modulation scheme has been described which allows a direct determination of the activation energy of elementary surface reactions. The practical value of the formalism has been illustrated by analyzing new experimental data concerning the oxidation of CO on the Pt(110) surface. The technique is by no means limited to bimolecular surface reactions, as discussed in detail elsewhere,[6] but this important class of reactions provides a rigorous test of the technique due to the inherent nonlinearity. At present, the major experimental limitation of the technique is the limited-frequency bandwidth. However, the present limit of observable frequencies should be able to be extended by several orders of magnitude by a combination of line-of-sight, differentially pumped mass-spectrometric detection and the use of chopped laser techniques to provide the modulation in temperature.

This work was supported by the National Science Foundation under Grant No. CHE-8206487.

[1]R. H. Jones, D. R. Olander, W. J. Siekhaus, and J. A. Schwarz, J. Vacuum Sci. Technol. **9**, 1429 (1972).

[2]M. P. D'Evelyn and R. J. Madix, Surf. Sci. Rep. **3**, 413 (1984).

[3]J. A. Schwarz and R. J. Madix, Surf. Sci. **46**, 317 (1974).

[4]M. Eigen, Discuss. Faraday Soc. **17**, 194 (1954).

[5]R. W. Arbesman and Y. G. Kim, Chem. Eng. Sci. **24**, 1627 (1969).

[6]J. R. Engstrom and W. H. Weinberg, to be published.

[7]Clearly, for both cases (i) and (ii), $\mathrm{tr}\mathbf{A}^2 >> |\mathbf{A}|$. Thus, $P_1 \cong -\mathrm{tr}\mathbf{A}$, $P_2/P_1 \cong |\mathbf{A}|/\mathrm{tr}\mathbf{A}^2 << 1$, and $z_i/P_1 \cong (\alpha_{\parallel} - \alpha_{\perp})/\mathrm{tr}\mathbf{A} << 1$.

[8]J. R. Engstrom and W. H. Wienberg, Rev. Sci. Instrum. **55**, 404 (1984).

[9]T. Engel and G. Ertl, Advan. Catal. **28**, 1 (1979).

[10]J. A. Fair and R. J. Madix, J. Chem. Phys. **73**, 3480 (1980).

[11]T. Matsushima, D. B. Almy, and J. M. White, Surf. Sci. **67**, 89 (1977); A. Golchet and J. M. White, J. Catal. **53**, 266 (1978).

[12]The preexponential factors were also evaluated for these reaction conditions and are given and discussed in detail elsewhere (Ref. 6).

[13]C. T. Campbell, G. Ertl, H. Kuipers, and J. Segner, J. Chem. Phys. **73**, 5862 (1980).

[14]N. Pacia, A. Cassuto, A. Pentenero, and B. Weber, J. Catal. **41**, 455 (1976).

[15]J. A. Fair and R. J. Madix, J. Chem. Phys. **73**, 3486 (1980). A subsequent estimate of the oxygen coverage present during the experiment was given as $\theta_O = 0.23$ (Ref. 2).

[16]P. A. Zhdan, G. K. Boreskov, W. F. Egelhoff, and W. H. Weinberg, Surf. Sci. **61**, 377 (1976).

CHAPTER 2

Analysis of Gas-Surface Reactions by Surface Temperature Modulation: I. Theoretical Formulation

[The text of Chapter 2 consists of an article coauthored with W. H. Weinberg, which has been submitted to *The Journal of Chemical Physics.*]

Abstract

The theoretical formulation of a frequency response technique, based on surface temperature modulation, for the study of surface reaction dynamics is described in detail. The formalism is developed for analyzing adsorption, desorption, and both unimolecular and bimolecular surface reactions. The evaluation of the activation barriers for the elementary surface reactions is straightforward even in the presence of strong nonlinearities and requires no knowledge of the composition or configuration (i.e., structure) of the adlayer. This capability provides a distinct advantage over competitive techniques such as modulated molecular beam reactive scattering. Although the evaluation of the preexponential factors of the rate coefficients is complicated by the presence of nonlinear effects (e.g., coverage-dependent rate parameters or a bimolecular reaction), in many cases the preexponential factors may also be evaluated in a straightforward manner.

I. Introduction

The study of transient phenomena occurring in chemically reacting systems often provides much additional information compared to measurements that are restricted to a steady state. Eigen originally proposed the application of perturbation techniques to the study of the kinetics of chemical reactions occurring in solution (**1**). Similar methods have been applied to the study of gas-surface reaction dynamics, a well-known example being the analysis of thermal desorption spectra to obtain the kinetic parameters that characterize the desorption reaction (**2**). Other relatively simple techniques involve measurements of the response of the gas phase reaction product signal to step or pulse changes in one of the state variables that specify the rate of reaction (**3**). More recently, *in situ* techniques involving electronic (**4,5**) and vibrational (**6,7**) spectroscopies have been employed to measure directly the time evolution of *adsorbed* surface species. Resolution approaching the ms time scale has been achieved in each case. Techniques that monitor the structure of the surface are also being applied in a time-resolved fashion (**8**).

To date, however, perhaps the most powerful transient technique developed for the investigation of chemical reaction dynamics on solid surfaces is modulated molecular beam reactive scattering (MMBRS) (**9,10**). It has proved to be an especially powerful technique for the investigation of *linear* surface processes such as unimolecular reactions, molecular desorption, and surface or bulk diffusion. For these simple cases, an analysis of the appropriate transfer function can provide kinetic parameters directly. However, substantial difficulties arise in the study of *nonlinear* surface processes, such as bimolecular reactions and/or reactions characterized by coverage-dependent rate coefficients (**11**). In general, two approaches can be taken to attempt to extend the applicability of MMBRS to the study of nonlinear surface processes: (i) an experimental linearization of the system response, and (ii) a complete, rigorous nonlinear analysis. Unfortunately, serious difficulties exist with both approaches.

The experimental linearization of the system response is realizable via MMBRS techniques by the superposition of a (large) constant reactant flux on the modulated reactant flux (**12**). With this approach, an analysis of the measured phase response $\phi(\omega)$ as a function of the modulation frequency ω can be utilized to obtain *apparent* reaction rate coefficients. For example, consider the *simple* nonlinear

case of adsorption and desorption described by the mass balance

$$d\theta(t)/dt = SF(t) - k_d[\theta(t),T]\theta(t) ,$$

where $\theta(t)$ is the fractional surface coverage, S is the (constant) probability of adsorption, $F(t)$ is the incident flux of reactant molecules, $k_d[\theta(t),T]$ is the *coverage-dependent* desorption rate coefficient, and T is the surface temperature. The phase response for the *linearized* system is given by

$$\phi(\omega) = -\tan^{-1}(\omega/\nu_d) ,$$

and

$$\nu_d = k_{d,s}[1 + \theta_s(\partial \ln k_d/\partial\theta)_s] ,$$

where ν_d is the *apparent* rate coefficient, $k_{d,s} \equiv k_d(\theta_s,T_s)$ is the *true* rate coefficient, and the subscript s refers to the values occurring at the steady state.

We see that the apparent rate coefficient is equivalent to the true rate coefficient *only* at very low coverages ($\theta_s << 1$) or in the absence of coverage-dependent rate parameters [$(\partial \ln k_d/\partial\theta)_s \sim 0$]. Furthermore, if the activation energy is to be evaluated, these restrictions must be satisfied for a range of temperatures sufficient for the construction of an Arrhenius plot (typically $\geq$ 50 K). Alternatively, the reactant pressure and surface temperature can be varied to maintain a constant coverage, but this requires *independent* knowledge of the coverage, often difficult to obtain at the steady state. Since $\nu_d \neq k_{d,s}$, one cannot determine the fractional coverage occurring at the steady-state (θ_s) by utilizing a mass balance on the adsorbate (in this case $SF_s = k_{d,s}\theta_s$) coupled with knowledge of the *apparent* rate coefficient. Rather, an independent technique must be employed to *measure* this steady-state fractional coverage. Obviously, these ideas apply also to other nonlinear reaction systems involving, for example, coverage-dependent adsorption, and second-order surface reactions.

The second approach to applying MMBRS to the study of nonlinear surface reaction systems consists of a rigorous nonlinear analysis of the waveform(s) of the reaction product(s). The fundamental assumption that must be made in this analysis is that one can write rate expressions that are sufficiently accurate to describe the mass balances for the adsorbed species. Whereas one can usually deduce the implicit coverage dependence, or "order", of an elementary surface reaction, the functional dependence of the kinetic rate parameters on the fractional coverage(s) cannot, in general, be deduced *a priori*. For

example, we have discovered that the activation energy [and preexponential factor, see Part II (13)] of the elementary reaction CO(a) + O(a) $\rightarrow$ CO_2(g) on the Pt(110)-(1x2) surface depends sensitively on the fractional coverage of oxygen adatoms, the functional dependence being quite nonlinear (**11**). In this case, the functional form sufficiently accurate to describe the coverage dependence would be, of necessity, very complex [e.g., $E_r(\theta)$ would be a cubic in θ]. Obviously, as the number of rate parameters describing the surface mass balances increases, the accuracy *and* uniqueness of the *set* of parameters determined via a nonlinear analysis become highly questionable.

These difficulties associated with nonlinearities can be circumvented by employing *surface temperature* modulation (**11,13,14**). The combined use of *both* surface temperature modulation and linearization methods permits a direct and *quantitative* analysis of the overall reaction energetics. Furthermore, under the appropriate experimental conditions, the frequency of modulation can be varied such that the measured response (in this case the *amplitude ratio*) will reflect the energetics of a *single elementary reaction*. Although, as with linearized MMBRS techniques, one can also obtain apparent reaction rate coefficients via surface temperature modulation, these coefficients are *not* used to evaluate the activation energy; i.e., *surface temperature modulation does make use of Arrhenius plots of apparent rate coefficients versus the reciprocal temperature to evaluate activation energies*. Rather, the magnitude of the amplitude ratio can be used to calculate directly the activation energy of a single elementary reaction utilizing data from only a *single set* of experimental conditions (i.e., reactant partial pressures and surface temperature). In addition, in principle, the analysis is not restricted to any particular adsorbate coverage regime; i.e., a wide range of reactant and product concentrations may be investigated. For the study of nonlinear reaction systems, these capabilities of surface temperature modulated mass spectrometry (STMMS) offer distinct advantages over studies utilizing MMBRS.

II. Theory

The rate of any surface reaction can be specified by the partial pressures of the reactant(s) and product(s), and the temperature of the surface. Thus, the rate of reaction and the composition of the adlayer (adsorbate coverages) can be considered as dependent variables (**16**). For any reaction, one can formulate mass balances for the relevant adsorbed species, which are given by rate expressions

describing adsorption, desorption and the surface reaction(s). (We do not consider explicitly here surface and bulk diffusion.) This set of coupled differential equations describes the surface reaction system. Linear frequency response techniques seek to identify the system parameters and/or the system transfer function by evaluating the response of a selected output state variable with respect to a periodically varied input state variable, or forcing function (1,9). For example, MMBRS utilizes a modulation in the reactant flux, while we shall consider here a modulation in the surface temperature (18). If we assume that the partial pressures of the reactants are constant, the mass balance equations are functions of both temperature and surface coverages, and they are in general nonlinear. However, any equation can be linearized about steady-state values, the validity of such a construction requiring experimental verification. This linearized set of simultaneous differential equations can then be combined with a mass balance (linearized also) on the selected gas phase reaction product to produce the relevant system transfer function. Thus, the system transfer function, determined experimentally by a comparison of the relevant input (surface temperature) and output [product partial pressure(s)] signals, can be used to evaluate the kinetic parameters.

We shall consider three general classes of surface reactions, namely: (1) adsorption-desorption equilibria (one-component system, where component implies surface species); (2) unimolecular surface reactions (two-component system); and (3) bimolecular surface reactions (three-component system). Since we are interested in *linearized* systems, we shall be able to obtain the general of the system transfer function without invoking any assumptions concerning the specific form of the rate expressions contained in the mass balance equations; i.e., the detailed dynamical information is contained in the constant coefficients of the linearized forms of the governing mass balance equations.

1. Adsorption-Desorption Equilibria

It is useful to consider two different cases explicitly, namely: (i) direct adsorption-desorption, and (ii) precursor-mediated adsorption-desorption (19,20).

(i) Direct Adsorption-Desorption

We shall consider reactions of the type

$$A(g) \underset{\rightarrow}{\overset{\leftarrow}{}} A(a) \quad \text{or} \quad A_2(g) \underset{\rightarrow}{\overset{\leftarrow}{}} 2A(a) ,$$

where in both cases there is only one surface species. A linearized mass balance on the surface species is given by

$$d\theta'(t)/dt = -a\theta'(t) - bT'(t) , \tag{1}$$

where $\theta'(t) \equiv \theta(t) - \theta_s$ is the *deviation* of the fractional surface coverage from the steady-state value (subscript s), and $T'(t) \equiv T(t) - T_s$ is the corresponding deviation of the surface temperature. The coefficient "a" (which has units of frequency) is composed of the appropriate combination of partial derivatives of the adsorption and desorption rate expressions, taken with respect to the fractional coverage and evaluated at the steady-state (e.g., if $d\theta/dt = r_a - r_d$, then $a \equiv -[\partial(r_a - r_d)/\partial\theta]_s$). Thus, "a" represents the apparent first-order rate coefficient of the linearized system, which may or may not be related simply to a (or a combination of) true rate coefficient(s) **(21)**. Similarly, the coefficient "b" is composed of appropriate combinations of partial derivatives with respect to temperature. Therefore, "b" represents the sensitivity of the adsorbate coverage to changes in the surface temperature, and, in general, its value is proportional to a (or a combination of) dimensionless activation energy(s) E/k_BT (22).

We consider now a mass balance on the reactant (in this case, identical to the product) in the gas phase. For a continuously pumped system in which the reactant is introduced at a constant rate, we have

$$dN_g'(t)/dt = -N_a d\theta'(t)/dt - N_g'(t)/\tau , \tag{2}$$

where $N_g'(t) \equiv N_g(t) - N_{g,s}$ is the deviation of the number of reactant molecules in the gas phase from the steady-state value, N_a is the number of adsites, and τ is the pumping time constant of the reactor. Taking the Laplace transforms of Eqs. (1) and (2) and combining, we obtain

$$(\tau p + 1)N_g^\dagger(p) = \left[\frac{N_a\tau}{N_{g,s}}\right]\left[\frac{bT_s(p/a)}{(p/a) + 1}\right]T^\dagger(p) , \tag{3}$$

where $N_g^\dagger(p) \equiv N_g'(p)/N_{g,s}$ and $T^\dagger(p) \equiv T'(p)/T_s$ with both functions being dimensionless, and p is the (complex) transform variable, which has units of frequency.

A practical expression for the term $N_a\tau/N_{g,s}$ can be obtained if we consider, for example, an experimental system in which the reactant is introduced via a directional doser resulting in a high beam-to-background pressure ratio (e.g., a multicapillary array or a conventional molecular beam

source). In this case, the rate of adsorption at steady state is equal to a constant fraction of the rate of introduction of the reactant. This fraction, which can be measured experimentally, is given by the quantity $S_s\eta$, where S_s is the probability of adsorption of the reactant at steady state [in general, $S = S(\theta,T)$], and η is the fraction of reactant molecules in the "beam" that strikes the crystal. Obviously, the value of $S_s\eta$ will lie between zero and unity. Since the quantity $N_{g,s}/\tau$ is equal to the rate of introduction of the reactant, Eq. (3) can be written as

$$(\tau p + 1)N_g^{\dagger} = S_s\eta \left[\frac{(p/a)}{(p/a) + 1}\right](bT_s/r_s)T^{\dagger}(p) , \tag{4}$$

where r_s is the rate of adsorption (and desorption) at steady state in units of $site^{-1}$–s^{-1}. The presence of the bothersome complicating factor, $S_s\eta$, is due to the fact that the "reactant" and the "product" are identical in this case.

We now consider specific forms for the expressions describing the rates of adsorption and desorption. For the rate of adsorption, we assume

$$r_a = (F/n_a)S(\theta,T) \equiv (F/n_a)S_0(1 - m\theta)^n\exp[-E_a(\theta)/k_BT_g] , \tag{5}$$

where F is the flux of reactant molecules at the surface, n_a is the concentration of adsites, $S(\theta,T) \equiv S_0(1 - m\theta)^n\exp[-E_a(\theta)/k_BT_g]$ is a coverage- and temperature-dependent probability of adsorption [e.g., m = 0 for coverage-independent adsorption, and m = 1 for nth-order Langmuir adsorption kinetics], and $E_a(\theta)$ is a coverage-dependent activation energy of adsorption. In the case of "direct" adsorption considered here, the *gas* temperature T_g should be used in the Boltzmann factor of Eq. (5), as shown. For the rate of desorption, we assume

$$r_d = \theta^n k_d(\theta,T) \equiv \theta^n n_a^{n-1} k_d^{(n)}(\theta)\exp[-E_d(\theta)/k_BT] , \tag{6}$$

where $k_d(\theta,T) \equiv n_a^{n-1}k_d^{(n)}(\theta)\exp[-E_d(\theta)/k_BT]$ is the nth-order desorption rate coefficient, $k_d^{(n)}(\theta)$ is the nth-order coverage-dependent preexponential factor of the desorption rate coefficient, and $E_d(\theta)$ is the coverage-dependent activation energy of desorption. Utilizing Eqs. (5) and (6) for the rates of adsorption and desorption, Eq. (4) reduces to

$$(\tau p + 1)N_g^{\dagger}(p) = S_s\eta \left[\frac{(p/\nu_d)}{(p/\nu_d) + 1}\right]\varepsilon_d T^{\dagger}(p) \equiv G(p)T^{\dagger}(p) , \tag{7}$$

where ν_d is the apparent rate coefficient given by

$$\nu_d \equiv \theta_s^{n-1} k_{d,s} \left\{ \frac{n}{(1 - m\theta_s)} + \theta_s \frac{\partial}{\partial \theta} \left[\ln(k_d^{(n)}) - \Delta\varepsilon_h \right]_s \right\}, \tag{8}$$

$\varepsilon_d \equiv (E_d/k_BT)_s$ is the dimensionless activation energy of desorption, and $\Delta\varepsilon_h = [(E_d/k_BT) - (E_a/k_BT_g)]$. Note that for the linear case of coverage-independent adsorption and first-order desorption described by coverage-independent rate parameters, the apparent and true rate coefficients become equivalent; i.e., $\nu_d = k_{d,s}$. Making the substitution $p = i\omega$ (23), the predicted frequency response of the experimentally determined parameters, the amplitude ratio (AR) and the phase difference (ϕ) of the input $[T^\dagger(p)]$ and output $[(\tau p + 1)N_g^\dagger(p)]$ functions, can be shown to be

$$AR(\omega) = |G(i\omega)| = S_s \eta \varepsilon_d [1 + (\nu_d/\omega)^2]^{-1/2}, \tag{9a}$$

and

$$\phi(\omega) \equiv \arg[G(i\omega)] = \tan^{-1}(\nu_d/\omega). \tag{9b}$$

These functional forms are displayed in Fig. 1. An analysis of experimental response data leads to a direct evaluation of the dimensionless activation energy of desorption ε_d, provided the product $S_s\eta$ is measured independently. Furthermore, if the coverage dependence of $E_a(\theta)$, $k_d^{(n)}(\theta)$ and $E_d(\theta)$ is weak and/or compensatory, or the coverage is small (i.e., $\theta_s << 1$), the preexponential factor of the desorption rate coefficient can also be evaluated via the apparent rate coefficient ν_d. However, for the cases of coverage-dependent adsorption and/or second-order desorption, the adsorbate coverage occurring at the steady state must also be known in order to evaluate the preexponential factor.

(ii) Precursor-Mediated Adsorption-Desorption

We shall consider reactions of the type

$$A(g) \underset{r_d^*}{\overset{r_a^*}{\rightleftarrows}} A^*(a) \underset{r_d}{\overset{r_a}{\rightleftarrows}} A(a),$$

where we make no assumptions concerning the molecularity of the adsorption, desorption and inter-conversion reactions [i.e., we do not exclude $A_2(g) \underset{\leftarrow}{\overset{\rightarrow}{\rightleftarrows}} A_2^*(a) \underset{\leftarrow}{\overset{\rightarrow}{\rightleftarrows}} 2A(a)$]. In this scheme, $A^*(a)$ represents the precursor state [species '2' below], and A(a) represents the chemisorbed state [species '1' below]. We do not make an explicit distinction between "intrinsic" precursor states (which exist over empty sites) and "extrinsic" precursor states (which exist over sites occupied by a chemisorbed species)

(20,24). The linearized mass balance equations on the two surface species may be written as

$$d\theta'(t)/dt = -\mathbf{A}\theta'(t) - \mathbf{B}T'(t) , \tag{10}$$

where $\theta'(t)$ and **B** are column vectors, and **A** is a (2x2) matrix. Taking the Laplace transform of Eq. (10), recognizing that **A** is nonsingular (25), and rearranging, we find

$$\theta'(p) = -(\mathbf{A} + p\mathbf{I})^{-1}\mathbf{B}T'(p) \equiv \mathbf{H}(p)T'(p) , \tag{11}$$

where **I** is the identity matrix, and $\mathbf{H}(p) \equiv -(\mathbf{A} + p\mathbf{I})^{-1}\mathbf{B}$. If the transfer functions $H_i(p)$ are expressed in terms of their zeros (z_i) and poles (P_1,P_2), then

$$H_i(p) = -b_i(p - z_i)/[(p - P_1)(p - P_2)] , \tag{12}$$

where $P_{1,2} = [-\mathrm{tr}\mathbf{A} \pm (\mathrm{tr}\mathbf{A}^2 - 4|\mathbf{A}|)^{1/2}]/2$, $z_i = (a_{ij}b_j - a_{jj}b_i)/b_i$, and (i,j) = (1,2) and (2,1). (Note that $P_1P_2 = |\mathbf{A}|$ and $P_1 + P_2 = -\mathrm{tr}\mathbf{A}$.)

A mass balance on the reactant (in this case, identical to the product) in the gas phase is given by

$$dN_g'(t)/dt = -N_a d(\theta_1' + \theta_2')/dt - N_g'(t)/\tau . \tag{13}$$

Taking the Laplace transform of Eq. (13) and combining the result with Eq. (11) yields

$$(\tau p + 1)N_g^{\dagger}(p) = -(N_a\tau/N_{g,s})p[\mathbf{U}\cdot\mathbf{H}(p)T_s]T^{\dagger}(p) , \tag{14}$$

where **U** is a unit column vector.

We now consider specific expressions for the rates of adsorption, desorption and interconversion given by the following: $r_a = \theta_2 k_a(\theta_1,T)S_1(\theta_1)$, where $k_a = k_a^{(1)}\exp[-E_a(\theta_1)/k_BT]$ and $S_1(\theta_1)$ represents the intrinsic coverage dependence of the chemisorption probability [e.g., $S_1(\theta_1) = S_{1,0}(1 - \theta_1)^n$]; $r_d = \theta_1^n k_d(\theta_1,T)f(\theta_2)$, where k_d is identical to the expression utilized in Eq. (6) and $f(\theta_2)$ accounts for the occupancy of the precursor state [e.g., $f(\theta_2) = (1 - \theta_2)$]; $r_d^* = \theta_2 k_d^*(T)$, where $k_d^*(T) = k_d^{(1)*}\exp[-E_d^*/k_BT]$; and $r_a^* = (F/n_s)S^*$ (i.e., a constant probability of unactivated adsorption into the precursor state). Note that we have assumed that the rates of both adsorption into and desorption from the precursor state are independent of the coverage of the chemisorbed state (26). In addition, we assume that the precursor state is in thermal equilibrium with the surface; i.e., the appropriate temperature in the rate expressions for r_a and r_d^* is the *surface* temperature. If $f(\theta_2) \cong 1$ (i.e., $\theta_2 << 1$), then $a_{12} \cong -(k_aS_1)_s$ and $a_{22} \cong k_{d,s}^* + (k_aS_1)_s$. Thus, the quantity $\alpha \equiv -a_{12}/a_{22}$ represents the probability that a molecule in the precursor state will be chemisorbed. The average residence time of a molecule in the precursor state is given by

$\tau_2 = 1/a_{22}$, whereas the corresponding residence time for the chemisorbed state is $\tau_1 = 1/a_1$, where $a_1 \equiv [\partial(r_d - r_a)/\partial\theta_1]_s$. [Note that $a_{11} = -a_{21} = a_1$, since $\partial(r_a^* - r_d^*)/\partial\theta_1 = 0$ in this case.] If the precursor state is short-lived with respect to both the chemisorbed state and the reciprocal of the modulation frequency, $a_{22} >> a_1$ and p, Eq. (14) reduces to

$$(\tau p + 1)N_g^\dagger(p) = S_s\eta \left[\frac{(p/\nu_d^*)}{(p/\nu_d^*) + 1}\right](\Delta\varepsilon_h^*)T^\dagger(p) \equiv G(p)T^\dagger(p) , \qquad (15)$$

where $S_s = S^*\alpha$, $\nu_d^* = (1 - \alpha)a_1$, and $\Delta\varepsilon_h^* = [(E_d - E_a + E_d^*)/k_BT]_s$ is the dimensionless heat of adsorption (recall that we have assumed that $E_a^* = 0$). The predicted frequency response of Eq. (15) is given by Eqs. (9a) and (9b), with the parameters ν_d and ε_d replaced by ν_d^* and $\Delta\varepsilon_h^*$. The close connection between Eqs. (15) and (7) is apparent if $S^*S_1(\theta_1)k_a(\theta_1,T)/k_d^*(T) = S(\theta,T)$ [see Eq. (5)], and $f(\theta_2) = 1$ (in this case, $a_1 = \nu_d$). The essential differences lie in the factor $1 - \alpha$ in the apparent rate coefficient $\nu_d^* = (1 - \alpha)\nu_d$ and between the quantities ε_d and $\Delta\varepsilon_h^*$. These differences may be understood when one realizes that we have assumed that desorption *must* proceed through the precursor state. Since all molecules or atoms leaving the chemisorbed state do not desorb into the gas phase (rather, a fraction α are readsorbed into the chemisorbed state), the apparent (i.e. measured) rate of desorption will be less than the rate at which molecules or atoms leave the chemisorbed state. Thus, $\nu_d^* = (1 - \alpha)\nu_d \leq \nu_d$. Likewise, the apparent activation energy of desorption is not equivalent to the activation energy associated with molecules or atoms leaving the chemisorbed state. Rather, it is equal to the total energy expenditure necessary to reach the gas phase, $E_d - E_a + E_d^*$. Since, in general, precursor states are bound weakly, i.e., $E_a, E_d^* \ll E_d$, this latter point may be of little practical consequence in the interpretation of experimental data.

2. Unimolecular Surface Reactions

We shall consider reactions of the type

$$A(g) \underset{\leftarrow}{\rightarrow} A(a) \underset{\leftarrow}{\rightarrow} B(a) \rightarrow B(g) ,$$

where we do not restrict the above reaction scheme to molecular first-order desorption reactions and nondissociative adsorption. It is instructive to consider two different cases explicitly, namely: (i) the reaction product is not trapped on the surface upon formation, but rather, it desorbs 'immediately' in a

reaction-limited fashion; and (ii) the reaction product is trapped on the surface for a significant period of time with respect to the average residence time of the reactant on the surface and the modulation period of the temperature forcing function.

(i) Unimolecular Surface Reaction in which the Product is not Trapped

If the reaction product is not trapped on the surface, we need consider only a mass balance on the reactant surface species (A, species '1'), given in linearized form by

$$d\theta_1'(t)/dt = -a_1\theta_1'(t) - b_1T'(t) , \tag{16}$$

where the definitions follow from those given in connection with Eq. (1). A mass balance on the reaction product (B, species '2') in the gas phase is given by

$$dN_2(t)/dt = N_a x(\theta_1)k_r(\theta_1,T) - N_2(t)/\tau , \tag{17}$$

where N_2 is the number of product molecules in the gas phase, $x(\theta_1)$ is the implicit coverage dependence of the surface reaction [i.e., the reaction "order", a simple case being $x(\theta_1) = \theta_1$], and $k_r(\theta_1,T) \equiv k_r^{(1)}(\theta_1)\exp[-E_r(\theta_1)/k_BT]$ is the coverage-dependent rate coefficient for the elementary, unimolecular surface reaction, $A(a) \rightarrow B(g)$. We neglect readsorption of the product and assume the surface reaction to be irreversible. Linearizing Eq. (17) about $\theta_{1,s}$ and T_s, taking the Laplace transform and combining the result with the transform of Eq. (16), we obtain

$$(\tau p + 1)N_2^\dagger(p) = \varepsilon_r\{1 + [\chi_1H_1'(p)/b_r]\}T^\dagger(p) \equiv \varepsilon_rG'(p)T^\dagger(p) . \tag{18}$$

where $N_2^\dagger(p) \equiv [N_2(p)/N_{2,s}] - 1$, $\varepsilon_r \equiv (E_r/k_BT)_s$ is the dimensionless activation energy of the unimolecular surface reaction, $\chi_1 = [\partial(xk_r)/\partial\theta_1]_s$, $H_1'(p) \equiv -b_1/(p + a_1)$, $b_r = (xk_r)_s\varepsilon_r/T_s$ and $G'(p) \equiv 1 + [\chi_1H_1'(p)/b_r]$. We see that in the limit of high frequencies ($p >> a_1$), the system transfer function $\varepsilon_rG'(p)$ will approach a constant value given by the dimensionless activation energy of the surface reaction $A(a) \rightarrow B(g)$ (i.e., ε_r).

A useful approximate form for the system transfer function $\varepsilon_rG'(p)$ can be obtained if we consider a reaction system in which the reaction probability upon adsorption is nearly unity (i.e., desorption rate of reactant << reaction rate). If the adsorption reaction is both essentially unactivated and only weakly dependent on coverage with respect to the surface reaction (in general, valid at low coverages of the reactant), then $b_1 \equiv b_r$ and $a_1 \equiv \chi_1$. In this case, the transfer function $\varepsilon_rG'(p)$ defined in Eq. (18) reduces

$$\varepsilon_r G'(p) = \varepsilon_r \frac{(p/\nu_r^{(1)})}{(p/\nu_r^{(1)}) + 1} , \tag{19}$$

where $\nu_r^{(1)} = \chi_1$. Note that this approximate transfer function is specified by two parameters $(\varepsilon_r, \nu_r^{(1)})$, whereas the exact form given by Eq. (18) is specified by three parameters [ε_r, a_1, and the product $\chi_1(b_1/b_r)$].

In certain cases, the apparent reaction rate coefficient $\nu^{(1)}$ can be used to extract useful information concerning the elementary unimolecular surface reaction. For example, if the implicit coverage dependence of the surface reaction is given by $x(\theta_1) = \theta_1$, then

$$\nu_r^{(1)} = k_{r,s}[1 + \theta_{1,s} \frac{\partial}{\partial \theta_1} (\ln k_r^{(1)} - E_r/k_B T)_s]. \tag{20}$$

If the coverage dependence of $E_r(\theta_1)$ and $k_r^{(1)}(\theta_1)$ is weak and/or compensatory or the reactant coverage is small, then the true rate coefficient is given approximately by the apparent rate coefficient $k_{r,s} \cong \nu_r^{(1)}$. Since the activation energy can be determined *independently* via the parameter ε_r, the preexponential factor can be calculated explicitly; in this case, $k_r^{(1)} = \nu_r^{(1)} \exp(\varepsilon_r)$. Finally, even in the presence of moderately coverage-dependent rate parameters, the apparent rate coefficient will most likely be within one order of magnitude of the true coefficient, i.e., on the order of typical experimental uncertainties associated with the evaluation preexponential factors.

(ii) Unimolecular Surface Reaction in which the Product is Trapped

The linearized mass balance equations on both surface species (A and B) may be written as

$$d\theta'(t)/dt = -\mathbf{A}\theta'(t) - \mathbf{B}T'(t) , \tag{21}$$

where $\theta'(t)$ and **B** are column vectors, and **A** is a (2x2) matrix. A mass balance on the reaction product in the gas phase may be written as

$$dN_2(t)/dt = N_a y(\theta_2) k_{d,2}(\theta_1, \theta_2, T) - N_2(t)/\tau , \tag{22}$$

where $y(\theta_2)$ is the implicit coverage dependence of the product desorption reaction [e.g., $y(\theta_2) = \theta_2^n$ for nth-order desorption], and $k_{d,2}(\theta_1, \theta_2, T) \equiv n_a^{n-1} k_{d,2}^{(n)}(\theta_1, \theta_2) \exp[-E_{d,2}(\theta_1, \theta_2)/k_B T]$ is the coverage-dependent rate coefficient for the desorption reaction. Again, we neglect readsorption of the reaction product. Linearizing Eq. (22) about $\theta_{i,s}$ and T_s, taking the Laplace transform, and combining the result with the

transform of Eq. (21), we obtain

$$(\tau p + 1)N_2^{\dagger}(p) = \varepsilon_{d,2}\{1 + [\boldsymbol{\psi}\cdot\mathbf{H}(p)/b_d]\}T^{\dagger}(p) \equiv \varepsilon_{d,2}G(p)T^{\dagger}(p), \tag{23}$$

where $\varepsilon_{d,2} \equiv (E_{d,2}/k_BT)_s$ is the dimensionless activation energy for the product desorption reaction, ψ is a column vector with components $\psi_i = [\partial(yk_{d,2})/\partial\theta_i]_s$, $\mathbf{H}(p) \equiv -(\mathbf{A} + p\mathbf{I})^{-1}\mathbf{B}$, $b_d = (yk_{d,2})_s\varepsilon_{d,2}/T_s$ and $G(p) \equiv 1 + [\boldsymbol{\psi}\cdot\mathbf{H}(p)/b_d]$. The components of $\mathbf{H}(p)$ are given by Eq. (12). Utilizing Eqs. (12) and (23), we see that in the limit of high frequencies the system transfer function $\varepsilon_{d,2}G(p)$ will approach a constant value that is given by the dimensionless activation energy for desorption of the reaction product (i.e., $\varepsilon_{d,2}$).

A useful limiting form of the system transfer funtion can be obtained if we consider the reactant species to be coupled weakly to the product species; i.e., we assume the mass balance on the reactant species A(a) to be independent of the surface coverage of the product species B(a). [In this case, $a_{11} = a_1$ and $a_{12} = 0$, where a_1 is defined in Eq. (16).] Clearly, this implies that the surface reaction is irreversible, and the coverage of the product is small with respect to the coverage of the reactant. In addition, we assume that the rate of desorption of the product is independent of the surface coverage of the reactant (i.e., $\psi_1 = 0$). With these assumptions, it can be shown that Eq. (23) reduces to

$$\varepsilon_{d,2}G(p) = \varepsilon_{d,2}\left[\frac{(p/a_{22})}{(p/a_{22}) + 1}\right] + \varepsilon_r\left[\frac{1}{1 + (p/a_{22})}\right]G'(p)\,, \tag{24}$$

where $G'(p)$ is defined as in Eq. (18) [i.e., $\varepsilon_rG'(p)$ is the transfer function for the reaction-limited desorption case]. It should be clear that the constant a_{22} will be approximated closely by the frequency (rate) of desorption of the reaction product. Thus, if we consider the limiting case corresponding to II.2(i) above, where a_{22} is large with respect to the modulation frequency, we find, for $p << a_{22}$, $\varepsilon_{d,2}G(p) \cong \varepsilon_rG'(p)$. As expected, the more general case considered here reduces to the simplified reaction-limited desorption case, when we consider weak coupling of the reactant mass balance to the surface coverage of the product and assume a rapid rate of desorption of the product species with respect to the modulation frequency.

The predicted experimental response for the unimolecular reaction system described by Eq. (24) is displayed in Fig. 2 for three specific cases. In order to both simplify the discussion and provide

meaningful physical insights into the behavior of the transfer function, these cases are embodied by the following three simplifying assumptions: (i) The adsorption reaction of the reactant is essentially independent of coverage and surface temperature with respect to the desorption and surface reactions; (ii) both the desorption of the reactant and the surface reaction are first order; and (iii) the rate parameters are independent of coverage. With these assumptions, the apparent rate coefficient of the reactant a_1 is given by the sum of the rate coefficients for the surface reaction and desorption of the reactant; i.e., $a_1 = k_{r,s} + k_{d,1,s}$. Likewise, the apparent rate coefficient of the surface reaction χ_1 is equal to the true rate coefficient of the surface reaction; i.e., $\chi_1 = k_{r,s}$. Thus, the reaction probability of the reactant upon adsorption ρ_1 is given by $\rho_1 = \chi_1/a_1$. Nonlinearities, e.g., coverage-dependent rate parameters, will act to make all of the above equalities approximations (albeit reasonably accurate). *However, the basic form of the transfer function versus frequency, most importantly, the frequency regimes for which the transfer function exhibits a constant value given by the dimensionless activation energy of a single elementary reaction, will remain essentially unchanged.*

Three separate frequency regimes are apparent from an inspection of Fig. 2(A). In the limit of zero frequency, i.e., much less than the rate of desorption of the reactant $\omega \ll k_{d,1,s} = (1 - \rho_1)a_1$, the phase is essentially zero and the magnitude of the amplitude ratio reflects directly the dimensionless apparent activation energy which, in this case, $AR(0) = (\varepsilon_r - \varepsilon_{d,1})(1 - \rho_1)$. For frequencies approximately equal to or greater than the apparent rate coefficient of the reactant (in this case, equivalent to the reciprocal of the average residence time of the reactant), and approximately equal to or less than the rate of desorption of the product, $2a_1 \leq \omega \leq a_{22}/2$, the amplitude ratio is equal to the dimensionless activation energy ε_r of the *unimolecular surface reaction.* Finally, for frequencies much greater than the rate of desorption of the product $\omega \gg a_{22}$, the amplitude ratio is equal to the dimensionless activation energy $\varepsilon_{d,2}$ of *desorption of the product.*

The validity of the limiting and/or approximate forms for the system transfer function given by Eq. (24) is clearly apparent in Fig. 2. Since in all three cases the average residence time of the product ($\tau_2 = 1/a_{22}$) is much less than that of the reactant ($\tau_1 = 1/a_1$), the product is weakly trapped and is formed in a reaction-limited fashion. Thus, for all three cases, the reaction-limited form given by

Eq. (18) is valid for frequencies $\omega \lesssim a_{22}/2$ as expected. Finally, case (c) of Fig. 2 represents a nearly unity reaction probability upon adsorption, and, consequently, consistent with the assumptions made above, it should be described well by the approximate form given by Eq. (19). We see that this is indeed the case for frequencies approximately equal to or greater than the rate of desorption of the reactant; i.e., $\omega \gtrsim 2k_{d,1,s} = 2(1 - \rho_1)a_1$. Furthermore, in this case, knowledge of both the activation energy of the surface reaction via the parameter ε_r, and the apparent rate coefficient $\chi_1 = \nu_r^{(1)}$ can lead to a direct evaluation of the preexponential factor via Eq. (20).

3. Bimolecular Surface Reactions

We shall consider reactions of the type

$$A(g) \underset{\leftarrow}{\overset{\rightarrow}{}} A(a) ,$$

$$B(g) \underset{\leftarrow}{\overset{\rightarrow}{}} B(a) ,$$

and

$$A(a) + B(a) \underset{\leftarrow}{\overset{\rightarrow}{}} C(a) \rightarrow C(g),$$

where again we make no assumptions concerning the molecularity of the adsorption and desorption reactions. As before, we shall consider explicitly two different cases to determine the effects of trapping of the product species on the predicted system response.

(i) Bimolecular Surface Reaction in which the Product is not Trapped

The linearized mass balance equations on the two reactant species (A and B) may be written as

$$d\theta'(t)/dt = -\mathbf{A}\theta'(t)/dt - \mathbf{B}T'(t) , \tag{25}$$

The mass balance on the reaction product in the gas phase (C, species '3') is given by

$$dN_3(t)/dt = N_a x(\theta_1,\theta_2)k_r(\theta_1,\theta_2,T) - N_3(t)/\tau , \tag{26}$$

where N_3 is the number of product molecules in the gas phase, $x(\theta_1,\theta_2)$ is the implicit coverage dependence of the surface reaction [a simple case being $x(\theta_1,\theta_2) = \theta_1\theta_2$], and $k_r(\theta_1,\theta_2,T) \equiv n_a k_r^{(2)}(\theta_1,\theta_2)\exp[-E_r(\theta_1,\theta_2)/k_BT]$ is the coverage-dependent rate coefficient describing the elementary, bimolecular surface reaction A(a) + B(a) $\rightarrow$ C(g). We neglect readsorption of the product and assume the surface reaction to be irreversible. Linearizing Eq. (26) about $\theta_{i,s}$ and T_s, taking the

Laplace transform and combining the result with the transform of Eq. (25) gives

$$(\tau p + 1)N_3^{\dagger}(p) = \varepsilon_r\{1 + [\boldsymbol{\chi}\cdot\mathbf{H}''(p)/b_r]\}T^{\dagger}(p) \equiv \varepsilon_r G''(p)T^{\dagger}(p) \ , \tag{27}$$

where $N_3^{\dagger}(p) \equiv [N_3(p)/N_{3,s}] - 1$, $\varepsilon_r \equiv (E_r/k_BT)_s$ is the dimensionless activation energy of the bimolecular surface reaction, $\boldsymbol{\chi}$ is a column vector with components $\chi_j \equiv [\partial(xk_r)/\partial\theta_j]_s$, $H''(p) = -(\mathbf{A} + pI)^{-1}\mathbf{B}$, $b_r \equiv (xk_r)_s\varepsilon_r/T_s$, and $G''(p) = 1 + [\boldsymbol{\chi}\cdot\mathbf{H}''(p)/b_r]$. The components of $H''(p)$ are given by Eq. (12). We see from Eqs. (12) and (27) that in the limit of high frequencies, the transfer function will approach a constant value given by the dimensionless activation energy of the elementary surface reaction A(a) + B(a) $\rightarrow$ C(g) (i.e., ε_r). In general, the approach to this very useful high frequency limit will be governed by the magnitude of poles P_1 and P_2 of the adsorbate transfer functions $H_i(p)$ [see Eq. (12)].

A useful approximate form for the system transfer function can be obtained if we consider a reaction system in which the reaction probability upon adsorption of both reactants is high (i.e., desorption rates << reaction rate). If the adsorption reactions are essentially unactivated, the components of the column vector **B** are approximated well by the corresponding surface reaction term; i.e., $b_i \equiv b_r$. Near unity reaction probabilities also imply that contributions to the components of the matrix **A** due to the partial derivative terms of the desorption rate expressions will be small with respect to partial derivative terms of the surface reaction rate expression. In addition, provided the adsorbate coverages are not near saturation levels (in general, where adsorption reactions become strongly coverage-dependent), the contributions of the partial derivative terms of the adsorption rate expressions will also be small with respect to the corresponding terms of the surface reaction rate expression. Under these conditions, one or both of the linearized rate coefficients of the bimolecular surface reaction (i.e., χ_1 and χ_2) will dominate in magnitude all of the linearized rate coefficients of the adsorption and desorption reactions of both reactants; i.e., $a_{ij} \equiv \chi_j$. Utilizing these approximations, it can be shown that the transfer function $\varepsilon_r G''(p)$ defined in Eq. (27) reduces to (28)

$$\varepsilon_r G''(p) = \varepsilon_r \frac{(p/\nu_r^{(2)})}{[(p/\nu_r^{(2)}) + 1]} \ , \tag{28}$$

where $\nu_r^{(2)} = \mathrm{tr}\mathbf{A} = \chi_1 + \chi_2$. Note that this approximate transfer function is specified by *two* parameters, whereas the exact form given by Eq. (27) is specified by *seven* parameters. In addition, for this specific case, Eq. (28) predicts that the *apparent* activation energy [i.e., $E_rG''(0)$] will be nearly zero with

respect to the actual activation energy of the surface reaction. Consequently, the experimental observation of both high reaction probabilities and low apparent activation energies relative to the activation energy of the surface reaction virtually assures the applicability of Eq. (28).

In addition to the obvious simplicity of the functional form of Eq. (28), under appropriate conditions the apparent rate coefficient $\nu_r^{(2)}$ can be used to extract useful information concerning the elementary surface reaction. As an example, for the case where the implicit coverage dependence of the surface reaction is given by $x(\theta_1,\theta_2) = \theta_1\theta_2$, we find that

$$\nu_r^{(2)} \equiv \chi_1 + \chi_2 = (\theta_1^* + \theta_2^*)k_{r,s} , \tag{29}$$

where

$$\theta_i^* = \theta_{i,s}\left[1 + \theta_{j,s}\frac{\partial}{\partial\theta_j}\,(\ln k_r^{(2)} - E_r/k_BT)_s\right] ,$$

and (i,j) = (1,2) and (2,1). If coverage-dependent effects can be assumed to be small and/or compensatory, $\nu_r^{(2)}$ and ε_r can be used to specify a minimum value for the preexponential factor of the surface reaction rate coefficient $n_s k_r^{(2)}$, i.e., $\nu_r^{(2)} \equiv (\theta_1 + \theta_2)n_s k_r^{(2)}\exp(-\varepsilon_r) \le n_s k_r^{(2)}\exp(-\varepsilon_r)$. Alternatively, if the surface coverages are known, the preexponential factor can be calculated explicitly. Finally, if $\theta_j \gg \theta_i$ and the rate coefficient k_r is only weakly dependent on θ_i, then the approximation $\nu_r^{(2)} \equiv (\theta_1 + \theta_2)k_{r,s}$ is still reasonably valid *even if* the rate coefficient is strongly dependent on θ_j. This is readily apparent from an inspection of Eq. (29) since coverage-dependent effects of θ_j are contained in the θ_i^* term.

(ii) Bimolecular Surface Reaction in which the Reaction Product is Trapped

In this case, the linearized mass balances on the three surfaces species are given by

$$d\boldsymbol{\theta}'(t)/dt = -\mathbf{A}\boldsymbol{\theta}'(t) - \mathbf{B}T'(t) , \tag{30}$$

where $\boldsymbol{\theta}'(t)$ and $\mathbf{B}$ are column vectors of dimension three, and $\mathbf{A}$ is a (3x3) matrix. A mass balance on the reaction product species in the gas phase may be written as

$$dN_3(t)/dt = N_a y(\theta_3)k_{d,3}(\boldsymbol{\theta},T) - N_3(t)/\tau , \tag{31}$$

where $y(\theta_3)$ is the implicit coverage dependence of the product desorption reaction, $k_{d,3}(\theta,T) \equiv n_s^{n-1}k_{d,3}^{(n)}(\theta)\exp[-E_{d,3}(\theta)/k_BT]$ is the coverage-dependent desorption rate coefficient, and $\theta \equiv (\theta_1,\theta_2,\theta_3)$ is the surface coverage column vector. We neglect readsorption of the reaction product.

Linearizing Eq. (31) about $\theta_{i,s}$ and T_s, taking the Laplace transform and combining the result with the transform of Eq. (30) gives

$$(\tau p + 1)N_3^{\dagger}(p) = \varepsilon_{d,3}\{1 + [\boldsymbol{\psi}\cdot\mathbf{H}(p)/b_d]\}T^{\dagger}(p) \equiv \varepsilon_{d,3}G(p)T^{\dagger}(p) , \tag{32}$$

where $\varepsilon_{d,3} \equiv [E_{d,3}/k_BT]_s$ is the dimensionless activation energy for desorption of the reaction product, ψ is a column vector with components $\psi_j = [\partial(yk_d)/\partial\theta_j]_s$, $\mathbf{H}(p) \equiv -(\mathbf{A} + p\mathbf{I})^{-1}\mathbf{B}$, $b_d = (yk_d)_s\varepsilon_{d,3}/T_s$, and $G(p) \equiv 1 + [\boldsymbol{\psi}\cdot\mathbf{H}(p)/b_d]$. Due to the form of the components of the vector $\mathbf{H}(p)$ in the limit of high frequencies (numerator terms of order p^2 and denominator terms of order p^3) the system transfer function will approach a constant value given by the dimensionless activation energy for desorption of the reaction product (i.e., $\varepsilon_{d,3}$).

As in the case of unimolecular surface reactions, it is of interest to consider the specific case in which the adsorbed reactants are coupled weakly to the reaction product. In particular, we assume the mass balances on the reactant species are independent of the surface coverage of the reaction product (i.e., $a_{13} = a_{23} = 0$). This implies that the surface reaction A(a) + B(a) $\rightarrow$ C(a) is irreversible and the coverage of the reaction product is small with respect to the reactants. In addition, we assume that the rate of desorption of the reaction product is independent of the surface coverages of the reactants (i.e., $\psi_1 = \psi_2 = 0$). With these assumptions, it can be shown that Eq. (32) reduces to

$$\varepsilon_{d,3}G(p) = \varepsilon_{d,3}\left[\frac{(p/a_{33})}{(p/a_{33}) + 1}\right] + \varepsilon_r\left[\frac{1}{1 + (p/a_{33})}\right]G''(p) , \tag{33}$$

where $G''(p)$ is defined in Eq. (27). As before, the constant a_{33} can be approximated by the rate of desorption of the reaction product. Thus, for the case in which trapping effects are expected to be small, i.e., a_{33} is large with respect to the modulation frequency, we have for $p << a_{33}$, $\varepsilon_{d,3}G(p) \cong \varepsilon_rG''(p)$; and the generalized transfer function reduces to the simplified, reaction-limited desorption transfer function defined in Eq. (27).

The predicted experimental response for the bimolecular surface reaction system described by Eq. (33) is displayed in Fig. 3 for three specific cases. It is not feasible to consider completely *all* possible forms of the transfer function for this complex bimolecular reaction system. Therefore, the three specific cases considered have been chosen carefully such that they will span the expected behavior of

the transfer function (29). As in the case of unimolecular surface reactions, it is useful to make a number of simplifying assumptions in order to increase the physical understanding of the behavior of the transfer function. These assumptions are the following: (i) the reaction probability upon adsorption of species '1' is unity, and the adsorption of '1' is independent of surface temperature and dependent equally on the coverage of both reactants; (ii) the adsorption of species '2' is independent of surface temperature and coverage; (iii) the desorption of '2' is first order and the bimolecular reaction is first order in each of the reactants; and (iv) the rate parameters are independent of coverage. Assumptions (i) and (iii) specify two coefficients of **A**, viz. $a_{11} = \alpha + \chi_1$ and $a_{12} = \alpha + \chi_2$, whereas (ii) and (iii) specify the other two, $a_{21} = \chi_1$ and $a_{22} = k_{d,2,s} + \chi_2$ and the reaction probability of '2', $\rho_2 = \chi_2/a_{22}$. Note that the ratio of the reactant coverages is given by $\theta_2/\theta_1 = \chi_1/\chi_2$. Again, nonlinearities, e.g., coverage-dependent rate parameters, will tend to make these equalities only approximations while exerting a negligible influence on the form of the transfer function versus frequency.

Case (a) in Fig. 3 represents a situation in which the coverage of '1' is both near the saturation level [thus $\alpha \gg \chi_1$ (30)] and much greater than the coverage of '2' (thus $\chi_1/\chi_2 = \theta_2/\theta_1 \ll 1$). In this case, the overall rate of reaction is most sensitive to changes in the coverage of '2'. In the limit of small reaction probabilities, the coverage of '2' is inversely proportional to the desorption rate constant $k_{d,2,s}$, and the apparent activation energy is approximately equal to the difference between the activation energies of reaction and desorption of '2'; i.e., $AR(0) \sim \varepsilon_r - \varepsilon_{d,2}$. From Fig. 3, we see that case (a) exhibits a negative apparent activation energy as expected since, in this case, $\varepsilon_r < \varepsilon_{d,2}$. As the frequency increases beyond a value of approximately $2(a_{11} + a_{22}) \cong 2a_{22} = 2/\tau_2$, where τ_2 is the average residence time of '2', the magnitude of the amplitude ratio is characteristic of the dimensionless activation energy ε_r of the *bimolecular surface reaction.* Finally, for frequencies much greater than the rate of desorption of the product a_{33}, the amplitude ratio is equal to the dimensionless activation energy $\varepsilon_{d,3}$ of *desorption of the product.*

Case (b) in Fig. 3 represents a situation in which the coverage of '2' is both at moderate levels [thus, $\alpha \cong \chi_2$ (30)] and much greater than the coverage of '1' ($\chi_2/\chi_1 << 1$). In this case, the overall rate of reaction is most sensitive to changes in the coverage of '1'. Since the reaction probability of '1' is

unity, the coverage of '1' will be determined by the rate of adsorption of '1', which, since $\theta_2 \gg \theta_1$ in this case, is most sensitive to changes in the coverage of '2'. In the limit of small reaction probabilities of '2', the coverage of '2' is inversely proportional to the desorption rate coefficient $k_{d,2,s}$. Thus, since a decrease in the coverage of '2' will result in an increase in the coverage of '1', and hence the overall rate, the apparent activation energy is the activation energy of desorption of '2', i.e., $AR(0) \cong \varepsilon_{d,2}$. From Fig. 3 we see that case (b) exhibits an apparent activation energy approximately equal to that of desorption of '2'. As the frequency increases beyond a value of approximately $2(a_{11} + a_{22}) = 2[(1/\tau_1) + (1/\tau_2)]$, where τ_i is the average residence time of 'i', the amplitude ratio is equal to the dimensionless activation energy of the bimolecular surface reaction. Again, for $\omega \gg a_{33}$, the amplitude ratio is equal to $\varepsilon_{d,3}$.

Case (c) in Fig. 3 represents a situation in which the coverages of both '1' and '2' are well below their saturation values ($\alpha/\chi_i << 1$). In addition, both reaction probabilities are near unity and, consequently, the apparent surface reaction rate coefficients χ_j supply the dominant contributions to a_{ij}. We see that the *apparent* activation energy is nearly zero with respect to that of the surface reaction ε_r. Thus, case (c) should be described well by the approximate form given by Eq. (28). From Fig. 3 we see this is the case for frequencies $0.1 \leq \omega \leq 500$ rad–s^{-1} (i.e., $\alpha \leq \omega \leq a_{22}/2$). Since the activation energy is determined independently via the parameter ε_r, the apparent rate coefficient $\nu_r^{(2)} = \chi_1 + \chi_2$ can be used in this case to evaluate the preexponential factor via Eq. (29), provided the reactant coverages are known. Finally, for $\omega \gg a_{33}$ the amplitude ratio is equal to $\varepsilon_{d,3}$.

Reviewing the material presented in Fig. 3 for a bimolecular surface reaction, we see that for *all* cases considered, despite the fact that the *apparent* energetics differs greatly, the amplitude ratio is equal to the dimensionless activation energy of the *bimolecular surface reaction* at sufficiently high frequencies. This "sufficiently high" frequency is given by the maximum value of the poles P_1, P_2 of the transfer function $\mathbf{H}''(p)$ [see Eq. (12)]. In most cases this maximum value is less than or equal to tr**A** (31). Furthermore, in many cases (e.g., reaction rates that are first- and or second-order in the adsorbate coverages), the quantity tr**A** is given by the sum of the reciprocals of the average residence times of the adsorbed reactants; i.e., $(1/\tau_1) + (1/\tau_2)$. Finally, since in all three cases the average residence time of

the product ($\tau_3 \equiv 1/a_{33}$) is much less than that of the reactants ($\tau_1 \equiv 1/a_{11}$, $\tau_2 \equiv 1/a_{22}$), the product is weakly trapped and is formed in a reaction-limited fashion. Thus, for all three cases, the reaction-limited form given by Eq. (27) is valid for frequencies $\omega \leq a_{33}/2$ as expected.

4. Generality of Formulation

The mass balance equations on the reaction products in the gas phase presented above were constructed to apply to continuously pumped reactors in which the average partial pressure of the reaction product is detected. However, these transfer functions can be related simply to the corresponding transfer functions developed to apply to systems utilizing line-of-sight differentially pumped mass spectrometric detection (32). In general, the approach taken above involved mass balances on the gas phase reaction product given by $dN_g/dt = r(\theta,T) - N_g/\tau$, whereas line-of-sight detection techniques typically measure the scattered intensity of the product molecules; i.e., $R_E(t) = r(\theta,T)$. It may be shown easily that $R_E^\dagger(p) = (\tau p + 1)N_g^\dagger(p)$, where $R_E^\dagger(p) = [R_E(p)/R_{E,s}] - 1$ and $N_g^\dagger(p) = [N_g(p)/N_{g,s}] - 1$. It was with this expression in mind that the transfer functions calculated previously [e.g., Eqs. (7), (15), (18), (23), (27) and (32)] were arranged such that the pumping term $\tau p + 1$ was grouped with the output variable $N_g^\dagger(p)$. Thus, the two experimental systems can be related simply via

$$R_E^\dagger(p) = (\tau p + 1)N_g^\dagger(p) = G(p)T^\dagger(p) ,$$

where G(p) represents the system transfer function.

It is important to note that the Laplace transform formalism employed here is suitable also for aperiodic forms of the temperature forcing function. Thus, our formulation is not restricted to periodically varied temperature forcing functions that are employed at different frequencies, although these typically provide the optimal method of analysis. For example, if a step-function in temperature is employed, the expected response in the time domain can be evaluated by inverting the product of the system transfer function and the transform of the forcing function, in this case given by $T^\dagger(p) \propto 1/p$.

Finally, extension of the formalism adopted here to more complex surface reaction systems should be straightforward utilizing the same basic strategy, i.e., construction of the system transfer function from the combination of linearized mass balance equations on both the relevant adsorbed surface species and the gas phase reaction product(s). For example, consider a unimolecular reaction of the

type

$$A(g) \underset{\leftarrow}{\overset{\rightarrow}{}} A(a) \underset{\leftarrow}{\overset{\rightarrow}{}} B(a) + C(a) \rightarrow B(g) + C(g) ,$$

where *two* decomposition products are formed. In this case, the adsorbate transfer function [**H**(p)] will be of dimension three. Two system transfer functions, each of which can be measured separately experimentally, will result from the combination of the adsorbate transfer function with the linearized mass balance equations describing the two gas phase reaction products. Unless both gas phase reaction products are formed in a single reaction-limited step, each system transfer function will contain unique information concerning the elementary surface reactions.

III. Summary

The theoretical formulation of a frequency response technique, based on surface temperature modulation, for the study of surface reaction dynamics has been described. The technique has the advantage of the availability of dynamical information provided by the use of a transient technique, whereas the values calculated for the kinetic parameters represent the values occurring at *steady state*, which are often difficult to obtain. The evaluation of the activation barriers for elementary surface reactions, such as desorption, unimolecular surface reactions A(a) $\rightarrow$ B(a), and bimolecular surface reactions A(a) + B(a) $\rightarrow$ C(a), is straightforward and requires no knowledge of the composition or configuration of the adlayer. This feature of STMMS, the straightforward analysis of the energetics of elementary surface reactions *even in the presence of strong nonlinearities*, provides the technique with a decided advantage over competing techniques such as MMBRS. Surface temperature modulation enjoys this advantage since apparent rate coefficients are *not* used to evaluate activation energies. Rather, by varying the modulation frequency appropriately, the amplitude ratio is equal to the dimensionless activation energy of a single elementary reaction for a *range* of frequencies. In most cases, the low frequency boundary of this range is given approximately by the (sum of the) reciprocal(s) of the average residence time(s) of the reactant(s) on the surface. Obviously, careful measurement of the *amplitude* as well as the phase of the input and output waveforms is required.

The evaluation of preexponential factors of surface reaction rate coefficients is complicated by the

presence of coverage-dependent effects and the requirement that the implicit coverage dependence of the reaction must be known. (Obviously, comparable difficulties exist also for MMBRS in the evaluation of these preexponential factors.) However, in many cases the prefactors can also be calculated in a straightforward manner. For example, for the case of coverage-independent adsorption and (first-order) molecular desorption, the preexponential factor can be calculated directly. Provided the adsorbate concentrations are known, the preexponential factors may be calculated also for the cases of coverage-dependent adsorption and/or second-order desorption [see Eq. (8)]. Concerning the more complex cases of unimolecular and bimolecular surface reactions, if reaction conditions are chosen appropriately, the measured apparent rate coefficients can be related simply to the true rate coefficients of the surface reactions [see Eqs. (20) and (29)]. In general, the reaction conditions must be chosen such that the reaction probability upon adsorption of the reactant(s) is nearly unity (admittedly, this is not always possible). In these cases, noting that for a bimolecular reaction the adsorbate concentrations must also be known, the preexponential factors can be calculated. Finally, in all cases, the presence of coverage-dependent rate parameters will tend to make the apparent rate coefficients only approximately equal to the true rate coefficients. However, in most cases this approximation will most probably be within one order of magnitude. Since the corresponding activation energies are determined *independently*, the error associated with evaluating preexponential factors via apparent rate coefficients will be on the order of typical experimental uncertainties.

Acknowledgment: This work was supported by the National Science Foundation under Grant No. CHE-8516615.

References

1. M. Eigen, Discuss. Faraday Soc. **17**, 194 (1954); M. Eigen and L. Maeyer, *Technique of Organic Chemistry*, Vol. 8, Pt. 2, Ed., A. Weissberger, Wiley, N.Y., 1963, p. 895.

2. D. Menzel, in *Chemistry and Physics of Solid Surfaces IV*, Eds., R. Vanselow and R. Howe, Springer-Verlag, Heidelberg-New York, 1982, p. 389.

3. C. O. Bennett, in *Catalysis under Transient Conditions*, ACS Symp. Ser. **178** (1982), p. 1.

4. M. Balooch, D. R. Olander, J. Abrefah and W. J. Siekhaus, Surface Sci. **149**, 285 (1985).

5. G. W. Rubloff, Surface Sci. **89**, 566 (1979); F. Steinbach and J. Schütte, Rev. Sci. Instrum. **54**, 1169 (1983).

6. W. Ho, J. Vacuum Sci. Technol. A **3**, 1432 (1985); B. A. Gurney and W. Ho, J. Vacuum Sci. Technol. A **3**, 1541 (1985).

7. D. A. Mantell, S. B. Ryali and G. L. Haller, Chem. Phys. Letters **102**, 37 (1983); D. A. Mantell, K. Kunimori, S. B. Ryali and G. L. Haller, Am. Chem. Soc. Div. Pet. Chem. Prep. **29**, 904 (1984).

8. M. P. Cox, G. Ertl and R. Imbihl, Phys. Rev. Letters **54**, 1725 (1985); E. Lang, P. Heilmann, G. Hanke, K. Heinz and K. Müller, Appl. Phys. **19**, 287 (1979).

9. R. H. Jones, D. R. Olander, W. J. Siekhaus and J. A. Schwarz, J. Vacuum Sci. Technol. **9**, 1429 (1972).

10. M. P. D'Evelyn and R. J. Madix, Surface Sci. Reports **3**, 413 (1984).

11. J. R. Engstrom and W. H. Weinberg, Phys. Rev. Letters **55**, 2017 (1985).

12. C. T. Foxon, M. R. Boudry and B. A. Joyce, Surface Sci. **44**, 69 (1974); J. A. Schwarz and R. J. Madix, Surface Sci. **46**, 317 (1974); D. R. Olander and A. Ullman, Internat. J. Chem. Kinetics **8**, 625 (1976).

13. J. R. Engstrom and W. H. Weinberg, J. Chem. Phys., submitted.

14. Although the use of surface temperature modulation has been proposed previously (15), the approach adopted here differs from past methodologies in several crucial respects. Steinbach et al. (15) emphasized the use of surface temperature modulation as a *modification* of MMBRS, their analysis involving exclusively the interpretation of *phase* response data in order to obtain *apparent* reaction rate coefficients. This approach offers no advantages over linearized MMBRS techniques. The true power of surface temperature modulation is realized only by the accurate measurement of *both the amplitude and the phase response.*

15. F. Steinbach and D. Hofer, Surface Sci. **79**, 311 (1979).

16. The configuration or structure of the adlayer can also be considered as a dependent variable. The effects of adsorbate structure on the mass balances are manifest in the form of the implicit coverage dependencies of the rate expressions that describe the various surface reactions. In particular, adsorbate structure can affect strongly the rate of bimolecular surface reactions. For example, Mukesh et al. (17) have developed model rate expressions to describe bimolecular surface reactions in which adsorbate domain formation occurs.

17. D. Mukesh, W. Morton, C. N. Kenney and M. B. Cutlip, Surface Sci. **138**, 237 (1984).

18. This difference in the nature of the forcing functions that are used produces the essential difference between the two techniques. With MMBRS, the amplitude response can be used to calculate reaction probabilities. With STMMS, the amplitude response can be used to calculate activation energies.

19. I. Langmuir, Chem. Rev. **6**, 451 (1929); J. B. Taylor and I. Langmuir, Phys. Rev. **44**, 423 (1933).

20. P. Kisliuk, J. Phys. Chem. Solids **3**, 95 (1957); **5**, 78 (1958).

21. In general, the contribution to the linearized rate coefficient "a" from a first-order rate expression such as molecular desorption or a unimolecular surface reaction is given approximately by the true rate coefficient itself. This approximation is exact in the absence of coverage-dependent rate parameters. On the other hand, the contribution from an nth-order Langmuir adsorption rate expression, $r_a = (F/n_a)S_0(1 - \theta)^n$, except near saturation coverages, is given approximately by the

product of the "order" n, the dimensionless impingement rate (units of site^{-1}–s^{-1}), and the initial probability of adsorption, i.e. $-(\partial r_a/\partial\theta)_s = n(F/n_a)S_0(1-\theta_s)^{n-1} = n(F/n_a)S_0$ for n=1 or $\theta_s << 1$. Note also that 1/a is approximately equal to the average residence time of the adsorbate.

22. The contribution to the linearized temperature coefficient "b" for thermally activated reactions characterized by Arrhenius rate coefficients of the form $k(T) = k^{(n)}\exp[-E/k_BT]$ is given by $\varepsilon r_s/T_s$, where $\varepsilon \equiv (E/k_BT)_s$ is the dimensionless activation energy, and r_s is the rate of the reaction at steady state. Thus, the contributions from most adsorption rate expressions will be essentially zero since many adsorption reactions are either unactivated or, certainly for "direct" adsorption, nearly independent of the *surface* temperature.

23. This convenient substitution arises from the simple relationship between the Laplace and Fourier transforms.

24. A. Cassuto and D. A. King, Surface Sci. **102**, 388 (1981).

25. Local stability considerations require **A** to be nonsingular; see, e.g., O. Bilous and N. R. Amundson, AIChE J. **1**, 513 (1955).

26. This approach describing precursor mediated adsorption kinetics, i.e., not distinguishing between "intrinsic" and "extrinsic" precursor states, is essentially equivalent to that presented previously by Ehrlich (**27**).

27. G. Ehrlich, J. Phys. Chem. **59**, 473 (1955).

28. Equation (28) can be derived in two different ways. (i) If $a_{ij} = \alpha_{ij} + \chi_j$, then $\alpha_{ij} \ll \chi_j$. Utilizing Eq. (12) for the transfer functions $H_i''(p)$, we find that one pole is given by $P_1 \cong -\mathrm{tr}\mathbf{A}$, the other pole by $P_2/P_1 \cong |\mathbf{A}|/\mathrm{tr}\mathbf{A} \ll 1$, and the zeroes by $z_i/P_1 \cong (\alpha_{ij} - \alpha_{jj})/\mathrm{tr}\mathbf{A} << 1$. Inserting into Eq. (27) and retaining only those terms of order tr**A**, we arrive directly at Eq. (28). (ii) Expanding $\mathbf{H}''(p)$ about (1/p), we find $\mathbf{H}''(p) = (-\mathbf{B}/p) + (\mathbf{AB}/p^2) + O(1/p^3)$. Utilizing this expansion and retaining only those terms of order tr**A** gives $G''(p) \cong 1 - (\nu_r^{(2)}/p) + (\nu_r^{(2)}/p)^2 + \cdots \cong (p/\nu_r^{(2)})/[(p/\nu_r^{(2)}) + 1]$, where $\nu_r^{(2)} = \mathrm{tr}\mathbf{A} \cong \chi_1 + \chi_2$.

29 Since only *stable* steady states are physically realizable, the choice of the coefficients of **A** cannot

be made arbitrarily. A stable steady-state is assured if $\mathrm{tr}\mathbf{A} > 0$ *and* $|\mathbf{A}| > 0$.

30. For example, if $r_{a,1} \propto (1 - \theta_1 - \theta_2)$, then $\alpha/\chi_j = \theta_j/(1 - \theta_1 - \theta_2)$. Thus, if $\theta_i \ll \theta_j$ then $\alpha/\chi_j \cong \theta_j/(1 - \theta_j)$.

31. If the steady-state is a *node*, i.e., perturbations from the steady state are followed by an exponentially decaying return to the steady state, then $|P_{1,2}| \leq \mathrm{tr}\mathbf{A}$. However, if the steady state is a *focus*, i.e., the return to the steady-state is an exponentially damped *oscillation*, then $|P_{1,2}| \leq |\mathbf{A}|^{1/2}$.

32. Obviously, if line-of-sight techniques are employed, effects due to the finite time-of-flight of the product molecules between the surface and the detector must be accounted for properly.

Table 1. Model Parameters Corresponding to Figure 3.[a]

	Apparent Rate Coefficents, s^{-1}			
Case	α	χ_1	χ_2	$k_{d,2,s}$
a	1.0	0.2	2.0	8.0
b	0.2	1.0	0.2	0.8
c	0.1	1.0	1.0	0.05
d	0.0	1.0	1.0	0.0

[a] Matrix **A** is given by $\mathbf{A} = \begin{bmatrix} (\alpha + \chi_1) & (\alpha + \chi_2) \\ \chi_1 & (\chi_2 + k_{d,2,s}) \end{bmatrix}$, and the reaction probabilities are $\rho_1 = 1.0$, $\rho_2 = \chi_2/a_{22}$.

Figure Captions

Figure 1: The predicted experimental response for the adsorption-desorption equilibrium described by Eq.(7) displayed both (A) quantitatively, in terms of a reduced amplitude ratio ($AR/S_s\eta\varepsilon_d$) and phase difference (ϕ) as a function of a reduced frequency (ω/ν_d), and (B) qualitatively, in terms of the vector $G(i\omega)$ in the complex plane. The arrow in (B) indicates increasing frequency. The two representations are related via $G(i\omega) = AR(\omega)\exp[i\phi(\omega)]$.

Figure 2: The predicted experimental response for the unimolecular surface reaction described by Eq.(24) displayed both (A) in terms of the amplitude ratio [$AR(\omega)$] and phase difference [$\phi(\omega)$], and (B) in terms of the complex vector $G(i\omega)$. The arrows in (B) indicate increasing frequency. Case (d) represents the approximate form given by Eq. (19).

Figure 3: The predicted experimental response for the bimolecular surface reaction described by Eq. (33) displayed both (A) in terms of the amplitude ratio [$AR(\omega)$] and phase difference [$\phi(\omega)$], and (B) in terms of the complex vector $G(i\omega)$. The arrows in (B) indicate increasing frequency. Case (d) represents the approximate form given by Eq. (28).

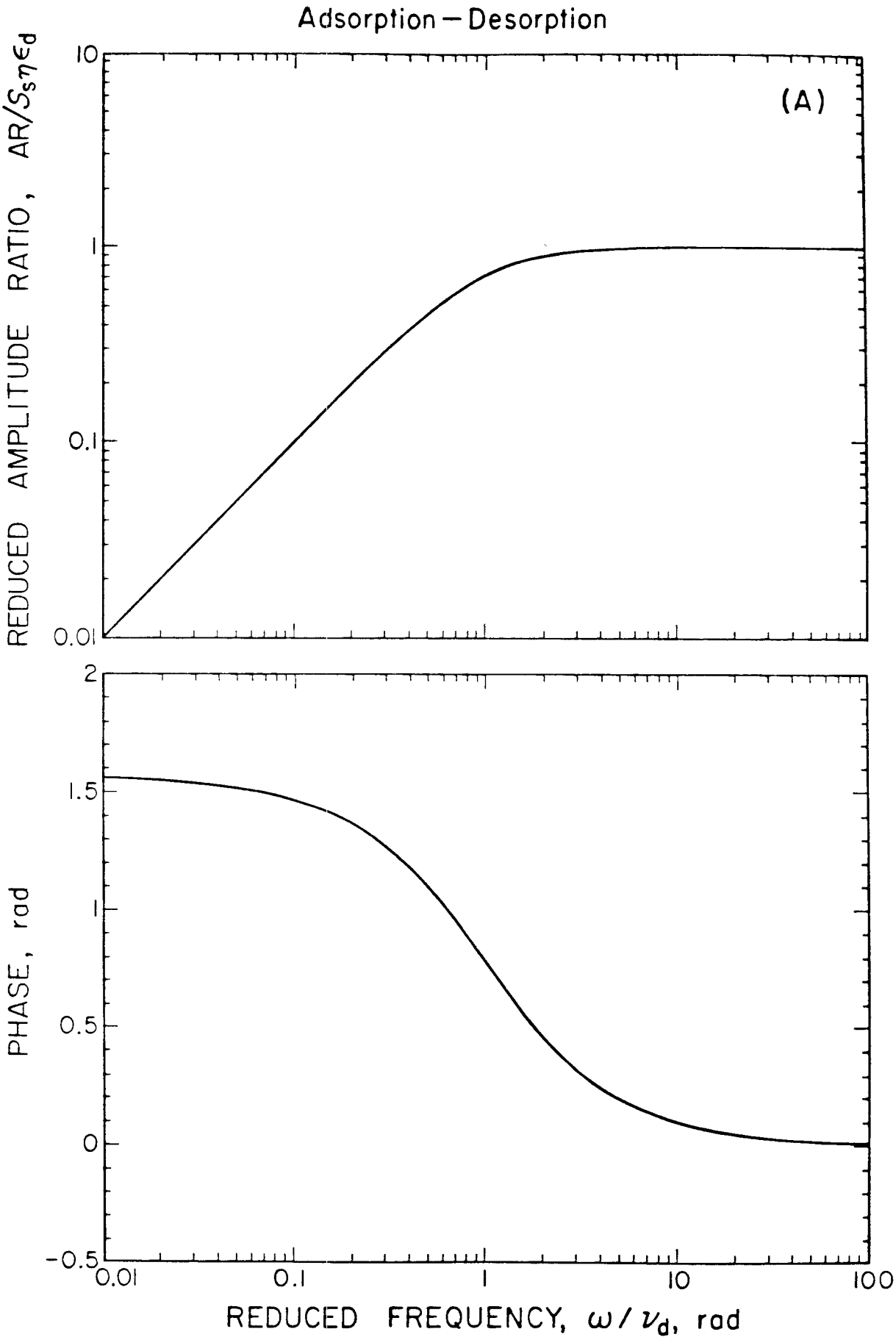
Adsorption — Desorption
(A)
REDUCED AMPLITUDE RATIO, $AR/S_s\eta\epsilon_d$
10
1
0.1
0.01
PHASE, rad
2
1.5
1
0.5
0
-0.5
0.01
0.1
1
10
100
REDUCED FREQUENCY, ω / ν_d, rad

Figure 1(A)

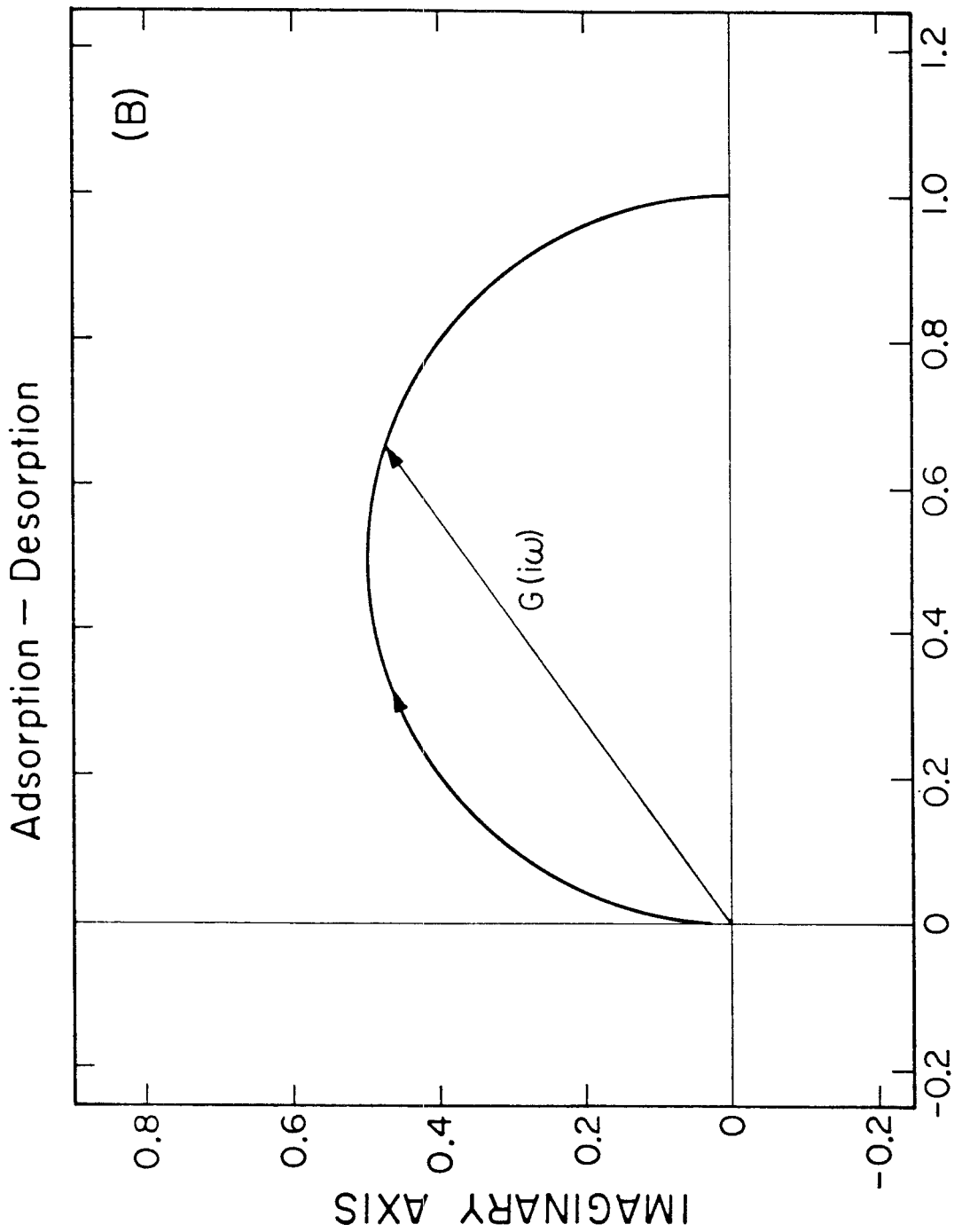
Adsorption — Desorption
(B)
G(iω)
IMAGINARY AXIS
REAL AXIS
0.8
0.6
0.4
0.2
0
-0.2
-0.2
0
0.2
0.4
0.6
0.8
1.0
1.2

Figure 1(B)

Unimolecular Surface Reaction

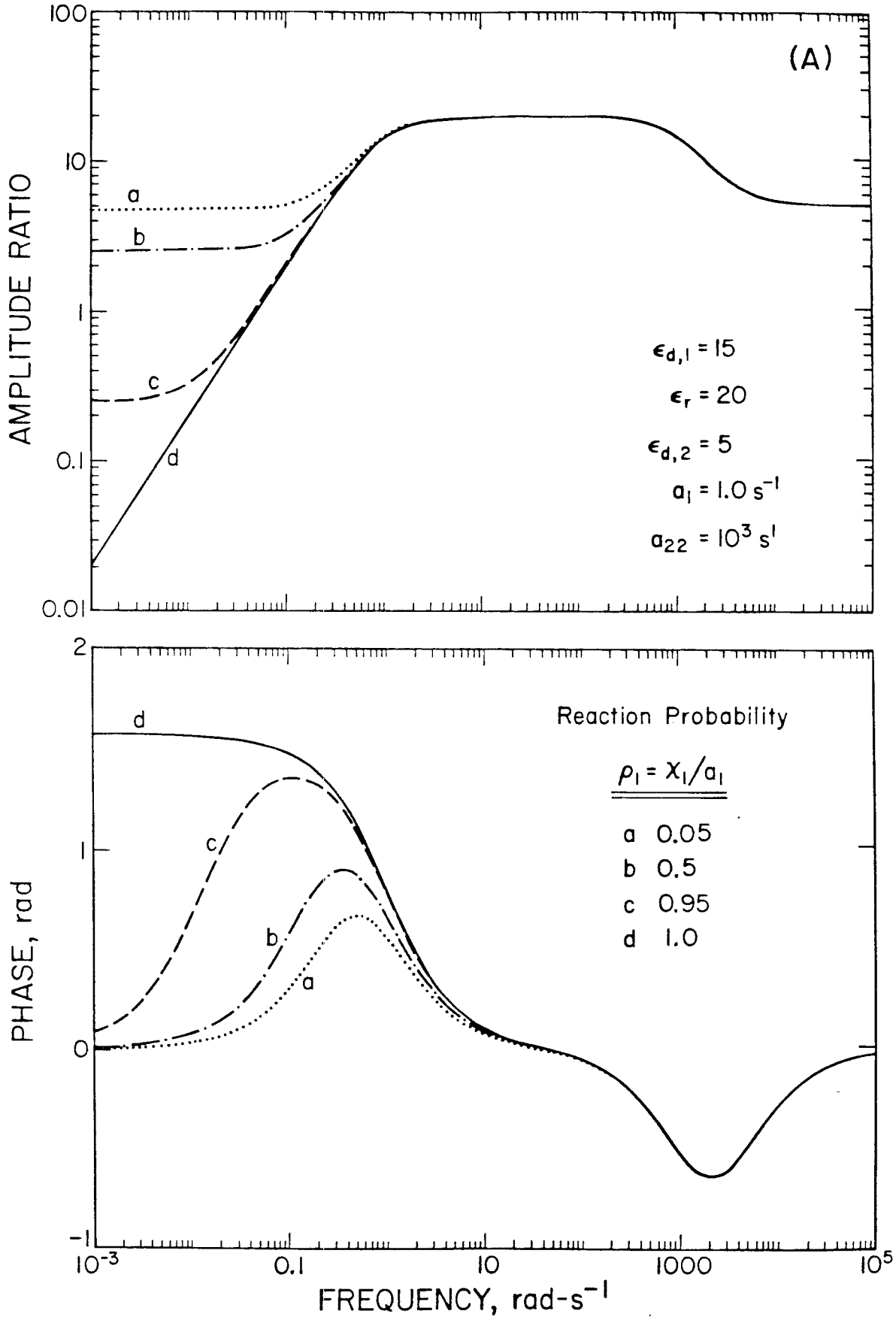

Figure 2(A)

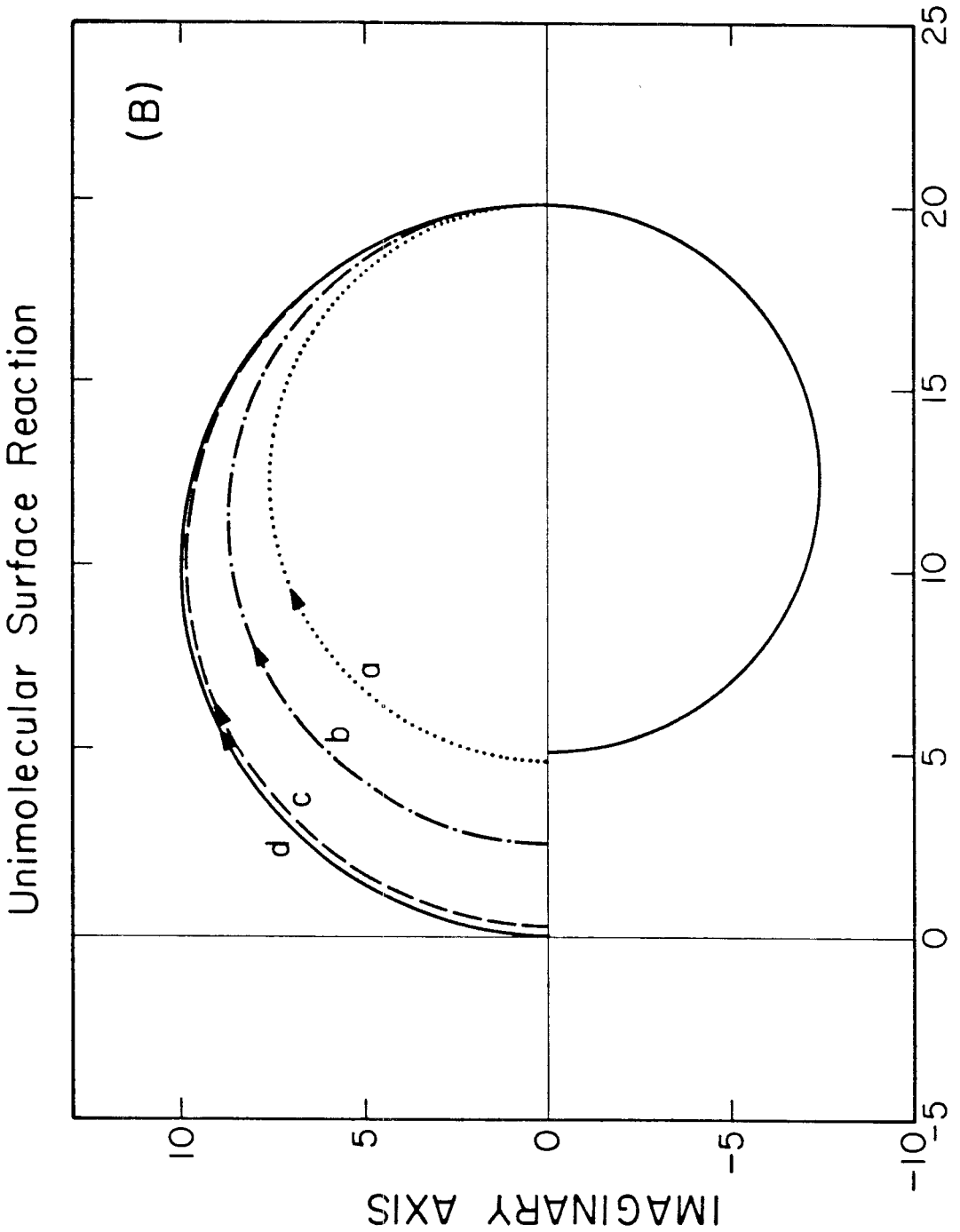
Unimolecular Surface Reaction
(B)
a
b
c
d
IMAGINARY AXIS
REAL AXIS
10
5
0
-5
-10
-5
0
5
10
15
20
25

Figure 2(B)

Bimolecular Surface Reaction

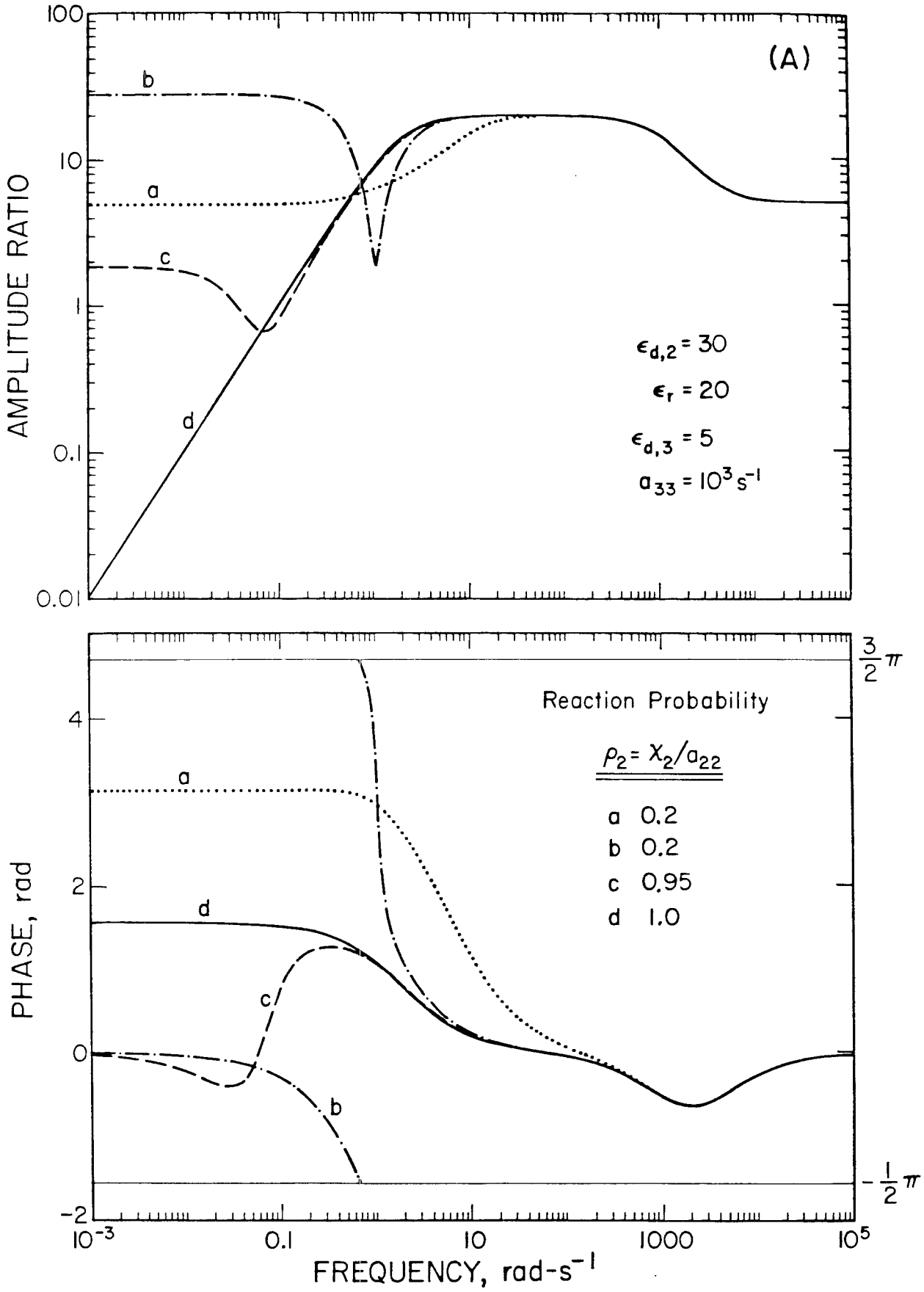

Figure 3(A)

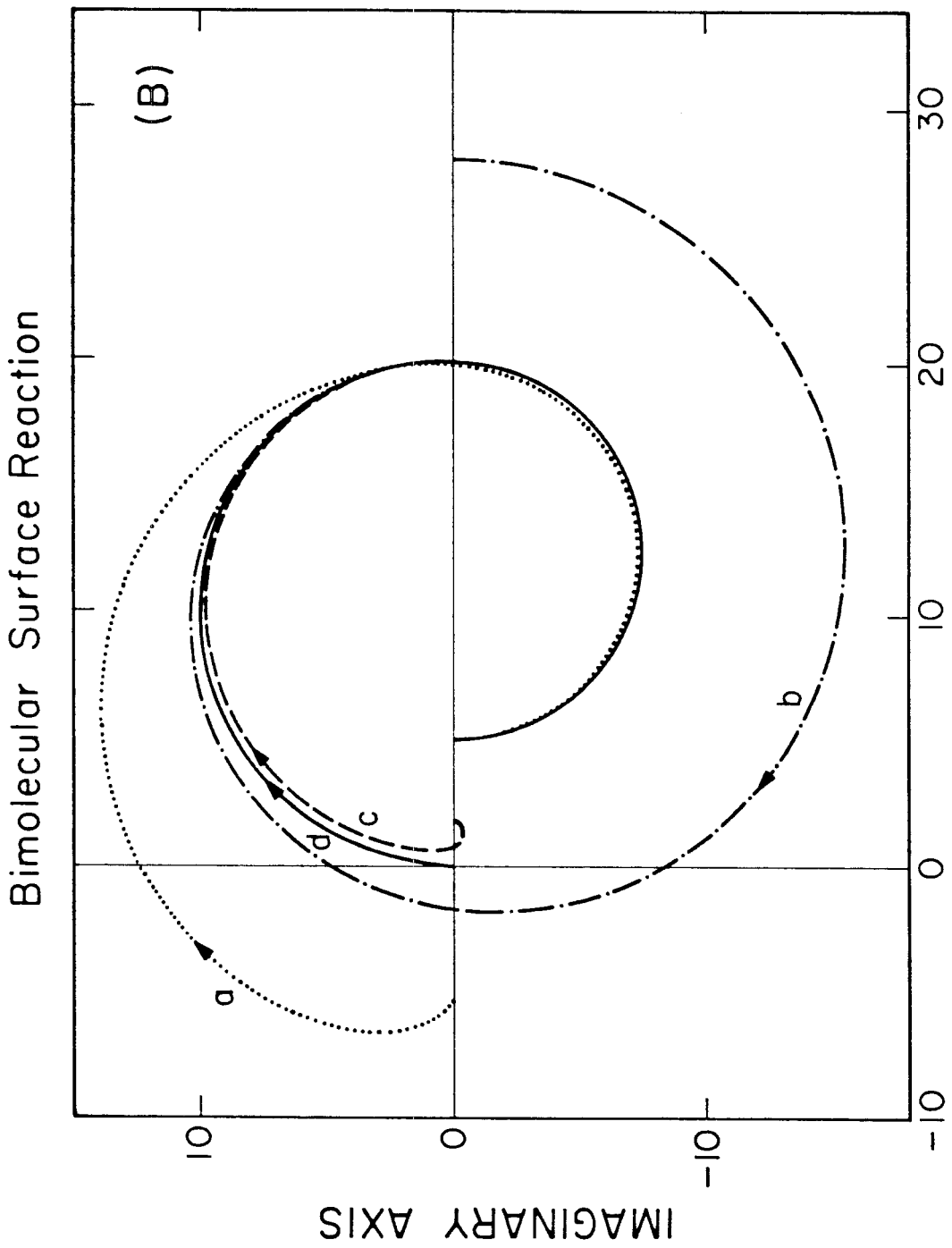
Bimolecular Surface Reaction
(B)
a
b
c
d
IMAGINARY AXIS
REAL AXIS
10
0
-10
-10
0
10
20
30

Figure 3(B)

CHAPTER 3

Analysis of Gas-Surface Reactions by Surface Temperature Modulation: II. Experimental Applications to the Adsorption and Oxidation of Carbon Monoxide on the Pt(110)-(1x2) Surface

[The text of Chapter 3 consists of an article coauthored with W. H. Weinberg, which has been submitted to *The Journal of Chemical Physics.*]

Abstract

Surface temperature modulation has been employed to investigate the adsorption, desorption and oxidation of CO on the Pt(110)-(1x2) surface. Examination of the adsorption-desorption equilibrium allows a determination of the kinetic parameters describing the desorption reaction. In the limit of zero coverage, the activation energy of desorption is 36 ± 1.5 kcal-mol^{-1} with a first-order preexponential factor of 3 x 10^{14} s^{-1}. As the coverage of CO increases, both parameters decrease in magnitude. The oxidation of CO has been studied with an emphasis on examining the kinetics of the elementary bimolecular surface reaction CO(a) + O(a) $\rightarrow$ CO_2(g). By varying both the reactant partial pressure ratio and the steady-state temperature of the surface, the reaction rate parameters have been evaluated for a variety of combinations of adsorbate concentrations occurring at steady state. The magnitudes of both the activation energy and the preexponential factor of the reaction rate coefficient have been found to correlate well with the oxygen adatom concentration. In the low coverage limit, the activation energy is 22 ± 1 kcal-mol^{-1}, and the preexponential factor is 3 x 10^{-3} cm^2–s^{-1}. As the oxygen adatom concentration increases beyond a fractional coverage of approximately 0.15, the magnitudes of both parameters drop precipitously to values given, respectively, by 8 ± 1 kcal-mol^{-1} and 10^{-10} cm^2–s^{-1}. The decrease in the activation energy at high oxygen coverages is explained by a decrease in the binding energies of the adsorbed reactants. The apparent decrease in the preexponential factor reflects also the *local* configuration of the reactants occurring at high oxygen coverages. The major contribution to the observed decrease in the preexponential factor is shown *not* to be due to reaction occurring at the edges of islands of oxygen adatoms. Rather, it is proposed that the energetically unfavorable configuration of reactants, which leads to a reduced activation energy, occurs with a low probability, and this leads to an anomalously low apparent preexponential factor.

I. Introduction

The adsorption and the oxidation of CO on transition metal surfaces have attracted particular attention both for their being model systems of fundamental gas-surface interactions, and for to their technological importance. On many transition metal surfaces, especially the Group VIII metals, the adsorption of CO has been found to be nondissociative and characterized by a nearly unity probability of adsorption (**1**). The binding energy is typically on the order of 30 kcal-mol^{-1}, indicative of (strong) chemisorption. Experimental studies employing both electronic and vibrational spectroscopies, coupled with theoretical calculations, have resulted in a thorough understanding of the nature of the chemical bond between the CO molecule and the metal surface (**2**). The oxidation of CO on transition metal surfaces, especially platinum, has been studied extensively (**3**) [dating to the time of Langmuir (**4**)], since both the reaction probability is high and the product CO_2 molecule interacts "weakly" with the surface upon formation. In view of the latter, studies of the distribution of energy in the translational and internal modes of the gas phase CO_2 product have led to a more complete description of the potential energy surface of the elementary bimolecular surface reaction between the adsorbed reactants (**5-7**). Of considerable interest is a determination of the influence that the adlayer composition has on the reaction dynamics. Clearly, a better understanding of the dynamics will be aided tremendously by independent knowledge of the integral rate parameters, i.e., the activation energy and the preexponential factor.

We have employed the technique of surface temperature modulation (**8,9**) to examine both the adsorption and the oxidation of CO on the Pt(110)-(1x2) surface. This technique permits a straightforward analysis of the energetics of *elementary* surface reactions, even for cases in which a *number* of elementary reactions contribute to the overall, *apparent* reaction energetics. In addition, the presence of coverage-dependent rate parameters does not preclude a direct determination of the activation energy; i.e., the activation energy can be evaluated for a *range* of reactant surface concentrations. The adsorption-desorption equilibrium of CO on the Pt(110)-(1x2) surface has been examined in order to evaluate the rate parameters that describe the desorption reaction $CO(a) \rightarrow CO(g)$. The oxidation of CO on this same surface has been examined to investigate explicitly the kinetics of the elementary surface reaction $CO(a) + O(a) \rightarrow CO_2(g)$. We shall emphasize particularly the coverage dependence of the

kinetic rate parameters, the results of which represent an important contribution to a more complete understanding of the surface reaction dynamics. Specifically, the *local* configuration of the reactants has been found to play a major role in determining the dynamics.

II. Experimental Procedures

The experiments described here were performed in an ion-pumped, stainless steel belljar that has been described previously (**10**). The base pressure of the belljar is below 1 x 10^{-10} Torr of reactive gases. Facilities are available for experimental studies involving mass spectrometry, low-energy electron diffraction (LEED), photoelectron spectroscopy (XPS and UPS) and Auger electron spectroscopy. The Pt(110) crystal was cut from a single crystalline boule of platinum and polished to within <0.5° of the (110) orientation by using standard metallographic techniques. The crystal was cleaned *in situ* by argon ion sputtering, heating in 5 x 10^{-7} Torr of oxygen at temperatures between 600 and 800 K, and high temperature annealing to 1400 K. Surface cleanliness was verified by Auger electron spectroscopy. Special care was taken to reduce the amount of silicon impurity in the sample to a negligible concentration, since Niehus and Comsa (**11**) have shown that its presence can be related directly to the formation of a "subsurface oxide" on Pt(111). After cleaning and annealing, the (1x2) LEED pattern characteristic of the clean, reconstructed surface was observed. Structural studies of this clean (1x2) surface have generally supported the "missing row" model as the correct geometrical structure of this reconstructed surface (**12**), and a recent study utilizing field ion microscopy appears to provide unequivocal evidence supporting the "missing row" model (**13**). The "missing row" reconstruction results in the formation of (111) microfacets, which are three atomic rows in width, and which are inclined at an angle of 109.5° with respect to one another.

Isotopic $C^{13}O$ (~90% C^{13}, Merck research grade, 99.99% purity) was utilized to increase the signal-to-noise ratio in the mass spectrometric detection. Research grade oxygen (99.99% purity) was supplied by Matheson. A directional beam doser, consisting of a multichannel array of capillaries (**14**) was employed to provide both careful control of reactant partial pressures (which is important for signal averaging) and a high beam-to-background pressure ratio (which improves the signal-to-noise ratio). Gases were admitted to the dosing line via capillary leaks from identical twin storage bulbs. The

reaction products in the gas phase were monitored with a quadrupole mass spectrometer (UTI 100C), while the temperature was measured by a thermocouple spotwelded to the back of the crystal.

Accurate temperature control was maintained by the use of an optimal control scheme, described elsewhere (**15**), which utilizes a laboratory microcomputer as the control element. (A complete physical description of the method used to heat and to cool the crystal is given elsewhere (**15**).) For a desired output (i.e., temperature) waveform, knowledge of the temperature control system transfer function produces directly the desired controller forcing function. In particular, if the desired output is given by $T(t) = T_s + T_A \sin\omega t$, it can be shown that

$$I'(t) = \frac{T_A}{\tau_c \rho(T_s)} \left[\omega\tau_c \cos\omega t + \sin\omega t\right] ,$$

where $I'(t) \equiv [i(t)]^2 - i_s^2$ is the deviation of the square of the applied current (proportional to the power input) from the value at steady state, τ_c is the thermal time constant of the crystal, $\rho(T_s)$ is proportional to the resistance of the support wires used to heat the crystal and inversely proportional to the heat capacity of the crystal, and ω is the radial frequency. A method for the accurate determination of the two parameters τ_c and $\rho(T)$ is given elsewhere (**15**).

The temperature control software has also been designed to control and to monitor the mass spectrometer. Thus, one routine provides data acquisition as well as control of the experiment. For each frequency of oscillation, after initial spurious transients have been reduced sufficiently (~15-50 s when a steady, periodic response has been achieved), data are collected and summed into a periodic array, increasing the signal-to-noise ratio. Typical periods of data collection for a single frequency and particular set of conditions [partial pressure(s) of reactant(s) and surface temperature] are 2.5-3 min in duration ($S/N \geq 10$). Once collected, the data are analyzed utilizing standard digital Fourier transform techniques (**16**). Since the input waveform (temperature) is nearly sinusoidal, only the results obtained at the fundamental frequency are used in the subsequent analysis.

The pumping time constant can be obtained easily and accurately by creating a step-function change in the rate of the particular surface reaction that affects the product concentration in the gas phase. The exact method that was employed varied for the two reaction systems studied here, as discussed below. An alternate method was also used that involved introducing a pulse of short duration of

the gas phase product species into the chamber via a leak line equipped with a solenoid-actuated valve (Allied #3M782). The intensity of the pulse was chosen to be approximately 5-10% of the steady-state intensity of gas phase product species in the reactor (i.e., the perturbation was linear). The results obtained by the two methods were in good agreement with one another.

A determination of the instrument response function is crucial for any frequency response technique (**17**). Utilizing standard techniques employing a function generator and an oscilloscope, distortions of the input (temperature) or output (mass spectrometer ion current) waveforms by the measurement electronics were found to be negligible for the frequency range employed (0.01-1.0 Hz). However, for any system sampling the rate of reaction over the entire surface of the crystal (e.g., a continuously pumped system), the desired input waveform is the *spatially averaged temperature* of the surface. Since we employ a spatially inhomogeneous method to heat and cool the crystal (**15**), this averaged temperature can be expected to differ from the temperature measured by the thermocouple at sufficiently high frequencies. A detailed analysis, presented elsewhere (**18**), shows that the power input (the square of the applied current) and the spatially averaged temperature can be related simply to one another. Thus, the microcomputer controlling the crystal temperature can be used to determine the frequency response of the measured temperature as a function of the spatially averaged temperature via the power input. The measured response was found to be linear for the amplitude of the temperature forcing functions used here, with the phase difference becoming significant at high frequencies, while the amplitude ratio was nearly unity for all frequencies. Independent measurements indicated that these effects were not related to spurious EMF signals due to IR drop or capacitive coupling caused by the heating current passing through the sample (**19**).

The measured response, taking the measured temperature as the output variable, is shown in Fig. 1. This result can be compared with that predicted theoretically from the time-dependent two-dimensional heat conduction equation solved for the appropriate crystal geometry and boundary conditions. The solution, given elsewhere (**18**), predicts a linear response between the measured- and spatially averaged temperatures. Thus, utilizing a value for the radial thermal time constant of the crystal of 1.27 s ($\tau_r = r^2/\kappa_c$, where r is the radius and κ_c is the thermal diffusivity of the crystal), the theoretical

response was calculated and is shown also in Fig. 1. The agreement between the measured response and the theoretically predicted response is *excellent*. Consequently, in the analysis below, the measured input waveform (temperature) has been adjusted accordingly to represent the spatially averaged temperature by utilizing the data displayed in Fig. 1.

III. Results and Discussion

1. CO Adsorption-Desorption Equilibrium on Pt(110)-(1x2)

The interaction of CO with the (110)-(1x2) surface of platinum has been examined for a gas phase pressure of approximately 6.5 x 10^{-8} Torr (20) and surface temperatures between 500 and 525 K. These experimental conditions were chosen on the basis of the range of realizable temperature forcing function frequencies. Essential to the application of the surface temperature modulation technique employed here is the experimental verification of the linearity assumption. A sufficient demonstration of linearity can be provided by examining the response of the gas phase product signal as the amplitude of the temperature forcing function is varied at constant frequency. The amplitude of the gas phase signal should vary linearly with the amplitude of the temperature, whereas the phase difference should be constant. Equivalently, the amplitude ratio can be calculated, and, as for the phase, its value should be constant. We choose the latter approach, since the results will also give an indication of the uncertainty in the values of the amplitude ratio (of obvious importance to the application of surface temperature modulation).

The amplitude ratio (AR) and phase difference of the gas phase signal [$N_g^\dagger$ of Eqs. (4) and (14) of part I (9), i.e., the dimensionless deviation of the product partial pressure from its steady-state value], detected by the mass spectrometer and corrected for the pumping term (i.e., $\tau p + 1$; see below) are plotted in Fig. 2 as a function of the (effective sinusoidal zero-to-peak) amplitude of the temperature forcing function (T_A). Both the amplitude ratio and the phase difference are independent of the amplitude of the temperature modulation, providing experimental proof of the linearity of the response. The two cases shown in Fig. 2 represent the lowest and highest frequencies employed in this particular study. The temperature amplitudes for these two frequencies utilized in the data that appear below are given by the median values shown in Fig. 2. These values bracket the amplitudes employed at intermediate

frequencies. Due to heat transfer limitations, smaller amplitudes are employed at higher frequencies, whereas larger amplitudes are desirable at the lower frequencies (where signal averaging is reduced) to diminish the uncertainty in the evaluation of the amplitude and phase. Not surprisingly, the poorest agreement occurs at low frequency with a small temperature amplitude.

A quantitative interpretation of the data presented here in terms of the kinetic parameters given in Eqs. (7) or (15) of Part I (**9**) is dependent upon an evaluation of the product $S_s\eta$ [equivalent to the fraction of molecules in the beam that both strike the crystal and adsorb, see Sect. II.1(i) of Part I (**9**)] and the pumping time constant τ of the chamber. Both parameters can be obtained by producing a step-function change in the rate of adsorption. Our measurements of the kinetics of adsorption of CO on the Pt(110)-(1x2) surface show that the probability of adsorption is essentially independent of coverage for fractional coverages below approximately 0.3, in agreement with previous investigations (**21-24**). Fair and Madix (**21**) have also found that the absolute value of the probability of adsorption of CO on Pt(110)-(1x2) is independent of temperature between 200 and 600 K. This coverage- and temperature-independence of the adsorption kinetics will be exploited to produce the desired step-function change in the rate of adsorption.

The specific procedure is as follows. The crystal, rotated out of line-of-sight of the beam doser, is flashed to desorb any molecules present on the surface due to adsorption from the background. Once the crystal has cooled to a temperature below 400 K, it is rotated quickly to be in line-of-sight of the beam doser, producing a step-function change in the rate of adsorption (**25**) [i.e., $r_a(t) = S_s\eta u(t)$, where u(t) is the Heaviside unit step function]. For sufficiently low reactant partial pressures (the impingement rates utilized here were approximately 0.03 site^{-1}–s^{-1}), the rate of adsorption will be constant for a significant period of time with respect to the pumping time constant of the chamber. During this period of time the partial pressure of the reactant (proportional to N_g) is given by

$$N_g(t)/N_{g,s} = 1 - S_s\eta[1 - \exp(-t/\tau)] \ .$$

Thus, the concentration of the reactant in the gas phase will decay exponentially, characterized by the pumping time constant of the reactor, to a new value given by $N_g = N_{g,s}(1 - S_s\eta)$. Provided the rate of adsorption is constant for a period of time such that $t >> \tau$, both the pumping time constant τ and the

product $S_s\eta$ can be obtained. We note that this procedure for obtaining an apparent probability of adsorption (i.e., $S_s\eta$) is essentially equivalent to that proposed previously by King and Wells (26).

In practice, the determination of the product $S_s\eta$ was quite reproducible utilizing this procedure (±5%). The determination of the pumping time constant compared well with the results obtained independently by employing the pulse-testing method utilizing the solenoid-activated value, as described in Sect. II. The more reproducible values for the pumping time constant obtained via the pulse-testing method are used in the analysis below.

As noted above, the probability of adsorption of CO on the Pt(110)-(1x2) surface is essentially independent of coverage at fractional coverages below approximately 0.3. This behavior is indicative of precursor-mediated adsorption kinetics, and the formalism developed in Sect. II.1(ii) of Part I (9) applies in this case. Since the residence time of CO in the precursor state is much less than both the residence time in the chemisorbed state and the reciprocal of the modulation frequency, the approximate form of the system transfer function given by Eq. (15) of part I is (9) appropriate. In addition, the observed temperature independence of the probability of adsorption between 200 and 600 K (21) indicates that the two activation energies E_a and E_d^* of Eq. (15) are essentially equal. (Recall that this equation assumes that adsorption into the precursor state is unactivated.) That is, based on the model utilized by Eq. (15), the temperature dependence of the probability of adsorption is contained in a factor given by $\exp[(E_a - E_d^*)/k_BT]$, and if $S \neq f(T)$, then $E_a = E_d^*$. Thus, in this case, the dimensionless heat of adsorption $\Delta\varepsilon_h^* = [(E_d - E_a + E_d^*)/k_BT]_s$ becomes equivalent to the dimensionless activation energy of desorption from the chemisorbed state $\varepsilon_d = (E_d/k_BT)_s$.

Amplitude and phase response data representing the system transfer function given by Eq. (15) are shown in Fig. 3 for a particular set of conditions with the same reactant partial pressure but different steady-state temperatures. We see that the experimental data are in quantitative agreement with Eqs. (9a) and (9b) of Part I (9) (where we replace ν_d and ε_d with ν_d^* and $\Delta\varepsilon_h^*$). In particular, the amplitude ratio approaches a constant value at high frequencies, whereas the phase difference varies from a value of $\pi/2$ to a value of zero as the frequency increases [see Fig. 1 of Part I (9)]. Thus, the data shown in Fig. 3 were fit to Eqs. (9a) and (9b) employing a least-squares functional minimization

routine based on a simplex method (27). The parameters obtained, $S_s\eta\Delta\varepsilon_h^*$ and ν_d^* (28), can be used to calculate directly the heat of adsorption and, under appropriate conditions, the preexponential factor of the desorption rate coefficient. Examination of Eq. (8) of Part I (9) indicates that the latter calculation should be justifiable at sufficiently low coverages (i.e., when $\theta_s[\partial(\ln k_d^{(1)} - \Delta\varepsilon_h^*)/\partial\theta]_s << 1$). Consequently, the fractional surface coverages occurring at steady state were estimated by heating the crystal rapidly while it was in line-of-site of the beam doser. The integrated area (vs. time) of the resulting desorption spectrum is proportional to the steady-state fractional surface coverage. By comparing the calculated area to the area obtained for saturation coverage at 350 K, of which the absolute value has been obtained (22), the absolute surface coverage can be calculated.

The calculated values for the heat of adsorption (essentially equivalent to the activation energy of desorption) and the preexponential factor of the desorption rate coefficient (calculated in two different ways; see below) are shown in Fig. 4 as a function of surface coverage. The three data points shown represent the same reactant partial pressure but different steady-state temperatures and are the average values obtained from two separate experiments under identical conditions. For reference purposes, the values obtained by modulated molecular-beam reactive scattering (MMBRS) (21) for the zero coverage limit are displayed on the left-hand ordinate in Fig. 4. We see that the kinetic parameters decrease in magnitude as the coverage increases and display a certain degree of compensatory behavior insofar as the rate of desorption is concerned, as has been observed previously (21-23). Extrapolating to zero coverage, the results obtained here compare very well with those obtained via MMBRS.

The preexponential factor is calculated by using Eq. (8) of Part I (9) with first-order desorption kinetics (n=1) and assuming coverage-independent adsorption kinetics (m=0), the latter being valid for the coverage range investigated. The solid line and open circles in Fig. 4 pertaining to $k_d^{(1)}$ were calculated by assuming that desorption from the chemisorbed state is direct (i.e., $\nu_d^* = k_{d,s}$), whereas the dashed line was calculated by assuming that CO, which desorbs from the chemisorbed state, is trapped in the precursor state [i.e., $\nu_d^* = (1 - \alpha)k_{d,s}$]. The latter calculation utilized a chemisorption probability of $\alpha = 0.7$ [$S^* = 1$ and $S^*\alpha = 0.7$ (21)]. Note that in this case the preexponential factor describes the elementary reaction $CO(a) \rightarrow CO^*(a)$, *not* $CO(a) \rightarrow CO(g)$. Although this is consistent with the

assumptions inherent in the derivation of Eq. (15), the possibility exists that the trapping mechanism may not be so efficient for CO *desorbed* from the chemisorbed state relative to CO *adsorbed* from the gas phase. Indeed, the presence of the precursor state was suggested by evidence concerning the adsorption kinetics (obtained at much lower temperatures). Thus, it is the lack of evidence concerning the trapping of molecules desorbed from the chemisorbed state that provides the motivation for calculating the preexponential factor for the case in which desorption is direct. In reality, the actual physical situation may lie between these two limiting cases, which cannot be distinguished experimentally as may be seen in Fig. 4. Unfortunately, the *form* of the experimentally measured response (e.g., the data of Fig. 3) also cannot resolve this matter, since the predicted functional forms for the direct and (approximated) precursor-mediated adsorption cases are identical [see Eq. (7) and (15) of Part I (9)].

2. CO Oxidation on Pt(110)-(1x2)

The oxidation of CO on the (110)-(1x2) surface of platinum has been examined for a CO partial pressure of approximately 4 x 10^{-9} Torr (20), oxygen-to-CO partial pressure ratios between approximately one and ten, and surface temperatures between 375 and 450 K. The general features of the CO oxidation reaction over the platinum metals have been reviewed by Ertl and Engel (3). For the reaction conditions considered here, the following four elementary reactions determine the steady-state rate of oxidation of CO: (1) the molecular adsorption of CO; (2) the dissociative adsorption of oxygen; (3) the desorption of CO; and (4) the surface reaction between adsorbed CO and oxygen adatoms to form the product CO_2. The rate of desorption of oxygen is negligible under these conditions. Since the desorption of CO_2 does not limit the overall rate of reaction (3), i.e., the product is not trapped, the formalism developed in Sect. II.3(i) of Part I (9) is appropriate.

We are most concerned with the dynamics of the surface reaction between CO admolecules and oxygen adatoms to produce CO_2. To date, the most reliable investigations of this elementary reaction on platinum surfaces have employed molecular beam techniques (29-31). The activation barrier has been found to be 22-24 kcal-mol^{-1} in the low coverage limit (29,30), while in the presence of high coverages of chemisorbed oxygen adatoms, the barrier has been observed to decrease to values between approximately 10 and 12 kcal-mol^{-1} (29,31).

The linearity of the response function was again verified experimentally by varying the amplitude of the temperature forcing function at fixed frequencies. The amplitude ratio and phase difference of the gas phase CO_2 product signal [$N_3^{\dagger}$ of Eq. (27) of Part I (9)], corrected for the pumping term, is shown in Fig. 5 as a function of the temperature amplitude. The linearity of the response function is evidenced by the independence of the amplitude ratio and phase difference with respect to the amplitude of the temperature modulation. The median values shown in Fig. 5 represent the temperature amplitudes for these two frequencies that were utilized in the data that appear below. These values bracket the amplitudes employed at intermediate frequencies.

The pumping time constant of the chamber was evaluated by imposing a step-function change in the rate of the surface reaction that produces CO_2. At sufficiently high temperatures ($\geq$650 K) under the conditions employed here, the overall rate of reaction was observed to be approximately first-order in the partial pressure of CO and nearly zero order in the partial pressure of oxygen. Since the rate of adsorption of CO is essentially independent of the oxygen adatom coverage (3), the overall rate of reaction is controlled by the relative rates of the surface reaction to produce CO_2 and the CO desorption reaction. Thus, if the CO partial pressure is reduced suddenly, the rate of the overall reaction will be reduced correspondingly. The time constant of the decay in the production of CO_2 will be less than the residence time of the adsorbed CO molecules in the absence of reaction. For temperatures above 650 K, we estimate a residence time for adsorbed CO on the clean surface that is below 0.01 s. (In the presence of oxygen adatoms, this residence time is smaller.) Thus, the resulting exponential decay of the gas phase product signal will reflect the pumping time constant of the chamber, since, in this case, it was much greater than the "reaction response time".

In actual practice, the CO and oxygen partial pressures are reduced suddenly by rotating the crystal quickly out of line-of-sight of the beam doser at high temperatures ($\geq$650 K). Since the background pressure is much less than the effective pressure of the beam doser ($\leq$5%), the rate of the surface reaction drops eventually to the background level (32). The values obtained by this procedure [$\tau \geq 0.3$ s (33)] were very reproducible and compared well with results obtained independently from the pulse-testing method utilizing the solenoid valve. The value of the pumping time constant was checked

periodically during the course of an experiment and was found to vary by less than ±5%.

Amplitude and phase response data representing the system transfer function $\varepsilon_r G''(p)$ [see Eq. (27) of Part I (**9**)] for a particular set of reaction conditions with the same reactant partial pressures but different steady-state temperatures are shown in Fig. 6. Due to both the limited frequency bandwidth of the temperature forcing functions and the advantages discussed in Part I (**9**), reaction conditions were chosen such that the restrictions placed on the use of Eq. (28) of Part I (**9**) were met. The advantages of using this "high-reaction-probability" approximate form include the simplicity of a two-parameter transfer function and the possibility of evaluating the preexponential factor via the apparent rate coefficient $\nu_r^{(2)}$ [see Eq. (29) of Part I (**9**)]. Concerning the restrictions placed on the use of this approximate form, the reaction probability of CO upon adsorption was measured to be greater than 0.9, whereas that for the adsorbed oxygen adatoms was unity for all reaction conditions considered. In addition, for these experimental conditions both the adsorption of CO (**21**) and the dissociative adsorption of oxygen (**34,35**) are essentially independent of the surface temperature. Finally, the observed *apparent* activation energies were such that $|G''(0)| \leq 0.05$ [see Sect. II.3(i) of Part I (**9**), and the discussion given elsewhere (**8**)]. Based on these experimental observations, the measured response should be described well by the approximate form of Eq. (28) for a wide range of frequencies. Curves representing Eq. (28), with the parameters ε_r and $\nu_r^{(2)}$ determined by the least-squares routine employed above (**27**), are displayed in Fig. 6. We see that the functional agreement of both the amplitude and the phase is excellent, which lends further support to the use of Eq. (28) for these reaction conditions. It is important to note that by utilizing the approximate form, the entire data set has been used in the analysis, which has increased greatly the sensitivity of the technique. *An analysis of the data shown in Fig. 6 leads to a direct determination of the activation energy of the elementary surface reaction via the parameter* ε_r *(i.e.,* $E_r \equiv k_B T_s \varepsilon_r$*).* For the two conditions shown, we find activation energies of approximately 21 and 17.5 kcal-mol^{-1} at 375 and 400 K.

To determine the effect of the composition of the adlayer on the kinetics of the surface reaction, a series of experiments were carried out at a constant CO partial pressure (3.8×10^{-9} Torr) and a varying oxygen partial pressure (between 6.8×10^{-9} and 3.4×10^{-8} Torr). Results similar to those presented in

Fig. 6 were obtained, and the activation energy of the surface reaction was evaluated for these various experimental conditions. These results are displayed in Fig. 7 (**36**). For small values of P_{O_2}/P_{CO}, the activation energy is virtually independent of the adlayer composition of which the latter is dictated by the surface temperature. The measured value of approximately 22 kcal-mol^{-1} is in excellent agreement with previous results in the low coverage limit on other platinum surfaces (**29,30**). Note that the *difference* between the activation energies for the desorption and the oxidation of CO was measured in this previous work to determine this low coverage value of the activation energy to reaction (29,30). For larger values of P_{O_2}/P_{CO}, the activation energy decreases markedly as the surface temperature is increased, as may be seen in Fig. 7.

To determine if this effect is related to structural changes in the overlayer, as has been postulated previously (**37**), the surface was monitored using LEED during all of the reaction conditions displayed in Fig. 7. For example, CO can form ordered superstructures on Pt(110) above coverages of 0.5, even removing the (1x2) clean surface reconstruction (**22**). In agreement with previous work (**22**), we observed a (1x1) LEED pattern at θ_{CO} = 0.5 and a p1g1(2x1) pattern at θ_{CO} = 1.0 in the presence of pure CO. On the other hand, in the presence of pure O_2, no ordered oxygen superstructures were observed for any coverage of oxygen adatoms which, again, is in agreement with previous experimental observations (**34**). Of most importance here, no ordered superstructures were observed during any reaction conditions; the (1x2) LEED pattern of the reconstructed surface was always maintained. However, upon reducing the temperature below approximately 375 K, the exact temperature depending on the partial pressure ratio P_{O_2}/P_{CO}, a (1x1) LEED pattern was observed concomitant to a complete extinguishing of the rate of production of CO_2. This latter observation suggests that a coverage of CO of θ_{CO} = 0.5 is sufficient to block completely the dissociative chemisorption of oxygen and, hence, the rate of oxidation of CO. Although separate disordered domains of CO(a) and O(a) remain a possibility (a *remote* possibility since adsorbate ordering is the major driving force for domain formation), a structural rearrangement of the overlayer seems unlikely as the cause of the observed behavior. Indeed, the presence of separate domains would imply the coexistence of high coverages of *both* reactants, which was not observed here based on our numerical calculations (see below) and is not observed at steady-state under

similar conditions (38,39).

An alternate, more reasonable explanation for the observed variation in the activation energy can be put forward. As stated earlier, high coverages of oxygen adatoms have been observed to have a profound effect on the activation barrier for the reaction, the observed large decrease having been attributed to a decrease in the binding energies of the adsorbed reactants (29). Fixing the level representing the transition state obviously results in a decrease in the barrier height. We believe a more plausible argument, however, includes a differential shift in *both the reactants and transition state*, the reactants shifting up more than the transition state (40).

Utilizing reaction rate measurements and the expressions for the rates of adsorption (both CO and O_2) and desorption (CO only) of the reactants determined from independent measurements and presented elsewhere (18), the adsorbate concentrations were calculated for the conditions shown in Fig. 7. The form of the calculated values as a function of temperature is in agreement with experimental measurements (38,39); i.e., there is a decrease in the CO coverage and a concomitant increase in the oxygen coverage as the temperature increases. As may be seen in Fig. 8, the variation of the activation energy of the surface reaction correlates well with fractional coverage of oxygen adatoms. Indeed, this is the *only* functional dependence of the activation energy of the elementary surface reaction on the composition of the adlayer that shows a consistent trend. Variation of the parameters used in the numerical model was found to result in differing absolute values for the coverage of oxygen (~±20%), while the *form* of the curve shown in Fig. 8 remained the same.

The variation of the activation energy with oxygen coverage is obviously quite nonlinear. In particular, the precipitous drop in the activation energy above $\theta_0 \cong 0.15$ suggests that configurational effects may be important. [Note that $\theta_0 = 0.4$ represents saturation (34,35).] In this picture, for $\theta_0 \leq 0.15$, CO admolecules are reacting with nearly independent oxygen adatoms, which are essentially equivalent to one another and isolated. However, for $\theta_0 > 0.15$ the adsorbed CO reacts in regions of higher (local) oxygen adatom concentration. This configuration of reactants serves to decrease the bond energy of the adsorbed reactants (3,41-44).

Examination of Eq. (29) of Part I (9) shows that if the particular functional form given by $x(\theta_1,\theta_2) = \theta_1\theta_2$ is chosen for the implicit coverage dependence [i.e., $r_r = x(\theta_1,\theta_2)k_r$] and coverage-dependent effects on the kinetic parameters are small and/or compensatory, the preexponential factor of the surface reaction rate coefficient can be calculated via the parameter $\nu_r^{(2)}$, provided the adsorbate coverages are known. We submit that this use of the parameter $\nu_r^{(2)}$ is valid for the reaction conditions represented in Fig. 8 if $\theta_0 \lesssim 0.15$. Due to the relatively low coverages of both reactants under these conditions (i.e., calculations indicate that $\theta_{CO} \lesssim 0.25$) adsorbate domain formation is unlikely. Since the temperature of reaction is relatively high, surface diffusion of CO is rapid, and the elementary surface reaction is certainly first order in the CO coverage. However, under these same conditions, the oxygen adatoms are relatively immobile (45). Nonetheless, provided all of the oxygen adatoms are *equivalent* and equally "accessible" which, in general, is valid at low coverages (where the adatoms are isolated), the surface reaction will also be first-order in the oxygen adatom coverage. Thus, since the activation energy is virtually independent of the adlayer composition below oxygen adatom coverages of approximately 0.15, we may assume that $\theta_{CO}^* + \theta_O^* = \theta_{CO} + \theta_O$ [see Eq. (29) of Part I (9)], and it follows directly that $k_r^{(2)} = \nu_r^{(2)}\exp(\varepsilon_r)/n_s(\theta_{CO} + \theta_O)$.

The values of the parameter $\nu_r^{(2)}$, corresponding to the reaction conditions of Fig. 7 and obtained via an analysis of data similar to those shown in Fig. 6, are displayed in Fig. 9. Utilizing these values, the measured values for the activation energies, and the calculated values for the adsorbate concentrations, we can calculate the corresponding values for the second-order preexponential factor of the reaction rate coefficient. These values of the preexponential factor are displayed in Fig. 8 as a function of the oxygen adatom concentration (46). Within experimental error, the preexponential factor is nearly independent of the adlayer composition below oxygen adatom coverages of approximately 0.15. In the limit of low coverages, the preexponential factor approaches a value of approximately 3×10^{-3} cm^2 $-s^{-1}$, accurate to within a factor of approximately five. This value for the low coverage limit of the preexponential factor is in excellent agreement with previous results on various surfaces of platinum (29), palladium (37) and rhodium (47), as well as the "normal" value of 10^{-2}–10^{-3} cm^2–s^{-1} predicted by transition state theory.

The preexponential factor has also been evaluated for oxygen adatom coverages above approximately 0.15. The validity of these calculations will be discussed below. We see that as the oxygen concentration increases beyond $\theta_O \cong 0.15$, the magnitude of the preexponential factor drops precipitously in concert with the activation energy, the rate parameters displaying compensatory behavior. For example, as the activation energy drops to a value of approximately 13 kcal-mol^{-1}, the preexponential factor decreases to a value of approximately 10^{-7} cm^2–s^{-1}, in agreement with previous work on other surfaces of platinum for similar oxygen adatom coverages, which were calculated in the same fashion (i.e., first order in θ_O) (**29,31**). As the activation energy continues to decrease to a value of approximately 8 kcal-mol^{-1}, the preexponential factor decreases further to a value of approximately 10^{-10} cm^2–s^{-1}.

Errors in the calculation of the preexponential factor for $\theta_O \gtrsim 0.15$ can arise from both coverage-dependent rate parameters, and the assumption of an incorrect implicit coverage dependence; i.e., $x(\theta_1,\theta_2) \neq \theta_1\theta_2$. Concerning the former, if the rate *parameters* compensate sufficiently for one another such that the rate *coefficient* is essentially independent of coverage, the calculation is valid. If the preexponential factors in Fig. 8 are the true values, it appears that significant compensation is indeed occurring. However, if the true preexponential factor is essentially constant, we find from the data in Fig. 8 that for $\theta_0 \cong 0.2$, $\{\theta_0\, \partial[E_r(\theta_0)/k_BT]/\partial\theta_0\}_s \cong -40$. Clearly, this value cannot totally account for the deviation of the preexponential factor by 10^7. Thus, if errors have been made in the calculation, the latter explanation is probably the major contributor; e.g., $x(\theta_{CO},\theta_O) = \theta_{CO}f(\theta_O)$, where $f(\theta_O) \ll \theta_O$.

Explanations for anomalously low apparent preexponential factors, such as those observed here at high oxygen adatom coverages have usually involved the following plausibility arguments: (1) effects due to adsorbate phase separation (**48**); and/or (2) abnormally high partition functions for the reactants resulting from the presence of "softened" vibrational modes for the adsorbed reactants (especially CO) (**31**). Concerning the latter, it is unlikely that an argument involving transition state theory and, for example, abnormally large vibrational partition functions for the reactants, could reasonably explain the apparent deviation of the preexponential factor by more than *seven* orders of magnitude. Concerning the former, the presence of oxygen adatom islands acts to limit the number of oxygen adatoms "accessi-

ble" for reaction with CO to those at the perimeter of islands [i.e., $x(\theta_1,\theta_2) \neq \theta_1\theta_2$ **(49)**]. This argument presupposes that the adsorption and/or reaction probability of CO is negligible within an oxygen adatom domain. If we assume that the islands are composed of a locally saturated oxygen adlayer (i.e., θ_O = 0.4), in order to account for the factor of 10^7 deviation of the preexponential factor the island diameter must be on the order of cm! Obviously, this size for an oxygen adatom island is physically unreasonable.

An alternate explanation for the apparently anomalously low preexponential factors can be put forward. We have argued that the decrease in the activation energy for $\theta_O \geq 0.15$ can be explained by a decrease in the binding energy of the reactants due to their local configuration. It is possible that this configuration of reactants occurs with a very low probability (i.e., on the order of 10^{-7}). Provided the relative reaction probability of this configuration of oxygen adatoms is much greater than that of isolated oxygen adatoms (e.g., due to a decrease in the binding energy of the oxygen adatoms in this configuration), this proposal would account for both an anomalously low preexponential factor and a lower activation energy of reaction, and it is consistent with other experimental observations (e.g., no deviation in overall rate). It is important to note that the rate parameters displayed in Fig. 8 are represented solely as a function of θ_O; i.e., they are independent of surface temperature. This result implies that this configuration of reactants is not intrinsically a function of surface temperature, which tends to rule out, for example, an equilibrium in the oxygen adlayer between low and high concentration adatom phases.

The results discussed above concerning the oxidation of CO emphasize the use of surface temperature modulation as an experimental tool for examining quantitatively the kinetics of elementary surface reactions. In the discussion that follows, we shall demonstrate that *mechanistic* information is also available. The predominance of the Langmuir-Hinshelwood mechanism in describing the oxidation of CO has been demonstrated clearly by Ertl et al. **(29,37)** on surfaces of platinum and palladium, and by Egelhoff et al. **(39,48)** on the (111) surface of iridium. We shall demonstrate that our experimental data support these conclusions.

By definition, the Langmuir-Hinshelwood mechanism involves a surface reaction between chem-

isorbed reactants, whereas the Eley-Rideal mechanism involves reaction between a chemisorbed reactant and a gas phase species (CO in this case) via direct collision or after adsorption into a weakly bound precursor state. For reaction via a direct collision, the rate may be expressed as $r_r = (F_{CO}/n_s)\theta_O k_r^{ER}(\theta_O,T)$. Thus, from the formalism developed in Sect. II.3 of Part I (**9**) [cf. Eq. (27)], we have $\chi_{CO} = 0$ and $\chi_O = (F_{CO}/n_s)k_r^{ER} = r_r/\theta_O$. We note that in this case the approximations inherent in the derivation of Eq. (28) will be satisfied only at low coverages of both species. This is valid for the data shown in Figs. 7 and 9 for the case of $P_{O_2}/P_{CO} = 1.8$. Thus, utilizing the expression $\nu_r^{(2)} = \chi_O = r_r/\theta_O$, the measured rate of reaction and the calculated coverages of oxygen (**50**), we find that the estimated values for the parameter $\nu_r^{(2)}$ are more than an order of magnitude smaller than those actually observed, which are shown in Fig. 9. Clearly, we can rule out any significant rate of reaction via the direct collision of gas phase CO with oxygen adatoms.

Reaction via a weakly bound precursor state of CO can also be discounted by the following argument. When the oxygen coverage is moderately high (i.e., $\theta_O \geq 0.10$) and the CO coverage is low ($\theta_{CO} << 1$), the partial derivative term with respect to θ_{CO} provides the dominant contribution to the parameter $\nu_r^{(2)}$. In addition, since the approximations inherent in the construction of Eq. (28) are satisfied for the reaction conditions examined here (verified by the experimentally measured system transfer function), we must have $\nu_r^{(2)} \cong \chi_{CO} = \theta_O k_r \gg k_d$, where k_d is the desorption rate coefficient for the reactive CO species. Consequently, $\nu_r^{(2)}$ can be used to specify a maximum desorption rate coefficient; or, equivalently, if we assume a reasonable value for the preexponential factor of the desorption rate coefficient, we can obtain a *minimum* value for the activation energy of desorption of CO. For example, utilizing $\nu_r^{(2)} = 1.5\ s^{-1}$ (i.e., $P_{O_2}/P_{CO} = 8.9$ and $T_s = 400$ K in Fig. 9) and $k_d^{(1)} = 10^{13}\ s^{-1}$, we find $E_{d,min} \cong 23$ kcal–mol^{-1}. This value for the desorption energy is beyond any reasonable value appropriate for a precursor state and obviously represents chemisorbed CO. Thus, the Langmuir-Hinshelwood mechanism is the only viable explanation for the experimental results.

IV. Conclusions

Surface temperature modulation (**8,9**) has been employed to investigate the interaction of CO with

the Pt(110)-(1x2) surface and the oxidation of CO by oxygen on this same surface. The adsorption-desorption equilibrium of CO was studied to determine the kinetic parameters describing the desorption reaction. These kinetic parameters were found to vary in sympathy with coverage, decreasing in magnitude as the coverage increases. Extrapolating to zero coverage, we find values for the activation energy of $E_d = 36 \pm 1.5$ kcal-mol^{-1} and for the preexponential factor of $k_d^{(1)} = 3 \times 10^{14}$ s^{-1}. By including trapping effects due to the presence of a precursor state, the value of the preexponential factor associated with the elementary reaction, CO(a) $\rightarrow$ CO*(a), may be as large as 1×10^{15} s^{-1} in the zero coverage limit. However, these two values are indistinguishable due to the experimental uncertainty (approximately a factor of five). The behavior of the kinetic parameters with coverage and the estimated values for the zero coverage limit are in excellent agreement with previously published results (**21-23**).

The oxidation of CO on Pt(110) was studied with particular emphasis on an examination of the elementary bimolecular surface reaction CO(a) + O(a) $\rightarrow$ CO_2(g). Despite the large number of fundamental studies directed at examining this surface reaction (**3**), surprisingly little quantitative information has been obtained concerning the variation of the kinetic parameters with surface coverage. Typically, measurements have been made under nonsteady-state conditions and/or only for limiting cases representing extremes in the composition of the adlayer (i.e., low coverages of both species, or relatively high oxygen adatom coverages).

The activation barrier for the elementary bimolecular surface reaction has been evaluated here in a direct fashion at a variety of steady-state conditions. The observed activation energy ranges between approximately 22 and 8 kcal-mol^{-1}. Calculations show that the coverages of both adsorbed reactants vary considerably for the conditions studied here. A strong correlation was found between the magnitude of the activation barrier and the coverage of oxygen adatoms. A precipitous drop in the magnitude of the activation barrier was observed as the fractional coverage of oxygen adatoms increased above approximately 0.15, the variation in the magnitude of the activation energy with oxygen coverage being quite nonlinear. This result is interpreted qualitatively as a manifestation of the crucial role that the local configuration of the reactants plays in determining the surface reaction dynamics. At relatively high oxygen coverages ($\theta_O \geq 0.15$), adsorbed CO reacts in regions of high local oxygen adatom concen-

tration. In these regions of the surface, the adsorbed reactants have reduced binding energies that lead directly to a decrease in the activation energy for the production of CO_2.

The preexponential factor for the elementary bimolecular surface reaction has been evaluated also for these reaction conditions. A value of $k_r^{(2)} = 3 \times 10^{-3}$ cm^2–s^{-1} was found for the low coverage limit, whereas concomitant with the variation of the activation energy, the magnitude of the preexponential factor drops precipitously as the oxygen coverage increases (i.e., $\theta_O \geq 0.15$), to an apparent value as low as 10^{-10} cm^2–s^{-1} at $\theta_O \cong 0.25$. The major factor contributing to this marked decrease in the preexponential factor is probably associated with the probability of occurrence (i.e. the concentration) of oxygen adatoms of high local density, not with the formation of separate adsorbate domains. In particular, we submit that the configuration of reactants leading to the observed decrease in the activation energy may occur with a very low probability (on the order of 10^{-7}). This, then, would explain the anomalously low preexponential factors at high oxygen adatom concentrations. Finally, knowledge of the approximate residence time of the adsorbed CO (i.e., $\tau_r \cong 1/\nu_r^{(2)}$) has demonstrated clearly that the CO oxidation reaction proceeds via the reaction of chemisorbed CO with oxygen adatoms; i.e., the Langmuir-Hinshelwood mechanism dominates.

In conclusion, a number of improvements to the surface temperature modulation technique as employed here come to mind. First, certainly for the frequencies used here, the technique can be coupled with time-resolved surface spectroscopies (**51-54**) or diffraction techniques (**55**) in order to provide direct complementary information concerning the composition and configuration of the adlayer. Specifically, time-resolved measurements of the fractional coverages of the adsorbed reactants could identify explicitly the adsorbate transfer functions [e.g., $\mathbf{H}''(p)$ of Eq. (27) of Part I (**9**)]. Combined with an evaluation of the system transfer function via measurements of the gas phase reaction product [e.g., $G''(p) \equiv 1 + \boldsymbol{\chi} \cdot \mathbf{H}''(p)/b_r$ of Eq. (27)], the partial derivative terms contained in the column vector $\boldsymbol{\chi}$ can be calculated. In principle, the variation of the partial derivative terms with respect to the fractional coverage of the adsorbed reactants could be used to deduce the form of the implicit coverage dependence of a bimolecular surface reaction (**56**). Alternatively, the energetics of (reversible) interconversion between stable surface species could be examined by the use of an appropriate surface spec-

troscopy coupled with a modulation in surface temperature. In this case, the formalism developed previously for homogeneous chemical kinetics should be sufficient (57).

Finally, the combined use of conventional, line-of-sight, differentially pumped mass spectrometric detection and laser heating techniques (58) would provide higher frequencies of the temperature forcing function. This would extend considerably the frequency bandwidth of the technique. Since direct measurement of the time evolution of the surface temperature produced by laser heating would be difficult if not impossible, a calibration procedure would have to be implemented, e.g., by considering a system for which the amplitude and phase response could be predicted by independent measurements. The adsorption-desorption equilibrium of CO detailed here should provide an ideal system for calibration purposes.

Acknowledgment: This work was supported by the National Science Foundation under Grant No. CHE-8516615.

References

1. See, e.g., T. Engel and G. Ertl, Advan. Catal. **20**, 1 (1979), and references therein.

2. See, e.g., S.-S. Sung and R. Hoffmann, J. Am. Chem. Soc. **107**, 578 (1985), and references therein.

3. G. Ertl in *Catalysis, Science and Technology*, J. R. Anderson and M. Boudart, Eds., Springer-Verlag, Berlin, 1983, p. 209; T. Engel and G. Ertl, Advan. Catal. **28**, 1 (1979).

4. I. Langmuir, Trans. Faraday Soc. **17**, 621 (1922).

5. J. Segner, C. T. Campbell, G. Doyen and G. Ertl, Surface Sci. **138**, 505 (1984).

6. L. S. Brown and S. L. Bernasek, J. Chem. Phys. **82**, 2110 (1985).

7. D. A. Mantell, K. Kunimori, S. B. Ryali, G. L. Haller and J. B. Fenn, Surface Sci. **172**, 281 (1986).

8. J. R. Engstrom and W. H. Weinberg, Phys. Rev. Letters **55**, 2017 (1985).

9. J. R. Engstrom and W. H. Weinberg, J. Chem Phys., submitted.

10. J. L. Taylor, D. E. Ibbotson and W. H. Weinberg, J. Chem. Phys. **69**, 4298 (1978).

11. H. Niehus and G. Comsa, Surface Sci. **102**, L14 (1981); H. Niehus and G. Comsa, Surface Sci. **93**, L147 (1980).

12. See, e.g., A. M. Lahee, W. Allison, R. F. Willis and K. H. Rieder, Surface Sci. **126**, 654 (1983); H. Niehus, Surface Sci. **145**, 407 (1984).

13. G. L. Kellogg, Phys. Rev. Letters **55**, 2168 (1985).

14. D. E. Ibbotson, T. S. Wittrig and W. H. Weinberg, Surface Sci. **110**, 294 (1981).

15. J. R. Engstrom and W. H. Weinberg, Rev. Sci. Instrum. **55**, 404 (1984).

16. E. O. Bingham, *The Fast Fourier Transform*, Prentice-Hall, Englewood Cliffs, N.J., 1974.

17. R. H. Jones, D. R. Olander, W. J. Siekhaus and J. A. Schwarz, J. Vacuum Sci. Technol. **9**, 1429 (1972).

18. J. R. Engstrom, PhD Thesis, California Institute of Technology, 1986.

19. S. J. Green and T. W. Hunt, in *Temperature*, Vol. 3, Pt. 2, C. M. Herzfeld and A. I. Dahl, Eds., Reinhold, N.Y., 1962, p. 695.

20. Beam doser pressures are calibrated such that the effective flux is calculated by using a gas phase temperature of 300 K.

21. J. A. Fair and R. J. Madix, J. Chem. Phys. **73**, 3480 (1980).

22. T. E. Jackman, J. A. Davies, D. P. Jackson, W. N. Unertl and P. R. Norton, Surface Sci. **120**, 389 (1982).

23. C. M. Comrie and R. M. Lambert, J. Chem. Soc. Faraday Trans. I **72**, 325 (1975).

24. R. W. McCabe and L. D. Schmidt, Surface Sci. **60**, 85 (1976).

25. For precursor-mediated adsorption an exact step-function change in the rate of irreversible adsorption or "uptake" cannot be obtained due to the presence of the precursor state. Utilizing the specific forms for the rate expressions consistent with Eq. (15) of Ref. 9 and assuming that adsorption into the chemisorbed state is irreversible, whereas adsorption into the precursor state is reversible, we find that for a step-function change in the reactant flux the resulting response in the rate of irreversible adsorption is proportional to $u(t)\{1 + [(1 - \alpha)/\alpha]\exp(-a_{22}t)\}$, where α is the probability of chemisorption from the precursor state, and $a_{22} = 1/\tau_2$ is the reciprocal of the average residence time in the precursor state. Thus, if $a_{22} \gg 1/\tau$ or $\alpha \cong 1$, the response of the rate of irreversible adsorption approximates a step-function change with respect to the response of the gas phase product signal; i.e., if the precursor state is short-lived with respect to the pumping time constant, the rate of irreversible adsorption will approximate a step-function change.

26. D. A. King and M. G. Wells, Surface Sci. **29**, 454 (1972).

27. J. A. Nelder and R. Mead, Computer J. **7**, 308 (1965).

28. Alternatively, if the pumping time constant τ is considered to be a *parameter* (i.e., a three-, rather than a two-parameter fit), the values estimated by the least-squares procedure are within approximately 10% of the independently measured values.

29. C. T. Campbell, G. Ertl, H. Kuipers and J. Segner, J. Chem. Phys. **73**, 5862 (1980).

30. N. Pacia, A. Cassuto, A. Pentenero and B. Weber, J. Catal. **41**, 455 (1976).

31. J. A. Fair and R. J. Madix, J. Chem. Phys. **73**, 3486 (1980).

32. In the calculation of the product signal $N_3^{\dagger}$, this constant background level is subtracted from the total signal.

33. The poppet valve separating the reaction chamber from the ion pumps was partially closed during these experiments to improve the back-mixing properties of the reactor and to minimize concentration gradients in the gas phase product. Thus, the measured time constants are larger than would be obtained were the poppet valve totally open.

34. M. Wilf and P. T. Dawson, Surface Sci. **65**, 399 (1977).

35. N. Freyer, M. Kiskinova, G. Pirug and H. P. Bonzel, Surface Sci. **166**, 206 (1986).

36. The data given by partial pressure ratios of P_{O_2}/P_{CO} = 3.2 and 5.5 represent the average values of two different experiments carried out under identical conditions. The values obtained for the activation energies (parameter $\nu_r^{(2)}$) were within approximately ±1 kcal-mol^{-1} (±20%) of the resulting mean values.

37. T. Engel and G. Ertl, J. Chem. Phys. **69**, 1267 (1978).

38. T. Matsushima, D. B. Almy and J. M. White, Surface Sci. **67**, 89 (1977); A. Golchet and J. M. White, J. Catal. **53**, 266 (1978).

39. P. A. Zhdan, G. K. Boreskov, W. F. Egelhoff and W. H. Weinberg, Surface Sci. **61**, 377 (1976).

40. K. J. Laidler, *Theories of Chemical Reaction Rates*, McGraw-Hill, New York, N.Y. 1969; M. G. Evans and M. Polanyi, Trans. Faraday Soc. **34**, 11 (1938).

41. J. L. Taylor, D. E. Ibbotson and W. H. Weinberg, Surface Sci. **90**, 37 (1979).

42. G. E. Thomas and W. H. Weinberg, J. Chem. Phys. **70**, 954 (1979).

43. H. Conrad, G. Ertl and J. Küppers, Surface Sci. **76**, 323 (1978).

44. J. L. Taylor, D. E. Ibbotson and W. H. Weinberg, Surface Sci. **79**, 349 (1979).

45. R. Lewis and R. Gomer, Surface Sci. **12**, 157 (1968).

46. The ordinate axes in Fig. 8 have been scaled to correspond to an "isokinetic temperature" of T_{iso} = 437 K. If the parameters compensate exactly for one another, then a differential change in the coverage (of oxygen in this case) will result in no change in the value of the reaction rate coefficient; i.e., by definition $\partial(k_B T_{iso} \ln k_r^{(2)} - E_r)/\partial\theta = 0$.

47. C. T. Campbell, S. K. Shi and J. M. White, J. Vacuum Sci. Technol. **16**, 605 (1979).

48. V. P. Ivanov, G. K. Boreskov, V. I. Savchenko, W. F. Egelhoff and W. H. Weinberg, J. Catal. **48**, 299 (1977).

49. For examples of model rate expressions that describe bimolecular surface reactions in which adsorbate domain formation occurs, see, for example, D. Mukesh, W. Morton, C. N. Kenney and M. B. Cutlip, Surface Sci. **138**, 237 (1984).

50. Note that the coverages are calculated without the need to invoke a mechanism for the bimolecular surface reaction.

51. M. Balooch, D. R. Olander, J. Abrefah and W. J. Siekhaus, Surface Sci. **149**, 285 (1985).

52. G. W. Rubloff, Surface Sci. **89**, 566 (1979); F. Steinbach and J. Schütte, Rev. Sci. Instrum. **54**, 1169 (1983).

53. W. Ho, J. Vacuum Sci. Technol. A **3**, 1432 (1985); B. A. Gurney and W. Ho, J. Vacuum Sci. Technol. A **33**, 1541 (1985).

54. D. A. Mantell, S. B. Ryali and G. L. Haller, Chem. Phys. Letters **102**, 37 (1983); D. A. Mantell, K. Kunimori, S. B. Ryali and G. L. Haller, Am. Chem. Soc. Div. Pet. Chem. Prep. 29, 904 (1984).

55. M. P. Cox, G. Ertl and R. Imbihl, Phys. Rev. Letters **54**, 1725 (1985); E. Lang, P. Heilmann, G. Hanke, K. Heinz and K. Müller, Appl. Phys. **19**, 287 (1979).

56. For example, if $x(\theta_1,\theta_2) = \theta_1\theta_2$ then $\chi_i = k_{r,s}\theta_j^*$, where (i,j) = (1,2) and (2,1); and θ_j^* is proportional to θ_j and is given by Eq. (29) of Ref. 9.

57. M. Eigen, Discuss. Faraday Soc. **17**, 194 (1954); M. Eigen and L. Maeyer, *Technique of Organic Chemistry*, Vol. 8, Pt. 2, Ed., A. Weissberger, Wiley, N.Y., 1963, p. 895.

58. T. J. Chuang, Surface Sci. Reports **3**, 1 (1983).

Figure Captions

Figure 1: Amplitude ratio (AR) and phase difference of the function $T_m'(p)/T_{av}'(p)$, where T_m' is the deviation of the measured temperature from its steady-state value, T_{av}' is the deviation of the spatially averaged temperature, and $p = i\omega$. (Note that $T_{m,s} = T_{av,s}$.) The circles represent the measured response, and the solid lines represent the predicted theoretical response utilizing a radial thermal time constant of $\tau_r = 1.27$ s.

Figure 2: Amplitude ratio (AR) and phase difference data representing the system transfer function $(\tau p + 1)N_g^\dagger(p)/T^\dagger(p) \equiv G(p)$, given by Eq. (15) of Part I (9), for the reaction $CO(g) \underset{\leftarrow}{\rightarrow} CO(a)$. The insensitivity of the response with respect to the amplitude of the temperature forcing function demonstrates the validity of the linearity assumption. Note the two different temperature scales.

Figure 3: Experimental data representing the system transfer function G(p), given by Eq. (15) of Part I (9), shown as a function of frequency in terms of the amplitude ratio (AR) and phase difference. The solid lines represent least-squares fits to Eqs. (9a) and (9b) of Part I (9), where $\nu_d = \nu_d^*$ and $\varepsilon_d = \Delta\varepsilon_h^*$, i.e., $AR(\omega) = S_s\eta\Delta\varepsilon_h^*/[(\nu_d^*/\omega)^2 + 1]^{1/2}$ and $\phi(\omega) = \tan^{-1}(\nu_d^*/\omega)$.

Figure 4: Activation energy E_d and preexponential factor $k_d^{(1)}$ of the desorption rate coefficient of CO from Pt(110) as a function of the surface coverage. $\theta_{CO} = 1$ is equivalent to 0.92×10^{15} molec-cm^{-2}. The open circles and solid line were calculated by assuming that the desorption reaction is direct, whereas the dashed line was calculated by assuming that desorption proceeds through a precursor state (see text). The values displayed on the ordinate were obtained by MMBRS (21).

Figure 5: Amplitude ratio (AR) and phase difference data representing the system transfer function $(\tau p + 1)N_3^\dagger(p)/T^\dagger(p) \equiv \varepsilon_r G''(p)$, given by Eq. (27) of Part I (9), for the reaction $CO(a) + O(a) \rightarrow CO_2(g)$. The insensitivity of the response with respect to the amplitude of the temperature forcing function demonstrates the validity of the linearity assumption. Note the two different temperature scales.

Figure 6: Experimental data representing the system transfer function $\varepsilon_r G''(p)$ given by Eq. (27) of Part I (9), shown as a function of frequency in terms of the amplitude ratio (AR) and phase difference. The solid lines represent least-squares fits to Eq. (28) of Part I (9), i.e., $AR(\omega) = \varepsilon_r/[(\nu_r^{(2)}/\omega)^2 + 1]^{1/2}$ and $\phi(\omega) = \tan^{-1}(\nu_r^{(2)}/\omega)$.

Figure 7: Activation energy for the surface reaction CO(a) + O(a) $\rightarrow$ CO_2(g) as a function of the surface temperature. $P_{CO} = 3.8 \times 10^{-9}$ Torr (20).

Figure 8: Activation energy and second-order preexponential factor for the surface reaction CO(a) + O(a) $\rightarrow$ CO_2(g) as a function of the calculated coverage of oxygen adatoms θ_O, where θ_O = 0.4 is saturation.

Figure 9: Apparent rate coefficient [$\nu_r^{(2)}$ of Eq. (28) of Part I (9)] of the surface reaction CO(a) + O(a) $\rightarrow$ CO_2(g) for the reaction conditions corresponding to the data given in Fig. 7. $P_{CO} = 3.8 \times 10^{-9}$ Torr (20).

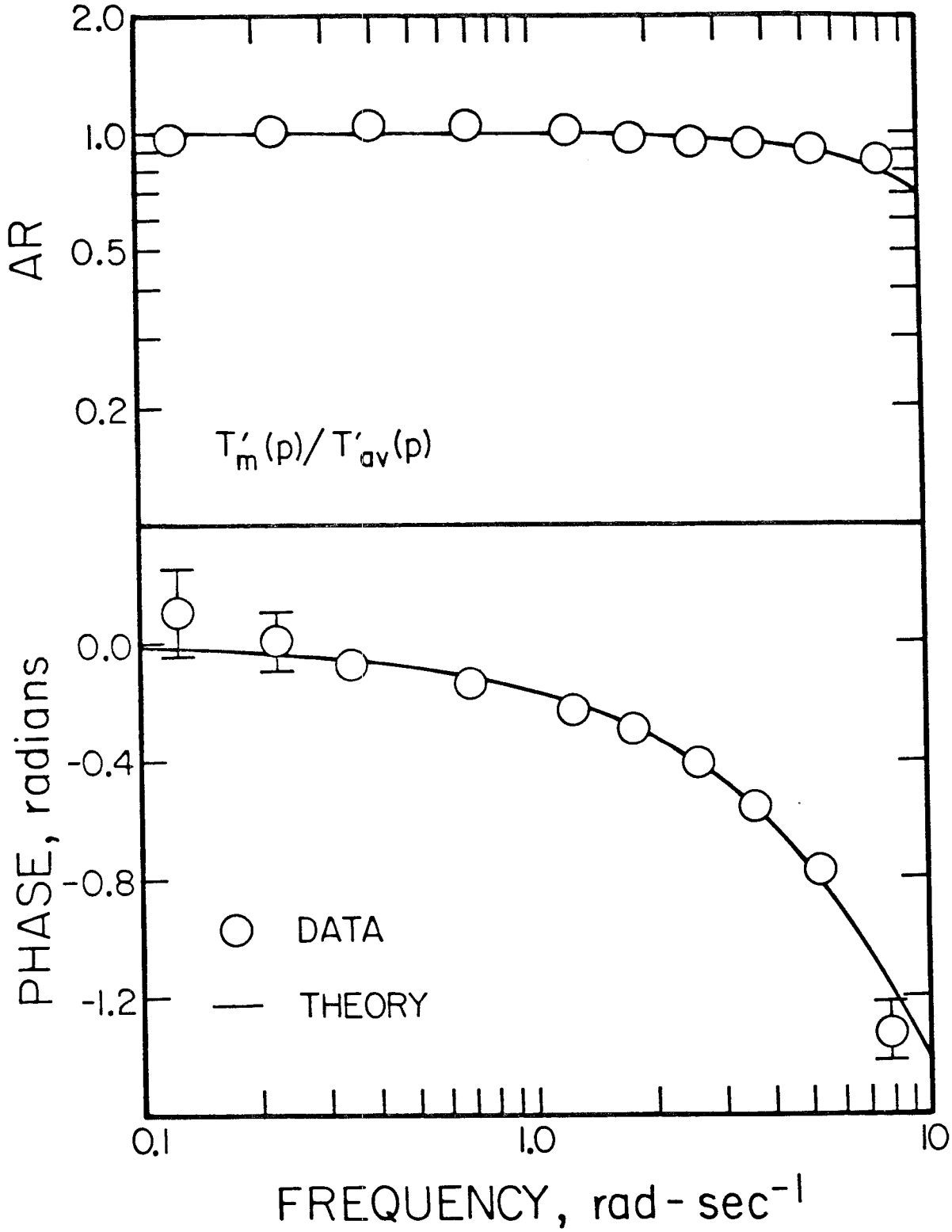
2.0
1.0
0.5
0.2
AR
$T'_m(p)/T'_{av}(p)$
0.0
-0.4
-0.8
-1.2
PHASE, radians
DATA
THEORY
0.1
1.0
10
FREQUENCY, rad-sec^{-1}

Figure 1

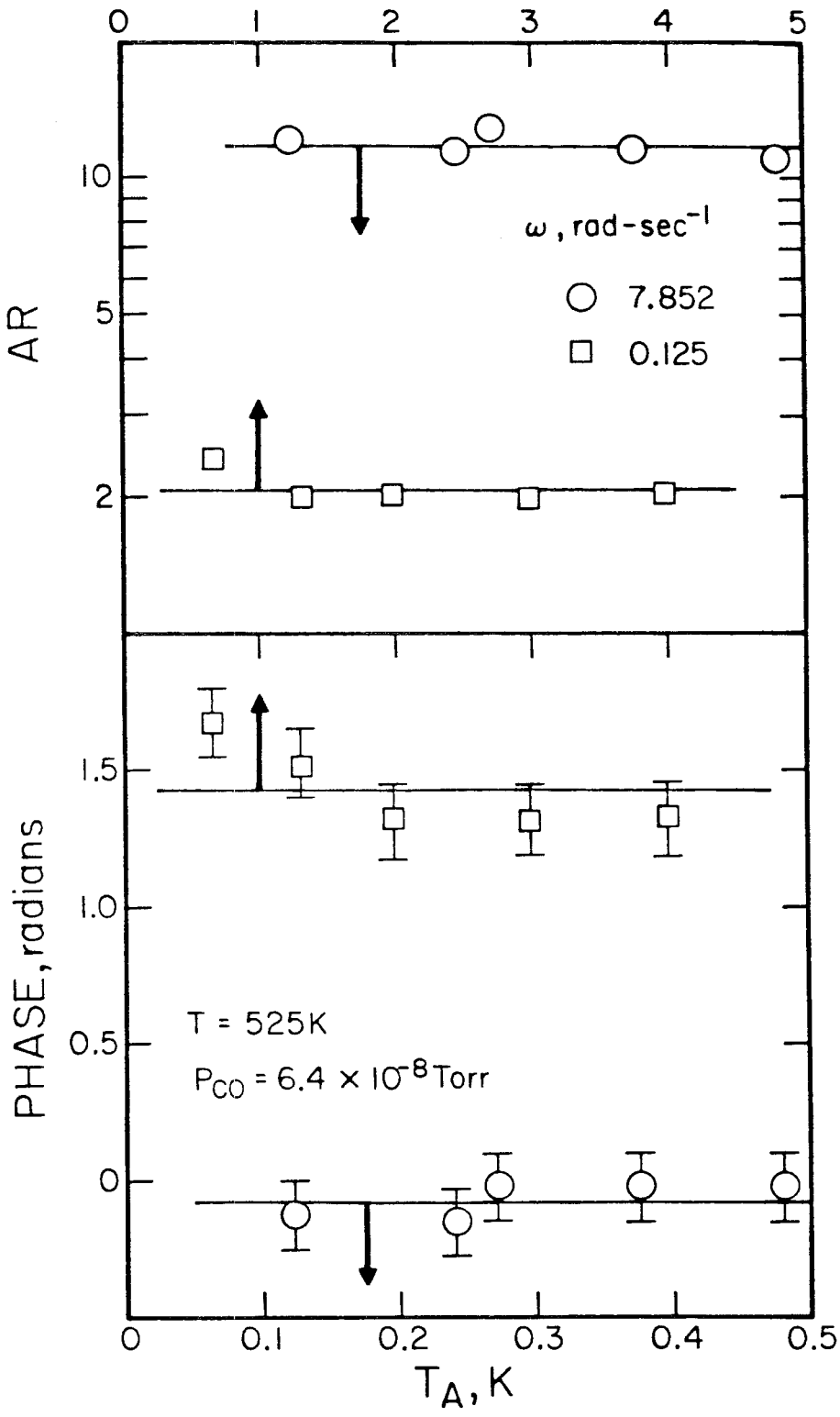
0
1
2
3
4
5
10
5
2
AR
ω, rad-sec⁻¹
7.852
0.125
1.5
1.0
0.5
0
PHASE, radians
T = 525K
P_CO = 6.4 × 10⁻⁸ Torr
0
0.1
0.2
0.3
0.4
0.5
T_A, K

Figure 2

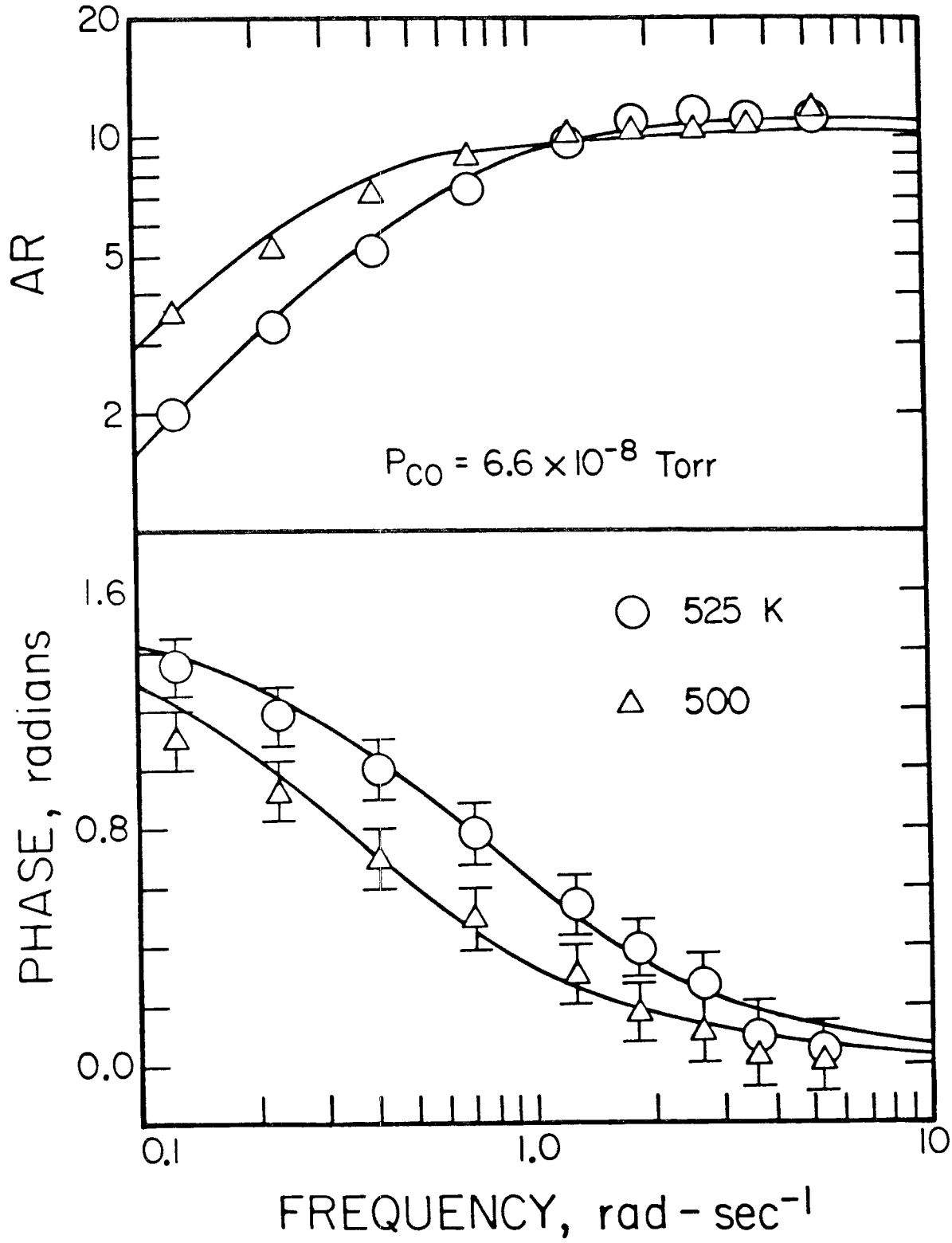
20
10
5
2
AR
$P_{CO} = 6.6 \times 10^{-8}$ Torr
1.6
0.8
0.0
PHASE, radians
525 K
500
0.1
1.0
10
FREQUENCY, rad - sec^{-1}

Figure 3

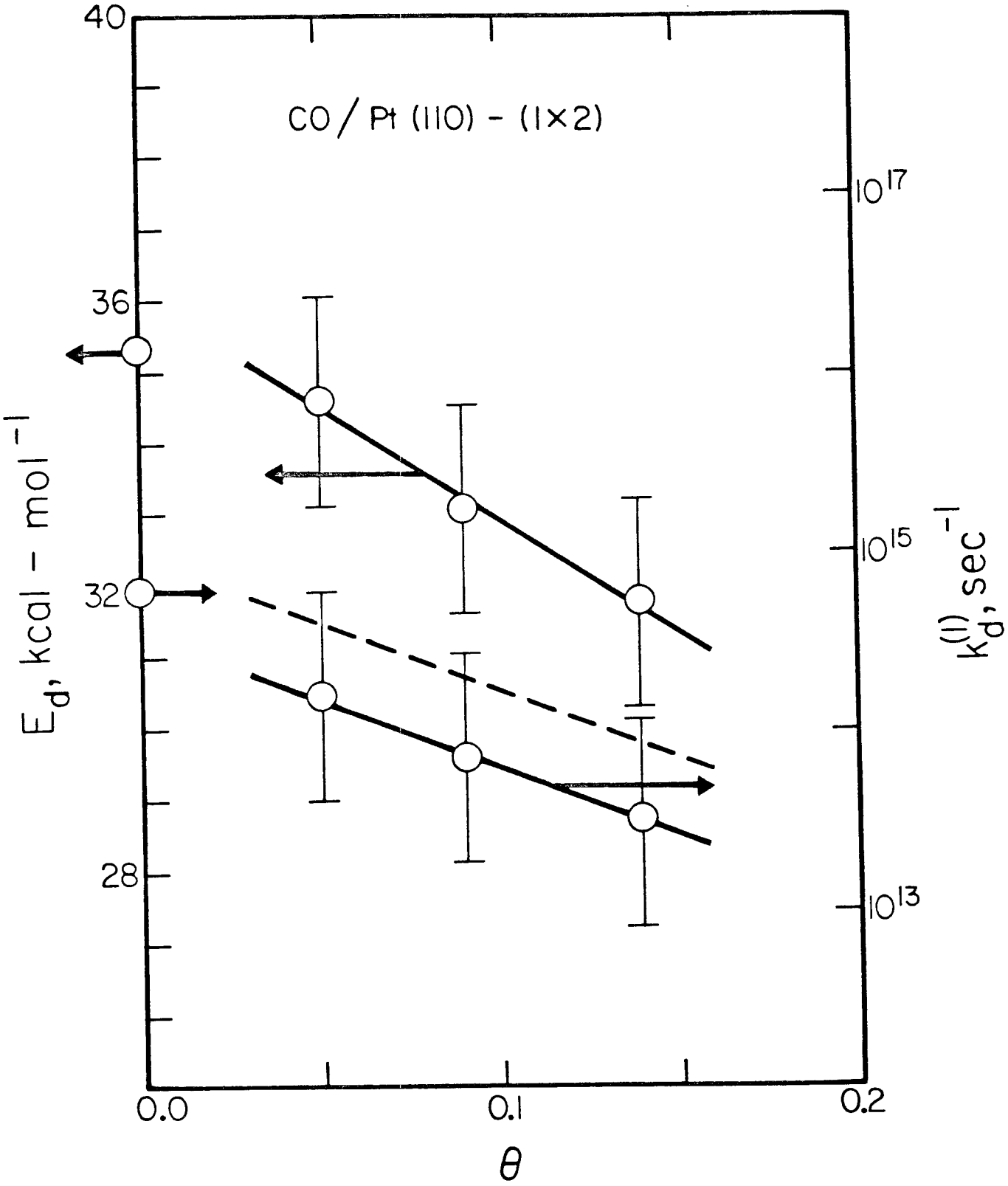
CO / Pt (110) - (1×2)
40
36
32
28
E_d, kcal - mol^{-1}
10^{17}
10^{15}
10^{13}
$k_d^{(1)}$, sec^{-1}
0.0
0.1
0.2
θ

Figure 4

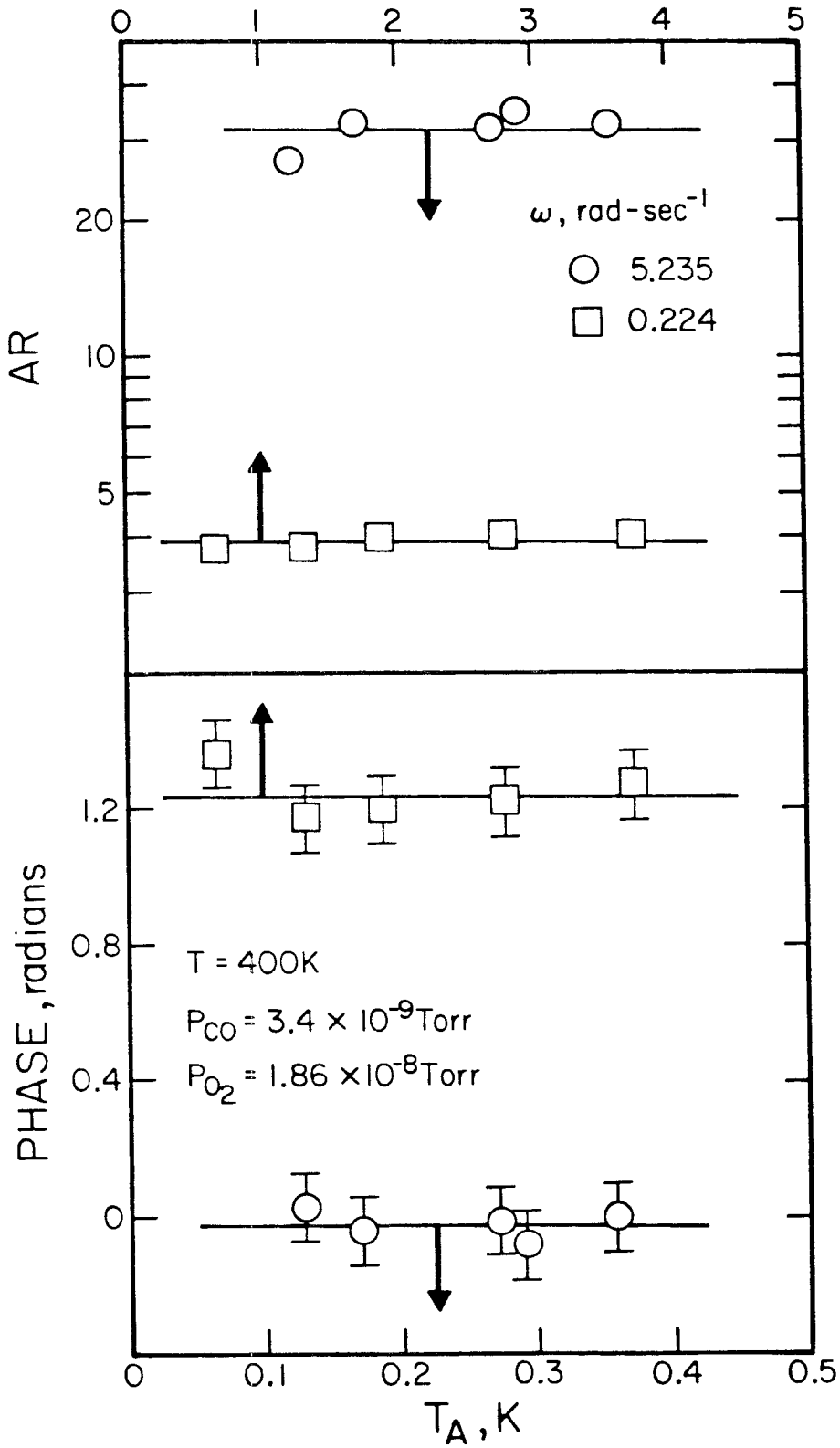
0
1
2
3
4
5
20
10
5
AR
ω, rad-sec⁻¹
5.235
0.224
1.2
0.8
0.4
0
PHASE, radians
T = 400K
P_{CO} = 3.4 × 10⁻⁹Torr
P_{O_2} = 1.86 ×10⁻⁸Torr
0
0.1
0.2
0.3
0.4
0.5
T_A, K

Figure 5

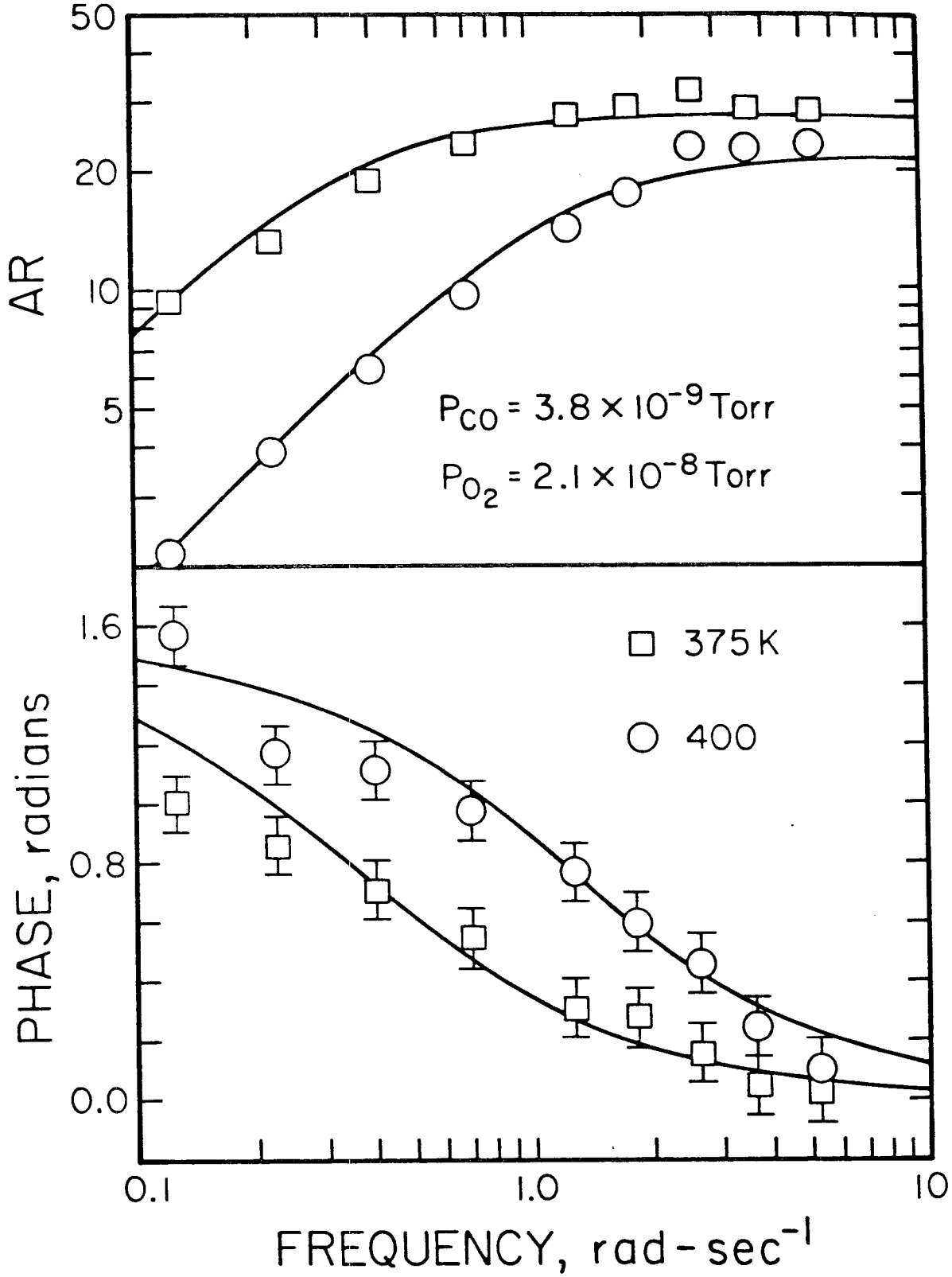
50
20
10
5
AR
$P_{CO} = 3.8 \times 10^{-9}$ Torr
$P_{O_2} = 2.1 \times 10^{-8}$ Torr
1.6
0.8
0.0
PHASE, radians
375 K
400
0.1
1.0
10
FREQUENCY, rad-sec^{-1}

Figure 6

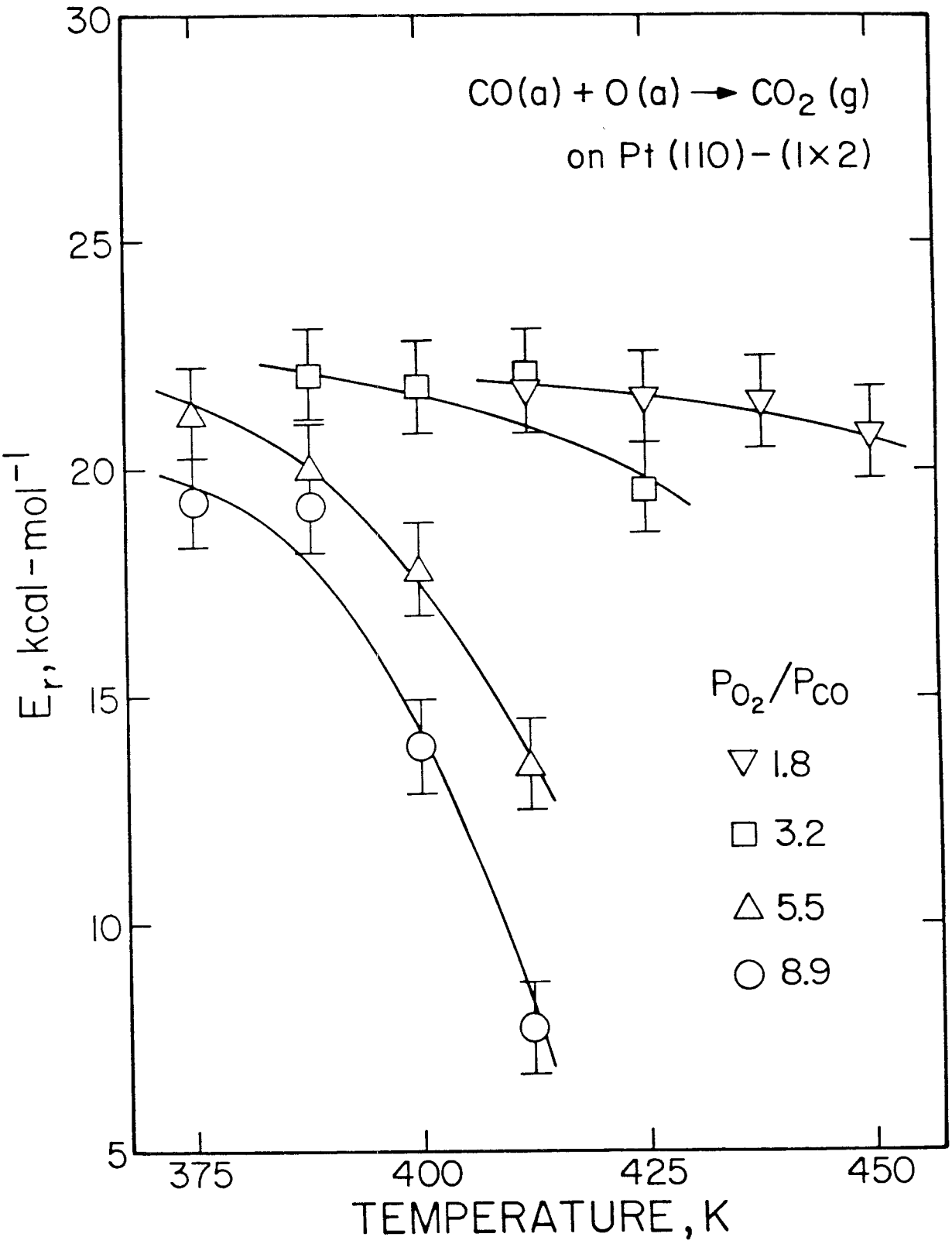
CO(a) + O(a) → CO2 (g)
on Pt (110)-(1×2)
Er, kcal-mol-1
TEMPERATURE, K
PO2/PCO
1.8
3.2
5.5
8.9
30
25
20
15
10
5
375
400
425
450

Figure 7

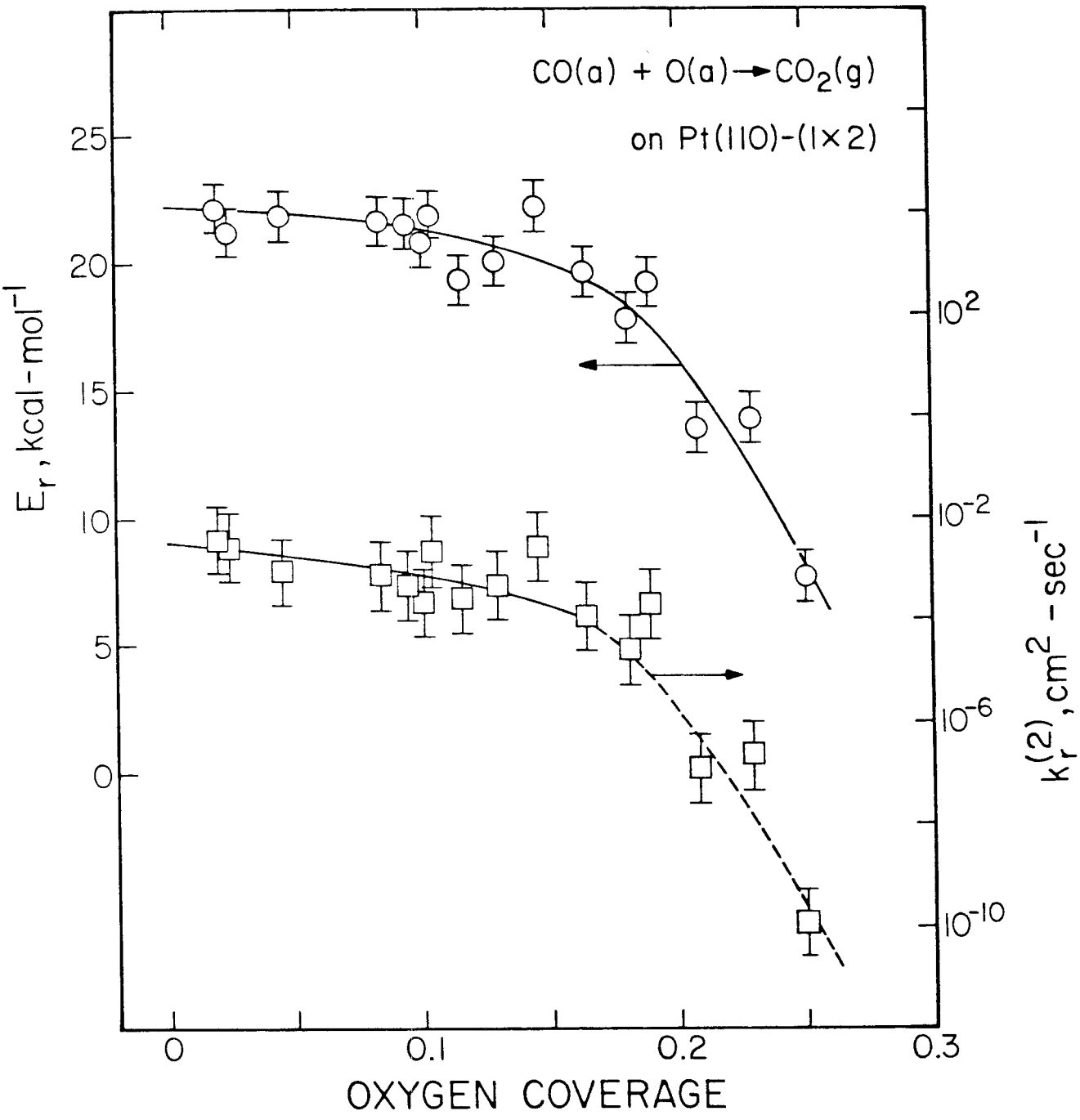
CO(a) + O(a)→CO2(g)
on Pt(110)-(1×2)
Er, kcal-mol-1
25
20
15
10
5
0
10^2
10^-2
10^-6
10^-10
kr(2), cm2 - sec-1
0
0.1
0.2
0.3
OXYGEN COVERAGE

Figure 8

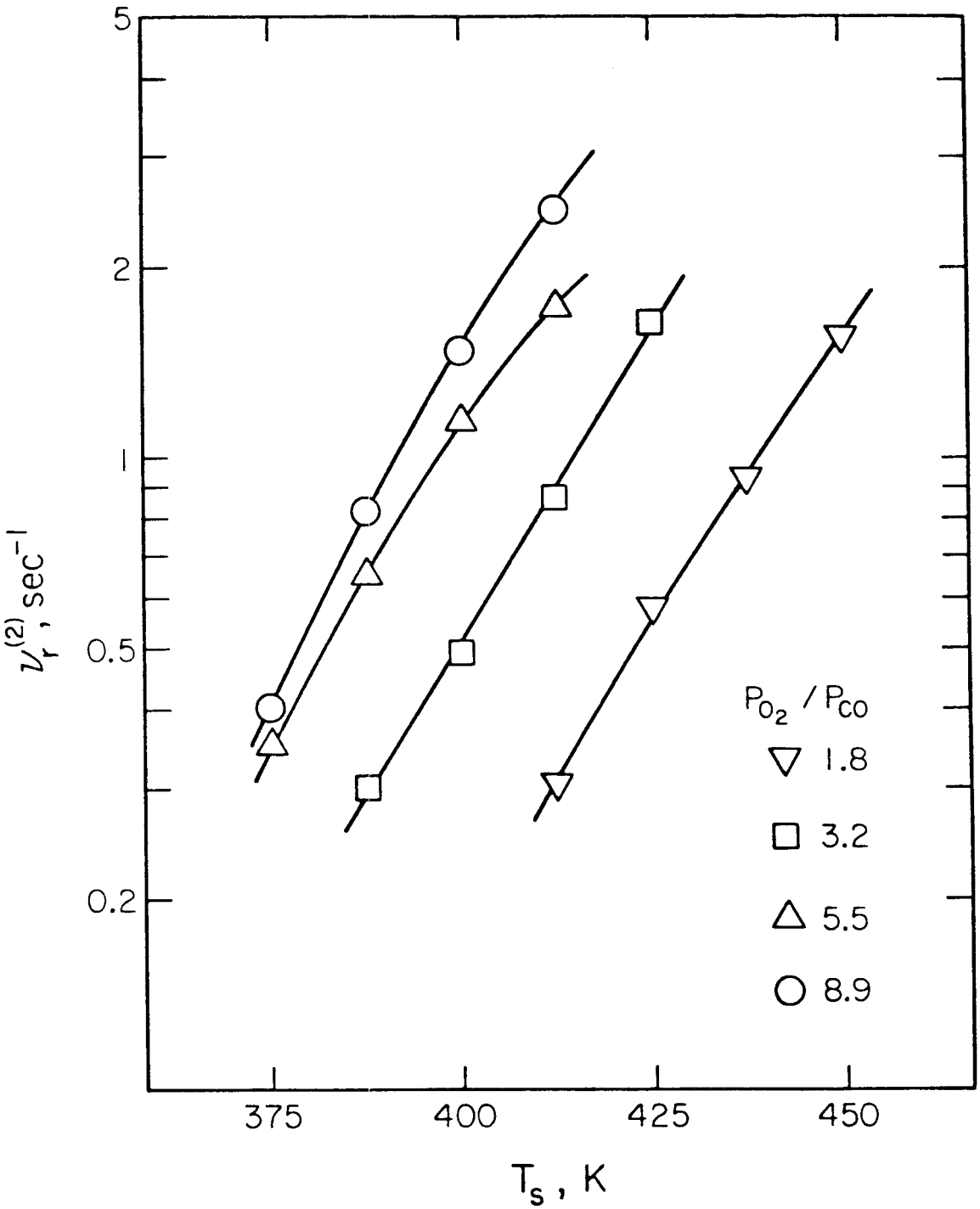

Figure 9

CHAPTER 4

The Chemisorption of Hydrogen on the (111) and (110)-(1x2) Surfaces of Iridium and Platinum

[The text of Chapter 4 consists of an article coauthored with W. Tsai and W. H. Weinberg, which has been submitted to *The Journal of Chemical Physics.*]

Abstract

The chemisorption of hydrogen on both the Ir(111) and Pt(110)-(1x2) surfaces has been examined under ultrahigh vacuum conditions with thermal desorption mass spectrometry, LEED and contact potential difference measurements. No ordered adsorbate superstructures were observed on either surface for partial pressures of hydrogen from 10^{-9} to 10^{-6} Torr and surface temperatures from 100 to 700 K, and the (1x2) reconstruction of the Pt(110) surface was stable under these same conditions. Hydrogen adsorbs dissociatively on the Ir(111) surface, the adsorption reaction described by second-order Langmuir kinetics with an initial probability of adsorption of 7×10^{-3}. The rate parameters describing the second-order desorption reaction of hydrogen from the Ir(111) surface are weakly dependent on coverage between fractional coverages of 0.1–0.3 and are given by $E_d \simeq 12.6$ kcal-mol^{-1} and $k_d^{(2)} \simeq 2 \times 10^{-6}$ cm^2-s^{-1}. However, beyond a fractional coverage of 0.3, the rate parameters decrease with increasing coverage. Hydrogen adsorbs dissociatively on the Pt(110)-(1x2) surface into two distinct adstates, the β_2 and β_1, the ratio of the saturation densities of the two states, β_2:β_1, being 1:2. Adsorption into the higher binding energy β_2-adstate is described by first-order Langmuir kinetics with an initial probability of adsorption of 0.46, whereas adsorption into the β_1-adstate is described by second-order Langmuir kinetics and an initial probability of adsorption of 0.022. The rate parameters describing the desorption reaction of hydrogen from the Pt(110)-(1x2) surface have been found to be *strongly* dependent on the coverage. In the coverage regime characteristic of the β_2-adstate ($\theta < 0.32$) the rate parameters are approximately symmetric about one-half of saturation of this state. Specifically, from the values for the zero-coverage limit of $E_d \simeq 18$ kcal-mol^{-1} and $k_d^{(2)} \simeq 10^{-4}$ cm^2-s^{-1}, the parameters first increase to maximum values of $E_d \simeq 26.5$ kcal-mol^{-1} and $k_d^{(2)} \simeq 0.3$ cm^2-s^{-1} at $\theta = 0.15$ and subsequently decrease approximately to the values for the zero coverage limit at $\theta = 0.32$. In the coverage regime characteristic of the β_1-adstate ($\theta > 0.32$), the activation energy decreases

continuously with increasing coverage from a value of $E_d \simeq 17$ kcal-mol^{-1} at $\theta = 0.35$, whereas the preexponential factor remains essentially constant with a value of 3×10^{-4} cm^2-s^{-1}. The contact potential difference for hydrogen on Pt(110)-(1x2) increases continuously with coverage to a value of 0.17 eV at $\theta = 0.30$, while as the coverage increases further, it decreases continuously approaching a value of -0.50 eV, at saturation. Probable binding states for the β_2- and β_1-adstates on the Pt(110)-(1x2) surface are inferred from both the adsorption and desorption kinetics and the contact potential difference measurements. Comparisons of the results obtained on the (111) and (110)-(1x2) surfaces of both iridium and platinum suggest strongly that *local* surface structure has a profound influence on the kinetics of adsorption of hydrogen on these surfaces. Surface structure apparently also has a profound influence on the desorption kinetics of hydrogen via the mediation of adatom-adatom interactions. Whereas both attractive and repulsive interactions are clearly manifest within the β_2-adstates on the (110)-(1x2) surfaces, only repulsive interactions are apparent on the (111) and for the β_1-adstates on the (110)-(1x2) surfaces.

I. Introduction

The study of the interaction of hydrogen with transition metal surfaces is of considerable fundamental importance since, for example, the most reliable theoretical calculations can be carried out to describe these systems. In addition, hydrogen plays a central role in a multitude of technologically important catalytic reactions that occur on transition metal surfaces, such as hydrocarbon processing and Fischer-Tropsch synthesis. Other topics of technological interest include the embrittlement of materials by hydrogen and the possible use of transition metals as hydrogen storage media. Not surprisingly, a multitude of investigations have been concerned with the chemisorption of hydrogen on various single crystalline surfaces of transition metals **(1)**, including the Group VIII metals **(2–22)**.

The primary thrust of the work described here is concerned with a detailed examination of the effects of surface structure on the dynamics of the elementary surface reactions that describe the adsorption and desorption of hydrogen. Previous studies have indicated that the presence of surface defects in the form of atomic steps can influence profoundly the kinetics of the adsorption and desorption reactions. For example, the initial probability of adsorption at step sites is nearly unity at surface temperatures of approximately 100 K and gas temperatures of approximately 300 K, whereas the corresponding probability on the "perfect" (111) surfaces of fcc transition metals is typically lower by an order of magnitude **(2–17)**. Recent work on the Ni(111) surface and the considerably more corrugated Ni(110) surface indicates that the low probability of adsorption on the (111) surface can be explained by the presence of an activation barrier to dissociative adsorption, whereas adsorption on the (110) surface is essentially unactivated **(16)**. The activation barrier on the Ni(111) surface is on the order of 2 kcal-mol^{-1}, as judged by a continuous increase of the probability of adsorption with increasing normal translational energy of H_2. This viewpoint is supported by work examining the adsorption kinetics of hydrogen on the stepped Ni(997) surface **(17)**. The effect of

surface structure on the kinetics of the desorption reaction is manifest in a higher activation energy of desorption in the low coverage limit for hydrogen adsorbed at step sites compared to hydrogen adsorbed at (111) terrace sites **(3,9,13,15)**. Clearly, both the binding energy of the hydrogen adatom and the activation barrier of dissociative adsorption are influenced by the surface structure.

We present here new experimental data concerning the chemisorption of hydrogen on both the Ir(111) and the Pt(110)-(1x2) surfaces. These data are compared and contrasted both with data obtained previously in our laboratory concerning the chemisorption of hydrogen on the Ir(110)-(1x2) surface **(18)**, and with data obtained by a number of investigators concerning the chemisorption of hydrogen on the Pt(111) surface **(2–9,19–22)**. The comparison of the (111) and (110)-(1x2) surfaces of both iridium and platinum is motivated in part by similarities (in addition to the obvious differences) in the *local* surface structure between the two surfaces. In particular, the clean (110) surfaces of both iridium **(23)** and platinum **(24)** reconstruct to form (111) microfacets, which are three atomic rows in width, and which are inclined at an angle of 109.5° with respect to one another (see Fig. 1). Consequently, the presence of structurally similar threefold hollow adsites on each surface might be manifest in similar adsorption and desorption kinetics. However, the corrugated (110)-(1x2) surface possesses unique adsites as a consequence of its geometry (*e.g.*, high coordination "trough" sites, *cf.* Fig. 1 and site B), which might influence greatly the dynamics of both the adsorption and desorption of hydrogen, especially at low surface coverages. For example, it has been generally observed that hydrogen prefers the highest coordination adsites that are available **(1)**.

II. Experimental Procedures

The experiments described here were performed in an ion-pumped, stainless steel belljar that has been described previously in detail **(25)**. The base pressure of the belljar is below 5 x 10^{-11} Torr of reactive gases. Facilities are available

for experimental studies involving mass spectrometry, low-energy electron diffraction(LEED), x-ray and UV-photoelectron spectroscopies, and Auger electron spectroscopy. The Ir(111) and Pt(110) crystals were cut from single crystalline boules and were polished to within 0.5° of the appropriate orientations using standard metallographic techniques. The iridium (platinum) crystal was cleaned *in situ* by argon ion sputtering, heating in 5 x 10^{-7} Torr of oxygen at a temperature of 1100 K (700 K), and annealing to 1600 K (1400 K). Surface cleanliness was verified by Auger electron and x-ray photoelectron spectroscopies. Special care was taken to reduce the concentration of silicon impurity in the platinum sample to a negligible level, since Niehus and Comsa **(26)** have shown that its presence is related to the formation of a "subsurface oxide" on Pt(111).

Research grade (99.995%) hydrogen and deuterium were utilized without further purification. Deuterium was employed in a number of desorption experiments in order to increase the sensitivity (*i.e.*, the signal-to-noise ratio) of the mass spectrometric detection and to examine qualitatively the isotopic mixing of the adatoms on the surface. Exposures were effected either by backfilling the chamber or by employing a (calibrated) directional beam doser **(27)**. The beam doser consists of a multichannel array of capillaries, and the gases are admitted to the dosing line behind this array via a separate capillary leak from a glass storage bulb. The gas pressure in the storage bulb (which determines the pressure at the doser) was monitored by a MKS Baratron gauge. A glass enclosure was installed around the ion source of the mass spectrometer for the thermal desorption mass spectrometric (TDMS) experiments **(28)**. This glass enclosure permits the desorption products to be sampled preferentially from the front of the crystal, thus minimizing spurious signals originating from desorption from the edges of the crystal, the mounting wire leads and the manipulator.

The single crystals were spotwelded to Ta wire leads, which were mounted on a precision manipulator. Heating was effected by passing current through the wire leads/crystal circuit, while cooling was accomplished by conduction through

the wire leads to support blocks that were in thermal contact with a reservoir of flowing liquid nitrogen. The temperature was measured by a W/5%Re-W/26%Re thermocouple spotwelded to the back of the crystal and referenced to an icepoint junction. Accurate temperature control was maintained by the use of an optimal control scheme, described elsewhere **(29)**, which utilizes a laboratory microcomputer as the control element. This control scheme is well suited for the generation of linear temperature ramps that were used here in connection with the measurement of thermal desorption spectra. A wide range of heating rates can be realized, and the temporal temperature profiles are sufficiently reproducible to permit the averaging of spectra (following suitable baseline corrections) in order to increase the signal-to-noise ratio. The temperature control software has been designed both to control and to monitor the mass spectrometer, and a single routine provides data acquisition as well as control of the experiment **(30)**.

Contact potential difference (CPD) measurements were made by employing the AC retarding potential technique of Nathan and Hopkins **(31)**. A high-stability, low-noise and low-drift power supply (Kepco PCX 100-0.2MAT) was utilized to provide the appropriate potentials for the (LEED) electron gun (Varian 981-2125). A standard carbon battery provided the retarding bias, and a biquad band-pass filter (gain of 10, Q-factor of 100, tuned to 7 kHz) was used to condition the output from the collector (*i.e.*, the crystal). Noise margins were 5 mV, and the CPD measurements were reproducible to within less than 10 mV at a bandwidth of 10 Hz (beam energy $\sim$ 45 V and beam current $\sim$ 0.1 μA).

III. Results

A. LEED Observations

1. Ir(111)

Under all conditions examined, *i.e.*, partial pressures of hydrogen from 10^{-9} to 10^{-6} Torr and surface temperatures from 100 to 700 K, no ordered adsorbate superstructures were observed, as judged by the absence of any additional fractional order LEED beams. This result is not surprising, as ordered superstructures of hydrogen are rare for hexagonally close-packed surfaces [excluding the degenerate (1x1) overlayer, the presence of which has been inferred for hydrogen on Ru(001) **(32)**, Pd(111) **(13)** and Pt(111) **(33)**]. A notable exception is the p(2x2)-2H superstructure that has been observed for hydrogen on the Ni(111) surface **(34,35)**. This submonolayer ($\theta_H = 0.5$) superstructure might occur on Ni(111) due to the considerably smaller lattice constant characteristic of the first-row transition metals. Basing our conclusions solely on qualitative LEED observations, we cannot rule out the possibility of an ordered (1x1) overlayer structure forming on the Ir(111) surface.

2. Pt(110)-(1x2)

As with the Ir(111) surface, no ordered adsorbate superstructures were observed under any conditions examined, and the (1x2) LEED pattern representative of the clean surface was always present. In addition, the adsorption of hydrogen did not remove the (1x2) clean surface reconstruction which occurs, for example, upon the adsorption of CO **(36)**. These observations are in agreement with those reported previously for the adsorption of hydrogen on the structurally similar Ir(110)-(1x2) surface **(18)**.

B. Hydrogen on Ir(111)

1. Desorption Kinetics

Thermal desorption spectra of H_2 from Ir(111), corresponding to ten different initial coverages that were obtained by varying the hydrogen exposure at 100 K, are shown in Fig. 2. The average heating rate β for each spectrum was 20 K-s^{-1} **(37)**. Several qualitative features of the desorption kinetics are immediately apparent from Fig. 2. Consistent with the availability of only one high coordination adsite **(38)**, the threefold hollow, the desorption spectra exhibit one desorption feature or "state." The peak temperature is observed to decrease continuously with increasing coverage, which is consistent with a second-order (adatom recombination) desorption reaction **(39)**. Broadening of the desorption spectra (*i.e.*, the FWHM increases more than the maximum intensity) is clearly evident at the higher coverages corresponding to exposures above approximately 10–20 L (1L $\equiv 10^{-6}$ Torr-s), indicative of the presence of repulsive adatom-adatom interactions. These desorption spectra are qualitatively similar to those obtained on other hexagonally close-packed surfaces of the Group VIII metals, *e.g.*, Pt(111) **(19)**, Rh(111) **(40)** and Ru(001) **(41,42)**. However, the Ni(111) surface provides an exception, the desorption spectra from this surface "splitting" into two "states" for fractional coverages above one-half of a monolayer [*i.e.*, the coverage corresponding to an optimally ordered (2x2) superstructure] **(35)**. Presumably, on Ni(111), the splitting of the desorption spectra and the formation of the submonolayer (2x2) superstructure are correlated.

The desorption kinetics were characterized quantitatively by employing an integral method involving variable heating rates **(43)**. This method permits the assessment of the coverage dependence of the integral kinetic rate parameters, *i.e.*, the activation energy of desorption [$E_d(\theta)$] and the (second-order) preexponential factor [$k_d^{(2)}(\theta)$] of the desorption rate coefficient. The variation of the (linear) heating rate permits an evaluation of the rate of desorption [proportional to the mass spectrometric intensity for a chamber that is pumped sufficiently rapidly **(39)**] as a function of temperature at a *fixed coverage*, the latter of which is determined by integrating the mass spectrometric intensity versus time. Depending on the energetics of the desorption reaction and the reproducibility of the temporal tem-

perature profiles (which permits the averaging of spectra), varying the heating rate by 1–2 orders of magnitude is sufficient for the construction of a set of Arrhenius plots. The activation energy of the desorption reaction for a particular adsorbate coverage can be evaluated from the Arrhenius plot of the rate of desorption as a function of the reciprocal surface temperature. By assuming an implicit coverage dependence (*i.e.*, order) for the desorption reaction, the preexponential factor of the desorption rate coefficient (assumed to be weakly dependent on temperature which is verified by the linearity of the Arrhenius construction) can also be evaluated as a function of adsorbate coverage. The major underlying assumption in this analysis is that the desorption reaction procedes via a direct, one-step process, with the rate of this reaction specified completely by the surface temperature and the adsorbate concentration **(44)**.

Arrhenius plots constructed from thermal desorption spectra of D_2 from Ir(111) that embodied two different fixed initial coverages and six different heating rates are shown in Fig. 3. Deuterium, which produces identical desorption spectra to those shown for hydrogen in Fig. 2, was employed to increase the sensitivity of the mass spectrometric detection (especially important at low heating rates). The heating rates were varied from 1.5 to 60 K-s^{-1}. Two different initial coverages, $\theta_0 = 0.148$ and $\theta_0 = 0.47$, were studied in order to emphasize two different coverage regimes. (An optimal signal-to-noise ratio is obtained by confining the analysis to the central part of the desorption peak, *i.e.*, $0.2\theta_0 \leq \theta \leq 0.8\theta_0$.) The former emphasized the low coverage limit, whereas the latter emphasized the low to moderate coverage regime. Higher coverages were not examined, since contamination of the surface by background gases (primarily CO) became significant. This was due to a combination of the relatively high exposures necessary to obtain a high coverage (exposures $\geq$ 100 L) and the low heating rates (total time for a complete spectrum $\geq$ 200 s) required by this method of analysis.

Making use of the data displayed in Fig. 3, we have evaluated the activation energy of desorption and the preexponential factor of the desorption rate coefficient

as a function of coverage. These results are shown in Fig. 4. The preexponential factor was evaluated by assuming that saturation density of hydrogen is 1.57×10^{15} atoms-cm^{-2} (the uncertainty associated with this assumption is negligible compared to other experimental uncertainties; see below) and that the desorption reaction is second order in the fractional coverage of hydrogen adatoms. The assumption of second-order kinetics is supported by the form of the desorption spectra displayed in Fig. 2 (see above) and the fact that adsorption is dissociative (*i.e.*, the *elementary* reaction, H(a) + H(a) $\rightarrow$ H_2(g), is obviously "bimolecular").

The coverage dependence of the rate parameters is evident from an inspection of Fig. 4. For a fractional coverage below 0.10, a significant variation in the rate parameters is observed— the activation energy of desorption decreases from 18 to 14 kcal-mol^{-1}, whereas the preexponential factor decreases from 1×10^{-3} to 1×10^{-5} cm^2-s^{-1}. Between fractional coverages of approximately 0.1 and 0.3 the rate parameters are essentially independent of coverage and are given by $E_d \simeq 12.6$ kcal-mol^{-1} and $k_d^{(2)} \simeq 2 \times 10^{-6}$ cm^2-s^{-1}. As the fractional coverage increases beyond 0.3, the rate parameters begin to decrease further. For coverages below approximately 0.1 and above approximately 0.3, a compensation effect is observed with the activation energy and preexponential factor varying in sympathy with coverage.

The strong coverage dependence of the rate parameters in the limit of low coverages is suggestive of the presence of a small concentration of defect sites at which the binding energy of the hydrogen adatoms is *intrinsically* greater. Since the probability of adsorption at defect sites is significantly greater than that at perfect (111) sites, as discussed above, these defect sites will be populated preferentially at low coverages. Moreover, since hydrogen adatoms are bound more strongly at defect sites, diffusion between adsites will not act to remove this preferential population as molecules are desorbed in a TDMS experiment. Thus, if defect sites are present, they will dominate the desorption kinetics at low coverages. This has been observed by Christmann and Ertl **(3,45)** who examined the chemisorption of hydrogen on Pt(111) and on a stepped Pt[9(111)x(111)] surface (*i.e.*, "defect

site" density of 10%). Between fractional coverages of 0.2 and 0.5, both surfaces of platinum exhibited similar activation energies of desorption. However, at coverages below 0.2 the activation energy of desorption on the (111) surface remained virtually constant, whereas on the stepped 9(111)x(111) surface it increased approximately linearly to a value ~ 3 kcal-mol^{-1} greater than that observed on the (111) surface in the limit of zero coverage. Since the divergence in the kinetic parameters occurred at $\theta = 0.2$ (*i.e.*, *not* 0.1), it is probable that there was significant mixing between (*i.e.*, recombination of) hydrogen adatoms at step sites and those at (111) terrace sites as molecules were desorbed. This behavior of the kinetic parameters observed on the Pt[9(111)x(111)] surface is essentially identical to that observed here on the Ir(111) surface and suggests the presence of a small percentage of defect sites on this Ir(111) surface. Furthermore, the approximate linear decrease in the activation energy for $\theta \leq 0.1$ on Ir(111) suggests that these defect sites may be step sites, as opposed to "point" defects for example. Scaling our results to those of Christmann and Ertl **(3)** would suggest that this Ir(111) surface has a defect density on the order of $\sim 5\%$.

The decrease in the activation energy of desorption at coverages above approximately 0.3 is explained best by the occurrence of repulsive adatom-adatom interactions (presumably "through-metal") at these adsorbate concentrations. These interactions act to decrease the (average) binding energy of the hydrogen adatoms and, hence, the activation energy of desorption. The fact that these interactions appear to become significant at a fractional coverage of approximately 0.3 is of particular interest, since the heat of adsorption of hydrogen on the Pt(111) surface, is also essentially constant below this coverage **(22)**. However, as the coverage increases beyond 0.3, the heat of adsorption decreases linearly. These results, both for hydrogen on Ir(111) and on Pt(111), suggest that next-nearest neighbor interactions between hydrogen adatoms are relatively weak, whereas nearest neighbor interactions are repulsive on these surfaces. That is, one can populate a hexagonal close-packed lattice [considering only one of the two inequivalent threefold hollow

sites as an adsite **(46)**] at a fractional coverage of one-third such that no nearest neighbor adatom pairs exist. However, for fractional coverages beyond one-third, the adlayer must contain nearest neighbor pairs. Thus, for fractional coverages beyond one-third, the occurrence of repulsive interactions between nearest neighbor hydrogen adatoms acts to decrease the (average) binding energy and, consequently, the activation energy of desorption.

The observation of a $(\sqrt{3}x\sqrt{3})R30°$ LEED pattern near $\theta = \frac{1}{3}$ would have lent considerable support to the above interpretation. However, over both Ir(111) (see above) and Pt(111) **(19)** no ordered hydrogen adatom superstructures have been observed near a coverage of one-third. This apparent discrepancy between the LEED observations and the measured energetics of desorption could be reconciled by one or both of the following: *(i)* the importance of (the apparently absent) *attractive* interactions between next-nearest neighbors in forming the ordered superstructure; and *(ii)* the occupation of both hcp and fcc threefold hollow sites at low (*i.e.*, $\theta \leq \frac{1}{3}$) hydrogen coverages.

2. Adsorption Kinetics

The adsorption kinetics of hydrogen and deuterium on Ir(111) at 100 K have been characterized by integration of thermal desorption spectra such as those shown in Fig. 2. The integrated area of the mass spectrometric intensity with respect to time is proportional to the adsorbate coverage, and these data (the fractional coverage versus the exposure) represent an integrated form of the adsorption kinetics. The mechanism of the adsorption reaction can be deduced by comparing these integrated data with integrated functional forms of various assumed rate expressions, *e.g.*, Langmuir adsorption kinetics **(47)** and precursor-mediated adsorption kinetics **(48)**. A quantitative assessment of the adsorption kinetics is dependent, however, upon the assignment of an absolute coverage, which specifies the value of the initial probability of adsorption. We shall assume that the saturation density of hydrogen

with respect to the metallic substrate density is $\theta_H^{sat} = 1$, or $n_s^{sat} = 1.57 \times 10^{15}$ atoms-cm^{-2}. This value is reasonable when compared with values obtained under similar conditions on other hexagonally close-packed surfaces of the Group VIII metals, *e.g.*, 0.8–0.9 on Pt(111) **(19,22)** and 0.85 ± 0.15 on Ru(001) **(42)**. Since the measurement of the absolute initial probability of adsorption via TDMS is typically accurate to only ~ 20%, this additional uncertainty is of minor importance.

The relative fractional coverage is displayed as a function of exposure in Fig. 5 for (a) hydrogen and (b) deuterium. The solid lines represent the results of least-squares fits of the data to second-order Langmuir adsorption kinetics; *i.e.*, the probability of adsorption is proportional to the square of the fraction of vacant surface sites, $(1 - \theta)^2$. The adsorption of both hydrogen and deuterium is well represented by a second-order Langmuir model, and both exhibit, within experimental error, an identical initial probability of adsorption of 7×10^{-3}. This value of the initial probability of adsorption is significantly lower than values obtained on other hexagonally close-packed surfaces of the Group VIII metals, *e.g.*, 0.05 on Ni(111) **(15)**, 0.65 on Rh(111) **(40)**, 0.1–0.25 on Ru(001) **(41,42)** and 0.016–0.1 on Pt(111) **(2,19,20)**. However, it is *identical* to that found for the lower binding energy β_1-adstate on the Ir(110)-(1x2) surface that has been attributed to adsorption on the (111) microfacets of this reconstructed (1x2) surface **(18)**. Second-order Langmuir adsorption kinetics have been reported for hydrogen on Rh(111) **(40)**, Ru(001) **(41,42)**, Pt(111) **(2,20)** and for the β_1-adstate on Ir(110)-(1x2). For small values of the initial probability of adsorption ($s_0 \ll 1$), Kisliuk's second-order precursor model **(48)** reduces to $s(\theta)/s_0 = (1 - \theta)^2/[1 + (K - 1)\theta]$, where $-s_0 \leq K \leq \infty$. Thus, if the parameter K is approximately equal to unity, this second-order precursor model becomes equivalent to and experimentally indistinguishable from Langmuir adsorption kinetics. The parameter K is equal to unity if the rates of desorption and migration from the precursor state are independent of the occupation of the underlying site; *i.e.*, except for adsorption, the intrinsic and extrinsic precursor states

are equivalent. Since s_0 is much less than unity in this case, we cannot rule out the possibility that the adsorption of hydrogen on Ir(111) proceeds through a weakly bound precursor state for which $K \sim 1$.

Consistent with the desorption kinetics discussed above, the adsorption kinetics also suggest the presence of a small fraction of defects on the Ir(111) surface studied here. These defect sites would be expected to increase the apparent probability of adsorption at low coverages. For example, Christmann and Ertl **(3)** have observed the initial probability of adsorption of hydrogen to increase by over a factor of three when comparing the stepped Pt[9(111)x(111)] surface ($s_0 = 0.34$) to a "perfect" Pt(111) surface ($s_0 \leq 0.1$), whereas above a fractional coverage of approximately 0.25, the two surfaces exhibited virtually identical (differential) adsorption kinetics. Examination of data comparable to those shown in Fig. 5(a) for the adsorption of hydrogen on this Ir(111) surface reveals that the coverages observed at low exposures ($\epsilon \leq 5$ L) are greater than those predicted from the "one-site" adsorption model plotted in Fig. 5. This is seen clearly for the low exposure data that are shown in Fig. 6. These data have been fit to a "two-site" adsorption model, which is defined by

$$\theta = x_s\theta_s + (1 - x_s)\theta_f$$

and

$$d\theta/d\epsilon = x_s s_{0,s}(1 - \theta_s)^n + (1 - x_s)s_{0,f}(1 - \theta_f)^2,$$

where $\epsilon \equiv 2F_{H_2}t/n_s$ is the exposure in units of atoms-site^{-1}, x_s is the fraction of defect (*e.g.*, step) sites and the subscripts "s" and "f" refer to "step" and "flat" (111) sites. If we assume that the defect sites exhibit behavior similar to that observed for the β_2-adstate on the Ir(110)-(1x2) surface **(18)**, namely, an initial probability of adsorption of unity (*i.e.*, $s_{0,s} = 1$), the data are in excellent *quantitative* agreement with the two-site adsorption model by assuming either first- or second-order Langmuir adsorption kinetics for the step sites (*i.e.*, n = 1 or 2) **(49)**. This agreement is shown explicitly in Fig. 6, where an optimum fit to the data was

obtained with a fraction of defect sites of 2.5%. (Note that if both $s_{0,s} = 0.5$ and $x_s = 0.05$ are assumed for example, the resulting fit is *considerably* worse.) Due to both the quantitative nature of this analysis and the use of only one assumption (*i.e.*, $s_{0,s} = 1$), this defect site density value of 2.5% is more reliable than the value of 5% implied from the previously discussed behavior of the desorption parameters.

In conclusion, we note that a determination of the defect site density in and of itself is not particularly interesting. Rather, the knowledge of the relative population of defect sites is often crucial to a more complete understanding of results obtained concerning other fundamental gas-surface interactions, *e.g.*, heterogeneous catalysis. For example, the product distribution from the hydrogenolysis of *n*-butane over iridium surfaces has been discovered to depend sensitively on the concentration of step sites **(50)** (specifically, low-coordination-number metal surface atoms), whereas these same defect sites are apparently crucial also for the relatively facile activation of C-H bonds in saturated hydrocarbons on surfaces of iridium **(51)**.

C. Hydrogen on Pt(110)-(1x2)

1. Desorption Kinetics

Thermal desorption spectra of D_2 from Pt(110)-(1x2) for nine different initial coverages are shown in Fig. 7. The linear heating rate produced by employing the digital temperature controller for each spectrum was 3.0 K-s^{-1}. As for the Ir(111) surface, hydrogen and deuterium produce thermal desorption spectra that are identical within experimental error. Unlike the Ir(111) surface, however, two distinct desorption peaks, or "states," are clearly apparent in Fig. 7. Previous work **(2,52)** did not resolve these two desorption features clearly due to the high heating rates that were employed in those studies ($\beta \geq 40$ K-s^{-1}). The state desorbing at approximately 300 K, which we label the β_2-adstate [consistent with previous work on the Ir(110)-(1x2) surface **(18)**], saturates at low exposures (*i.e.*, a high

probability of adsorption). The narrow width of the thermal desorption peaks from this β_2-adstate (FWHM $\sim$ 30 K; compare Fig. 7 to Fig. 2) suggests the presence of *attractive* adatom-adatom interactions **(39)**. The state desorbing near 200 K, which we label as the β_1-adstate, saturates at much larger exposures compared to the β_2-adstate, and the peak temperature decreases continuously with increasing coverage, indicative of second-order desorption. Broadening of the desorption peaks of the β_1-adstate is apparent also, quite similar to that observed on Ir(111) (*cf.* Fig. 2), and this suggests the presence of repulsive adatom-adatom interactions. The ratio of the saturation densities of the two adstates, β_2:β_1, is approximately 1:2. These thermal desorption spectra are *very* similar to those obtained on the Ir(110)-(1x2) surface **(18)**.

Deuterium and hydrogen were adsorbed sequentially to determine the approximate extent of exchange between the two adstates. Thermal desorption spectra of D_2, HD and H_2 (not corrected for differences in pumping speeds or mass spectrometric sensitivities), obtained at a heating rate of 3.0 K-s^{-1} following the sequential exposures of 0.64 L of D_2 and 8.5 L of H_2, are shown in Fig. 8. This exposure of D_2 populates approximately 85% of the β_2-adstate, whereas this additional exposure of H_2 fills the remainder of the β_2-adstate and populates approximately 35% of the β_1-adstate (see Fig. 11 below). Thus, the initial coverage of hydrogen adatoms and deuterium adatoms is approximately equal. There is significant exchange between the two adstates during the course of the TDMS experiment, occurring apparently at temperatures as low as 200 K. Similar thermal desorption spectra are obtained if the exposure sequence is reversed. These results are in (qualitative) agreement with results obtained from similar isotopic exchange experiments carried out on the Ir(110)-(1x2) surface **(18)**.

The desorption kinetics was characterized quantitatively by employing the integral method involving variable heating rates described above. In this case, the heating rates were varied from 2 to 25 K-s^{-1}. Three to four spectra were measured at each heating rate and summed to increase the signal-to-noise ratio. Two different

initial coverages, $\theta_0 = 0.37$ and $\theta_0 = 0.70$, were employed in order to examine two different coverage regimes: in this case, the β_2- and β_1-adstates. Specifically, the lower initial coverage was utilized to examine fractional coverages below $\sim$ 0.35, and the higher initial coverage to examine fractional coverages between $\sim$ 0.35 and 0.65. We note that *serious* errors could arise if the *entire* coverage range were examined by utilizing a single high initial coverage. These errors would arise from the decreasing resolution of the two desorption features at high heating rates ($\beta \gg 3$ K-s^{-1}), as observed in previous work **(2,52)**. Since desorption from the β_1-adstate is characterized by a lower activation energy (lower desorption temperature), the β_1 peak will shift upward in temperature more than the β_2 peak as the heating rate is increased, resulting in a mixing of the two desorption features at intermediate coverages (*i.e.*, $0.2 \leq \theta \leq 0.45$). Errors can be avoided, at least for desorption from the β_2-adstate, by employing an initial coverage representative of (essentially) only the β_2-adstate, *i.e.*, $\theta_0 = 0.37$.

Making use of data from Arrhenius plots similar to those shown in Fig. 3, we have evaluated the activation energy of desorption and the preexponential factor of the desorption rate coefficient as a function of surface coverage. These results are shown in Fig. 9. The preexponential factor was evaluated by our assuming that the saturation density of hydrogen is 1.60 x 10^{15} atoms-cm^{-2} (see below) and that the desorption reaction is second order. The rate parameters are strongly dependent on coverage, especially for desorption from the β_2-adstate. In addition, over the coverage range characteristic of the β_2-adstate, a compensation effect is clearly apparent, both rate parameters first increasing and then decreasing with coverage. In particular, from a zero coverage limit of approximately 18 kcal-mol^{-1}, the activation energy of desorption first increases to a value of 26.5 kcal-mol^{-1} at a fractional coverage of 0.15 and then decreases to a value of approximately 18 kcal-mol^{-1} as the coverage increases to a value of 0.32, *i.e.*, saturation of the β_2-adstate. Concomitantly, from a zero coverage limit of approximately 10^{-4} cm^2-s^{-1}, the preexponential factor first increases to a value of 0.3 cm^2-s^{-1} and then decreases

to a value of approximately 10^{-3} cm^2-s^{-1}. The approximate symmetry of the rate parameters about a fractional coverage of $\theta \sim 0.15$ (*i.e.*, one-half of saturation of the β_2-adstate) is provocative.

The initial increase in the activation energy of desorption as the fractional coverage increases to a value of 0.15 is due to attractive adatom-adatom interactions at these adsorbate concentrations. The presence of attractive interactions in the adlayer was implied by the narrow width of the β_2-adstate desorption peak. These interactions act to increase the (average) binding energy of the hydrogen adatoms and, hence, the activation energy of desorption, since the activation energy of adsorption is essentially zero for the β_2-adstate (adsorption probability near unity; see below). An initial increase in the activation energy of desorption has been observed also for hydrogen on the (110) surfaces of both iridium **(18)** and nickel (somewhat less pronounced) **(14)**. The fact that these attractive interactions are much more apparent on fcc (110) surfaces, compared to fcc (111) surfaces, for example, implies that surface structural effects are important.

The (110) surfaces of fcc metals consist of close-packed rows of atoms separated by one-dimensional channels (see Fig. 1). Evidence exists supporting the location of the low coverage β_2-adstate of hydrogen as being in the pseudo-fourfold hollow "trough" sites present on (110) surfaces **(18)**. For the Pt(110)-(1x2) surface, the saturation density of the β_2-adstate is approximately equal to the density of these "trough" sites, *i.e.*, one hydrogen adatom per fourfold hollow site at saturation. It appears that these one-dimensional channels can mediate particularly well "through lattice" attractive adatom-adatom interactions between *next*-nearest neighbors along the [001] channel direction. From this point of view, the decrease in the activation energy of desorption between fractional coverages of approximately 0.15 and 0.30 is due to the occurrence of *repulsive* adatom-adatom interactions between *nearest* neighbors. If both attractive next-nearest neighbor and repulsive nearest neighbor interactions occur, one might expect to observe ordering in one di-

mension along the [001] direction at a fractional coverage corresponding to one-half saturation of the β_2-adstate (*i.e.*, $\theta = 0.15$). However, if the interaction *between* adjacent channels were sufficiently weak that ordering in *two* dimensions did not occur (*i.e.*, no correlation between the one-dimensional channels), one would not expect to observe a new LEED pattern different from the clean surface (1x2) pattern. Since no new LEED patterns were observed we can exclude *two*-dimensional ordering in the β_2-adstate, whereas *one*-dimensional ordering remains a distinct possibility.

The coverage dependence of the kinetic rate parameters of the β_1-adstate is also apparent from an inspection of Fig. 9. The activation energy of desorption decreases approximately linearly with increasing coverage from a value of 17 kcal-mol^{-1} at $\theta = 0.35$ to a value of 13 kcal-mol^{-1} at $\theta = 0.65$, whereas the preexponential factor maintains an essentially constant value of approximately 3 x 10^{-4} cm^2-s^{-1}. The decrease of the activation energy is again due to the occurrence of repulsive adatom-adatom interactions which act to decrease the binding energy of the hydrogen adatoms. It is important to note that desorption from the β_1-adstate occurs in the presence of a fully occupied β_2-adstate. Thus, in addition to interactions *within* the β_1-adstate, interactions *between* the β_1- and β_2-adstates may contribute also to the repulsive energy, which leads to a decrease in the activation energy of desorption from the β_1-adstate.

2. Adsorption Kinetics

The adsorption kinetics of hydrogen and deuterium on Pt(110)-(1x2) at 120 K have been characterized by integration of thermal desorption spectra similar to those shown in Fig. 7. The fractional coverage of deuterium adatoms is displayed as a function of exposure in Fig. 10, and hydrogen exhibits identical adsorption kinetics. The absolute coverage has been assigned by comparing the integrated intensities of thermal desorption spectra corresponding to saturated overlayers at 120 K and at 170 K. The saturation density of deuterium adatoms at 170 K has

been measured to be 1.07±0.1 x 10^{15} atoms-cm^{-2} **(36)**. As may be seen in Fig. 10, the adsorption kinetics are represented by two distinct regimes corresponding to the β_2- and β_1-adstates. Since the two adstates exhibit vastly different adsorption kinetics, they can be examined separately.

The fractional coverages, relative to each of the adstate saturation values, are displayed as a function of exposure in Fig. 11 for (a) the β_2- and (b) the β_1-adstate. The solid lines represent the results of least-squares fits of the data to (a) first-order and (b) second-order Langmuir adsorption kinetics. The adsorption of deuterium into the β_2-adstate is characterized by an initial probability of adsorption of 0.45, whereas the corresponding probability for the β_1-adstate is considerably smaller, 0.024. Analysis of the adsorption kinetics of hydrogen results in values for the initial probability of adsorption of 0.46 for the β_2-adstate and 0.022 for the β_1-adstate, *i.e.*, experimentally indistinguishable from deuterium.

Since the adsorption of hydrogen is dissociative, the observation of *first*-order Langmuir adsorption kinetics $[s(\theta)/s_0 = (1-\theta)]$ for the β_2-adstate is somewhat unexpected. However, the β_2-adstate on the structurally similar Ir(110)-(1x2) surface exhibits first-order Langmuir adsorption kinetics **(18)**. First-order adsorption kinetics has been reported also for hydrogen on the (111) and (100) surfaces of nickel **(14)**. The initial probability of adsorption of 0.46 for the β_2-adstate compares well to both the value of 0.33 reported previously by Lu and Rye **(2)** for the Pt(110) surface and the value of 0.34 attributed to adsorption at step sites on the Pt[9(111)x(111)] surface **(3)**.

As for the β_1-adstate on Pt(110)-(1x2), second-order Langmuir adsorption kinetics has been reported both for the β_1-adstate on the Ir(110)-(1x2) surface, as well as for the hexagonally close-packed surfaces of Rh **(40)**, Ru **(41,42)**, Pt **(2,20)** and Ir (this work). The value of 0.022 for the initial probability of adsorption compares well to the value of 0.016 reported by Lu and Rye for hydrogen adsorption on Pt(111) **(2)**, supporting the proposition that, as for the Ir(110)-(1x2) surface

(18), the β_1-adstate can be attributed to adsorption on the (111) microfacets of the reconstructed Pt(110)-(1x2) surface. Finally, as for the Ir(111) surface, second-order Langmuir adsorption kinetics, characterized by a small initial probabilty of adsorption, cannot be distinguished by these experiments from precursor-mediated kinetics in which the precursor state interacts weakly with the surface.

3. Contact Potential Difference Measurements

Contact potential difference (CPD) measurements have been carried out in order to evaluate the work function change ($\Delta\varphi$) upon adsorption of hydrogen on the Pt(110)-(1x2) surface. These measurements can provide information concerning electron transfer between the adsorbate and the substrate, *i.e.*, the dipole moment of the adsorbate-substrate complex. For the data presented here, the CPD has been measured as a function of time while the surface was exposed to a constant partial pressure of hydrogen. Since the adsorption kinetics of hydrogen on the Pt(110)-(1x2) surface is characterized by two distinct regimes, a relatively lower partial pressure was employed to examine the CPD for the β_2-adstate (approximately 2 x 10^{-8} Torr), whereas a higher one was employed for the β_1-adstate (approximately 5 x 10^{-7} Torr). Making use of the coverage versus exposure relationships shown in Figs. 10 and 11, the CPD was evaluated as a function of coverage.

The CPD for hydrogen adsorbed on the Pt(110)-(1x2) surface at 120 K is shown in Fig. 12 as a function of the (total) fractional coverage. Adsorption into the β_2-adstate results in an increase in the CPD, reaching a maximum of 0.17 eV at a coverage of 0.3. As the coverage increases beyond 0.3, characteristic of adsorption into the β_1-adstate, the CPD decreases, approaching a value of -0.50 eV at saturation. For coverages below approximately 0.2 and above approximately 0.4 the CPD varies linearly with coverage, indicating that the dipole moment of the adsorbed hydrogen adatoms is constant at these concentrations (*i.e.*, depolarization effects are small). The calculated values for the dipole moments (μ) are +0.12 D

for the β_2-adstate ($\theta \leq 0.2$), and -0.17 D for the β_1-adstate ($\theta \geq 0.4$), where 1D $\equiv$ 1 esu-cm. The nonlinear variation in the CPD at the intermediate coverages between 0.2 and 0.4 is due primarily to the partial filling of the β_1-adstate prior to the filling of the β_2-adstate and the occurrence of depolarization effects within the β_2-adstate. Note that depolarization effects are absent in the β_1-adstate as the coverage approaches saturation.

An initial *increase* in the CPD, followed by a continuous *decrease* has been observed for hydrogen adsorbed on both the Ir(110)-(1x2) surface **(18)** and the stepped Pt[9(111)x(111)] surface **(3)**. On the structurally similar Ir(110)-(1x2) surface, the CPD increases linearly to a maximum of 0.30 eV at a coverage of 0.33 (μ = +0.14 D), corresponding to the filling of the higher binding energy β_2-adstate. As the lower binding energy β_1-adstate populates, the CPD decreases and approaches a saturation value of -0.14 eV (obtained at a surface temperature of 140 K). On Pt[9(111)x(111)], the CPD increases to a maximum of 0.02 eV at a coverage of 0.25 and then decreases continuously to a value of -0.36 eV at saturation coverage. For coverages beyond 0.7, the CPD of this stepped platinum surface becomes indistinguishable from that obtained on the Pt(111) surface, where the CPD is observed to decrease continuously from zero coverage **(19,21)**.

The apparent disparity in the sign of the dipole moment for the low coverage, higher binding energy states {the β_2-adstates on the (110)-(1x2) surfaces of Pt and Ir, and the "step sites" on Pt[9(111)x(111)]}, and the lower binding energy states [the β_1-adstates and (or) the (111) "terrace sites"] can be explained by the following arguments. Clearly, the continuous decrease in the CPD observed on Pt(111) **(19,21)** is due to electron donation from the hydrogen adatoms to the metal surface. Since we attribute the β_1-adstates to adsorption on the (111) microfacets of the (110)-(1x2) surfaces, this explanation holds also for the observed decrease in the CPD for the filling of the β_1-adstates. The increase in the CPD for the β_2-adstates can be interpreted as either *(i)* electron donation from the metal surface to the hydrogen adatoms, assuming the adatoms lie above the image dipole plane

of the surface, or *(ii)* electron donation from the hydrogen adatoms to the metal surface (as for the β_1-adstates) with the adatoms lying *below* the image plane (*e.g.*, the pseudo-fourfold hollow "trough" sites, *cf.* Fig. 1). The latter viewpoint, the β_2-adstate being located in the troughs, was adopted previously to explain the CPD behavior on the Ir(110)-(1x2) surface on the basis of adsorption-induced changes in the UV photoelectron spectra **(18)**. We believe this interpretation is also very plausible for the results obtained here on the Pt(110)-(1x2) surface {and elsewhere on the Pt[9(111)x(111)] surface **(3)**, adsorption at the inner corner of the steps being below the image plane **(53)**}. Indeed, the proposition of the pseudo-fourfold hollow adsite for the β_2-adstate is consistent with the observation that, in general, hydrogen binds preferentially at high coordination adsites **(1)**.

4. Coadsorption of CO and H_2

The coadsorption of hydrogen and carbon monoxide on the Pt(110)-(1x2) surface has been studied in order to examine the perturbations by CO on the adsorption and desorption of hydrogen. It is of interest to review briefly the results obtained previously concerning the coadsorption of CO and H_2 on the structurally similar Ir(110)-(1x2) surface **(55)**. The adsorption of hydrogen on an Ir(110)-(1x2) surface exposed previously to CO results in less hydrogen occupying the high binding energy β_2-adstate, shifting preferentially the occupancy to the β_1-adstate. This preferential shift occurs also for the postadsorption of CO on a hydrogen precovered surface. In both cases, the adsorption of one-half of a monolayer of CO poisons or displaces completely all of the hydrogen chemisorbed in the β_2-adstate, shifting the occupancy to the β_1-adstate.

Thermal desorption spectra of H_2 from Pt(110)-(1x2), corresponding to the same initial coverage of hydrogen (ϵ_{H_2} = 0.39 L, θ_H = 0.26, *i.e.*, 80% of saturation of the β_2-adstate) and six different subsequent exposures of CO at 120 K are shown in Fig. 13(A). Since the linear heating rate was 15 K-s^{-1}, the spectra are

shifted to higher temperatures with respect to those given in Fig. 7 for the clean surface (where $\beta = 3.0$ K-s^{-1}). In all cases, H_2 desorption was complete prior to any desorption of CO ($T \geq 400$ K). For exposures of CO below approximately 1 L, desorption from the β_2-adstate is suppressed progressively with increasing CO exposures, whereas desorption between 200 and 300 K (characteristic of the β_1-adstate on the clean surface) increases concomitantly. For exposures above 1 L, the H_2 thermal desorption peak shifts down further in temperature, the peak shifting to approximately 200 K. Integration of these thermal desorption spectra indicates that displacement of hydrogen from the surface at 120 K has not occurred for these exposures of CO. In addition, no new LEED patterns were observed for these exposure sequences for temperatures between 120 and 300 K **(56)**. This observation, coupled with the fact that H_2 desorption from the β_2-adstate is extinguished completely at coverages of CO below 0.5, indicates that (long-range) adsorbate segregation, which, for example, occurs on the Rh(111) surface **(58)**, is not occurring.

Three desorption regimes, dependent upon the CO postexposure, are apparent in Fig. 13(A). At zero postexposure, desorption is exclusively from the β_2-adstate. For postexposures between approximately 0.5 and 1 L, the β_2-adstate has been virtually extinguished, and the desorption peaks are very similar to those expected if the hydrogen adatoms were merely displaced [*i.e.*, no additional CO(a)-H(a) interactions] to the β_1-adstate (*cf.* Fig. 7 and $\epsilon_{D_2} = 8$ L). For postexposures above 1 L, this "β_1-like" adstate is suppressed, and a new "state" with a peak temperature of approximately 200 K begins to dominate the desorption spectra. If exposures below $\sim$ 1 L displace completely hydrogen adatoms to the β_1-adstate, it is reasonable to assume that exposures above 1 L ($\theta_{CO} \geq 0.4$) may lead to repulsive interactions between the CO admolecules and the hydrogen adatoms. These interactions would explain the observed shift in the desorption peak to lower temperature, *i.e.*, from $\sim$ 250 K to $\sim$ 200 K.

Contact potential difference measurements were carried out to test the above hypothesis concerning the effects of coadsorbed CO on the chemisorption of hydro-

gen. Since the two clean surface adstates of hydrogen are characterized by dipole moments of opposite sign (*cf.* Fig. 12), displacement of adatoms from one adstate to another should result in large changes in the CPD whereas (non-displacing) interactions between the CO admolecules and the hydrogen adatoms may only marginally affect the CPD (assuming we can account for the CPD due solely to the CO). An experiment was conducted in order to measure the CPD for the exposure sequence represented by the thermal desorption spectra shown in Fig. 13(A). Specifically, the CPD was measured as a function of time while the clean Pt(110)-(1x2) surface was exposed to 0.39 L of hydrogen, followed by a constant partial pressure of CO of 5 x 10^{-8} Torr. These data are shown in Fig 13(B). The CPD for CO adsorbed on the clean surface is shown also for reference purposes (within experimental error, the adsorption kinetics of CO were found to be identical for the clean surface and for this precoverage of hydrogen). From Fig. 13(B) we see that the CPD decreases precipitously upon the initial exposure of CO, decreasing to $\sim$ -0.02 eV at an exposure of 0.3 L and further to $\sim$ -0.21 eV at 1 L. Above exposures of approximately 1 L, the CPD is essentially constant at $\sim$ -0.22 eV.

These results for the CPD are entirely consisitent with the above interpretation concerning the thermal desorption spectra. For exposures below approximately 1 L, the CPD decreases rapidly as the hydrogen adatoms are displaced to the β_1-adstate. However, for exposures above approximately 1 L, little change in the CPD is observed, consistent with the occurrence of (non-displacing) interactions between the CO admolecules and the hydrogen adatoms, which lead to the observed changes in the thermal desorption spectra.

The effect of preadsorbed CO on the chemisorption of hydrogen on the Pt(110)-(1x2) surface was studied briefly. It was found that an exposure of 1.1 L of CO (θ_{CO} $\sim$0.4) blocked completely the adsorption of H_2 into the β_2-adstate. The resulting adsorption into the β_1-adstate was characterized by an initial probability of adsorption of 0.016 and second-order Langmuir kinetics, *i.e.*, very similar to the clean surface on which $s_0 = 0.022$ and second-order Langmuir kinetics also applied.

The thermal desorption spectra from this CO precovered surface were found to be similar to those expected for hydrogen adatoms which were merely displaced to the β_1-adstate, *e.g.*, spectrum d in Fig. 13(A). Finally, adsorption of hydrogen on this CO precovered surface resulted in a continuous decrease in the CPD, consistent with preferential adsorption into the β_1-adstate.

In summary, the post- or preadsorption of CO on the Pt(110)-(1x2) surface poisons hydrogen adsorption into the β_2-adstate and shifts its occupation to the β_1-adstate, consistent with earlier work on the structurally similar Ir(110)-(1x2) surface **(55)**. At low to moderate coverages of CO ($\theta_{CO} \leq 0.4$), the CO acts merely to displace the hydrogen adatoms from the β_2- to the β_1-adstate. However, at CO coverages above one-half of a monolayer, repulsive interactions between the CO admolecules and the hydrogen adatoms leads to a reduced binding energy of the hydrogen adatoms and hence, a lower desorption temperature for hydrogen.

IV. Discussion

The results obtained here concerning the chemisorption of hydrogen on both the Ir(111) and Pt(110)-(1x2) surfaces have illustrated clearly the importance of surface structure and its influence on the rates of both adsorption and desorption. The initial probability of adsorption can vary by as much as two orders of magnitude when one compares the close-packed (111) and the corrugated (110)-(1x2) surfaces of both iridium and platinum. However, the adsorption kinetics characteristic of the lower binding energy β_1-adstates on the (110)-(1x2) surfaces are virtually identical to those observed on the corresponding (111) surfaces. The desorption kinetics are also influenced strongly by the surface structure. The (110)-(1x2) surfaces possess unique adsites as a consequence of their geometry, and these sites are related directly to the observation of an additional [with respect to the (111) surfaces] higher binding energy β_2-adstate. In addition, these (110)-(1x2) surfaces apparently mediate particularly well attractive adatom-adatom interactions between the hydrogen

adatoms in this higher binding energy β_2-adstate. As for the adsorption kinetics, the desorption kinetics characteristic of the lower binding energy β_1-adstates on the (110)-(1x2) surfaces are very similar to those observed on the corresponding (111) surfaces. In the discussion that follows, we shall quantify these comparisons of the adsorption and desorption kinetics of hydrogen on the (111) and (110)-(1x2) surfaces of both iridium and platinum.

The adsorption kinetics of hydrogen on the (111) and (110)-(1x2) surfaces of both iridium and platinum are summarized in Table 1 in terms of the initial probabilities of adsorption (s_0) and the functional dependencies of the reaction on the fractional coverage [$f(\theta)$] **(59)**. In all cases, the kinetics were evaluated at surface temperatures between 100 and 150 K and for gas temperatures of approximately 300 K. The dominant role of the surface structure in determining the rate of the adsorption reaction is clearly apparent. Adsorption into the β_2-adstates of both iridium and platinum is characterized by near unity initial probabilities of adsorption and first-order Langmuir adsorption kinetics. These values of s_0 imply that adsorption into the β_2-adstates is not activated.

The importance of the *local* surface structure is supported by the observation of both essentially identical values of the initial probabilities of adsorption and identical second-order Langmuir kinetics for adsorption on the (111) surfaces and into the β_1-adstates on the (110)-(1x2) surfaces. The striking similarity of the adsorption kinetics for these two adstates on macroscopically distinct surfaces is due to the presence of structurally similar threefold hollow adsites. This result was not totally unexpected; however, it is somewhat suprising that (111) microfacets that are only three atomic rows in width exhibit essentially identical rates of adsorption as a "perfect" (111) surface. The low values observed for the initial probabilities of adsorption on the (111) surfaces could be explained by the presence of an activation barrier for dissociative adsorption. Previous work employing molecular beam techniques has suggested that this barrier is on the order of 0.4–1.5 kcal-mol^{-1} on the Pt(111) surface **(7,8)**. As discussed above, more recent work on the adsorption

of hydrogen on the Ni(111) surface **(16)** implicates the presence of an activation barrier of approximately 2 kcal-mol^{-1} on this structurally similar close-packed surface. In addition, in agreement with our point of view, adsorption on the Ni(110) surface was found to be essentially unactivated.

The kinetic parameters that describe the desorption reaction, the activation energy of desorption, and the second-order preexponential factor of the desorption rate coefficient are displayed as a function of surface coverage in Fig. 14 for iridium and Fig. 15 for platinum (activation energy only) **(60)** for both the (111) surface and the β_1-adstate on the (110)-(1x2) surface. The abscissae have been scaled such that the *absolute* adsorbate concentrations are equal for the two adstates on any vertical line.

For coverages above approximately 0.1, the kinetic parameters for each adstate on the iridium surfaces are given by similar values. However, in the limit of zero coverage, the kinetic parameters characteristic of this Ir(111) surface are closer to the zero coverage limit on the Ir(110)-(1x2) surface, which are characteristic of the β_2-adstate. This observation supports the proposition argued above that the desorption kinetics at coverages below 0.1 are dominated by the presence of defect sites (*e.g.*, step sites) participating in the desorption reaction. Consequently, the zero coverage limit on a perfect Ir(111) surface might be expected to be characterized by the (coverage-independent) values measured here for for coverages between 0.1 and 0.3, *i.e.*, $E_d \simeq 12.6$ kcal-mol^{-1} and $k_d^{(2)} \simeq 2 \times 10^{-6}$ cm^2-s^{-1}. Note that the former is close to the value of $\sim$ 13.5 kcal-mol^{-1} for the zero coverage limit of the β_1-adstate on the Ir(110)-(1x2) surface.

For fractional coverages above 0.3, or approximately one-third of a monolayer, the activation energy of desorption on the Ir(111) surface begins to decrease. We believe this is due to the occurrence of repulsive adatom-adatom interactions between nearest neighbors which decrease the (average) binding energy of the hydrogen adatoms and hence, the activation energy of desorption. However, for the β_1-adstate on the Ir(110)-(1x2) surface, a continuous decrease in the activation en-

ergy is observed. This result could be explained also by the occurrence of repulsive interactions between the adatoms which, for the Ir(110-(1x2) surface, are apparently of longer range than those on the (111) surface. More likely is the possibility that since desorption from the β_1-adstate occurs in the presence of a fully occupied β_2-adstate, the two adstates being essentially nearest neighbors (*cf.* Fig. 1), the β_2-adstate acts to mediate these (apparently) long-range repulsive interactions between adatoms in the β_1-adstate.

As may be seen in Fig. 15, on the platinum surfaces, the activation energies of desorption vary with the surface coverage in a manner similar to that observed on the iridium surfaces. For fractional coverages below 0.3, the activation energy of desorption on the Pt(111) surface is essentially independent of the coverage. In addition, although it was not investigated quantitatively, Norton *et al.* **(22)** found evidence for hydrogen that was more strongly bound at coverages below approximately 0.05, presumably due to defect sites. As the coverage increases beyond 0.3, the activation energy of desorption decreases due to the occurrence of repulsive interactions between nearest neighbor hydrogen adatoms. For the β_1-adstate on the Pt(110)-(1x2) surface, the activation energy of desorption decreases continuously with increasing coverage, indicative of the occurrence of repulsive interactions at all adsorbate concentrations for which the β_2-adstate may play a mediating role. In the limit of zero coverage the two adstates exhibit a similar activation energy of desorption of approximately 16 kcal-mol^{-1}, emphasizing again the similarity of the two adstates.

The kinetic parameters that describe the desorption of hydrogen from the (110)-(1x2) surfaces of both iridium and platinum are displayed in Fig. 16 as a function of surface coverage. The dominant influence of the surface structure is clearly apparent. For both surfaces, the parameters vary sympathetically with surface coverage, first increasing and subsequently decreasing, in the coverage regime characteristic of the β_2-adstate ($\theta \leq 0.33$). The activation energies of desorption for the β_1-adstates ($\theta \geq 0.33$) decrease continuously with increasing coverage, whereas the preexponen-

tial factors remain essentially constant. The rate parameters for the Pt(110)-(1x2) surface are symmetric about a coverage equal to one-half of saturation of the β_2-adstate. This result has been interpreted as a manifestation of the occurrence of attractive adatom-adatom interactions between next-nearest neighbors and repulsive interactions between nearest neighbors which, in this case, are apparently of approximately equal strength. The rate parameters for the Ir(110)-(1x2) surface appear to be asymmetric in the β_2-adstate coverage regime. However, these results should be treated with some caution as one high initial coverage (θ=0.8) was used to evaluate the entire coverage regime displayed in Fig. 16 (see above). It is probable that at the high heating rates (as large as 110 K-s^{-1}) employed to evaluate the parameters, significant mixing occurred between the β_1- and β_2-adstates in the intermediate coverage regime ($0.2 \leq \theta \leq 0.45$). On the other hand, a mismatch in the strength of the attractive and repulsive interactions could contribute also to the observed asymmetry. In any case, the interpretation involving attractive adatom-adatom interactions at low coverages and repulsive interactions as the β_2-adstate approaches saturation remains valid also for the Ir(110)-(1x2) surface.

V. Conclusions

The major conclusions of this work examining the chemisorption of hydrogen on both the Ir(111) and the Pt(110)-(1x2) surfaces can be summarized as follows:

1. Hydrogen adsorbs dissociatively on the Ir(111) surface, the adsorption reaction described by second-order Langmuir kinetics with an initial probability of adsorption of 7 x 10^{-3}.
2. The rate parameters describing the desorption of hydrogen from the Ir(111) surface are weakly dependent on coverage between fractional coverages of 0.1 and 0.3 and are given by $E_d \simeq 12.6$ kcal-mol^{-1} and $k_d^{(2)} \simeq 2 \times 10^{-6}$ cm^2-s^{-1}. The activation energy of desorption decreases continuously with coverage above

$\theta = 0.3$, indicative of the occurrence of repulsive interactions between nearest neighbor hydrogen adatoms.

3. Both the variation in the desorption rate parameters at coverages below approximately 0.1 and the observation of an apparently higher probability of adsorption for this same coverage regime suggest that the Ir(111) surface examined here may contain a fraction of defect sites on the order of 2.5–5.0%.
4. Hydrogen adsorbs dissociatively on the Pt(110)-(1x2) surface into two distinct adstates which are designated as the β_2 and β_1. The ratio of the saturation densities of the two adstates, β_2:β_1, is 1:2. Adsorption into the higher binding energy β_2-adstate is described by first-order Langmuir kinetics with an initial probability of adsorption of 0.46. Adsorption into the β_1-adstate is described by second-order Langmuir kinetics with an "initial" probability of adsorption of 0.022.
5. The rate parameters describing the desorption of hydrogen from the Pt(110)-(1x2) surface depend strongly on the coverage. From the values for the zero coverage limit given by $E_d \simeq 18$ kcal-mol^{-1} and $k_d^{(2)} \simeq 10^{-4}$ cm^2-s^{-1}, the rate parameters first increase to maximum values given by $E_d \simeq 26.5$ kcal-mol^{-1} and $k_d^{(2)} \simeq 0.3$ cm^2-s^{-1} at $\theta = 0.15$ and subsequently decrease to approximately the values for the zero coverage limit at $\theta = 0.32$, *i.e.*, saturation of the β_2-adstate. The variation of the parameters in this coverage regime is symmetric about a coverage equal to one-half of saturation of the β_2-adstate, implicating the occurrence of attractive adatom-adatom interactions between next-nearest neighbors and repulsive interactions between nearest neighbor hydrogen adatoms. In the coverage regime characteristic of the β_1-adstate, the activation energy decreases linearly with increasing coverage from $E_d \simeq 17$ kcal-mol^{-1} at $\theta = 0.35$, whereas the preexponential factor maintains a constant value of $k_d^{(2)} \simeq 3 \times 10^{-4}$ cm^2-s^{-1}.
6. Adsorption of hydrogen on the clean Pt(110)-(1x2) surface results in a continuous increase in the CPD, reaching a maximum value of 0.17 eV at a coverage

of $\theta = 0.30$, *i.e.*, nearly saturation of the β_2-adstate. Adsorption into the β_1-adstate results in a continuous decrease in the CPD, approaching a value of -0.50 eV at saturation. The initial increase in the CPD is attributed to the β_2-adstate's being located below the image dipole plane of the surface, in the pseudo-fourfold hollow "trough" sites.

7. The pre- or postadsorption of CO on the Pt(110)-(1x2) surface poisons hydrogen adsorption into the β_2-adstate, preferentially shifting its occupation to the β_1-adstates.
8. Surface structure has been found to have a profound influence on the kinetics of the adsorption of hydrogen. Comparisons of the results obtained on the (111) and (110)-(1x2) surfaces of both iridium and platinum suggest strongly that the *local* surface structure is the major determining factor. This viewpoint is supported by the striking similarities observed between the adsorption kinetics for the (111) surfaces and for the β_1-adstates on the (110)-(1x2) surfaces of both iridium and platinum, the latter adstates attributed to adsorption on the (111) microfacets of these reconstructed surfaces.
9. The desorption kinetics have also been found to be influenced profoundly by the surface structure. The (110)-(1x2) surfaces of both iridium and platinum possess unique [with respect to the (111) surfaces] pseudo-fourfold hollow adsites, these sites associated with the higher binding energy β_2-adstates, which are not observed on the (111) surfaces. Whereas both attractive and repulsive adatom-adatom interactions within the β_2-adstates are mediated by the (110)-(1x2) surfaces, only repulsive interactions are apparent on the (111) surfaces and for the β_1-adstates on the (110)-(1x2) surfaces.

Acknowledgement:

This work was supported by the National Science Foundation under Grant No. CHE-8516615.

References

1. Z. Knor, in: *Catalysis: Science and Technology*, Eds. J. R. Anderson and M. Boudart, Springer-Verlag, Berlin, Vol. 3, p. 231 (1982).
2. K. E. Lu and R. R. Rye, Surface Sci. **45**, 677 (1974).
3. K. Christmann and G. Ertl, Surface Sci. **60**, 365 (1976).
4. B. E. Nieuwenhuys, Surface Sci. **59**, 430 (1976).
5. R. W. McCabe and L. D. Schmidt, Proc. 7^{th} Intern. Vac. Congr. and 3^{rd} Intern. Conf. Solid Surfaces (Vienna 1977) p. 1201.
6. D. M. Collins and W. E. Spicer, Surface Sci. **69**, 85 (1977); D. M. Collins and W. E. Spicer, Surface Sci. **69**, 114 (1977).
7. R. J. Gale, M. Salmeron and G. A. Somorjai, Phys. Rev. Letters **38**, 1027 (1977); M. Salmeron, R. J. Gale and G. A. Somorjai, J. Chem. Phys. **67**, 5324 (1977).
8. M. Salmeron, R. J. Gale and G. A. Somorjai, J. Chem. Phys. **70**, 2807 (1979).
9. B. Poelesma, G. Mechtersheimer and G. Comsa, Surface Sci. **111**, L728 (1981); B. Poelesma, G. Mechtersheimer and G. Comsa, Surface Sci. **111**, 519 (1981).
10. G. E. Gdowski, J. A. Fair and R. J. Madix, Surface Sci. **127**, 541 (1983).
11. B. E. Nieuwenhuys, D. I. Hagen, G. Rovida and G. A. Somorjai, Surface Sci. **59**, 155 (1976).
12. J. M. Derochette and J. Marien, Phys. Stat. Solidi (a) **39**, 281 (1977).
13. H. Conrad, G. Ertl and E. E. Latta, Surface Sci. **41**, 435 (1974).
14. K. Christmann, O. Schober, G. Ertl and M. Neumann, J. Chem. Phys. **60**, 4528 (1974).
15. A. Winkler and K. D. Rendulic, Surface Sci. **118**, 19 (1982).
16. H. J. Robota, W. Vielhaber, M. C. Lin, J. Segner and G. Ertl, Surface Sci. **155**, 101 (1985).
17. H. Karner, M. Luger, H. P. Steinruck, A. Winkler and K. D. Rendulic, Surface

Sci. **163**, L641 (1985).

18. D. E. Ibbotson, T. S. Wittrig and W. H. Weinberg, J. Chem. Phys. **72**, 4885 (1980).
19. K. Christmann, G. Ertl and T. Pignet, Surface Sci. **54**, 365 (1976).
20. R. W. McCabe and L. D. Schmidt, Surface Sci. **65**, 169 (1977).
21. P. R. Norton and J. W. Goodale, Solid State Commun. **31**, 223 (1979).
22. P. R. Norton, J. A. Davies and T. E. Jackman, Surface Sci. **121**, 103 (1982).
23. C.-M. Chan, M. A. Van Hove, W. H. Weinberg and E. D. Williams, Solid State Commun. **30**, 47 (1979); C.-M. Chan, M. A. Van Hove, W. H. Weinberg and E. D. Williams, Surface Sci. **91**, 430 (1980).
24. See *e.g.*, G. L. Kellogg, Phys. Rev. Letters **55**, 2168 (1985); H. Niehus, Surface Sci. **145**, 407 (1984); A. M. Lahee, W. Allison, R. F. Willis and K. H. Rieder, Surface Sci. **126**, 654 (1983).
25. J. L. Taylor, D. E. Ibbotson and W. H. Weinberg, J. Chem. Phys. **69**, 4298 (1978).
26. H. Niehus and G. Comsa, Surface Sci. **102**, L14 (1981); H. Niehus and G. Comsa, Surface Sci. **93**, L147 (1980).
27. D. E. Ibbotson, T. S. Wittrig and W. H. Weinberg, Surface Sci. **110**, 294 (1981).
28. P. Feulner and D. Menzel, J. Vacuum Sci. Technol. **17**, 662 (1980).
29. J. R. Engstrom and W. H. Weinberg, Rev. Sci. Instrum. **55**, 404 (1984).
30. J. R. Engstrom, PhD Thesis, California Institute of Technology, 1987.
31. R. Nathan and B. J. Hopkins, J. Phys. E **7**, 851 (1974).
32. P. Hoffmann and D. Menzel, Surface Sci. **152/153**, 382 (1985).
33. J. Lee, J. P. Cowin and L. Wharton, Surface Sci. **130**, 1 (1983); I. Batra, Surface Sci. **87**. L97 (1984).
34. J. Behm, K. Christmann and G. Ertl, Solid State Commun. **28**, 763 (1978).
35. M. A. Van Hove, G. Ertl, K. Christmann, J. Behm and W. H. Weinberg, Solid State Commun. **28**, 373 (1978); K. Christmann, J. Behm, G. Ertl, M. A. Van

Hove and W. H. Weinberg, J. Chem Phys. **70**, 4168 (1979).

36. T. E. Jackmann, J. A. Davies, D. P. Jackson, W. N. Unertl and P. R. Norton, Surface Sci. **120**, 389 (1982).
37. The digital temperature controller was not employed in the measurement of these spectra.
38. In actual fact, there are two inequivalent threefold hollow sites when the second substrate layer is taken into account.
39. C.-M. Chan, R. Aris and W. H. Weinberg, Appl. Surface Sci. **1**, 360 (1978); C.-M. Chan and W. H. Weinberg, Appl. Surface Sci. **1**, 377 (1978).
40. J. T. Yates, P. A. Thiel and W. H. Weinberg, Surface Sci. **84**, 427 (1979).
41. J. A. Schwarz, Surface Sci. **87**, 525 (1979).
42. H. Shimizu, K. Christmann and G. Ertl, J. Catal. **61**, 412 (1980).
43. J. L. Taylor and W. H. Weinberg, Surface Sci. **78**, 259 (1978).
44. This assumption may break down, for example, if *(i)* desorption proceeds through a precusor state or if *(ii)* adsorbate domain formation occurs. That is, the kinetics of *(i)* the rate of exchange between the precursor state and the chemisorbed state, or *(ii)* the rate of domain formation/dissipation can influence the apparent rate of desorption. Concerning case *(i)*, see, *e.g.*, D. A. King, Surface Sci. **64**, 43 (1977), and R. Gorte and L. D. Schmidt, Surface Sci. **76**, 559 (1978).
45. Although the values of the kinetic parameters reported by Christmann and Ertl **(3)** have been challenged insofar as their *quantitative* accuracy is concerned **(9,22)**, a *qualitative* (internal) comparison of the results obtained on the two surfaces is nonetheless pedagogical. Indeed, both Christmann and Ertl **(3)** and Comsa *et al.* **(9)** report a difference in the activation energies of desorption from defect (step) sites and perfect (111) sites of $E_d^{step} - E_d^{(111)} \sim 3$ kcal-mol^{-1}.
46. Hydrogen appparently adsorbs preferentially on the hcp-type site (*i.e.*, the threefold hollow site directly above a second-layer substrate metal atom) on Pt(111) at $\theta = 1$ **(33)**, whereas both inequivalent threefold hollow adsites are

apparently populated on Ni(111) at $\theta = 0.5$ **(34,35)**.

47. I. Langmuir, Chem. Rev. **6**, 451 (1929); J. B. Taylor and I. Langmuir, Phys. Rev. **44**, 423 (1933).
48. P. Kisliuk, J. Phys. Chem. Solids **3**, 95 (1957); **5**, 78 (1958).
49. The relative disagreement between the "one"- and "two-site" adsorption models becomes progressively smaller as the coverage increases. Note that the *integral* adsorption kinetics still differ appreciably at $\theta \sim 0.15$, whereas the *differential* kinetics (*i.e.*, $d\theta/d\epsilon$) are essentially identical for $\theta \geq 0.05$.
50. J. R. Engstrom, D. W. Goodman and W. H. Weinberg, J. Am. Chem. Soc. **108**, 4653 (1986).
51. P. D. Szuromi, J. R. Engstrom and W. H. Weinberg, J. Chem. Phys. **80**, 508 (1984).
52. R. W. McCabe and L. D. Schmidt, Surface Sci. **60**, 85 (1976).
53. This adsorption site, the bridge site in the inner corner of the step (equivalent to the pseudo-fourfold hollow designation used here) is supported by high resolution electron energy-loss spectra of hydrogen adsorbed on a Pt[6(111)x(111)] surface **(54)**.
54. A. M. Baro and H. Ibach, Surface Sci. **92**, 237 (1980).
55. D. E. Ibbotson, T. S. Wittrig and W. H. Weinberg, Surface Sci. **97**, 297 (1980).
56. Carbon monoxide forms ordered phases on the Pt(110)-(1x2) surface at temperatures above 300 K for $\theta \geq 0.5$ [(1x1) LEED pattern] and $\theta \geq 0.9$ [(2x1)*p*1*g*1 LEED pattern] **(36)**. Also, at temperatures below 250 K, a metastable c(8x4) superstructure has been reported for a saturation coverage ($\theta = 1$) of CO **(57)**.
57. T. E. Jackman, J. A. Davies, D. P. Jackson, P. R. Norton and W. N. Unertl, J. Phys. C **15**, L99 (1982).
58. E. D. Williams, P. A. Thiel, W. H. Weinberg and J. T. Yates, Jr., J. Chem. Phys. **72**, 3496 (1980).
59. There is considerable disagreement in the literature concerning the adsorption kinetics of hydrogen on the Pt(111) surface. As shown in Table 1, Lu and

Rye **(2)** report second-order Langmuir kinetics and an initial probability of adsorption of 0.016. However, both Christmann *et al.* **(19)** and McCabe and Schmidt **(20)** could not fit the kinetics to any "one-site" models and reported an initial probability of adsorption of 0.1. It is of interest to note that for fractional coverages beyond $\sim$ 0.2, the data of Christmann *et al.* **(19)** are described well by second-order Langmuir kinetics and an "initial" probability of adsorption of 0.024.

60. An *approximate* heat of adsorption of D_2 on the Pt(111) surface was measured by Norton *et al.* **(22)**. The values reported (and used here) were approximate since a fixed gas temperature was employed. Nonetheless, the effects of a fixed gas temperature and the probable presence of an activation barrier to dissociative adsorption (on the order of 1 kcal-mol^{-1}) are within other experimental uncertainties such that we may equate approximately the heat of adsorption and the activation energy of desorption.

Table 1

Hydrogen Adsorption Kinetics on Iridium and Platinum [a)]

	Iridium			Platinum		
	s_0	$f(\theta)$	Ref.	s_0	$f(\theta)$	Ref.
(111)	7 x 10^{-3}	$(1-\theta)^2$	b)	0.016	$(1-\theta)^2$	**(2,59)**
(110)-(1x2) β_1-adstate	7 x 10^{-3}	$(1-\theta)^2$	**(18)**	0.022	$(1-\theta)^2$	b)
(110)-(1x2) β_2-adstate	1.0	$(1-\theta)$	**(18)**	0.46	$(1-\theta)$	b)

a) In all cases, the kinetics were evaluated at surface temperatures of 100 to 150 K, and for gas temperatures of approximately 300 K.

b) This work.

Figure Captions

Figure 1. Structural models for the (110)-(1x2) and (111) surfaces of iridium and platinum. A and B represent two probable locations for the hydrogen adatoms in the higher binding energy β_2-adstates observed on the (110)-(1x2) surfaces (see text), A being a twofold bridge site, and B being a pseudo-fourfold hollow site. C and D denote the preferred hydrogen binding sites both on the (111) surfaces and for the β_1-adstates on the (110)-(1x2) surfaces which, on both surfaces, are inequivalent threefold hollow sites.

Figure 2. Thermal desorption spectra of hydrogen from the (111) surface as a function of exposure of hydrogen. The surface temperature during adsorption was 100 K, and the average heating rate (β) for each spectrum was 20 K-s^{-1} **(37)**.

Figure 3. Arrhenius plots obtained for deuterium desorption from the Ir(111) surface by varying the heating rate and maintaining a constant initial coverage of a) 0.148 and b) 0.47.

Figure 4. Activation energy (E_d) and second-order preexponential factor ($k_d^{(2)}$) of the desorption rate coefficient for D_2 desorption from Ir(111) as a function of fractional surface coverage. The squares were obtained from the data presented in Fig. 3(a) ($\theta_0 = 0.148$), the circles from Fig. 3(b) ($\theta_0 = 0.47$).

Figure 5. The coverage-exposure relationship for (a) hydrogen and (b) deuterium on the Ir(111) surface. The solid lines represent least-squares fits of the data to second-order Langmuir kinetics with an initial probability of adsorption of (a) 7.1 x 10^{-3} for H_2 and (b) 7.0 x 10^{-3} for D_2.

Figure 6. The coverage-exposure relationship for low exposures of hydrogen to the Ir(111) surface. In this coverage regime, the "two-site" adsorption model (*i.e.*, the fraction of defect sites, $x_s = 0.025$ and n = 1 or 2; see text) provides a superior fit of the data with respect to the "one-site" model (*i.e.*, $x_s = 0.0$) **(49)**.

Figure 7. Thermal desorption spectra of deuterium from the Pt(110)-(1x2) surface as a

function of exposure of deuterium. The surface temperature during adsorption was 120 K and the linear heating rate for each spectrum was 3.0 K-s^{-1}. The ratio of the saturation densities of the two adstates, β_2:β_1, is approximately 1:2.

Figure 8. Thermal desorption spectra of D_2, HD and H_2 from a coadsorbed layer of hydrogen and deuterium. In this experiment, 0.64 L of D_2 was exposed first, populating approximately 85% of the β_2-adstate, and, subsequently, 8.5 L of H_2 was exposed. The surface temperature during adsorption was 120 K, and the linear heating rate was 3.0 K-s^{-1}.

Figure 9. Activation energy (E_d) and second-order preexponential factor ($k_d^{(2)}$) of the desorption rate coefficient for D_2 desorption from Pt(110)-(1x2) as a function of fractional surface coverage.

Figure 10. The coverage-exposure relationship for deuterium on the Pt(110)-(1x2) surface. The solid line has been drawn to facilitate the presentation. The coverage regimes representative of the β_2- and β_1-adstates are marked to emphasize the vastly different kinetics exhibited by the two states.

Figure 11. Analytic fits to the adsorption kinetics of D_2 on the Pt(110)-(1x2) surface derived from the data shown in Fig. 10. (a) The adsorption kinetics for D_2 into the β_2-adstate fit to a first-order Langmuir model with an initial probability of adsorption of 0.45. The coverage has been normalized to saturation of the β_2-adstate. (b) The adsorption kinetics for D_2 into the β_1-adstate fit to a second-order Langmuir model with an initial probability of adsorption of 0.024. The coverage has been normalized to saturation of the β_1-adstate.

Figure 12. The CPD of hydrogen on the Pt(110)-(1x2) surface as a function of fractional coverage at 120 K. The coverage regimes representative of the β_2- and β_1-adstates are marked to emphasize the (apparently) different charge transfer characteristics of the two adstates.

Figure 13. (A) Thermal desorption of H_2 from preadsorbed hydrogen (0.39 L, $\theta_H = 0.26$) exposed to varying amounts of CO (0–4.4 L CO, $\theta_{CO} = 0$–0.8). The surface

temperature during adsorption was 120 K, and the linear heating rate was 15 K-s^{-1}. The coverage of hydrogen was constant with these CO exposures. (B) The CPD for the exposure sequence represented by the thermal desorption spectra given in (A). The surface was exposed to 0.39 L of H_2, followed by a constant partial pressure of CO of 5 x 10^{-8} Torr. The dashed line in (B) represents the CPD for CO exposed to a *clean* Pt(110)-(1x2) surface.

Figure 14. Comparison of the desorption rate parameters, the activation energy (E_d) and the second-order preexponential factor ($k_d^{(2)}$), for hydrogen on the Ir(111) surface and for the β_1-adstate on the Ir(110)-(1x2) surface as a function of fractional coverage. The abscissae have been scaled such that the absolute adsorbate concentrations are equal for the two adstates. The zero coverage limit for the Ir(110)-(1x2) surface is shown for reference purposes. The data for the Ir(110)-(1x2) surface are from Ibbotson *et al.* **(18)**.

Figure 15. Comparison of the activation energies of desorption (E_d) for deuterium on the Pt(111) surface and for the β_1-adstate on the Pt(110)-(1x2) surface as a function of fractional coverage. The abscissae have been scaled such that the absolute adsorbate concentrations are equal for the two adstates. The data for the Pt(111) surface are from Norton *et al.* **(22,60)**.

Figure 16. Comparison of the desorption rate parameters, the activation energy (E_d) and the second-order preexponential factor ($k_d^{(2)}$), for hydrogen on the (110)-(1x2) surfaces of both iridium and platinum as a function of fractional coverage. The data for the Ir(110)-(1x2) surface are from Ibbotson *et al.* **(18)**.

Ir, Pt (110)-(1×2)

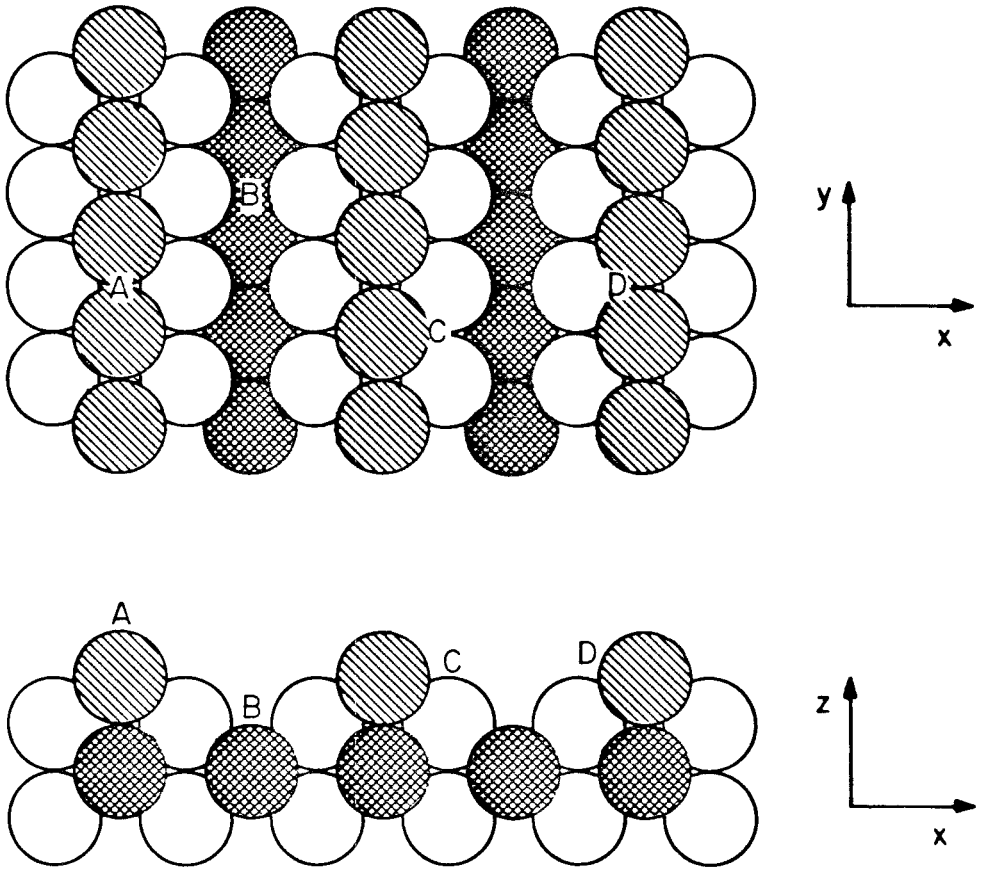

Ir, Pt (111)

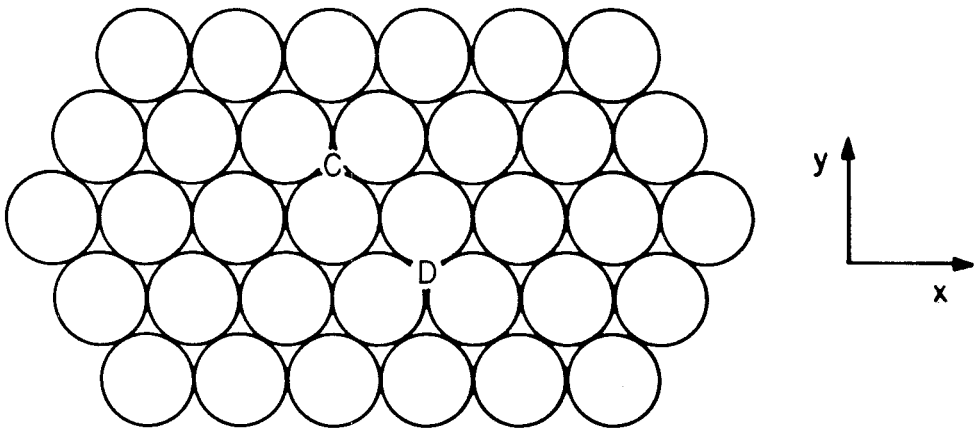

Figure 1

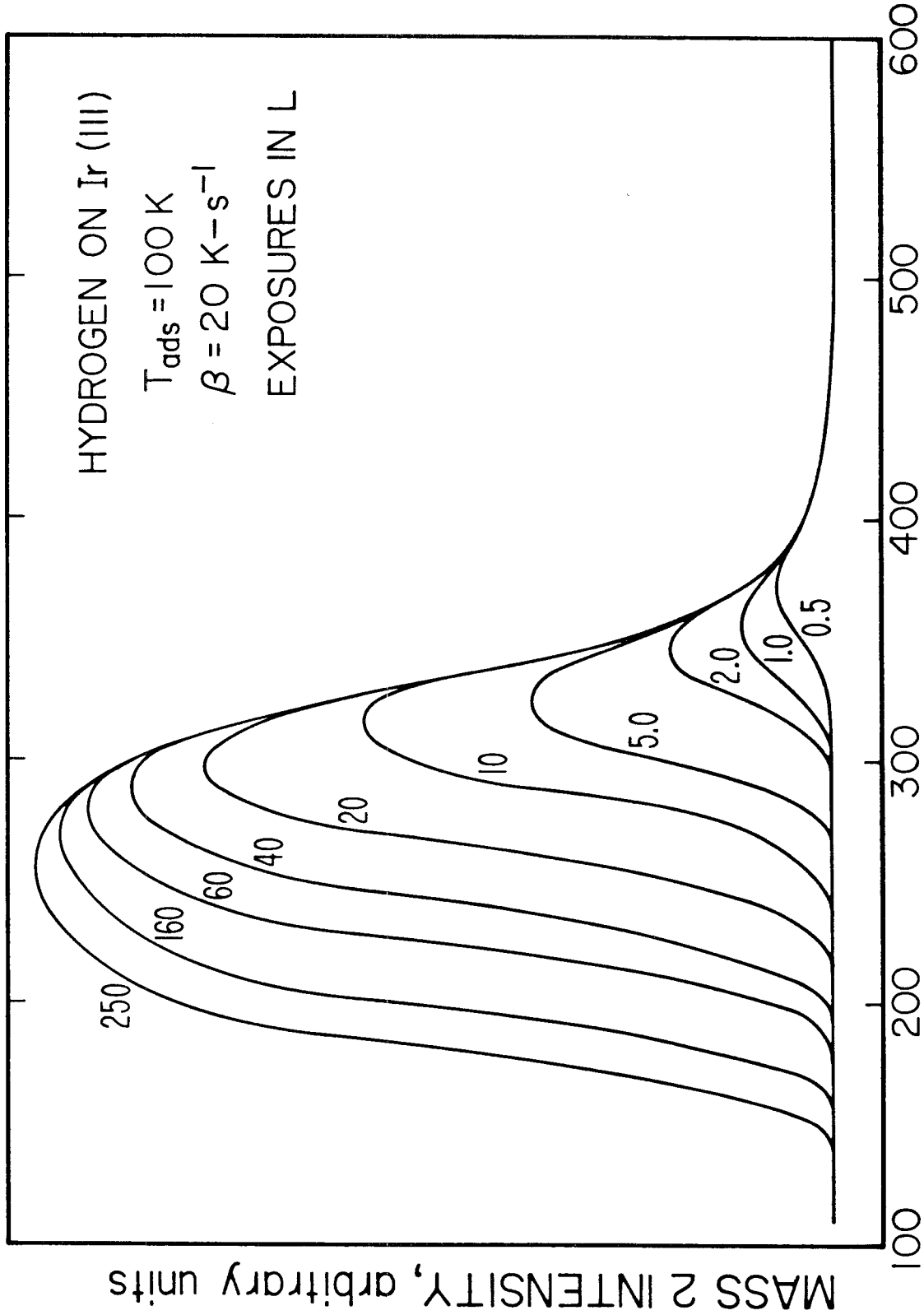
HYDROGEN ON Ir (111)
T_{ads} = 100 K
β = 20 K-s^{-1}
EXPOSURES IN L
250
160
60
40
20
10
5.0
2.0
1.0
0.5
100
200
300
400
500
600
TEMPERATURE, K
MASS 2 INTENSITY, arbitrary units

Figure 2

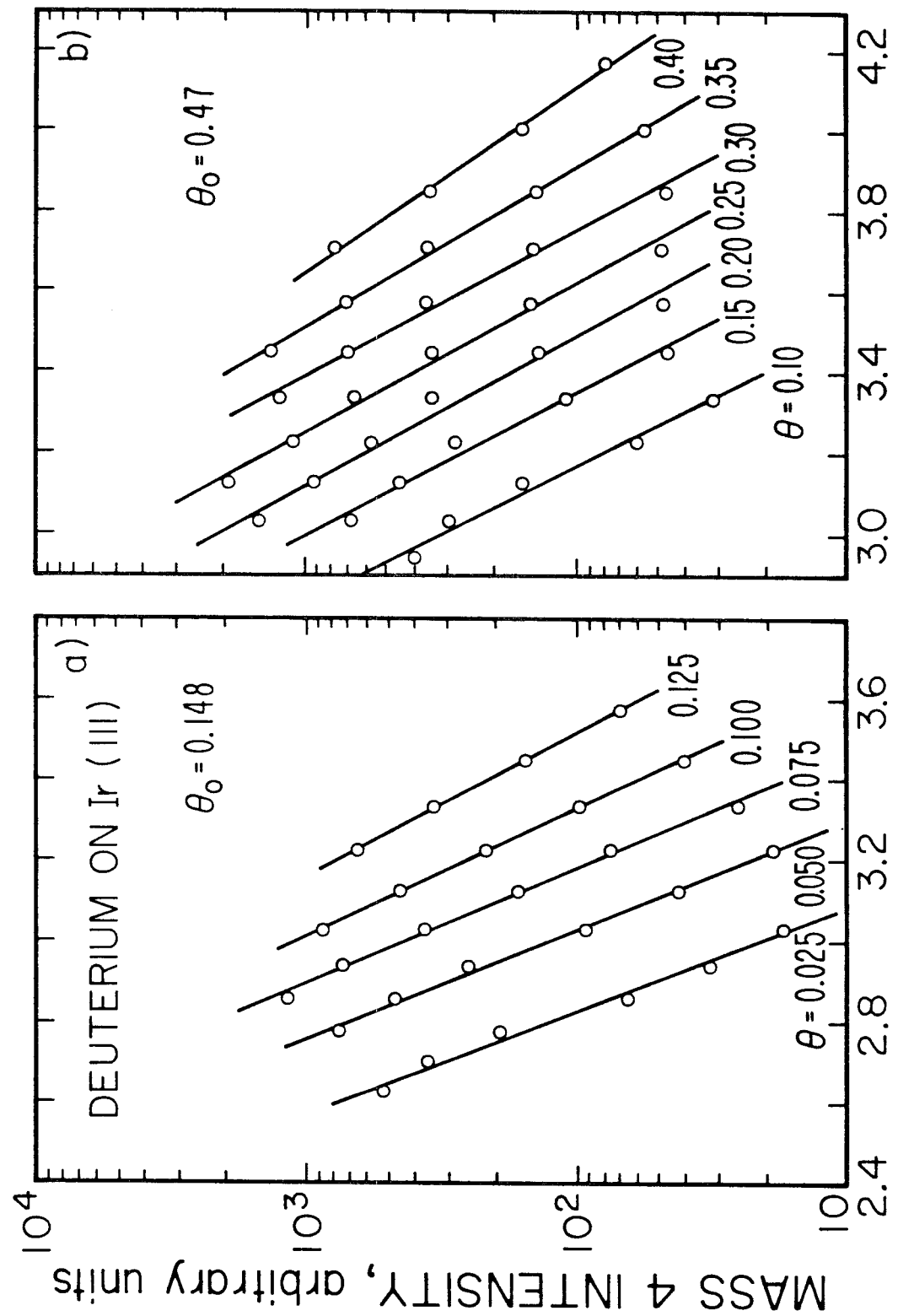
MASS 4 INTENSITY, arbitrary units
DEUTERIUM ON Ir (111)
a)
$\theta_o = 0.148$
$\theta = 0.025$
0.050
0.075
0.100
0.125
b)
$\theta_o = 0.47$
$\theta = 0.10$
0.15
0.20
0.25
0.30
0.35
0.40
1000/T

Figure 3

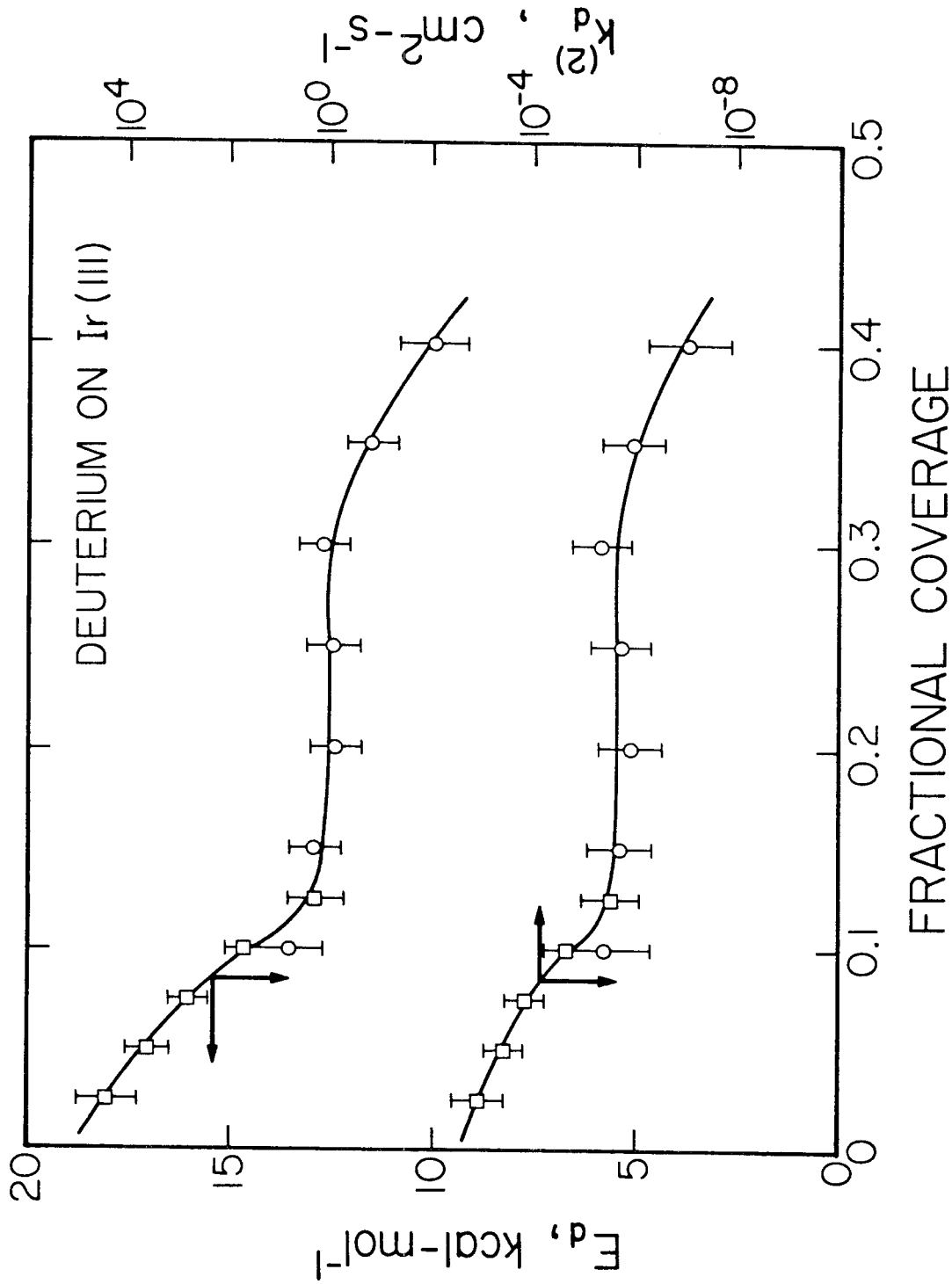
DEUTERIUM ON Ir(III)
E_d, kcal-mol^{-1}
$k_d^{(2)}$, cm^2-s^{-1}
FRACTIONAL COVERAGE
0
5
10
15
20
10^{-8}
10^{-4}
10^{0}
10^{4}
0.1
0.2
0.3
0.4
0.5

Figure 4

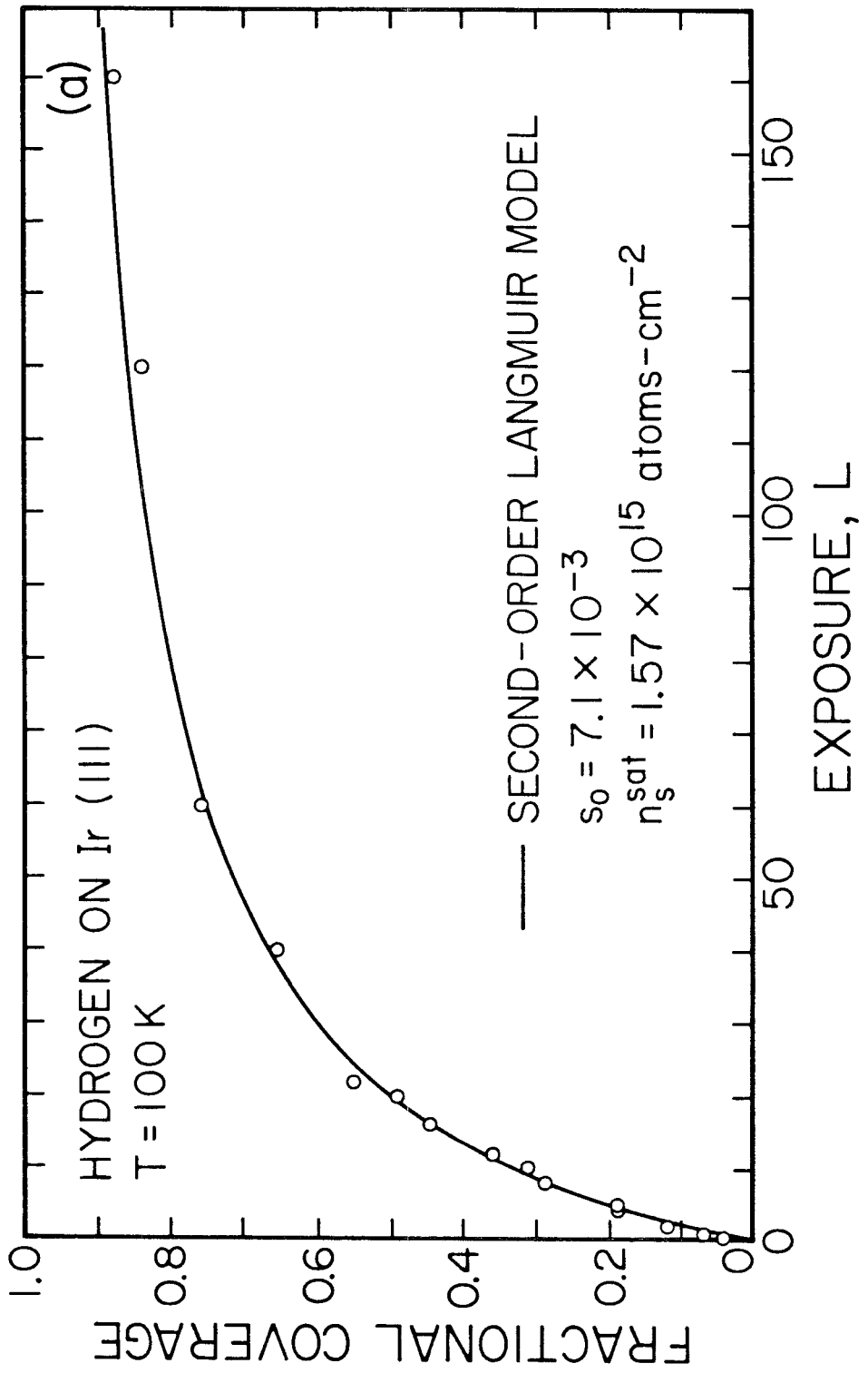
(a)
HYDROGEN ON Ir (111)
T = 100 K
SECOND-ORDER LANGMUIR MODEL
$s_o = 7.1 \times 10^{-3}$
$n_s^{sat} = 1.57 \times 10^{15}$ atoms-cm^{-2}
FRACTIONAL COVERAGE
EXPOSURE, L
0
0.2
0.4
0.6
0.8
1.0
0
50
100
150

Figure 5(a)

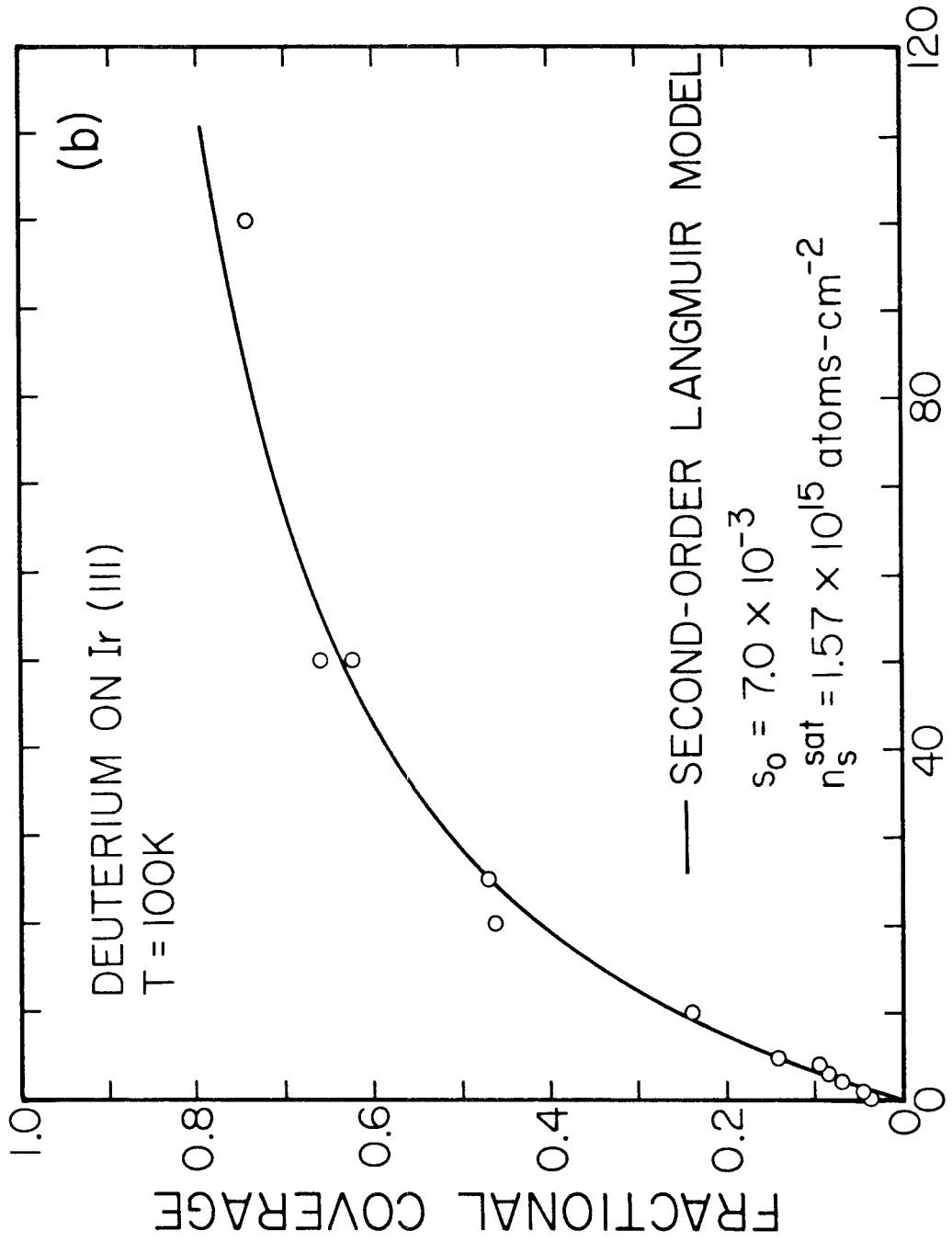
(b)
DEUTERIUM ON Ir (111)
T = 100K
— SECOND-ORDER LANGMUIR MODEL
$s_o = 7.0 \times 10^{-3}$
$n_s^{sat} = 1.57 \times 10^{15}$ atoms-cm^{-2}
FRACTIONAL COVERAGE
EXPOSURE, L
0
0.2
0.4
0.6
0.8
1.0
40
80
120

Figure 5(b)

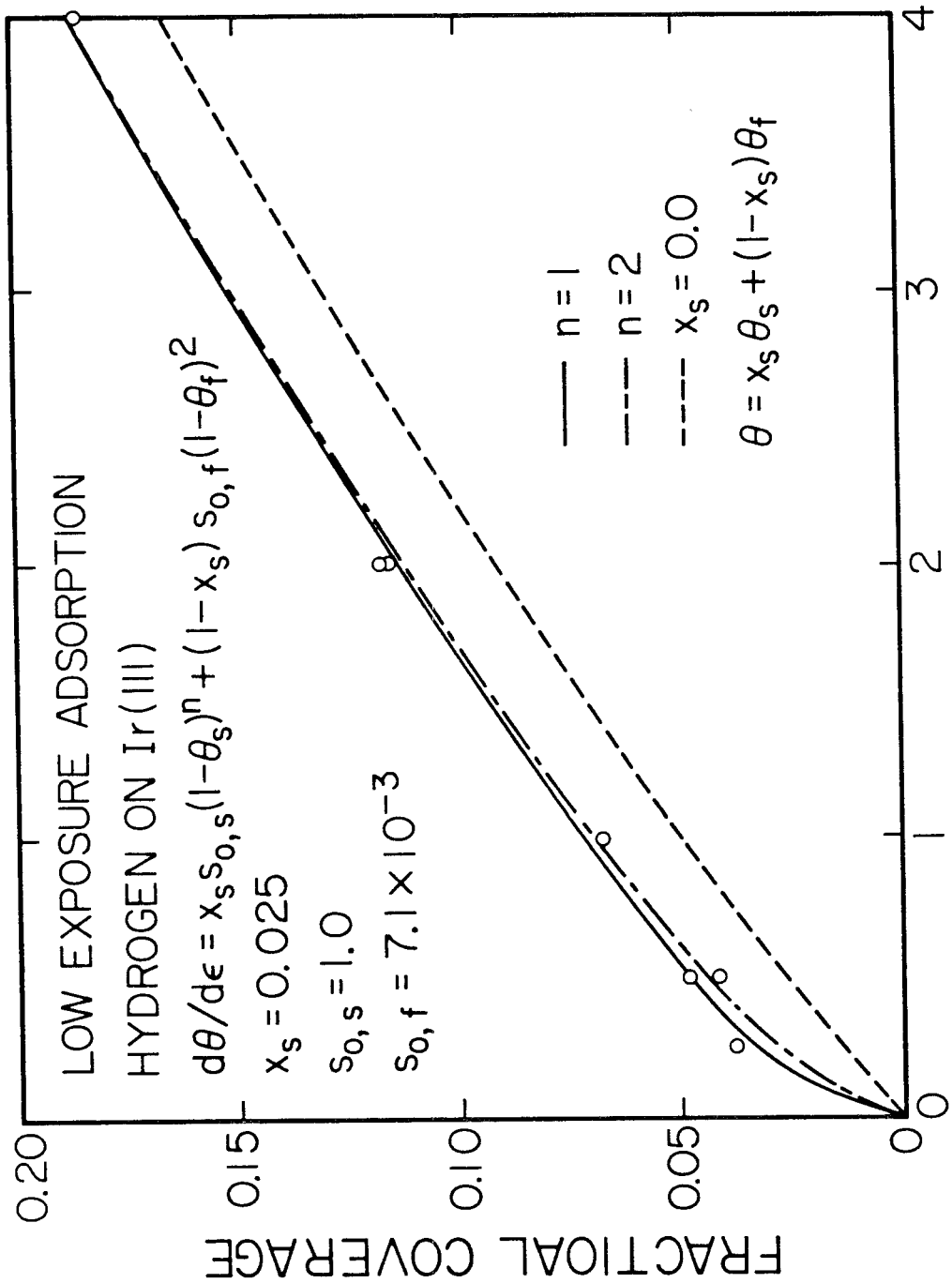
LOW EXPOSURE ADSORPTION
HYDROGEN ON Ir(111)
$d\theta/d\epsilon = x_s s_{o,s}(1-\theta_s)^n + (1-x_s)\, s_{o,f}(1-\theta_f)^2$
$x_s = 0.025$
$s_{o,s} = 1.0$
$s_{o,f} = 7.1 \times 10^{-3}$
n = 1
n = 2
$x_s = 0.0$
$\theta = x_s\theta_s + (1-x_s)\theta_f$
FRACTIOAL COVERAGE
EXPOSURE, L
0.20
0.15
0.10
0.05
0
1
2
3
4

Figure 6

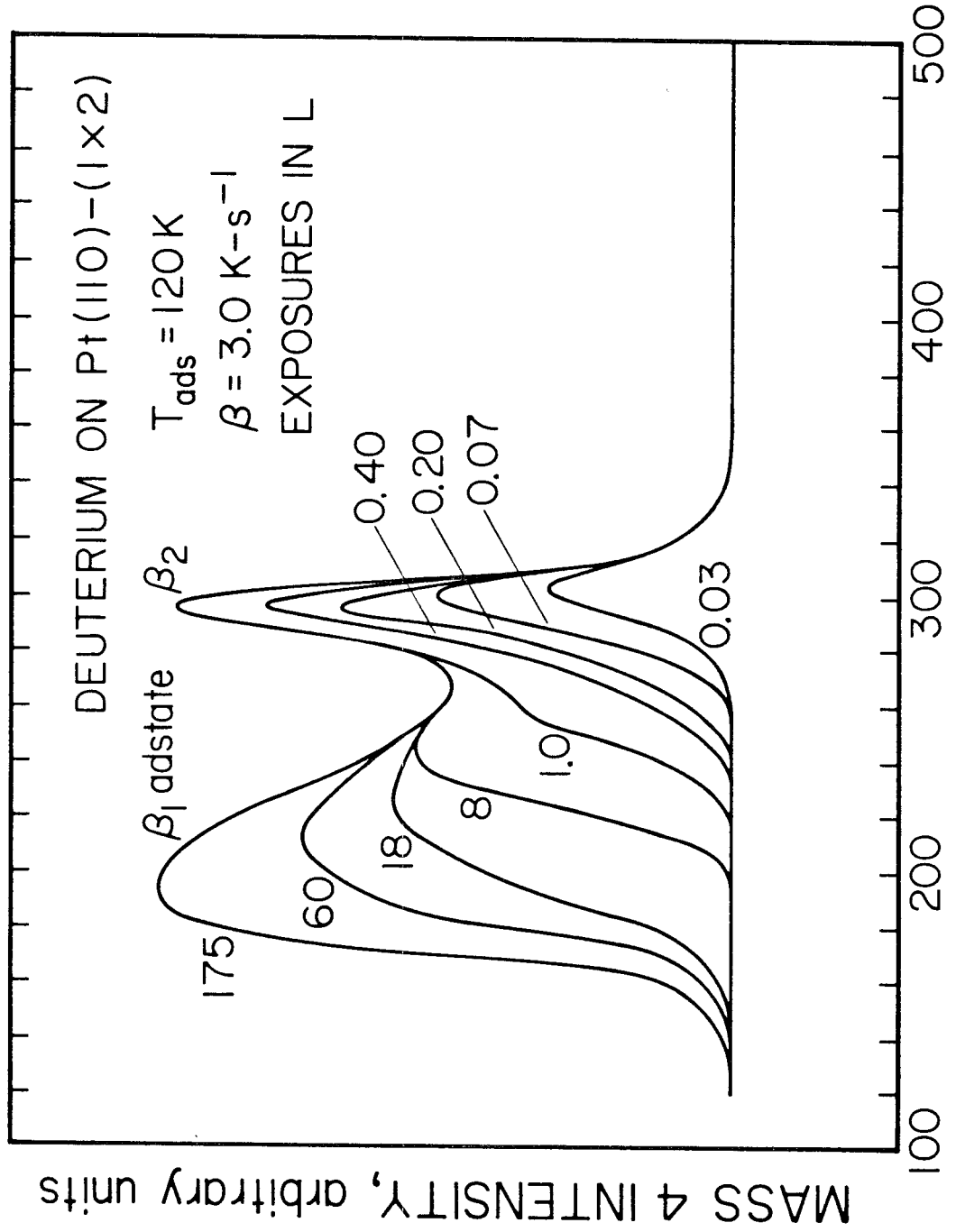
DEUTERIUM ON Pt(110)-(1×2)
T_{ads} = 120 K
β = 3.0 K-s^{-1}
EXPOSURES IN L
β_1 adstate
β_2
175
60
18
8
1.0
0.40
0.20
0.07
0.03
MASS 4 INTENSITY, arbitrary units
100
200
300
400
500
TEMPERATURE, K

Figure 7

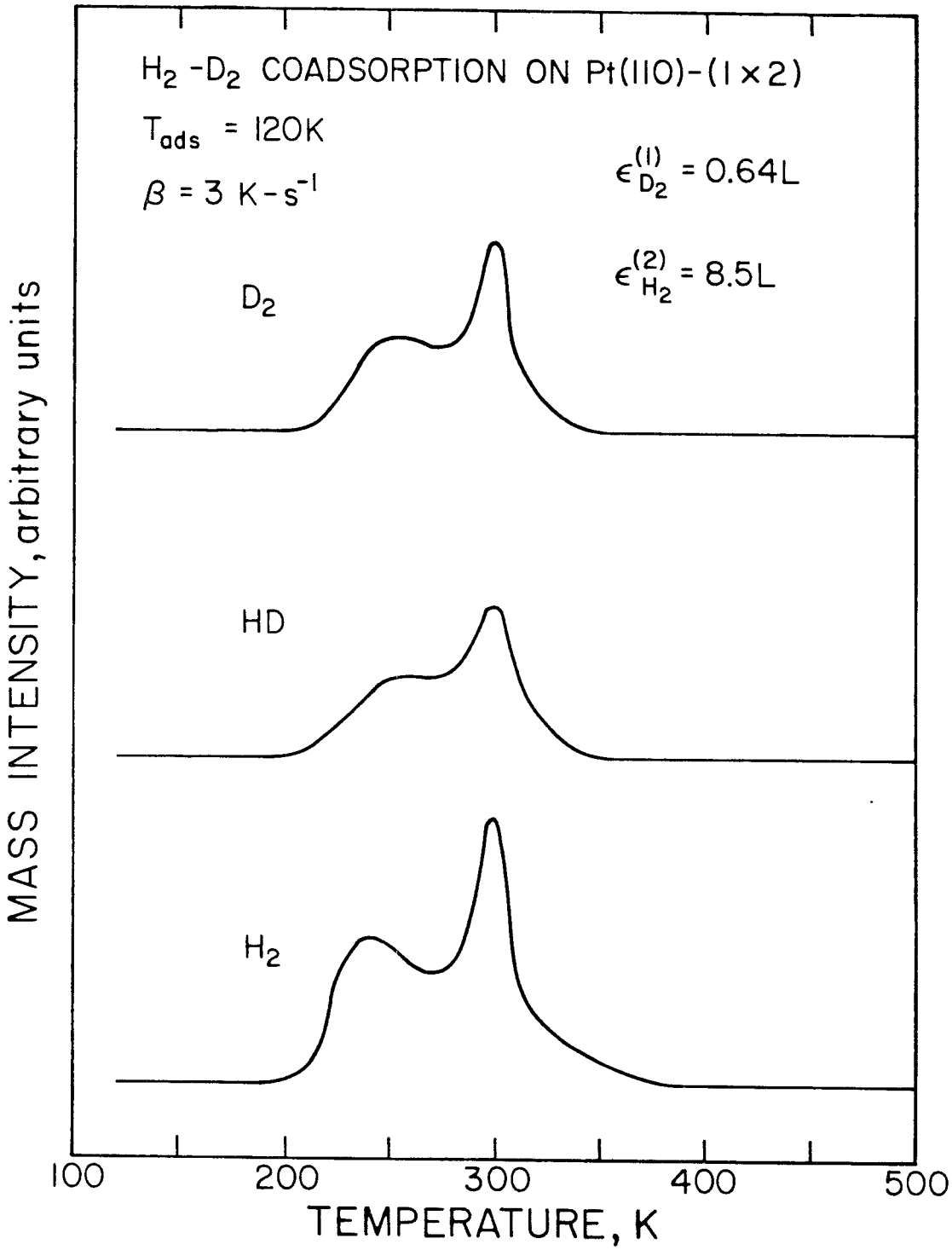
H2 -D2 COADSORPTION ON Pt(110)-(1×2)
Tads = 120K
β = 3 K-s-1
ε(1)D2 = 0.64L
ε(2)H2 = 8.5L
D2
HD
H2
MASS INTENSITY, arbitrary units
100
200
300
400
500
TEMPERATURE, K

Figure 8

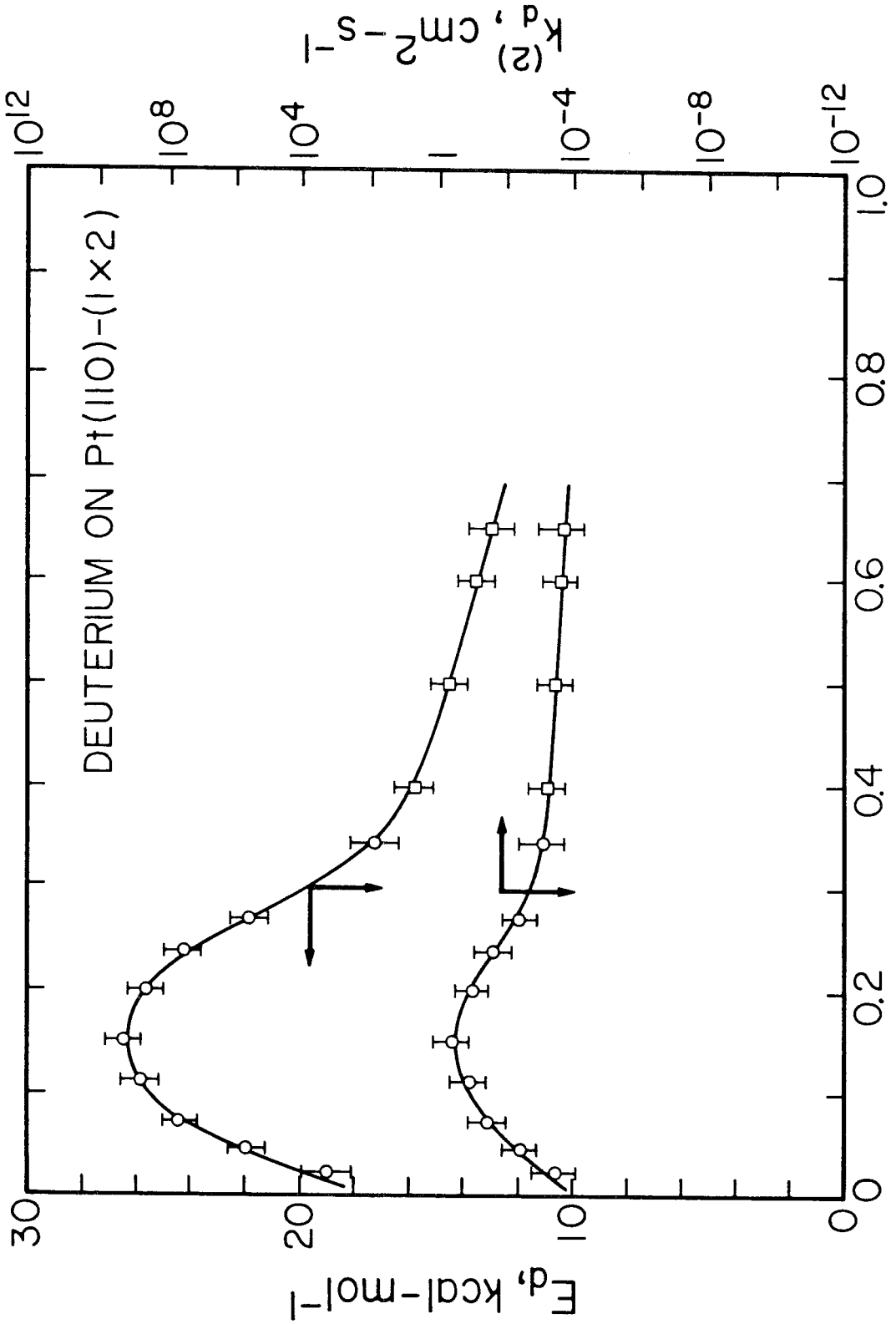
DEUTERIUM ON Pt(110)-(1×2)
E_d, kcal-mol^{-1}
$k_d^{(2)}$, cm^2-s^{-1}
FRACTIONAL COVERAGE
30
20
10
0
0.0
0.2
0.4
0.6
0.8
1.0
10^{12}
10^{8}
10^{4}
1
10^{-4}
10^{-8}
10^{-12}

Figure 9

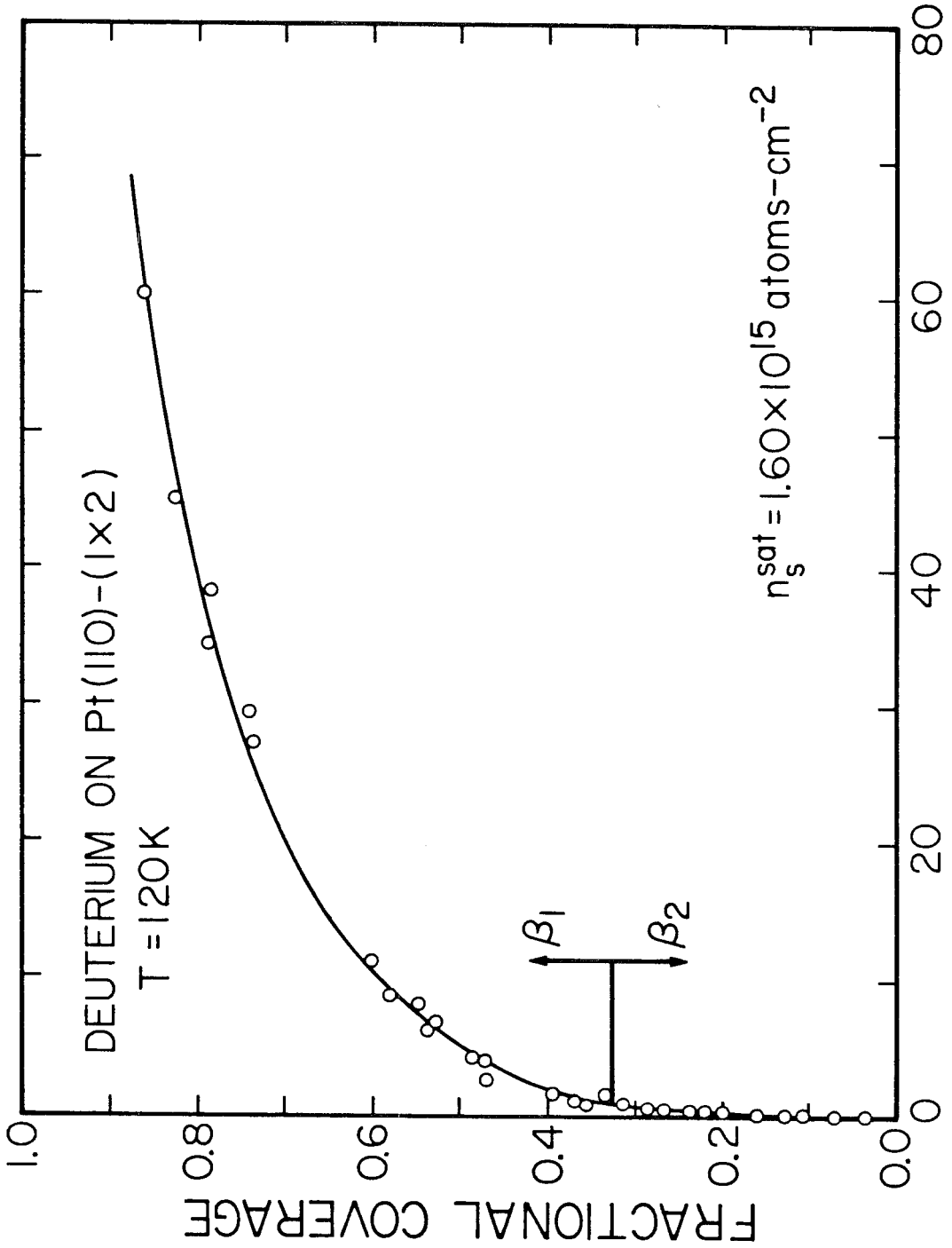
DEUTERIUM ON Pt(110)-(1×2)
T = 120K
$n_s^{sat} = 1.60 \times 10^{15}$ atoms-cm^{-2}
β_1
β_2
FRACTIONAL COVERAGE
EXPOSURE, L
0.0
0.2
0.4
0.6
0.8
1.0
0
20
40
60
80

Figure 10

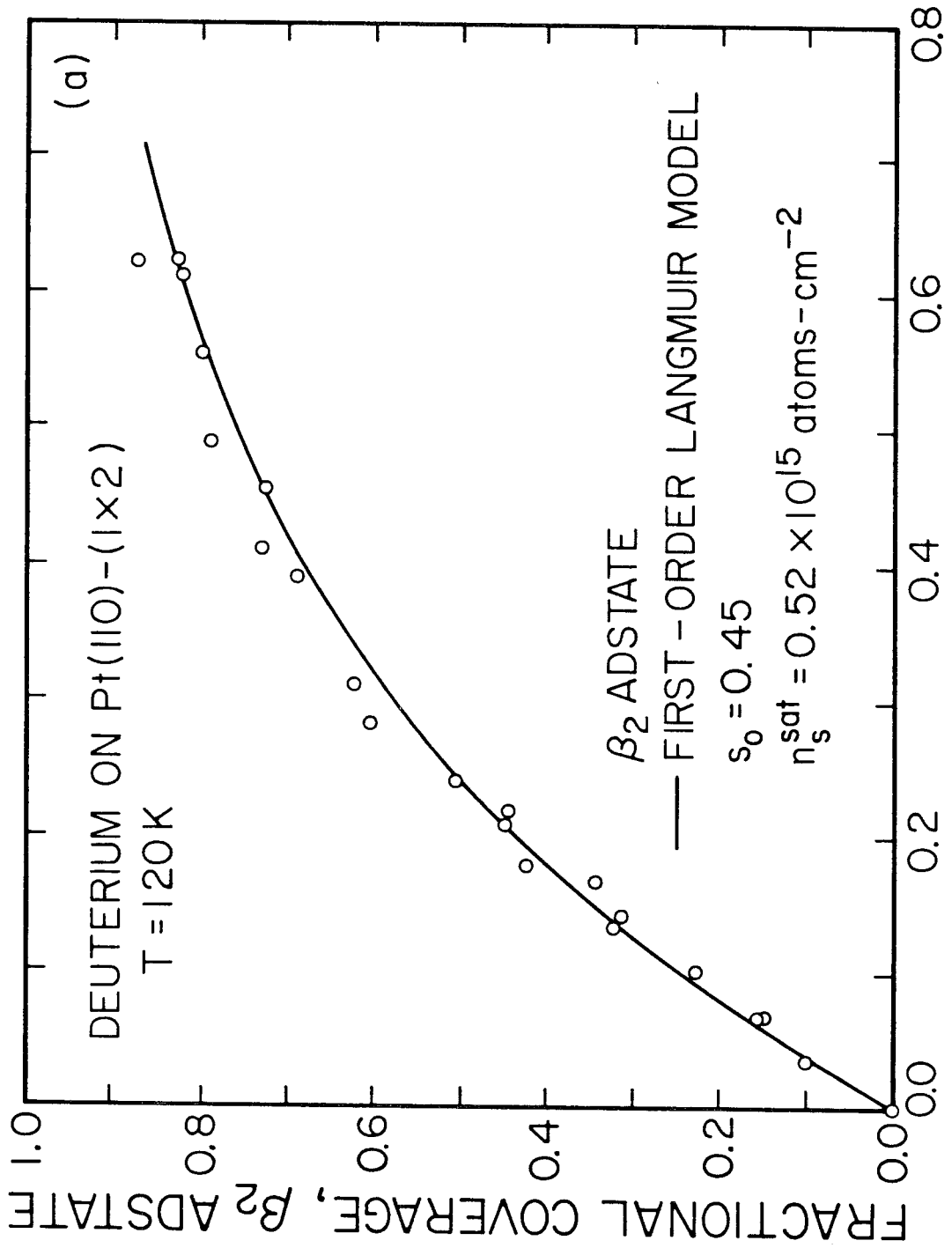
(a)
DEUTERIUM ON Pt(110)-(1×2)
T = 120 K
β_2 ADSTATE
FIRST-ORDER LANGMUIR MODEL
$s_0 = 0.45$
$n_s^{sat} = 0.52 \times 10^{15}$ atoms-cm^{-2}
FRACTIONAL COVERAGE, θ_{β_2} ADSTATE
EXPOSURE, L
0.0
0.2
0.4
0.6
0.8
1.0

Figure 11(a)

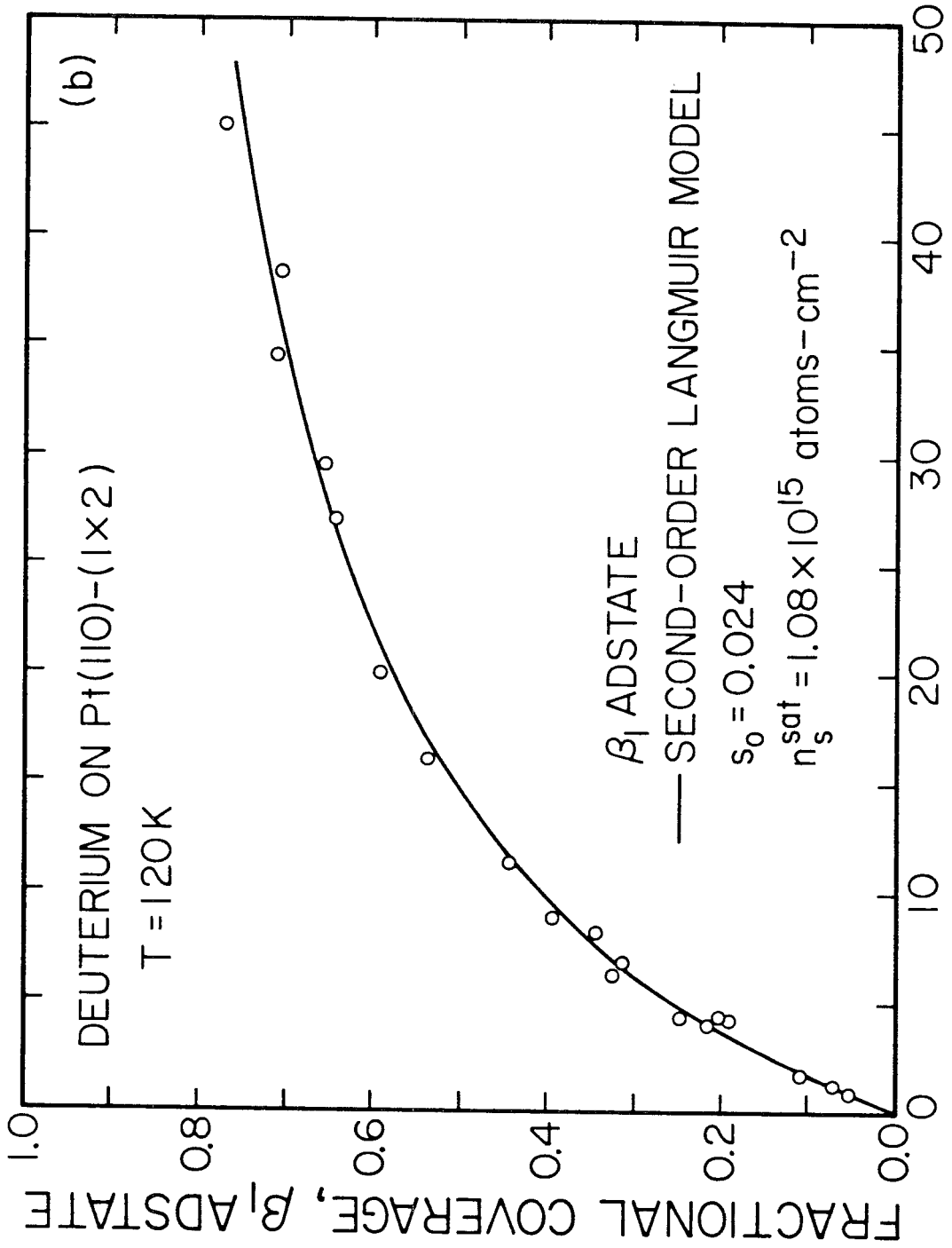
(b)
DEUTERIUM ON Pt(110)-(1×2)
T = 120 K
β_1 ADSTATE
— SECOND-ORDER LANGMUIR MODEL
$s_0 = 0.024$
$n_s^{sat} = 1.08 \times 10^{15}$ atoms-cm^{-2}
FRACTIONAL COVERAGE, $\theta_{\beta_1 ADSTATE}$
EXPOSURE, L
0.0
0.2
0.4
0.6
0.8
1.0
0
10
20
30
40
50

Figure 11(b)

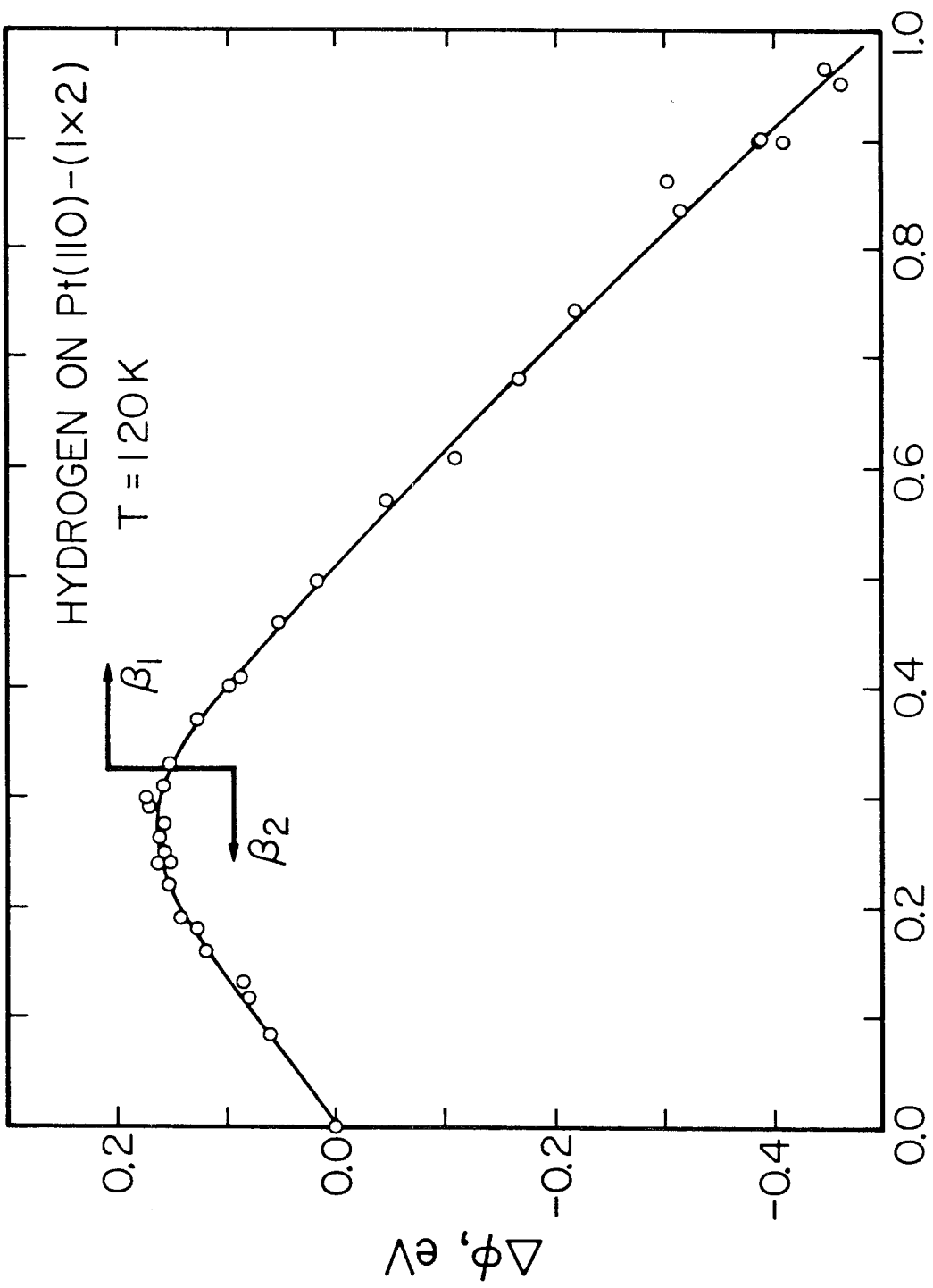
HYDROGEN ON Pt(110)-(1x2)
T = 120 K
β1
β2
Δφ, eV
0.2
0.0
-0.2
-0.4
0.0
0.2
0.4
0.6
0.8
1.0
FRACTIONAL COVERAGE

Figure 12

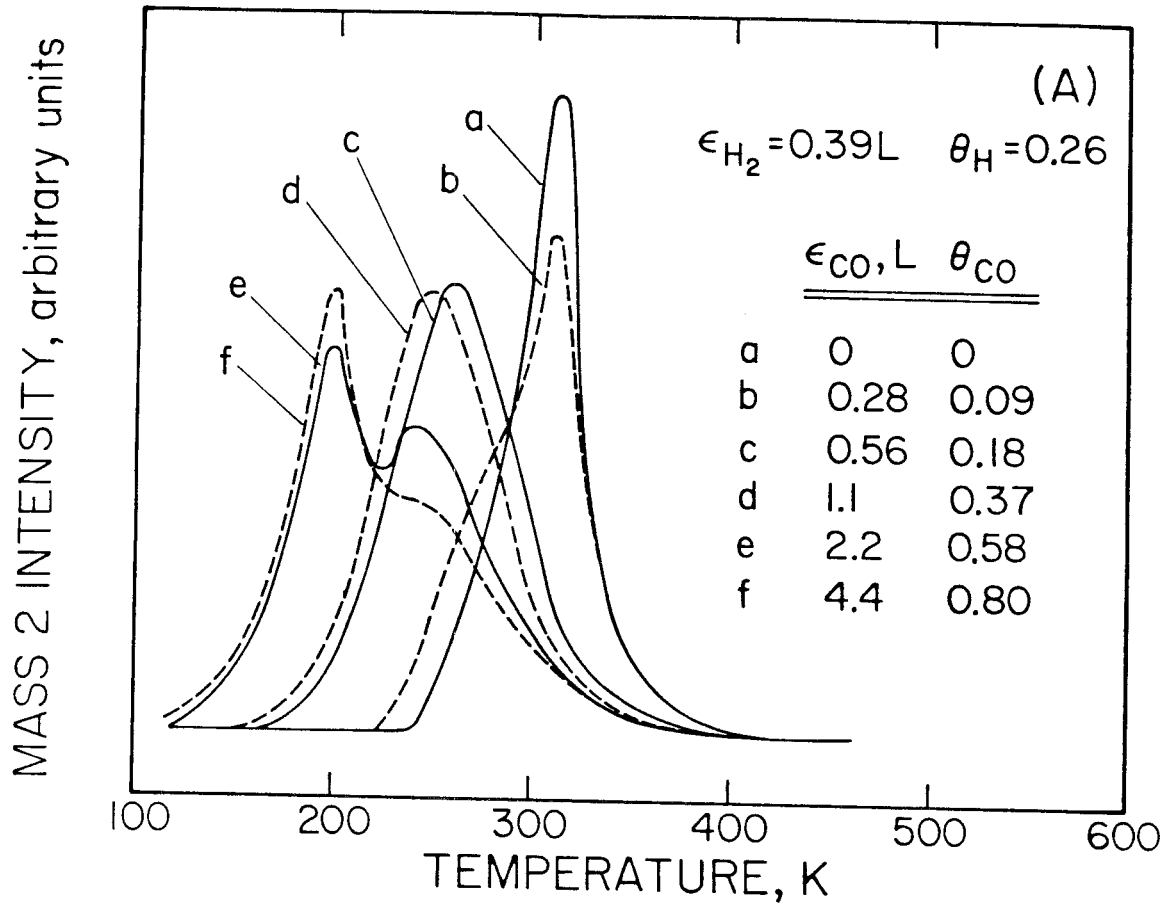
(A)
ϵ_{H_2}=0.39L θ_H=0.26
ϵ_{CO}, L θ_{CO}
a 0 0
b 0.28 0.09
c 0.56 0.18
d 1.1 0.37
e 2.2 0.58
f 4.4 0.80
MASS 2 INTENSITY, arbitrary units
100 200 300 400 500 600
TEMPERATURE, K

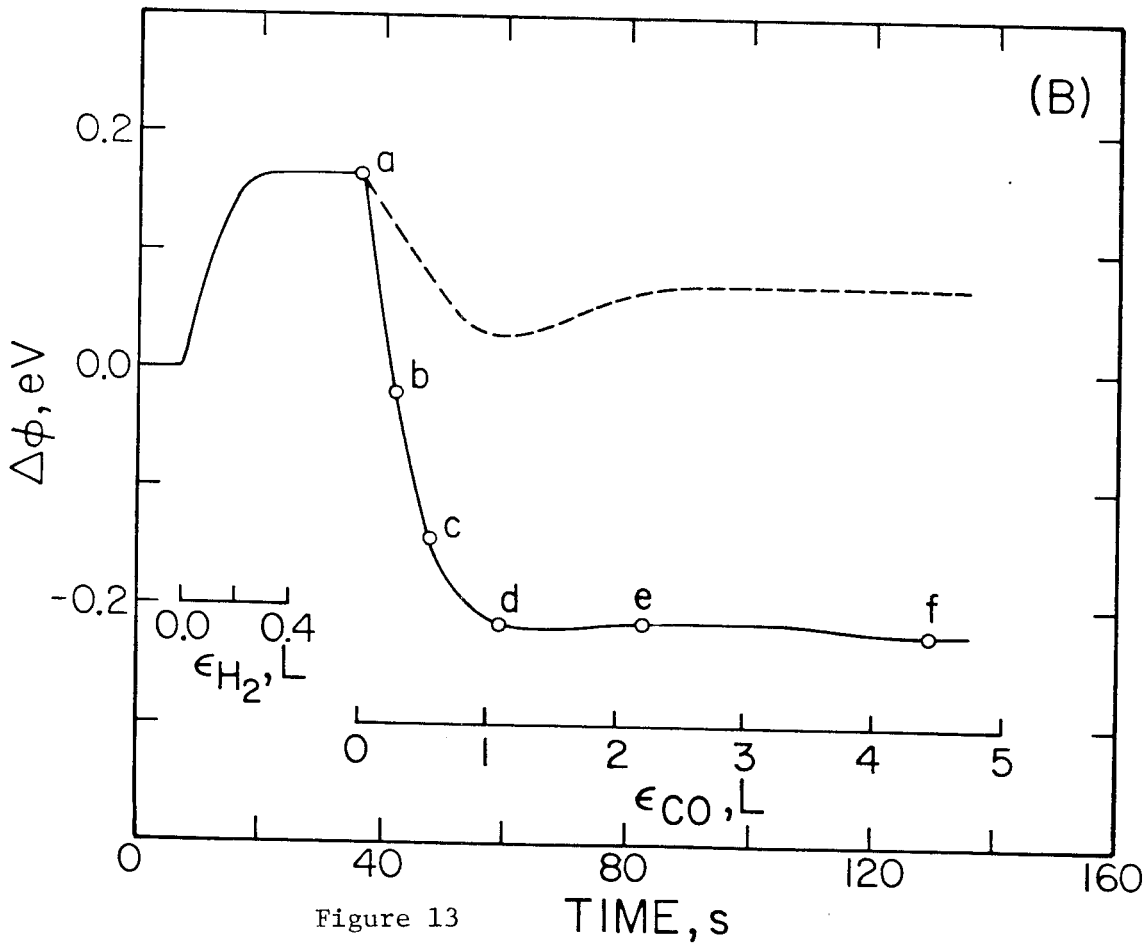
(B)
0.2
0.0
-0.2
$\Delta\phi$, eV
0.0 0.4
ϵ_{H_2}, L
0 1 2 3 4 5
ϵ_{CO}, L
0 40 80 120 160
TIME, s

Figure 13

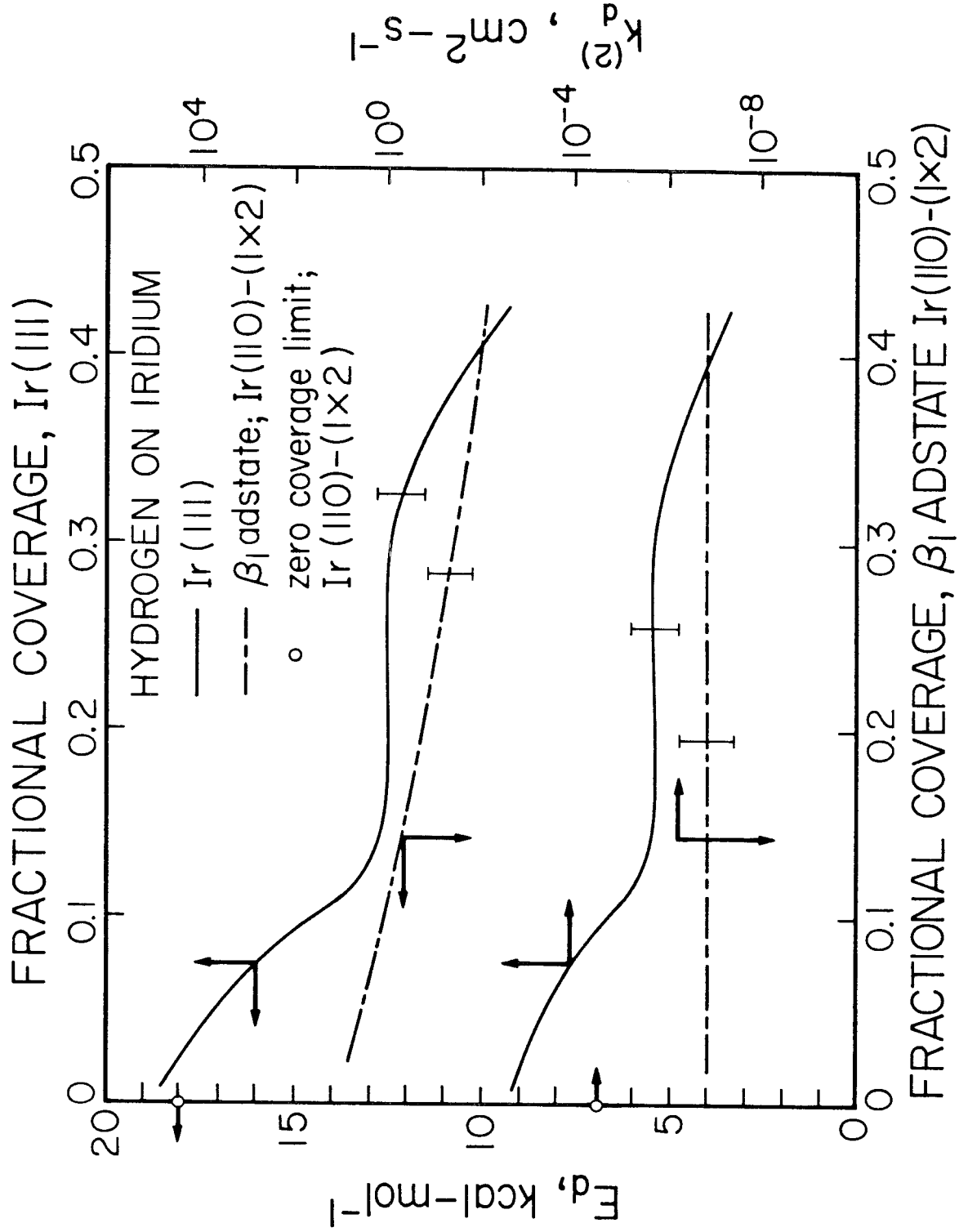
HYDROGEN ON IRIDIUM
Ir (111)
β1 adstate; Ir(110)-(1×2)
zero coverage limit; Ir (110)-(1×2)
FRACTIONAL COVERAGE, Ir(111)
FRACTIONAL COVERAGE, β1 ADSTATE Ir(110)-(1×2)
Ed, kcal-mol-1
k(2)d , cm2-s-1
0
0.1
0.2
0.3
0.4
0.5
20
15
10
5
0
10^4
10^0
10^-4
10^-8

Figure 14

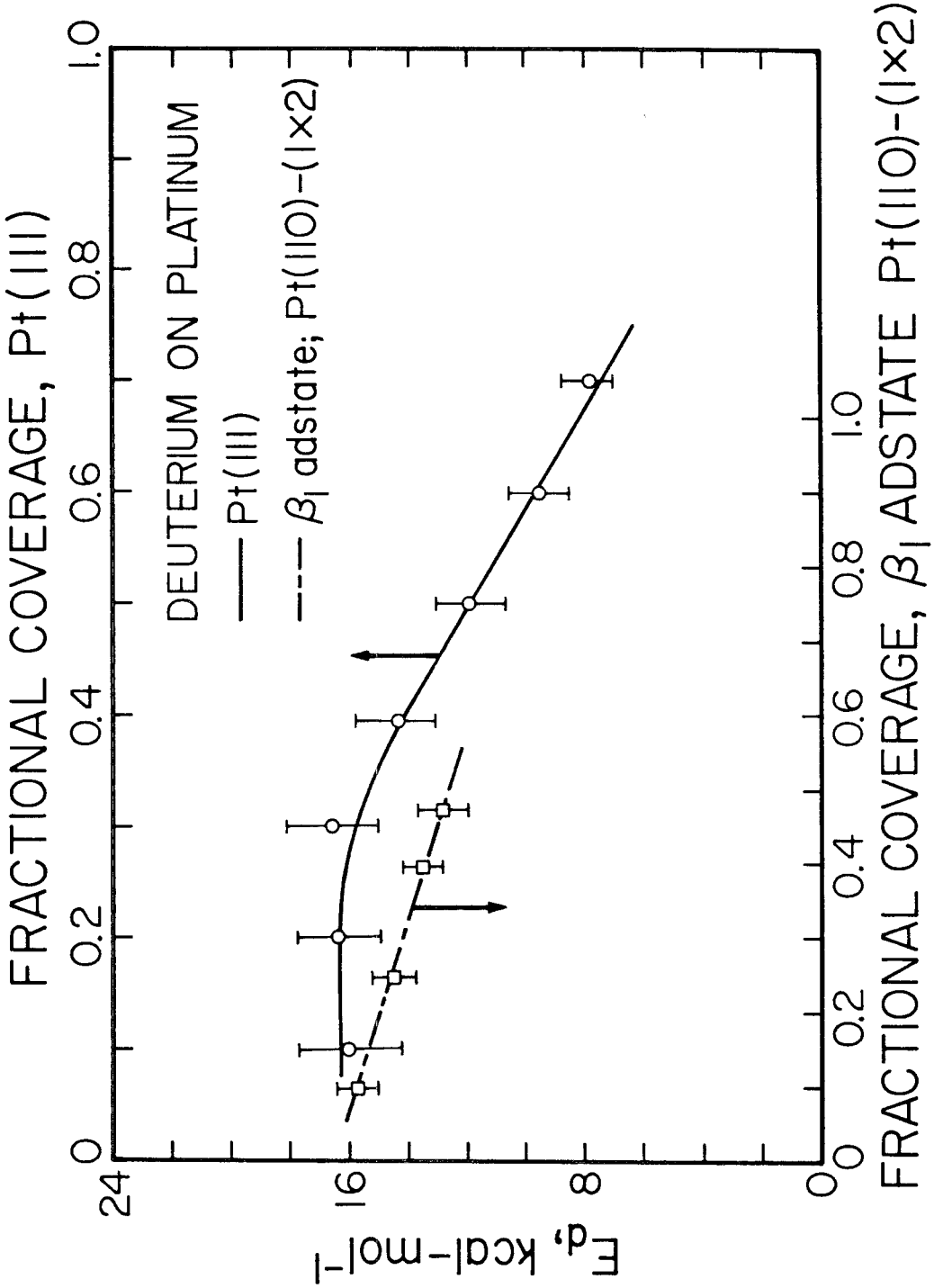
FRACTIONAL COVERAGE, Pt(111)
FRACTIONAL COVERAGE, β_1 ADSTATE Pt(110)-(1×2)
E_d, kcal-mol^{-1}
DEUTERIUM ON PLATINUM
Pt(111)
β_1 adstate; Pt(110)-(1×2)
0
0.2
0.4
0.6
0.8
1.0
8
16
24

Figure 15

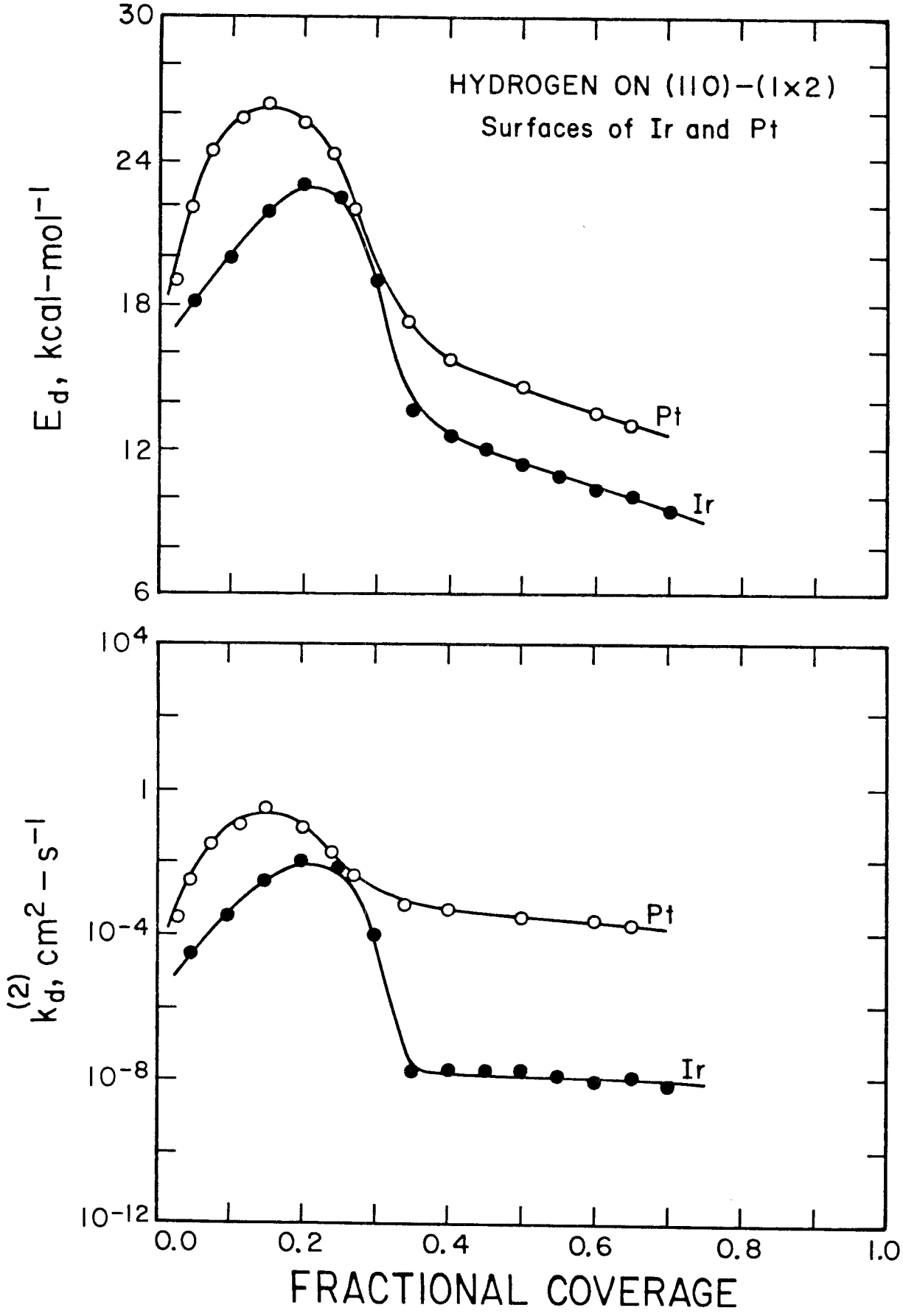
HYDROGEN ON (110)–(1×2)
Surfaces of Ir and Pt
E_d, kcal-mol^{-1}
30
24
18
12
6
Pt
Ir
$k_d^{(2)}$, cm^2-s^{-1}
10^4
1
10^{-4}
10^{-8}
10^{-12}
Pt
Ir
0.0
0.2
0.4
0.6
0.8
1.0
FRACTIONAL COVERAGE

Figure 16

CHAPTER 5

Hydrogenolysis of *n*-Butane over the (111) and (110)-(1x2) Surfaces of Iridium: A Direct Correlation between Catalytic Selectivity and Surface Structure

[The text of Chapter 5 consists of an article coauthored with D. W. Goodman and W. H. Weinberg, which has appeared in *The Journal of American Chemical Society* **108**, 4653 (1986).]

Reprinted from the Journal of the American Chemical Society, 1986, *108*, 4653.
Copyright © 1986 by the American Chemical Society and reprinted by permission of the copyright owner.

Hydrogenolysis of *n*-Butane over the (111) and (110)-(1×2) Surfaces of Iridium: A Direct Correlation between Catalytic Selectivity and Surface Structure†

J. R. Engstrom‡ and D. W. Goodman*

Surface Science Division, Sandia National Laboratories Albuquerque, New Mexico 87185

W. H. Weinberg*

Division of Chemistry and Chemical Engineering California Institute of Technology Pasadena, California 91125

Received March 24, 1986

The importance of surface structure in determining the activity and selectivity of various classes of heterogeneously catalyzed reactions is well-known. Boudart[1] has applied Taylor's concept of "active centers"[2] to catalysis by supported metals, stressing the need to examine the sensitivity of the *specific activity* (per site basis) to the average metallic particle size ("dispersion"). Although many reactions over supported catalysts, including the hydrogenolysis of alkanes, have been found to be "structure-sensitive",[1] a microscopic understanding of this variation in catalytic properties with particle size has remained elusive. Except in the limit of nearly atomic dispersion, changes in the surface of the catalyst particle with size will be geometric,[3] involving variations in the relative number of atoms in high-symmetry microfacets and at low-coordination-number edge and corner positions where these high-symmetry planes intersect.[5]

Foger and Anderson[6] have reported that the selectivity for the hydrogenolysis of n-C_4H_{10} by supported Ir catalysts is extremely sensitive to the average metal particle size.[7] The structure sensitivity is most apparent for clusters of diameter $\lesssim$40 Å, where there is a rapid change in the average coordination number of the metal surface atoms.[11] Since the use of oriented single crystals as catalysts allows an *unambiguous* assessment of the effects of

† Work performed at Sandia National Laboratories and supported by the U.S. Department of Energy under Contract DE-AC04-76DP00789. We acknowledge the partial support of the Office of Basic Energy Sciences, Division of Chemical Science.

‡ Visiting from the Division of Chemistry and Chemical Engineering, California Institute of Technology, Pasadena, CA 91125.

(1) Boudart, M. *Adv. Catal.* **1969**, *20*, 153.

(2) Taylor, H. S. *Proc. R. Soc. London, Ser. A* **1925**, *108*, 105.

(3) Any perturbation in the electronic properties will result from the differing *surface* geometries. Strong metal–support interactions are negligible for nonreducible oxides such as Al_2O_3 and SiO_2, whereas they may be significant for reducible oxides such as TiO_2.[4]

(4) See, e.g.: Foger, K. In *Catalysis—Science and Technology*; Anderson, J. R., Boudart, M., Eds.; Springer-Verlag: Berlin, 1984; Vol. 6, p 227 and references therein.

(5) van Hardeveld, R.; Hartog, F. *Adv. Catal.* **1972**, *22*, 75.

(6) Foger, K.; Anderson, J. R. *J. Catal.* **1979**, *59*, 325.

(7) Similar results have been reported for the hydrogenolysis of n-C_4H_{10} by supported Pt[8] and the hydrogenolysis of n-C_5H_{12} by supported Pt[9] and Rh.[10]

(8) (a) Leclercq, G.; Trochet, J.; Maurel, R. *C. R. Acad. Sci., Ser. C* **1973**, *276*, 1353. (b) Guczi, L.; Gudkov, B. S. *React. Kinet. Catal. Lett.* **1978**, *9*, 343.

(9) Brunelle, J.-P.; Sugier, A.; Le Page, J.-F. *J. Catal.* **1976**, *43*, 273.

(10) Yao, H. C.; Shelef, M. *J. Catal.* **1979**, *56*, 12. Yao, H. C.; Yu Yao, Y.-F.; Otto, K. *J. Catal.* **1979**, *56*, 21.

(11) Poltorak, O. M.; Boronin, V. S. *Russ. J. Phys. Chem.* **1966**, *40*, 1436.

0002-7863/86/1508-4653$01.50/0 © 1986 American Chemical Society

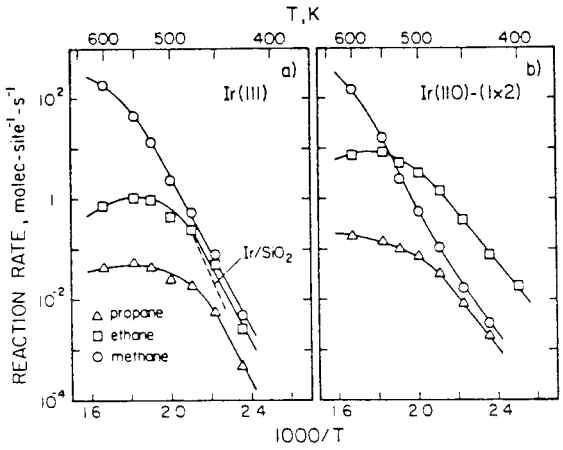

Figure 1. Specific reaction rates for the hydrogenolysis of n-C_4H_{10} over (a) an Ir(111) surface ($n_s = 1.57 \times 10^{15}$ sites cm^{-2}) and (b) and Ir-(110)-(1×2) surface ($n_s = 1.93 \times 10^{15}$ sites cm^{-2}). The partial pressure of n-C_4H_{10} (>99.95% purity) is 1 torr, and that of H_2 (99.999% purity) is 100 torr. The dashed line in (a) represents data obtained by Foger and Anderson[6] over a 0.98 wt % Ir/SiO_2 catalyst ($\bar{d}_{Ir} = 70$ Å; dispersion of 16%) extrapolated to our reactant partial pressures and plotted in terms of conversion. These data agree well with those for the Ir(111) surface.

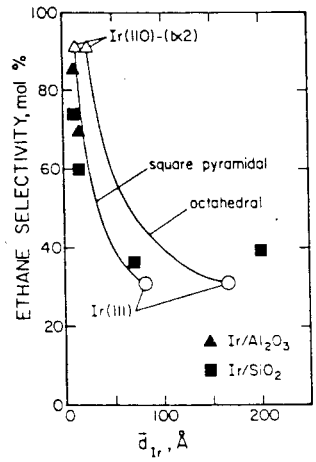

Figure 2. Selectivity for C_2H_6 production (mol % of total products) from the hydrogenolysis of n-C_4H_{10} over Ir catalysts plotted as a function of the mean Ir particle size. Data for the supported catalysts are from Foger and Anderson.[6] The abscissae for the two single-crystalline surfaces were determined by a calculated "effective particle size", as described in the text. The solid curves represent theoretical interpolations between the single-crystalline surfaces based on the specified geometrical shapes, as described in the text. The reaction temperature is in all cases ~475 K.

surface geometry,[12] we have investigated the hydrogenolysis of n-C_4H_{10} over the close-packed (111) and the corrugated (110)-(1×2) surfaces of Ir. The clean Ir(110) surface is reconstructed into a (1×2) superstructure,[13] which contains a large fraction (25%) of low-coordination-number (C_7[5]) edge atoms, whereas a perfect (111) surface contains no such atoms. If the ratio of the number of edge atoms to the number of face atoms influences the mechanism of this reaction, the (110)-(1×2) and (111) surfaces should be decisive in quantifying the connection between catalytic selectivity and *local* surface structure.

The experiments were performed in a high-pressure reaction chamber linked to an ultrahigh vacuum (UHV) analysis chamber in which facilities are available for Auger electron spectroscopy (AES) and ion sputtering.[12] The crystals were cleaned in the UHV chamber by Ar^+ sputtering, heating in 5×10^{-7} torr of O_2 at 700 K, and annealing to 1600 K. Reaction products were detected by gas chromatography.

Steady-state rates of the reaction of n-C_4H_{10} with H_2 for conversions below ~1% over both surfaces are shown in Figure 1, plotted in an Arrhenius form. Post-reaction surface characterization by AES indicated the presence of a *submonolayer* carbonaceous residue, the fractional coverage of which was nearly independent of reaction conditions; i.e., $\theta_c \cong 0.34 \pm 0.08$ on Ir(111) and $\theta_c \cong 0.24 \pm 0.08$ on Ir(110)-(1×2).[14] The only reaction products observed were CH_4, C_2H_6, and C_3H_8. The decrease in the apparent activation energy ("rollover") at $T \gtrsim 500$ K is associated with a depletion in the steady-state coverage of hydrogen.[12] Of more importance is the fact that the selectivities are quite different for the two surfaces where linear Arrhenius behavior is observed ($T \lesssim 475$ K). In this regime, the *major* reaction pathways are n-$C_4H_{10} + 2H_2 \rightarrow 2CH_4 + C_2H_6$ on Ir(111) and n-$C_4H_{10} + H_2 \rightarrow 2C_2H_6$ on Ir(110)-(1×2), with apparent activation energies of 34 ± 2 kcal mol^{-1} and 22 ± 2 kcal mol^{-1}. The profound difference in selectivity that is observed suggests that *different intermediates exist on the two surfaces.*

In order to compare the results of Foger and Anderson[6] to those reported here, we must compute an "effective particle size" for the (111) and (110)-(1×2) surfaces. *We shall introduce the ratio of the number of edge (C_7) atoms to the number of (111) face (C_9) atoms as the appropriate criterion of the "effective particle size".* The (110)-(1×2) surface contains one C_7 atom and two C_9 atoms per unit cell, a ratio of 1/2. The ratio for the (111) surface is determined both by defects and by the edge of the crystal (edge area/surface area $\lesssim 1/10$). On the basis of hydrogen chemisorption data for this (111) surface,[16] the ratio C_7/C_9 is ~1/20. Assuming the supported catalyst particles form shapes of either octahedral or square-pyramidal (half-octahedral) structure,[17] the effective mean particle diameters are approximately 24 or 13 Å for the (110)-(1×2) surface, and 166 or 81 Å for the (111) surface, respectively.[18]

The selectivity for C_2H_6 production for both the supported catalysts[6] and the two single-crystalline surfaces are shown in Figure 2 as a function of the mean particle diameter.[19] Theoretically calculated curves, normalized to the specific activities of the two single-crystalline surfaces and interpolated by using the ratio C_7/C_9 as a basis, are also shown in Figure 2. Obviously, there is an *excellent* correlation between the selectivity for C_2H_6 production and the mean Ir particle size. Based on our results, *the observed increase in C_2H_6 selectivity with decreasing particle size is identified clearly with the increasing participation of low-coordination-number surface atoms.*

We have also observed that the specific rates (and selectivities) of hydrogenolysis of C_3H_8 over Ir(111) *and* Ir(110)-(1×2) and of n-C_4H_{10} over Ir(111) are virtually identical, with apparent activation energies of 34 ± 2 kcal mol^{-1}.[20] This implicates the presence of structurally similar, adsorbed intermediates in these

(12) Goodman, D. W.; Kelley, R. D.; Madey, T. E.; Yates, J. T., Jr. *J. Catal.* **1980**, *63*, 226. Goodman, D. W. *Acc. Chem. Res.* **1984**, *17*, 194.

(13) Chan, C.-M.; Van Hove, M. A.; Weinberg, W. H.; Williams, E. D. *Solid State Commun.* **1979**, *30*, 47. Chan, C.-M.; Van Hove, M. A.; Weinberg, W. H.; Williams, E. D. *Surf. Sci.* **1980**, *91*, 430.

(14) It has been shown previously that the (1×2) reconstruction of the Ir(110) surface is *not* removed by the presence of any coverage of hydrocarbon residues or surface carbon and hydrogen for temperatures between 100 and 800 K.[15]

(15) Weinberg, W. H. In *Surv. Prog. Chem.* **1983**, *10*, 1. Szuromi, P. D.; Weinberg, W. H. *Surf. Sci.* **1985**, *149*, 225.

(16) Engstrom, J. R.; Tsai, W.; Weinberg, W. H. manuscript in preparation. Szuromi, P. D.; Engstrom, J. R.; Weinberg, W. H. *J. Chem. Phys.* **1984**, *80*, 508.

(17) See, e.g.: Burch, R. In *Catalysis (Specialist Periodical Reports)*; Bond, G. C., Webb, G., Eds.; The Royal Society of Chemistry: London, 1985; Vol. 8, p 149 and references therein.

(18) These two geometrical shapes will bracket other probable regular polyhedra, e.g., cubo-octahedra or cubes.

(19) Note that for the reaction n-$C_4H_{10} + H_2 \rightarrow 2C_2H_6$, the selectivity for ethane is 100%; whereas for the reaction n-$C_4H_{10} + 2H_2 \rightarrow 2CH_4 + C_2H_6$, the selectivity for ethane is 33%.

(20) Engstrom, J. R.; Goodman, D. W.; Weinberg, W. H., manuscript in preparation.

reactions. For n-C_4H_{10} hydrogenolysis over Ir(110)-(1×2), however, both the specific rate (apparent activation energy of 22 ± 2 kcal mol^{-1}) and the selectivity (to C_2H_6) are qualitatively different, indicative of the presence of a qualitatively different surface intermediate. Furthermore, by varying the partial pressures of the reactants, we have observed that *whatever* the intermediate from n-C_4H_{10} on Ir(110)-(1×2) is, it is *less dehydrogenated* than either the intermediate from n-C_4H_{10} on Ir(111) or the intermediate from C_3H_8 on both surfaces.[20] These observations suggest *strongly* that the occurrence of this particular intermediate on Ir(110)-(1×2) is a consequence of the corrugation of this surface rather than, for example, the presence of a particular, disordered carbonaceous residue on the surface. A very plausible intermediate in n-C_4H_{10} hydrogenolysis over Ir(110)-(1×2) is a metallacycle pentane. For example, it is known that transition-metal homogeneous complexes containing metallacycle pentane ligands can decompose thermally to two C_2H_4 ligands,[21] which would be hydrogenated to C_2H_6 under our experimental conditions, in agreement with the observed selectivity. The corollary to this hypothesis is that metallacycle pentane formation is favored on those surfaces that contain low-coordination-number metal atoms, and which is *necessary* from a stereochemical point of view on the two single-crystalline surfaces discussed here.

To summarize, the selectivity for C_2H_6 production from the hydrogenolysis of n-C_4H_{10} over Ir catalysts scales with the concentration of low-coordination-number metal surface atoms. This observation and detailed interpretation are limited neither to n-C_4H_{10} nor to Ir, however. Rather, they serve to illustrate the profound importance of local surface structure in dictating the occurrence of particular reaction intermediates and, hence, catalytic *selectivity*.

Registry No. Ir, 7439-88-5; butane, 106-97-8.

---

(21) (a) Grubbs, R. H.; Miyashita, A. *J. Am. Chem. Soc.* **1978**, *100*, 1300. Grubbs, R. H.; Miyashita, A.; Liu, M.; Burk, P. *J. Am. Chem. Soc.* **1978**, *100*, 2418. (b) Diversi, P.; Ingrosso, G.; Lucherni, A. *J. Chem. Soc., Chem. Commun.* **1977**, *52*. (c) McLain, S. J.; Wood, C. D.; Schrock, R. R. *J. Am. Chem. Soc.* **1977**, *99*, 3519. (d) McDermott, J. X.; Wilson, M. E.; Whitesides, G. M. *J. Am. Chem. Soc.* **1976**, *98*, 6529. (e) Harvie, I. J.; McQuillin, F. J. *J. Chem. Soc., Chem. Commun.* **1974**, 806. (f) Cassar, L.; Eaton, P. E.; Halpern, J. *J. Am. Chem. Soc.* **1970**, *92*, 3515. (g) Jacobson, D. B.; Freiser, B. S. *J. Am. Chem. Soc.* **1983**, *105*, 7492. (h) Armentrout, P. B.; Beauchamp, J. L. *J. Am. Chem. Soc.* **1981**, *103*, 6628.

CHAPTER 6

The Hydrogenolysis of Ethane, Propane, *n*-Butane and Neopentane over the (111) and (110)-(1x2) Surfaces of Iridium

[The text of Chapter 6 consists of an article coauthored with D. W. Goodman and W. H. Weinberg, which has been submitted to *The Journal of American Chemical Society.*]

Abstract

The hydrogenolysis of ethane, propane, *n*-butane and neopentane has been investigated over the (111) and (110)-(1x2) single crystalline surfaces of iridium at reactant partial pressures from 0.2 and 5.0 Torr of hydrocarbon, 20 to 500 Torr of hydrogen and for surface temperatures from 400 to 700 K. A coupled high pressure reactor-ultrahigh vacuum (UHV) analysis chamber was employed, which permitted both the measurement of the specific rates of reaction and *in situ* pre- and post-reaction surface characterization utilizing standard UHV techniques. Both the apparent reaction kinetics (*i.e.*, activation energies and preexponential factors) and the dependencies of the rates of reaction on the reactant partial pressures (*i.e.*, apparent reaction "orders") were examined in detail. Post-reaction surface analysis by Auger electron spectroscopy indicated the presence of a *submonolayer* carbonaceous residue, the coverage of which was both nearly identical on both surfaces, and essentially independent of reaction conditions, *i.e.*, surface temperature and reactant partial pressures. Titration of these residues with hydrogen produced only methane in all cases, suggesting that the carbonaceous residue plays the role of a "spectator." The major reaction channels for all of the reactants examined, with the exception of *n*-butane, involve the cleavage of a single carbon-carbon bond, resulting in a "demethylization" of the parent hydrocarbon. For *n*-butane, the major reaction channels on the two surfaces are $n\text{-}C_4H_{10}+2H_2 \rightarrow 2CH_4+C_2H_6$ on Ir(111) and $n\text{-}C_4H_{10} + H_2 \rightarrow 2C_2H_6$ on Ir(110)-(1x2). In all cases, as the temperature is increased sufficiently, the apparent activation energy decreases, and, concomitantly, the selectivity for methane increases greatly. These changes have been identified explicitly with a depletion in the steady-state coverage of hydrogen adatoms as the temperature is increased. A mechanistic model involving a rate-limiting irreversible unimolecular C-C bond cleavage step has been employed to describe the variations in the both the specific activity and selectivity of hydrogenolysis with variations in the reactant partial pressures. The successful application of the mechanism to

the data, with the exception of *n*-butane on Ir(110)-(1x2), permitted the deduction of the stoichiometries of the adsorbed parent hydrocarbon fragments (*i.e.*, the reaction intermediates). In all cases, the implied stoichiometries are consistent with the proposition that hydrogenolysis proceeds through a partially dehydrogenated intermediate that is multiply bound to the surface via one or more metal surface atoms. The hydrogenolysis of *n*-butane over the Ir(110)-(1x2) surface is not described well by the mechanism involving irreversible C-C bond cleavage; rather, a mechanism involving reversible C-C bond cleavage in a symmetrical reaction intermediate best describes the data. Concerning the implicated reaction intermediates, the hydrogenolysis of ethane proceeds through different reaction intermediates, the parent fragment on the Ir(110)-(1x2) surface being more extensively dehydrogenated. Both the specific activity and the implicated reaction intermediates (*i.e.*, mechanisms) for both propane and neopentane are nearly indistinguishable on the two surfaces. The selectivity for the hydrogenolysis of *n*-butane on the two surfaces has been identified with the occurrence of particular adsorbed reaction intermediates on each surface. The intermediate that leads to the high selectivity for ethane on the Ir(110)-(1x2) surface is a mononuclear metallacycle pentane. The formation of this intermediate is sterically forbidden on (111) surfaces. The implication of this latter result (*i.e.*, different mechanisms for *n*-butane hydrogenolysis) on related reactions of saturated hydrocarbons, such as skeletal isomerization and cyclization, is discussed briefly.

I. Introduction

The study of the reactions of saturated hydrocarbons with hydrogen over transition metal surfaces is of considerable technological importance, most notably in connection with the hydroprocessing of petrochemical feedstocks. The hydrogenolysis of saturated hydrocarbons represents a major subset of the reactions that have been observed over supported transition metal catalysts which also include, for example, skeletal isomerization and cyclization. For many of these reactions the *specific* activity (per site basis) and/or selectivity has been found to be sensitive to the average metallic particle size. This "structure-sensitivity" **(1)** has been attributed to a number of effects, which include variations in the electronic and/or geometric nature of the catalyst surface with particle size. Considerable effort has already been made in this area **(2–7)** which, unfortunately, has not yet led to a complete *microscopic* understanding of the observed variations in the catalytic properties with particle size. For example, few correlations exist between the structure of the catalyst surface and the relevant adsorbed reaction intermediates that act to control the activity and/or selectivity of a particular catalyst.

We have undertaken a fundamental examination of the role of surface structure in the hydrogenolysis of various short-chain alkanes over two oriented single crystalline surfaces of iridium. The use of oriented single crystals as catalysts allows an *unambiguous* assessment of the effects of surface geometry **(8)** or, equivalently, surface electronic structure as a consequence of its geometry. For example, previous work **(9–11)** has indicated that the specific rates of hydrogenolysis of various alkanes differ considerably over two high-symmetry single crystalline surfaces of nickel, namely the Ni(100) and Ni(111) planes. It is important to note that for idealized catalyst particle shapes (*e.g.*, cubo-octahedra), the relative number of atoms in these two high-symmetry microfacets will vary with particle size. One also expects a variation in the relative number of atoms in the low-coordination-number edge and corner positions where these high symmetry planes intersect. In order to

determine the importance of the latter, we have employed the close-packed (111) and the corrugated (110)-(1x2) surfaces of iridium as model catalysts. The clean Ir(110) surface reconstructs into a (1x2) superstructure **(12)**, which contains a large fraction (25%) of low-coordination-number [C_7 **(13)**] edge atoms, whereas a perfect (111) surface contains no such atoms (*cf.* Fig. 1). The (1x2) reconstruction is expected to be stable *under reaction conditions*, *e.g.*, in the presence of adsorbed hydrocarbon residues and/or surface carbon and hydrogen **(14)**. Thus, if the ratio of the number of edge atoms to the number of face atoms influences the dynamics and/or mechanism of a particular reaction, then the (110)-(1x2) and (111) surfaces should be decisive in quantifying the connection between catalytic activity and/or selectivity and *local* surface structure.

We shall consider here the reactions of ethane, propane, *n*-butane and neopentane with hydrogen over these two single crystalline surfaces of iridium. By examining the reactions of these four hydrocarbons of differing structure, various adsorption mechanisms can be isolated and their relative contributions can be evaluated; *e.g.*, "1,2" adsorption is prohibited for neopentane, whereas "1,4" adsorption is possible only for *n*-butane. In addition, since single crystalline catalysts are essentially not affected by the heat and mass transfer limitations associated with supported metal catalysts, the reaction conditions (*i.e.*, reactant partial pressures and surface temperature) can be varied over a wide range. These data can be utilized to evaluate the apparent kinetics of the reaction and the selectivity as a function of surface temperature. Moreover, by varying the reactant partial pressures, the importance of proposed reaction mechanisms can be assessed, and, in principle, the stoichiometry of the relevant adsorbed intermediates can be deduced **(15–16)**. Finally, by comparing the results obtained on both surfaces, we hope to determine the role of surface structure in dictating the particular adsorbed intermediates in each case and, hence, the catalytic selectivity.

II. Experimental Procedures

The experiments described here were performed in a high pressure reaction chamber (total volume $\simeq$ 600 cm^3) linked to an ultrahigh vacuum (UHV) analysis chamber, similar to that described previously **(8)**. The chambers, which are pumped separately, are connected by a metal valve, and the base pressure in both is 10^{-10} Torr. In the UHV analysis chamber, facilities are available for Auger electron spectroscopy, ion sputtering and mass spectrometry. The catalyst samples are attached to a retraction bellows and can be translated vertically to various positions in either chamber. The single crystal catalysts of iridium (total surface area $\simeq$ 1 cm^2) were mounted on tungsten leads and were heated resistively. The temperature was controlled manually and was measured with a W/5%Re-W/26%Re thermocouple spotwelded to the crystal. The crystals were cleaned in the UHV analysis chamber by argon ion sputtering, heating in 5 x 10^{-7} Torr of oxygen at 700 K, and annealing to 1600 K. Surface cleanliness was verified by Auger electron spectroscopy.

The ethane (99.99%), propane (99.97%) and *n*-butane (99.9%) employed in these experiments were research purity from Matheson. The neopentane was ultrahigh purity (99.995%) from API Standard Reference Materials. The hydrogen was ultrahigh purity (99.999%) **(17)**. The hydrocarbons were purified further by degassing at 80 K, followed by triple distillation from a liquid pentane/solid pentane bath. Reaction products were detected by gas chromatography which, in this case, is superior to mass spectrometric detection (*e.g.*, there are no complications due to the interpretation of cracking patterns). Absolute reaction rates were calculated by utilizing the measured volume of the reactor, the reaction time period (*i.e.*, batch reactor kinetics), and the measured geometrical surface areas of the crystals. Concerning the latter, integration of thermal desorption spectra of saturated adlayers of CO, the absolute coverage of which is known for both the Ir(111) **(19)** and Ir(110)-(1x2) **(20)** surfaces, confirmed the geometrical measurements. Specific rates were calculated by using substrate densities of 1.57 x 10^{15} cm^{-2} and 1.93 x 10^{15} cm^{-2} for the (111) and (110)-(1x2) surfaces, respectively. The corresponding saturation coverages of hydrogen (in these cases, the coverage that is irreversibly adsorbed at 100

K), commonly used to determine metallic surface areas of supported catalysts, are within approximately 20% of these substrate densities in each case **(21,22)**. However, it should be noted that if the low-coordination-number (C_7) surface atoms provide the "active sites" for a particular reaction (*cf.* Fig. 1), then this procedure will *under*estimate the specific rate for the Ir(110)-(1x2) surface by a factor of four.

III. Results

A. The Ir(111) Surface

Specific rates of hydrogenolysis of ethane, propane, *n*-butane and neopentane over the Ir(111) surface are shown in Figs. 2(a)–(d), plotted in Arrhenius form. These data represent *steady-state* reaction rates, as verified by measuring the total amount of product formed after various times of reaction, typically 50–2000 s, depending on the temperature. No induction periods were detected. To avoid secondary reactions, conversions were restricted typically to below 1%. The standard reactant partial pressure ratio, H_2/C_nH_{2n+2}, was 100/1, with a hydrocarbon pressure of 1.0 Torr.

Post-reaction surface characterization by Auger electron spectroscopy indicated the presence of a *submonolayer* carbonaceous residue, the fractional coverage of which, in all cases, was essentially independent of reaction conditions [surface temperature *and* reactant partial pressures (see below)]. The measured values for the coverages are given in Table 1 in terms of a fractional carbon coverage, where $\theta_C = 1$ is equivalent to the substrate density, *i.e.*, in this case, 1.57 x 10^{15} atoms-cm^{-2}. We see that there is an approximately linear increase in the carbon coverage with increasing size of the parent hydrocarbon (*i.e.*, the coverage of the carbonaceous residue with respect to an equivalent parent admolecule is nearly constant at 0.1 molec-site^{-1}). Post-reaction thermal desorption of the surface containing the carbonaceous residue produced only H_2, which, in all cases, gave a broad desorption feature, evolving H_2 from approximately 350 to 800 K and exhibiting a

peak temperature of approximately 500 K. No attempts were made to determine the average stoichiometry (C_xH_y) of this carbonaceous residue since it is *not* representative of the relevant adsorbed reaction intermediates under reaction conditions. This important point was demonstrated explicitly by returning the catalyst to the reaction chamber (*i.e.*, after the reactants had been pumped away) and titrating the carbonaceous residue with pure hydrogen at the relevant reaction temperature. Methane was the only product observed in all cases; *e.g.*, no "C_{n-1}" products were produced.

As may be seen from Fig. 2, the only reaction products observed were methane, ethane, propane and isobutane. With the exception of *n*-butane, the major reaction channels at sufficiently low temperatures ($T \leq 475$ K) are given by

$$C_nH_{2n+2} + H_2 \rightarrow CH_4 + C_{n-1}H_{2(n-1)+2} \ ,$$

i.e., the products expected from the cleavage of a single carbon-carbon bond. For *n*-butane, the major reaction channel is given by

$$n - C_4H_{10} + 2H_2 \rightarrow 2CH_4 + C_2H_6 \ ,$$

i.e., two carbon-carbon bonds are cleaved.

No isomerization products were detected from either *n*-butane (*i.e.*, isobutane) or neopentane (*i.e.*, isopentane or *n*-pentane). For the case of *n*-butane, based on the sensitivity of our gas chromatographic detection, the maximum rate of production of isobutane is below 10^{-4} molec-site^{-1}s^{-1} for all reaction conditions considered. This observation is consistent with the fact that, to the best of our knowledge, the isomerization of *n*-butane to isobutane has not been reported over iridium catalysts. A similar analysis for neopentane was hampered by the fact that the isomerization products would have been located on the trailing edge of the (considerably larger) parent hydrocarbon chromatographic peak. A conservative estimate places the maximum rate of isomerization below that of the total rate of hydrogenolysis. This estimate is consistent with previous work. For example, both Boudart and Ptak

(23) and Foger and Anderson **(24)** reported an isomerization rate (to isopentane) over silica-supported iridium catalysts, which was approximately one-third of the rate of hydrogenolysis. On the other hand, over iridium films, neither Anderson and Avery **(25)** nor Taylor and Clarke **(26)** could detect any isomerization of neopentane.

The apparent kinetic rate parameters obtained from the data shown in Fig. 2 at temperatures where linear Arrhenius behavior is observed are given in Table 2 for each of the major reaction channels. At a common surface temperature of 475 K, propane and *n*-butane exhibit comparable rates of reaction, whereas ethane and neopentane react more slowly by approximately an order of magnitude. However, despite the very different structure of these four hydrocarbons, the *apparent* rate parameters are remarkably similar, *i.e.*, all $k_{app}^{(0)} \simeq 10^{13\pm1}$ molec-site^{-1}-s^{-1} and $E_{app} \simeq 34 \pm 3$ kcal-mol^{-1}. Depending on the detailed mechanism of the *overall* reaction in each case, *e.g.*, the extent of dehydrogenation of the adsorbed reaction intermediates, based solely on these data, we cannot rule out the possibility that this agreement is fortuitous (*i.e.*, the apparent rates are determined by several elementary steps). A comparison of these data to those reported previously by Foger and Anderson **(24)** over a silica-supported iridium catalyst (0.98 wt %, $\bar{d}_{Ir}$ = 70 Å, dispersion of 16% and extrapolated to our reactant partial pressures) is shown in Figs. 2(a,c,d), and there is good agreement in all cases.

As may be seen in Fig. 2, dramatic changes in the selectivity and apparent reaction kinetics occur for propane, *n*-butane and neopentane as the temperature is increased above approximately 475 K. The apparent activation energy of the rate of *conversion* decreases, and the selectivity for "complete" hydrogenolysis to methane increases at the expense of the "C_{n-1}" products. These changes, which we shall designate as "rollover," can be identified explicitly with a depletion in the steady-state coverage of hydrogen, which, in turn, affects both the selectivity and the apparent reaction kinetics.

The observed "rollover" can be identified with the steady-state coverage of

hydrogen adatoms by varying the hydrogen partial pressure at a temperature near the onset of the nonlinear Arrhenius behavior. In order to assess various mechanistic models, it is necessary to vary also the hydrocarbon partial pressure. Therefore, reaction rates were measured for variations in both the hydrogen and hydrocarbon partial pressures, while maintaining a constant fixed partial pressure of the other and a fixed temperature. These data are shown in Figs. 3–5 for propane, *n*-butane and neopentane, respectively. It is important to note that the coverages of the carbonaceous residue remained essentially identical to those given in Table 1, as the partial pressures were varied. Thus, any changes observed in the activity and/or selectivity can *not* be associated with a transformation in the composition of the adlayer (*e.g.*, "self-poisoning" due to the carbonaceous residue). As may be seen in Figs. 3–5, a reduction in the hydrogen partial pressure near the onset of "rollover" has the same effect as an increase in the temperature; *i.e.*, the selectivity for methane increases greatly. Since both reducing the hydrogen partial pressure and increasing the surface temperature result in a decrease in the hydrogen coverage, *"rollover" is clearly associated with a depletion in surface hydrogen.*

A number of qualitative features of the dependencies of the specific rates of hydrogenolysis on the reactant partial pressures are apparent in Figs. 6(a)–(d), where the specific rates are plotted in terms of total *conversion* of the parent alkane. We see that, in all cases, the apparent reaction "order" (*i.e.*, $\partial \ln R / \partial \ln P$) in the hydrocarbon partial pressure, P_{HC}, varies from ~ 1 to ~ 0 as P_{HC} is increased. On the other hand, the "order" in the hydrogen partial pressure varies from ~ 0 to large negative values, ≤ -1, as P_{H_2} is increased. Similar behavior has been reported, for example, concerning ethane hydrogenolysis over a number of supported Group VIII metal catalysts **(2)**. Returning to Figs. (3)–(5), the sensitivity of the *selectivity* of hydrogenolysis is quite different. In particular, the selectivity is essentially independent of P_{HC}, whereas at low P_{H_2}, the selectivity for the production of "C_{n-1}" ("C_{n-2}" for *n*-butane) hydrocarbons decreases sharply as P_{H_2} is reduced.

Quantitative analysis of the data shown in Figs. 3–6 is possible by employing

a mechanisitic scheme similar to those proposed previously by both Cimino *et al.* **(15)** and Sinfelt **(16)**. The major assumptions of the model employed here, which is described in detail in the Appendix, may be summarized as follows: *(i)* pseudo-equilibrium is maintained between the gas phase reactants and a partially dehydrogenated hydrocarbon fragment (carbon skeleton remaining intact) and the adsorbed hydrogen adatoms; *(ii)* the (slow) rate-limiting step involves an irreversible carbon-carbon bond cleavage in the adsorbed hydrocarbon species, and *(iii)* hydrogenation of the resulting fragments (or additional C-C bond cleavage and subsequent hydrogenation) is rapid with respect to the C-C bond cleavage reaction. Assumption *(i)* involves the following set of reactions:

$$C_nH_{2n+2}(g) \rightleftharpoons C_nH_x(a) + 2\alpha H(a) \tag{1}$$

$$H_2(g) \rightleftharpoons 2H(a)\ , \tag{2}$$

where $\alpha = (2n+2-x)/2$. Note that "reaction" (1) embodies one or more elementary steps. Assumption *(ii)* involves the reaction

$$C_nH_x(a) \rightarrow C_mH_y(a) + C_{n-m}H_z(a)\ , \tag{3}$$

where the resulting fragments, $C_mH_y(a)$ and $C_{m-n}H_z(a)$, are subsequently rapidly hydrogenated.

An analysis of the mechanistic scheme outlined by Eqs. (1)–(3), presented in the Appendix, results in the following expression for the total rate of hydrogenolysis (*i.e.*, conversion of the parent hydrocarbon) as a function of the partial pressures of the reactants:

$$R_C = k_C\theta_{C_nH_x} = \frac{k_CK^{\dagger}P_{HC}}{K^{\dagger}P_{HC} + P_{H_2}^{\alpha+\frac{1}{2}}}\ , \tag{4}$$

where k_C is the rate coefficient for the reaction given by Eq. (3), $\theta_{C_nH_x}$ is the fractional coverage of the species $C_nH_x(a)$, and $K^{\dagger}$ is a combination of rate coefficients for the reactions given in Eqs. (1) and (2), which is defined explicitly in the

Appendix. Note that Eq. (4) predicts that the apparent "order" of the reaction in the hydrocarbon partial pressure will vary from 1 to 0 as P_{HC} is increased, whereas that for hydrogen will vary from 0 to $-(\alpha + \frac{1}{2})$ as P_{H_2} is increased, consistent with the experimental observations. Consequently, in principle, the stoichiometry of the adsorbed parent hydrocarbon fragment (*i.e.*, $x = 2(n - \alpha) + 2$) can be determined by varying the reactant partial pressures.

The major difference between the expression derived here and given by Eq. (4), and those derived previously **(15,16)**, lies in the presence of an additional power of $\frac{1}{2}$ in the partial pressure of hydrogen. This term is a result of considering explicitly the competition of the reactants for adsorption sites; *e.g.*, hydrogen adatoms can block the adsorption and/or dehydrogenation of the parent alkane by occupying sites normally active for dissociation. If one neglects this site-blocking effect by hydrogen, one would tend to overestimate the extent of dehydrogenation of the apparent reaction intermediate by one hydrogen atom.

The data given in Figs. 6(a)–(d) have been fit to the functional form given by Eq. (4). The optimal parameters were obtained utilizing a least-squares functional minimization routine based on a simplex method **(27)** where, initially, the constant α was allowed to vary arbitrarily (*i.e.*, it was not fixed to half-integer values). Subsequently, the set of parameters which produced the best, statistically significant fit were re-fit to the data by rounding off α and fixing its value to the nearest half-integer.

The agreement between the experimental data and the behavior predicted by Eq. (4) is excellent, as may be seen from Fig. 6. For ethane and propane the dimensionless standard deviation between the model and the data is approximately 15%. For *n*-butane, the data are somewhat better described by $\alpha = \frac{1}{2}$ (standard deviation of 15 %) **(28)**, compared to $\alpha = 1$ (standard deviation of 25 %), although, in both cases, the uncertainties between the model and the data are on the order of the experimental uncertainty ($\sim \pm 20\%$). Neopentane is fit equally well by values for α of 2 and $2\frac{1}{2}$, in both cases the standard deviation being approximately

20%. The stoichiometries for the adsorbed hydrocarbon fragments that are implied by these data are summarized in Table 3. Consistent with the proposition that hydrogenolysis proceeds through a partially dehydrogenated intermediate that is multiply bound to the surface by one or more metal atoms, we see that, in all cases (with the possible exception of *n*-butane), at least two hydrogen atoms are removed from the parent molecule.

The success of applying the mechanistic model described by Eqs. (1)–(3) to the experimental data permits a quantitative interpretation of the "rollover" phenomena via the use of Eq. (4). At high partial pressures of hydrogen, $P_{H_2}^{\alpha+\frac{1}{2}} \gg K^{\dagger}P_{HC}$, and the reaction rate is given by $k_C K^{\dagger} P_{HC}/P_{H_2}^{\alpha+\frac{1}{2}}$. Thus, the apparent activation energy is given by $E_{app} \simeq E_C + \Delta H^{\dagger}$, where E_C is the activation energy of the C-C bond cleavage reaction of Eq. (3), and $\Delta H^{\dagger}$ is the total enthalpy change for the set of reactions given by $C_nH_{2n+2}(g) + H(a) \rightarrow C_nH_x(a) + (\alpha + \frac{1}{2})H_2(g)$ **(29)**. However, as the partial pressure of hydrogen is reduced to an extent such that $P_{H_2}^{\alpha+\frac{1}{2}} \ll K^{\dagger}P_{HC}$, the reaction rate is given by k_C, and the apparent activation energy is given by $E_{app} \simeq E_C$. Equating temperatures below "rollover" with high hydrogen partial pressures and temperatures above with low pressures, would imply that the enthalpy change $\Delta H^{\dagger}$ is positive, since "rollover" is accompanied by a decrease in the apparent activation energy (with respect to conversion).

Support for this proposal can be obtained by determining the apparent reaction "orders" in the reactant partial pressures at different temperatures (*i.e.*, by varying the reactant partial pressures about fixed, averaged values at different temperatures). For example, over Ir blacks **(30)**, and under similar reaction conditions, the apparent order in P_{H_2} for ethane hydrogenolysis was found to increase continuously with temperature from $\sim -1\frac{1}{2}$ at 450 K to $\sim -\frac{1}{2}$ at 575 K. This experimental observation implies that the coefficient $K^{\dagger}$ increases with temperature and, therefore, $\Delta H^{\dagger}$ must be positive [*i.e.*, if $K^{\dagger}P_{HC} \ll P_{H_2}^{\alpha+\frac{1}{2}}$, the order in P_{H_2} is $\sim -(\alpha + \frac{1}{2})$, whereas, if $K^{\dagger}P_{HC} \gg P_{H_2}^{\alpha+\frac{1}{2}}$, the order in P_{H_2} is ~ 0].

The data shown in Figs. 3–5 can be utilized to the interpret the changes

observed in the selectivities in the "rollover" regime. For example, propane reacts to form a C_2 and a C_1 species via the reaction given by Eq. (3). If sufficient hydrogen adatoms are present, these species will be hydrogenated rapidly, producing ethane and methane. However, if the hydrogen adatom concentration is depleted, as is the case in the "rollover" regime, the C_2 species could react further with the surface to produce two C_1 species, and eventually, methane. This reaction could involve, for example, partial dehydrogenation of the C_2 species and almost certainly formation of an addition carbon-metal bond. It should be clear that we can describe this situation by again employing a scenario such as that given by Eqs. (1)–(3) except, in this case, *for the C_2 species.* Thus, we shall consider the reactions

$$C_mH_{y'}(a) + 2\beta H(a) \rightleftharpoons C_mH_{2m+1}(a) + H(a) \rightarrow C_mH_{2m+2}(g) \tag{5}$$

and

$$C_mH_{y'}(a) \rightarrow C_\ell H_u(a) + C_{m-\ell}H_v(a) \ , \tag{6}$$

where $\beta = (2m + 2 - y')/2$. In this case, we have neglected readsorption of the C_mH_{2m+2} product, clearly valid at low conversions. Proceeding in a similar fashion as for the derivation of Eq. (4), the specific procedure detailed in the Appendix, we find that the C_m selectivity with respect to the total C_n conversion at a constant temperature is given by

$$S_{C_m} \equiv \frac{R_{C_m}}{R_C} = \frac{k_S P_{H_2}^{\beta}}{1 + k_S P_{H_2}^{\beta}} \ , \tag{7}$$

where k_S represents a combination of rate coefficients, given explicitly in the Appendix. Note that, in agreement with the experimental observations, this selectivity is not a function of P_{HC}. It is also important to note that y' of Eq. (5) is not necessarily equal to y of Eq. (3). That is, subsequent to (or simultaneous with) the initial C-C bond cleavage, the C_m species may dehydrogenate further prior to additional C-C bond cleavage. In any case, y' of Eq. (5) will provide a *minimum* value for y of Eq. (3), whereas x, obviously, represents the maximum value. In

evaluating the minimum limiting value of y, we exclude the possibility that additional C-C bond cleavage could be preceded by a hydrogenation step. Note that if y were determined exactly by utilizing Eq. (7), the stoichiometry of Eq. (3) would be completely specified, since x is determined independently from Eq. (4).

The data presented in Figs. 3(a)–5(a) for propane, *n*-butane and neopentane have been fit to Eq. (7) by utilizing a least-squares routine similar to that described above. The results are shown in Figs. 7(a)–(c). We see that the data are described well by this model. Specifically, the standard deviation between the data and this model for propane and *n*-butane is $\sim$ 7%, whereas for neopentane, which is fit equally well by $\beta = 2$ or $2\frac{1}{2}$, it is $\sim$ 11%. (Note that the experimental uncertainty associated with evaluating *selectivities*, as opposed to specific activities, is relatively smaller, approximately $\pm$ 5%.) The (minimum) hydrogen contents of the C_m fragments implied by these data are summarized in Table 3.

B. The Ir(110)-(1x2) Surface

Specific rates of hydrogenolysis of ethane, propane, *n*-butane and neopentane over the Ir(110)-(1x2) surface are shown in Figs. 8(a)–(d) in Arrhenius form. These data represent steady-state reaction rates, obtained for conversions that were restricted typically to below 1%. The standard reactant partial pressure ratio, H_2/C_nH_{2n+2}, in all cases was 100/1, with a hydrocarbon partial pressure of 1.0 Torr.

Post-reaction surface characterization by Auger electron spectroscopy indicated the presence of a submonolayer carbonaceous residue on the Ir(110)-(1x2) surface. The measured values for the fractional coverages, which, in all cases considered here and below, were essentially independent of reaction conditions (surface temperature *and* reactant partial pressures), are given in Table 4 in terms of a fractional carbon coverage. As was observed on the Ir(111) surface, there is an approximately linear increase in the carbon coverage with increasing size of the parent hydrocarbon. Furthermore, the fractional coverages observed on each surface are *very* similar to

one another (*cf.* Tables 1 and 4). These similarities tend to rule out the possibility that surface sites unique to the (110)-(1x2) surface were being poisoned selectively. On the other hand, if activity and/or selectivity differences are observed between the two surfaces studied here for a particular reaction, it is unlikely that these differences would be a manifestation of a particular configuration of the carbonaceous residue present on each of the surfaces. Finally, post-reaction thermal desorption of the carbonaceous adlayer produced only H_2, and the resulting desorption spectra were similar to those observed from the (111) surface. Titration of the carbonaceous adlayer with hydrogen produced only methane in all cases.

As with the Ir(111) surface, the only reaction products observed were methane, ethane, propane and isobutane. No isomerization products were detected from either *n*-butane or neopentane [where we must qualify our estimates for the maximum rates of isomerization in the same manner as with the (111) surface; see Sec. III.A]. With the exception of *n*-butane, the major reaction channels at sufficiently low temperatures ($T \leq 500$ K) are given by

$$C_nH_{2n+2} + H_2 \rightarrow CH_4 + C_{n-1}H_{2(n-1)+2} \ .$$

For *n*-butane on the Ir(110)-(1x2) surface, the major reaction channel is given by

$$n\text{-}C_4H_{10} + H_2 \rightarrow 2C_2H_6 \ .$$

Of the four reactions on the two surfaces considered here, the hydrogenolysis of *n*-butane on the Ir(110)-(1x2) surface is the only one that does not produce methane from the major reaction channel. Hence, the *selectivity* for the hydrogenolysis of *n*-butane by iridium catalysts is sensitive to the structure of the surface.

The apparent kinetic rate parameters obtained from the data shown in Fig. 8 are given in Table 5 for each of the major reaction channels. At a common temperature of 475 K the reaction rates in terms of conversion may be ordered as follows: *n*-butane > propane > neopentane > ethane. In addition, unlike the Ir(111) surface, the apparent reaction rate parameters differ considerably for the four hydrocarbons

considered here. Specifically, the parameters for the hydrogenolysis of ethane are given by $k_{app}^{(0)} \simeq 6 \times 10^{18}$ molec-site^{-1}-s^{-1} and $E_{app} \simeq 49 \pm 2$ kcal-mol^{-1}; those for propane and neopentane are similar to one another and are given by $k_{app}^{(0)} \simeq 1 \times 10^{14}$ molec-site^{-1}-s^{-1} and $E_{app} \simeq 35 \pm 2$ kcal-mol^{-1}, and those for *n*-butane are given by $k_{app}^{(0)} \simeq 1 \times 10^{9}$ molec-site^{-1}-s^{-1} and $E_{app} \simeq 22 \pm 2$ kcal-mol^{-1}. It is of interest to note that the values obtained on the (111) and (110)-(1x2) surfaces for the hydrogenolysis of propane and neopentane are nearly indistinguishable. However, the apparent activation energy for ethane hydrogenolysis is much greater over the (110)-(1x2) surface, whereas that for *n*-butane hydrogenolysis is considerably smaller with respect to that observed on the (111) surface. These results suggest that different intermediates may exist on the two surfaces for these latter two reactions.

Consistent with the observations over the Ir(111) surface, dramatic changes in the selectivity and apparent reaction kinetics occur for propane, *n*-butane and neopentane hydrogenolysis on the (110)-(1x2) surface, as the temperature is increased above approximately 500 K. Again, these "rollover" phenomena are associated with a depletion in the steady-state coverage of hydrogen. Moreover, by comparing the results obtained over the two surfaces, the *source* of the hydrogen can be identified explicitly. For example, the relative selectivity for ethane with respect to methane from the hydrogenolysis of propane, *i.e.*, $R_{C_2H_6}/R_{CH_4}$, is approximately equal to $\frac{1}{3}$ at 500 K on Ir(111) and at 550 K on Ir(110)-(1x2) [*cf.* Figs. 2(b) and 8(b)]. Since our results implicate the presence of essentially identical reaction intermediates on both surfaces for this reaction (see below and Tables 3 and 6), the observed difference in the onset of "rollover" is due primarily to differing energetics of the adsorption of hydrogen. Consequently, since "rollover" occurs at a higher temperature on the Ir(110)-(1x2) surface, this surface must possess hydrogen adsites characterized by a higher binding energy than those available on an Ir(111) surface.

Independent measurements of the adsorption and desorption kinetics of hydro-

gen on *clean* (111) and (110)-(1x2) surfaces of Ir have verified explicitly the presence of a higher binding energy adstate on the (110)-(1x2) surface **(21,22)**. However, calculations suggest that this higher binding energy adstate on the (110)-(1x2) surface should be saturated for *all* reaction conditions considered here. That is, it is probable that "rollover" is associated with depletion of hydrogen adatoms from the lower binding energy adstate on the (110)-(1x2) surface. Unfortunately, the kinetic parameters describing the desorption of hydrogen were not evaluated for coverages near saturation on the two Ir surfaces considered here. Nonetheless, extrapolating the data obtained at lower coverages ($\theta \leq 0.5$) suggests that hydrogen is more strongly bound on Ir(110)-(1x2), compared to Ir(111) in the limit of fractional coverages approaching unity. The agreement between these results obtained on clean surfaces and those obtained here under reaction conditions [*i.e.*, both implicating hydrogen being more strongly bound on the (110)-(1x2) surface] point to the surface metal atoms as the source of the hydrogen. This identification, for example, obviously rules out any mechanism involving the carbonaceous adlayer acting as a "hydrogen-transfer agent."

Verification of the role of hydrogen in the "rollover" phenomena was again provided by varying the partial pressures of the reactants at a temperature near the onset of "rollover." These data for the Ir(110)-(1x2) surface are shown in Fig. 9–11 for propane, *n*-butane and neopentane. As was found on the Ir(111) surface, for all reactions conditions considered in Figs. 9–11, the coverages of the carbonaceous residue were essentially identical to those given in Table 4. We see that a reduction in the partial pressure of hydrogen has the same effect as an increase in the temperature for propane and neopentane, namely, the selectivity for methane increases greatly. However, for *n*-butane, a reduction in the hydrogen partial pressure results in a decrease in the total rate of *conversion*; *e.g.*, as P_{H_2} is reduced from 100 to 20 Torr, the total rate of conversion of *n*-butane decreases by a factor of approximately five. In this case, unlike propane and neopentane, the decrease in the rate of production of ethane is *not* compensated by a corresponding increase in the rate

of production of methane (*i.e.*, conversion of *n*-butane to ethane dominates for all P_{H_2} displayed in Fig. 10; even at 20 Torr of H_2, conversion to ethane is approximately a factor of four times that to methane). Rather, in this case, the slight increase in methane production with decreasing P_{H_2} is probably associated with the corresponding decrease in the *propane* production. These observations suggest that two distinct reaction pathways are operating simultaneously for *n*-butane on Ir(110)-(1x2); namely, the major pathway is $n\text{-}C_4H_{10} + H_2 \rightarrow 2C_2H_6$, whereas the minor one is $n\text{-}C_4H_{10} + H_2 \rightarrow CH_4 + C_3H_8$.

The observed positive order in P_{H_2} for the rate of conversion of *n*-butane for pressures below 100 Torr (observed also for neopentane to a lesser extent, see below) might be explained by either of the following: *(i)* surface hydrogen is participating in the C-C bond cleavage reaction given in Eq. (4); or *(ii)* the C-C bond cleavage reaction is reversible (*i.e.*, overall, hydrogenolysis is positive order in P_{H_2}). The plausibility of these two explanations is considered below.

The data shown in Fig. 9 for propane and similar data for ethane have been fit to the functional form given by Eq. (4), utilizing the least-squares procedure described above. These data are shown in Figs. 12(a) and (b). The data for ethane are fit well by $\alpha = 2$, with a standard deviation of 18%, whereas propane is fit well by $\alpha = 1$, with a standard deviation of 23%. The stoichiometries for the adsorbed reaction intermediates implied by these data are summarized in Table 6. Note that the stoichiometry of the intermediate for propane is identical to that observed on the Ir(111) surface, which, together with the similarites between the apparent kinetics, suggests that similar pathways may exist on both surfaces for this reaction.

The data presented in Fig. 11 for neopentane are plotted in Fig. 12(d) in terms of total conversion. We see that for partial pressures below approximately 200 Torr, the apparent order in P_{H_2} is positive and nearly equal to $\frac{1}{2}$. This small positive order in P_{H_2} can be rationalized if the rate-limiting C-C bond cleavage of Eq. (3) involves a bimolecular reaction between the hydrocarbon fragment and a hydrogen adatom (*i.e.*, $R_C = k_C \theta_{C_nH_x} \theta_H$) **(31)**. Employing the mechanistic scheme detailed in the

Appendix, it can be shown that if one assumes that C-C bond cleavage involves a bimolecular reaction with a hydrogen adatom, the resulting expression for the rate of hydrogenolysis is given by a form similar to Eq. (4). In particular, the essential difference lies in the presence of a $P_{H_2}^{1/2}$ factor in the numerator. Consequently, the data for neopentane have been fit to the product of the expression given in Eq. (4) and $P_{H_2}^{1/2}$. We see that the data for neopentane are fit equally well by values for α of 2 and $2\frac{1}{2}$, in both cases the standard deviation being 23%. Note that, as with propane, the stoichiometries of the apparent reaction intermediates form neopentane over the two surfaces are identical to each other (*cf.* Tables 3 and 6).

The data presented in Fig. 10 for *n*-butane are plotted in Fig. 12(c) in terms of total conversion. As discussed above in connection with Fig. 10, the apparent order in P_{H_2} is positive and is equal to approximately unity for partial pressures of hydrogen below 100 Torr. However, unlike neopentane, it is difficult to reconcile a positive order in P_{H_2} of ~ 1 in terms of hydrogen participating in the C-C bond cleavage reaction. On the other hand, since hydrogenolysis does involve the incorporation of hydrogen, *i.e.*, "overall" it is positive order in P_{H_2} (*e.g.*, $C_4H_{10} + H_2 \rightarrow 2C_2H_6$), one possible interpretation of this result is that C-C bond cleavage is reversible. That is, in the absence of a sufficient concentration hydrogen adatoms, the reverse reaction of Eq. (3) will compete with the hydrogenation of the product fragments. If the product fragments are "reasonably" hydrogen-deficient (*e.g.*, 2 or more hydrogen atoms), the apparent order in P_{H_2} for the hydrogenation of the fragments will be unity or greater. Consequently, the mechanism described by Eqs. (1)–(3) was altered to include also the case where the C-C bond cleavage reaction is reversible. We replace Eq. (3) with the reaction

$$C_nH_x(a) \rightleftharpoons 2C_mH_y(a) \tag{8}$$

and Eq. (5), the product fragment hydrogenation step, with the (set of) reaction(s)

$$C_mH_y(a) + 2\delta H(a) \rightarrow C_mH_{2m+2}(g)\ , \tag{9}$$

where, to simplify matters, we will consider "symmetric" C-C bond cleavage reactions only. An analysis, detailed in the Appendix, indicates that the "selectivity" of hydrogenation (*i.e.*, the probability that the product fragments, once formed, will be hydrogenated) can be approximated by

$$S_{hyd} \equiv \frac{R_{hyd}}{R_C} = \frac{k_h P_{H_2}^{\delta}}{1 + k_h P_{H_2}^{\delta}} , \tag{10}$$

where k_h is a combination of rate coefficients given explicitly in the Appendix, and R_C is the rate of the C-C bond cleavage, which is still given by Eq. (4). Utilizing the expression for R_C, the rate of hydrogenolysis becomes

$$R_{hyd} = \frac{k_C K^{\dagger} P_{HC}}{K^{\dagger} P_{HC} + P_{H_2}^{\alpha+\frac{1}{2}}} \frac{k_h P_{H_2}^{\delta}}{1 + k_h P_{H_2}^{\delta}} . \tag{11}$$

We see that Eq. (11) predicts that the apparent order in P_{H_2} will vary from $\delta = (\alpha + 1)/2$ to zero and finally to $-(\alpha + \frac{1}{2})$, as P_{H_2} is increased.

The data for *n*-butane hydrogenolysis over the Ir(110)-(1x2) surface have been fit to Eq. (11), utilizing the least-squares procedure described above. These results are shown in Fig. 12(c), where an optimal fit was obtained with $\alpha = 1$ and $\delta = 1$. Moreover, the quality of the fit (standard deviation of 15%) is excellent. Consequently, this result implies that the major reaction channel for *n*-butane hydrogenolysis over the Ir(110)-(1x2) surface involves a reversible, symmetric C-C bond cleavage.

The data for the *minor* reaction channel for *n*-butane hydrogenolysis over Ir(110)-(1x2), *i.e.*, $n\text{-}C_4H_{10} + H_2 \rightarrow CH_4 + C_3H_8$, can be examined also by employing either of the mechanistic schemes described above. These data are shown in Fig. 13(a) in terms of the total $CH_4 + C_3H_8$ conversion and are described well by Eq. (4), the mechanism involving *irreversible* C-C bond cleavage. The data are described well by either $\alpha = \frac{1}{2}$ or 1 **(28)**, the standard deviation being approximately 18% in both cases. Note that these parameters are essentially identical to those obtained for the major reaction channel on the Ir(111) surface, where $\alpha = \frac{1}{2}$ or 1.

The C_m selectivity in the "rollover" regime was examined quantitatively by employing Eq. (7). The results, obtained by utilizing the least-squares procedure, are shown in Figs. 14(a) and (b) for propane and neopentane, and in Fig. 13(b) for the minor reaction channel of *n*-butane. The data for propane are described somewhat better by $\beta = 2\frac{1}{2}$ (standard deviation of 5%) as opposed to $\beta = 2$ (standard deviation of 8%), those for neopentane equally well by $\beta = 2$ or $2\frac{1}{2}$ (standard deviation of 12%), and those for the minor reaction channel of *n*-butane equally well by $\beta = 1\frac{1}{2}$ or 2 (standard deviation of 8%). The stoichiometries of the product fragments implied by these data are given in Table 6. The stoichiometry for the product fragment for the major reaction channel of *n*-butane was determined previously by the agreement of the data with Eq. (11), where $\delta = 1$. Note that the product fragments from neopentane (and possibly propane) are the same on both the (111) and (110)-(1x2) surfaces (as was the case for the parent fragments).

IV. Discussion

A. Ethane

Ethane hydrogenolysis has been reported to be sensitive to changes in the average metallic particle size over silica-supported catalysts of both Rh **(32,33)** and Ni **(34)**. For example, Yates and Sinfelt **(32)** reported maximum specific activities over Rh/SiO_2 catalysts for average metal crystallite sizes between 10 and 40 Å, whereas for particle sizes above 100 Å, the activity decreased by $1–1\frac{1}{2}$ orders of magnitude. Similar results were reported by Martin and Dalmon **(34)** over Ni/SiO_2 catalysts of varying particle size. Recent work by Lee and Schmidt **(33)** on Rh/SiO_2 catalysts and by Goodman **(9)** on oriented Ni single crystals suggests that the observed variations in the specific activity may be due to structural changes in the catalyst surface with increasing particle size. In particular, the work of Goodman **(9)** implicates the importance of the relative number of surface atoms in (100) and (111) microfacets of the metal crystallite, as the particle size is varied.

In contrast to the observations over Rh and Ni, Foger and Anderson **(24)** reported differences in the specific activities over alumina- and silica-supported Ir of less than a factor of three between catalysts with average particle sizes of 15 and 70 Å. Apparently the nature of the metal exerts considerable influence on the degree of sensitivity of the catalytic properties to changes in the average particle size. However, it must be noted that comparisons based solely on specific activities at a particular set of reaction conditions can be misleading unless there happen to be no variations in the apparent reaction kinetics or apparent reaction "orders" in P_{HC} and P_{H_2}. Examination of the data obtained here with the (111) and (110)-(1x2) surfaces of Ir illustrates this point clearly; *i.e.*, for temperatures below approximately 550 K, the (111) surface is more active than the (110)-(1x2), whereas above 550 K, the opposite is true. This observation is a manifestation of the different apparent reaction kinetics observed on the two surfaces. For the limited temperature range examined by Foger and Anderson **(24)** (T $\simeq$ 525–550 K, *cf.* Fig. 2), the specific activities over the Ir(111) and Ir(110)-(1x2) surfaces are very similar, supporting their observed lack of any strong sensitivity to particle size.

As may be seen from Tables 2 and 5, the apparent reaction kinetics differ considerably for ethane hydrogenolysis over the two surfaces considered here; *e.g.*, $E_{app} \simeq 35$ kcal-mol^{-1} and $k_{app}^{(0)} \simeq 1 \times 10^{13}$ molec-site^{-1}-s^{-1} on Ir(111) and $E_{app} \simeq 49$ kcal-mol^{-1} and $k_{app}^{(0)} \simeq 6 \times 10^{18}$ molec-site^{-1}-s^{-1} on Ir(110)-(1x2). These differences can be explained by either *(i)* different reaction mechanisms; or *(ii)* the same mechanism in which the rates and energetics of one or more elementary steps differ. From Tables 3 and 6 we see that distinct reaction intermediates are implicated on the two surfaces, namely, C_2H_4 on Ir(111) and C_2H_2 on Ir(110)-(1x2). Consequently, the differences between the apparent reaction kinetics is evidently due to the different reaction intermediates (mechanisms). It is of interest to note that the correlation between a more extensively dehydrogenated intermediate and a higher apparent activation energy has been observed previously for ethane hydrogenolysis

over a number of metals **(35)** and for the hydrogenolysis of various C_5 hydrocarbons over Pt/Al_2O_3 catalysts **(36)**. The most plausible explanation for this correlation involves the reaction mechanism described above by Eqs. (1)–(3). Specifically, the enthalpy change for the set of reactions $C_2H_6(g)+H(a) \rightarrow C_2H_x(a)+(\alpha+\frac{1}{2})H_2(g)$ **(29)** is considered to be positive (*i.e.*, $\Delta H^{\dagger} > 0$), for which the endothermicity increases with greater values of α. Thus, since $E_{app} \simeq E_C + \Delta H^{\dagger}$ for temperatures below the onset of "rollover," the apparent activation energy will increase as α increases.

The differing extents of dehydrogenation of the reaction intermediates on each surface can be explained by arguments based purely on structural considerations. It is accepted generally that ethane hydrogenolysis proceeds through an intermediate in which both carbon atoms are bound to the surface. The apparent reaction intermediate implicated on the Ir(111) surface, C_2H_4, is consistent with a species bound to the surface via two σ carbon-metal bonds. Moreover, this adsorbed species is expected to maintain its sp^3 hybridization (*i.e.*, further dehydrogenation will most likely lead to either re-hybridization or considerable strain in the C-C bond). The apparent reaction intermediate implicated on the Ir(110)-(1x2) surface, C_2H_2, is consistent with either a symmetrical species, $HCCH$, or an assymetrical species, CCH_2. An $HCCH$ species would be expected to lose the sp^3 hybridization of the parent alkane, C_2H_6, upon forming two carbon-metal double bonds. However, the CCH_2 species might be able to maintain its original sp^3 hybridization due to the configuration of the metal surface atoms on the Ir(110)-(1x2). In particular, it is important to realize that the Ir(110)-(1x2) surface can be thought of as consisting of three-atom-wide (111) microfacets, which are inclined towards one another at an angle of 109.5° (*i.e.*, nearly 90°, *cf.* Fig. 1). Consequently, it is conceivable that on the (110)-(1x2) surface a species might form that would involve one carbon atom being triply bound to one of the (111) microfacets, whereas the other carbon atom (which binds the two hydrogen atoms) would bind to the *opposing* (111) microfacet, this configuration permitting the CCH_2 species to maintain its sp^3 hybridization

(*i.e.*, without experiencing considerable C-C bond strain). This interpretation could explain the C_2H_2 stoichiometry observed on the (110)-(1x2) surface. If this is indeed the proper explanation, the unique catalytic properties of the (110)-(1x2) surface with respect to the (111) for ethane hydrogenolysis are a manifestation of the *high* coordination "trough" adsites [C_{11} atoms, *cf.* Fig. 1 **(13)**] available on this surface.

B. Propane

In comparison to ethane, considerably less work has been carried out concerning propane hydrogenolysis by metal catalysts **(37–39)**. The first-row Group VIII transition metals have been found to promote complete hydrogenolysis, *i.e.*, production of methane, with Ni exhibiting a somewhat higher selectivity for ethane compared to Fe and Co **(38)**. On the other hand, over both alumina-supported Ru **(37,38)** and Pt **(39)**, and Pt blacks **(40)**, the selectivities for both ethane and methane have been found to be nearly equal; *i.e.*, apparently one carbon-carbon bond is cleaved. In all cases the apparent reaction "orders" with respect to P_{HC} were nearly unity, whereas those with respect to P_{H_2} were typically between -1 and -2, consistent with our observations here. Finally the selectivity for ethane was found to decrease with increasing temperature **(37)**. This selectivity shift with increasing temperature is clearly associated with the "rollover" phenomena observed here.

Examination of the results given in Tables 2 and 5 shows that both the specific activities and the apparent kinetic rate parameters are essentially identical over the Ir(111) and Ir(110)-(1x2) surfaces. Furthermore, as may be seen from Tables 3 and 6, the stoichiometries of the adsorbed parent hydrocarbon fragments are also identical. These observations suggest strongly that the reaction mechanism on both surfaces is the same.

Knowledge of the stoichiometries of the adsorbed intermediates, coupled with comparisons to the other reactions considered here, permits speculation as to the nature of the dominant mechanism. For example, the stoichiometry of the adsorbed

intermediate, C_3H_6, is consistent with a species bound to the surface via two single carbon-metal bonds, which may involve more than one metal surface atom. Since *different* adsorbed intermediates were implicated for ethane on the two surfaces, and ethane must be bound "1,2", it is probable that this species is bound through the terminal carbon atoms, *i.e.*, "1,3" adsorption. A "1,3" diadsorbed species is consistent with either a mononuclear metallacycle butane **(41)** or a binuclear metallacycle pentane **(42)**. Interconversion between metallacycle butanes and metallacarbenes and adsorbed olefins is well known in organometallic chemistry and is of special importance to olefin metathesis **(43)**. Not surprisingly, the importance of metallacycle butanes in heterogenous catalysis and the hydrogenolysis of alkanes has been suggested previously **(5)**. Carbon-carbon bond cleavage of a metallacycle butane to form a methylidene and adsorbed ethylene, followed by rapid hydrogenation of these species, would be consistent with our experimental observations, *i.e.*, production of methane and ethane. On the other hand, a binuclear metallacycle pentane also provides an attractive candidate for the reaction intermediate. For example, for and sp^3 hybridized $C_3H_6(a)$ species, the C_1-C_3 internuclear distance is $\sim$ 2.52 Å, a value which is within 10% of the nearest neighbor Ir-Ir spacing of 2.72 Å. Consequently, we would expect minimal C-C bond strain in the carbon framework for a binuclear metallacycle pentane.

Obviously, it is virtually impossible to discriminate between these proposals based on our results. However, it is important to note that the implicated $C_2H_{y'}$ product fragments from the hydrogenolysis of propane are evidently more dehydrogenated than the C_2H_x parent hydrocarbon fragments formed from (gas phase) ethane [certainly on Ir(111), possibly on Ir(110)-(1x2); *cf.* Tables 3 and 6]. Since the same mechanistic scheme was utilized to determine the stoichiometries in each case, the differing extents of dehydrogenation observed suggest that C-H bond cleavage may accompany the C-C bond cleavage reaction of Eq. (3). If this is the case, the implication is that metallacycle butane decomposition to a methylidene and an adsorbed ethylene is not important for the hydrogenolysis of propane.

We have also measured the specific rates of hydrogenolysis of cyclopropane over both the Ir(111) and Ir(110)-(1x2) surfaces **(18)**. These data can be used to lend further support to our interpretation of the "rollover" phenomenon via the use of Eq. (4). Specifically, the reaction of cyclopropane with hydrogen over these two Ir surfaces has been found to follow two distinct reaction pathways— the major product was propane, whereas the minor products were equal amounts of ethane and methane **(18)**. Since variation of the reactant partial pressures indicated that the reaction rate via the minor channel c-$C_3H_6 + 2H_2 \rightarrow CH_4 + C_2H_6$ was essentially zero order in both P_{HC} and P_{H_2}, presumably the apparent kinetics of this minor reaction channel were not affected by a pseudo-equilibrium between the gas phase reactants and an adsorbed hydrocarbon fragment. Rather, the hydrogenolysis of cyclopropane to methane and ethane is apparently limited by the decomposition (C-C bond cleavage) of an adsorbed hydrocarbon species, this species being formed readily from cyclopropane compared to propane, *e.g.*, ring-opening of cyclopropane to directly form a diadsorbed species, $C_3H_6(a)$. Thus, for cyclopropane, the apparent reaction kinetics should reflect *directly* the energetics of the C-C bond cleavage reaction.

The specific rates of hydrogenolysis (to ethane and methane) of both propane and cyclopropane on the Ir(110)-(1x2) surface are shown in Fig. 15 in terms of conversion. We see that there is an *excellent* correlation between the apparent activation energy of propane hydrogenolysis for temperatures above the onset of "rollover" and that of cyclopropane hydrogenolysis. (Note also that "rollover," with respect to changes in the apparent activation energy, does not occur for cyclopropane under these reaction conditions.) This correlation supports our assignment of the apparent activation energy below "rollover" to the quantity $E_C + \Delta H^\dagger$, where $\Delta H^\dagger$ is positive, and that above, solely to the activation energy of the C-C bond cleavage reaction, E_C. Specifically, the enthalpy change for $C_3H_8(g) + H(a) \rightarrow C_3H_6(a) + \frac{3}{2}H_2(g)$, implicated by these data is approximately 12–13 kcal-mol^{-1}.

This value for $\Delta H^\dagger$ can be used to calculate the binding energy of the ad-

sorbed hydrocarbon fragment, $C_3H_6(a)$. In particular, $\Delta H^{\dagger} = 2D_{C-H} - \frac{1}{2}\Delta H_{H_2} - D_{H-H} - D_{C_3H_6}$, where D_{C-H} (D_{H-H}) is the C-H (H-H) bond dissociation energy, ΔH_{H_2} is the heat of adsorption of hydrogen on Ir(110)-(1x2), and $D_{C_3H_6}$ is the binding energy of the reaction intermediate. If propane adsorbs "1,3," the D_{C-H} $\simeq$ 98 kcal-mol^{-1}, whereas for the expected high coverages of hydrogen adatoms under our reaction conditions, $-\Delta H_{H_2} \leq 10$ kcal-mol^{-1} **(21)**. Utilizing these values and $D_{H-H} \simeq 104$ kcal-mol^{-1}, we find that $D_{C_3H_6} \simeq 85 \pm 1$ kcal-mol^{-1}, which implies a carbon-metal bond strength of 42–43 kcal-mol^{-1}.

C. *n*-Butane

The study of the hydrogenolysis of *n*-butane permits an examination of *selectivity*, in addition to activity, variations with surface structure, since for a reaction involving the cleavage of a single C-C bond, two product distributions are possible, *i.e.*, $CH_4 + C_3H_8$ and $2C_2H_6$. As was the case with propane, on Ni "complete" hydrogenolysis to methane has been found to predominate **(10,44)**, whereas over alumina-supported Ru, the three expected products (CH_4, C_2H_6 and C_3H_8) were formed in approximately equal amounts **(45)**. Of particular interest here, over both Pt-**(46)** and Ir-**(24)** supported catalysts, the product distributions have been found to be sensitive to the metal particle size; in particular, the selectivity for ethane production was found to increase dramatically as the particle size decreased **(47)**.

Foger and Anderson **(24)** have reported that the selectivity for the hydrogenolysis of *n*-butane is extremely sensitive to the average metallic particle size. This "structure sensitivity" is most evident for clusters of diameter $\leq$ 40 Å, where there is a rapid change in the average coordination number of the metal surface atoms **(13,48)**. The immediate implication of these results is that the mechanism and, hence, the catalytic selectivity, are being dictated by the structure of the surface. In order to quantify the connection between the catalytic selectivity and the *local* surface structure, we have compared these results for supported Ir catalysts of vary-

ing particle size to those obtained here over the Ir(111) and Ir(110)-(1x2) surfaces **(49)**.

In order to make this comparison, we have computed an "effective particle size" **(49)** for the (111) and (110)-(1x2) surfaces utilizing the ratio of the number of edge (C_7) atoms to the number of (111) face (C_9) atoms as the appropriate criterion **(50)**. For example, the (110)-(1x2) surface contains one C_7 atom and two C_9 atoms per unit cell, a ratio of $\frac{1}{2}$. The ratio for the (111) surface is determined both by defects and the edge of the crystal (edge area/surface area $\leq 1/10$). For a perfect (111) surface it would be zero. On the basis of hydrogen chemisorption data, which have been shown to be sensitive to the presence of defects such as atomic steps **(22)**, the ratio for this (111) surface is $\sim \frac{1}{20}$. Assuming the supported catalyst particles form shapes of either octahedral or square-pyramidal (half-octahedral) structure **(52)**, we find that the effective mean particle diameters are approximately 24 or 13 Å for the Ir(110)-(1x2) surface, and 166 or 81 Å for the (111) surface, respectively **(53)**.

The selectivity for ethane production for both the supported catalysts **(24)** and the two single crystalline surfaces are shown in Fig. 16 as a function of the mean particle diameter **(54)**. Theoretically calculated curves, normalized to the specific activities of the two single crystalline surfaces and interpolated by using the ratio C_7/C_9 as a basis, are also shown in Fig. 16. Obviously, there is an *excellent* correlation between the selectivity for ethane production and the mean Ir particle size. Based on our results, *the observed increase in ethane selectivity with decreasing particle size is identified clearly with the increasing participation of low-coordination-number surface atoms.*

Examination of the results given in Tables 2 and 5 for the apparent reaction kinetics and in Tables 3 and 6 for the implied stoichiometries of the reaction intermediates suggests *strongly* that different mechanisms are operative for *n*-butane hydrogenolysis over the Ir(111) and Ir(110)-(1x2) surfaces. For example, over the Ir(111) surface both the activity and apparent reaction kinetics for the hydrogenolysis of propane and *n*-butane are very similar to one another, implicating similar

reaction pathways. The parent hydrocarbon fragment from *n*-butane over Ir(111) (assuming $\alpha = 1$ is correct), C_4H_8 is consistent with a di-σ (metal-carbon) bonded intermediate. Since two C-C bonds are cleaved for the major reaction channel on Ir(111), the rate limiting step might involve abstraction of the "dangling" methyl group from a "1,3" diadsorbed species (where we choose "1,3" due to the similarity with propane). Subsequently (or simultaneous to the "demethylization"), the remaining "1,3,3" C_3 fragment would react further in essentially the same manner as propane, and the resulting overall product distribution would be $2CH_4 + C_2H_6$, consistent with the experimental observations. On the other hand, if $\alpha = \frac{1}{2}$ is correct, and a C_4H_9 species is the appropriate intermediate, this scenario may still apply. Specifically, the rate-limiting step could be (irreversible) formation of a "1,3" diadsorbed species, accompanied by rapid C-C bond cleavage as described for the C_4H_8 intermediate. Regardless of the specific structures of the intermediates, the rate-limiting step is evidently the *irreversible* cleavage of a C-C bond, as judged by the fit to the mechanistic model that is shown in Fig. 6(c).

For *n*-butane hydrogenolysis on the Ir(110)-(1x2) surface the apparent reaction kinetics, the implied reaction intermediates and the selectivity all differ considerably from those observed on the Ir(111) surface for *n*-butane and on both surfaces for propane. These observations virtually assure that a distinct reaction mechanism is operative on the (110)-(1x2) surface for *n*-butane hydrogenolysis. As demonstrated in Fig. 12(c), the mechanism providing the best fit to the data is given by

$$n\text{-}C_4H_{10}(g) \rightleftharpoons C_4H_8(a) + 2H(a)$$

$$C_4H_8(a) \rightleftharpoons 2C_2H_4(a)$$

$$C_2H_4(a) + 2H(a) \rightarrow C_2H_6(g)\ .$$

Again the stoichiometry of the parent fragment, C_4H_8, is consistent with a di-σ bonded intermediate. However, in this case, the most plausible structure is a "1,4" diadsorbed species, or more specifically, a *metallacycle pentane.* The importance of "1,4" intermediates in alkane hydrogenolysis has been suggested by both

Leclercq *et al.* **(55)** and Zimmer *et al.* **(56)**, based on the observation that 2,2,3,3-tetramethylbutane cleaves readily to isobutane over Pt/Al_2O_3 and Pt blacks, and by Kane and Clarke **(57)**, based on the observation of a high selectivity for the production of ethane and isobutane from the hydrogenolysis of 2,2-dimethylbutane over Pt-Au films **(58)**. However, the most compelling evidence derives from precedents in organometallic chemistry, namely, the work of Grubbs and co-workers **(60)** concerning *reversible* bisolefin–metallacycle pentane interconversion in transition metal homogeneous complexes. For example, it is known that transition metal complexes containing metallacycle pentane ligands can decompose thermally to two ethylene ligands **(60)**, *i.e.*, the *exact* reaction implicated by the mechanism shown above.

Further evidence for the metallacycle intermediate (implicitly *mono*nuclear) can be provided if one considers its stereochemistry on the two surfaces considered here. For example, utilizing bond lengths and bond angles for Ir **(61)** and Pt **(62)** complexes containing metallacycle pentane ligands, one finds that significant repulsion is expected between the α-hydrogens and the adjacent Ir atoms on a (111) surface. However, no such repulsion is expected if one coordinates the ligand about the low-coordination-number C_7 atom on the (110)-(1x2) surface. Since these C_7 atoms are not present on a (111) surface, *the absence of the mononuclear metallacycle pentane intermediate on Ir(111) can be explained purely on a stereochemical basis.*

Anderson and co-workers **(63)** have suggested previously that the formation of "carbocyclic" intermediates, which were suggested to be partially responsible for the skeletal isomerization of C_5 and C_6 hydrocarbons over Pt (especially for highly dispersed catalysts), is favored on low-coordination-number surface metal atoms. Although a recent review has challenged this interpretation **(5)**, a complete understanding is hampered by the fact that there are apparently two "cyclic" mechanisms, "selective" and "non-selective" **(64)**. Finlayson *et al.* **(65)** have demonstrated recently that the "selective" mechanism for the cyclization of 2,2,4,4-tetramethylpentane on Ir, Pt, Rh, and Pd films proceeds through a "1,5" di-σ

bonded intermediate, presumably a mononuclear metallacycle hexane. Since the C-Ir-C bond angle is certainly greater for a metallacycle hexane compared to a metallacycle pentane, we would predict that this "selective cyclic mechanism" is sterically forbidden on the Ir(111) surface. This conclusion extends the proposition made by Finlayson *et al.* **(65)** that substitution at the 1,5 terminal carbon atoms (*e.g.*, alkyl groups) will sterically hinder metallacycle hexane formation; *i.e.*, the *α-hydrogens* should provide sufficient steric hindrance on the (111) surface.

Finally, the apparent reversibility of metallacycle pentane and bisethylene interconversion observed here over the Ir(110)-(1x2) surface (the reversibility consistent with the work of Grubbs *et al.* **(60)**) suggests that this mechanism may be important for the *isomerization* of higher hydrocarbons, *e.g.*, branched butanes or pentanes. For example, Garin *et al.* **(66)** have invoked (somewhat exotic) "1,2" and "1,3 ethyl-shift" mechanisms to explain the product distribution from the isomerization of ^{13}C-labeled 2- and 3-methylpentanes over alumina-supported Ir catalysts. Interestingly, these "novel" mechanisms predominated on the most highly dispersed catalysts studied ($\bar{d}_{Ir} \simeq 10$ Å). We note that virtually all of their experimental observations can be rationalized by invoking a mechanism involving reversible metallacycle (substituted) pentane–bisolefin interconversion; *e.g.*, for 3-methylpentane the olefins would be ethylene and 1-butene. If one permits rotation about and/or migration of the double-bond(s) prior to recyclization, the former of which has been observed experimentally **(60)**, the isomerization product distribution can be completely accounted for. The fact that these mechanisms predominate on highly dispersed catalysts that contain a large fraction of low-coordination-number surface metal atoms, lends further support to our proposition.

D. Neopentane

The reaction of neopentane with hydrogen on transition metal catalysts, especially on Pt **(67)**, has attracted particular interest since both isomerization (to isopentane) and hydrogenolysis products have been observed. In addition, corre-

lations have been made between the fraction of surface atoms in (111) microfacets and the isomerization selectivity with respect to that of hydrogenolysis **(67–69)**. Specifically, isomerization is favored over large metal crystallites of low dispersion. However, as discussed above in Sec. III.A, there is considerable disagreement in the literature concerning the observation of the isomerization of neopentane over iridium catalysts **(23-26)**. In cases where isomerization was observed **(23,24)**, its specific rate was less than $\frac{1}{3}$ that of hydrogenolysis. Finally, if the concentration of (111) microfacets influences the mechanism of the reaction of neopentane on Ir, a comparison of the (111) and (110)-(1x2) surfaces will be of little use since, in terms of C_9 atoms or threefold hollow (B_3) sites **(13)**, the density of these microfacets are nearly equal (and nearly equally accessible to a neopentane molecule).

An examination of Tables 2, 3, 5 and 6 shows that the specific activities, the apparent reaction kinetics, and the implied reaction intermediates (both parent and product) are essentially identical on the Ir(111) and Ir(110)-(1x2) surfaces. As with propane, these observations implicate the presence of similar reaction mechanisms on these two surfaces. However, unlike propane, for example, the parent hydrocarbon fragment from neopentane is extensively dehydrogenated; *i.e.*, apparently 4–5 hydrogen atoms are removed. This extent of dehydrogenation suggests that three carbon atoms may be bound to the surface, à la the "triadsorbed" intermediate proposed previously by Anderson and Avery **(25)**. Carbon-carbon bond cleavage of this "triadsorbed" intermediate would produce a diadsorbed isobutane fragment, which could conceivably form an additional carbon-metal bond and "triadsorb" also. The implicated stoichiometries of the product fragment, C_4H_5 or C_4H_6, are consistent with both a "diadsorbed" and "triadsorbed" species.

Isomerization products of neopentane were not detected on either surface. Nevertheless, the formation of ethane and propane may follow a similar reaction channel. That is, if ethane and propane merely resulted from successive "demethylizations" of the parent neopentane molecule, we would not expect ethane and propane to be formed in equal amounts. On the other hand, if neopentane were to isomerize to an

adsorbed (dehydrogenated) isopentane species, a single C-C bond cleavage in this intermediate could result in the production of equal amounts of ethane and propane. As may be seen in Fig. 2(d), on the Ir(111) surface, ethane and propane are not produced stoichiometrically at any reaction temperature. However, as shown in Fig. 5, these two products behave similarly with respect to P_{HC} and P_{H_2}. On Ir(110)-(1x2), as shown in Fig. 8(d), ethane and propane are produced stoichiometrically a temperatures of 475 K, and the products behave similarly with respect to P_{HC} and P_{H_2}, as shown in Fig. 11. These observations suggest that if ethane and propane are formed from a isopentane "precursor," the subsequent C-C bond cleavage on the (110)-(1x2) surface is more selective. This selective cleavage over the (110)-(1x2) surface could be a manifestation of a mechanism involving a metallacycle pentane forming from the 2-methylbutane (*i.e.*, isopentane) "precursor," with the subsequent C-C bond cleavage proceeding in the same manner as *n*-butane does on this surface.

V. Conclusions

We have examined the hydrogenolysis of various short-chain alkanes over the Ir(111) and Ir(110)-(1x2) surfaces in order to quantify the relationship between surface structure and both catalytic activity and selectivity. In particular, these two surfaces were chosen primarily in order to evaluate explicitly the role of low-coordination-number metal surface atoms in alkane hydrogenolysis. We have employed four different hydrocarbons of differing size and structure in an attempt to isolate and investigate the importance of a number of possible adsorption mechanisms. These mechanisms, or equivalently, the adsorbed reaction intermediates, act to control the catalytic selectivity.

Post-reaction surface analysis revealed the presence of a carbonaceous residue, the coverage of which was always at *submonolayer* levels, essentially independent of reaction conditions, *i.e.*, surface temperature *and* reactant partial pressures. The

coverage of the carbonaceous residue was nearly identical over both surfaces, and it increased approximately linearly with the number of carbon atoms in the parent hydrocarbon. Titration of these residues with hydrogen produced only methane, demonstrating that the carbonaceous residue essentially plays the role of a "spectator."

The major reaction channels for all of the reactants examined, with the exception of *n*-butane over the Ir(111) surface, involved the cleavage of a single carbon-carbon bond. These major reaction channels could be described by a "demethylization" of the parent hydrocarbon, with the exception of *n*-butane on the Ir(110)-(1x2) surface, which produced two ethane molecules. In all cases, as the temperature was increased sufficiently, the apparent activation energy decreased, and, concomitantly, the relative production of methane increased greatly. These changes, which we have designated as "rollover," are associated with a depletion in the steady-state concentration of hydrogen adatoms. This was demonstrated explicitly by varying the hydrogen partial pressure at a temperature near the onset of "rollover." Furthermore, since "rollover" occurred at a higher temperature over the Ir(110)-(1x2) surface, this surface containing hydrogen adsites characterized by a higher binding energy with respect to the (111) (in the limit of both low and high coverages) **(21,22)**, we were able to identify explicitly the source of the hydrogen adatoms with the metal surface atoms, *i.e.*, not the carbonaceous residue.

A mechanistic model involving a rate-limiting irreversible unimolecular C-C bond cleavage step, similar to those proposed previously by both Cimino *et al.* **(15)** and Sinfelt **(16)**, was able to describe accurately the variations in the specific rates of hydrogenolysis with variations in the reactant partial pressures. In order to describe both the specific activity and the selectivity of hydrogenolysis, it was discovered that the mechanism could be applied most advantageously by varying the reaction conditions at a temperature near the onset of "rollover." The successful application of the mechanism permitted the deduction of the stoichiometries of the adsorbed parent hydrocarbon fragments (*i.e.*, the reaction intermediates). In all cases, the

implied stoichiometries were consistent with the proposition that hydrogenolysis proceeds through a partially dehydrogenated intermediate that is multiply bound to the surface via one or more metal surface atoms. Examination of the variation in the selectivity as the hydrogen partial pressure was varied in the "rollover" regime also permitted the deduction of the (minimum) stoichiometries of the adsorbed *product* hydrocarbon fragments. The hydrogenolysis of *n*-butane over the Ir(110)-(1x2) surface could not be described by the mechanism involving irreversible C-C bond cleavage. Rather, a mechanism involving reversible C-C bond cleavage in a symmetrical reaction intermediate was found to provide a superior fit to the data.

Ethane hydrogenolysis was determined to proceed through different reaction intermediates, the parent fragment over the Ir(110)-(1x2) surface being more extensively dehydrogenated. We interpreted this result as a manifestation of the availability of *high* coordination adsites on the (110)-(1x2) surface. Both propane and neopentane hydrogenolysis were found to be nearly indistinguishable on the two surfaces. These results can be interpreted by invoking reaction intermediates that are bound to two or more adjacent metal surface atoms. However, the participation of a mononuclear metallacycle butane in the hydrogenolysis of propane remains a distinct possibility. By comparing the specific rates of hydrogenolysis (to methane and ethane) of propane and cyclopropane **(18)** on the Ir(110)-(1x2) surface, we have lent considerable support to our assignment of the apparent activation energy to $E_{app} \simeq E_C + \Delta H^{\dagger}$ for temperatures below "rollover," and $E_{app} \simeq E_C$ for temperatures above.

The selectivity for the hydrogenolysis of *n*-butane on the two surfaces has been identified with the occurrence of particular adsorbed reaction intermediates on each surface. Specifically, by comparing our results to those reported previously over supported iridium catalysts of varying metallic particle size **(24)**, a direct correlation has been discovered between the selectivity for ethane production and the concentration of low-coordination-number metal surface atoms **(49)**. Based on the implicated reaction mechanism and precedents from organometallic chemistry **(60)**,

the adsorbed reaction intermediate which leads to the high selectivity for ethane is a mononuclear metallacycle pentane. The formation of this intermediate is sterically forbidden on (111) surfaces. The logical extension of this observation has led us to propose that other mechanisms involving, for example, mononuclear metallacycle hexanes **(65)** may also be forbidden on (111) surfaces. On the other hand, the observed reversibility of the metallacycle pentane–bisethylene interconversion has led us to propose that these metallacycle pentane intermediates may be involved in the isomerization of higher hydrocarbons such as branched butanes and pentanes.

Appendix

Mechanistic Model Describing the Hydrogenolysis of Alkanes over Ir

A mechanistic scheme is developed in the following to describe both the specific rate and the selectivity of the hydrogenolysis of alkanes over iridium. Emphasis is placed on utilizing the data concerning the variations of the specific rates with the reactant partial pressures in order to deduce the stoichiometries of the apparent reaction intermediates. In addition, a major goal is to obtain a more complete understanding of the "rollover" phenomena which, as discussed above, involves both an increase in the selectivity for methane, and a concomitant decrease in the apparent activation energy with respect to total conversion as the temperature is increased. Any mechanism proposed must be consistent with the experimental observations reported above. In particular, with the exception of *n*-butane over the Ir(110)-(1x2) surface [and possibly neopentane over Ir(110)-(1x2)], we have observed the following:

1. Dependence of the total rate of hydrogenolysis (*i.e.*, with respect to conversion) on the reactant partial pressures

   (i) Apparent "order" in P_{HC} varies from $\sim$ 1 to $\sim$ 0 as P_{HC} is increased

   (ii) Apparent "order" in P_{H_2} varies from $\sim$ 0 to large negative values, $\sim$ -1 to -3, as P_{H_2} is increased

2. Selectivity of hydrogenolysis near the onset of "rollover," *i.e.*, single, in comparison to multiple, C-C bond cleavage

   (i) Selectivity of hydrogenolysis is independent of P_{HC}

   (ii) Selectivity of hydrogenolysis depends strongly on P_{H_2}, with the methane production increasing sharply as P_{H_2} is reduced.

We shall consider the following set of elementary reactions to be necessary and sufficient to describe the hydrogenolysis of alkanes over iridium. For the dissociative adsorption of the parent alkane we assume

$$C_nH_{2n+2}(g) + i\sigma \rightleftharpoons C_nH_{2n+1}(a) + H(a) \ , \qquad (i)$$

with corresponding forward and reverse rate coefficients, k_1 and k_{-1}. The term, σ, represents a "vacant site"; *i.e.*, $\theta_\sigma \equiv 1 - \sum_n \theta_n$, where θ_n are the fractional coverages of all adsorbed species. In this case, "i" vacant sites are required for adsorption. The next step we consider is a "secondary adsorption" reaction, involving the formation of an additional carbon-metal bond, given by

$$C_nH_{2n+1}(a) + j\sigma \rightleftharpoons C_nH_{2n}(a) + H(a) \ , \qquad (ii)$$

with corresponding forward and reverse rate coefficients, k_2 and k_{-2}. In this case, "j" vacant sites are required for the forward reaction. Additional dehydrogenation of the adsorbed hydrocarbon fragment is allowed (although not required) by the following reactions:

$$C_nH_{2n}(a) + \sigma \rightleftharpoons C_nH_{2n-1}(a) + H(a) \qquad (iii)$$

$$\vdots$$

$$C_nH_{x+1}(a) + \sigma \rightleftharpoons C_nH_x(a) + H(a) \ , \qquad (\ell)$$

with corresponding rate coefficients k_3 and k_{-3} for the first reaction, and k_ℓ and $k_{-\ell}$ for the "ℓ" reaction, where $\ell = (2n+2) - x$. In each case, the forward reactions require one vacant site. The C-C bond cleavage step is given by the irreversible unimolecular reaction

$$C_nH_x(a) \rightarrow C_mH_y(a) + C_{n-m}H_z(a) \ , \qquad (iv)$$

with rate coefficient k_C. Subsequent hydrogenation (or additional hydrogenolysis) of the C_m and C_{n-m} fragments are assumed to be rapid with respect to this step. Finally, the adsorption of hydrogen is given by

$$H_2(g) + 2\sigma \rightleftharpoons 2H(a) \ , \qquad (v)$$

with rate coefficients k_{H_2} and k_{-H_2}. Second-order adsorption kinetics have been observed for hydrogen over both Ir(111) (all coverages) **(22)**, and for the high coverage adstate on Ir(110)-(1x2) (*i.e.*, as demonstrated below the appropriate adstate for the reaction conditions considered above) **(21)**. It is *imperative* to note that the above mechanistic scheme can be utilized to describe the variation of the *selectivity* of hydrogenolysis. For example, if we consider the hydrogenolysis of propane to methane and ethane, we merely reverse the sequence for an adsorbed C_2H_y fragment; *i.e.*, the fragment can cleave irreversibly to two C_1 fragments and form methane via Eq. (4), or it can be hydrogenated (also irreversible at low conversions) and form ethane via Eqs. (i)–(ℓ).

Under reaction conditions similar to those considered above, the rates of the exchange of alkanes with deuterium over iridium blacks have been found to be several orders of magnitude more rapid than the corresponding rates of hydrogenolysis **(30)**. In addition, the initial product distributions indicated that the amount of exchange was extensive (*e.g.*, the average deuterium content for ethane was D_4) **(30)**. Similar results have been reported over single crystalline surfaces of platinum **(70)**. These experimental observations suggest that the "reaction probability" of the alkane upon dissociative adsorption is small (*i.e.*, the probability that it will undergo C-C bond cleavage compared to being hydrogenated and returned to the gas phase). Consequently, we may equate approximately the rates of the forward and reverse reactions of Eq. (1):

$$k_1 P_{HC} \theta_\sigma^i \simeq k_{-1} \theta_{C_nH_{2n+1}} \theta_H \ , \qquad (A.1)$$

where P_{HC} is the partial pressure of the alkane, C_nH_{2n+2}, and the θ_n designate fractional surface concentrations.

The experimental observation of extensive exchange of the alkane with deuterium suggests that the forward and reverse reactions of Eqs. (*ii*)-(*ℓ*) are fast with respect to both the C-C bond cleavage reaction [Eq. (*iv*)], and the reverse (hydrogenation) reaction of Eq. (*i*), which forms the parent alkane. Consequently, we can relate the surface coverages, $\theta_{C_nH_{2n+1}}$ and $\theta_{C_nH_x}$ by equating approximately the forward and reverse reactions of Eqs. (*ii*)-(*ℓ*):

$$\theta_{C_nH_x} \simeq \frac{\prod_{n=2}^{\ell} K_n \theta_{C_nH_{2n+1}} \theta_\sigma{}^{j-1}}{\phi^{\ell-1}} \tag{A.2}$$

where $K_n = k_n/k_{-n}$, $\phi \equiv \theta_H/\theta_\sigma$, and $\ell \geq 2$.

Under the reaction conditions considered above, and utilizing rate parameters describing the adsorption and desorption of hydrogen from both Ir(111) **(22)** and Ir(110)-(1x2) **(21)**, we expect the "reaction probability" of hydrogen to be small (*i.e.*, most of the hydrogen desorbs, rather than participating in the overall reaction $C_nH_{2n+2} + H_2 \rightarrow CH_4 + C_{n-1}H_{2n}$). Consequently, we may equate approximately the rates of the forward and reverse reactions of Eq. (5):

$$\theta_H/\theta_\sigma \equiv \phi \simeq (K_{H_2} P_{H_2})^{1/2} \ , \tag{A.3}$$

where $K_{H_2} = k_{H_2}/k_{-H_2}$. Finally, the total rate of hydrogenolysis from Eq. (*iv*) is given by

$$R_C = k_C \theta_{C_nH_x} \tag{A.4}$$

To proceed, we shall assume that the only adsorbed species in significant concentrations are hydrogen adatoms and the $C_nH_x(a)$ species; *i.e.* $1 \simeq \theta_\sigma + \theta_H + \theta_{C_nH_x}$. Combining Eqs. (A.1)-(A.4), we find that in order to be consistent with the experimental observations given above concerning the apparent "orders" in the reactant partial pressures, we must have $i + j = 3$. Thus, for the total rate of hydrogenolysis we find

$$R_C = \frac{k_C K_\pi P_{HC}}{K_\pi P_{HC} + \phi^{\ell}(\phi + 1)} \ , \tag{A.5}$$

where $K_\pi = \prod_{n=1}^{\ell} K_n$. For our reaction conditions we expect $\phi \gg 1$ or $\theta_H \gg \theta_\sigma$ **(71)**, and we find

$$R_C = \frac{k_C K^\dagger P_{HC}}{K^\dagger P_{HC} + P_{H_2}^{\alpha+\frac{1}{2}}} , \tag{A.6}$$

where $K^\dagger = K_\pi/(K_{H_2})^{\alpha+\frac{1}{2}}$ and $\alpha = \ell/2$. From Eq. (A.6) we see that the apparent order in P_{H_2} approaches a value of $-(\alpha+\frac{1}{2})$ at sufficiently high partial pressures of hydrogen. Consequently, by determining the value of α from experimental data, the stoichiometry of the relevant intermediate for the rate-limiting C-C bond cleavage reaction [Eq. (iv)] can be deduced via $x = 2(n-\alpha)+2$. It is of interest to note that in the limit of low hydrogen adatom coverages, $\phi \ll 1$, for which Eq. (A.5) reduces to $R_C \simeq k_C K' P_{HC}/(K' P_{HC} + P_{H_2}^{\alpha})$, where $K' = K_\pi/K_{H_2}^{\alpha}$. This functional form for the rate of hydrogenolysis is essentially identical to that derived previously by Sinfelt **(16)**, where it was assumed that the competition between the reactants for adsorption sites is minimal (obviously valid in the limit of low hydrogen adatom coverages).

To derive an expression for the selectivity of hydrogenolysis we shall consider the mechanistic scheme given by Eqs. (i)–(v). However, in this case, we do not consider the forward reaction of Eq. (i); *i.e.*, the reverse reaction of Eq. (i) is irreversible, an approximation that is clearly valid at low conversions of the parent alkane. Proceeding in a similar fashion as above, the rate of hydrogenation of the product hydrocarbon fragment, $C_m H_{y'}$ (*i.e.*, in all cases except *n*-butane, $C_m H_{2m+2} \equiv C_{n-1} H_{2n}$; see above), is given by Eq. (i):

$$R_{C_m} = k_{-1} \theta_{C_m H_{2m+1}} \theta_H . \tag{A.7}$$

The rate of the irreversible "secondary" C-C bond cleavage is given by

$$R'_C = k'_C \theta_{C_m H_{y'}} , \tag{A.8}$$

where, again, the subsequent hydrogenation of the resulting fragments is rapid with respect to this step. Since the "primary" C-C bond cleavage reaction is irreversible,

we must have $R_C = R_{C_m} + R'_C$ at steady state. Thus, the selectivity for the rate of production of C_mH_{2m+2} with respect to the total rate of conversion of C_nH_{2n+2} is given by

$$S_{C_m} \equiv \frac{R_{C_m}}{R_C} = \frac{(R_{C_m}/R'_C)}{1+(R_{C_m}/R'_C)} \ . \tag{A.9}$$

Utilizing Eq. (A.2) to relate the surface coverages, $\theta_{C_mH_{y'}}$ and $\theta_{C_mH_{2m+1}}$, and combining with Eqs. (A.7)–(A.9), we find that, in order to be consistent with the experimental observations reported above, we must have $j = 2$. The resulting expression for the selectivity of hydrogenolysis is given by

$$S_{C_m} = \frac{k_S P_{H_2}^{\beta}}{1+k_S P_{H_2}^{\beta}} \ , \tag{A.10}$$

where $\beta = \frac{1}{2}[(2m+2)-y']$ and $k_S = [k_{-1}K_{H_2}^{\beta}/(\prod_{n=2}^{\beta/2}K_n)k'_C]$. Thus, the apparent order in P_{H_2} for the C_m selectivity varies from β to 0 as P_{H_2} is increased. Determination of β via the evaluation of experimental data will permit the deduction of the stoichiometry of the product hydrocarbon fragment, $C_mH_{y'}$, via $y' = 2(m-\beta)+2$.

In order to reconcile the proposed hydrogenolysis reaction mechanism with our experimental observations, we have concluded the following: from the derivation of the total rate expression, $i+j=3$, whereas from the derivation of the selectivity expression, $j=2$. If the proposed mechanism can be used to describe both of these reactions, as was done here (*i.e.*, single and multiple C-C bond cleavage), then we must have $i=1$. A value of unity for i implicates first-order Langmuir kinetics for the dissociative adsorption of the parent alkane, a somewhat unexpected result. However, this implication does not totally contradict the to-date theoretical expectations and experimental observations. For example, in certain cases, dissociative adsorption via a molecular "precursor" is approximated well by first-order Langmuir kinetics **(72)**. On the other hand, unfortunately, little experimental data exist concerning the coverage dependence of the probability for dissociative adsorption of alkanes. In the particular case of the Ir(110)-(1x2) surface **(14,73)**, where the dissociative adsorption reaction could be examined under well-controlled (ultrahigh

vacuum) conditions, it was discovered that the probability for dissociative adsorption was related *linearly* to the availability of the implicated "active sites." Thus, this experimental observation tends to support, rather than contradict, a value for i of unity.

The mechanism described by Eqs. (i)–(v) may be altered also to include the case where the C-C bond cleavage reaction is reversible. That is, we replace Eq. (iv') with the reaction

$$C_nH_x(a) \rightleftharpoons 2C_mH_y(a) \ , \qquad (iv')$$

with forward and reverse rate coefficients, k_C and k_{-C}. To simplifiy matters, we consider "symmetric" C-C bond cleavage reactions only. (Modification to include "assymmetrical" cases is straightforward.) For the symmetrical case, $m = y/2$ and $y = x/2$. To proceed, we assume that the concentration of the $C_mH_y(a)$ species is not perturbed appreciably by the reversibility of the C-C bond cleavage reaction, an approximation that is valid provided C-C bond cleavage is still slow with respect to the hydrogenation/dehydrogenation reactions of Eqs. (i)–(ℓ). Thus, as derived above, the rate of C-C bond cleavage R_C is given by Eq. (A.6). Given the rate of C-C bond cleavage, the rate of hydrogenolysis will be given by the product of this rate and the "selectivity" for hydrogenation of the product fragments. This "selectivity" is is given by

$$S_{hyd} \equiv \frac{R_{hyd}}{R_C} = \frac{(R_{hyd}/R_{-C})}{1 + (R_{hyd}/R_{-C})} \ , \qquad (A.11)$$

where R_{hyd} is the rate of hydrogenation of the product fragments, and R_{-C} is the rate of the reverse reaction of Eq. (iv'). Note that at steady state we must have $R_C = R_{hyd} + R_{-C}$, where, in this case, we have neglected the rate of "secondary" C-C bond cleavage R'_C (an assumption that can be verified experimentally, for example, by the observation of a selectivity of hydrogenolysis that is independent of P_{H_2}). The rate of hydrogenation of the product fragments can be derived, as was done above, by combining Eqs. (A.7) and (A.2). For the rate of recombination of

the product fragments we assume that

$$R_{-C} \simeq k_{-C}\theta_{C_mH_y} \tag{A.11}$$

This assumption (*i.e.*, first- as opposed to second-order in $\theta_{C_nH_y}$) will be a reasonable approximation for the cases in which the rate of recombination is faster than the rate of hydrogenation, $R_{-C} > R_{hyd}$, and a poor approximation for the cases in which $R_{hyd} \gg R_{-C}$. Since S_{hyd} is approximately unity and essentially independent of P_{H_2} in the latter case (*i.e.*, where the approximation is poor), serious errors should not result in employing Eq. (A.11). [Note that if the hydrogenation of the two product fragments, C_mH_y, is "symmetric," *i.e.*, neither or both are hydrogenated, the approximation made in Eq. (A.11) is excellent for all reaction conditions.] Combining Eqs. (A.2), (A.7), (A.10) and (A.11) we find that

$$S_{hyd} = \frac{k_h P_{H_2}^{\delta}}{1 + k_h P_{H_2}^{\delta}} , \tag{A.12}$$

where $\delta = \frac{1}{2}[(2m+2) - y] = (\alpha+1)/2$ and $k_h = [k_{-1}K_{H_2}^{\delta}/(\prod_{n=2}^{\delta/2} K_n)k_{-C}]$. The total rate of hydrogenolysis is equal to the rate of hydrogenation of the product fragments, $R_{hyd} = S_{hyd}R_C$, which is given by the product of Eqs. (A.12) and (A.6):

$$R_{hyd} = \frac{k_h P_{H_2}^{\delta}}{1 + k_h P_{H_2}^{\delta}} \frac{k_C K^{\dagger} P_{HC}}{K^{\dagger} P_{HC} + P_{H_2}^{\alpha+\frac{1}{2}}} . \tag{A.13}$$

From Eq. (A.13) we see that the apparent order in P_{H_2} is given by a positive value of $\delta = (\alpha+1)/2$ at low P_{H_2}, whereas it approaches a negative value of $-(\alpha+\frac{1}{2})$ at high P_{H_2}; *i.e.*, the total rate of hydrogenolysis will exhibit a ***maximum*** with respect to the partial pressure of hydrogen.

References

1. M. Boudart, Advan. Catal. **20**, 153 (1969).
2. J. H. Sinfelt, Catal. Rev. **3**, 175 (1969); Advan. Catal. **23**, 91 (1973).
3. J. R. Anderson, Advan. Catal. **23**, 1 (1973).
4. J. K. A. Clarke and J. J. Rooney, Advan. Catal. **25**, 125 (1976).
5. F. G. Gault, Advan. Catal. **30**, 1 (1981).
6. Z. Paál and P. Tétényi, in: *Catalysis (Specialist Periodical Reports)*, G. C. Bond and G. Webb Eds., The Royal Society of Chemistry, London, Vol. 5, p. 80 (1982).
7. G. L. C. Maire and F. G. Garin, in *Catalysis— Science and Technology*, J. R. Anderson and M. Boudart Eds., Springer-Verlag, Berlin, Vol. 6, p. 161 (1984).
8. D. W. Goodman, R. D. Kelley, T. E. Madey and J. T. Yates Jr., J. Catal. **63**, 226 (1980); D. W. Goodman, Acc. Chem. Res. **17**, 194 (1984).
9. D. W. Goodman, Surface Sci. **123**, L679 (1982).
10. D. W. Goodman, Proc. 8^{th} Internal. Congr. Catal., Berlin, Vol. 4, p. 3 (1984).
11. D. W. Goodman, J. Vac. Sci. Technol. A **2**, 873 (1984).
12. C.-M. Chan, M. A. Van Hove, W. H. Weinberg and E. D. Williams, Solid State Commun., **30**, 47 (1979); C.-M. Chan, M. A. Van Hove, W. H. Weinberg and E. D. Williams, Surface Sci. **91**, 430 (1980).
13. R. van Hardeveld and F. Hartog, Advan. Catal. **22**, 75 (1972).
14. W. H. Weinberg, in: *Survey of Progress in Chemistry*, Vol. 10, p. 1 (1983).
15. A. Cimino, M. Boudart and H. S. Taylor, J. Phys. Chem. **58**, 796 (1954).
16. J. H. Sinfelt, J. Catal. **27**, 468 (1972).
17. Ultrahigh purity reactants are desirable in order to reduce any extraneous contamination of the catalyst surface. For example, olefins, if present in sufficient concentrations, can lead to an increased concentration of adsorbed carbonaceous residue **(18)**.

18. J. R. Engstrom, D. W. Goodman and W. H. Weinberg (in preparation).

19. C. M. Comrie and W. H. Weinberg, J. Chem. Phys. **64**, 250 (1976).

20. J. L. Taylor, D. E. Ibbotson and W. H. Weinberg, J. Chem. Phys. **69**, 4298 (1978).

21. D. E. Ibbotson, T. S. Wittrig and W. H. Weinberg, J. Chem. Phys. **72**, 4885 (1980).

22. J. R. Engstrom, W. Tsai and W. H. Weinberg (submitted for publication).

23. M. Boudart and L. D. Ptak, J. Catal. **16**, 90 (1970).

24. K. Foger and J. R. Anderson, J. Catal. **59**, 325 (1979).

25. J. R. Anderson and N. R. Avery, J. Catal. **5**, 446 (1966); **7**, 315 (1967).

26. J. F. Taylor and J. K. A. Clarke, Z. Phys. Chem., N. F. **103**, 216 (1976).

27. J. A. Nedler and R. Mead, Computer J. **7**, 308 (1965).

28. A value for α of $\frac{1}{2}$ is not strictly consistent with the assumptions made in the mechanistic model that is described in the Appendix, *i.e.*, where the implicit assumption is $\alpha \geq 1$. In particular, to reconcile $\alpha = \frac{1}{2}$, the secondary adsorption step, $C_nH_{2n+1}(a) \rightarrow C_nH_{2n}(a) + H(a)$, must be irreversible, and must represent the rate-limiting C-C bond cleavage reaction.

29. By writing the set of reactions, $C_nH_{2n+2}(g)+H(a) \rightarrow C_nH_x(a)+(\alpha+\frac{1}{2})H_2(g)$, we do *not* mean to imply an elementary reaction between the gas phase hydrocarbon and a hydrogen adatom. On the contrary, the proper interpretation is that a hydrogen adatom must be *desorbed* in order to create a vacant site to facilitate the chemisorption and/or dehydrogenation of the hydrocarbon.

30. A. Sárkány, K. Matusek and P. Tétényi, J. Chem. Soc. Faraday I **73**, 1699 (1977).

31. Another possible explanation for the observed small positive order in P_{H_2} is that the initial C-C bond cleavage reaction of Eq. (3) is no longer rate-limiting. In particular, for neopentane, a reduction in P_{H_2} increases the selectivity for methane production greatly; *i.e.*, multiple C-C bond cleavage becomes the dominant pathway. If the "secondary" C-C bond cleavage reactions (and sub-

sequent hydrogenations) are not rapid with respect to the initial C-C bond cleavage reaction, these secondary reactions can limit the overall rate of reaction. For example, if the coverages of the product fragments become siginificant, their presence on the surface can block the dissociative adsorption of the parent hydrocarbon. The fact that "complete" hydrogenolysis of neopentane involves the scission of *four* C-C bonds, as opposed to two for propane, suggests that this interpretaion may be important for neopentane.

32. D. J. C. Yates and J. H. Sinfelt, J. Catal. **8**, 348 (1967).
33. C. Lee and L. D. Schmidt, J. Catal. **101**, 123 (1986).
34. G. A. Martin and J. A. Dalmon, C. R. Acad. Sci. Paris C, **286**, 127 (1978).
35. J. H. Sinfelt, W. F. Taylor and D. J. C. Yates, J. Phys. Chem. **69**, 95 (1965).
36. F. Garin and F. G. Gault, J. Am. Chem. Soc. **97**, 4466 (1975).
37. C. J. Machiels and R. B. Anderson, J. Catal. **58**, 253 (1979).
38. D. G. Tajbl, Ind. Eng. Chem. Proc. Res. Devel. **8**, 364 (1969).
39. G. Leclercq, L. Leclercq and R. Maurel, J. Catal. **44**, 68 (1976).
40. L. Guczi, A. Sárkány and P. Tétényi, Faraday Trans. **70**, 1971 (1974).
41. J. L. Herrison and Y. Chauvin, Makromol. Chem. **141**, 161 (1970).
42. See, *e.g.*, K. H. Theopold and R. G. Bergman, J. Am. Chem. Soc. **102**, 5695 (1980); K. M. Motyl, J. R. Norton, C. K. Schauer and O. P. Anderson, J. Am. Chem. Soc. **104**, 7325 (1982); M. J. Krause and R. G. Bergman, J. Am. Chem. Soc. **107**, 2972 (1985).
43. R. H. Grubbs, Prog. Inorg. Chem. **24**, 1 (1978); N. Calderon, J. P. Lawrence and E. A. Ofstead, Adv. Organomet. Chem. **17**, 449 (1979).
44. J. R. Anderson and B. G. Baker, Proc. Roy. Soc. (London) **402**, A271 (1963).
45. J. C. Kempling and R. B. Anderson, Ind. Eng. Chem. Proc. Res. Devel. **9**, 116 (1970).
46. (a) G. Leclercq, J. Trochet and R. Maurel, C. R. Acad. Sci., Ser. C **276**, 1353 (1973); (b) L. Guczi and B. S. Gudkov, React. Kinet. Catal. Lett. **9**, 343 (1978).

47. A high selectivity for ethane production from the hydrogenolysis of *n*-butane has been observed also for Pt-Ir/Al_2O_3 bimetallic catalysts: see J. R. Bernard, J. Bousquet and P. Turlier, Proc. 7th Internal. Congr. Catal., Tokyo, paper A7 (1980).

48. O. M. Poltorak and V. S. Boronin, Russ. J. Phys. Chem. **40**, 1436 (1966).

49. J. R. Engstrom, D. W. Goodman and W. H. Weinberg, J. Am. Chem. Soc. **108**, 4653 (1986).

50. Alternatively, we could have computed the C_7/C_9 ratio of the supported metal particles and evaluated subsequently the ethane selectivity as a function of this ratio **(48)**. However, this calculation presumes that both the particle shape and the effective diameters of the supported catalysts are known to high accuracy. Consequently, since we *do* know the C_7/C_9 ratio to high accuracy for the single crystals, we have chosen to compute "effective particle diameters."

51. See, *e.g.*, J.-P. Brunelle, A. Sugier and J.-F. Le Page, J. Catal. **43**, 273 (1976).

52. See, *e.g.*, R. Burch in: *Catalysis (Specialist Periodical Reports)*, G. C. Bond and G. Webb Eds., The Royal Society of Chemistry, London, Vol. 8, p. 149 (1985), and references therein.

53. These two geometrical shapes bracket other probable regular polyhedra, *e.g.* cubo-octahedra or cubes.

54. Note that for the reaction $n\text{-}C_4H_{10} + H_2 \rightarrow 2C_2H_6$, the selectivity for ethane is 100%, whereas for the reaction $n\text{-}C_4H_{10} + 2H_2 \rightarrow 2CH_4 + C_2H_6$, the selectivity for ethane is 33%.

55. G. Leclercq, L. Leclercq and R. Maurel, J. Catal. **50**, 87 (1977).

56. H. Zimmer, P. Tétényi and Z. Paál, J. Chem. Soc. Faraday Trans. I **78**, 3573 (1982).

57. A. F. Kane and J. K. A. Clarke, J. C. S. Faraday I **76**, 1640 (1980).

58. It is of interest to note that Zimmer *et al.* **(56)**, examining the rates of C-C bond cleavage (hydrogenolysis) of substituted butanes at the C_2-C_3 bond, observed maxima in the specific rates with respect to P_{H_2}, consistent with our

observations for *n*-butane on Ir(110)-(1x2). Based on our mechanism involving metallacycle pentane–bisolefin interconversion, the specific value of P_{H_2} at the maximum should be inversely proportional to the rate of hydrogenation of the resulting olefins. Since the rate of olefin hydrogenation decreases with increasing alkyl substitution about the double bond **(59)**, *i.e.*, the rates of hydrogenation follow the order: ethylene > propylene > isobutylene, we would expect that the maxima in P_{H_2} for the hydrogenolysis of substituted butanes will follow the order: 2,2-dimethylbutane < 2,2,3-trimethylbutane < 2,2,3,3-tetramethylbutane. Indeed, this is exactly what Zimmer *et al.* observed **(56)**.

59. M. Kraus, Adv. Catal. **29**, 151 (1980).
60. R. H. Grubbs and A. Miyashita, J. Am. Chem. Soc. **100**, 1300 (1978); R. H. Grubbs, A. Miyashita, M. Liu and P. Burk, J. Am. Chem. Soc. **100**, 2418 (1978).
61. (a) A. R. Fraser, P. H. Bird, S. A. Bezman, J. R. Shapley, R. White and J. A. Osborn, J. Am. Chem. Soc. **95**, 597 (1973); (b) P. Diversi, G. Ingrosso, A. Lucheni, W. Porzio and M. Zocchi, J. C. S. Chem. Comm., 811 (1977).
62. A. Cheethan, R. J. Puddephatt, A. Zalkin, D. H. Templeton and L. K. Templeton, Inorg. Chem. **15**, 299 (1976).
63. J. R. Anderson, R. J. MacDonald and Y. Shimoyama, J. Catal. **20**, 147 (1971).
64. G. Maire, G. Plouidy, J. C. Prudhomme and F. G. Gault, J. Catal. **4**, 556 (1965).
65. O. E. Finlayson, J. K. A. Clarke and J. J. Rooney, J. C. S. Faraday Trans. I **80**, 191 (1984).
66. F. Garin, P. Girard, F. Weisang and G. Maire, J. Catal. **70**, 215 (1981).
67. M. Boudart, A. W. Aldag, L. D. Ptak and J. E. Benson, J. Catal. **11**, 35 (1968).
68. K. Foger and J. R. Anderson, J. Catal. **54**, 318 (1978).
69. J. M. Domínguez and M. J. Yacamán, J. Catal. **64**, 223 (1980).
70. F. Zaera and G. A. Somorjai, J. Phys. Chem. **84**, 3211 (1985).

71. For example, utilizing rate parmeters representative of the clean Ir(110)-(1x2) surface **(21)**, at P_{H_2} = 100 Torr and T = 500 K, $\phi \sim 10$.

72. P. Kisliuk, J. Phys. Chem. Solids **5**, 78 (1958).

73. T. S. Wittrig, P. D. Szuromi and W. H. Weinberg, J. Chem. Phys. **76**, 3305 (1982).

Table 1

Carbonaceous Residue Following Hydrogenolysis Reactions

Ir(111) Surface

Reactant	Fractional Carbon Coverage, θ_C
Ethane	0.17 ± 0.04
Propane	0.28 ± 0.10
n-Butane	0.34 ± 0.08
Neopentane	0.45 ± 0.10

Table 2

Apparent Kinetic Rate Parameters of Hydrogenolysis[a)]

Ir(111) Surface

Reaction Temperature range	R(475K)[b)] molec-site^{-1}-s^{-1}	$k_{app}^{(0)}$ molec-site^{-1}-s^{-1}	E_{app} kcal-mol^{-1}
$C_2H_6 + H_2 \rightarrow 2CH_4$ 450–550 K	1.1 x 10^{-3}	1.0 x $10^{13\pm1}$	34.7 ± 2
$C_3H_8 + H_2 \rightarrow CH_4 + C_2H_6$ 425–450 K	1.0 x 10^{-2}	4.7 x $10^{13\pm1}$	33.5 ± 2
n-$C_4H_{10} + 2H_2 \rightarrow 2CH_4 + C_2H_6$ 425–500 K	2.7 x 10^{-2}	7.4 x $10^{12\pm1}$	31.6 ± 2
neo-$C_5H_{12} + H_2 \rightarrow CH_4 + i$-$C_4H_{10}$ 450–475 K	2.1 x 10^{-3}	1.2 x $10^{14\pm1}$	36.4 ± 2

a) Rate parameters were fit to the total conversion by utilizing the expression $R = k_{app}^{(0)} exp(-E_{app}/k_B T)$. Reactant partial pressures were 1.0 Torr of hydrocarbon and 100 Torr of hydrogen.

b) Reaction rate is in terms of total conversion.

Table 3

Apparent Reaction Intermediates[a)]

Ir(111) Surface

Reactant	Parent Fragment	Product Fragment
$C_nH_{2n+2}(g)$	$C_nH_x(a)$	$C_mH_{y'}(a)$
C_2H_6	C_2H_4	—
C_3H_8	C_3H_6	C_2H_2
n-C_4H_{10}	C_4H_8 or C_4H_9	C_2H_1
neo-C_5H_{12}	C_5H_7 or C_5H_8	C_4H_5 or C_4H_6

a) Reaction mechanism is given by the following (also see text):

$$C_nH_{2n+2}(g) \rightleftharpoons C_nH_x(a) + 2\alpha H(a)$$

$$C_nH_x(a) \rightarrow C_mH_y(a)$$

$$C_mH_y(a) \rightleftharpoons C_mH_{y'}(a) + 2\beta H(a) \rightarrow C_mH_{2m+2}(g)\ .$$

Table 4

Carbonaceous Residue Following Hydrogenolysis Reactions

Ir(110)-(1x2) Surface

Reactant	Fractional Carbon Coverage, θ_C
Ethane	0.18 ± 0.07
Propane	0.21 ± 0.04
n-Butane	0.24 ± 0.08
Neopentane	0.44 ± 0.13

Table 5

Apparent Kinetic Rate Parameters of Hydrogenolysis[a)]

Ir(110)-(1x2) Surface

Reaction Temperature range	R(475K)[b)] molec-site^{-1}-s^{-1}	$k_{app}^{(0)}$ molec-site^{-1}-s^{-1}	E_{app} kcal-mol^{-1}
$C_2H_6 + H_2 \rightarrow 2CH_4$ 475–575 K	1.3 x 10^{-4}	5.8 x $10^{18\pm1}$	49.4 ± 2
$C_3H_8 + H_2 \rightarrow CH_4 + C_2H_6$ 425–525 K	1.5 x 10^{-2}	1.2 x $10^{14\pm1}$	34.7 ± 2
n-$C_4H_{10} + H_2 \rightarrow 2C_2H_6$ 400–475 K	7.8 x 10^{-2}	1.1 x $10^{9\pm1}$	22.2 ± 2
neo-$C_5H_{12} + H_2 \rightarrow CH_4 + i$-$C_4H_{10}$ 450–500 K	4.2 x 10^{-3}	6.2 x $10^{13\pm1}$	35.6 ± 2

a) Rate parameters were fit to the total conversion by utilizing the expression $R = k_{app}^{(0)} exp(-E_{app}/k_B T)$. Reactant partial pressures were 1.0 Torr of hydrocarbon and 100 Torr of hydrogen.

b) Reaction rate is in terms of total conversion.

Table 6

Apparent Reaction Intermediates[a)]

Ir(110)-(1x2) Surface

Reactant		Parent Fragment	Product Fragment
$C_nH_{2n+2}(g)$		$C_nH_x(a)$	$C_mH_{y'}(a)$
C_2H_6		C_2H_2	—
C_3H_8		C_3H_6	C_2H_1 or C_2H_2
n-C_4H_{10}	major	C_4H_8	C_2H_4
	minor	C_4H_8 or C_4H_9	C_3H_4 or C_3H_5
neo-C_5H_{12}		C_5H_7 or C_5H_8	C_4H_5 or C_4H_6

a) Reaction mechanism is given by the following (also see text):

$$C_nH_{2n+2}(g) \rightleftharpoons C_nH_x(a) + 2\alpha H(a)$$

$$C_nH_x(a) \rightarrow C_mH_y(a)$$

$$C_mH_y(a) \rightleftharpoons C_mH_{y'}(a) + 2\beta H(a) \rightarrow C_mH_{2m+2}(g)\ .$$

For the major channel of *n*-butane, the second reaction (C-C bond cleavage) is reversible and $y = y'$, $m = n/2$, and $y = x/2$.

Figure Captions

Figure 1. Structural models for the (110)-(1x2) and (111) surfaces of iridium. The z-axis is perpendicular to the plane of the surface. The C_n designate the coordination numbers of the metal surface atoms **(13)**.

Figure 2. Specific reaction rates (*product* molecule-site-s^{-1}) for the hydrogenolysis of (a) ethane, (b) propane, (c) *n*-butane and (d) neopentane over the Ir(111) surface. The partial pressure of hydrocarbon was 1.0 Torr, whereas that of hydrogen was 100 Torr. The dashed lines in (a), (c) and (d) represent data obtained by Foger and Anderson **(24)** over a 0.98 wt% Ir/SiO_2 catalyst ($\bar{d}_{Ir}$ = 70 Å, dispersion of 16%) extrapolated to our reactant partial pressures and plotted in terms of conversion.

Figure 3. Specific reaction rates for the hydrogenolysis of propane over the Ir(111) surface. (a) The partial pressure of propane was fixed at 1.0 Torr as the partial pressure of hydrogen was varied. (b) The partial pressure of hydrogen was fixed at 100 Torr as the partial pressure of propane was varied.

Figure 4. Specific reaction rates for the hydrogenolysis of *n*-butane over the Ir(111) surface. (a) The partial pressure of *n*-butane was fixed at 1.0 Torr as the partial pressure of hydrogen was varied. (b) The partial pressure of hydrogen was fixed at 100 Torr as the partial pressure of *n*-butane was varied.

Figure 5. Specific reaction rates for the hydrogenolysis of neopentane over the Ir(111) surface. (a) The partial pressure of neopentane was fixed at 1.0 Torr as the partial pressure of hydrogen was varied. (b) The partial pressure of hydrogen was fixed at 100 Torr as the partial pressure of neopentane was varied.

Figure 6. Analytic fits of the specific reaction rates in terms of conversion (*parent* molec-site-s^{-1}) to Eq. (4) for (a) ethane, (b) propane, (c) *n*-butane and (d) neopentane over the Ir(111) surface. The circles represent the cases for which the

partial pressure of hydrogen was fixed at 100 Torr as the partial pressure of the hydrocarbon was varied. The squares represent the cases for which the partial pressure of hydrocarbon was fixed at 1.0 Torr as the partial pressure of the hydrogen was varied. The central data point, corresponding to the standard reactant partial pressures (*i.e.*, $P_{HC} = 1$ Torr and $P_{H_2} = 100$ Torr), applies to both curves. The optimal, statistically significant values of α are displayed in each case.

Figure 7. Analytic fits of the C_m selectivity, with respect to C_n conversion, to Eq. (7) for (a) propane, (b) *n*-butane and (c) neopentane over the Ir(111) surface. In all cases the partial pressure of the hydrocarbon was 1.0 Torr. The optimal, statistically significant values of β are displayed in each case.

Figure 8. Specific reaction rates (product molecule-site-s^{-1}) for the hydrogenolysis of (a) ethane, (b) propane, (c) *n*-butane and (d) neopentane over the Ir(110)-(1x2) surface. The partial pressure of hydrocarbon was 1.0 Torr, whereas that of hydrogen was 100 Torr.

Figure 9. Specific reaction rates for the hydrogenolysis of propane over the Ir(110)-(1x2) surface. (a) The partial pressure of propane was fixed at 1.0 Torr as the partial pressure of hydrogen was varied. (b) The partial pressure of hydrogen was fixed at 100 Torr as the partial pressure of propane was varied.

Figure 10. Specific reaction rates for the hydrogenolysis of *n*-butane over the Ir(110)-(1x2) surface. (a) The partial pressure of *n*-butane was fixed at 1.0 Torr as the partial pressure of hydrogen was varied. (b) The partial pressure of hydrogen was fixed at 100 Torr as the partial pressure of *n*-butane was varied.

Figure 11. Specific reaction rates for the hydrogenolysis of neopentane over the Ir(110)-(1x2) surface. (a) The partial pressure of neopentane was fixed at 1.0 Torr as the partial pressure of hydrogen was varied. (b) The partial pressure of hydrogen was fixed at 100 Torr as the partial pressure of neopentane was varied.

Figure 12. Analytic fits of the specific reaction rates in terms of conversion (*parent* molec-site-s^{-1}) to Eq. (4) for (a) ethane, (b) propane, and (d) neopentane, and to Eq. (11) for (c) *n*-butane over the Ir(110)-(1x2) surface. The circles represent the cases for which the partial pressure of hydrogen was fixed at 100 Torr as the partial pressure of the hydrocarbon was varied. The squares represent the cases for which the partial pressure of hydrocarbon was fixed at 1.0 Torr as the partial pressure of the hydrogen was varied. The central data point, corresponding to the standard reactant partial pressures (*i.e.*, $P_{HC} = 1$ Torr and $P_{H_2} = 100$ Torr), applies to both curves. The optimal, statistically significant values of α are displayed in each case. The data for neopentane were fit to a modified form of Eq. (4), namely, the product of the expression given by Eq. (4) and $k_b P_{H_2}^{1/2}$, where k_b is a constant coefficient (see text).

Figure 13. Analytic fits of (a) the specific reaction rate to Eq. (4) and (b) the C_3 selectivity to Eq. (7) for the *minor* reaction channel of *n*-butane hydrogenolysis over the Ir(110)-(1x2) surface, *i.e.*, $n\text{-}C_4H_{10} + H_2 \rightarrow CH_4 + C_3H_8$. The optimal, statistically siginificant values of α and β are dispayed in each case.

Figure 14. Analytic fits of the C_m selectivity, with respect to C_n conversion, to Eq. (7) for (a) propane and (b) neopentane over the Ir(110)-(1x2) surface. In all cases the partial pressure of the hydrocarbon was 1.0 Torr. The optimal, statistically significant values of β are displayed in each case.

Figure 15. Specific rates of hydrogenolysis of propane (this work) and cyclopropane **(18)** to ethane and methane over the Ir(110)-(1x2) surface. The partial pressure of propane was 1.0 Torr, that of cyclopropane was 2.0 Torr, and that of hydrogen was 100 Torr. The values displayed for the apparent activation energies were obtained from least-squares fits to the total rate of conversion to methane and ethane.

Figure 16. Selectivity for ethane production (mol % of total products) from the reaction of *n*-butane with hydrogen over Ir catalysts plotted as a function of the mean

Ir particle size. Data for the supported catalysts are from Foger and Anderson **(24)**. The abscissae for the two single crystalline surfaces were determined by a calculated "effective particle size," as described in the text. The solid curves represent theoretical interpolations between the single crystalline surfaces based on the specified geometrical shapes, as described in the text. The reaction temperature in all cases is $\sim$ 475 K.

Ir(110)-(1×2)

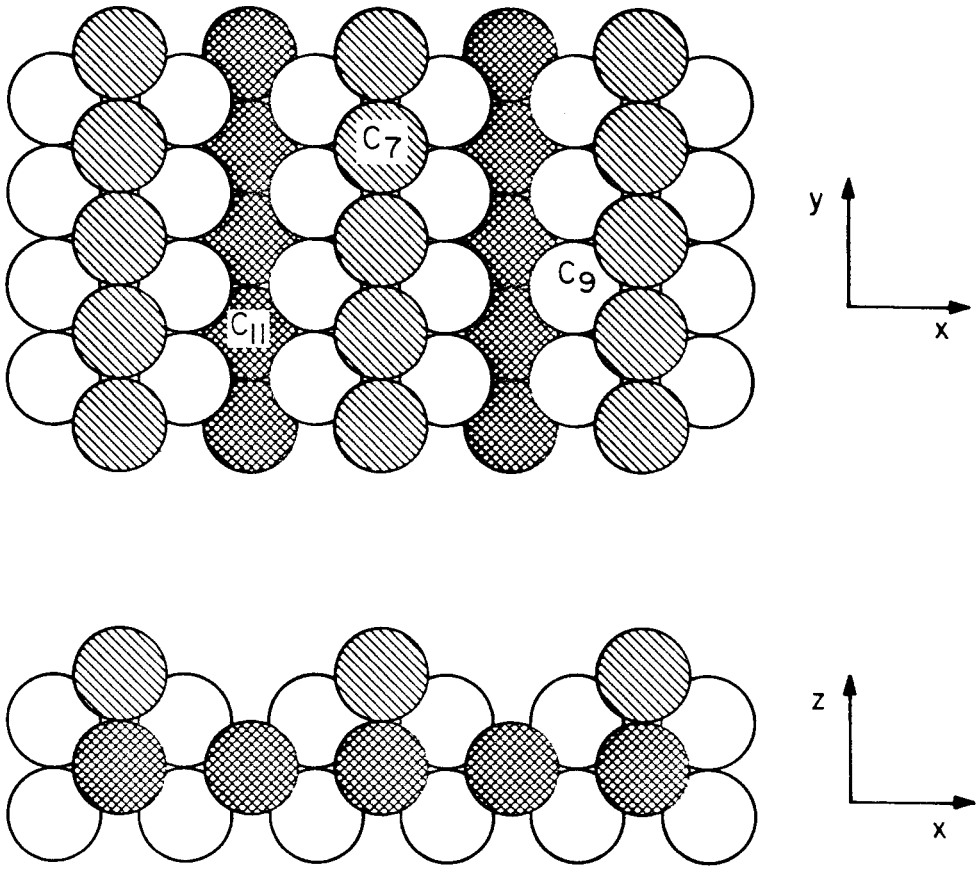

Ir(111)

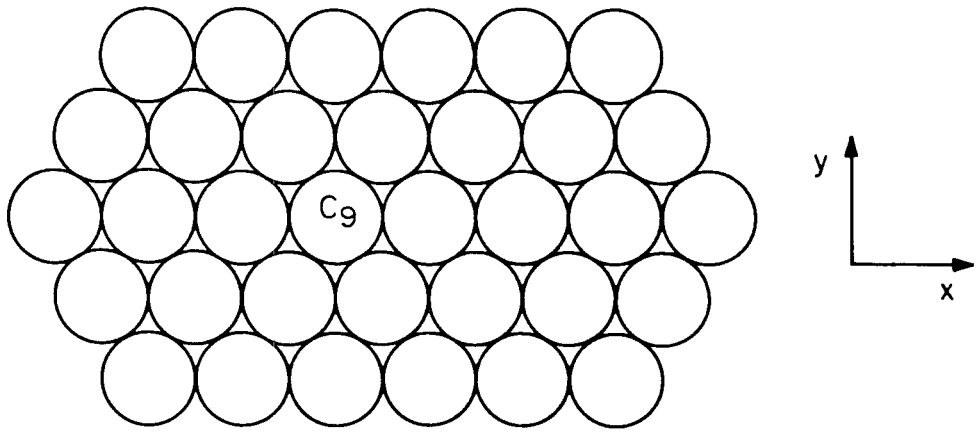

Figure 1

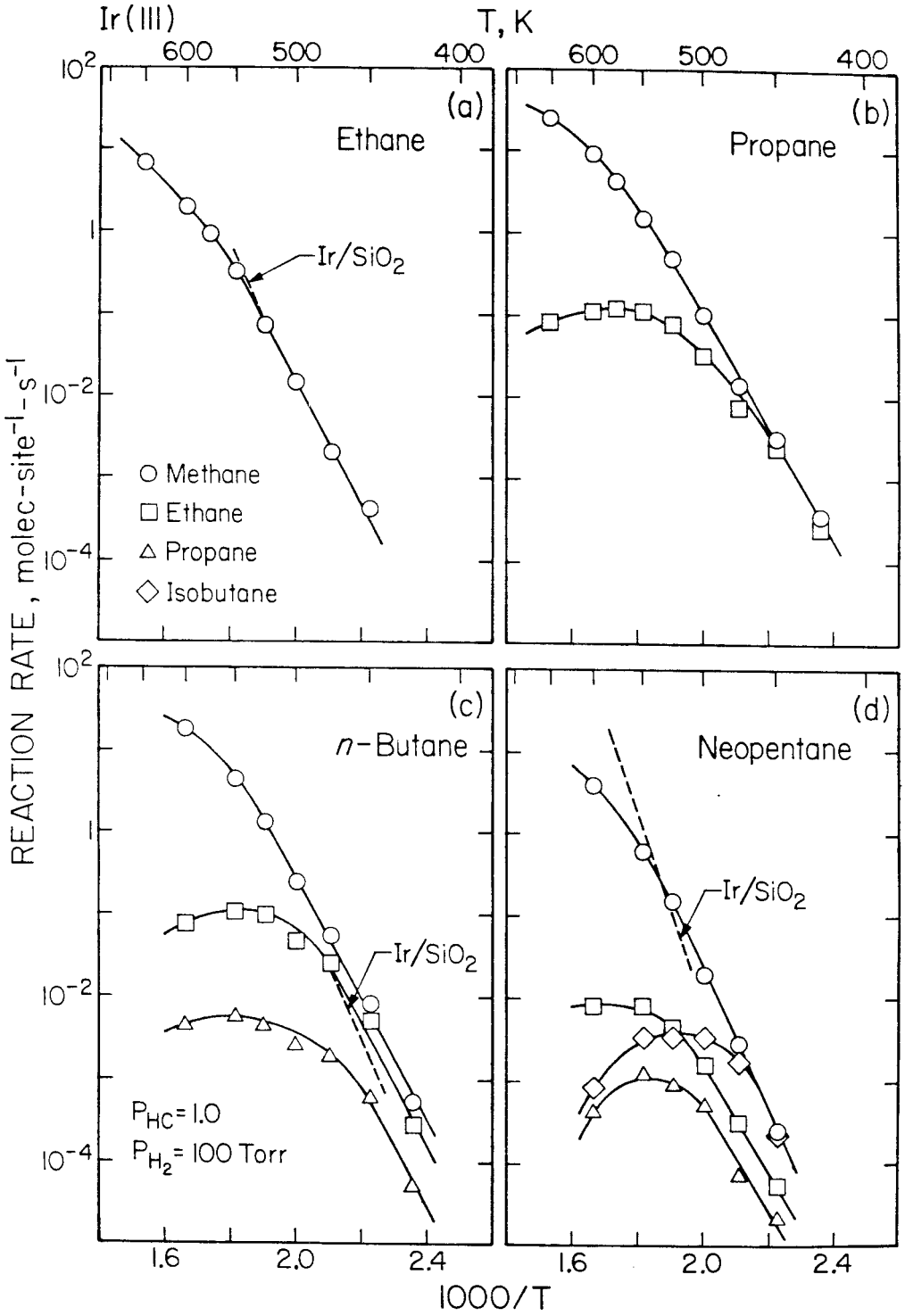
Ir(III)
T, K
600
500
400
(a)
Ethane
(b)
Propane
Ir/SiO2
O Methane
□ Ethane
△ Propane
◇ Isobutane
(c)
n-Butane
(d)
Neopentane
PHC= 1.0
PH2= 100 Torr
REACTION RATE, molec-site-1-s-1
1000/T
1.6
2.0
2.4

Figure 2

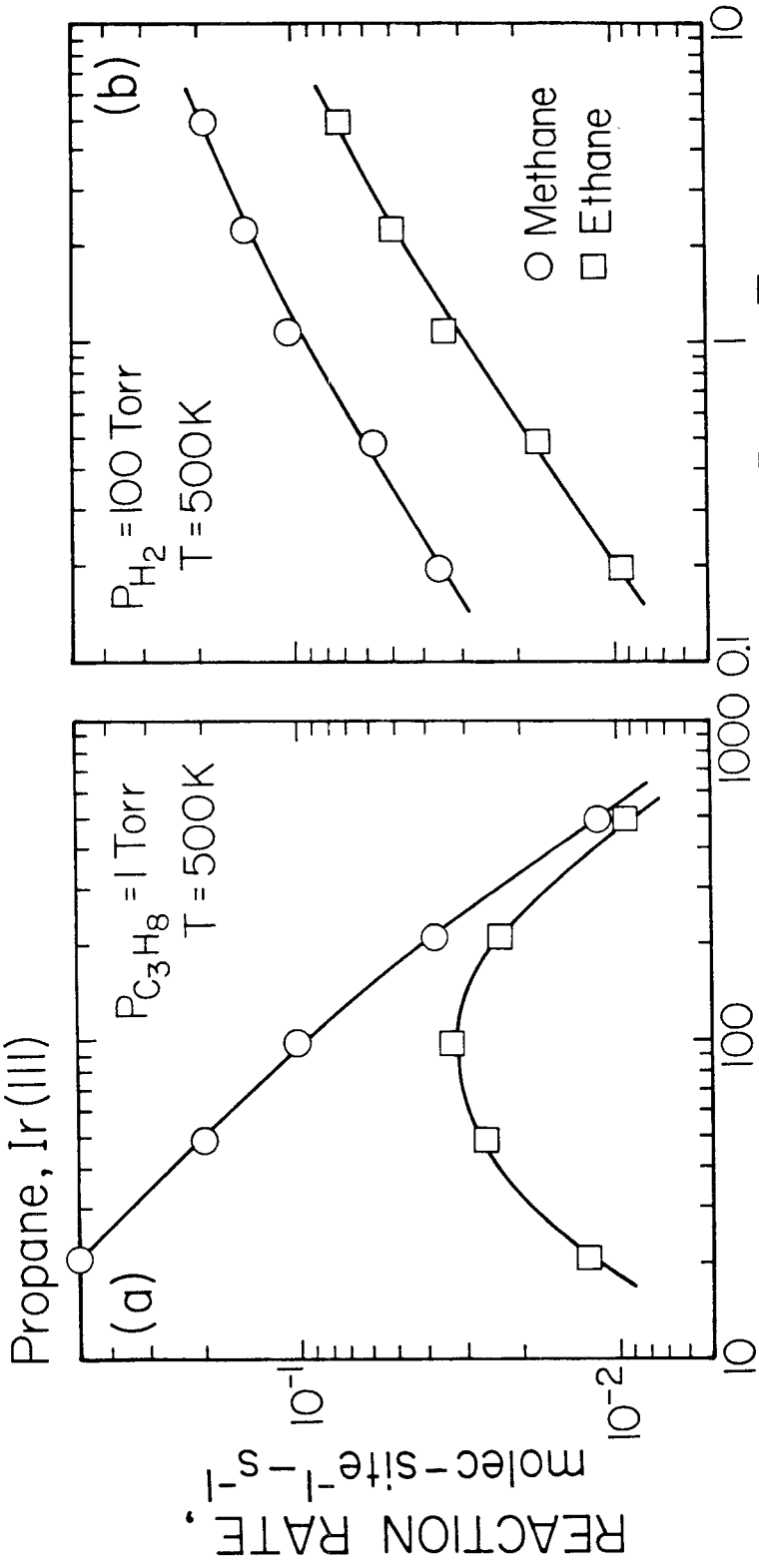
Propane, Ir(111)
REACTION RATE, molec-site^{-1}-s^{-1}
(a)
$P_{C_3H_8}$ = 1 Torr
T = 500K
P_{H_2}, Torr
(b)
P_{H_2} = 100 Torr
T = 500K
O Methane
□ Ethane
$P_{C_3H_8}$, Torr

Figure 3

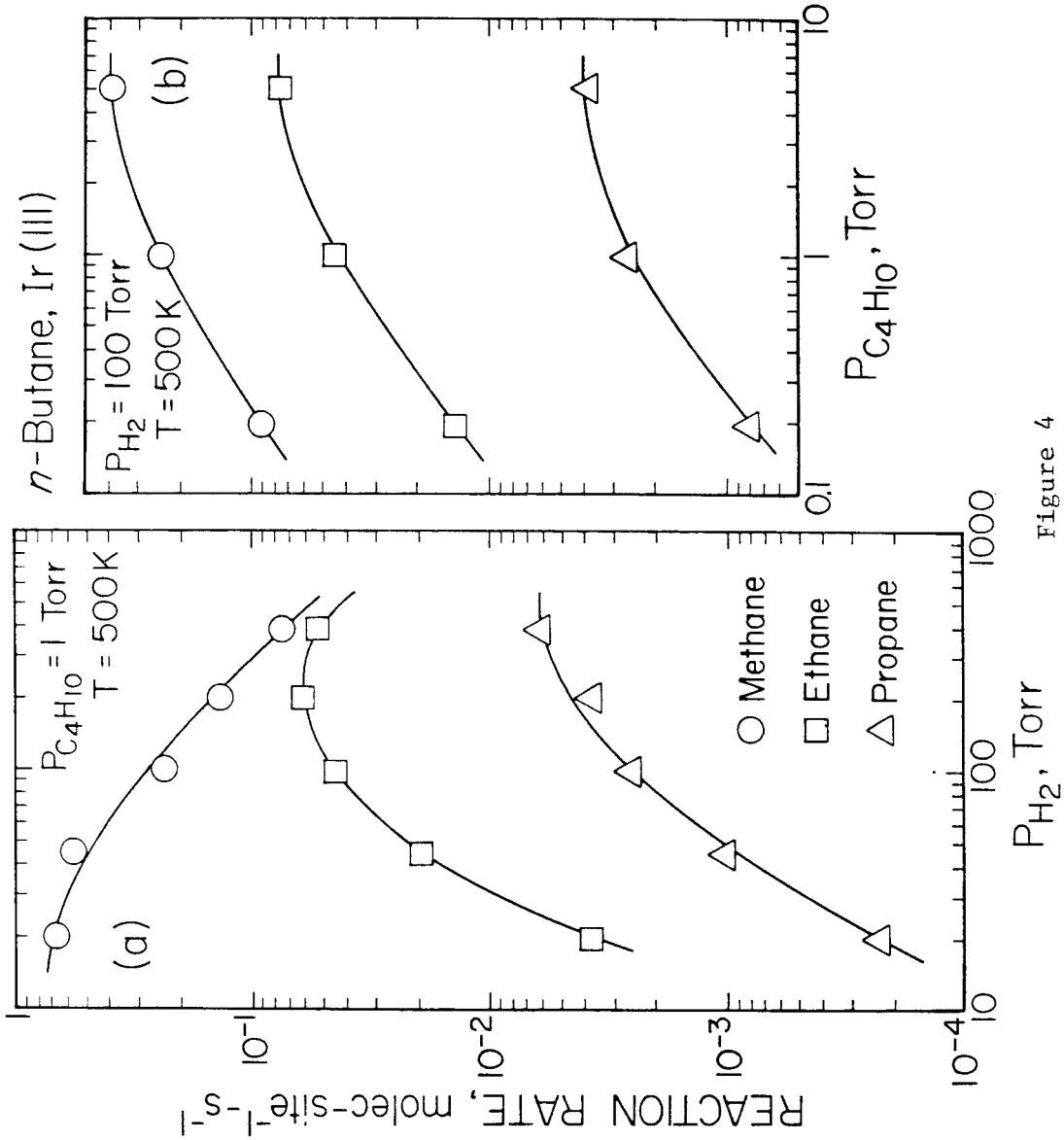
n-Butane, Ir (111)
(a)
$P_{C_4H_{10}}$ = 1 Torr
T = 500K
(b)
P_{H_2} = 100 Torr
T = 500 K
○ Methane
□ Ethane
△ Propane
REACTION RATE, molec-site^{-1}-s^{-1}
P_{H_2}, Torr
$P_{C_4H_{10}}$, Torr

Figure 4

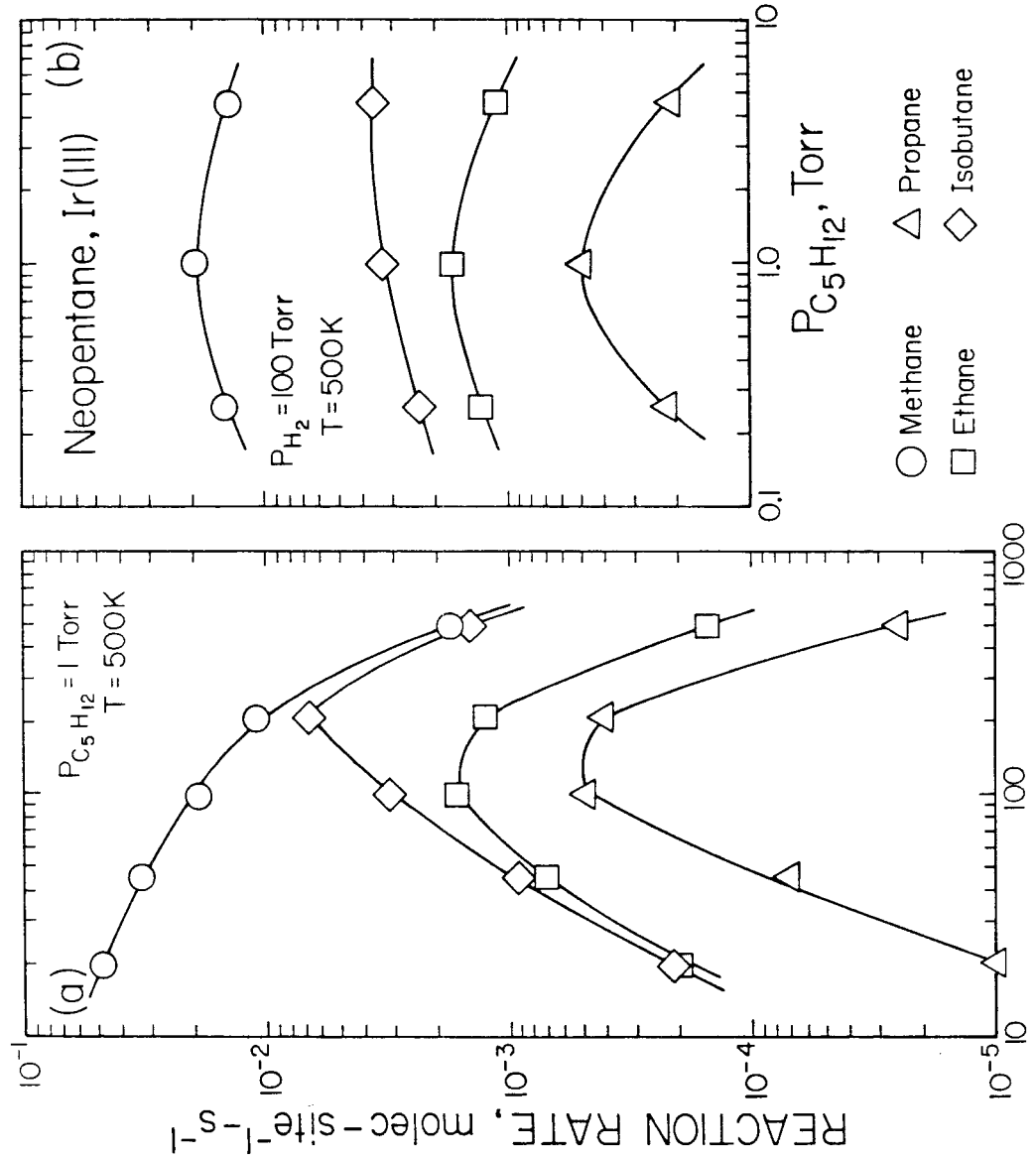
Neopentane, Ir(111)
(b)
P_{H_2} = 100 Torr
T = 500K
$P_{C_5H_{12}}$, Torr
0.1
1.0
10
(a)
$P_{C_5H_{12}}$ = 1 Torr
T = 500K
REACTION RATE, molec-site^{-1}-s^{-1}
10^{-1}
10^{-2}
10^{-3}
10^{-4}
10^{-5}
10
100
1000
P_{H_2}, Torr
Methane
Ethane
Propane
Isobutane

Figure 5

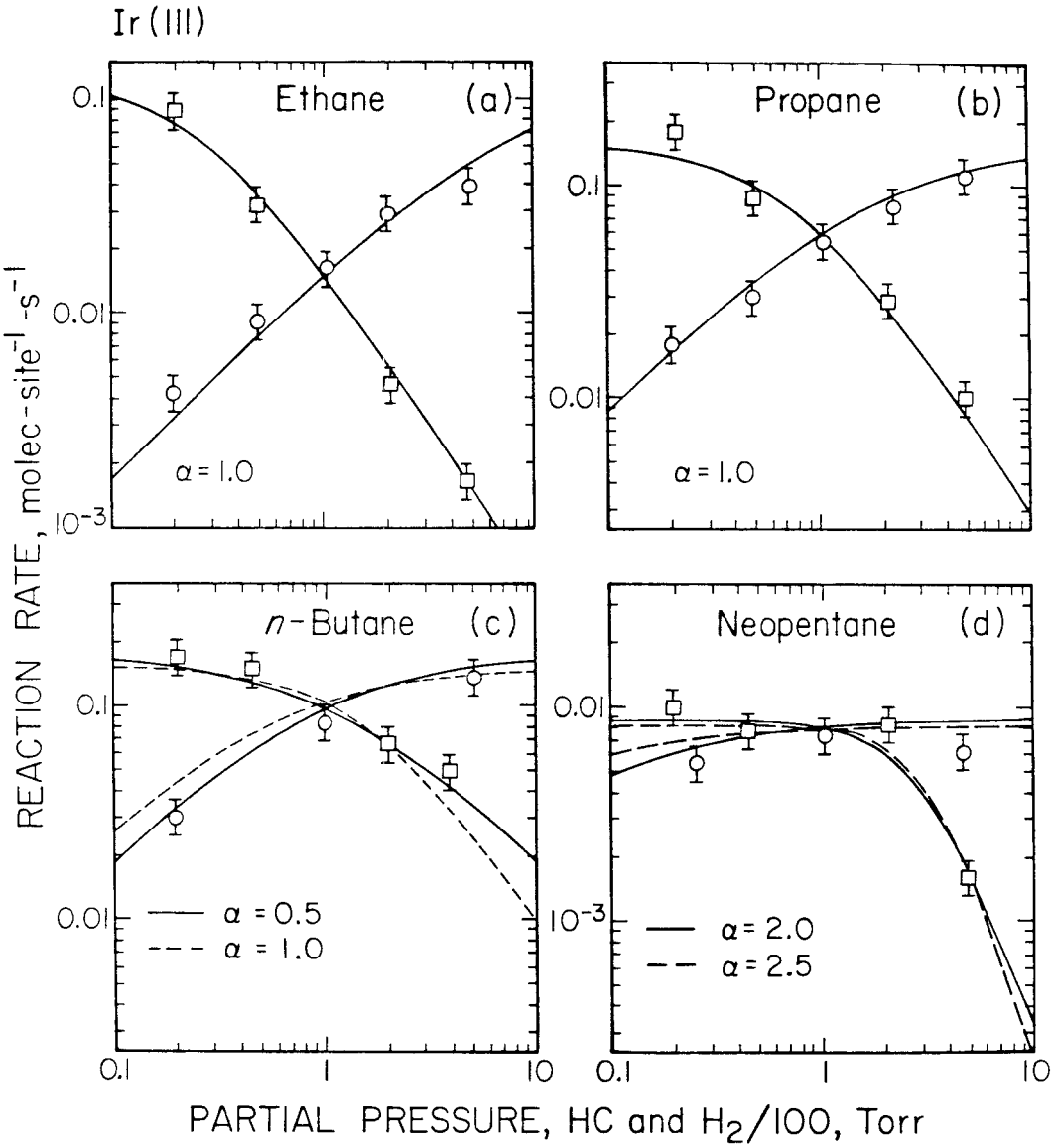
Ir (III)
Ethane (a)
Propane (b)
n-Butane (c)
Neopentane (d)
α = 1.0
α = 1.0
α = 0.5
α = 1.0
α = 2.0
α = 2.5
REACTION RATE, molec-site⁻¹-s⁻¹
PARTIAL PRESSURE, HC and H2/100, Torr
0.1
0.01
10⁻³
1
10

Figure 6

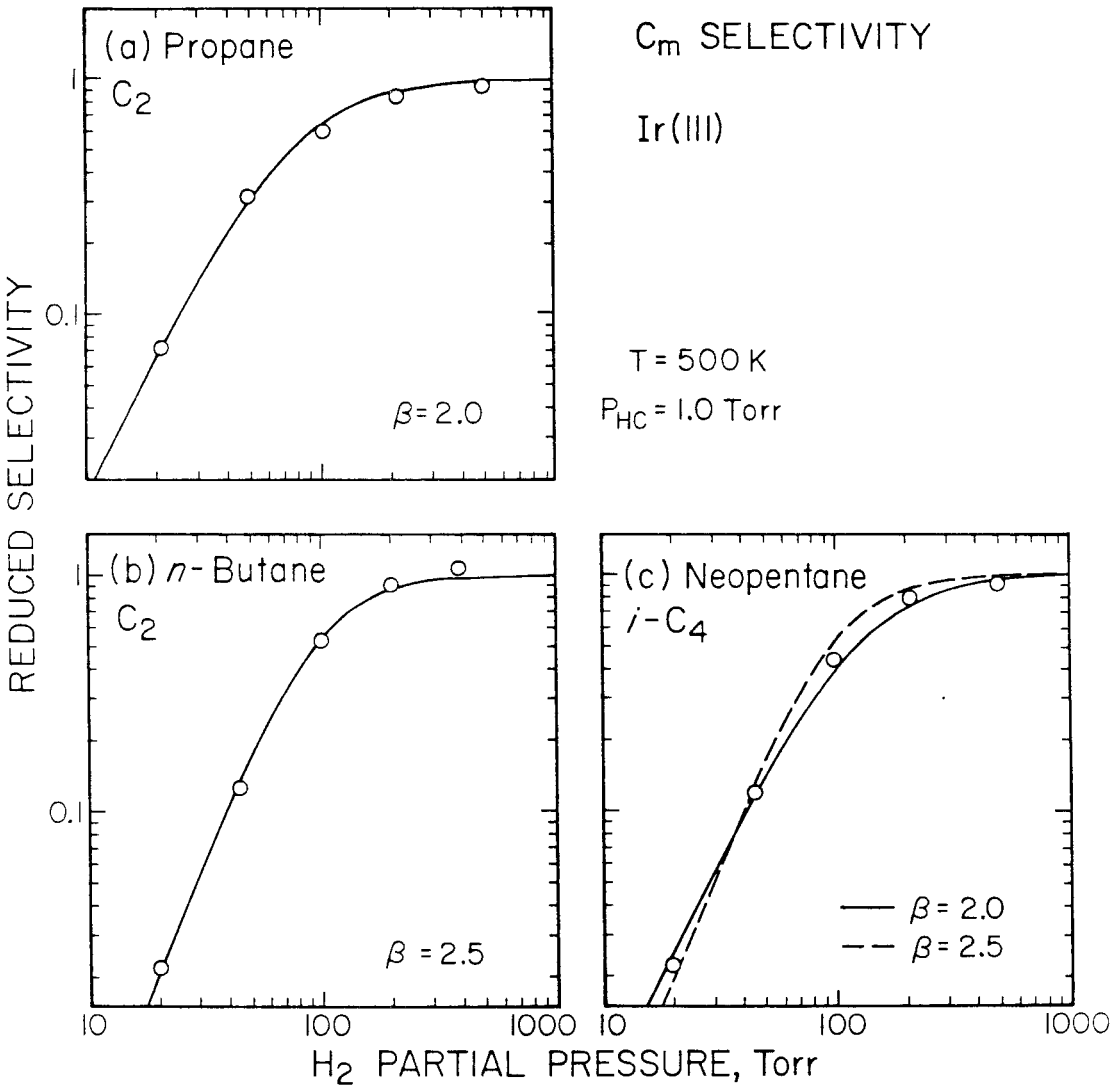
(a) Propane
C_2
$\beta = 2.0$
(b) n-Butane
C_2
$\beta = 2.5$
(c) Neopentane
i-C_4
$\beta = 2.0$
$\beta = 2.5$
C_m SELECTIVITY
Ir(III)
T = 500 K
P_{HC} = 1.0 Torr
REDUCED SELECTIVITY
1
0.1
10
100
1000
H_2 PARTIAL PRESSURE, Torr

Figure 7

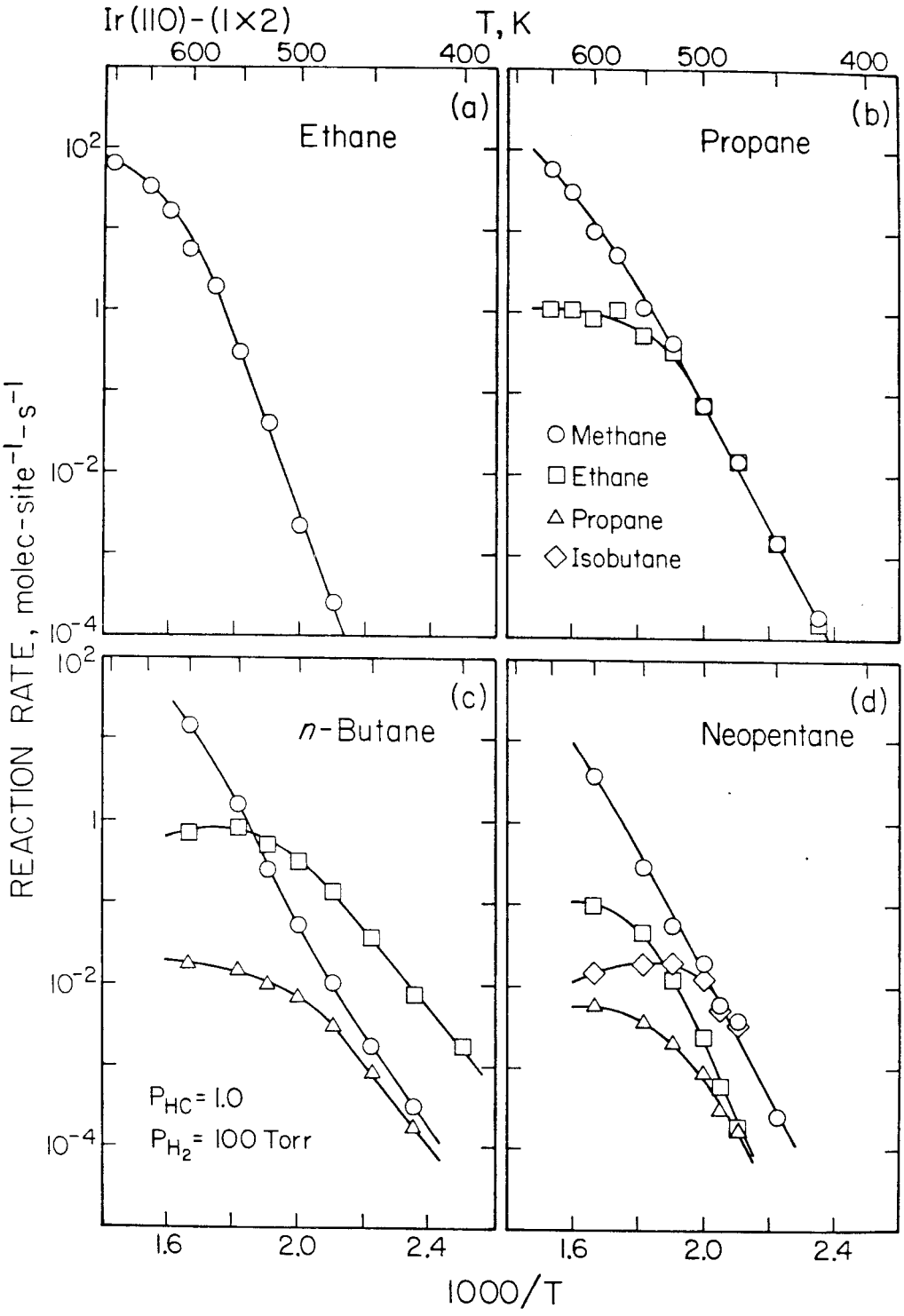
Ir(110)-(1×2)
T, K
600
500
400
(a)
Ethane
(b)
Propane
(c)
n-Butane
(d)
Neopentane
REACTION RATE, molec-site^{-1}-s^{-1}
10^2
1
10^{-2}
10^{-4}
Methane
Ethane
Propane
Isobutane
P_{HC} = 1.0
P_{H_2} = 100 Torr
1.6
2.0
2.4
1000/T

Figure 8

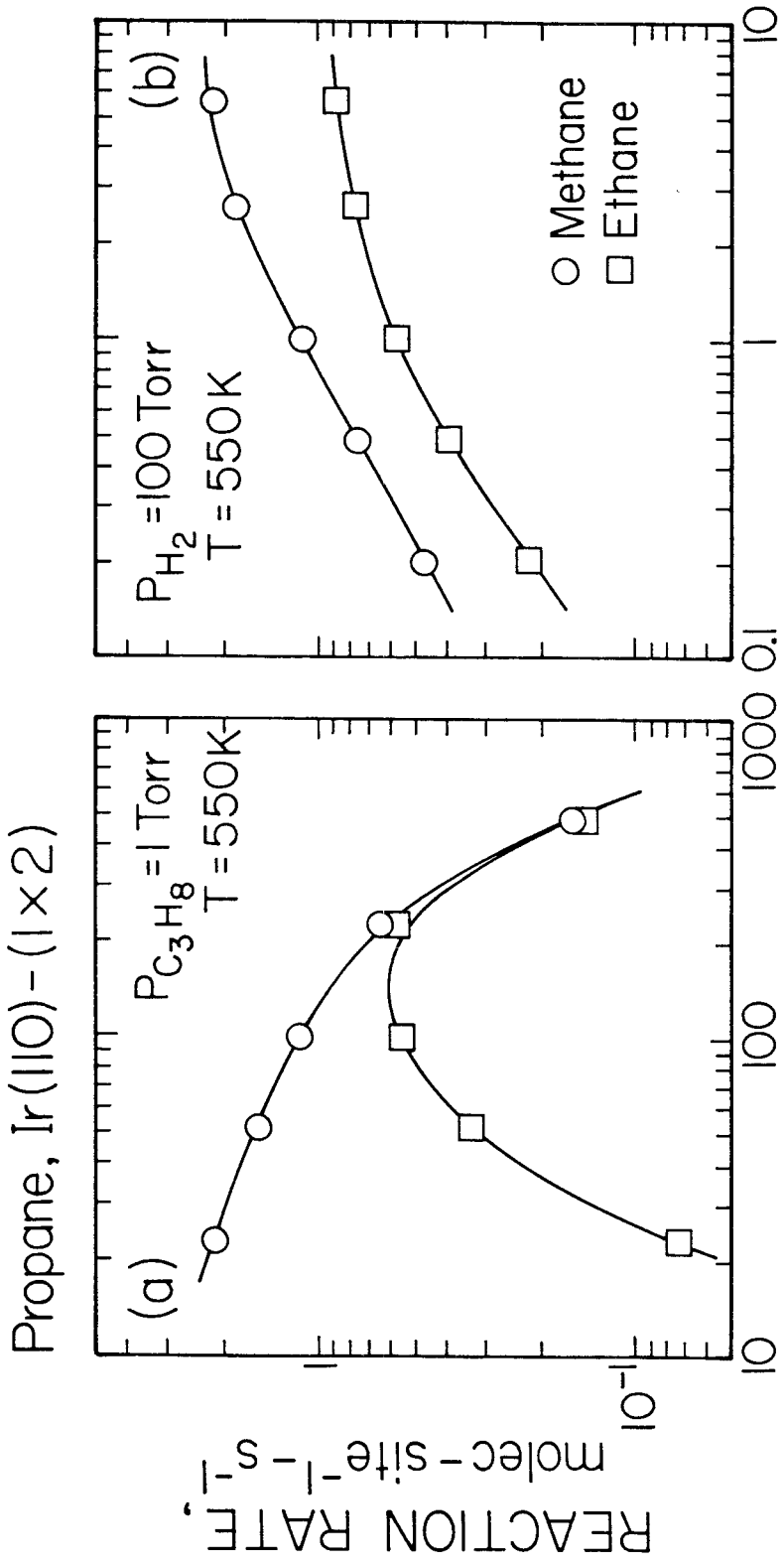
Propane, Ir(110)-(1×2)
REACTION RATE, molec-site^{-1}-s^{-1}
(a)
$P_{C_3H_8}$=1 Torr
T=550K
P_{H_2}, Torr
(b)
P_{H_2}=100 Torr
T=550K
O Methane
□ Ethane
$P_{C_3H_8}$, Torr

Figure 9

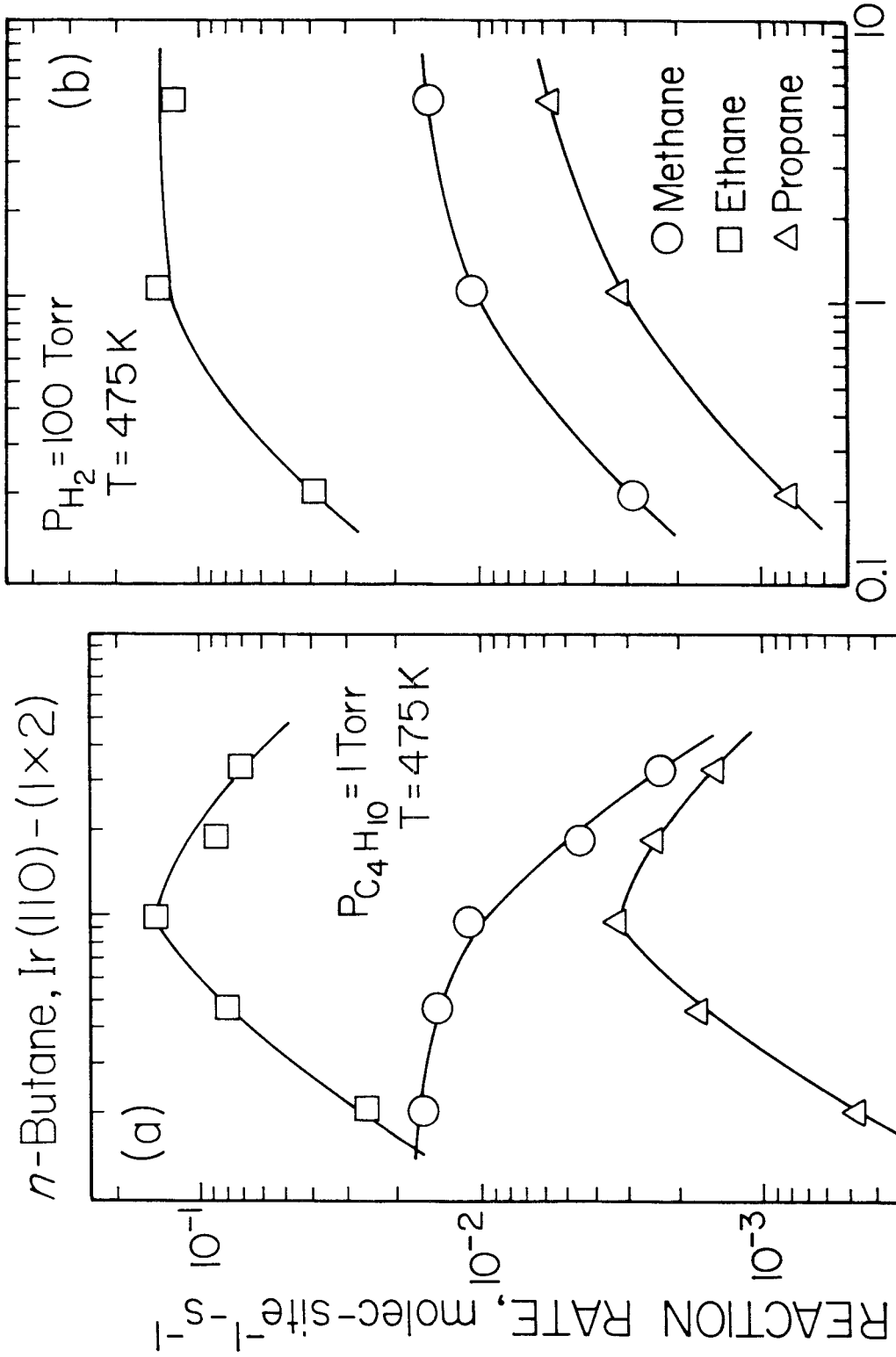
n-Butane, Ir (110)-(1×2)
(a)
$P_{C_4H_{10}}$ = 1 Torr
T = 475 K
REACTION RATE, molec-site^{-1}-s^{-1}
10^{-1}
10^{-2}
10^{-3}
10
100
1000
P_{H_2}, Torr
(b)
P_{H_2} = 100 Torr
T = 475 K
Methane
Ethane
Propane
0.1
1
10
$P_{C_4H_{10}}$, Torr

Figure 10

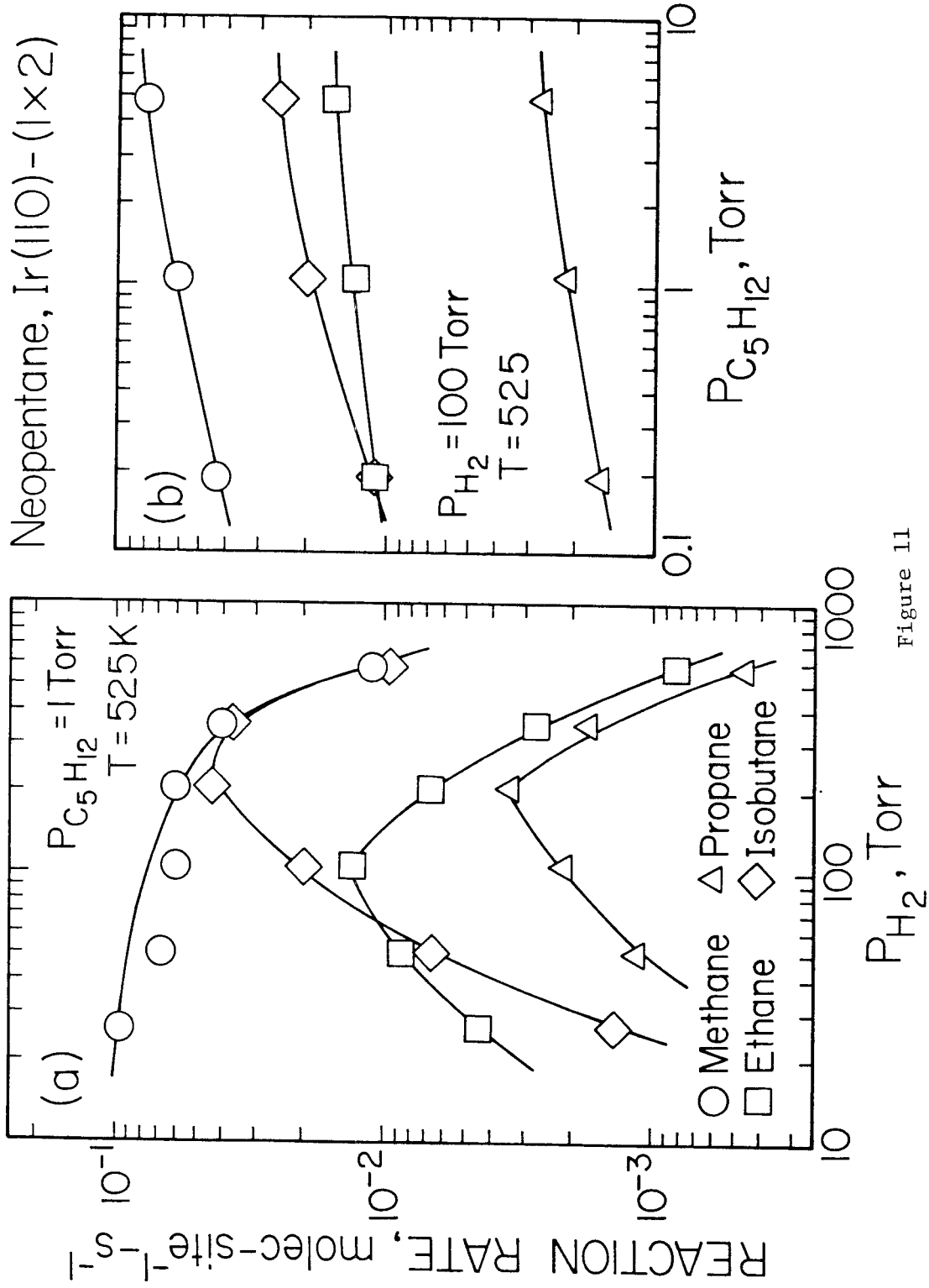
Neopentane, Ir(110)-(1×2)
(a)
$P_{C_5H_{12}}$ = 1 Torr
T = 525 K
(b)
P_{H_2} = 100 Torr
T = 525
REACTION RATE, molec-site^{-1}-s^{-1}
10^{-1}
10^{-2}
10^{-3}
10
100
1000
0.1
1
10
P_{H_2}, Torr
$P_{C_5H_{12}}$, Torr
Methane
Ethane
Propane
Isobutane

Figure 11

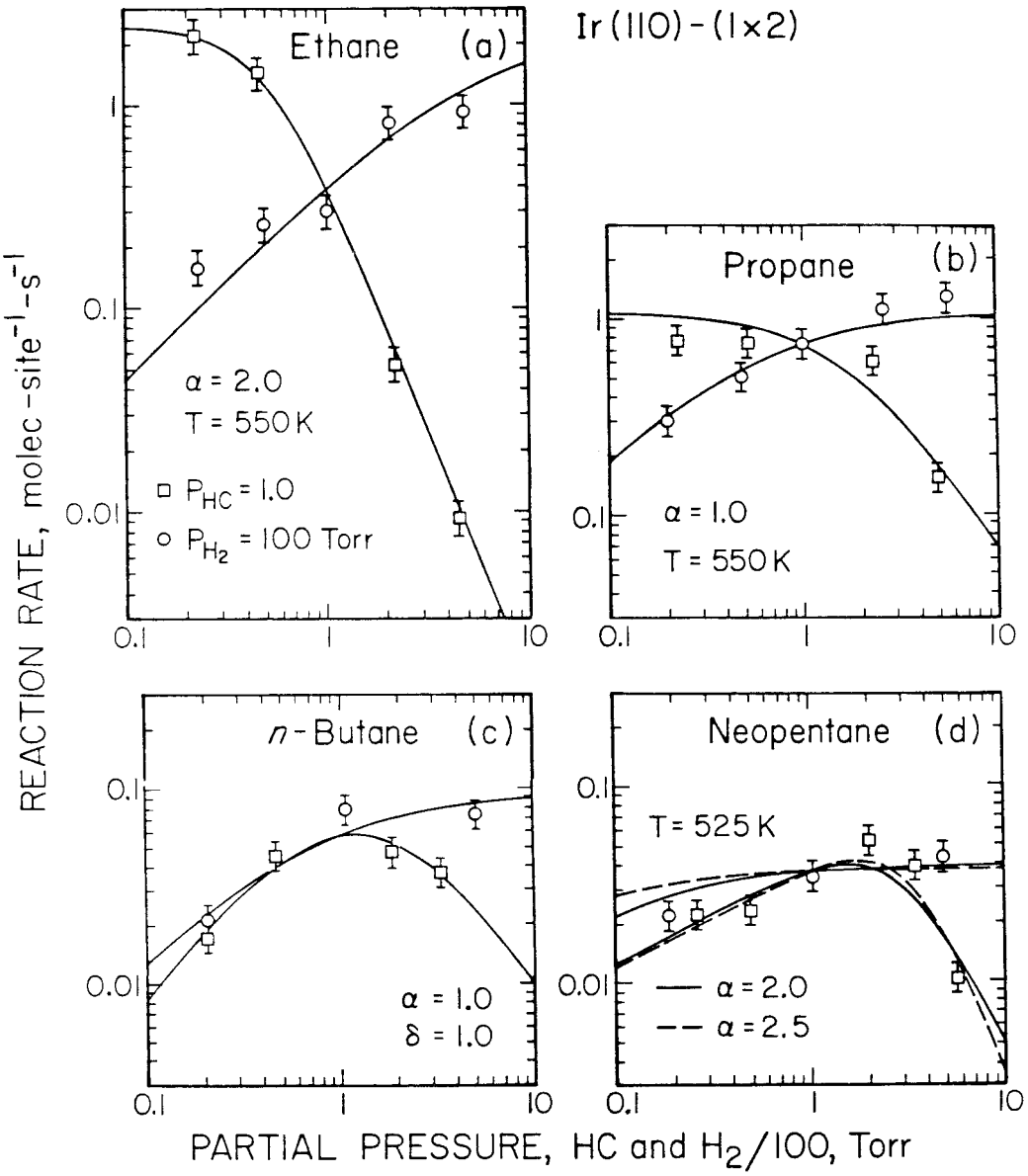
Ir(110)-(1×2)
Ethane (a)
α = 2.0
T = 550 K
□ P_{HC} = 1.0
○ P_{H_2} = 100 Torr
Propane (b)
α = 1.0
T = 550 K
n-Butane (c)
α = 1.0
δ = 1.0
Neopentane (d)
T = 525 K
— α = 2.0
-- α = 2.5
REACTION RATE, molec-site^{-1}-s^{-1}
PARTIAL PRESSURE, HC and H_2/100, Torr

Figure 12

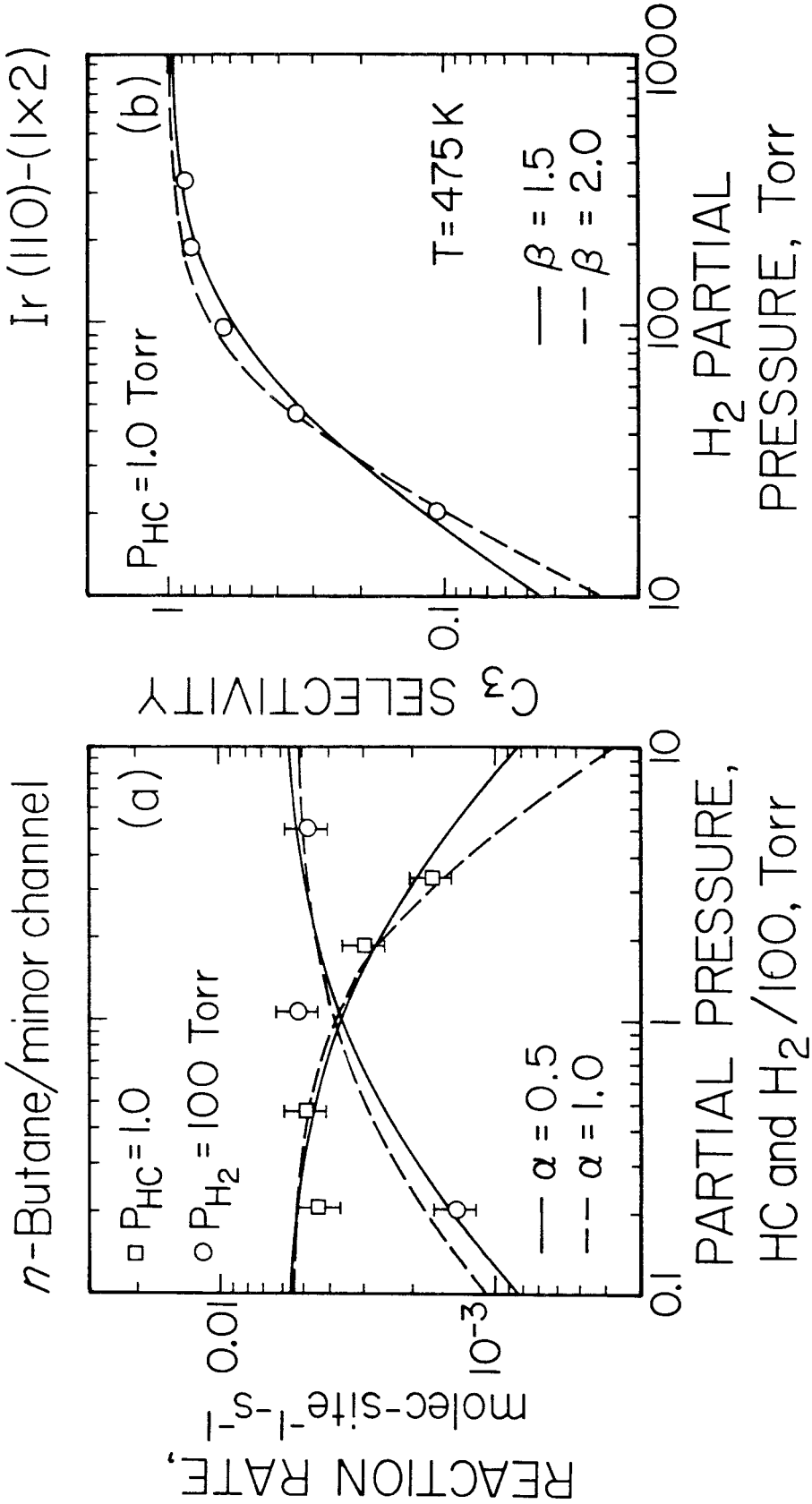
Ir (110)-(1×2)
(a)
n-Butane/minor channel
□ P_{HC} = 1.0
○ P_{H_2} = 100 Torr
— α = 0.5
-- α = 1.0
REACTION RATE, molec-site^{-1}-s^{-1}
0.01
10^{-3}
0.1
1
10
PARTIAL PRESSURE, HC and H_2/100, Torr
(b)
P_{HC} = 1.0 Torr
T = 475 K
— β = 1.5
-- β = 2.0
C_3 SELECTIVITY
1
0.1
10
100
1000
H_2 PARTIAL PRESSURE, Torr

Figure 13

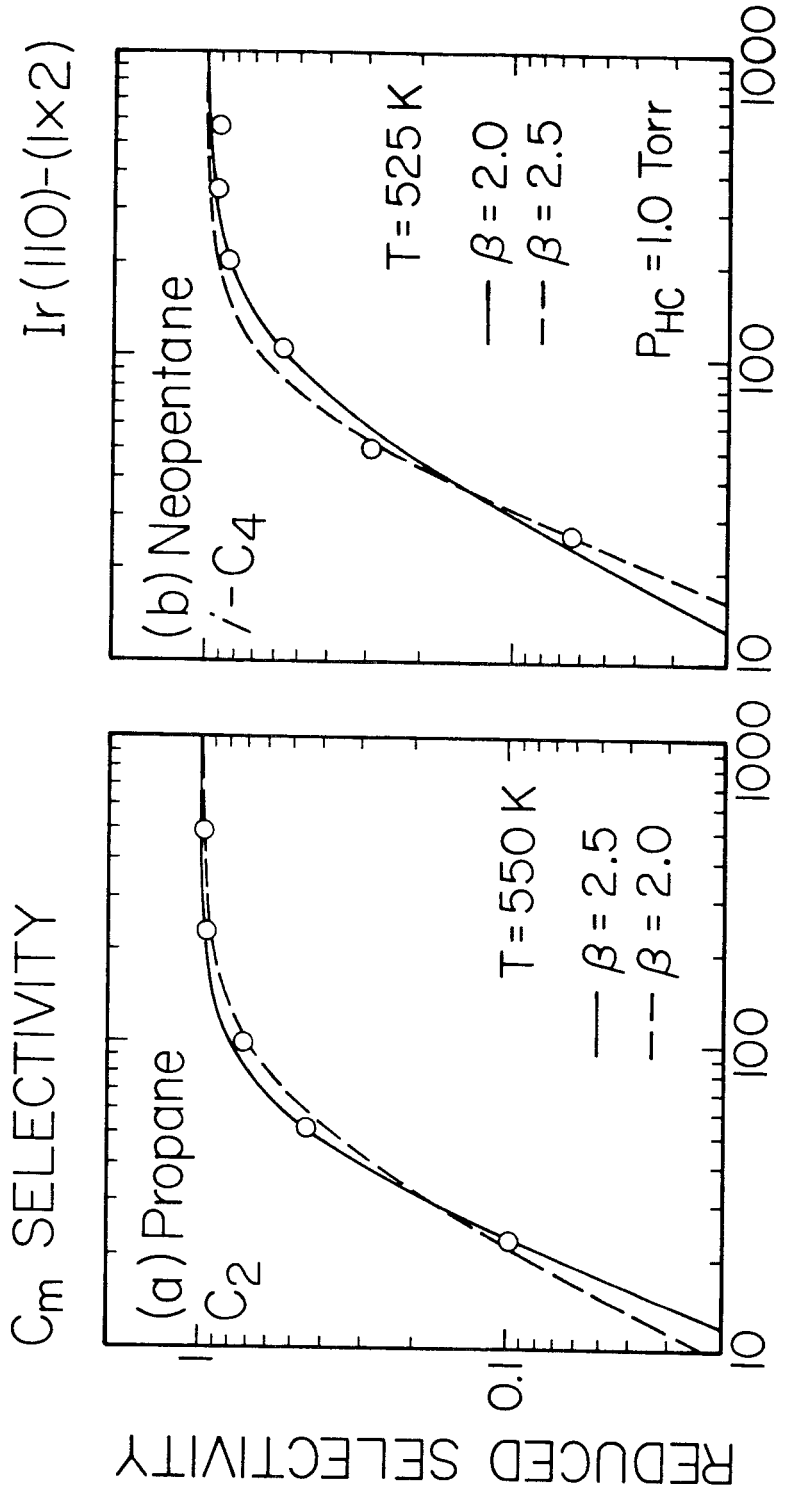
Ir(110)-(1×2)
C_m SELECTIVITY
REDUCED SELECTIVITY
(a) Propane
C_2
T=550 K
β=2.5
β=2.0
(b) Neopentane
i-C_4
T=525 K
β=2.0
β=2.5
P_{HC}=1.0 Torr
1
0.1
10
100
1000
H_2 PARTIAL PRESSURE, Torr

Figure 14

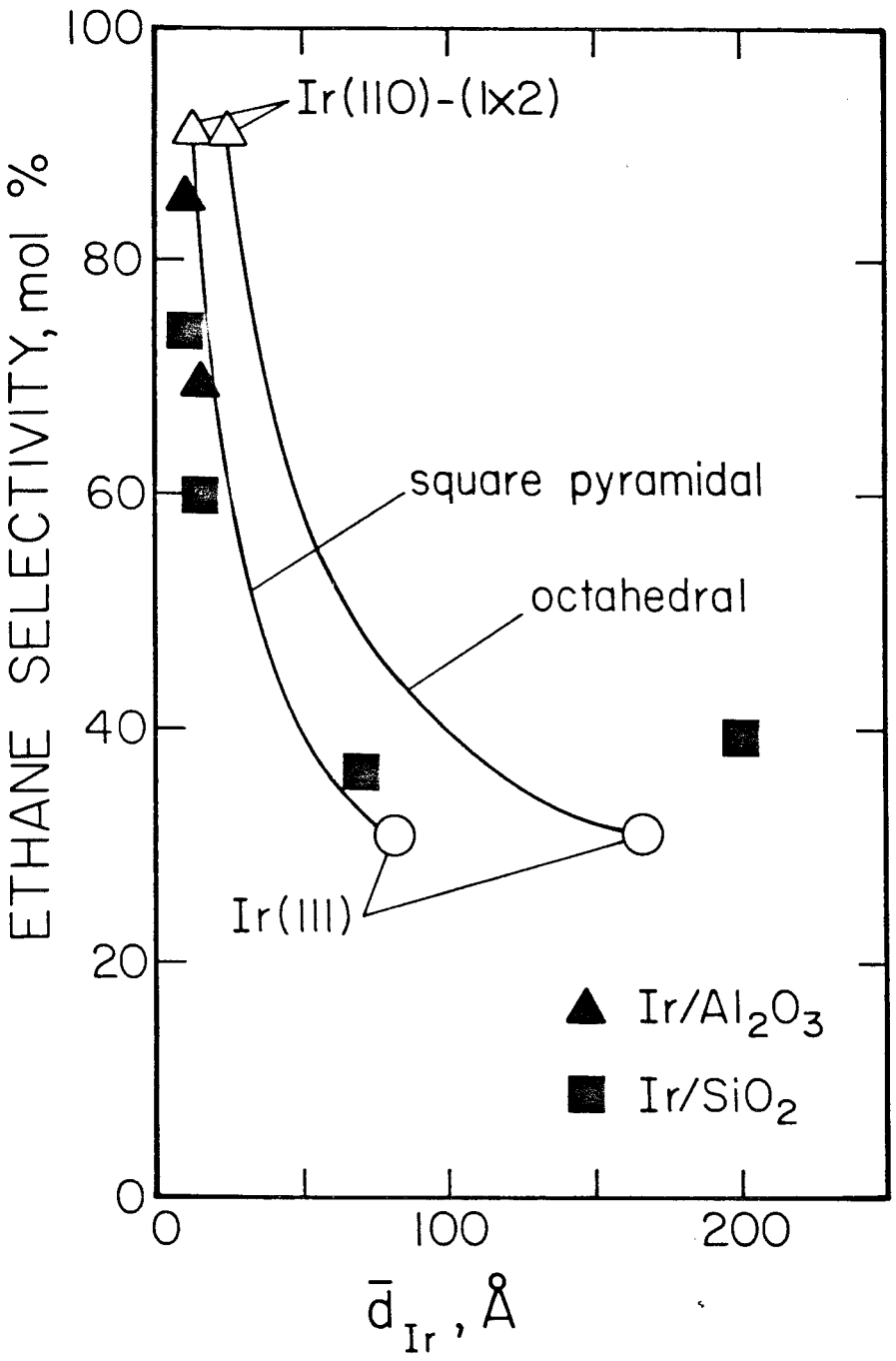
100
80
60
40
20
0
ETHANE SELECTIVITY, mol %
Ir(110)-(1x2)
square pyramidal
octahedral
Ir(111)
Ir/Al2O3
Ir/SiO2
0
100
200
d̄Ir, Å

Figure 15

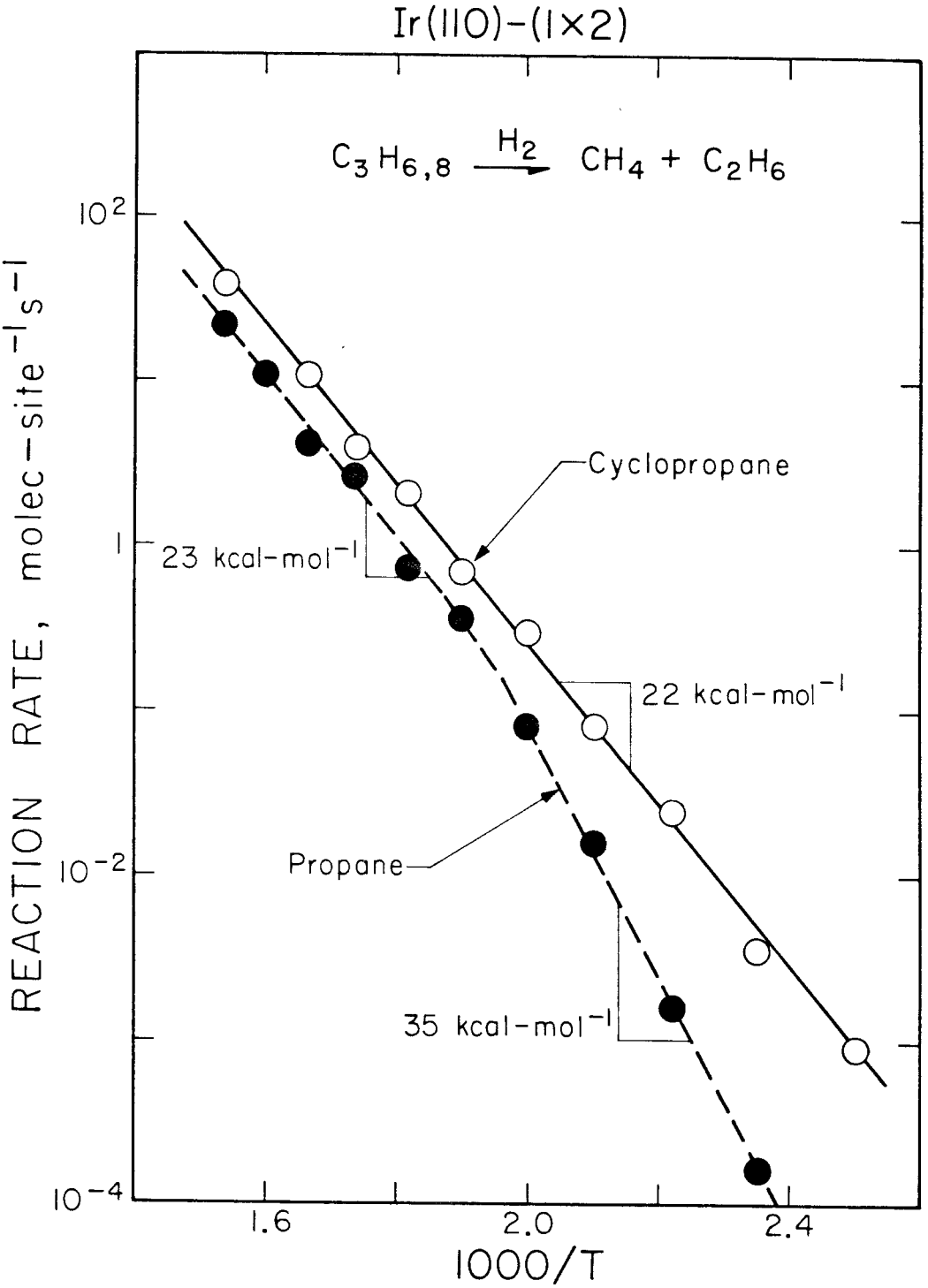
Ir(110)-(1×2)
C3H6,8 H2 CH4 + C2H6
REACTION RATE, molec-site-1s-1
10^2
1
10^-2
10^-4
Cyclopropane
23 kcal-mol-1
22 kcal-mol-1
Propane
35 kcal-mol-1
1.6
2.0
2.4
1000/T

Figure 16

CHAPTER 7

The Reaction of Cyclopropane, Methylcyclopropane and Propylene with Hydrogen on the (111) and (110)-(1x2) Surfaces of Iridium

[The text of Chapter 7 consists of an article coauthored with D. W. Goodman and W. H. Weinberg, which has been submitted to *The Journal of Physical Chemistry.*]

Abstract

The hydrogenation, isomerization and hydrogenolysis of cyclopropane, methylcyclopropane and propylene have been investigated on the (111) and (110)-(1x2) single crystalline surfaces of iridium at reactant partial pressures from 0.4 to 10 Torr of hydrocarbon, 20 to 500 Torr of hydrogen, and for surface temperatures from 400 to 600 K. A coupled high pressure reactor/ultrahigh vacuum (UHV) analysis chamber was employed, which permitted both the measurement of the specific rates of reaction, and *in situ* pre- and post-reaction surface characterization utilizing standard UHV techniques. Both the apparent reaction kinetics (*i.e.*, activation energies and preexponential factors) and the dependencies of the rates of reaction on the reactant partial pressures (*i.e.*, apparent reaction "orders") were examined in detail. Post-reaction surface analysis revealed the presence of a carbonaceous residue, the coverage of which was found to vary with the reaction conditions. For cyclopropane at the "standard" reactant partial pressures (P_{HC} = 2.0 Torr and P_{H_2} = 100 Torr) and for temperatures between 400 and 600 K, the fractional coverage of the residue was essentially constant at $\theta_C \simeq 0.5$ on both surfaces. The reaction of cyclopropane and hydrogen was described by two major reaction channels on both surfaces, namely, the hydrogenation to propane and the hydrogenolysis to methane and ethane, with the hydrogenation channel dominating for temperatures below 500 K. On both surfaces the apparent activation energy of hydrogenation was approximately 9–10 kcal-mol^{-1}, whereas that of hydrogenolysis was 23–27 kcal-mol^{-1}. The Ir(110)-(1x2) surface was found to be more active than the (111) surface for both the hydrogenation and the hydrogenolysis of cyclopropane; in both cases, the specific activity (per metal surface atom basis) on Ir(110)-(1x2) was greater by a factor of approximately $3\frac{1}{2}$. Comparison of our results to those reported previously for both supported Ni and Pt catalysts suggests that this activity difference could be due to a greater intrinsic activity (for these reactions) possessed by the low-coordination-number (C_7) metal surface atoms present on the (110)-(1x2) surface. For temperatures near 575–600 K, as the partial pressure ratio, P_{HC}/P_{H_2}, was increased sufficiently [$>$ 30 on Ir(111), $>$ 10 on Ir(110)-(1x2)], the coverage of the carbonaceous residue increased dramatically, approaching a coverage of one monolayer. Concomitant with the transformation in the composition of the adlayer, the selectivity of the reaction of cyclopropane and hydrogen was found to shift from-

methane (hydrogenolysis) to propylene (isomerization). We have associated this selectivity shift with a perturbation in the catalytic properties of the metal surface by the high coverage carbonaceous residue, which results in a change in either the binding energy or structure of the adsorbed reaction intermediate normally associated with hydrogenolysis. The hydrogenolysis of cyclopropane was found to be qualitatively different from the hydrogenolysis of propane. In particular, for cyclopropane on both surfaces, there was no variation in the apparent reaction kinetics over the entire temperature range investigated ($T \simeq 400$–600 K). This difference between cyclopropane and propane is due to the relative facility and irreversibility of forming the appropriate adsorbed intermediate from cyclopropane. The hydrogenation of methylcyclopropane on both the Ir(111) and the Ir(110)-(1x2) surface was found to be dominated by the production of *n*-butane for the reaction conditions considered here. This result was interpreted qualitatively by invoking parallel reaction mechanisms for the production of *n*-butane and isobutane, with the *n*-butane channel exhibiting a higher apparent activation energy, thus, dominating at the higher temperatures. The hydrogenolysis of methylcyclopropane was found to be similar to that found for cyclopropane on both surfaces. However, a selectivity difference was observed between the two surfaces for hydrogenolysis; the product distributions for the major reaction channels were $CH_4 + C_3H_8$ on Ir(111) and $CH_4 + C_2H_6 + C_3H_8$ on Ir(110)-(1x2). The absence of ethane in the major hydrogenolysis channel on the Ir(111) surface can be explained on a stereochemical basis if formation of the appropriate intermediate proceeds through an "edge complex"; the formation of the intermediate associated with ethane production being sterically forbidden on the Ir(111) surface. Finally, the Ir(110)-(1x2) surface was found to possess a greater specific activity with respect to the Ir(111) surface for the hydrogenation of propylene. This experimental observation, coupled with a number of others, suggested strongly a superior hydrogenation capacity for the Ir(110)-(1x2) surface. A simple explanation for these observations and the associated implication is that the hydrogen adatom concentration is greater on the Ir(110)-(1x2) surface due to the presence of a higher binding energy adstate for hydrogen on this surface.

I. Introduction

The reaction of cyclopropane with hydrogen on a variety of transition metal surfaces has attracted considerable attention since, depending on the reaction conditions, two distinct reaction channels can be observed, namely, "hydrogenation" to form propane, and "hydrogenolysis" to form methane and ethane **(1–13)**. The "hydrogenation" pathway might be expected to exhibit some similarities to olefin hydrogenation, whereas the "hydrogenolysis" pathway might resemble alkane (*e.g.*, propane) hydrogenolysis. Consequently, from the examination of a relatively simple product distribution (methane, ethane and propane), two (presumably) fundamentally different reaction pathways can be examined simultaneously.

This idealized view of the two major reactions of cyclopropane with hydrogen downplays the obvious differences between cyclopropane and both olefins and alkanes. Concerning the hydrogenation pathway, whereas evidence has been obtained for the existence of a "π-like" nondissociated adsorbed cyclopropane complex **(14)**, obviously C-C bond activation (*i.e.*, ring-opening) must precede the hydrogenation step. In regard to the hydrogenolysis pathway, unlike alkanes, C-H bond activation in the parent cyclopropane molecule is generally irreversible as evidenced by the lack of the observation of significant exchange between cyclopropane and deuterium over most transition metal surfaces **(15)**.

The reaction of cyclopropane with hydrogen has been reported to be slightly "structure sensitive" **(11,12)**; *i.e.*, the catalytic properties have been found to vary with the morphology (dispersion) of the supported metal. For example, on silica-supported nickel catalysts of varying metallic particle size, the activity for both reaction pathways was found to reach a maximum value for crystallites with an average diameter of 12Å **(12)**. The *specific* activity (per site basis) for this particle size was approximately a factor of three greater than that observed with much larger crystallites of average diameters of $\geq$ 50 Å. Similar behavior was reported for both alumina- and silica-supported platinum catalysts **(11)**. This sensitivity of the

catalytic properties to the structure of the surface for supported catalysts has been corroborated by more recent work by Goodman **(13)** on oriented single crystalline surfaces of nickel.

We have undertaken a fundamental examination of the role of surface structure in the reaction of cyclopropane with hydrogen on two orientations of iridium single crystals, namely, the close-packed (111) and the corrugated (110)-(1x2) surfaces (*cf.* Fig. 1). The clean Ir(110)-(1x2) surface reconstructs into a (1x2) superstructure **(16)**, which contains a large fraction (25%) of low-coordination-number [C_7 **(17)**] edge atoms, whereas a perfect (111) surface contains no such atoms. The (1x2) reconstruction is expected to be stable *under reaction conditions*, *e.g.*, in the presence of adsorbed hydrocarbon residues and/or surface carbon and hydrogen **(18–21)**.

We have considered also the reaction of both methylcyclopropane and propylene with hydrogen on these two surfaces of iridium. Comparisons are also made to previous work on propane hydrogenolysis on these same two iridium surfaces **(22)**. The study of methylcyclopropane can elucidate a more detailed picture of the reaction mechanisms. For example, by examining the relative rates of *n*-butane and isobutane production as a function of reaction conditions, particular adsorbed intermediates of the hydrogenation reaction are suggested. On the other hand, the selectivity for the production of methane and propane versus (two molecules of) ethane suggests intermediates relevant to the hydrogenolysis reaction. Finally, the study of the hydrogenation of propylene can be useful for a more complete understanding of the mechanism of the hydrogenation reaction of cyclopropane. For example, if both propylene and propane are produced from a common intermediate from the reaction of cyclopropane, comparison to propylene hydrogenation may implicate the nature of the rate-limiting step (or steps); *e.g.*, the rate-limiting step could involve either the rate of formation of the particular adsorbed intermediate, or the rate at which this intermediate is hydrogenated.

II. Experimental Procedures

The experiments reported here were performed in a high-pressure reaction chamber (total volume $\simeq$ 600 cm^3) linked to a UHV analysis chamber, similar to that described previously **(23)**. The chambers, which are pumped separately, are connected by a metal valve, and the base pressure in both is 10^{-10} Torr. Facilities are available in the UHV analysis chamber for Auger electron spectroscopy (AES), ion sputtering and mass spectrometry. The catalyst samples are attached to a retraction bellows and can be translated vertically to various positions in either chamber. The single crystal catalysts of iridium (total surface area $\simeq$ 1 cm^2) were mounted on wire leads and were heated resistively. The temperature was controlled manually and was measured with a W/5%Re-W/26%Re thermocouple spotwelded to the crystal. The crystals were cleaned in the UHV analysis chamber by argon ion sputtering, heating in 5 x 10^{-7} Torr of oxygen at 700 K, and annealing to 1600 K. Surface cleanliness was verified by Auger electron spectroscopy.

The cyclopropane (99.0%) and propylene (99.6%) employed in these experiments were research purity from Matheson. The methylcyclopropane was ultrahigh purity (99.95%) from API Standard Reference Materials. The hydrogen was ultrahigh purity (99.999%). The hydrocarbons were purified further by degassing at 80 K, followed by triple distillation from a liquid pentane/solid pentane bath. Reaction products were detected by gas chromatography, which, in this case, is superior to mass spectrometric detection (*e.g.*, there are no complications due to the interpretation of cracking patterns). Absolute reaction rates were calculated by utilizing the measured volume of the reactor, the reaction time period (batch reactor kinetics), and the measured geometrical surface areas of the crystals. Integration of thermal desorption spectra of saturated overlayers of CO, the absolute coverage of which is known for both the Ir(111) **(24)** and Ir(110)-(1x2) **(25)** surfaces, confirmed the geometrical measurements of the surface areas. Specific rates were calculated by using substrate densities of 1.57 x 10^{15} cm^{-2} and 1.93 x 10^{15} cm^{-2} for the (111) and (110)-(1x2) surfaces, respectively. The corresponding saturation coverages of hydrogen, commonly used to determine metallic surface areas of supported catalysts,

are within approximately 20% of these substrate densities in each case **(26,27)**. However, it should be noted that if either the low-coordination-number (C_7) or the high-coordination-number (C_{11}) surface atoms provide the only "active sites" for a particular reaction (*cf.* Fig. 1), then this normalization will *under*estimate the specific rate for the Ir(110)-(1x2) surface by a factor of four.

III. Results

A. Cyclopropane

1. The Ir(111) Surface

Specific rates (product molec-site^{-1}-s^{-1}) of the reaction of cyclopropane with hydrogen over the Ir(111) surface are shown in Fig. 2, plotted in Arrhenius form. These data represent *steady-state* reaction rates as verified by measuring the total amount of product formed after various times of reaction, typically 50–2000 s, depending on the temperature. No induction periods were detected. To both avoid secondary reactions and maintain approximately constant reactant partial pressures, conversions were restricted typically to below 1%. The standard reactant partial pressure ratio, H_2/c-C_3H_6, was 100/2, with a cyclopropane pressure of 2.0 Torr.

Post-reaction surface characterization by AES indicated the presence of a *submonolayer* carbonaceous residue, the fractional coverage of which was essentially independent of temperature for these reactant partial pressures. The measured value for the fractional coverage of carbon on the surface is given in Table 1. Post-reaction thermal desorption of the surface containing the carbonaceous residue produced only H_2, which, in all cases, gave a broad desorption feature from approximately 350 to 800 K, exhibiting a peak temperature of approximately 500 K (see below and Fig. 7). No attempts were made to determine the average stoichiometry (C_xH_y) of this carbonaceous residue, since it is *not* representative of the relevant adsorbed reaction

intermediates under reaction conditions. This important point was demonstrated explicitly by returning the catalyst to the reaction chamber (after the reactants had been pumped away) and titrating the carbonaceous residue with pure hydrogen at the relevant reaction temperatures. Methane was the only reaction product observed in all cases; *i.e.*, no C_2 or C_3 products were produced.

As may be seen in Fig. 2, the only reaction products observed were methane, ethane, ethylene, propane and propylene (total C_3 product refers to propane and propylene). The two major reaction channels at low temperatures ($T \leq 450$ K) are given by

$$c\text{-}C_3H_6 + H_2 \rightarrow C_3H_8 \ ,$$

i.e., the (dominant) "hydrogenation" pathway, and

$$c\text{-}C_3H_6 + 2H_2 \rightarrow CH_4 + C_2H_6 \ ,$$

i.e., the "hydrogenolysis" pathway. The production of ethylene is associated with the hydrogenolysis pathway. It is immediately evident from Fig. 2 that the apparent activation energy for the production of propane is much lower than that for the production of methane and ethane (and ethylene). In addition, the rate of hydrogenation is much greater than that of hydrogenolysis. Extrapolating these rates to lower temperatures, it becomes clear why the hydrogenolysis reaction was not observed by previous workers employing supported iridium catalysts at lower temperatures ($T \leq 375$ K) **(4,7)**. The apparent kinetic rate parameters obtained from the data shown in Fig. 2 (for $T \leq 450$–500 K) are given in Table 2 for the two major reaction channels. The apparent activation energy of 9.9 ± 1 kcal-mol^{-1} observed here for the hydrogenation of cyclopropane agrees well with previous work on supported iridium catalysts, where values of 9.8–11.5 **(3,4)** and 13 kcal-mol^{-1} **(7)** were obtained.

As the temperature is increased above approximately 475 K, a number of changes in the reaction product distribution are observed. Whereas linear Arrhenius behavior is apparent with respect to the *total* C_3 production for temperatures

up to approximately 550 K, the selectivity for propylene increases with increasing temperature. The linear Arrhenius behavior suggests that propylene and propane are formed from a common intermediate, whereas the increase in propylene production is best explained by a depletion in the steady-state coverage of hydrogen adatoms with increasing temperature. Above temperatures of approximately 500 K, the relative production of ethane and ethylene decreases, while the production of methane increases. The change in the selectivity of the hydrogenolysis pathway is *not* accompanied by any change in the apparent reaction kinetics. This is evident in Fig. 3, where the total rate of hydrogenolysis to C_1 and C_2 products is plotted in an Arrhenius form in terms of cyclopropane *conversion*. In particular, a least-squares fit of the data shown in Fig. 3 results in essentially identical apparent rate parameters as those given in Table 2 (which were fit to $T \leq 500$ K); namely, $k_{app}^{(0)} \simeq 1.1 \times 10^{11\pm1}$ molec-site-s^{-1} and $E_{app} \simeq 27.3 \pm 1$ kcal-mol^{-1}. This observation is unlike that found for alkane hydrogenolysis, where concomitant with the increase in the selectivity for methane, a change was also observed in the apparent reaction kinetics **(22)**. Thus, for cyclopropane, the nature of the mechanism of the hydrogenolysis reaction [*i.e.*, which step(s) is (are) rate-limiting] does not vary for temperatures between 400 and 600 K at these reactant partial pressures.

The dependence of the specific rates of reaction on the reactant partial pressures has been examined at two different temperatures. Data are shown in Fig. 4 where reaction rates were measured for variations in both the hydrogen and cyclopropane partial pressures, while maintaining a constant partial pressure of the other and a constant temperature of 450 K. This temperature corresponds to the onset of an appreciable rate of propylene production (*cf.* Fig. 2). As may be seen in Fig. 4, both decreasing the hydrogen partial pressure and increasing the hydrocarbon partial pressure lead to an increase in the rate of propylene production. Similar behavior is observed for the hydrogenolysis pathway insofar as the rate of ethylene production. These observations are consistent with a reaction mechanism in which hydrogen and cyclopropane compete for the same adsorption sites. Thus, increas-

ing the temperature, decreasing the hydrogen partial pressure, and increasing the cyclopropane partial pressure all act to deplete the steady-state coverage of hydrogen adatoms and, hence, shift the selectivity to the more dehydrogenated products, propylene and ethylene.

The apparent reaction "order" (*i.e.*, $\partial \ln R / \partial \ln P$) in P_{HC} for the hydrogenation/isomerization pathway (*i.e.*, *total* C_3 production) is approximately unity for cyclopropane partial pressures below 2.0 Torr and decreases somewhat at higher pressures. With respect to the hydrogen partial pressure, a *maximum* is observed, the apparent order decreasing from ~ 1 to $\sim -\frac{1}{2}$ as P_{H_2} is increased. A maximum in the rate of production of propane as a function of the hydrogen partial pressure from the reaction of cyclopropane and hydrogen has been observed previously over supported iridium catalysts **(4)**, consistent with our observations here. The $-\frac{1}{2}$ order in P_{H_2} for hydrogen partial pressures above 100 Torr is consistent with a mechanism involving competition between the reactants for adsorption sites; *i.e.*, hydrogen is acting to block the adsorption of cyclopropane. The positive order in P_{H_2} for pressures below 100 Torr suggests that the hydrogenation step may not be rapid with respect to the overall rate of reaction. That is, if we exclude the possibility that hydrogen is required (*i.e.*, acts as a reactant in a bimolecular reaction) for either the adsorption and/or (C-C bond) dissociation reactions of cyclopropane, then to reconcile a positive order in P_{H_2}, the hydrogenation reaction to form propane cannot be rapid with respect to the preceding reaction steps. Utilizing similar reasoning, since the *total* rate of C_3 production is positive order in P_{H_2} in this pressure regime, we propose that if propane and propylene are formed from a common intermediate, it may be more dehydrogenated than propylene (*e.g.*, a C_3H_5(a) adsorbed species).

In contrast to the hydrogenation pathway, the total rate of hydrogenolysis (*i.e.*, total conversion of cyclopropane to methane, ethane and ethylene) is only weakly dependent on the reactant partial pressures. The apparent order with respect to P_{HC} is essentially zero, whereas that with respect to P_{H_2} is nearly zero and exhibits

a small positive value ($\sim \frac{1}{2}$) for hydrogen partial pressures below 100 Torr. These observations should be contrasted with those found for alkane (including propane) hydrogenolysis **(22)**, where in the regime where linear Arrhenius behavior was observed, the reaction rates are approximately first order in hydrocarbon partial pressure and large negative order ($\leq -1\frac{1}{2}$) in hydrogen partial pressure. The orders for alkane hydrogenolysis can be rationalized in terms of a pseudo-equilibrium between the gas phase hydrocarbon and hydrogen and an adsorbed, dehydrogenated parent hydrocarbon fragment. The behavior of the hydrogenolysis pathway observed here suggests that this pseudo-equilibrium does not occur for cyclopropane. Rather, formation of the appropriate reaction intermediate is relatively facile and irreversible for cyclopropane.

The sensitivity of the specific rates of reaction on the reactant partial pressures is considerably different at higher temperatures where dramatic changes in the selectivity are observed (*cf.* Fig. 2). This is reflected in the data that are shown in Fig. 5, which represent a constant temperature of 575 K. If $P_{H_2}/P_{HC} > 30$, the apparent orders in P_{HC} are nearly unity for hydrogenation and essentially zero for hydrogenolysis, whereas the orders in P_{H_2} are $\sim 1\frac{1}{2}$ for hydrogenation and nearly zero for hydrogenolysis (with respect to C_1 and C_2 conversion). In addition, the selectivity for ethane increases greatly with the hydrogen partial pressure.

Concerning the hydrogenation pathway and $P_{H_2}/P_{HC} > 30$, the positive order in P_{H_2} is consistent with the data of Fig. 4 for $P_{H_2} \leq 100$ Torr. The order of unity in P_{HC} for hydrogenation is also consistent both with the data of Fig. 4 and with the general observation that the order in P_{HC} increases from zero to unity as the temperature is increased **(3,4)**.

Concerning the hydrogenolysis pathway and $P_{H_2}/P_{HC} > 30$, the apparent orders in both P_{HC} and P_{H_2} are essentially zero (with respect to C_1 and C_2 conversion), in agreement with the data of Fig. 4, which were obtained at 450 K. The similar reaction orders for the hydrogenolysis pathway observed at 450 and 575

K corroborate the constancy of the apparent reaction kinetics for this channel for the reaction conditions considered here (*cf.* Fig. 3). On the other hand, the dramatic decrease in the ethane selectivity with decreasing hydrogen partial pressure is readily understood from complimentary results obtained for alkane hydrogenolysis **(22)**. In particular, the decrease in the ethane selectivity is due to the increasing occurrence of multiple carbon-carbon bond cleavage as the hydrogen concentration is depleted; *i.e.*, the probability increases that a C_2 fragment will cleave to two C_1 fragments as opposed to hydrogenating to form ethane.

The most notable feature of the data shown in Fig. 5 is that a dramatic shift in the selectivity is observed for $P_{H_2}/P_{HC} < 30$. This virtual step-function change in the selectivity from methane (hydrogenolysis) to propylene (isomerization) is accompanied by and probably due to a nearly irreversible transformation in the composition of the adlayer. Post-reaction surface characterization via AES indicates that the carbon coverage increases from a value of $\theta_C \simeq 0.46$ to values of $\theta_C \simeq 0.8$–1.0, as P_{H_2}/P_{HC} is reduced below a value of 30 at a temperature of 575 K. The specific values for the carbon coverage corresponding to the reaction conditions given by Fig. 5 are shown in Fig. 6(b). The data of Fig. 5 are also shown in Fig. 6(a) where they are plotted in terms of a hydrogenation/isomerization (C_3) selectivity and a hydrogenolysis (C_1 and C_2) selectivity. Clearly, the hydrogenolysis pathway dominates on the "low" carbon coverage surface ($\theta_C \simeq 0.46$), whereas the hydrogenation/isomerization pathway dominates on the highly carburized surface ($\theta_C \simeq 0.8$–1.0).

The cause of the selectivity shift may be better understood if we consider in more detail the nature of the highly carburized surface. First of all, the high carbon coverage residue was considerably less reactive than the low coverage residue. For example, titrating the residue corresponding to $\theta_C \simeq 0.96$ of Fig. 6 in pure hydrogen ($\sim$ 100 Torr) for 300 s at 575 K reduced the carbon coverage by only 10 %, whereas a similar treatment of the low coverage residue produces essentially a clean surface. In addition, post-reaction thermal desorption of the high coverage residue

(monitoring H_2, the only observed product) shows that it contains (relatively) less hydrogen compared to the low coverage residue. Thermal desorption spectra representative of the low and high coverage residues are shown in Fig. 7. Integration of these spectra indicates that on a per-carbon-atom basis, the high coverage residue contains approximately 70% less hydrogen than the low coverage residue. This result suggests that the high coverage residue is extensively dehydrogenated with virtually all of the carbon atoms bound strongly to the surface.

The strongly bound carbonaceous residue, approaching one monolayer in coverage, can be expected to perturb appreciably the ability of the metal surface to bind the relevant reaction intermediates. Although the carburized surface can be expected to lead to a lower steady-state concentration of hydrogen adatoms and, hence, an increase in the relative amount of unsaturated products (*e.g.*, propylene), this is *not* the proper explanation. That is, if the hydrogen adatom concentration is the sole cause of the observed behavior, then the selectivity shift should be from propylene to *propane* as P_{H_2} is increased. However, since the selectivity shift is to *methane* (hydrogenolysis), the implication is that either the structure or the binding energy of the adsorbed hydrocarbon intermediate is changed significantly on the carburized surface. For example, it is generally accepted that hydrogenolysis proceeds through intermediates that are bound strongly to the surface via metal-carbon bonds. Thus, the perturbation of the surface by the high coverage residue could weaken the binding energy of the intermediate such that its residence time becomes too short for significant carbon-carbon bond cleavage to occur.

The dramatic shift in the selectivity from hydrogenolysis to isomerization, due in this case to "self-poisoning" of the metal surface by the reactants, has been observed previously. Under similar conditions (P_{H_2} = 1.0 Torr, P_{H_2} = 100 Torr, and T = 550 K) for the reaction of cyclopropane and hydrogen on a Ni(111) surface, Goodman **(13)** observed a selectivity shift of similar magnitude upon the addition of $\frac{1}{3}$ of a monlayer of sulfur (*i.e.*, with respect to a initially clean Ni surface). Since sulfur is expected to perturb the electronic structure of the metal surface to a greater

extent than carbon (due to its greater electronegativity), it is not surprising that the addition of only $\frac{1}{3}$ of a monolayer produces a comparable effect to that observed for a full monolayer of carbon. Although "geometric" factors are certainly important for a carbonaceous residue approaching a coverage of one monolayer, these observations suggest that a significant perturbation in the electronic properties of the Ir(111) surface by the high carbon coverage residue may also be important.

2. The Ir(110)-(1x2) Surface

Specific rates of the reaction of cyclopropane with hydrogen on the Ir(110)-(1x2) surface are shown in Fig. 8, plotted in an Arrhenius form. These data represent steady-state reaction rates, obtained for conversions that were restricted typically to below 1%. The standard reactant partial pressure ratio, $H_2/c\text{-}C_3H_6$, was 100/2, with a cyclopropane partial pressure of 2.0 Torr.

Post-reaction surface characterization by AES indicated the presence of a sub-monolayer carbonaceous residue on the Ir(110)-(1x2) surface. The measured value for the fractional coverage, which was essentially independent of temperature for these reactant partial pressures, is given in Table 1 in terms of a fractional carbon coverage. Clearly, the fractional coverages of carbon observed on both surfaces for the reaction of cyclopropane and hydrogen are *very* similar to one another. This similarity tends to rule out the possibility that surface sites unique to the (110)-(1x2) surface are being poisoned selectively. On the other hand, if activity and/or selectivity differences are observed between the two surfaces for a particular reaction channel, it is unlikely that these differences would be a manifestation of a particular configuration of the carbonaceous residue present on each of the surfaces. Finally, post-reaction thermal desorption of the carbonaceceous adlayer produced only H_2, and the resulting desorption spectra were similar to those observed from the (111) surface (*cf.* Fig. 7, spectrum a). Titration of the carbonaceous adlayer with hydrogen produced only methane in all cases.

The only reaction products observed on the Ir(110)-(1x2) surface were methane,

ethane and propane. In particular, no unsaturated hydrocarbons (*e.g.*, ethylene or propylene) were produced, in contrast to the observations on the Ir(111) surface. Again, the product distribution is described by two major reaction channels for temperatures below approximately 500 K: the hydrogenation pathway to form propane, and the hydrogenolysis pathway to form methane and ethane. Qualitatively, both the relative rates and the apparent activation energies for these two reaction channels with respect to each other agree with the observations over the Ir(111) surface. The apparent rate parameters obtained from the data shown in Fig. 8 (for $T \leq$ 475 K) are given in Table 3 for the two major reaction channels. The apparent activation energies observed for the (110)-(1x2) surface are very similar to, although somewhat smaller than, those observed on the (111) surface— the difference being approximately 1 kcal-mol^{-1} for hydrogenation (*i.e.*, on the order of the experimental uncertainty), and $3\frac{1}{2}$ kcal-mol^{-1} for hydrogenolysis (*cf.* Tables 2 and 3). In terms of absolute activities, at a temperature of 450 K, the Ir(110)-(1x2) surface is more active than the Ir(111) surface for both reaction channels by a factor of approximately $3\frac{1}{2}$. (Note that this value is dependent on the particular site density chosen for the two surfaces.)

As with the Ir(111) surface, as the temperature is increased above approximately 500 K, the production of ethane decreases, while the production of methane increases. [Note that the relative selectivity for ethane begins to decrease at lower temperatures over Ir(111), in agreement with results obtained previously concerning propane hydrogenolysis **(22)**.] Again, this change in the selectivity of the hydrogenolysis channel is not accompanied by any change in the apparent reaction kinetics. This is evident in Fig. 9, where the total rate of hydrogenolysis to C_1 and C_2 products is plotted in terms of cyclopropane conversion. A least-squares fit of these data gives apparent rate parameters of $k_{app}^{(0)} \simeq 1.3 \times 10^{9\pm1}$ molec-site-s^{-1} and $E_{app} \simeq 22.2 \pm 1$ kcal-mol^{-1}, essentially identical to those given in Table 3, which were fit to $T \leq 525$ K. The decrease in the selectivity for ethane is best described in this case also by an increasing probability of multiple carbon-carbon bond cleav-

age due to the decreasing concentration of hydrogen adatoms as the temperature is increased.

The dependence of the specific rates of reaction on the reactant partial pressures have been examined at two different temperatures. Data are shown in Fig. 10, where reaction rates were measured at 425 K as a function of both the hydrogen and cyclopropane partial pressures, while maintaining a constant partial pressure of the other. Concerning the hydrogenation pathway, the apparent reaction order in P_{HC} is nearly zero ($\leq \frac{1}{2}$), whereas that in P_{H_2} is nearly unity for $P_{H_2} \leq 200$ Torr and evidently takes on a negative value for hydrogen partial pressures above 200 Torr. As with the Ir(111) surface, a maximum is observed in the rate of propane production as a function of the hydrogen partial pressure. Concerning the hydrogenolysis pathway, both the apparent reaction order in P_{HC} and P_{H_2} are essentially zero, in agreement with the observations on the Ir(111) surface.

The sensitivity of the specific rates of reaction with respect to the reactant partial pressures differs considerably at the higher temperature of 600 K, as may be seen in Fig. 11. For the hydrogen-rich conditions ($P_{H_2}/P_{HC} > 15$), the behavior is qualitatively similar to that observed on the Ir(111) surface. Specifically, for the hydrogenation pathway, the apparent order in P_{H_2} is essentially unity and that with respect to P_{HC} is approximately $\frac{1}{2}$. Again the order with respect to P_{HC} for the hydrogenation pathway is larger at the higher temperature. With respect to the hydrogenolysis pathway, the apparent reaction orders in both P_{HC} and P_{H_2} are essentially zero (with respect to C_1 and C_2 conversion), in agreement with the observations at 425 K. Finally, the selectivity for ethane increases greatly with P_{H_2}, consistent with the proposal that hydrogen adatoms (in sufficient concentration) inhibit multiple C-C bond cleavage.

The onset of the selectivity shift observed on the Ir(111) surface is apparent for the Ir(110)-(1x2) surface for relatively hydrogen-lean partial pressure ratios ($P_{H_2}/P_{HC} \leq 10$). As with the Ir(111) surface, the shift is from methane (hydrogenolysis) to propylene (isomerization), as P_{H_2}/P_{HC} is reduced sufficiently.

Post-reaction surface characterization via AES indicated that for $P_{H_2}/P_{HC} > 15$ the carbon coverage was approximately constant at $\theta_C \simeq 0.59 \pm 0.06$, whereas for $P_{H_2}/P_{HC} \simeq 10$, the coverage was $\theta_C \simeq 0.72$–0.90. The fact that this shift occurs on Ir(110)-(1x2) at lower hydrogen-to-hydrocarbon partial pressure ratios indicates that it is more difficult to carburize the (110)-(1x2) surface. This could be due to a superior hydrogenation capacity of the (110)-(1x2) surface, which is supported, for example, by the lack of the observation of any unsaturated hydrocarbon products at the standard reactant partial pressure ratio (*cf.* Fig. 8), whereas olefins were observed over the Ir(111) surface.

B. Methylcyclopropane

1. The Ir(111) Surface

Specific rates of the reaction of methylcyclopropane with hydrogen on the Ir(111) surface are shown in Fig. 12 plotted in Arrhenius form. The coverage of the carbonaceous residue determined via post-reaction surface characterization by AES is given in Table 1. The coverage of the residue was essentially independent of the reaction conditions considered here and below, and its value is nearly equal to that observed for cyclopropane on this same surface at similar reaction conditions.

As may be seen in Fig. 12, a variety of products are observed from the reaction of methylcyclopropane and hydrogen on the Ir(111) surface, namely, methane, ethane, ethylene, propane, propylene, isobutane, *n*-butane, and a mixture of 1- and 2-butenes. [Isobutene could not be detected due to overlap with the (considerably larger) *n*-butane and 1- and 2-butene chromatographic peaks.] The most notable feature of the data shown in Fig. 12 is the predominance of the formation of *n*-butane (and 1- and 2-butenes) from the hydrogenation channel. The major hydrogenation/isomerization channel on the Ir(111) surface is given by

$$c\text{–}C_3H_5CH_3 + H_2 \rightarrow n\text{–}C_4H_{10} \text{ or } n\text{–}C_4H_8 \ ,$$

whereas the major hydrogenolysis channel is given by

$$c\text{-}C_3H_5CH_3 + 2H_2 \rightarrow CH_4 + C_3H_8 \ .$$

The corresponding minor reaction channels involve hydrogenation to isobutane and hydrogenolysis to ethane. Note that at a temperature of 425 K, conversion of methylcyclopropane to (two molecules of) ethane is approximately $\frac{1}{15}$ of that to methane and propane.

The apparent kinetic rate parameters obtained from the data shown in Fig. 12 are given in Table 2 for the two major reaction channels. The parameters for the hydrogenation/isomerization pathway were fit to the total *n*-C_4 (*i.e.*, *n*-butane and 1- and 2-butene) conversion, whereas those for hydrogenolysis were fit to the rate of $C_1 + C_3$ production. Compared to the reaction of cyclopropane on this same surface at a temperature of 450 K, the rate of hydrogenation/isomerization of methylcyclopropane is approximately a factor of six greater, whereas the rate of hydrogenolysis is greater by a factor of approximately two. The apparent activation energy for hydrogenation/isomerization of methylcyclopropane ($\sim$ 14 kcal-mol^{-1}) is greater than that for cyclopropane ($\sim$ 10 kcal-mol^{-1}), whereas for hydrogenolysis the opposite is true, $\sim$ 20 kcal-mol^{-1} for methylcyclopropane and $\sim$ 27 kcal-mol^{-1} for cyclopropane. As with cyclopropane, the relative fraction of unsaturated products increases with increasing surface temperature, consistent with a depletion in the steady-state coverage of hydrogen adatoms as the temperature is increased.

Based on previous work with Group VIII metals **(4,8)**, the observation here of a high selectivity for *n*-butane (as opposed to isobutane) is somewhat surprising. For example, for similar reactant partial pressures at temperatures near or below 273 K, isobutane has been found to be the major reaction product on both supported Pt (P_{HC} = 50 Torr and P_{H_2} = 50 Torr) **(4)** and Pd, Ni, and Pt films (P_{HC} = 10 Torr and P_{H_2} = 100 Torr) **(8)**. Similar behavior has been reported for the hydrogenation of gemdimethylcyclopropane by several Group VIII metal films and supported catalysts; *i.e.*, the production of neopentane dominates **(9)**. This

apparent disagreement with the work reported here can be rationalized by examining the temperature dependence of the selectivity for *n*-butane versus isobutane. In particular, both Bond and Newham **(4)** and Anderson and Avery **(8)** have found that with Pt catalysts, the relative selectivity for *n*-butane increases dramatically with temperature, from a value of approximately $\frac{1}{20}$ at 275 K to a value of nearly unity at 500–525 K. This observation is qualitatively consistent with our experimental measurements on Ir. Extrapolating our data shown in Fig. 12 to lower temperatures indicates that the rates of *n*-butane and isobutane production should become equivalent at a temperature of approximately 300–325 K. The fact that the temperature for which the relative selectivity for *n*-butane and isobutane is nearly unity is apparently considerably lower for Ir with respect to Pt, could be intrinsic, or could be due to differing reaction conditions between our work and previous investigations (*i.e.*, as demonstrated below, the dependence of isobutane production on P_{HC} and P_{H_2} differs from that for *n*-butane).

The dependence of the specific rates of reaction on the reactant partial pressures has been examined at a temperature of 425 K. These data are shown in Fig. 13. With respect to the total production of *n*-C_4 molecules, the apparent orders in P_{HC} and P_{H_2} are essentially zero. Consistent with a decreasing fraction of *n*-butane production with increasing temperature, the apparent order in P_{H_2} for *n*-butane is positive and is essentially equal to unity. The fact that at a similar temperature of 425 K the order for cyclopropane in P_{HC} is larger (~ 1) than that for methylcyclopropane (~ 0) suggests, as has been previously suggested **(4)**, that the adsorbed methylcyclopropane species is either bound more strongly to the surface and/or formed more easily (*i.e.*, its coverage is nearer the saturation level and thus, the order in P_{HC} is nearly zero). With respect to the minor hydrogenation pathway (the production of isobutane) the order in P_{HC} varies between ~ 1 and $\sim \frac{1}{2}$ as P_{HC} is increased, whereas the apparent order in P_{H_2} is approximately $1–1\frac{1}{2}$. Thus, the sensitivity (*i.e.*, the apparent orders) of the two hydrogenation/isomerization pathways differ with respect to each other, suggesting that different intermediates

may be involved. Concerning the major hydrogenolysis pathway (the formation of methane, propane and propylene), the order in P_{HC} is zero, whereas that in P_{H_2} is nearly zero and exhibits a small positive value ($\sim \frac{1}{2}$) for $P_{H_2} \leq 50$ Torr. These observations are consistent with those observed for cyclopropane hydrogenolysis on this same surface where both orders were essentially zero.

2. The Ir(110)-(1x2) Surface

Specific rates of the reaction of methylcyclopropane with hydrogen over the Ir(110)-(1x2) surface are shown in Fig. 14 plotted in an Arrhenius form. The coverage of the carbonaceous residue following the reaction is given in Table 1. The coverage of the residue was essentially independent of the reaction conditions considered here and below, and its value is essentially identical to that observed for methylcyclopropane over the Ir(111) surface. The insensitivity of the coverage of the carbonaceous residue to the structure of the surface suggests strongly that the residue plays the role of a "spectator" species.

The products observed on the Ir(110)-(1x2) surface were methane, ethane, propane, isobutane, *n*-butane and a mixture of 1- and 2-butenes. (Again, the production of isobutene could not be resolved.) Unlike the Ir(111) surface, but in agreement with the results for cyclopropane over this same surface, unsaturated hydrogenolysis products, *i.e.*, ethylene and propylene in this case, are not observed on the Ir(110)-(1x2) surface. In addition, the selectivity for *n*-butane begins to decrease at a higher temperature on the (110)-(1x2) surface [*e.g.* the selectivity, *n*-C_4H_{10}/total *n*-C_4, is equal to $\frac{1}{2}$ at 450 K on Ir(110)-(1x2) in contrast to 400 K on Ir(111)]. These results suggest again a superior hydrogenation capacity of the Ir(110)-(1x2) surface. As may be seen from Fig. 14, the dominant hydrogenation/isomerization channel involves the production of *n*-butane and "linear" butenes, as was the case for the Ir(111) surface. However, unlike the Ir(111) surface, there *apparently* is no dominant hydrogenolysis channel on Ir(110)-(1x2). Rather, both the production of $CH_4 + C_3H_8$ and $2C_2H_6$ exhibit similar activities

and (possibly fortuitously) similar apparent kinetic rate parameters. Recall that the production of CH_4 + C_3H_8 was the dominant hydrogenolysis channel over the Ir(111) surface.

The apparent kinetic rate parameters obtained from the data shown in Fig. 14 are given in Table 3 for the two major reaction channels. The parameters for the hydrogenation/isomerization pathway were fit to the total *n*-C_4 conversion, whereas those for hydrogenolysis were fit to the total rate of conversion to C_1 + C_2 + C_3 products. In comparison to the reaction of cyclopropane on this same surface at a temperature of 450 K, the rate of hydrogenation/isomerization of methylcyclopropane is approximately a factor of seven greater, whereas the rate of hydrogenolysis of methylcyclopropane is a factor of two *smaller*. Comparing the two surfaces for the reaction of methylcyclopropane at a temperature of 450 K, the activities for hydrogenolysis are essentially equivalent, whereas the specific rate of hydrogenation/isomerization is greater on the Ir(110)-(1x2) surface by approximately a factor of four. The apparent activation energies for the two reaction channels of methylcyclopropane on the two surfaces are very similar to one another. In particular, on the Ir(110)-(1x2) surface, a value of $\sim$ 14 kcal-mol^{-1} is found for the hydrogenation/isomerization pathway, whereas $\sim$ 19 kcal-mol^{-1} is found for the hydrogenolysis pathway.

The product distribution observed from the hydrogenolysis pathway on the Ir(110)-(1x2) surface, *i.e.*, equal amounts of methane, ethane and propane, can be explained by the following argument. The products from the major reaction channel of hydrogenolysis result from the cleavage of two C-C bonds; *i.e.*, first the ring is opened, and subsequently a second C-C bond is cleaved in the resulting adsorbed complex, leaving two hydrocarbon "fragments," which are hydrogenated (or desorbed for the unsaturated species) to the observed products. If we consider a completely random scission of two C-C bonds in the parent molecule methylcyclopropane, restricting C-C bond scission to the ring carbons (*i.e.*, the weakest C-C bonds), there are three possible combinations; two result in the production of CH_4

+ C_3H_8, and one results in the production of $2C_2H_6$. Thus, for a completely random scission of two C-C bonds in the methylcyclopropane ring, the expected product distribution is equal amounts of methane, ethane and propane, *exactly* what is observed on the Ir(110)-(1x2) surface. The fact that the production of ethane involves scission of the two C-C bonds adjacent to the methyl group, and that this pathway is apparently a minor channel over Ir(111) (*i.e.*, the surface for which the metal surface atoms are relatively more coordinatively saturated), suggests that steric factors may be involved in the observed hydrogenolysis selectivity.

The dependencies of the specific rates of reaction on the reactant partial pressures have been examined at a temperature of 425 K. These data are shown in Fig. 15. With respect to the total production of *n*-C_4 molecules, the apparent order in P_{HC} is essentially zero, whereas that in P_{H_2} exhibits a small postive value ($\sim \frac{1}{2}$) for $P_{H_2} \leq 100$ Torr. Consistent with a decreasing fraction of *n*-butane production with increasing temperature, the apparent order in P_{H_2} for *n*-butane is positive. However, the apparent order in P_{H_2} is smaller on the (110)-(1x2) surface with respect to the (111) for identical reaction conditions, suggesting a superior hydrogenation capacity of the (110)-(1x2) surface. On the other hand, as was the case for the Ir(111) surface, at a temperature of 425 K on the Ir(110)-(1x2) surface, the order in cyclopropane in P_{HC} is larger ($\sim \frac{1}{2}$) than that for methylcyclopropane (~ 0), suggesting that the adsorbed methylcyclopropane species is bound more strongly to the surface and/or formed more easily. With respect to the minor hydrogenation pathway, *i.e.*, the production of isobutane, the order in P_{HC} varies between ~ 1 and $\sim \frac{1}{2}$ as P_{HC} is increased, whereas the apparent order in P_{H_2} is approximately $\frac{1}{2}$–$1\frac{1}{2}$. Again, the differing sensitivities (*i.e.*, apparent orders) of the two hydrogenation/isomerization pathways suggest that different intermediates may be involved. Concerning the hydrogenolysis pathway, the orders in both P_{HC} and P_{H_2} are essentially zero for all the products observed, suggesting that, in agreement with the apparent reaction kinetics, methane, ethane and propane are formed from a similar intermediate.

C. Propylene

1. The Ir(111) Surface

The reaction of propylene with hydrogen on the Ir(111) surface was examined briefly. Steady-state rates of reaction are shown in Fig. 16(a) plotted in Arrhenius form. The coverage of the carbonaceous residue corresponding to these reaction conditions is shown in Fig. 16(b). We see that there is a dramatic increase in the coverage of the residue for temperatures above approximately 500 K. In particular, for $T \leq 500$ K, $\theta_C \simeq 0.5 \pm 0.1$, whereas for $T \geq 550$ K, $\theta_C \simeq 1.0 \pm 0.1$. Post-reaction thermal desorption of the near monolayer coverage residue produced spectra similar to spectrum b shown above in Fig. 7. Note that for identical reactant partial pressures, the coverage of the carbonaceous residue was independent of temperature for the reaction of cyclopropane over this same surface.

The only reaction products observed on the Ir(111) surface for the reaction conditions considered here were methane, ethane, ethylene and propane. Two major reaction channels were observed: the hydrogenation of propylene to propane, and hydrogenolysis to methane and a mixture of ethane and ethylene, the relative selectivity for ethylene increasing with increasing temperature. In comparison to cyclopropane over this same surface at a temperature of 450 K, the rate of production of propane is a factor of approximately seven more rapid from propylene, whereas the rate of hydrogenolysis is nearly equivalent from either reactant. The former observation suggests that if cyclopropane and propylene are hydrogenated to propane from a similar intermediate, then the rate of formation of this intermediate from cyclopropane must be less rapid than from propylene.

The specific rate of conversion via the hydrogenolysis channel was fit to an Arrhenius expression, and the apparent kinetic rate parameters obtained are given in Table 2. The run-to-run accuracy of our rate measurements ($\sim \pm 20\%$) precluded a quantitative assessment of the kinetics of hydrogenation, although as expected, the apparent activation energy is evidently quite small (≤ 5 kcal-mol^{-1}). We see that

the parameters found for propylene hydrogenolysis are similar to those found for cyclopropane; *e.g.*, the apparent activation energies are within approximately 3 kcal-mol^{-1} of each other. However, unlike cyclopropane, nonlinear Arrhenius behavior is observed in the temperature range examined, T $\simeq$ 400–600 K. The concomitant decrease in the apparent activation energy of hydrogenolysis and increase in the coverage of the carbonaceous residue for temperatures above 500 K suggest that the nonlinear behavior is due to the transformation in the adlayer composition.

To obtain supporting evidence for the proposition involving the adlayer transformation, the partial pressure of propylene was varied at a fixed partial pressure of hydrogen and two different fixed temperatures. These data are shown in Figs. 17 and 18 for temperatures of 450 and 575 K. As may be seen in Fig. 17, at a temperature of 450 K, *i.e.*, in the linear Arrhenius region, the apparent order in P_{HC} for the hydrogenolysis channel is essentially zero, whereas that for hydrogenation exhibits a small positive value ($\leq \frac{1}{2}$). The relative rate of ethylene production decreases with P_{HC}, consistent with a more hydrogen-rich partial pressure ratio. Most importantly, at 450 K, the coverage of the carbonaceous residue is essentially constant at a value of $\theta_C \simeq 0.54 \pm 0.08$.

In contrast, as may be seen from Fig. 18, as P_{H_2}/P_{HC} is increased above approximately 200–500 at a temperature of 575 K, there is a shift in both the adlayer composition and the selectivity. Specifically, as P_{H_2}/P_{HC} is increased, the coverage of the residue is reduced by approximately a factor of 2, whereas the selectivity shifts from hydrogenation (propane) to hydrogenolysis (methane). This behavior, *i.e.*, a dramatic decrease in the hydrogenolysis selectivity over a highly carburized surface, is exactly what was observed for cyclopropane on Ir(111) as shown in Fig. 6. The essential difference between these two reactants in regard to these phenomena is that smaller partial pressure ratios, P_{HC}/P_{H_2}, are sufficient to lead to the highly carburized surface for propylene ($\sim \frac{1}{100}$) with respect to cyclopropane ($\sim \frac{1}{20}$). This is presumably due to the relative "ease" and/or strength of chemisorption of propylene with respect to cyclopropane.

2. The Ir(110)-(1x2) Surface

Steady-state rates of the reaction of propylene with hydrogen on the Ir(110)-(1x2) surface are shown in Fig. 19(a) plotted in an Arrhenius form. The coverage of the carbonaceous residue corresponding to these reaction conditions is shown in Fig. 19(b). As with the Ir(111) surface, on the Ir(110)-(1x2) surface there is a sharp increase in the coverage of the residue, in this case occurring near a temperature of 550 K. The fact that this adlayer transformation occurs at a higher temperature on Ir(110)-(1x2) implicates again a superior resistance to "self-poisoning" and carburization for this surface.

The only reaction products observed for the reaction conditions considered here were methane, ethane, ethylene and propane. The two major reaction channels were again the hydrogenation of propylene to propane, and hydrogenolysis to methane and a mixture of ethane and ethylene, with the relative selectivity for ethylene increasing with increasing temperature. In comparison to cyclopropane over this same surface at a temperature of 450 K, the rate of production of propane is a factor of approximately 25 more rapid from propylene, whereas the rate of hydrogenolysis is nearly equivalent from either reactant. In comparison to propylene on Ir(111) at a temperature of 450 K, the rate of hydrogenation to propane is a factor of approximately 14 greater on the Ir(110)-(1x2) surface, whereas the rate of hydrogenolysis is more rapid on Ir(110)-(1x2) by a factor of approximately 3. The larger rate of hydrogenation of propylene and the higher selectivity for ethane observed on the Ir(110)-(1x2) surface implicate again a superior hydrogenation capacity of this surface.

The specific rate on conversion via the hydrogenolysis channel was fit to an Arrhenius expression, and the apparent kinetic rate parameters obtained are given in Table 3. We see that the parameters found for propylene hydrogenolysis compare well to those found both for cyclopropane on Ir(110)-(1x2) and for propylene on Ir(111). In addition, as with the Ir(111) surface, the nonlinear Arrhenius behav-

ior apparent above 500 K can be attributed to the transformation in the adlayer composition.

IV. Discussion

The hydrogenation of cyclopropane to propane has been reported to be slightly "structure-sensitive" **(28)** over both supported Ni **(12)** and Pt **(11)**, in agreement with our results reported here for the two single crystalline surfaces of Ir. In particular, our experimental measurements indicate that the specific activity (for both hydrogenation and hydrogenolysis) of the Ir(110)-(1x2) surface is greater than that of the Ir(111) surface by approximately a factor of $3\frac{1}{2}$. This difference in the specific activities is on the order of those reported previously for the supported Ni **(12)** and Pt **(11)** catalysts of varying particle size, where larger specific activities were found for the smaller particles. However, it is significantly less than that reported for the single crystalline (111) and (100) surfaces of Ni **(13)**, where a difference of greater than an order of magnitude was found.

With respect to our experimental measurements, the results obtained for the supported Ni catalysts of varying metallic particle size are most intriguing. In particular, these workers reported a specific activity (of hydrogenation *and* hydrogenolysis) for catalysts with an average crystallite diameter of 12 Å that was a factor of three greater than that observed for much larger crystallites with average diameters of $\geq$ 50 Å. Previous work we have carried out concerning the hydrogenolysis of *n*-butane on these same Ir(110)-(1x2) and Ir(111) surfaces led us to compare results from the Ir single crystals to supported Ir catalysts of varying particle size **(29)**. In this case, in order to make a comparison, we computed "effective particle sizes" for the single crystalline surfaces by utilizing the ratio of the number of edge (C_7) atoms to the number of (111) face (C_9) atoms as the appropriate criterion (*cf.* Fig. 1). In particular, depending on the particular polyhedron chosen for the crystallite shape, the "effective particle sizes" are 13–24 Å for the Ir(110)-(1x2) surface

and 81–166 Å for the Ir(111) surface. (Utilizing the Ni-Ni lattice spacing, we find that the "effective particle size" for the Ir(110)-(1x2) surface is 12–22 Å.) Thus, the results obtained here [implicating a greater specific activity for the Ir(110)-(1x2) surface] and those obtained for supported Ni catalysts [implicating a greater specific activity for crystallites with average diameters of 12 Å] can be reconciled if the low-coordination-number (C_7) atoms possess an activity for this reaction that is intrinsically greater than that possessed by the more highly coordinated (111) face (C_9) atoms. If this is the case, the intrinsic activity difference could be related to differences in the local electronic density between C_7 and C_9 atoms.

The results obtained for cyclopropane on the Ir(111) surface suggested that propane and propylene were formed from a common intermediate (*cf.* Figs. 2 and 4). For example, a reasonable structure for this intermediate is a 1,2 di-σ bound C_3H_6(a) species. However, the observation of a positive order in P_{H_2} for the total rate of C_3 (propane and propylene) production can be rationalized if the common intermediate is more dehydrogenated than propylene, *e.g.*, a C_3H_5(a) species. One species that is consistent with the stoichiometry, C_3H_5, is an η^3-allyl. Addition of a hydrogen atom at the 1 or 3 postions of an η^3-allyl would produce either the aforementioned 1,2 di-σ bound C_3H_6 or an adsorbed propylene. Additional hydrogenation would lead to propane, whereas desorption would lead to propylene, consistent with the observations on the Ir(111) surface. This interpretation is obviously not unique. However, there are precedents from organometallic chemistry that involve the reaction of transition metal homogeneous complexes with cyclopropanes, which lead to the coordination of an η^3-allyl ligand. Interestingly, one such system involves an Ir(I) complex **(30)**.

The hydrogenolysis of cyclopropane to methane and ethane [and ethylene on Ir(111)] was found to be qualitatively different from the hydrogenolysis of propane. For example, for the entire range of temperatures considered over both surfaces (*cf.* Figs. 3 and 9), there was no observable variation in the apparent reaction

kinetics. This was corroborated by the lack of any significant variation in the apparent reaction "orders"— both the order in P_{HC} and P_{H_2} being essentially zero. These observations can be interpreted by a reaction mechanism involving relatively facile formation of the appropriate adsorbed intermediate (*i.e.*, the step which "opens" the ring), with the rate-limiting step being (secondary) C-C bond cleavage in the adsorbed intermediate (*i.e.*, subsequent hydrogenation, desorption or additional hydrogenolysis are rapid with respect to C-C bond cleavage in the adsorbed intermediate). The major difference between this mechanism and that proposed previously for propane (alkane) hydrogenolysis is that formation of the appropriate intermediate is both facile and irreversible for cyclopropane.

A reasonable reaction for the first (facile) step is oxidative addition of cyclopropane to the Ir surface (*i.e.*, ring-opening), forming a "1,3" C_3H_6 diadsorbed species. The leading candidate for the adsorbed species is a metallacycle butane since, for example, the most common route to (synthesis of) metallacycle butanes in organometallic chemistry is the addition of cyclopropane to complexes of transition metals in low formal oxidation states **(31)**. Of particular interest here, the fragmentation of metallacycle butane ligands in homogeneous transition metal complexes to form olefins and carbenes is well known **(32)** and, thus, provides an established mechanism for hydrogenolysis. The observation of the production of ethylene from the hydrogenolysis channel on Ir(111) suggests that a metallacycle butane is the dominant intermediate (and mechanism) for hydrogenolysis. The absence of the production of ethylene on Ir(110)-(1x2) (excepting the "severe" reaction conditions of Fig. 11) does not necessarily suggest a different mechanism; rather, it may be a manifestation of the superior hydrogenation capacity of the Ir(110)-(1x2) surface, for which there is ample evidence (see below).

The most significant result concerning the reaction of methylcyclopropane on the two Ir surfaces considered here is the (somewhat surprising) dominance of the production of *n*-butane (and 1- and 2-butenes) from the hydrogenation (isomerization) channel. This result can be interpreted qualitatively, as discussed above in

Sec. III.B.1, by considering two parallel reaction channels, with the production of *n*-butane exhibiting a higher apparent activation energy. In this picture, in agreement with expectations, the weakest C-C bond of methylcyclopropane (*i.e.*, the C_2-C_3 bond) is cleaved at low temperatures. This interpretation, of course, does not explain *why* *n*-butane production dominates at high temperatures.

Clues as to the nature of the reaction mechanism that leads to the production of *n*-butane can be obtained by examining the specific cases for which a high selectivity for *n*-butane has been observed. For example, Anderson and Avery **(8)** observed a product ratio, n-C_4H_{10}:i-C_4H_{10}, of 2:1 from the reaction of methylcyclopropane with deuterium on tungsten films at temperatures of 290–310 K (P_{HC} = 10 Torr and P_{H_2} = 100 Torr). Of particular interest, under the identical reaction conditions, the major products were *deuteromethylcyclopropanes*, where the exchange with the parent methylcyclopropane was limited to the "ring hydrogens." On the other hand, under similar reaction conditions on Pd, Ni and Pt films (T = 210–270 K, identical P_{HC} and P_{H_2}), the product ratio, n-C_4H_{10}:i-C_4H_{10}, was always less than 1:10 (*i.e.*, isobutane dominated), *and* no deuteromethylcyclopropanes were detected. Chevreau and Gault **(9)** have reported similar results concerning the reactions of gemdialkylcyclopropanes. For example, on tungsten films, the major reaction product from 1,1′-dimethylcyclopropane was isopentane, and its relative rate of production (selectivity) increased with temperature; *e.g.*, isopentane represented 80% of the products at 275 K, and 98 % at 575 K. These results suggest that in cases for which C-H bond activation (apparently) precedes C-C bond activation **(33)**, the ring opens next to the most substituted carbon atom.

Gault and co-workers **(10)** have also examined the reaction of 1,2 *cis*- and *trans*-dimethylcyclopropanes with hydrogen on Pt, Ni and Pd films at temperatures between 275 and 325 K (P_{HC} = 5 Torr and P_{H_2} = 60 Torr). In all cases, isopentane was the major reaction product. However, *n*-pentane was detected, and its relative rate of production increased with temperature. Most importantly, on Pt films, for example, the relative selectivity for *n*-pentane was approximately 20%

from the *cis* isomer, whereas it was only 1% from the *trans* isomer. These results may be interpreted, as they have been recently **(35)**, by invoking a "flat" adsorbed intermediate (or transition state), *i.e.*, the plane of the ring being parallel to the metal surface, for the production of *n*-pentane, and "edge-on" dissociative adsorption [essentially that described above for metallacycle butane formation **(31)**] for the production of isopentane. It is of interest to note that both of the mechanisms discussed here for the production of *n*-butane from methylcyclopropane— C-H bond activation preceding (or concomitant with) C-C bond activation, or a "flat" adsorbed intermediate— would appear to suggest the (eventual) participation of an η^3-allyl species in the hydrogenation channel.

The selectivity difference observed between Ir(111) and Ir(110)-(1x2) concerning the hydrogenolysis pathway for methylcyclopropane can be explained on the basis of structural considerations. The presence of propylene from the major (hydrogenolysis) reaction channel on Ir(111) suggests, as was the case for cyclopropane, the involvement of a metallacycle butane in the hydrogenolysis channel. If the pathway to this intermediate is involves an "edge complex," as has been discussed elsewhere **(31)**, then the presence of the methyl group may provide a steric limitation as to the activation of the C_1-C_2 bond. Since the presence of ethane (or ethylene) from the hydrogenolysis of methylcyclopropane can only be described (for this mechanism) by the fragmentation of a metallacycle butane that has been formed from the activation of the C_1-C_2 bond, the selectivity observed for the hydrogenolysis channel should be decisive in determining if a steric limitation exists on either surface. In fact, the selectivity is quite different for the major reaction channels on the two surfaces— the product distribution is $CH_4 + C_3H_8$ on Ir(111), whereas it is $CH_4 + C_2H_6 + C_3H_8$ on Ir(110)-(1x2). This result can be interpreted readily by considering the stereochemistry of the two surfaces. In particular, an "edge complex" involving the C_1-C_2 bond of methylcyclopropane and the C_9 atoms of the Ir(111) surface is precluded by the presence of the methyl group, whereas an "edge complex" involving the C_1-C_2 bond may be formed with the low-coordination-number

C_7 atoms, which are present (in significant concentrations) only on the Ir(110)-(1x2) surface. Consequently, the absence of ethane in the major hydrogenolysis channel on Ir(111) can be explained purely on a stereochemical basis. It is important to note that, as evidenced by the dominant production of *n*-butane, activation of the C_1-C_2 bond *does* occur on Ir(111) for the hydrogenation/isomerization channel—the selectivity for hydrogenation of methylcyclopropane being essentially identical to that found on the Ir(110)-(1x2) surface. This observation implies that, on both surfaces, the production of *n*-butane from methylcyclopropane does not involve an "edge complex," rather, possibly the "flat" intermediate suggested above.

Finally, comment must be made on the apparent superior hydrogenation capacity of the Ir(110)-(1x2) surface. The experimental evidence for this superior hydrogenation capacity includes the following observations:

(i) Unsaturated products (ethylene and propylene) are not observed from the reaction of cyclopropane and hydrogen on Ir(110)-(1x2) at the standard reactant partial pressures (P_{HC} = 2.0 Torr and P_{H_2} = 100 Torr).

(ii) Higher partial pressure ratios, P_{HC}/P_{H_2}, are necessary to "carburize" the Ir(110)-(1x2) surface from the reaction of cyclopropane and hydrogen.

(iii) Unsaturated hydrogenolysis products (ethylene and propylene) are not observed from the reaction of methylcyclopropane and hydrogen on Ir(110)-(1x2) at the standard reactant partial pressures (P_{HC} = 2.0 Torr and P_{H_2} = 100 Torr). In addition, for identical reaction conditions, the selectivity for *n*-butane (with respect to total *n*-C_4) is greater on Ir(110)-(1x2).

(iv) The specific rate of hydrogenation of propylene is greater on the Ir(110)-(1x2) surface.

(v) The selectivity for ethylene from the reaction of propylene and hydrogen is greater on Ir(110-(1x2). In addition, higher temperatures are necessary to "carburize" the Ir(110)-(1x2) surface for this reaction.

Independent measurements of the adsorption and desorption kinetics of hydrogen on the *clean* (111) and (110)-(1x2) surfaces of Ir have verified explicitly the presence of a higher binding energy adstate on the (110)-(1x2) surface **(26,27)**. Thus, for all reaction conditions (*i.e.*, P_{H_2} = 100 Torr and T = 400–600 K), we expect that the hydrogen adatom concentration will be greater on the Ir(110)-(1x2) surface. This could explain the superior hydrogenation capacity of the Ir(110)-(1x2) surface. It must be noted, however, that if one utilizes the clean surface values for the parameters that describe the kinetics of adsorption and desorption **(26,27)**, the coverage of hydrogen (with respect to vacant sites **(22)**) is calculated to be near the saturation level on *both* surfaces. Consequently, this interpretation may not be completely correct, and other more subtle effects may be involved. For example, the carbonaceous residue (near a coverage of $\theta_C \simeq 0.5$ at the standard reactant partial pressures) may perturb the binding energy of the hydrogen adatoms such that the hydrogen coverages are not near saturation, and, thus, do differ significantly. On the other hand, it is also possible that the Ir(110)-(1x2) surface binds olefins more strongly than the Ir(111) surface such that the rate of desorption cannot compete with that of hydrogenation on the Ir(110)-(1x2) surface.

V. Conclusions

We have examined the hydrogenation, isomerization and hydrogenolysis of cyclopropane, methylcyclopropane and propylene on the Ir(111) and Ir(110)-(1x2) surfaces. In particular, these two surfaces were chosen primarily in order to evaluate explicitly the role of low-coordination-number metal surface atoms in these reactions. The (110)-(1x2) surface was found to be more active than the (111) surface for both the hydrogenation (to propane) and the hydrogenolysis (to methane and ethane) of cyclopropane. Comparison of our results to those reported previously for both supported Ni **(12)** and Pt **(11)** catalysts suggests that this activity difference could be due to a greater intrinsic activity of the low-coordination-number

(C_7) metal surface atoms for these reactions.

Post-reaction surface analysis revealed the presence of a carbonaceous residue, the coverage of which was found to vary with both the reaction conditions, and the particular reaction (*i.e.*, reactant) examined. For cyclopropane at the "standard" reactant partial pressures (P_{HC} = 2.0 Torr and P_{H_2} = 100 Torr) and for temperatures between 400 and 600 K, the coverage of the residue was essentially constant at $\theta_C \simeq 0.5$ on both surfaces. However, for temperatures near 575–600 K, as the partial pressure ratio, P_{HC}/P_{H_2}, was increased sufficiently [> 30 on Ir(111), > 10 on Ir(110)-(1x2)], the coverage of the residue increased dramatically, approaching a coverage of one monolayer. Concomitant with the transformation in the composition of the adlayer, the selectivity of the reaction of cyclopropane and hydrogen was found to shift from methane (hydrogenolysis) to propylene (isomerization). We have associated this selectivity shift with a perturbation in the catalytic properties of the metal surface by the high coverage carbonaceous residue. This perturbation results in either (or possibly both) a reduction in the binding energy, or a change in the structure of the adsorbed reaction intermediate normally associated with hydrogenolysis. Consequently, the selectivity is shifted to the (relatively facile) isomerization reaction.

On the Ir(111) surface, propane and propylene are formed from a common intermediate from the reaction of cyclopropane. Possible structures for the reaction intermediate have been discussed; one such possible intermediate is an η^3-allyl. Although propylene is not observed for the same reaction conditions on Ir(110)-(1x2), there is no evidence to suggest that a different intermediate is involved [*i.e.*, there is ample evidence that the (110)-(1x2) surface possesses a superior hydrogenation capacity]. The hydrogenolysis of cyclopropane was found to be qualitatively different from the hydrogenolysis of propane **(22)**. In particular, for cyclopropane on both surfaces, there was no variation in the apparent reaction kinetics over the entire temperature range investigated (T $\simeq$ 400–600 K). This difference between cyclopropane and propane is due to the relative facility and irreversibility of form-

ing the appropriate adsorbed intermediate from cyclopropane. The observation of the production of ethylene on Ir(111) from the hydrogenolysis channel, coupled with precedents from organometallic chemistry **(31,32)**, suggests that the adsorbed intermediate is a mononuclear metallacycle butane. Again, since a superior hydrogenation capacity for the Ir(110)-(1x2) surface has been implicated, the lack of the observation of ethylene on Ir(110)-(1x2) does not exclude the possibility that this mechanism is dominant on both surfaces.

The hydrogenation of methylcyclopropane on both the Ir(111) and the Ir(110)-(1x2) surface was found to be dominated by the production of *n*-butane for the reaction conditions considered here. This result was interpreted qualitatively by invoking parallel reaction mechanisms for the production of *n*-butane and isobutane, with the *n*-butane channel exhibiting a higher apparent activation energy and, thus, dominating at the higher temperatures. Possible mechanisms that lead to the production of *n*-butane were discussed. Different apparent reaction "orders" in P_{HC} and P_{H_2} for the production of *n*-butane compared to isobutane suggest that different intermediates (mechanisms) may be involved for the two hydrogenation pathways. The hydrogenolysis of methylcyclopropane was found to be similar to that found for cyclopropane on both surfaces. The observation of the production of propylene on the Ir(111) surface is again consistent with the participation of a metallacycle butane in the hydrogenolysis channel. Furthermore, the selectivity difference observed between the two surfaces for the major hydrogenolysis channels would appear to support this mechanism. In particular, the absence of ethane in the major hydrogenolysis channel on the Ir(111) surface can be explained on a stereochemical basis if metallacycle butane formation proceeds through an "edge complex" **(31)**— *i.e.*, the presence of the methyl group prevents activation of the C_1-C_2 bond in methylcyclopropane by the more coordinatively saturated C_9 atoms of the Ir(111) surface.

Finally, the Ir(110)-(1x2) surface was found to possess a greater specific activity with respect to the Ir(111) surface for the hydrogenation of propylene. This obser-

vation, coupled with a number of others (see discussion above), suggested strongly a superior hydrogenation capacity for the Ir(110)-(1x2) surface. One relatively simple explanation for these observations and the associated implication is that the hydrogen adatom concentration is greater on the Ir(110)-(1x2) surface due to the presence of a previously identified **(26,27)**, higher binding energy adstate for hydrogen on this surface.

References

1. G. C. Bond and J. Sheridan, Trans. Faraday Soc. **48**, 713 (1952).
2. G. C. Bond and J. Turkevich, Trans. Faraday Soc. **50**, 1335 (1954).
3. J. Addy and G. C. Bond, Trans. Faraday Soc. **53**, 368 (1957); **53**, 377 (1957); **53**, 383 (1957); **53**, 388 (1957);
4. G. C. Bond and J. Newham, Trans. Faraday Soc. **56**, 1501 (1960).
5. J. H. Sinfelt, D. J. C. Yates and W. F. Taylor, J. Phys. Chem. **69**, 1877 (1965).
6. W. F. Taylor, D. J. C. Yates and J. H. Sinfelt, J. Catal. **4**, 374 (1965).
7. R. A. Dalla Betta, J. A. Cusumano and J. H. Sinfelt, J. Catal. **19**, 343 (1970).
8. J. R. Anderson and N. R. Avery, J. Catal. **8**, 48 (1967).
9. T. Chevreau and F. G. Gault, J. Catal. **50**, 124 (1977).
10. G. Maire, G. Plouidy, J. C. Prudhomme and F. G. Gault, J. Catal. **4**, 556 (1965).
11. J. W. E. Coenen, W. M. T. M. Schats and R. Z. C. van Meerten, Bull. Soc. Chim. Belg. **88**, 435 (1979).
12. M. Boudart, A. Aldag, J. E. Benson, N. A. Dougharty and C. Girvin Harkins, J. Catal. **6**, 92 (1966).
13. D. W. Goodman, J. Vac. Sci. Technol. A **2**, 873 (1984).
14. F. M. Hoffmann, T. E. Felter and W. H. Weinberg, J. Chem. Phys. **76**, 3799 (1982); T. E. Felter, F. M. Hoffmann, P. A. Thiel and W. H. Weinberg, Surface Sci. **130**, 163 (1983).
15. Deuterocyclopropanes have been observed from the exchange of cyclopropane and deuterium over tungsten films at temperatures near 275 K **(8)**. In fact, deuterocyclopropanes were the *major* reaction products in this case. Deuterium exchange with the parent hydrocarbon has also been reported on supported Rh, Ir and Pt catalysts at temperatures near 375 K **(3)**. In comparison to both the tungsten films **(8)** and the corresponding rates of propane production for these supported catalysts, the rates of exchange were considerably less over these

Group VIII metals, *e.g.*, approximately 1% of the rate of propane production at 375 K.

16. C.-M. Chan, M. A. Van Hove, W. H. Weinberg and E. D. Williams, Solid State Commun. **30**, 47 (1979);C.-M. Chan, M. A. Van Hove, W. H. Weinberg and E. D. Williams, Surface Sci. **91**, 430 (1980).
17. R. van Hardeveld and F. Hartog, Advan. Catal. **22**, 75 (1972).
18. T. S. Wittrig, P. D. Szuromi and W. H. Weinberg, J. Chem. Phys. **76**, 716 (1982).
19. T. S. Wittrig, P. D. Szuromi and W. H. Weinberg, Surface Sci. **116**, 414 (1982).
20. P. D. Szuromi, J. R. Engstrom and W. H. Weinberg, J. Chem. Phys. **80**, 508 (1984).
21. W. H. Weinberg, in: *Survey of Progress in Chemistry*, Vol. 10, p. 1 (1983).
22. J. R. Engstrom, D. W. Goodman and W. H. Weinberg, J. Am. Chem. Soc. (submitted for publication).
23. D. W. Goodman, R. D. Kelley, T. E. Madey and J. T. Yates Jr., J. Catal. **63**, 226 (1980); D. W. Goodman, Acc. Chem. Res. **17**, 194 (1984).
24. C. M. Comrie and W. H. Weinberg, J. Chem. Phys. **64**, 250 (1976).
25. J. L. Taylor, D. E. Ibbotson and W. H. Weinberg, J. Chem. Phys. **69**, 4298 (1978).
26. D. E. Ibbotson, T. S. Wittrig and W. H. Weinberg, J. Chem. Phys. **72**, 4885 (1980).
27. J. R. Engstrom, W. Tsai and W. H. Weinberg (submitted for publication).
28. M. Boudart, Adv. Catal. **20**, 153 (1969).
29. J. R. Engstrom, D. W. Goodman and W. H. Weinberg, J. Am. Chem. Soc. **108**, 4653 (1986).
30. T. M. Tulip and J. A. Ibers, J. Am. Chem. Soc. **101**, 4201 (1979).
31. R. J. Puddephatt, Coord. Chem. Rev. **33**, 149 (1980).
32. See, *e.g.*, D. A. Straus and R. H. Grubbs, Organomaetallics **1**, 1658 (1982).

33. C-H bond activation of cyclopropanes has been observed to precede C-C bond activation (*i.e.*, ring-opening) with certain transition metal homogeneous complexes **(35)**.

34. See, *e.g.*, R. A. Periana and R. G. Bergman, J. Am. Chem. Soc. **106**, 7272 (1984).

35. A. G. Zsigmond, F. Notheisz and M, Bartók, *Proc. 5th Internal. Symp. Catal., Varna 1983*, **1**, 345 (1983).

Table 1

Carbonaceous Residues Following Reactions

Reactant	Fractional Carbon Coverage, θ_C
Ir(111) Surface	
Cyclopropane	0.48 ± 0.08
Methylcyclopropane	0.52 ± 0.10
Ir(110)-(1x2) Surface	
Cyclopropane	0.49 ± 0.11
Methylcyclopropane	0.54 ± 0.09

Table 2

Apparent Kinetic Rate Parameters[a)]

Ir(111) Surface

Reaction Temperature range	R(450K)[b)] molec-site^{-1}-s^{-1}	$k_{app}^{(0)}$ molec-site^{-1}-s^{-1}	E_{app} kcal-mol^{-1}
c-$C_3H_6 + H_2 \rightarrow C_3H_8$ 375–450 K	0.156	1.00 x $10^{3\pm0.5}$	9.9 ± 1
c-$C_3H_6 + 2H_2 \rightarrow CH_4 + C_2H_6$ 400–500 K	6.8 x 10^{-3}	5.4 x $10^{10\pm1}$	26.6 ± 2
c-$C_3H_5CH_3 + H_2 \rightarrow$ n-C_4H_{10} 375–475 K	0.92	3.9 x $10^{6\pm0.5}$	13.6 ± 1
c-$C_3H_5CH_3 + 2H_2 \rightarrow$ $CH_4 + C_3H_8$ 375–450 K	1.12 x 10^{-2}	6.6 x $10^{7\pm1}$	20.4 ± 2
$C_3H_6 + 2H_2 \rightarrow CH_4 + C_2H_6$ 400–500 K	5.6 x 10^{-3}	1.46 x $10^{9\pm1}$	23.8 ± 2

a) Rate parameters were fit to the total conversion within the specified temperature range by utilizing the expression $R = k_{app}^{(0)} exp(-E_{app}/k_B T)$. Reactant partial pressures were 2.0 Torr of hydrocarbon and 100 Torr of hydrogen.

b) Reaction rate is in terms of total conversion.

Table 3

Apparent Kinetic Rate Parameters[a)]

Ir(110)-(1x2) Surface

Reaction Temperature range	R(450K)[b)] molec-site^{-1}-s^{-1}	$k_{app}^{(0)}$ molec-site^{-1}-s^{-1}	E_{app} kcal-mol^{-1}
c-$C_3H_6 + H_2 \rightarrow C_3H_8$ 375–450 K	0.54	7.8 x $10^{3\pm0.5}$	8.7 ± 1
c-$C_3H_6 + 2H_2 \rightarrow CH_4 + C_2H_6$ 400–525 K	2.5 x 10^{-2}	3.0 x $10^{9\pm1}$	23.0 ± 2
c-$C_3H_5CH_3 + H_2 \rightarrow n$-$C_4H_{10}$ 375–475 K	3.6	2.2 x $10^{7\pm0.5}$	14.2 ± 1
c-$C_3H_5CH_3 + 2H_2 \rightarrow$ $CH_4 + C_2H_6 + C_3H_8$ 375–475 K	1.28 x 10^{-2}	1.32 x $10^{7\pm1}$	18.6 ± 2
$C_3H_6 + 2H_2 \rightarrow CH_4 + C_2H_6$ 400–450 K	1.70 x 10^{-2}	9.3 x $10^{10\pm1}$	26.3 ± 2

a) Rate parameters were fit to the total conversion within the specified temperature range by utilizing the expression $R = k_{app}^{(0)} exp(-E_{app}/k_B T)$. Reactant partial pressures were 2.0 Torr of hydrocarbon and 100 Torr of hydrogen.

b) Reaction rate is in terms of total conversion.

Figure Captions

Figure 1. Structural models for the (110)-(1x2) and (111) surfaces of iridium. The z-axis is perpendicular to the plane of the surface. The C_n designate the coordination numbers of the metal surface atoms **(15)**.

Figure 2. Specific reaction rates (*product* molec-site-s^{-1}) for the reaction of cyclopropane and hydrogen on the Ir(111) surface. The partial pressure of cyclopropane was 2.0 Torr, whereas that of hydrogen was 100 Torr.

Figure 3. Specific rates of hydrogenolysis of cyclopropane to methane, ethane and ethylene on the Ir(111) surface, plotted in terms of cyclopropane conversion. The partial pressure of cyclopropane was 2.0 Torr, and that of hydrogen was 100 Torr.

Figure 4. Specific reaction rates for the reaction of cyclopropane and hydrogen on the Ir(111) surface at a temperature of 450 K. (a) The partial pressure of cyclopropane was fixed at 2.0 Torr as the partial pressure of hydrogen was varied. (b) The partial pressure of hydrogen was fixed at 100 Torr as the partial pressure of cyclopropane was varied.

Figure 5. Specific reaction rates for the reaction of cyclopropane and hydrogen on the Ir(111) surface at a temperature of 575 K. (a) The partial pressure of cyclopropane was fixed at 2.0 Torr as the partial pressure of hydrogen was varied. (b) The partial pressure of hydrogen was fixed at 100 Torr as the partial pressure of cyclopropane was varied.

Figure 6. (a) Relative selectivity for hydrogenation/isomerization (C_3) and hydrogenolysis ($C_1 + C_2$) from the reaction of cyclopropane and hydrogen on the Ir(111) surface at a temperature of 575 K. The reaction conditions are identical to those given in Fig. 5. (b) The coverage of the carbonaceous residue at the corresponding reaction conditions.

Figure 7. Thermal desorption spectra, monitoring H_2, of the carbonaceous residue following the reaction of cyclopropane and hydrogen on the Ir(111) surface at the conditions indicated.

Figure 8. Specific reaction rates for the reaction of cyclopropane and hydrogen on the Ir(110)-(1x2) surface. The partial pressure of cyclopropane was 2.0 Torr, whereas that of hydrogen was 100 Torr.

Figure 9. Specific rates of hydrogenolysis of cyclopropane to methane and ethane on the Ir(110)-(1x2) surface, plotted in terms of cyclopropane conversion. The partial pressure of cyclopropane was 2.0 Torr, and that of hydrogen was 100 Torr.

Figure 10. Specific reaction rates for the reaction of cyclopropane and hydrogen on the Ir(110)-(1x2) surface at a temperature of 425 K. (a) The partial pressure of cyclopropane was fixed at 2.0 Torr as the partial pressure of hydrogen was varied. (b) The partial pressure of hydrogen was fixed at 100 Torr as the partial pressure of cyclopropane was varied.

Figure 11. Specific reaction rates for the reaction of cyclopropane and hydrogen on the Ir(110)-(1x2) surface at a temperature of 600 K. (a) The partial pressure of cyclopropane was fixed at 2.0 Torr as the partial pressure of hydrogen was varied. (b) The partial pressure of hydrogen was fixed at 100 Torr, as the partial pressure of cyclopropane was varied.

Figure 12. Specific reaction rates for the reaction of methylcyclopropane and hydrogen on the Ir(111) surface. The partial pressure of methylcyclopropane was 2.0 Torr, whereas that of hydrogen was 100 Torr.

Figure 13. Specific reaction rates for the reaction of methylcyclopropane and hydrogen on the Ir(111) surface at a temperature of 425 K. (a) The partial pressure of methylcyclopropane was fixed at 2.0 Torr as the partial pressure of hydrogen was varied. (b) The partial pressure of hydrogen was fixed at 100 Torr, as the partial pressure of methylcyclopropane was varied.

Figure 14. Specific reaction rates for the reaction of methylcyclopropane and hydrogen on the Ir(110)-(1x2) surface. The partial pressure of methylcyclopropane was 2.0 Torr, whereas that of hydrogen was 100 Torr.

Figure 15. Specific reaction rates for the reaction of methylcyclopropane and hydrogen on the Ir(110)-(1x2) surface at a temperature of 425 K. (a) The partial pressure of methylcyclopropane was fixed at 2.0 Torr as the partial pressure of hydrogen was varied. (b) The partial pressure of hydrogen was fixed at 100 Torr as the partial pressure of methylcyclopropane was varied.

Figure 16. (a) Specific reaction rates for the reaction of propylene and hydrogen on the Ir(111) surface. The partial pressure of propylene was 2.0 Torr, whereas that of hydrogen was 100 Torr. (b) The coverage of the carbonaceous residue at the corresponding reaction conditions.

Figure 17. Specific reaction rates for the reaction of propylene and hydrogen on the Ir(111) surface at a temperature of 450 K. The partial pressure of hydrogen was fixed at 100 Torr as the partial pressure of propylene was varied.

Figure 18. (a) Specific reaction rates for the reaction of propylene and hydrogen on the Ir(111) surface at a temperature of 575 K. The partial pressure of hydrogen was fixed at 100 Torr as the partial pressure of propylene was varied. (b) The coverage of the carbonaceous residue at the corresponding reaction conditions.

Figure 19. (a) Specific reaction rates for the reaction of propylene and hydrogen on the Ir(110)-(1x2) surface. The partial pressure of propylene was 2.0 Torr, whereas that of hydrogen was 100 Torr. (b) The coverage of the carbonaceous residue at the corresponding reaction conditions.

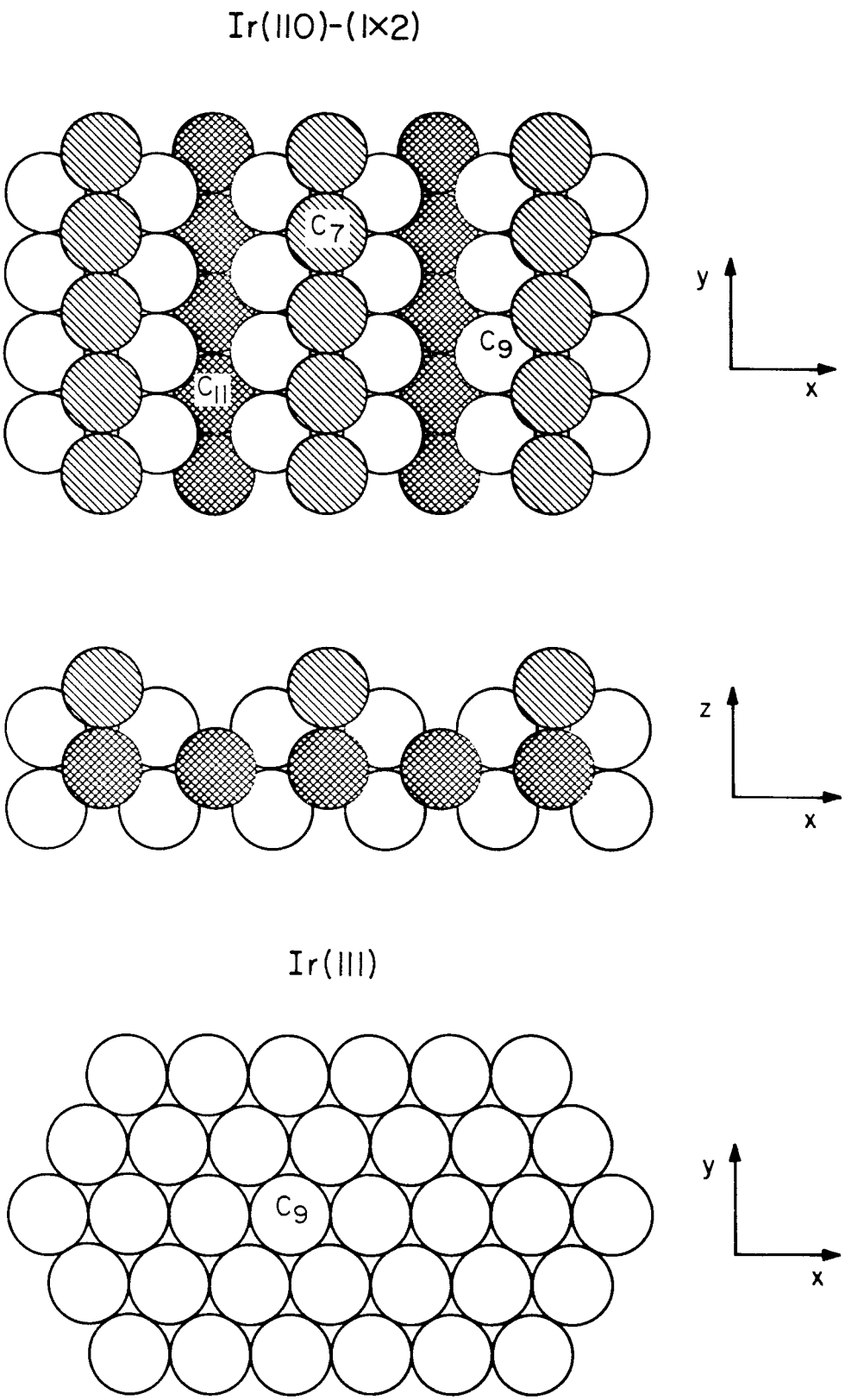

Figure 1

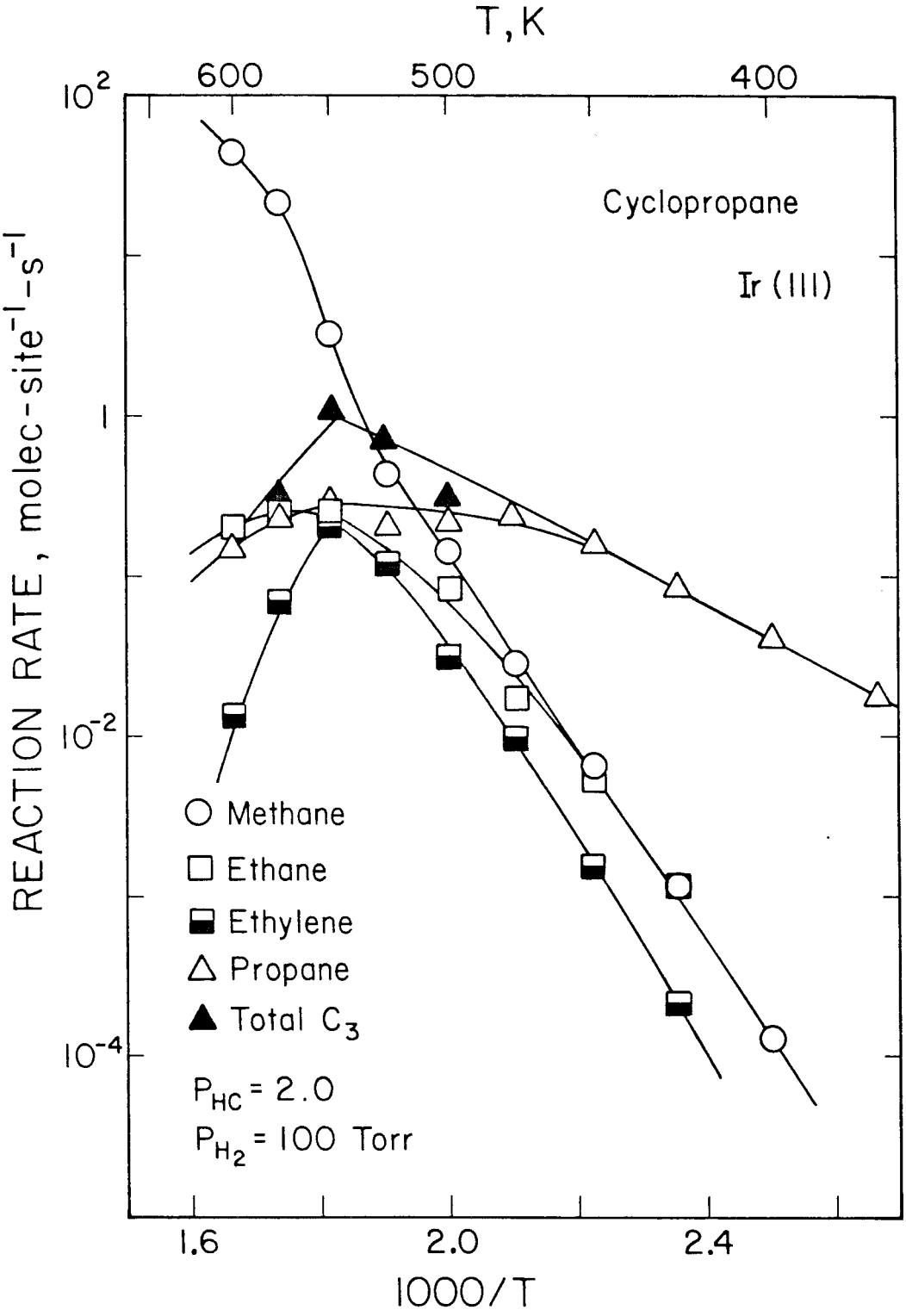
T, K
600
500
400
10^2
1
10^{-2}
10^{-4}
REACTION RATE, molec-site^{-1}-s^{-1}
Cyclopropane
Ir (111)
Methane
Ethane
Ethylene
Propane
Total C_3
P_{HC} = 2.0
P_{H_2} = 100 Torr
1.6
2.0
2.4
1000/T

Figure 2

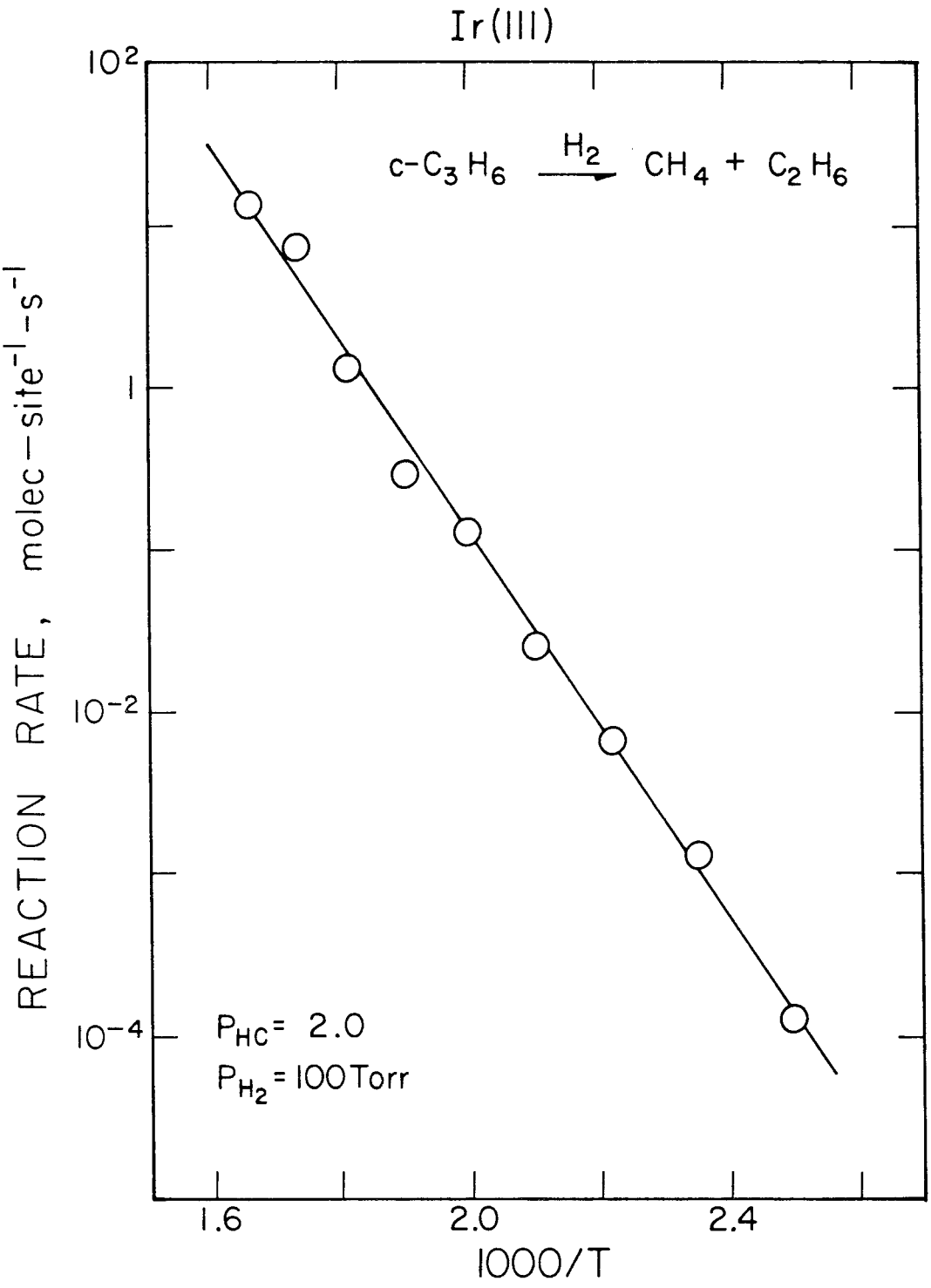
Ir(III)
$c\text{-}C_3H_6 \xrightarrow{H_2} CH_4 + C_2H_6$
REACTION RATE, molec−site^{-1}−s^{-1}
10^2
1
10^{-2}
10^{-4}
P_{HC}= 2.0
P_{H_2}= 100 Torr
1.6
2.0
2.4
1000/T

Figure 3

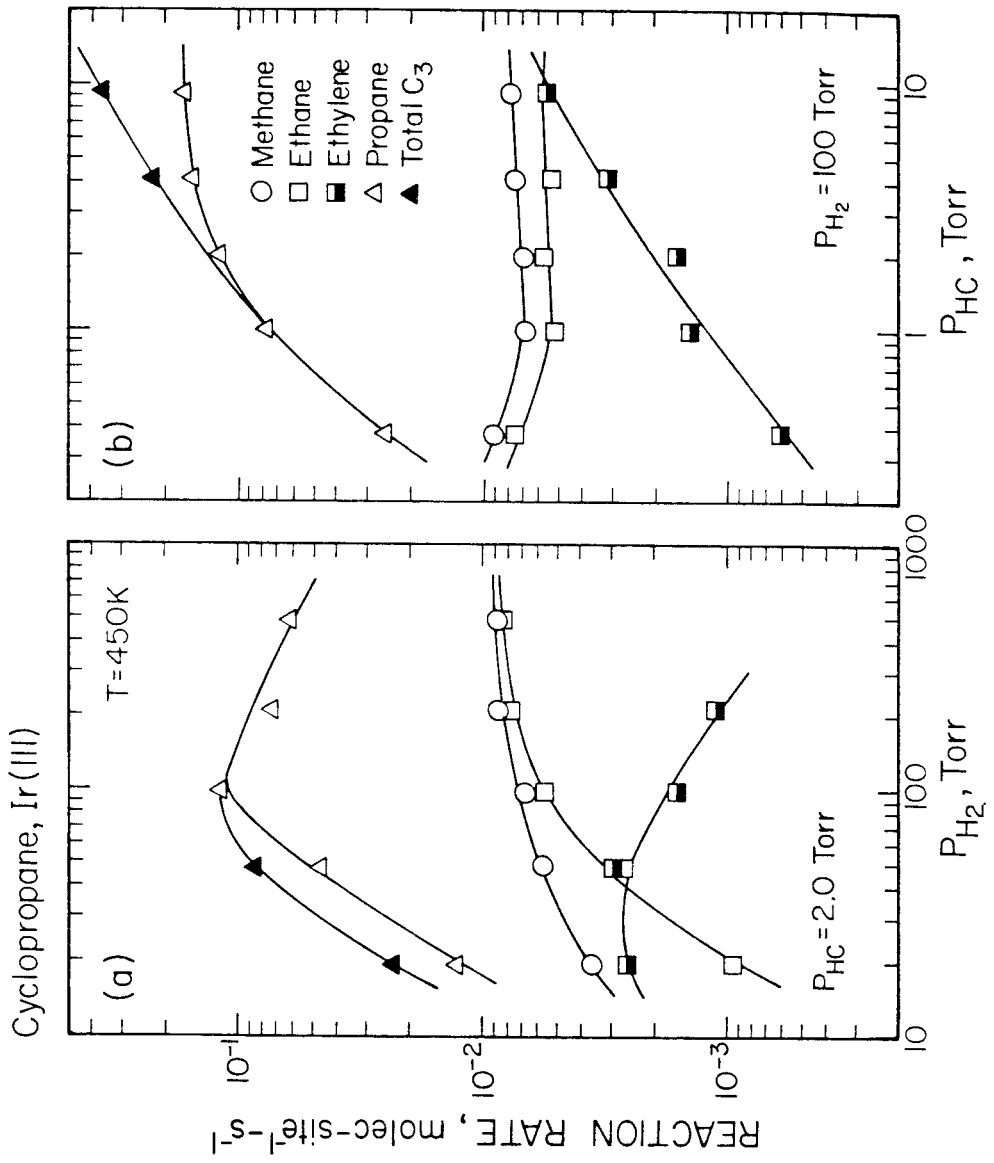
Cyclopropane, Ir(111)
(a)
T=450K
(b)
Methane
Ethane
Ethylene
Propane
Total C_3
P_{HC}=2.0 Torr
P_{H_2}=100 Torr
REACTION RATE, molec-site^{-1}-s^{-1}
10^{-1}
10^{-2}
10^{-3}
10
100
1000
1
P_{H_2}, Torr
P_{HC}, Torr

Figure 4

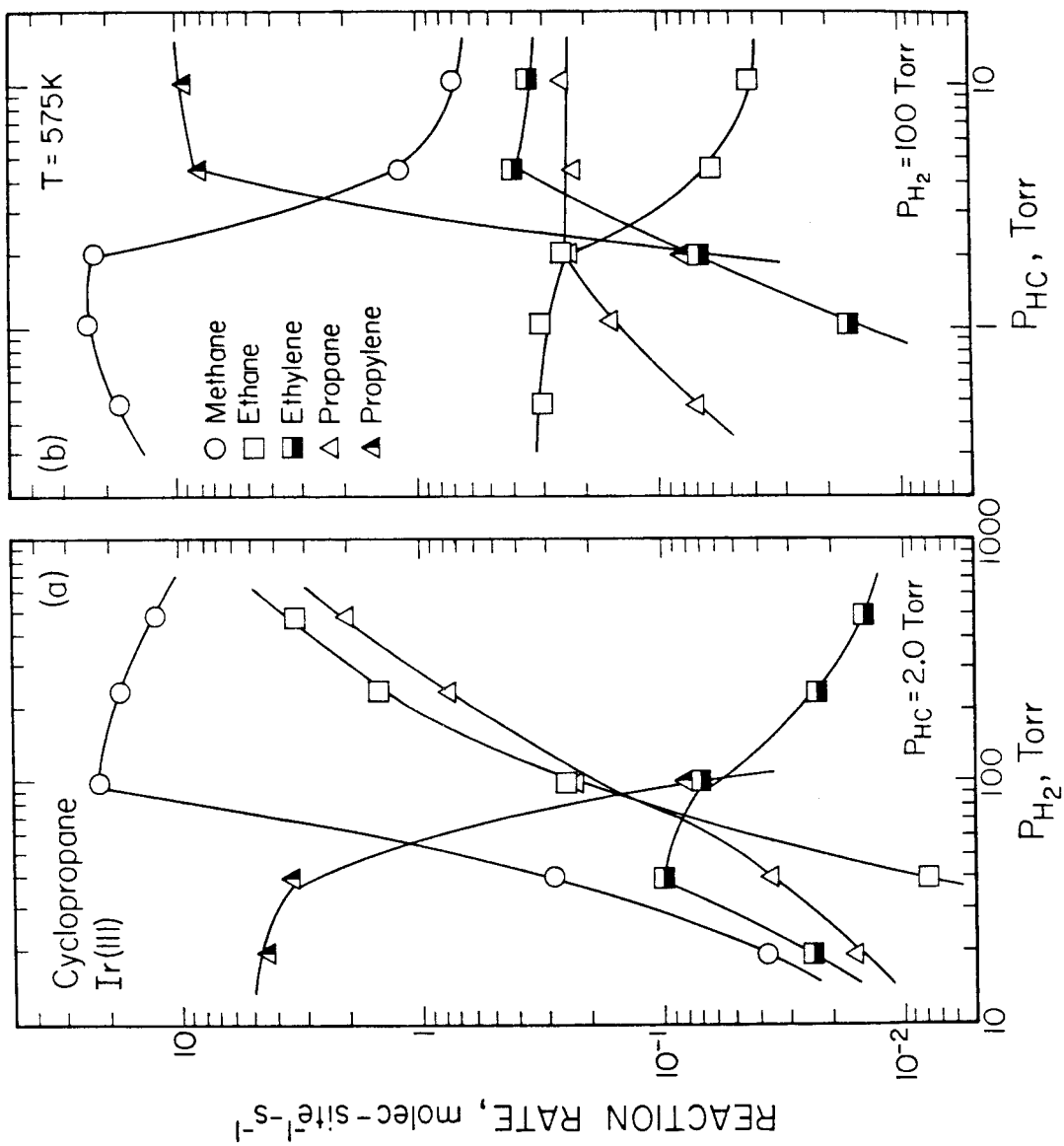
REACTION RATE, molec-site^{-1}-s^{-1}
10
1
10^{-1}
10^{-2}
(a)
Cyclopropane
Ir(111)
P_{HC} = 2.0 Torr
10
100
1000
P_{H_2}, Torr
(b)
T = 575K
Methane
Ethane
Ethylene
Propane
Propylene
P_{H_2} = 100 Torr
1
10
P_{HC}, Torr

Figure 5

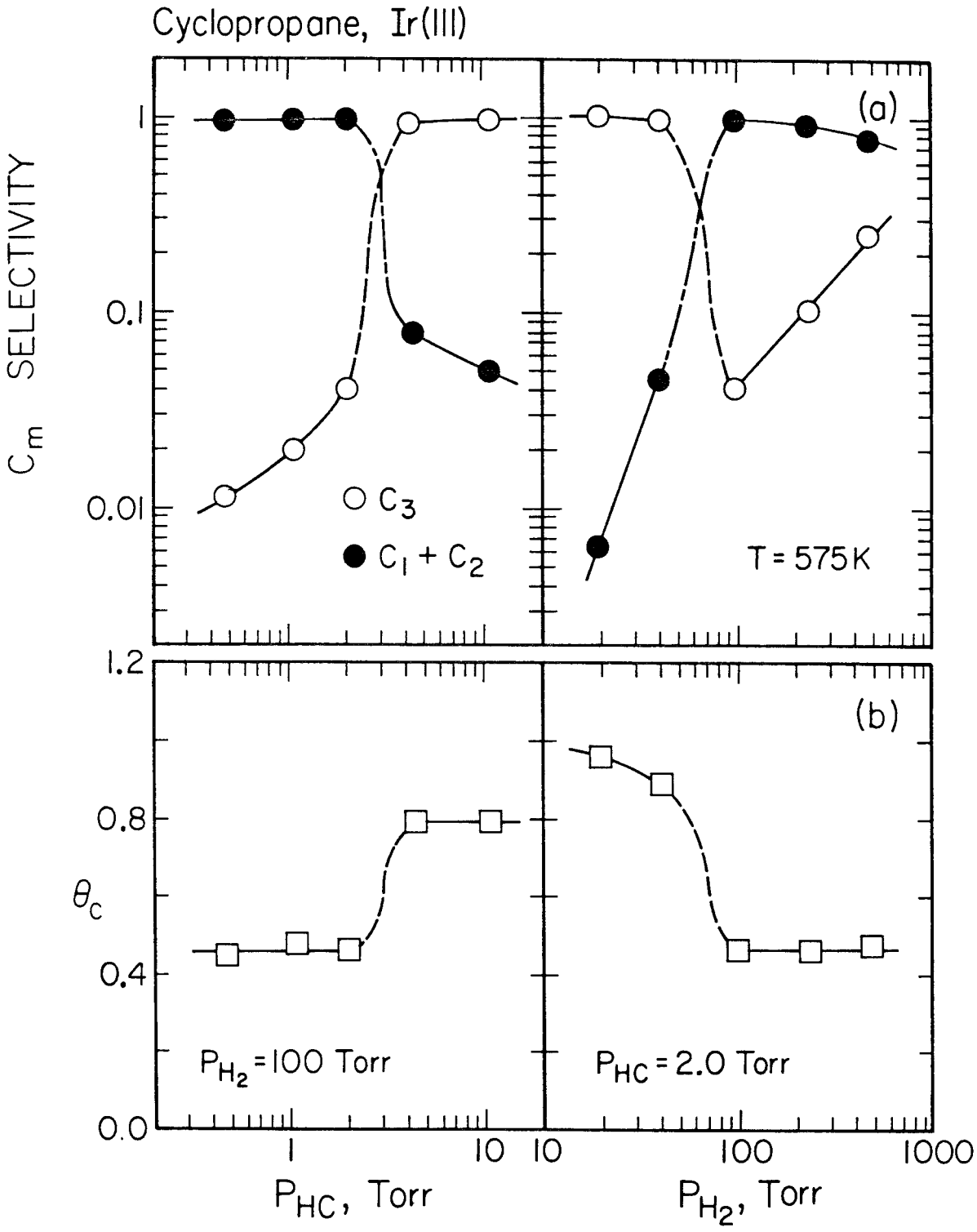
Cyclopropane, Ir(111)
C_m SELECTIVITY
1
0.1
0.01
○ C_3
● $C_1 + C_2$
(a)
T = 575K
1.2
0.8
0.4
0.0
θ_C
(b)
P_{H_2} = 100 Torr
P_{HC} = 2.0 Torr
1
10
10
100
1000
P_{HC}, Torr
P_{H_2}, Torr

Figure 6

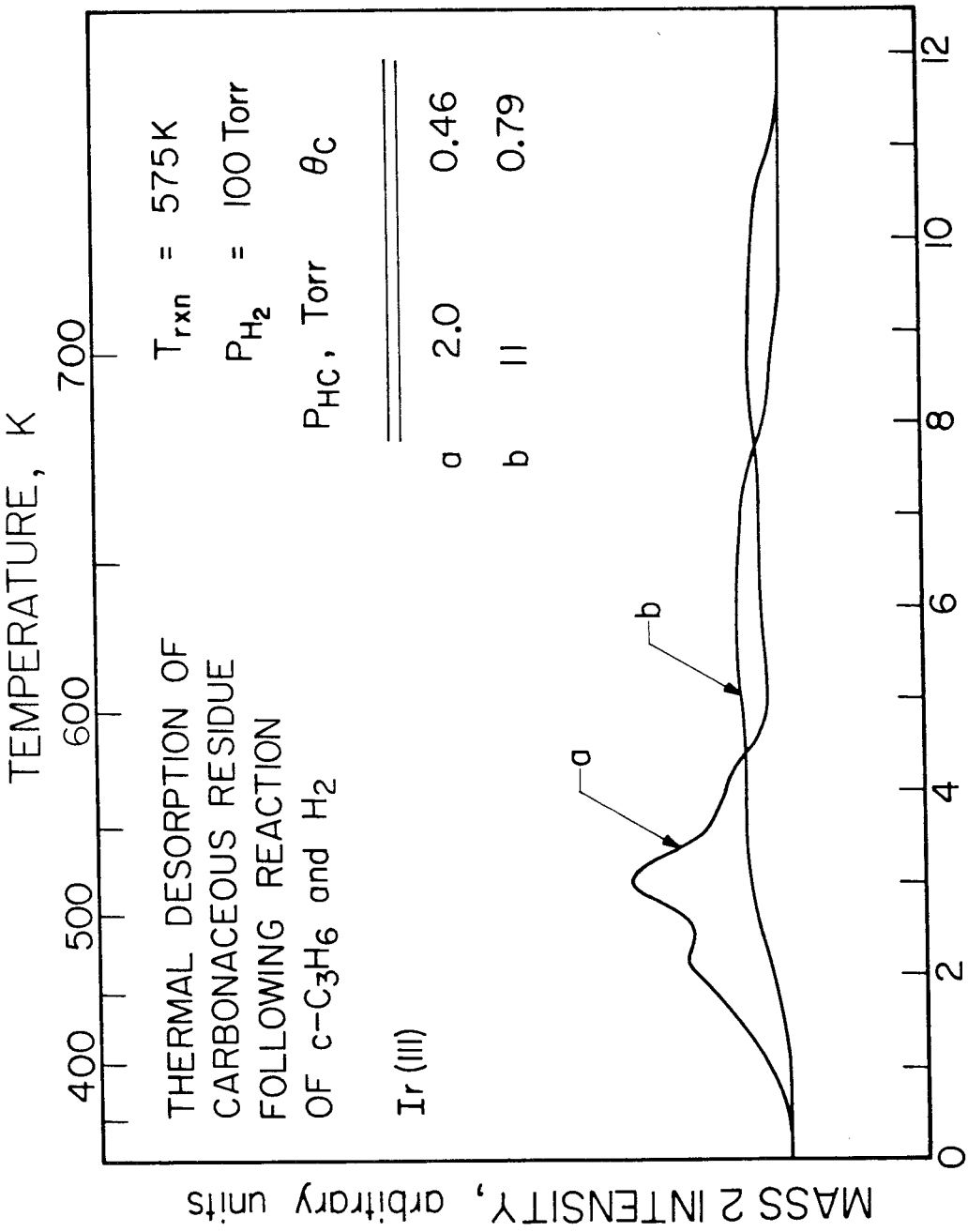
TEMPERATURE, K
400
500
600
700
THERMAL DESORPTION OF
CARBONACEOUS RESIDUE
FOLLOWING REACTION
OF c-C3H6 and H2
Ir (111)
Trxn = 575K
PH2 = 100 Torr
PHC, Torr θC
a 2.0 0.46
b 11 0.79
a
b
MASS 2 INTENSITY, arbitrary units
0
2
4
6
8
10
12
TIME, s

Figure 7

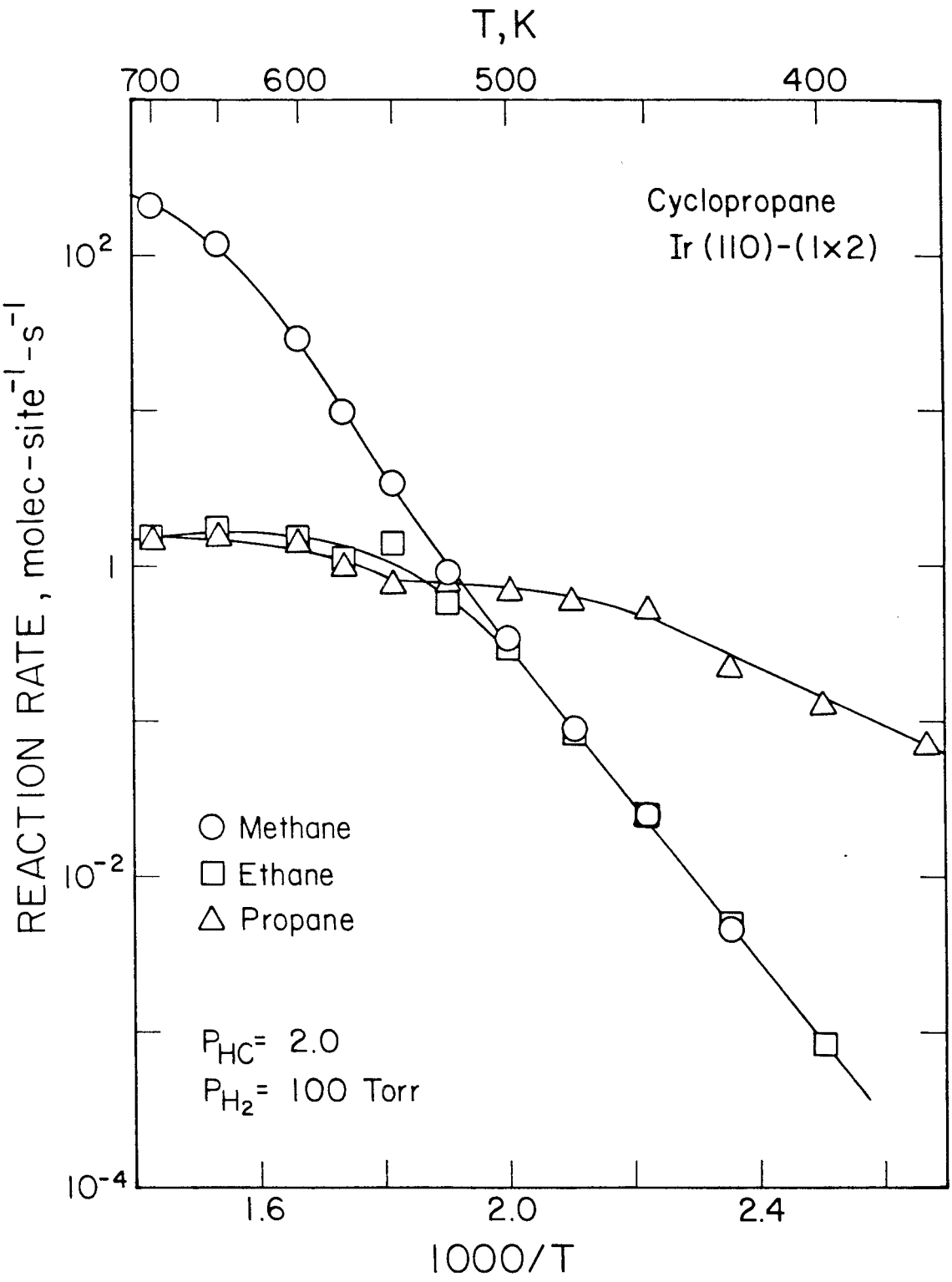
T, K
700
600
500
400
Cyclopropane
Ir (110)-(1×2)
10^2
1
10^{-2}
10^{-4}
REACTION RATE, molec-site^{-1}-s^{-1}
Methane
Ethane
Propane
P_{HC}= 2.0
P_{H_2}= 100 Torr
1.6
2.0
2.4
1000/T

Figure 8

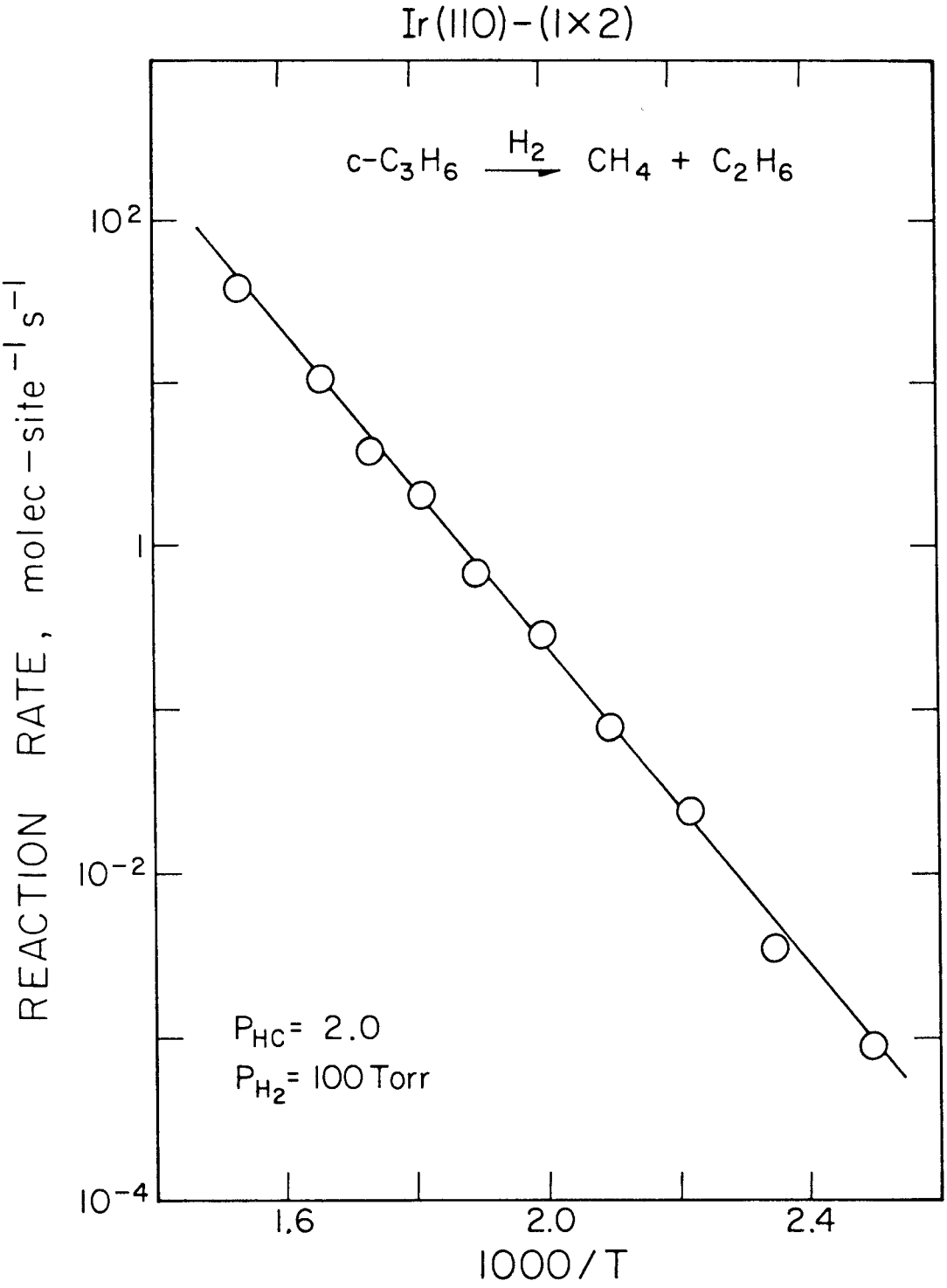
Ir(110)-(1×2)
c-C3H6 H2 CH4 + C2H6
REACTION RATE, molec-site-1 s-1
10^2
1
10^-2
10^-4
PHC= 2.0
PH2= 100 Torr
1.6
2.0
2.4
1000/T

Figure 9

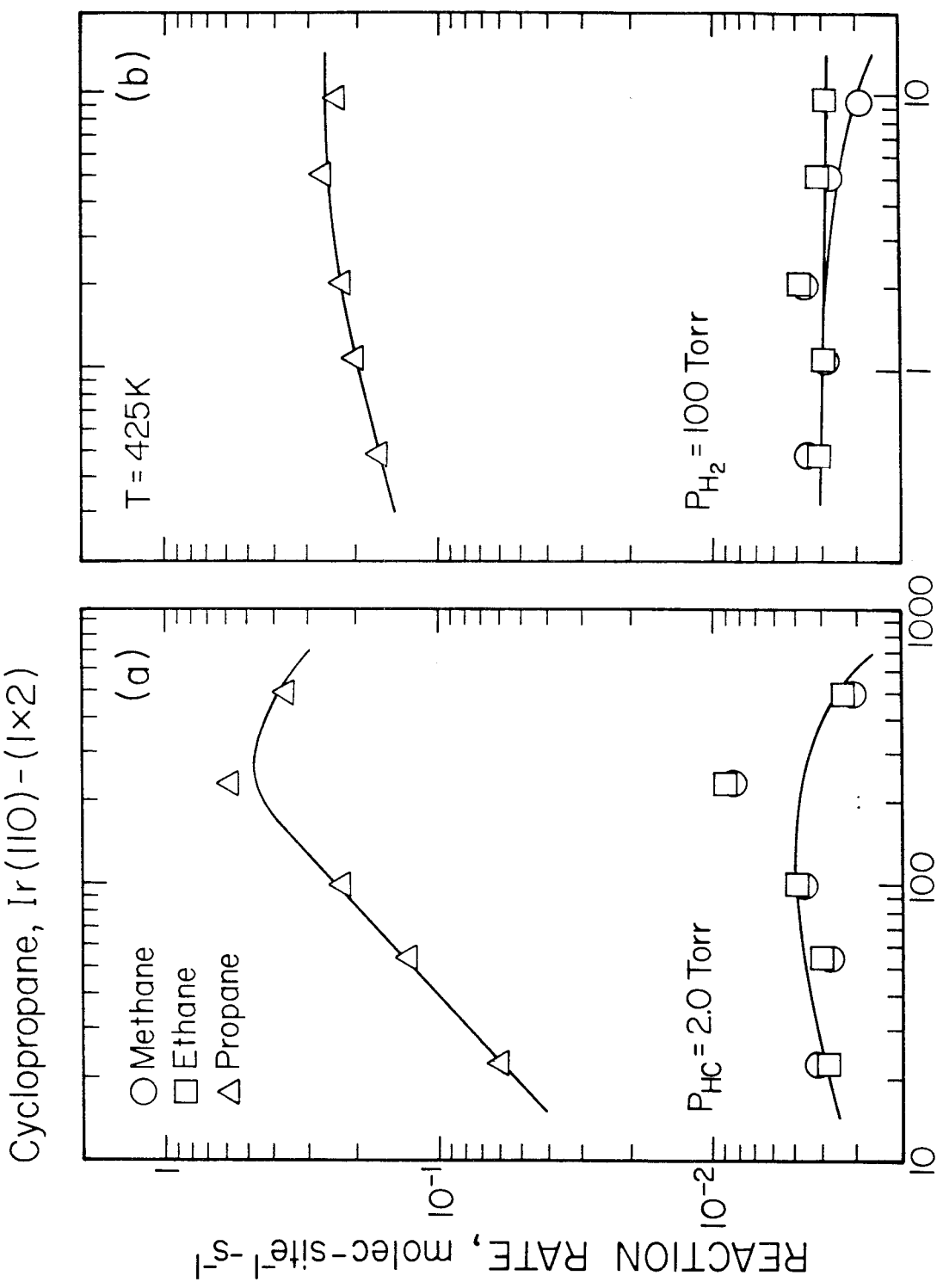
Cyclopropane, Ir(110)-(1×2)
REACTION RATE, molec-site^{-1}-s^{-1}
(a)
(b)
○ Methane
□ Ethane
△ Propane
P_{HC} = 2.0 Torr
T = 425K
P_{H_2} = 100 Torr
P_{H_2}, Torr
P_{HC}, Torr
10^{-1}
10^{-2}
10
100
1000
1
10

Figure 10

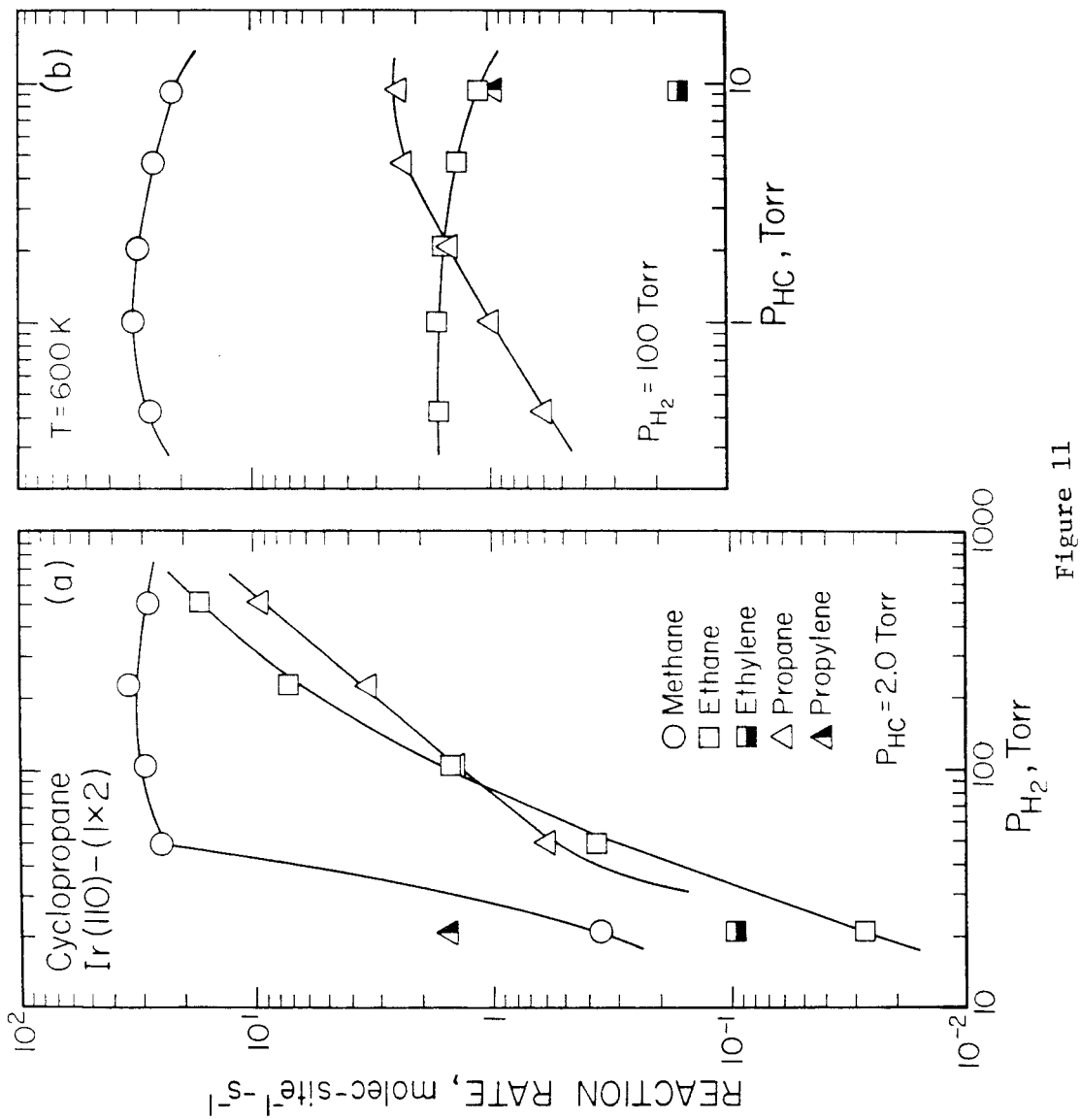
(a)
Cyclopropane
Ir(110)-(1×2)
Methane
Ethane
Ethylene
Propane
Propylene
P_{HC} = 2.0 Torr
REACTION RATE, molec-site^{-1}-s^{-1}
P_{H_2}, Torr
(b)
T = 600 K
P_{H_2} = 100 Torr
P_{HC}, Torr

Figure 11

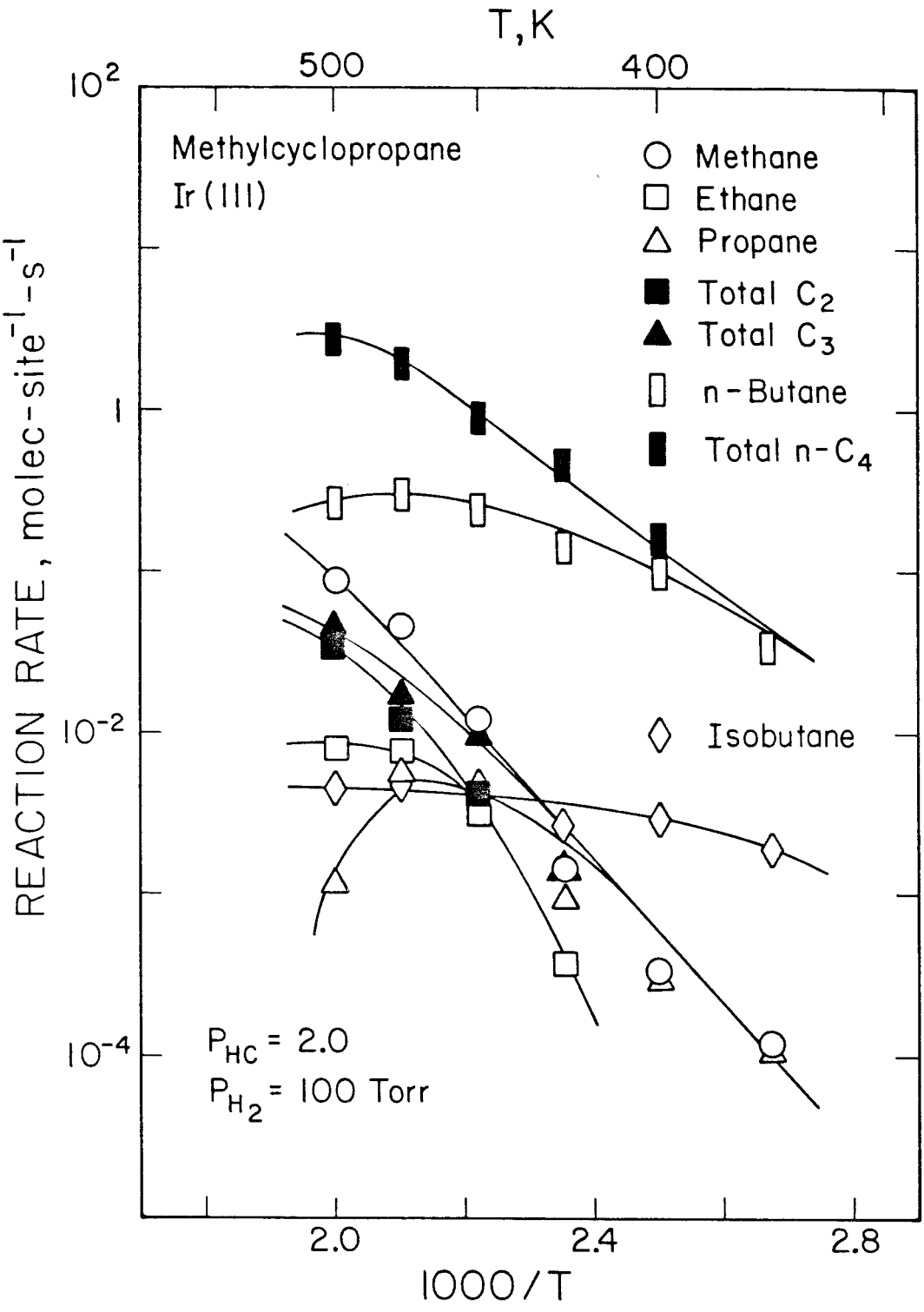
T, K
500
400
10^2
1
10^{-2}
10^{-4}
REACTION RATE, molec-site^{-1}-s^{-1}
Methylcyclopropane
Ir (111)
Methane
Ethane
Propane
Total C_2
Total C_3
n-Butane
Total n-C_4
Isobutane
P_{HC} = 2.0
P_{H_2} = 100 Torr
2.0
2.4
2.8
1000/T

Figure 12

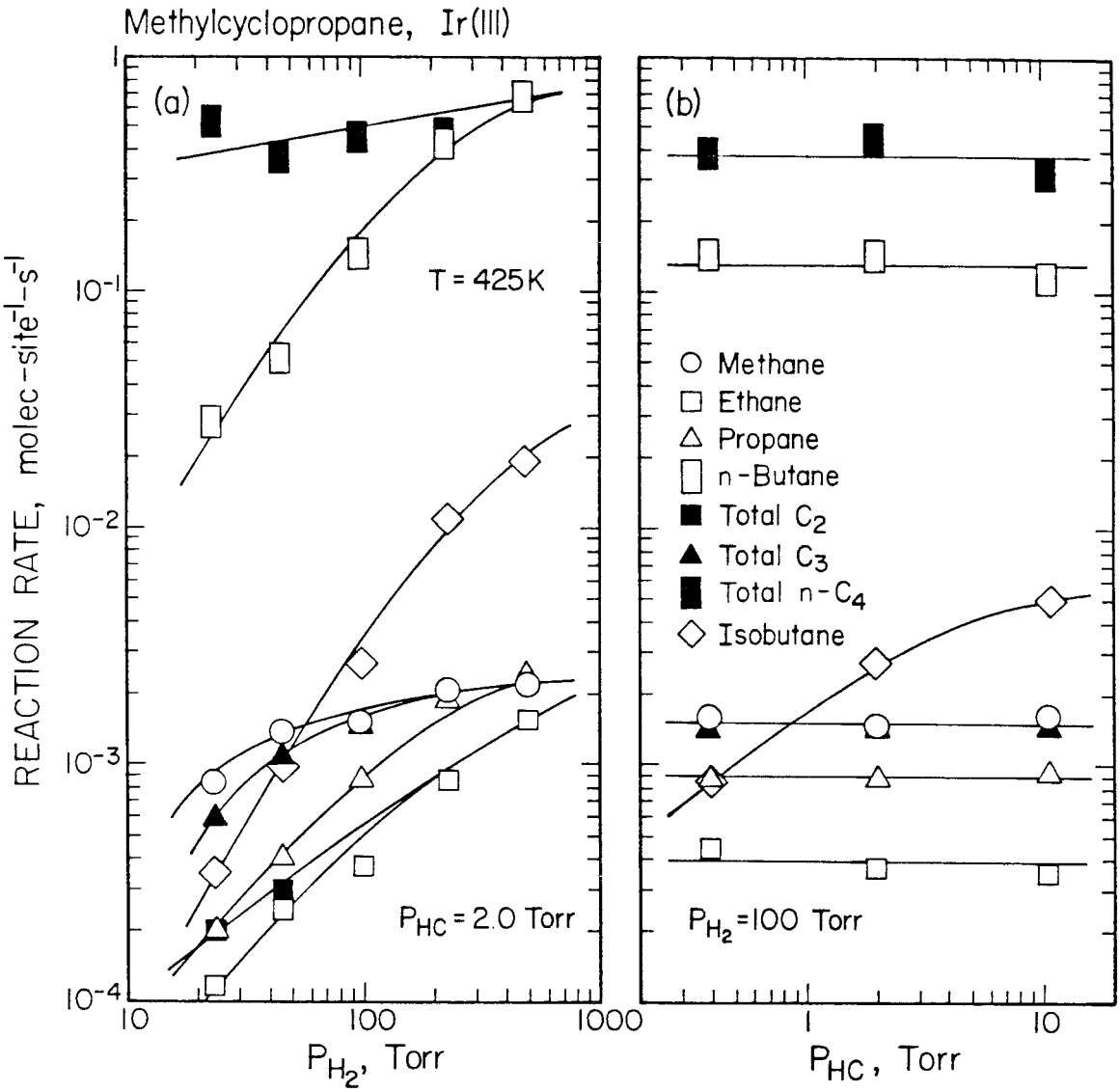
Methylcyclopropane, Ir(III)
(a)
(b)
T = 425K
P_{HC} = 2.0 Torr
P_{H_2}=100 Torr
Methane
Ethane
Propane
n-Butane
Total C_2
Total C_3
Total n-C_4
Isobutane
REACTION RATE, molec-site^{-1}-s^{-1}
10^{-1}
10^{-2}
10^{-3}
10^{-4}
10
100
1000
1
10
P_{H_2}, Torr
P_{HC}, Torr

Figure 13

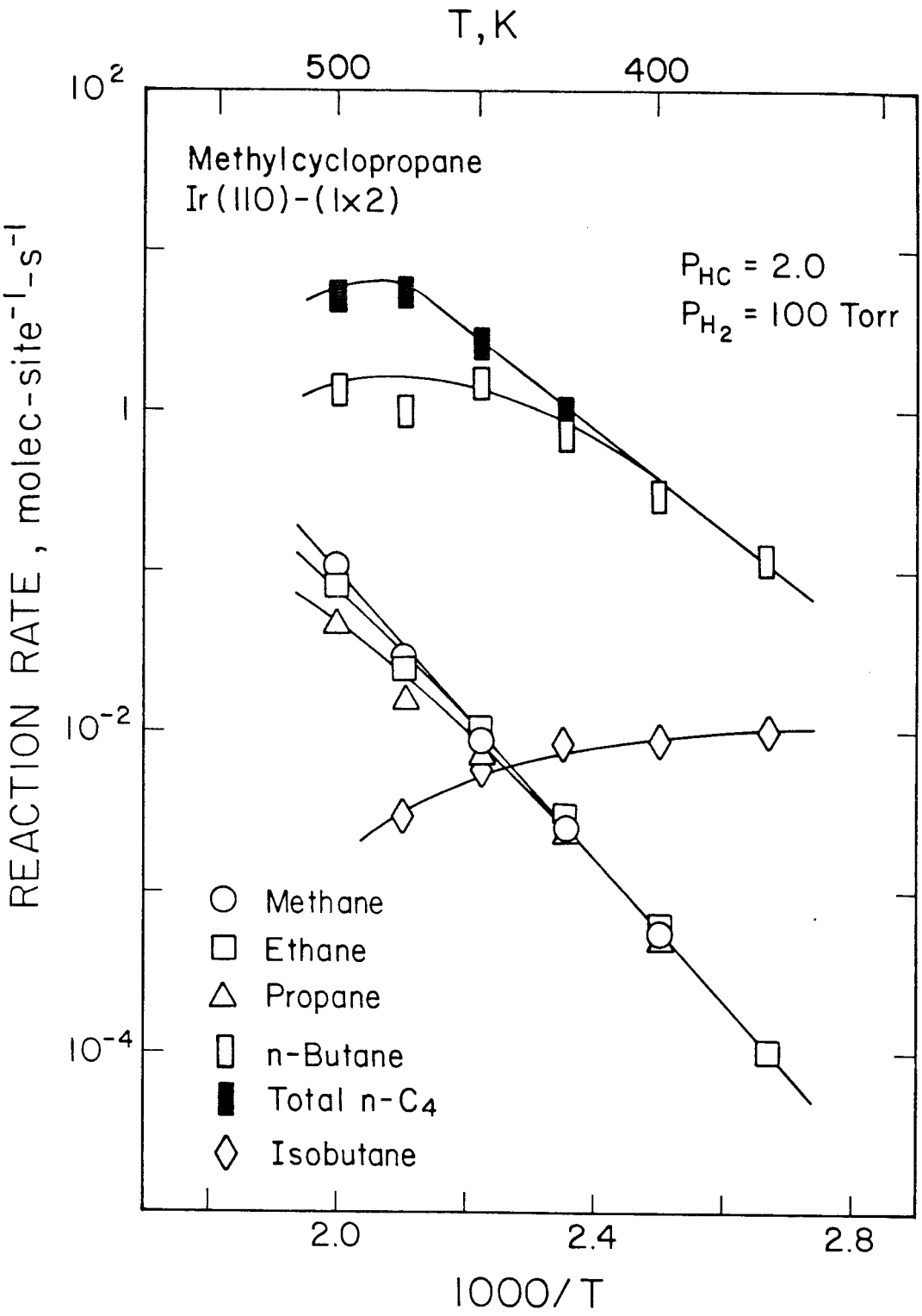
T, K
500
400
10^2
1
10^{-2}
10^{-4}
REACTION RATE, molec-site^{-1}-s^{-1}
Methylcyclopropane
Ir(110)-(1x2)
P_{HC} = 2.0
P_{H_2} = 100 Torr
Methane
Ethane
Propane
n-Butane
Total n-C_4
Isobutane
2.0
2.4
2.8
1000/T

Figure 14

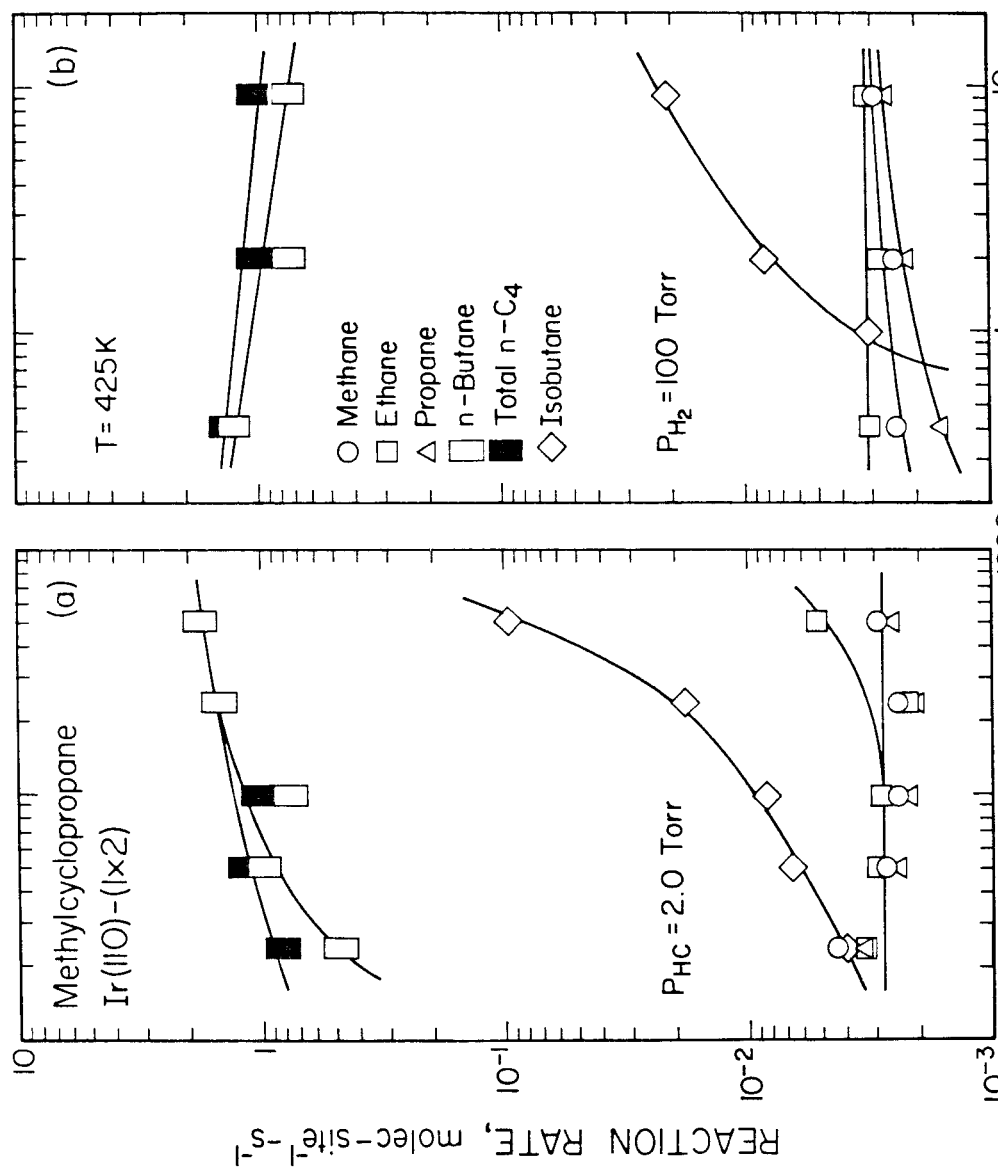
Methylcyclopropane
Ir(110)-(1×2)
(a)
(b)
T= 425K
O Methane
□ Ethane
△ Propane
□ n-Butane
■ Total n-C4
◇ Isobutane
P_HC = 2.0 Torr
P_H2 = 100 Torr
REACTION RATE, molec-site-1-s-1
P_H2, Torr
P_HC, Torr
10
1
10-1
10-2
10-3
100
1000

Figure 15

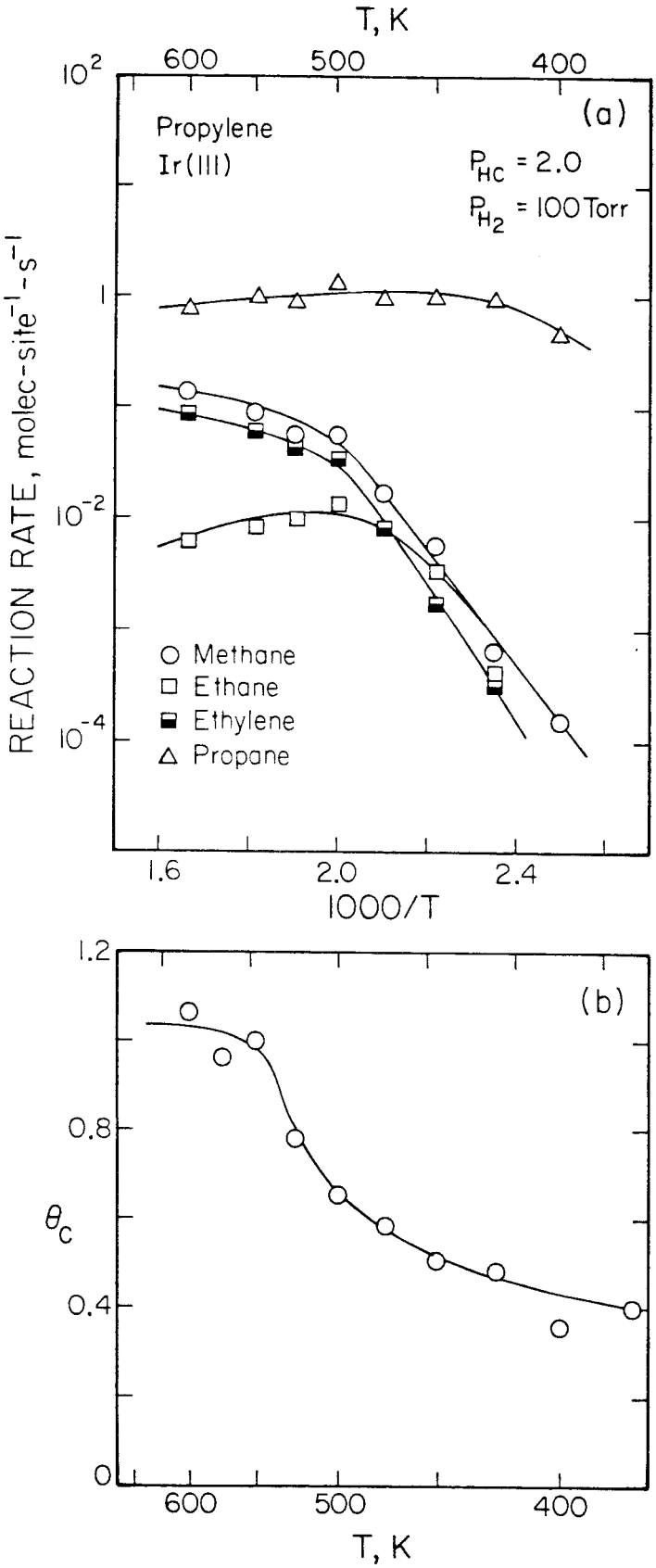
T, K
600
500
400
(a)
Propylene
Ir(111)
P_{HC} = 2.0
P_{H_2} = 100 Torr
REACTION RATE, molec-site^{-1}-s^{-1}
10^2
1
10^{-2}
10^{-4}
O Methane
□ Ethane
■ Ethylene
△ Propane
1.6
2.0
2.4
1000/T
(b)
1.2
0.8
0.4
0
θ_C
600
500
400
T, K

Figure 16

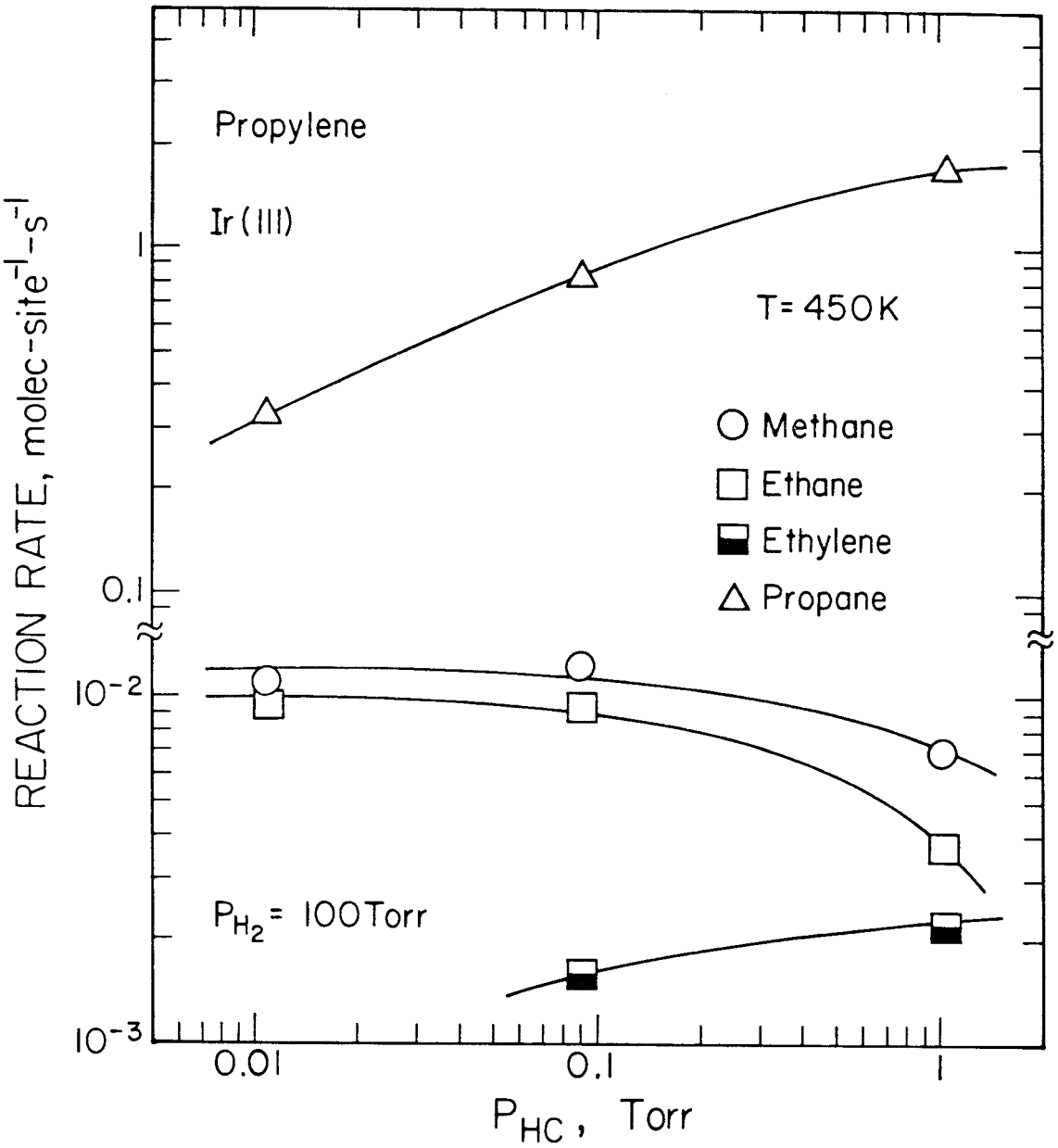
Propylene
Ir (111)
T= 450K
Methane
Ethane
Ethylene
Propane
P_{H_2} = 100Torr
REACTION RATE, molec-site^{-1}-s^{-1}
1
0.1
10^{-2}
10^{-3}
0.01
0.1
1
P_{HC}, Torr

Figure 17

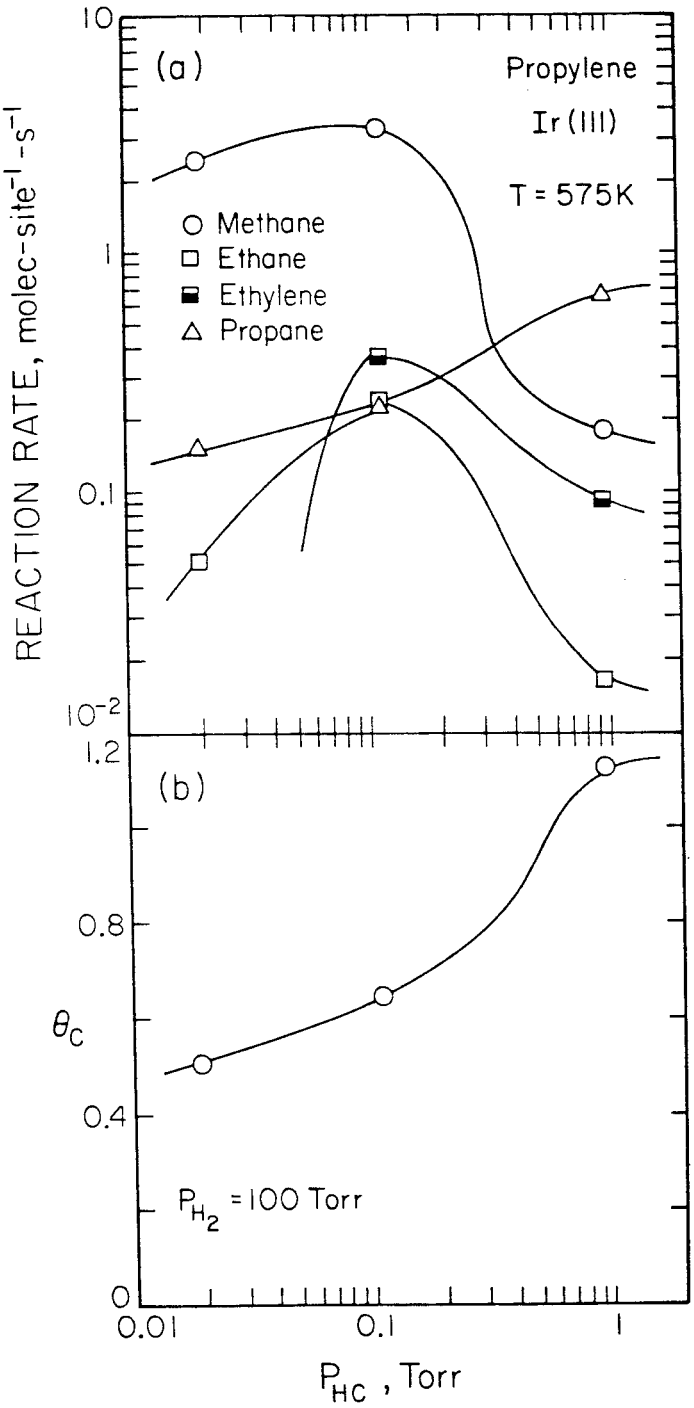
(a)
Propylene
Ir(111)
T = 575K
Methane
Ethane
Ethylene
Propane
REACTION RATE, molec-site^{-1}-s^{-1}
10
1
0.1
10^{-2}
(b)
θ_C
1.2
0.8
0.4
0
P_{H_2} = 100 Torr
0.01
0.1
1
P_{HC}, Torr

Figure 18

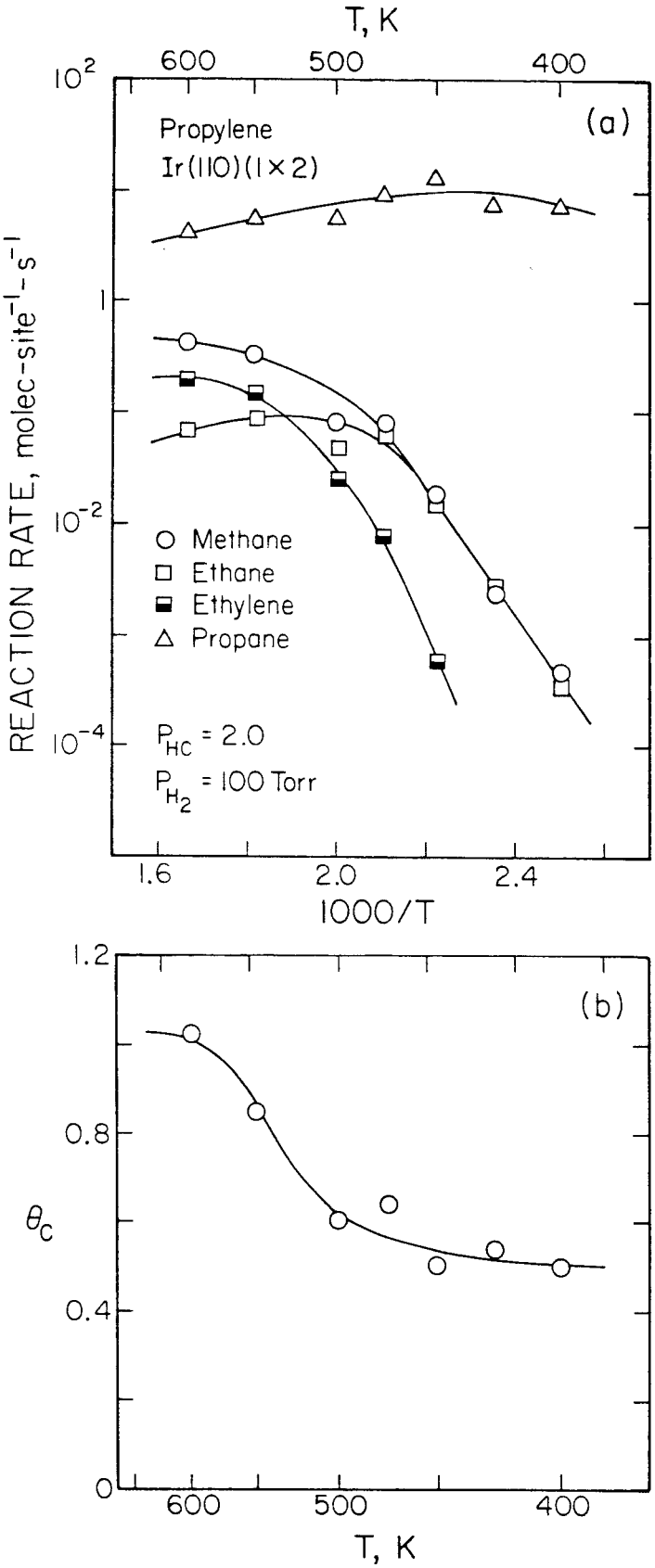
T, K
600
500
400
10^2
Propylene
Ir(110)(1×2)
(a)
1
10^{-2}
10^{-4}
REACTION RATE, molec-site^{-1}-s^{-1}
O Methane
□ Ethane
■ Ethylene
△ Propane
P_{HC} = 2.0
P_{H_2} = 100 Torr
1.6
2.0
2.4
1000/T
1.2
(b)
0.8
θ_C
0.4
0
600
500
400
T, K

Figure 19

CONCLUSIONS

Chapters 1–3

The theoretical formulation of a frequency response technique, based on surface temperature modulation, for the study of the kinetics of elementary gas-surface reactions has been described in detail. The technique possesses a distinct advantage over competitive techniques, such as modulated molecular beam reactive scattering, since the evaluation of activation barriers for elementary surface reactions is straightforward even in the presence of strong nonlinearities, and requires no knowledge of the composition and/or configuration of the adlayer. The technique was employed successfully to investigate the adsorption, desorption and oxidation of CO on the Pt(110)-(1x2) surface. In particular, the oxidation of CO was studied with emphasis being placed on examining the kinetics of the elementary bimolecular surface reaction $CO(a) + O(a) \rightarrow CO_2(g)$. The results concerning the coverage-dependence of the kinetic parameters, spanning a large range of adsorbate concentrations, represent the most complete and detailed data set yet obtained for this reaction on platinum, despite a plethora of previous work examining this same reaction. The activation energy was found to correlate well with the oxygen adatom concentration, the variation being quite nonlinear. This nonlinear variation was interpreted as a manifestation of the dominant role that the local configuration of the reactants play in determining the reaction dynamics. It has been suggested that the power of the technique can be increased significantly by either coupling it with time-resolved, surface-sensitive spectroscopies or utilizing localized (*e.g.*, laser) heating techniques to provide the modulation in surface temperature and, thus, considerably extending the frequency bandwidth.

Chapter 4

The chemisorption of hydrogen on both the Ir(111) and Pt(110)-(1x2) surfaces was examined by employing primarily thermal desorption mass spectrometry. The

structure of the surface was found to have a profound influence on the kinetics of both the adsorption and desorption of hydrogen. For example, certainly on the Ir surfaces and possibly on the Pt surfaces, the kinetics of the adsorption of hydrogen on (111) microfacets, which are three atomic rows in width was found to be essentially identical to that observed on a "perfect" (111) surface. Surface structure was also found to influence greatly the desorption kinetics of hydrogen via the mediation of "through-metal" adatom-adatom interactions. In particular, both attractive and repulsive interactions were clearly manifest within the higher binding energy β_2-adstates on the (110)-(1x2) surfaces, these β_2 states associated with adsorption into one-dimensional channels, which are composed of high-coordination "trough" sites. However, only repulsive interactions were apparent on the (111) surfaces or for the lower binding energy β_1-adstates on the (110)-(1x2) surfaces, these β_1 states associated with adsorption on the (111) microfacets.

Chapters 5–7

The hydrogenolysis of several alkanes and cycloalkanes was examined on both the (111) and (110)-(1x2) single crystalline surfaces of iridium. The choice of these two surfaces proved to be decisive for the unambiguous assessment of the effects of surface geometry on both catalytic activity and selectivity. Concerning the hydrogenolysis of alkanes, excepting the special case of *n*-butane on Ir(110)-(1x2), a mechanism involving a rate-limiting unimolecular C-C bond cleavage in an adsorbed, dehydrogenated hydrocarbon fragment was found to describe well the variations in both the specific activity and selectivity of hydrogenolysis with variations in the reactant partial pressures. In cases where similar activities and selectivities were observed over the two surfaces, essentially identical reaction intermediates (mechanisms) were implicated. On the other hand, in cases where different activities and/or selectivities were observed over the two surfaces, distinct reaction intermediates (mechanisms) were implicated. In the particular case of the reaction of *n*-butane, the selectivity for ethane was identified explicitly with the participation

(concentration) of low-coordination-number metal surface atoms. The proposition of a mononuclear metallacycle pentane as the relevant reaction intermediate for the production of ethane was found to provide a particularly elegant, although not unique, interpretation of the observed correlation between catalytic selectivity and surface structure. Concerning the hydrogenolysis and hydrogenation of cycloalkanes, the Ir(110)-(1x2) surface was found to possess a greater specific activity with respect to the Ir(111) surface for both the hydrogenation (to propane) and the hydrogenolysis (to methane and ethane) of cyclopropane. This result was interpreted by invoking a greater intrinsic activity (for these reactions) for the low-coordination-number metal surface atoms, these C_7 atoms present in higher concentrations on the Ir(110)-(1x2) surface. Unlike the reactions of alkanes, for cyclopropane at "severe" reaction conditions (*i.e.*, large hydrocarbon-to-hydrogen partial pressure ratios and/or high temperatures), a transformation in the composition of the adlayer was observed, with the coverage of the carbonaceous residue approaching one monolayer. Concomitant with the adlayer transformation, the selectivity shifted dramatically from methane (hydrogenolysis) to propylene (isomerization). The dominance of the presumably facile isomerization channel on the "carburized" surface was interpreted as a manifestation of a weakened interaction between the metal surface and the adsorbed intermediate that normally leads to hydrogenolysis.

APPENDIX A

Design and Construction of a Digital Temperature Controller for Use in Surface Studies

[The text of Appendix A consists of an article coauthored with W. H. Weinberg, which has appeared in *Review of Scientific Instruments* **55**, 404 (1984).]

Design and construction of a digital temperature controller for use in surface studies

J. R. Engstrom and W. H. Weinberg

Division of Chemistry and Chemical Engineering, California Institute of Technology, Pasadena, California 91125

(Received 29 August 1983; accepted for publication 5 December 1983)

An optimal crystal temperature control scheme is proposed which utilizes a minicomputer as the controller element. The controller design is based on standard frequency response techniques applied to an accurate and readily characterizable physical model. Specific control strategies for the production of both linear and step-function temperature profiles, commonly employed in surface studies, are presented and evaluated.

PACS numbers: 07.20.Dt, 68.90. + g, 82.80.Di

INTRODUCTION

Accurate crystal temperature control represents a largely unaddressed problem in modern surface science. This is surprising in view of its vital role in the characterization of such fundamental surface phenomena as the rates of thermal desorption, surface reactions, and surface diffusion. In particular, recent innovations in the implementation of mass spectrometry[1] and in the measurement of work function changes,[2,3] both techniques applicable to the characterization of surface kinetic processes, demonstrate the need for more accurate crystal temperature control. Here an optimal control strategy is described that utilizes a laboratory minicomputer as the controller element. Advantages of the proposed scheme include an accurate and easily characterizable physical model, in addition to a controller element capable of reproducing virtually any temperature profile desired. Application of specific control modes for thermal desorption mass spectrometry and complementary techniques utilizing work function change measurements are discussed. In particular, the utility of the method is illustrated by considering explicitly thermal desorption spectra of D_2 from Ir(111).[4]

I. SYSTEM CHARACTERIZATION

The development of a physical model that properly describes the system under consideration is crucial to any process control scheme. The experimental configuration to be considered is shown in the inset of Fig. 1(a). A highly polished single crystalline disk (approximately 5–10 mm in diameter and 1–2 mm in thickness with a mass of approximately 0.5–1 g) is spotwelded to Ta support wires (approximately 10–15 mil in diameter) which are mounted on a precision manipulator. Heating of the crystal is effected by passing current through the wire leads/crystal circuit, whereas cooling is provided by conduction through the leads to the mounting blocks which are in thermal contact with a reservoir of flowing liquid nitrogen. Thermal gradients across the crystal can be neglected due to the large cross-sectional area of the crystal compared to that of the wire leads.[5] Relevant physical constants are also displayed in Fig. 1. The transient energy balance may be written as

$$m_c \hat{C}_{p,c} \frac{dT}{dt} = i^2 R(T) + k_w A_w \left.\frac{dT_w}{dz}\right|_b + \epsilon A_c (T_{ch}^4 - T^4), \quad (1)$$

where m_c, $\hat{C}_{p,c}$, T, ϵ, and A_c are the mass, specific heat, temperature, emittance and surface area of the crystal; i and $R(T)$ the current passed through and the temperature-dependent, effective resistance of the circuit; k_w, A_w, T_w, and z the thermal conductivity, cross-sectional area, temperature and axial coordinate of the wire leads; T_{ch} the temperature of the chamber walls, and t the time.

A number of simplifying assumptions can be made at this point. Due to the low emittance of a highly polished single crystal surface and the moderate temperatures which are usually encountered (e.g., $T \lesssim 1000$ K), the radiation term can be neglected. In addition, approximating the conduction term as linear [i.e., $dT_w/dz \approx 2(T_b - T)/l_w$] gives

$$m_c \hat{C}_{p,c} \frac{dT}{dt} = i^2 R(T) - \left(\frac{2k_w A_w}{l_w}\right)(T - T_b), \quad (2)$$

where T_b is the temperature of the support blocks, and l_w the length of the wire leads.[6] Equation (2) may be written as

$$\frac{d\theta}{dt} = I\rho(\theta) - \kappa\theta + \kappa\theta_b, \quad (3)$$

where θ is a dimensionless temperature defined by $\theta \equiv T(\mathrm{K})/100 - 1$; I is equal to i^2; $\rho(\theta)$ is a reduced effective resistance, which is a function of θ; and κ is the reciprocal of the conductive cooling time constant. The quantities θ, θ_b, and I are all considered to be functions of time. At steady state, Eq. (3) becomes

$$0 = I_s \rho(\theta_s) - \kappa\theta_s + \kappa\theta_{b,s}, \quad (4)$$

where the subscript s refers to steady state.[7]

In order to characterize the system using the model presented here θ_b, κ, and $\rho(\theta)$ must be evaluated. Due to the large "thermal inertia" of the support assembly with respect to the crystal, θ_b can be assumed to be constant (independent of θ) over the time span of a typical experiment (clearly, it will increase with θ). Moreover, $\theta_{b,s}$ can be estimated by measuring the temperature of the crystal (θ_s) with the current (I_s) set to zero. The cooling time constant (κ^{-1}) may be obtained easily by starting at $\theta = \theta_{b,s}$, applying current for a

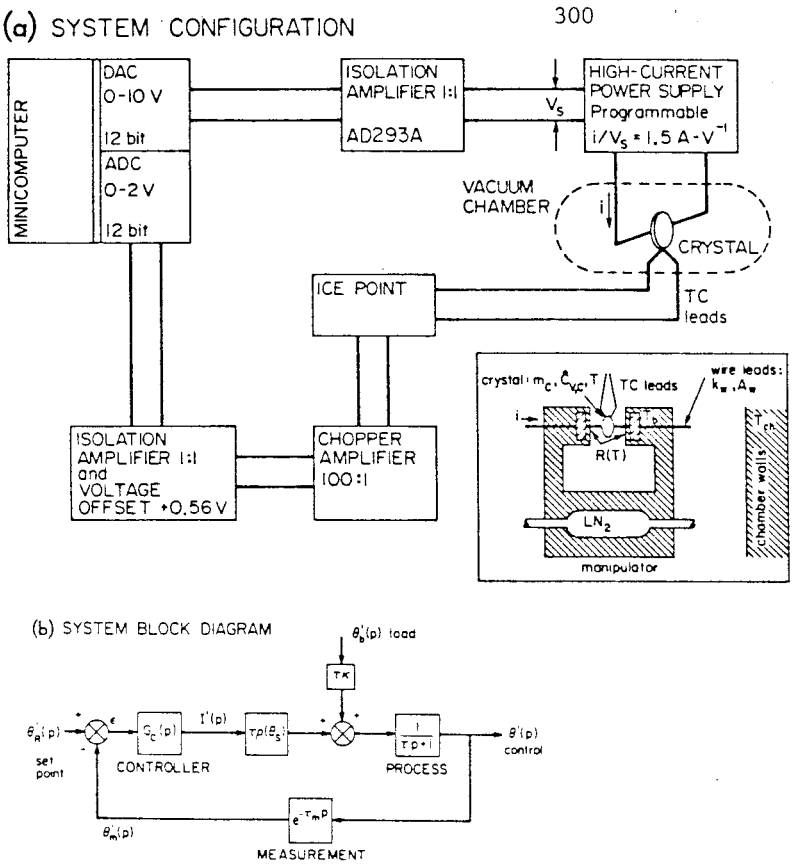

FIG. 1. (a) Control system configuration. Inset displays the physical configuration of the crystal and support assembly. (b) System block diagram in the transform variable domain.

short period of time (so that $\theta_{b,s}$ can be approximated as constant) to heat the crystal, and by then setting the current to zero. Exponential temperature decay results and, in particular,

$$\theta - \theta_{b,s} = (\theta - \theta_{b,s})_0 \exp(-\kappa t), \tag{5}$$

from which the evaluation of κ is straightforward. The determination of $\rho(\theta)$ is more difficult and time consuming. Beginning at $\theta = \theta_{b,s}$, a constant current is applied, and θ is measured after a "sufficient" time interval has passed, with a pseudo-steady-state having been achieved. In this context, "sufficient" means that any further increases in the temperature of the crystal are primarily due to an increase in the $\kappa\theta_b$ term of Eq. (3) and not the $I\rho(\theta)$ term. In practice, a sufficient time interval is approximately $5/\kappa$. Rearrangement of Eq. (4) yields

$$\rho(\theta_s) = \frac{\kappa(\theta_s - \theta_{b,s})}{I_s}. \tag{6}$$

Hence, by varying the applied current (I_s), different pseudo-steady-state temperatures (θ_s) will result, and $\rho(\theta)$ can be fit to θ via Eq. (6).

Although the characterization scheme proposed here is relatively crude, implementation has shown it to be sufficiently accurate to describe the open-loop characteristics of the system. In addition, this model is quickly characterizable, which represents a distinct advantage for the typical experimental system in which crystals often have to be removed, replaced, and/or remounted—procedures which result in a variation of the physical response of the system.

II. CONTROLLER DESIGN

The controller design scheme proposed here utilizes classical linear system control.[8] However, as is readily apparent from Eq. (3), the $I\rho(\theta)$ term is nonlinear. Linearizing Eq. (3) and combining the result with Eq. (4) yields

$$\frac{d\theta'}{dt} = \rho(\theta_s)I' + \left(\frac{\partial\rho}{\partial\theta}\bigg|_{\theta_s} I_s - \kappa\right)\theta' + \kappa\theta_b', \tag{7}$$

where $\theta' = \theta - \theta_s$, etc. represent deviation variables. Taking Laplace transforms and rearranging gives

$$\theta'(p) = \frac{\tau\rho(\theta_s)}{\tau p + 1} I'(p) + \frac{\tau\kappa}{\tau p + 1}\theta_b'(p), \tag{8}$$

where

$$\tau = \left(\kappa - \frac{\partial\rho}{\partial\theta}\bigg|_{\theta_s} I_s\right)^{-1},$$

and p is the transform variable. Construction of the closed-loop block diagram corresponding to the first-order system represented by Eq. (8) is displayed in Fig. 1(b). A measurement block has been added to account for the inherent time lag of the digital signal processing (i.e., FORTRAN coding), as well as any physical effects due to the response of the thermocouple circuit. The essential elements of the controller are shown explicitly, where $G_c(p)$ is the controller transfer

function, $\theta'_m = \theta' \exp(-\tau_m p)$ the measured variable, $\theta'_R = \theta_{set} - \theta_s$ the set point variable, and $\epsilon = \theta'_R - \theta'_m$ the error.

The controller design based on the open-loop transform function is straightforward utilizing standard frequency response techniques.[9] Specifically, for the model proposed here (i.e., a first-order system with measurement lag), the corresponding cross-over frequency is given by the transcendental relation

$$\pi = \omega_{co}\tau_m + \tan^{-1}(\omega_{co}\tau), \tag{9}$$

where τ_m is the measurement lag time constant, τ is the system time constant [cf. Eq. (8)], and ω_{co} is the cross-over frequency. The amplitude ratio (AR) is given by

$$AR(\omega) = \frac{\tau\rho(\theta_s)}{[(\omega\tau)^2 + 1]^{1/2}}. \tag{10}$$

For specific design purposes, the ultimate gain (K_u) and the ultimate period (P_u) are the relevant design parameters, where

$$K_u = 1/AR(\omega_{co}) \text{ and } P_u = 2\pi/\omega_{co}.$$

Optimal controller settings are obtained from the above by the scheme of Ziegler and Nichols[11] for proportional, proportional-integral (PI), and proportional-integral-derivative (PID) controller modes as listed in Table I. For proportional-derivative (PD) control, controller settings suggested by Cohen and Coon[12] are given by

$$K_c = \frac{1}{\tau_m \rho(\theta_s)}\left(\frac{5}{4} + \frac{\tau_m}{6\tau}\right) \approx \frac{5}{4\tau_m \rho(\theta_s)}$$

and

$$\tau_D = \tau_m\left(\frac{6 - 2(\tau_m/\tau)}{22 + 3(\tau_m/\tau)}\right) \approx \frac{3\tau_m}{11},$$

where the approximate forms follow when $\tau_m \ll \tau$. It should be emphasized that for both these control schemes the recommended controller settings should be used as first estimates, with subsequent "fine tuning" governed by the behavior that is observed upon variation of the recommended settings.

III. DESIGN SPECIFICS

It would appear from the results of the previous section that the design problem for crystal temperature control has been solved. However, due to the use of digital signal processing and the stringent demands placed on the controller by the required temperature profiles of various experimental methods, this is not the case. Consequently, it is advantageous to reexamine the calculated control design parameters.

As noted previously, measurement lag is inherent to a digital control system due to the need for signal processing. Unfortunately, excessive measurement lag leads to poor controller performance and system instability. Thus, any coding should be as brief as possible to minimize time lags. On the other hand, additional signal processing is often desired to improve controller performance. Specifically, for thermal desorption measurements, where the temperature is ramped linearly, it is obvious that the controller "steady-state" load signal (J) must be continually updated.[13] Furthermore, it is desirable to update the controller settings, essentially simulating a nonlinear controller. Using the parameters characterizing an actual experimental system [i.e., κ, $\rho(\theta)$ and τ_m], the ultimate gain and ultimate period were calculated as functions of temperature (θ), and the results are displayed in Fig. 2. Clearly, the ultimate gain is a strong function of temperature, while the ultimate period is virtually constant. Examination of Eqs. (8)–(10) reveals that this behavior is expected if $\rho(\theta)$ is a strong function of temperature and $\tau \gg \tau_m$. This has been found to be the case for all experimental systems studied. Moreover, the ultimate gain and the ultimate period can be approximated by

$$K_u \approx \frac{\pi}{[2\tau_m \rho(\theta_s)]} \text{ and } P_u \approx 4\tau_m.$$

The implementation of these results into a control scheme should be obvious. If one is continually updating the set point (i.e., ramping the temperature), it will be desirable also to continually update the appropriate gain. However, the appropriate (i.e., derivative, integral) time constants need not be changed. The preceding suggestions have been incorporated into the FORTRAN coding which represents the most crucial element of the control scheme.

IV. CONTROLLER CONSTRUCTION

A simplified schematic diagram of the system configuration is displayed in Fig. 1(a). The use of a digital minicomputer which can duplicate the control strategy outlined previously represents the key element of the control system. The software utilized by the minicomputer is displayed in Fig. 3 in the form of a FORTRAN flow chart. The coding used in the actual routine is of standard sophistication and requires no special programming techniques. Standard numerical techniques are used in the computation of the integral and derivative error terms, and in the iterative solution of Eq. (9) for the crossover frequency. MACRO service routines provide

TABLE I. Ziegler–Nichols controller settings.

Type of control	Controller transfer function $G_c(p)$	Gain K_c	Integral time constant τ_I	Derivative time constant τ_D
Proportional	K_c	$0.5\,K_u$	—	—
Proportional integral (PI)	$K_c(1 + 1/\tau_I p)$	$0.45\,K_u$	$P_u/1.2$	—
Proportional-integral derivative (PID)	$K_c(1 + 1/\tau_I p + \tau_D p)$	$0.6\,K_u$	$P_u/2$	$P_u/8$

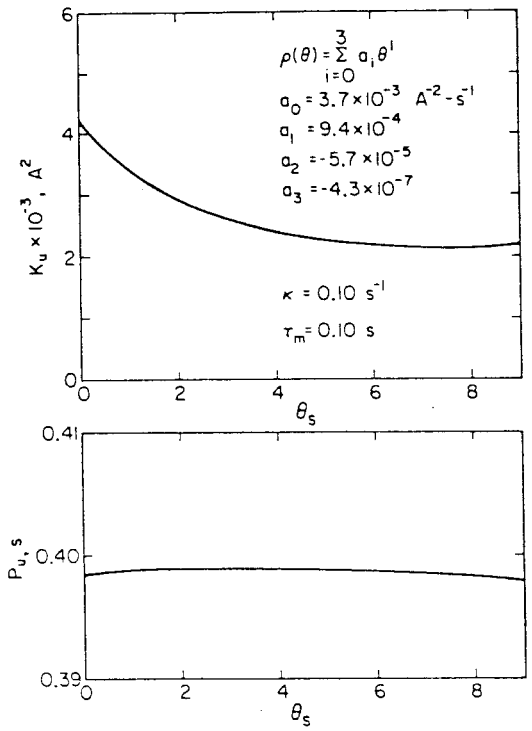

FIG. 2. Temperature dependence of controller design parameters—ultimate gain (K_u) and ultimate period (P_u), based on parameters characterizing an actual experimental system.

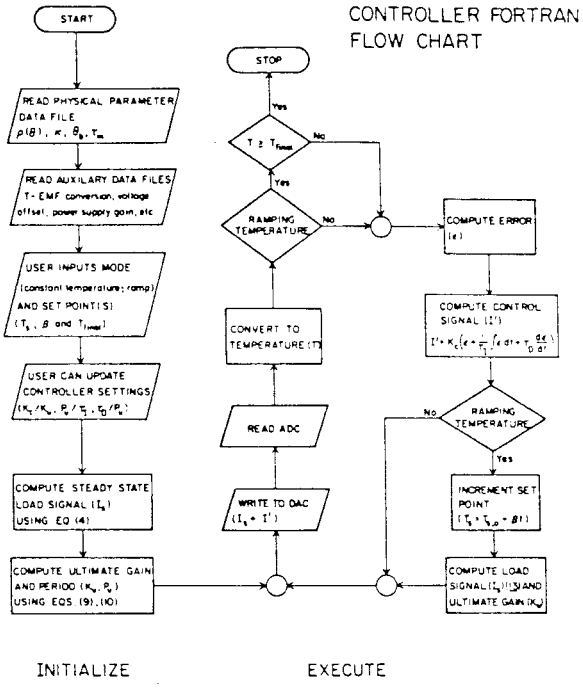

FIG. 3. FORTRAN flow chart for minicomputer software.

access to the DAC and ADC, as well as absolute time interfacing.

The peripheral electronic hardware is also of standard construction. The specific electronic circuits used in the construction of the control system are displayed in Fig. 4. The EMF amplifier, shown in Fig. 4(a), utilizes a noninverting chopper operational amplifier (AD 260K) having low noise and ultralow drift. The use of a W/5%Re–W/26%Re thermocouple spotwelded on the back of the crystal permits temperatures to be measured from 77 to 2200 K.[14] The high-current power supply, shown in Fig. 4(b), provides a programmable current source with a gain (i/V_s) of 1.5 Ω^{-1} (15 A max), stable to within 0.5%. The dc offset current through the crystal is 1 mA, while the ac noise component was found to be 5 mA p.-p. The 741 operational amplifier provides a sufficiently fast slew rate of 0.5 V/μs.

At present the controller is capable of ramping the temperature over a wide range of specified rates (values ranging from 0.1 to 200 K s^{-1} have been obtained), or holding the temperature constant. Both options can be performed with either a 100%-ON duty cycle or a 50%-ON/50%-OFF duty cycle. In particular, the modulation mode allows accurate temperature control to be interfaced with experimental techniques (e.g., work function change measurements[3]) otherwise not realizable due to the presence of electric fields associated with the current passing through the crystal.

V. PERFORMANCE EVALUATION

Actual temperature profiles produced by the use of the controller are shown in Fig. 5 for the linear temperature ramp mode (a), and the constant temperature mode, adjusted to approximate a step-function change (b). In particular, the step function change is approximated by the choice of PD control combined with a suitably high gain. Typically, a linear temperature ramp is employed in the measurement of thermal desorption spectra. Use of the step-function change in temperature, coupled with a measurement of the adsorbate surface coverage (e.g., via the work-function change measurement), permits a characterization of isothermal desorption kinetics.[15,16] However, the implementation of virtually any desired temperature profile is possible with minor modifications to the FORTRAN coding.

The temperature controller described here has been used in the measurement of thermal desorption spectra of D_2 from Ir(111).[4] Following the method of Taylor and Weinberg,[17] thermal desorption spectra were obtained with heating rates varying from 0.8 to 190 K s^{-1}. Representative thermal desorption spectra (a) and temperature profiles (b) are shown in Fig. 6. Clearly, the temperature profiles are very nearly linear. Using these (and other similar) thermal desorption spectra, Arrhenius plots were constructed, allowing an evaluation of the kinetic parameters as a function of coverage. The results are displayed in Fig. 7 and are discussed in detail elsewhere.[4]

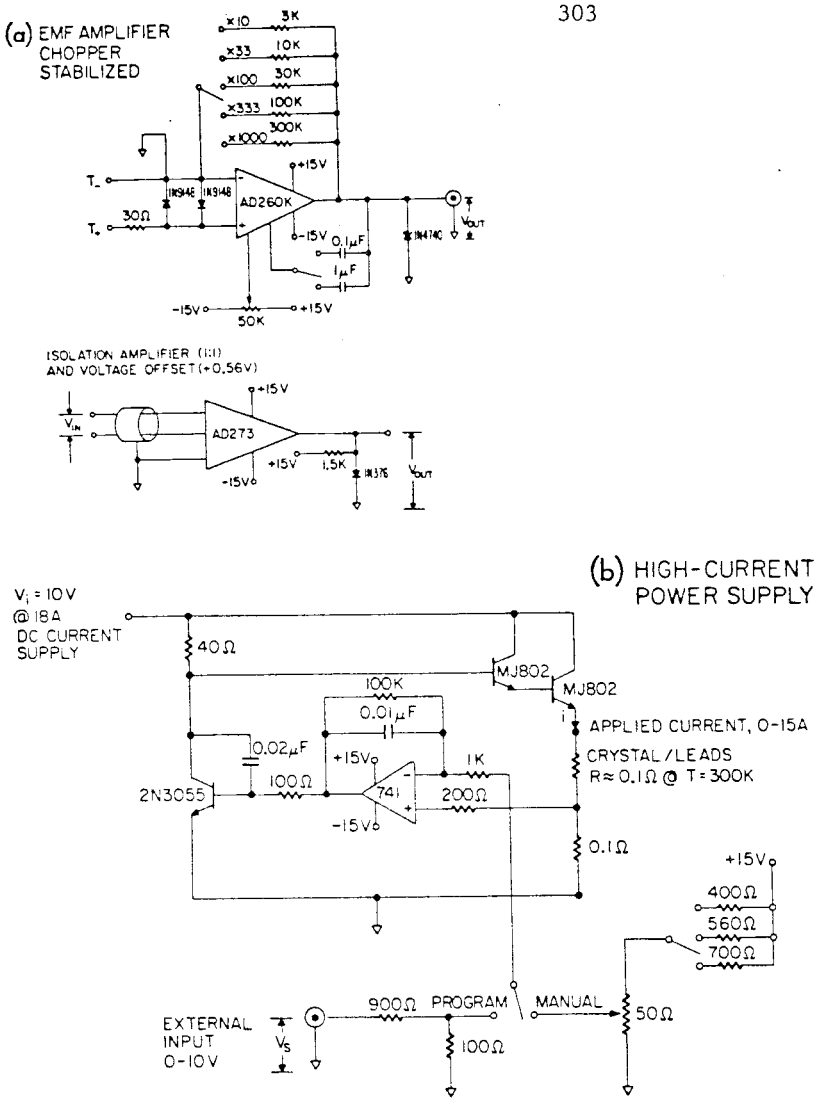

FIG. 4. Schematic diagrams for: (a) thermocouple EMF amplifier; and (b) programmable high-current power supply.

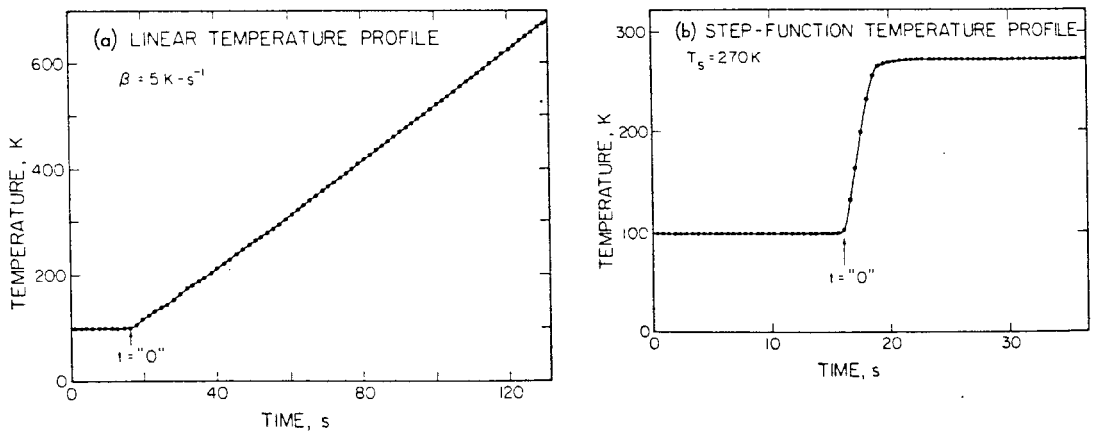

FIG. 5. Temperature profiles produced by the use of the control system shown in Fig. 1(a): (a) temperature ramp mode, heating rate of 5 K s^{-1}; and (b) constant temperature mode adjusted to approximate a step-function change in temperature with a set point of 270 K.

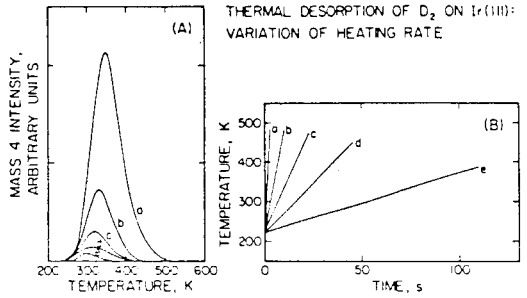

FIG. 6. Thermal desorption spectra of D_2 from Ir(111): (a) desorption spectra, and (b) corresponding temperature profiles. The heating rates are (a) 63, (b) 18, (c) 10, (d) 5.1, and (e) 1.5 K s^{-1}. The initial fractional coverage is 0.15.

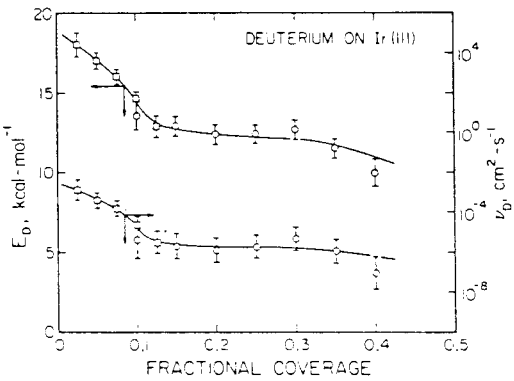

FIG. 7. Activation energy (E_d) and preexponential factor (ν_d) of the desorption rate coefficient for D_2 desorption from Ir(111) as a function of fractional surface coverage.[4] Initial fractional coverages are 0.15 (squares) and 0.47 (circles).

ACKNOWLEDGMENT

This research was supported by the National Science Foundation under Grant No. CHE82-06487.

[1]P. Feulner and D. Menzel, J. Vac. Sci. Technol. **17**, 662 (1980).
[2]H. A. Engelhardt, P. Feulner, H. Pfnür, and D. Menzel, J. Phys. E **10**, 1133 (1977).
[3]J. L. Taylor and W. H. Weinberg, J. Vac. Sci. Technol. **15**, 1811 (1978).
[4]J. R. Engstrom and W. H. Weinberg (to be published).
[5]Since the materials of interest (the crystal and the wire leads) possess similar thermal and electrical properties (i.e., resistivities), the dominant factor affecting the rate of heat transfer is the geometrical configuration of the crystal/wire leads circuit. Consequently, the crystal can be approximated as a constant temperature bath, due to its low electrical and thermal resistance resulting from its large axial cross-sectional area in comparison to the wire leads.
[6]Equation (2) is exact if one assumes that the crystal and support blocks can be represented by constant temperature baths, that all physical (material) constants are independent of temperature, and that there is negligible radiative heat transfer. This can be shown easily by solving the steady-state energy balance for the wire leads, $d^2T_w/dz^2 = i^2R_w/k_wA_wl_w$, and imposing the boundary conditions $T_w|_b = T_b$, $T_w|_c = T$ and $dT_w/dz|_c = 0$.
[7]Equations (3) and (4) can be generalized to systems utilizing other methods of heating the crystal (e.g., electron bombardment), provided the rate of energy input to the crystal can be represented by a term of the form $cf(\theta)$, where c is a constant and f is a function of θ. Furthermore, in non-UHV environments, convective heat transfer can be treated by the addition of a linear term [i.e., $hA_c(T_g - T)$ or $\kappa'\theta_g - \kappa'\theta$], which will result in a modified reciprocal of the cooling time constant ($\kappa + \kappa'$) and an additional load term ($\kappa'\theta_g$).
[8]D. R. Coughanowr and L. B. Koppel, *Process Systems Analysis and Control* (McGraw-Hill, New York, 1965).
[9]Although the analysis presented here is based on analog (continuous) control, while implementation utilizes a digital (discrete) controller element, the approximation involved is reasonable due to the speed of the controller element with respect to the process, i.e., $\tau_m \ll \tau$. For processes where τ_m and τ are of comparable magnitude, sampled-data control system design should be implemented.[10] Transformation of Eq. (8) from the Laplace domain to the z domain and subsequent controller design is straightforward.
[10]W. L. Luyben, *Process Modeling, Simulation, and Control for Chemical Engineers* (McGraw-Hill, New York, 1973).
[11]J. C. Ziegler and N. B. Nichols, Trans. ASME **64**, 759 (1942).
[12]G. H. Cohen and G. A. Coon, Trans. ASME **75**, 827 (1953).
[13]In this case, Eq. (3) is solved for the pseudo-steady-state load signal (I) using $dT/dt = \beta$.
[14]D. R. Sandstrom and S. P. Withrow, J. Vac. Sci. Technol. **14**, 748 (1977).
[15]H. Pfnür, P. Feulner, H. A. Engelhardt, and D. Menzel, Chem. Phys. Lett. **59**, 481 (1978).
[16]H. A. Engelhardt and D. Menzel, Surf. Sci. **57**, 591 (1976).
[17]J. L. Taylor and W. H. Weinberg, Surf. Sci. **78**, 259 (1978).

APPENDIX B

Spatial Temperature Distribution of the Crystal Surface

The physical configuration utilized in the experiments described here is depicted to approximate scale in Fig. 1. The single crystal, cut and polished into a thin circular disk (approximately 0.5 mm in thickness), is spotwelded to two 15 mil diameter Ta wire leads which are mounted on a precision manipulator. Heating is effected by passing current through the wire leads/crystal circuit, while cooling is accomplished by conduction through the wire leads to support blocks which are in thermal contact with a reservoir of flowing liquid nitrogen. Since the wire leads are of much smaller cross sectional area than the crystal, nearly all of the joule heating ($\propto i^2R$) occurs in the wire leads. Thus, internal heating of the crystal by the applied current can be neglected. Furthermore, for the temperatures of interest ($100 \lesssim T \lesssim 1000$ K), cooling or heating by radiation can be neglected. Finally, since the support blocks approximate a constant temperature bath due to their large "thermal inertia", the steady-state solutions of the governing heat conduction equations predict a parabolic temperature profile across the wire leads and a constant temperature profile across the crystal. This temperature profile is shown in Fig. 1.

We shall be interested in periodic, time-dependent solutions superposed on the steady-state solutions of the governing heat conduction equations. As a first approximation, we shall separate the solution to the overall problem into the two following issues: the temperature profile across the wire leads, and the temperature profile across the crystal.

The temperature profile across the wire leads can be assumed to be one-dimensional. The governing energy balance is given by

$$\frac{1}{\tau_w}\frac{\partial^2 T(z,t)}{\partial z^2} + q(t) = \frac{\partial T(z,t)}{\partial t},$$

where $\tau_w \equiv l^2/\kappa_w$ is the radial time constant of the wire, l is the length of the wire leads, κ_w is the thermal diffusivity, $z \equiv x/l$ is the dimensionless length, $q(t) = i(t)^2R/\rho\hat{c}Al$ is the power input, i(t) is the applied current, R is the resistance, ρ is the mass density, $\hat{c}$ is the specific heat, and A is the cross sectional area. We assume that the deviation from steady-state is sufficiently small such that the resistance is approximately constant. A useful approximation is to fix the endpoint temperatures as constant, i.e. $T|_{z=0} = T_b$ (the support block temperature) and $T|_{z=1} = T_c$ (the crystal temperature). This is reasonable if the amplitude of the modulation of the crystal temperature is small compared to the total temperature gradient across the wire leads $(T_c - T_b)$, which is always the case. After nondimensionalizing the temperature, we have

$$\frac{1}{\tau_w}\frac{\partial^2 T^\dagger(z,t)}{\partial z^2} + q'(t) = \frac{\partial T^\dagger(z,t)}{\partial t},$$

where $T^\dagger = (T - T_b)/(T_c - T_b)$ and $q' = q/(T_c - T_b)$. We seek solutions of the form

$$T^\dagger(z,t) = \mathrm{Re}[u(z)e^{i\omega t}] + T_s^\dagger(z),$$

given that $q'(t) = \mathrm{Re}[Ie^{i\omega t}] + q_s'$, where ω is the radial frequency, and I is proportional to the modulated power input. The 's' subscripts designate the steady-state values.

The steady-state solution follows directly by applying the boundary conditions $T_s^\dagger|_{z=0} = 0$, $T_s^\dagger|_{z=1} = 1$, and $[\partial T_s^\dagger/\partial z]_{z=1} = 0$. These three boundary conditions arise by considering q_s' to be a variable. Specifically, we find $T_s^\dagger(z) = 2z[1 - (z/2)]$, and $q_s' = 2/\tau_w$. The time-dependent solution is found by solving

$$\frac{1}{\tau_w}\frac{\partial^2 u(z)}{\partial z^2} + I = i\omega u(z)$$

and applying the boundary conditions $u|_{z=0,1} = 0$. We find

$$u(z) = \frac{I\tau_w}{\beta^2}\left\{1 - \frac{2\sinh(\beta/2)}{\sinh(\beta)}\cosh[\beta(z - 1/2)]\right\},$$

where $\beta = (\omega\tau_w)^{1/2}\exp(i\pi/4)$. Of special interest is the flux at the crystal edge (i.e. z = 1), since this will represent the power input to the crystal. Differentiating, we find

$$-\frac{\partial u}{\partial z}\bigg|_{z=1} = 2I\tau_w\frac{[\sinh(\beta/2)]^2}{\beta\sinh(\beta)} \qquad \text{(B.1)}$$

and

$$\lim_{\beta \to 0}\left\{-\frac{\partial u}{\partial z}\bigg|_{z=1}\right\} = \frac{I\tau_w}{2}.$$

Thus, for small $\omega\tau_w$, the flux at the crystal will be in phase and proportional to the square of the applied current.

For the materials used here, we estimate a time constant for the wire leads of approximately 0.1 s. Using a radial frequency of 10 rad-s^{-1}, we find the phase difference between the square of the applied current and the flux at the crystal to be $\lesssim$0.1 rad. Thus, for the frequencies of interest here ($\lesssim$10 rad-s^{-1}), the phase of the power input to the crystal is approximated well by the phase of the square of the applied current. Similarly, the amplitude ratio of the flux at the crystal to the square of the applied current is essentially constant for the frequencies of interest.

As stated above, the steady-state solution for the crystal temperature is given by a constant. Thus, the time-dependent solution is found by solving

$$\kappa_c \nabla^2 T'(r,\theta,t) = \partial T'(r,\theta,t)/\partial t \ ,$$

where $T' \equiv T - T_c$ is the deviation from the steady-state temperature, and κ_c is the thermal diffusivity of the crystal. We assume solutions of the form

$$T'(r,\theta,t) = \mathrm{Re}[u(r,\theta)e^{i\omega t}] \ ,$$

where $u(r,\theta)$ will be complex in general. Consequently,

$$\frac{1}{\tau_c} \nabla'^2 u(r',\theta) = i\omega u(r',\theta) \ ,$$

where $\tau_c \equiv r_o^2/\kappa_c$ is the radial time constant of the crystal , r_o is the radius of the crystal, and $r' \equiv r/r_o$ is the dimensionless radial coordinate. We apply the following boundary conditions: symmetry about $\theta = 0, -\pi$; $[\partial u/\partial\theta]_{\theta=\pm\pi/2} = 0$; and the solution is bounded at $r = 0$. Solving the above equation by separation of variables, we find

$$u(r',\theta) = b_o J_o(\alpha r') + \sum_{n=1}^{\infty} b_n J_{2n}(\alpha r')\cos(2\alpha\theta) \ ,$$

where $\alpha = (\omega\tau_c)^{1/2}\exp(-i\pi/4)$, the b_n's are constants to be determined, and the J_n are Bessel functions of the first kind of integral order. The final boundary condition is given by a flux condition at $r' = 1$:

$$\left.\frac{\partial u}{\partial r'}\right|_{r'=1} = F(\theta) = \begin{cases} F \ , & 0 \le \theta \le \psi \\ 0 \ , & \psi \le \theta \le \pi/2 \end{cases} ,$$

where F is real, and we need specify only one quadrant due to the previously applied symmetry conditions. Thus, the quantity $2r_o\sin\psi$ represents the "area" of contact with one wire lead. Making use of the orthogonality of the eigenfunctions $\cos(2\alpha\theta)$, we find the complete solution is given by

$$u(r',\theta) = \frac{2F}{\pi}\left\{\frac{-\psi}{\alpha J_1(\alpha)}J_o(\alpha r') + \sum_{n=1}^{\infty}\frac{\sin(2n\psi)}{2n[\alpha J_{2n}'(\alpha)]}J_{2n}(\alpha r')\cos(2\alpha\theta)\right\}.$$

Two specific temperatures are of interest, namely the temperature at r' = 0 (i.e. the approximate, measured temperature), and the spatially averaged temperature. For the spatially averaged temperature $\bar{u}$, we find

$$\bar{u}e^{i\omega t} = \frac{8F\psi}{\pi(\omega\tau_c)}\exp[i(\omega t - \pi/2)]. \tag{B.2}$$

For the temperature at the origin, where $u_o \equiv u(0,\theta)$, we find

$$u_o e^{i\omega t} = \frac{4F\psi}{\pi[\alpha J_1(\alpha)]}\exp[i(\omega t - \pi)]. \tag{B.3}$$

In the limit of low frequencies, $\alpha \to 0$, we find

$$\lim_{\alpha \to 0} u_o e^{i\omega t} = \frac{8F\psi}{\pi(\omega\tau_c)}\exp[i(\omega t - \pi/2)] = \bar{u}e^{i\omega t}.$$

Thus, as expected, the two temperatures are equivalent at sufficiently low frequencies. Finally, we can relate these two temperatures to the periodically varied flux into the crystal. The total flux is given by

$$e^{i\omega t}\int_0^{2\pi} F(\theta)d\theta = 4F\psi e^{i\omega t}. \tag{B.4}$$

From Eqs. (B.2) and (B.4), we see that there will be a constant phase lag of $\pi/2$ between the spatially averaged temperature and the power input (i.e. the flux at r' = 1). In addition, the amplitude of the spatially averaged temperature will be inversely proportional to the frequency at constant power input.

To conclude, the above analysis can be summarized as follows:

1. For the frequencies of interest ($\omega \lesssim 10$ rad$-s^{-1}$), the power input to the crystal is approximated by the square of the applied current [see Eq. (B.1)].

2. The spatially averaged temperature will have a constant phase lag of $\pi/2$ with respect to the power input, and its amplitude will be inversely proportional to the frequency [see Eqs. (B.2) and (B.4)].

3. The spatially averaged temperature and the approximate, measured temperature can be related via Eqs. (B.2) and (B.3). Specifically,

$$u_o/\bar{u} = \alpha/2J_1(\alpha)\,, \tag{B.5}$$

where $\alpha = (\omega\tau_c)^{1/2}\exp(-i\pi/4)$. The amplitude ratio and phase response follow directly by taking the modulus and argument of the complex quantity given by Eq. (B.5).

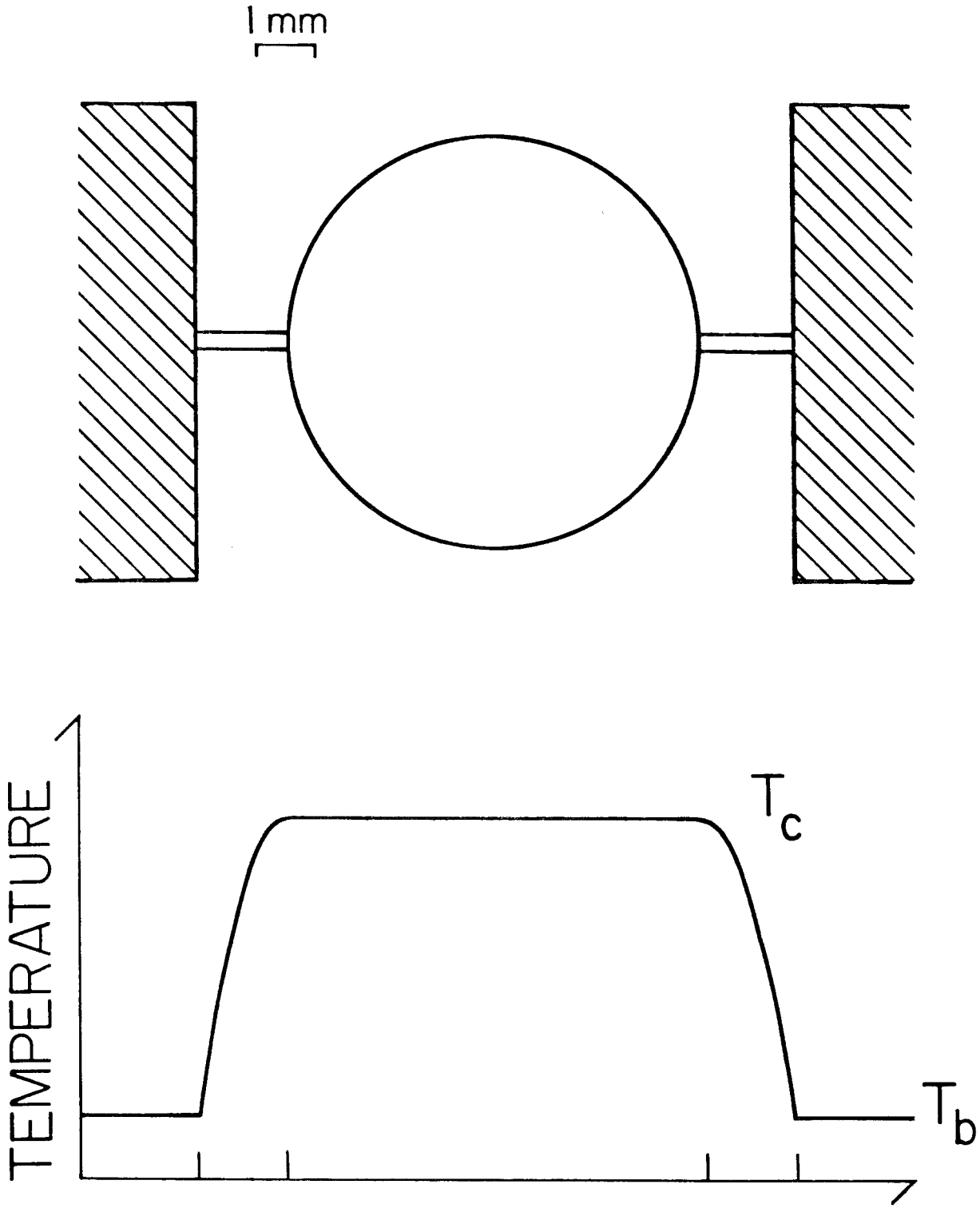

Figure 1. Physical configuration of the crystal and support assembly, and the predicted steady-state temperature profile.

APPENDIX C

Numerical Model Describing the Oxidation of CO on Pt(110)-(1x2)

For the reaction conditions described above in Chapter 3, we consider four elementary reactions to be necessary and sufficient to describe the overall rate of reaction: (1) the molecular adsorption of CO; (2) the dissociative adsorption of oxygen; (3) the desorption of CO; and (4) the surface reaction between CO admolecules and oxygen adatoms to form CO_2. Since the CO_2 reaction product is not trapped on the surface **(1)**, we need not consider a seperate desorption step for CO_2. We shall first describe the rate expressions for the first three elementary reactions (*i.e.*, those required for the calculation of the reactant coverages), as deduced by independent measurements.

The adsorption of CO on Pt(110)-(1x2) has been observed to follow first-order precursor-mediated adsorption kinetics with an initial probability of adsorption of 0.7–1.0 **(2-5)**. This behavior was confirmed by our experimental measurements (see Chapter 3). On a Pt(111) surface, high coverages of oxygen adatoms have been observed to have a negligible effect on the probability of adsorption of CO **(6)**. On a Ir(110)-(1x2) surface, the probability of adsorption of CO was also found to be independent of oxygen adatom coverage **(7)**. Thus, for the rate expression describing the adsorption of CO, we utilize the empirical functional form given by Comrie and Lambert **(4)** and confirmed by our measurements here

$$r_a^{CO} = (F_{CO}/n_s) S_0^{CO} (1 - \theta_{CO}^{\xi}) \ , \qquad \text{(C.1)}$$

where F_{CO} is the flux of CO molecules at the surface, n_s is the concentration of surface atoms where, in this case, $n_s = 0.92 \times 10^{15}$ atoms-cm^{-2}, S_0^{CO} is the initial probability of adsorption, measured here to be unity, $\theta_{CO} \equiv n_{CO}/n_s$ where n_{CO} is the CO admolecule concentration, and ξ is a surface mobility parameter **(8)**. In this case, $\xi = 4$. The saturation fractional coverage of CO admolecules has been

measured to be unity on Pt(110)-(1x2) **(3)**. Alternate functional forms describing the first-order precursor kinetics could be utilized, with only negligible changes in the final results occurring.

The dissociative adsorption of oxygen on Pt(110)-(1x2) has been found to be best described by second-order Langmuir kinetics **(9-11)**, with an initial probability of adsorption reported to be between 0.3 and 0.5 **(10-12)**. Adsorbed CO is known to affect strongly the probability of adsorption of oxygen **(1)**. Thus, for the rate expressions describing the dissociative adsorption of oxygen, we assume

$$r_a^{\mathrm{O}} = 2(F_{\mathrm{O}_2}/n_s)S_0^{\mathrm{O}_2}(1 - C_{\mathrm{CO}}\theta_{\mathrm{CO}} - C_{\mathrm{O}}\theta_{\mathrm{O}})^2 \ , \qquad \text{(C.2)}$$

where F_{O_2} is the flux of oxygen molecules at the surface, $S_0^{\mathrm{O}_2}$ is the initial probability of adsorption, where the optimal value was found to be 0.5 (following several self-consistency checks, see below), $\theta_{\mathrm{O}} \equiv n_{\mathrm{O}}/n_s$ where n_{O} is the oxygen adatom concentration, and C_{CO} and C_{O} are constants. For a Pd(111) surface, the formation of an ordered overlayer of CO admolecules at $\theta_{\mathrm{CO}} = \frac{1}{3}$ prevents the dissociative adsorption of oxygen **(1)**. On Pt(110)-(1x2), CO forms ordered phases at surface coverages of $\theta_{\mathrm{CO}} = 0.5$ [giving a (1x1) LEED pattern], and $\theta_{\mathrm{CO}} = 1.0$ [giving a (2x1)p1g1 LEED pattern]**(3)**. We would expect oxygen adsorption to be negligible for CO coverages above $\theta_{CO} \geq 0.5$ on Pt(110)-(1x2). Indeed, this proposition is supported by the experimental observation of a (1x1) LEED pattern (*i.e.*, $\theta_{\mathrm{CO}} = 0.5$), concomitant to a complete extinguishing of the rate of production of CO_2 over the Pt(110)-(1x2) surface (see Chapter 3). Thus, we choose a value for the constant C_{CO} of 2.0. Finally, we choose a value for the constant C_{O} of 2.5, since the saturation value for the fractional surface coverage of oxygen adatoms on Pt(110)-(1x2) has been found to be $\theta_{\mathrm{O}}^{sat} = 0.4$, or $n_{\mathrm{O}}^{sat} \simeq 3.5 \times 10^{14}$ atoms-cm^{-2} **(9,11)**

Studies of the desorption of CO from the clean Pt(110)-(1x2) surface (*i.e.*, no oxygen adatoms present) have demonstrated that the kinetic parameters describing the desorption reaction vary with coverage **(2-4)**. This behavior is supported by the data presented above in Chapter 3 (see Fig. 4). Evidence exists also for repulsive

interactions between CO admolecules and oxygen adatoms **(7,13,14)**, which are manifest in a reduction of the activation energy for desorption of CO **(7)**. In particular, on an Ir(110)-(1x2) surface **(7)**, the kinetic parameters describing the desorption reaction of CO are described well by expressions given by

$$r_d^{CO} = \theta_{CO} k_d^{(1)}(\theta_{CO}, \theta_O) exp[-E_d(\theta_{CO}, \theta_O)/k_B T], \qquad (C.3)$$

where

$$k_d^{(1)}(\theta_{CO}, \theta_O) = k_d^0 exp[-\alpha_{CO}\theta_{CO} - \alpha_O \theta_O^{1/2}],$$

and

$$E_d(\theta_{CO}, \theta_O) = E_d^0 - \beta_{CO}\theta_{CO} - \beta_O \theta_O^{1/2}.$$

Here $k_d^{(1)}(\theta_{CO}, \theta_O)$ is a coverage-dependent preexponential factor, and $E_d(\theta_{CO}, \theta_O)$ is a coverage-dependent activation energy. The linear dependence of the kinetic parameters on the fractional coverage of CO on a Pt(110)-(1x2) surface is supported by independent measurements obtained elsewhere **(3)** and above in Chapter 3 (see Fig. 4). Specific values chosen for the kinetic parameters were the following: $k_d^0 = 3$ x 10^{14} s^{-1}, $\alpha_{CO} = 7.0$, $E_d^0 = 34$ kcal-mol^{-1}, and $\beta_{CO} = 16$ kcal-mol^{-1}. Utilizing this model, we find that the predicted values of the kinetic parameters and the measured values are within experimental uncertainty (see Fig. 4 of Chapter 3). The values chosen for the parameters describing the oxygen coverage dependence have been extrapolated from those obtained on the Ir(110)-(1x2) surface **(7)**. Specifically, the parmeters have been scaled to account for the different values of the saturation coverages of oxygen on the two surfaces [$\theta_O^{sat} = 0.4$ on Pt(110)-(1x2) and $\theta_O^{sat} = 1.0$ on Ir(110)-(1x2) **(15)**]. The optimal values for Pt(110)-(1x2) were found to be (following self-consistency checks, see below) $\alpha_O = 16$ and $\beta_O = 17$ kcal-mol^{-1}.

Reaction rate measurements, combined with Eqs. (C.1)–(C.3), can be used to calculate the fractional coverages of the adsorbed species. In particular, the mass balances for the adsorbed species at fixed reactant partial pressures are given by

$$d\theta_O/dt = r_a^O(\theta_O, \theta_{CO}) - r_r(T) \ , \qquad (C.4)$$

and

$$d\theta_{CO}/dt = r_a^{CO}(\theta_{CO}) - r_d^{CO}(\theta_{CO}, \theta_O) - r_r(T) \qquad (C.5)$$

where $r_r(T)$ is the *measured* rate of reaction (*i.e* production of CO_2). At steady-state, the time derivative terms are zero, and we may solve the above two equations for the surface coverages (θ_O, θ_{CO}) at a particular temperature. A simplex method **(16)** was used to calculate the steady-state values for the adsorbate concentrations. Specifically, the calculation routine for a specific set of reaction conditions (P_{O_2},P_{CO}) was initiated at a datum point corresponding to a negligible coverage of CO (*i.e.*, T $\geq$ 500 K for the reaction conditions considered in Chapter 3). This permits an accurate estimation of the oxygen coverage to be made [*i.e.*, Eq. (C.4) becomes a quadratic equation in θ_O]. Coupled with an initial estimation of θ_{CO} $\simeq$ 0, both the convergence of the simplex routine and the resulting adsorbate concentrations are obtained rapidly. The calculation is continued by moving to the next datum point (a temperature difference of approximately 1 K) and utilizing the steady-state adsorbate concentrations obtained at the previous point to provide the initial input. This procedure results in smoothly varying adsorbate concentrations and represents accurately the particular reaction rate branch corresponding to the data shown in Fig. 7 of Chapter 3. Thus, this procedure was followed in the construction of Fig. 8. The adsorbate concentrations calculated for the reaction conditions given in Fig. 7 of Chapter 3 are shown in Fig. 1 of this appendix.

Finally, in order to provide a self-consistency check for the numerical model employed here, the calculated surface coverages were used to calculate the rate parameters describing the surface reaction CO(a) + O(a) $\rightarrow$ CO_2(g). In order to do this an implicit coverage dependence [*i.e.*, $x(\theta_1, \theta_2)$, see Chapters 2 and 3] must be chosen. Specifically, it was assumed that the rate of the surface reaction could be expressed as

$$r_r(\theta_O, \theta_{CO}, T) = n_s \theta_{CO} \theta_O k_r^{(2)} exp(-E_r/k_B T), \qquad (C.6)$$

where $k_r^{(2)}$ is a second-order reaction rate preexponential factor taken to be a con-

stant, and E_r is the activation energy of the reaction, taken also to be a constant. The implicit coverage dependence of the reaction, $\theta_{CO}\theta_O$, is expected to hold for situations for which the coverages of the reactants are relatively low. These assumptions (low coverages and coverage-independent rate parameters) are expected to be reasonable for the case $P_{O_2}/P_{CO} = 1.8$ at the temperatures represented by the data shown in Fig. 7 of Chapter 3. Utilizing reaction rate measurements for the case $P_{O_2}/P_{CO} = 1.8$, we calculated the steady-state coverages for temperatures between 400 and 475 K, and the quantity $r_r/\theta_{CO}\theta_O$ was plotted in Arrhenius fashion as a function of the reciprocal temperature. The resulting data were well represented by a line described by values of the kinetic parameters given by $k_r^{(2)} = 3.3 \times 10^{-4}$ cm^2-s^{-1} and $E_r = 22$ kcal-mol^{-1}. In comparison, the average *measured* values **(17)** for these reaction conditions ($P_{O_2}/P_{CO} = 1.8$ and T = 412–450 K) were found to be $k_r^{(2)} = 1.0 \times 10^{-3\pm0.7}$ cm^2-s^{-1} $E_r = 21.4 \pm 1$ kcal-mol^{-1}. The excellent agreement between the measured values and the calculated values lends support to the quantitative accuracy of the numerical model employed here to describe the oxidation of CO over the Pt(110)-(1x2) surface.

References

1. T. Engel and G. Ertl, Advan. Catal. **28**, 1 (1979).
2. J. A. Fair and R. J. Madix, J. Chem. Phys. **73**, 3480 (1980).
3. T. E. Jackman, J. A. Davies, D. P. Jackson, W. N. Unertl and P. R. Norton, Surface Sci. **120**, 389 (1982).
4. C. M. Comrie and R. M. Lambert, J. Chem. Soc. Faraday Trans. I **72**, 325 (1975).
5. R. W. McCabe and L. D. Schmidt, Surface Sci. **60**, 85 (1976).
6. C. T. Campbell, G. Ertl, H. Kuipers and J. Segner, J. Chem. Phys. **73**, 5862 (1980).
7. J. L. Taylor, D. E. Ibbotson and W. H. Weinberg, Surface Sci. **90**, 37 (1979).
8. R. P. H. Gasser and E. B. Smith, Chem. Phys. Letters **1**, 457 (1967).
9. M. Wilf and P. T. Dawson, Surface Sci. **65**, 399 (1977).
10. V. S. Sundaram and P. H. Dawson, Surface Sci. **146**, L593 (1984).
11. N. Freyer, M. Kiskinova, G. Pirug and H. P. Bonzel, Surface Sci. **166**, 206 (1986).
12. R. Ducros and R. P. Merrill, Surface Sci. **55**, 227 (1976).
13. G. E. Thomas and W. H. Weinberg, J. Chem. Phys. **70**, 954 (1979).
14. H. Conrad, G. Ertl and J. Küppers, Surface Sci. **76**, 323 (1978).
15. J. L. Taylor, D. E. Ibbotson and W. H. Weinberg, Surface Sci. **79**, 349 (1979).
16. J. A. Nedler and R. Mead, Computer J. **7**, 308 (1965).
17. Actually, only the activation energies were measured independent of any knowledge of the reactant coverages.

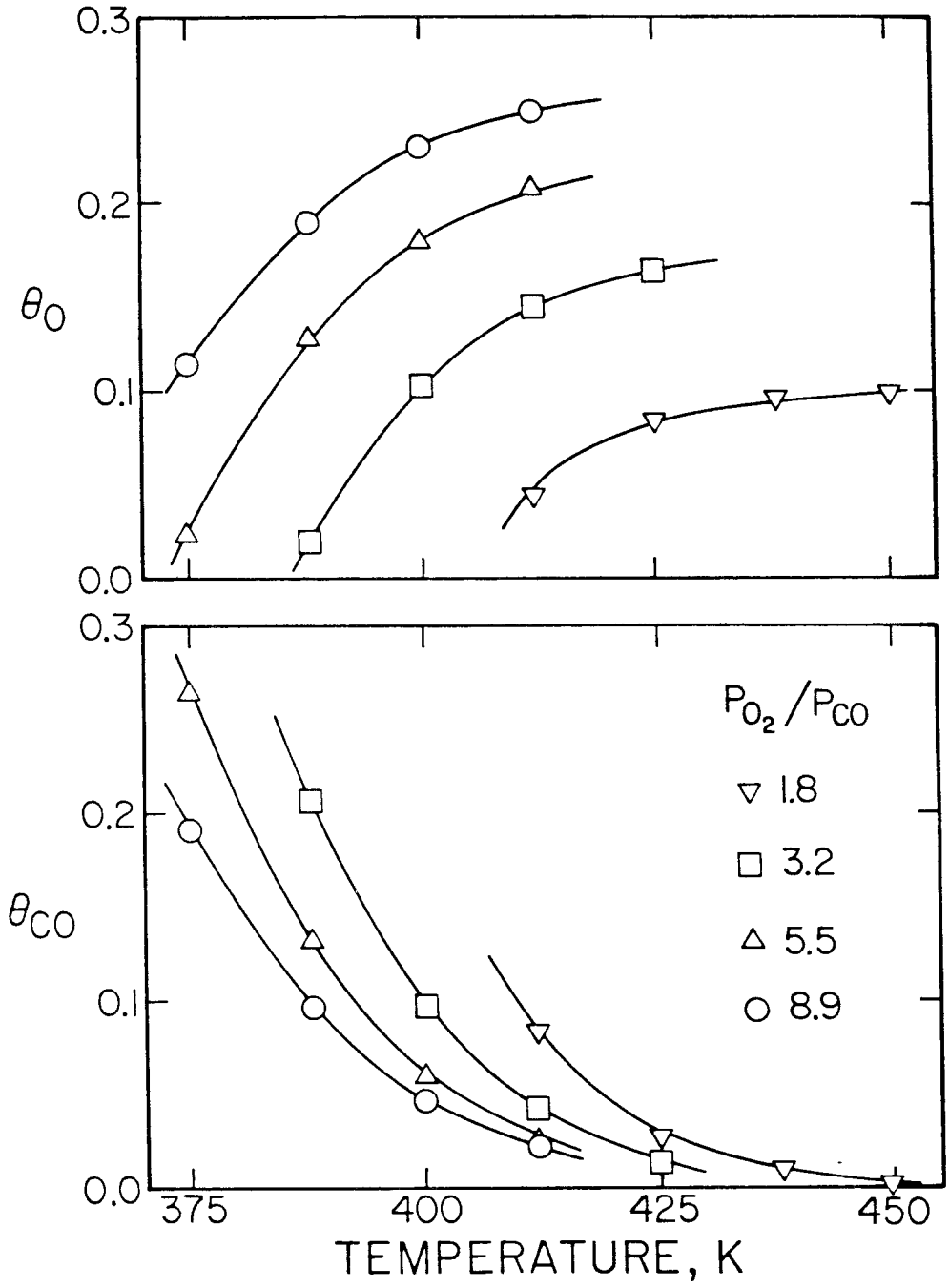

Figure 1.

The calculated adsorbate concentrations corresponding to the reaction conditions given in Fig. 7 of Chapter 3. Note that $\theta_O = 0.4$ and $\theta_{CO} = 1.0$ represent the respective saturation values on the Pt(110)-(1x2) surface.

APPENDIX D

The Reaction of Saturated and Unsaturated Hydrocarbons with the (110)-(1x2) and (111) Surfaces of Iridium

[The text of Appendix D consists of an article coauthored with P. D. Szuromi and W. H. Weinberg, which has appeared in *The Journal of Chemical Physics* **80**, 508 (1984).]

The reaction of saturated and unsaturated hydrocarbons with the (110)-(1×2) and (111) surfaces of iridium[a)]

P. D. Szuromi,[b)] J. R. Engstrom, and W. H. Weinberg
Division of Chemistry and Chemical Engineering, California Institute of Technology, Pasadena, California 91125

(Received 19 July 1983; accepted 16 September 1983)

The dehydrogenation of propane, cyclopropane, propylene, propyne, and allene has been investigated on the reconstructed Ir(110)-(1×2) surface. Annealing adlayers of these hydrocarbons (at low coverages) leads to the formation of surface hydrogen and hydrocarbon fragments of approximate stoichiometry C_3H_2. The importance of the β_2' adsite of hydrogen on this surface of Ir has been demonstrated further by poisoning studies with hydrogen, CO and surface carbon. The Ir(111) surface was found to dehydrogenate propylene but neither propane nor cyclopropane under the same reaction conditions, indicating a strong effect of surface geometry for the C–H bond activation of alkanes.

I. INTRODUCTION

A fundamental study of the interaction of hydrocarbon molecules with well-characterized transition metal surfaces is important as a means of gaining insight into the more general mechanisms of various reactions of hydrocarbons on transition metal catalyst surfaces. The relationship of particular adsites to various reaction pathways can be understood better by studying the reactions on different orientations of single crystals. In turn, if hydrocarbons which vary widely in electronic and geometric structure dehydrogenate in a very similar manner on a surface, then the presence of a particularly reactive adsite on that surface is implicated.

The adsorption and decomposition (dehydrogenation) of ethane, propane, cyclopropane, isobutane, and neopentane have been studied on the reconstructed Ir(110)-(1×2) surface primarily by thermal desorption mass spectrometry (TDMS).[1-3] Dynamic low-energy electron diffraction (LEED) calculations indicate that the clean surface reconstructs to form (111) microfacets which are three atomic rows in width, and which are inclined at an angle of 109.4° with respect to one another.[4] While previous studies of the interaction of saturated hydrocarbons with other single crystalline surfaces of group VIII metals under UHV conditions have observed generally nondissociative chemisorption,[5-7] the adsorption of alkanes on the Ir(110)-(1×2) surface is dissociative even at low temperatures ($\lesssim$ 130 K) and leads to dehydrogenation due to a particularly reactive (β_2') adsite.[1-3]

Here the interaction of cyclopropane and propane with Ir(110)-(1×2) is compared with that of three unsaturated hydrocarbons which also contain three carbon atoms, namely, propylene, propyne, and allene. On the Pt(111) surface, the dehydrogenation of a number of alkenes, including propylene, was found to vary markedly with the particular hydrocarbon molecule.[8] It will be shown that despite the wide variation in electronic and geometric structure of these five hydrocarbons, their dehydrogenation in the presence of vacant β_2' adsites is remarkably similar. The importance of this adsite will be demonstrated both by its selective poisoning on the Ir(110)-(1×2) surface and by comparison with the close-packed Ir(111) surface. In both cases, the absence of the β_2' adsite causes the dehydrogenation of the hydrocarbons to be correlated to the geometric and electronic structure of the individual adsorbates. This is a further indication that the unusual ability of the Ir(110)-(1×2) surface to activate C–H bonds in alkanes is primarily either a geometric effect, or an electronic effect induced by its particular surface geometry.

II. EXPERIMENTAL PROCEDURES

The experiments were performed in an ion-pumped stainless steel bell jar which has been described in detail previously.[9] The base pressure of the bell jar was below 4×10^{-11} Torr of reactive contaminants. The hydrocarbon exposures were carried out with a directional beam doser consisting of a multichannel array of capillaries.[10] During dosing, the crystal was positioned ~3 mm from the face of the doser. This provides a beam pressure-to-background pressure ratio of over 100:1. The unit of exposure that is employed for the beam doser is the Torr s and refers to the product of the time of exposure and the pressure in the storage bulb of the doser. The storage bulb supplies gas through a capillary to the doser head leading into the vacuum system. Therefore, the flux of gas into the vacuum system is proportional to the pressure in the storage bulb. For the gases employed in this study, an exposure of 1 L is approximately equivalent to 3 Torr s for propane, 2.5 Torr s for cyclopropane, and 3.5 Torr s for propylene. Although the proportionality factor was not measured for propyne and allene, by assuming reasonable ion gauge sensitivities it is estimated to be between 3 and 4 Torr s. The temperature of adsorption was in all cases between 90 and 100 K. Heating rates between 10 and 15 K s^{-1} were used in performing thermal desorption experiments on this surface. The crystals were cleaned of surface carbon produced by the dehydrogenation of the hydrocarbons in the following manner. The Ir(110)-(1×2) surface was exposed to 1×10^{-7} Torr of O_2 for 2–2.5 min at a

[a] Supported by the National Science Foundation under Grant No. CHE82-06487.

[b] National Science Foundation Predoctoral Fellow.

 0021-9606/84/010508-10$02.10 © 1984 American Institute of Physics

crystal temperature of 900 K, and then heated to 1600 K to desorb the oxygen. The Ir(111) surface was exposed to 5×10^{-8} Torr of O_2 for 2–2.5 min at a crystal temperature of 1100 K, and then heated to 1600 K to desorb the oxygen.

The hydrogen coverage calibration that is used to determine the concentration of dissociatively adsorbed hydrocarbon molecules on the Ir(110)-(1×2) surface involves a titration of the hydrogen with adsorbed oxygen as described previously.[11] The hydrogen concentration on this surface following an exposure of 0.5 L of H_2 is $(7.3\pm1.0)\times10^{14}$ atoms cm^{-2}.

The hydrocarbon gases used in this study were purified by cryogenic distillation, and all gases were checked for purity mass spectrometrically after admission into the ultrahigh vacuum system.

III. EXPERIMENTAL RESULTS

A. Adsorption on Ir(110)-(1×2)

1. Thermal desorption of hydrogen from hydrocarbon overlayers

The dehydrogenation of cyclopropane and propane overlayers on Ir(110)-(1×2) has been studied previously in this laboratory by thermal desorption mass spectrometry.[1-3] Thermal desorption spectra of hydrogen obtained from saturated overlayers of these dissociatively adsorbed hydrocarbons are shown in Figs. 1(A) and 1(B). From the absolute hydrogen coverage calibration obtained for this surface, the absolute coverages of dissociatively adsorbed cyclopropane and propane were found to be $(2.1\pm0.2)\times10^{14}$ and $(1.1\pm0.3)\times10^{14}$ molecules cm^{-2}, respectively. In Fig. 1(C) thermal desorption spectra of hydrogen are shown resulting from an exposure of the clean surface (a) to 0.5 L of hydrogen, which saturates the β_2 adstate, (b) to 2 L of hydrogen, and (c) to 300 L of hydrogen, which saturates both the β_1 and β_2 adstates.[11]

The thermal desorption of hydrogen from dissociatively adsorbed cyclopropane and propane both exhibit features which we have defined previously as the β_2' and γ adstates. The β_2' adstate is similar in intensity and temperature maximum to the β_2 adstate of hydrogen on the clean surface, suggesting that the β_2' adstate arises from the desorption of hydrogen from metallic sites similar to the β_2 adsite. The high temperature γ adstate arises from hydrogen which is more strongly bound than any hydrogen which is adsorbed on the Ir substrate. This implies that the desorption of hydrogen from the γ adstate is limited by the dehydrogenation of hydrocarbon fragments on the surface (i.e., the cleavage of C–H bonds). This is not surprising since the formation of surface fragments by the adsorption of unsaturated hydro-

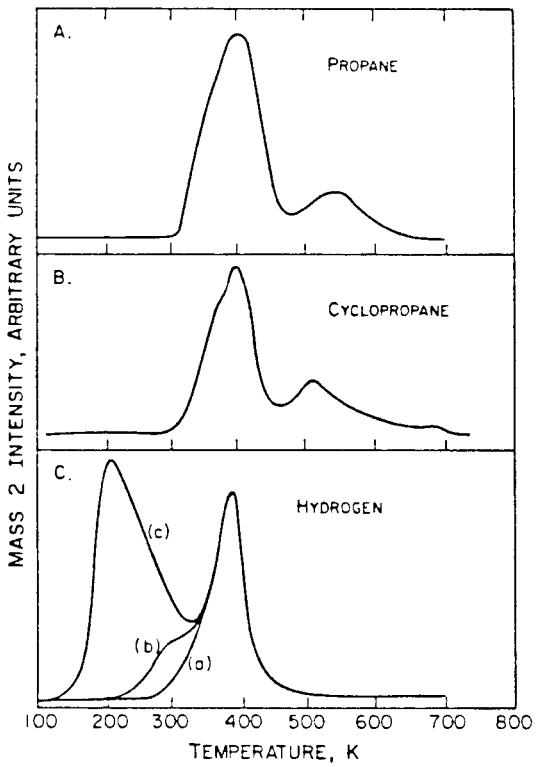

FIG. 1. Thermal desorption of hydrogen resulting from exposure of the Ir(110)-(1×2) surface to: A. 6 Torr s of propane (saturation). B. 4 Torr s of cyclopropane (saturation). C. (a) 0.5 L of hydrogen (saturation of β_2 adstate), (b) 2 L of hydrogen, (c) 300 L of hydrogen (saturation of β_1 and β_2 adstates).

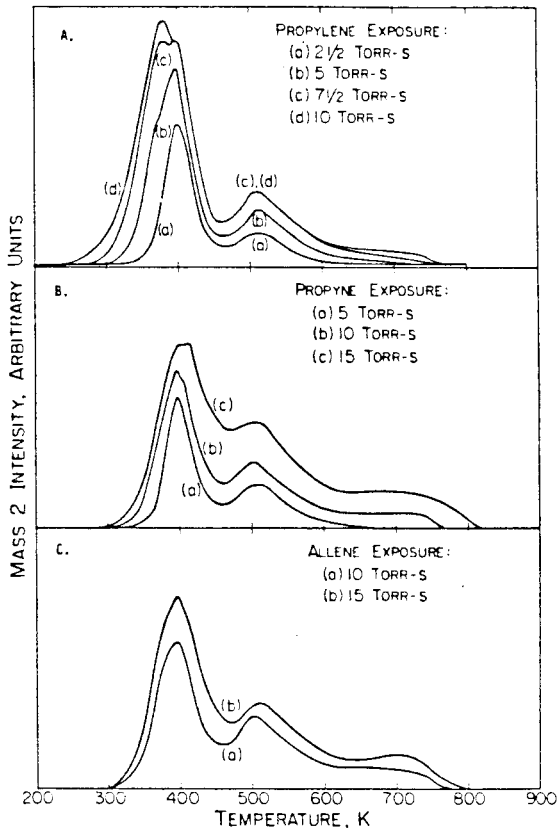

FIG. 2. Thermal desorption of hydrogen as a function of exposure of the Ir(110)-(1×2) surface to: A. Propylene, B. Propyne, C. Aliene. Exposures are shown adjacent to the corresponding spectra.

carbons has been observed spectroscopically on other metals.[12–14] The thermal desorption of hydrogen from a saturated, dissociatively adsorbed adlayer of propane exhibits, in addition, a low temperature shoulder on the β_2' peak, which has been defined as the α adstate.[3] As has been discussed previously, this adstate is due to the dehydrogenation of relatively less stable hydrocarbon fragments on the surface.[3]

It has been shown that the low temperature (α, β_2') and high temperature (γ) adstates for both propane and cyclopropane develop at the same rate with increasing coverage. The quantity R has been defined as the ratio of the peak areas of the α and β_2' adstates to that of the γ adstate.[3] For propane, R has the value 3.2 ± 0.3, while for cyclopropane the value is 2.1 ± 0.3. These ratios indicate that the fragment(s) associated with the γ adstate have an average composition of C_3H_2. The γ adstate is stable if the surface on which it is present is annealed to 400 K for times on the order of one minute, i.e., it is stable in the presence of vacant β_2' adsites.[1] It was also shown that the coverage–exposure relationship for the dissociative adsorption of cyclopropane is linear.[1]

Thermal desorption spectra of hydrogen after exposures of (a) 2.5, (b) 5, (c) 7.5, and (d) 10 Torr s of propylene to the clean surface are shown in Fig. 2(A). The thermal desorption spectra of hydrogen, and hence, of the irreversibly adsorbed adlayer of propylene are observed to saturate after an exposure of 10 Torr s. At low exposures, only two thermal desorption features are observed: one with a peak maximum at 550 K which we define as the γ adstate, and a second with a peak maximum at 400 K which we define as the β_2' adstate. At higher exposures (>2.5 Torr s), a third state, which we define as the α adstate, is observed as a low temperature shoulder of the β_2' adstate. At saturation, the peak maximum of the α adstate is observed at 370 K. Also, the γ adstate shows the development of a high temperature tail which extends to 750 K. The absolute coverage of the *irreversibly* adsorbed propylene adlayer at saturation was determined to be $(2.5 \pm 0.3) \times 10^{14}$ molecules cm^{-2} by the hydrogen coverage calibration.

The formation of α adstates has been observed previously. However, in each case the α adstate has been observed to develop with a commensurate increase in the γ thermal desorption adstate. However, in comparing the thermal desorption spectra of hydrogen from the 7.5 Torr s [Fig. 2(A)(c)] and 10 Torr s [Fig. 2(A)(d)] exposures, it can be seen that the α adstate continues to develop, independently of both the γ and β_2' adstates. Obviously, the ratio R cannot be a constant with respect to coverage, and in fact it increases from ~ 2.0 at low coverages to ~ 2.8 at saturation. However, since the peak shape of the β_2 adstate for hydrogen on the clean Ir(110)-(1×2) surface is well defined, it is possible to make a reasonable separation of the β_2' and α peak areas. In Fig. 3, a comparison is made between the thermal desorption spectra of hydrogen for (a) 10 Torr s of propylene which saturates the irreversibly adsorbed adstates, and (b) 0.5 L of hydrogen which saturates β_2 adstate on the clean surface. If the α and β_2' adstates are separated by comparing the peak to the appropriate β_2 feature of the clean surface (i.e., the area outside the β_2 envelope on the low temperature side is

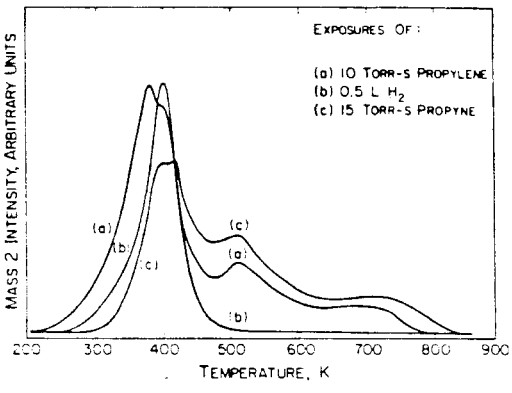

FIG. 3. Thermal desorption of hydrogen resulting from exposure of the Ir(110) surface to: (a) 10 Torr s of propylene. (b) 0.5 L of hydrogen. (c) 15 Torr s of propyne.

the α adstate area), then it can be shown that the ratio of the β_2' peak area to the γ peak area, defined as R', is to within 5% a constant with respect to coverage, and has the value 2.0 ± 0.2. If the α adstates of the thermal desorption spectra of hydrogen from propylene are subtracted, the resulting spectra (for equivalent coverages) appear to be identical (to within $<5\%$) in both peak maximum temperature and intensity to thermal desorption spectra of hydrogen from cyclopropane overlayers.

In Fig. 4, the coverage of the dissociatively adsorbed propylene ($\alpha + \beta_2' + \gamma$), of the β_2' and γ adstates and of the α adstate, as determined by hydrogen thermal desorption, are plotted with respect to propylene exposure. Note that the coverage of dissociatively adsorbed propylene does not vary linearly with respect to propylene exposure. The α adstate exhibits a sinusoidal development, increasing weakly between 0.5 and 5 Torr s, strongly between 5 and 7.5 Torr s, and again weakly between 7.5 and 10 Torr s. This would indicate that β_2' adsites must be nearly saturated by reaction with propylene before the α adstate begins to populate appreciably.

The thermal desorption spectra of hydrogen after adsorption of propyne and allene are shown as a function of

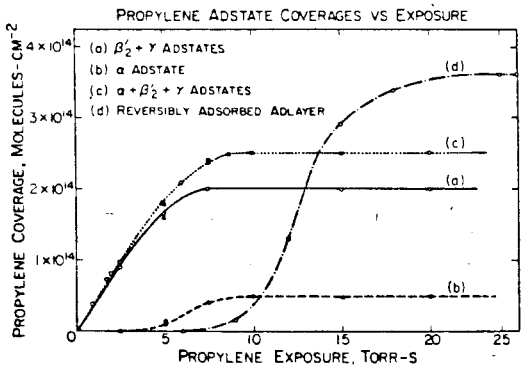

FIG. 4. Surface coverages of propylene adstates as a function of exposure to the Ir(110)-(1×2) surface.

exposure in Figs. 2(B) and 2(C), respectively, with exposures of propyne of (a) 5, (b) 10, and (c) 15 Torr s, and with exposures of allene of (a) 10 and (b) 15 Torr s. Since their thermal desorption spectra were found to be very similar, the results will be discussed together. At low coverages, both exhibit a γ and a β_2' thermal desorption adstate. At exposures up to 10 Torr s, R for these hydrocarbons is 1.0 ± 0.1, and thus the stoichiometry of the γ adstate is approximately C_3H_2.

At high coverages, the β_2' and γ adstates show a broad trailing edge extending to ~ 800 K. This can be observed by comparing Fig. 3(c), 15 Torr s of propyne, which saturates the irreversibly adsorbed adlayer, with Fig. 3(b), 0.5 L of hydrogen, which saturates the β_2 adstate on the clean surface. Note that the intensity of the β_2' peak maximum is not so fully developed at saturation as it had been for propane, cyclopropane, and propylene. Also, note that in this case no low temperature broadening is observed. Beyond an exposure of 10 Torr s, the apparent value of R ceases to remain a constant, falling to 0.75 ± 0.1, or an apparent stoichiometry of $C_3H_{2.3}$. However, it is possible that propyne and allene can be adsorbed at low temperatures and high coverages without dehydrogenation, due to the lack of vacant β_2' adsites. As the temperature of the surface is increased, hydrogen in the β_2' adsites desorbs, making these adsites available. The molecularly adsorbed hydrocarbon can then dehydrogenate, causing the evolution of reaction-limited hydrogen to appear as a high temperature broadening of the β_2' desorption feature. This mechanism also results in the formation of fragments which dehydrogenate in the same temperature regime as the γ adstate. This conjecture is supported by considering the ratio of the area of the β_2' adstate to the area of the γ adstate while including the high temperature broadening of the β_2' adstate. In this case, R maintains a constant value of 1.0 ± 0.1. It appears that additional propyne or allene can adsorb on the surface after the β_2' adsites have been poisoned and that the fragments formed by their partial dehydrogenation have a stoichiometry of $\sim C_3H_2$. The absolute coverages of the irreversibly adsorbed propyne and allene adlayers, as determined by the hydrogen coverage calibration, are $(4.0 \pm 0.4) \times 10^{14}$ and $(3.6 \pm 0.4) \times 10^{14}$ molecules cm^{-2}, respectively.

2. Thermal desorption of molecular hydrocarbons

For each of the hydrocarbon molecules that has been studied, no hydrocarbon other than the one originally adsorbed was observed in the thermal desorption mass spectra. Parent peak spectra for each hydrocarbon adsorbed *molecularly* at saturation coverage are shown in Fig. 5. No desorption peaks of the molecular hydrocarbons were observed above 170 K. For propylene, propyne, and allene, only a single peak structure is observed with desorption maxima at saturation coverage between 115 and 120 K. The coverage–exposure relationship for molecularly adsorbed propylene is shown in Fig. 4(d). Note that almost no propylene is adsorbed molecularly until the *irreversibly* adsorbed adlayer approaches saturation coverage. It has also been shown that cyclopropane and propane exhibit little or no formation of

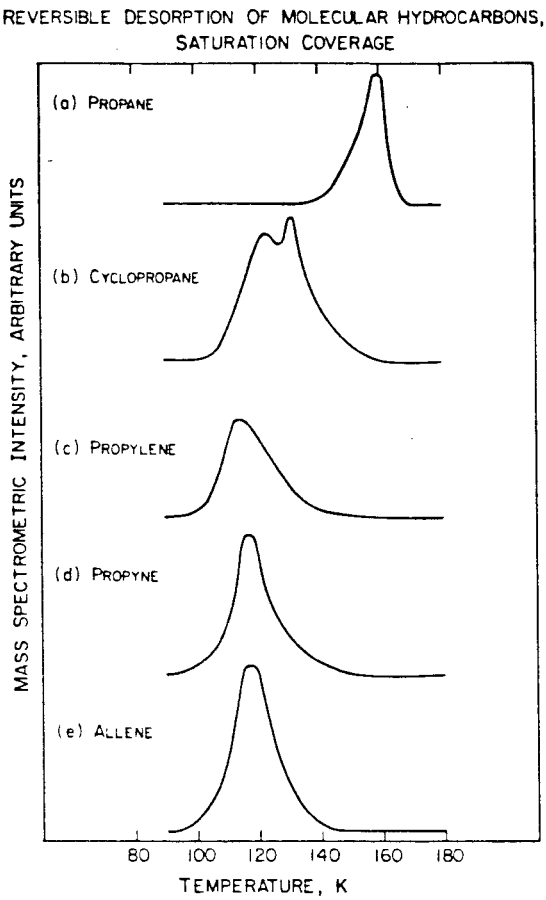

FIG. 5. Thermal desorption spectra of saturated molecular adstates on the Ir(110)-(1 × 2) surface: (a) Propane (mass 43), (b) Cyclopropane (mass 42), (c) Propylene (mass 42), (d) Propyne (mass 40), (e) Allene (mass 40).

the molecular adlayer until saturation of the dissociatively adsorbed adlayer is completed.[1,3]

This separation of the regimes of dissociative and molecular adsorption, coupled with the hydrogen coverage calibration which has been measured for this surface, permits the coverage of the molecular adlayer to be measured through uptake experiments.[1] In these experiments, the hydrocarbon parent peak signal (I_p) is monitored with the molecular beam doser on. When the crystal is out of the beam, this signal maintains a steady state value. When the crystal is turned into the beam, the signal drops, reflecting the adsorption of the hydrocarbon on the crystal. The signal eventually rises to a new steady-state value $I_{p,\infty}$. The difference $I_{p,\infty} - I_p$ reflects the probability of adsorption of the hydrocarbon by the surface, and the integral over time of this function is proportional to the coverage. In the initial phases of the uptake, the adsorption is completely that of the *dissociatively* adsorbed hydrocarbon molecules. Hence, the coverage of the hydrocarbon on the surface in this regime can be determined from thermal desorption spectra of hydrogen. This measurement determines the constant of proportionality

between the relative and absolute coverages for both dissociative and molecular adsorption. Using this technique, it was determined previously that the saturation coverage of molecularly adsorbed cyclopropane was $(6.6 \pm 1) \times 10^{14}$ molecules cm^{-2}. Saturation coverages of the molecular adlayers have been determined for propane to be $(4.2 \pm 0.7) \times 10^{14}$ molecules cm^{-2}, and for propylene $(3.6 \pm 0.6) \times 10^{14}$ molecules cm^{-2}.

3. Postadsorption of hydrogen and propylene on annealed propylene adlayers

A saturated adlayer of propylene annealed to 800 K retains no hydrogen. This surface retains some reactivity for subsequent dehydrogenation of propylene, but its activity is poisoned by the presence of surface carbon. This is illustrated in Fig. 6. In Fig. 6(a), the hydrogen thermal desorption spectrum after a 10 Torr s exposure of propylene on the clean surface is shown. In Fig. 6(b), the thermal desorption spectrum of hydrogen is shown after a 10 Torr s exposure of propylene to the surface which remained after the measurement of Fig. 6(a). In Fig. 6(c), the thermal desorption spectrum of hydrogen is shown after a 10 Torr s exposure of propylene to the surface which remained after the measurement of Fig. 6(b). A comparison of the integrated intensities of the thermal desorption peaks indicates that the activity of the surface is poisoned successively by ~60% after each exposure. The poisoning of β_2' adsites causes the decomposition of the hydrocarbon to shift to relatively higher temperatures. In Figs. 6(d) and 6(e), hydrogen thermal desorption spectra are shown for hydrogen adsorption on the surface after the measurement of Fig. 6(a), the exposures being 0.5 and 5 L of H_2, respectively. The adsorption of hydrogen is poisoned by the carbon on the surface as well, and for the exposure of 0.5 L [which normally saturates the β_2 adstate on the clean Ir(110)-(1×2) surface], the poisoning is again 60%. This is in agreement with the strong link that has already been established between surface activity for propylene dehydrogenation through abstraction of hydrogen from the hydrocarbon by the surface and the availability of β_2' adsites.

4. Coadsorption of hydrogen

As reported previously, the preadsorption of hydrogen into the β_2 adsite on the clean Ir(110)-(1×2) surface causes a linear decrease in the saturation coverage of dissociatively adsorbed cyclopropane and propane.[2,3] For propylene, propyne, and allene, this poisoning effect by preadsorbed hydrogen was not observed. In Fig. 7, thermal desorption spectra of hydrogen are shown for various precoverages of hydrogen and propylene exposures. In each case, a new low temperature feature is observed which is similar to the β_1 adstate on the clean surface,[11] and which is defined as the β_1' adstate. In Fig. 7, 5 Torr s of propylene was exposed to (a) the clean surface, (b) a surface exposed previously to 0.5 L H_2, and (c) a surface exposed previously to 10 L of H_2. Note that no changes occur in the intensities of the γ adstate. Hence, precoverage of hydrogen does not measurably change the probability of adsorption of dissociatively adsorbed propylene. While the intensity of the γ adstate remains unchanged, there is an apparent enhancement in the integrated intensity of the β_2' and α adstates. The α adstate is actually unchanged—its apparent enhancement is due to simultaneous desorption from the β_1' adstate. The enhancement of the β_2' adstate is due to the saturation of the β_2 adstate on the clean surface. The intensity of the β_1' adstate increases with increasing precoverage of hydrogen, as is most explicitly shown by comparison of Figs. 7(a) and (b). The sums of the thermal desorption areas for the separate exposures are in each case equal within experimental uncertainty to the areas obtained in the coadsorption measurements. This indicates

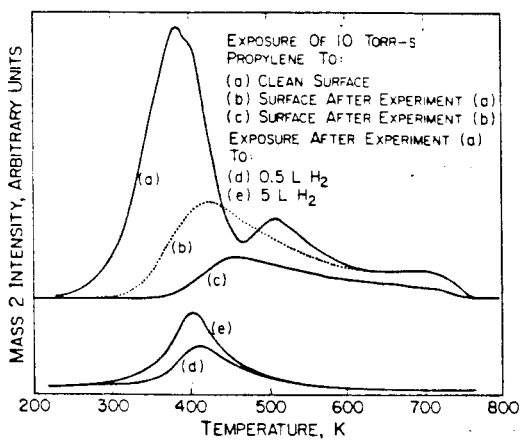

FIG. 6. Thermal desorption spectra of hydrogen resulting from exposure of 10 Torr s of propylene to: (a) The clean Ir(110) surface. (b) The surface after experiment (a). (c) The surface after experiment (b); and resulting from exposure of the surface after experiment (a); (d) 0.5 L of hydrogen, (e) 5 L of hydrogen.

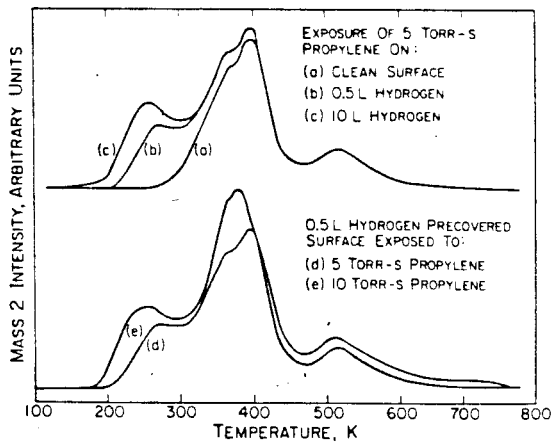

FIG. 7. Thermal desorption spectra of hydrogen resulting from exposure of 5 Torr of propylene to the following: (a) The clean Ir(110)-(1×2) surface. (b) Surface (a) exposed to 0.5 L of hydrogen. (c) Surface (a) exposed to 10 L hydrogen; and from exposure of the Ir(110)-(1×2) surface to 0.5 L of hydrogen followed by exposure to: (d) 5 Torr s of propylene. (e) 10 Torr s of propylene.

that little if any preadsorbed hydrogen is desorbed during the exposure to propylene at 100 K.

In Figs. 7(d) and 7(e), 5 and 10 Torr s of propylene were exposed to a surface previously exposed to 0.5 L H_2. In both cases, the intensity of the γ adstates is unchanged compared to exposures of propylene on the clean surface. The β_2' and α adstates appear to be enhanced, again due to the previous saturation of the β_2 adstate and the concurrent desorption from the β_1' adstate, respectively. The intensity of the β_2' adstate increases with increasing propylene postexposure as well.

Similar reactivity has been observed for the adsorption of propyne and allene on surfaces preexposed to hydrogen, i.e., the formation of a β_1' adstate. Not surprisingly, the unsaturated hydrocarbon molecules react more readily with the surface than do the saturated hydrocarbons studied previously.

The formation of the β_1' adstate by postexposure of propylene to the surface precovered with hydrogen could arise from two sources. One is that hydrogen from the irreversible adsorption of propylene shifts hydrogen adsorbed in the β_2 adstate to the β_1' adstate. Another is that preadsorbed hydrogen remains unshifted, and that propylene reacts to yield β_1' hydrogen, presumably through a different mechanism. Both possibilities would cause the intensity of the β_1' adstate to increase with both increasing hydrogen and propylene exposures. The former explanation is more likely since the γ adstates observed for a given exposure of propylene are the same on both the clean and on the hydrogen precovered surfaces, suggesting that a similar reaction occurs in both cases. Moreover, such shifting of hydrogen from the β_2 to the β_1 adstate has been observed previously on this surface with the coadsorption of hydrogen and CO.[15]

Isotopic labeling cannot distinguish between these two possibilities. As shown in Fig. 8, isotopic exchange occurs readily among adstates during the thermal desorption experiment. Thermal desorption spectra of H_2, HD, and D_2 are shown for 10 Torr s of propylene exposed to a surface preexposed to 0.5 L of deuterium. While deuterium was initially adsorbed only in the β_2 adstate, it appears in all adstates (β_1', α, β_2', and γ) in the desorption measurement. This result is similar to that reported previously for isobutane.[3] The appearance of deuterium in the γ adstate indicates that exchange must occur below 400 K between the hydrocarbon fragments and the hydrogen adsorbed on the metal surface.

Previously, it was shown that the *postadsorption* of hydrogen on propane adlayers at 100 K causes an increase in the amount of propane that desorbs molecularly and a decrease in the amount of hydrogen that desorbs from the γ adstate.[3] Less than 40% of the dehydrogenation reactivity remained after 4 L of hydrogen was postadsorbed on a saturated propane adlayer at 100 K. This reactivity is probably due to the fact that hydrogen is not a completely effective poison under these conditions, rather than a residual reactivity of the surface at 100 K. For cyclopropane and propylene, this effect was not observed. No increases were observed in the concentration of the molecularly adsorbed hydrocarbons when hydrogen was postadsorbed, i.e., both cyclopropane and propylene are chemisorbed strongly at 100 K. At saturation coverages of the dissociatively adsorbed adlayers of cyclopropane and propylene, no additional hydrogen was observed to adsorb (i.e., $< 10^{13}$ molecules cm^{-2}).

5. Coadsorption of CO

The coadsorption of CO can be used to determine the relative energetics of chemisorption of surface species. On the Ir(110)-(1×2) surface, it can be used to help differentiate between reaction-limited and desorption-limited hydrogen that is observed in thermal desorption spectra. The coadsorption of CO has been carried out with propane, cyclopropane, and propylene. In all cases investigated, the preadsorption of CO causes the dissociative adsorption of these three hydrocarbon molecules to be poisoned, i.e., no hydrogen desorbs when 2.5 L of CO is preadsorbed. Thermal desorption spectra of hydrogen are shown in Fig. 9 for a saturation exposure of propylene (10 Torr s) on the clean surface and on surfaces with various preexposures of CO. Two effects are observed. First, the total coverage of propylene decreases

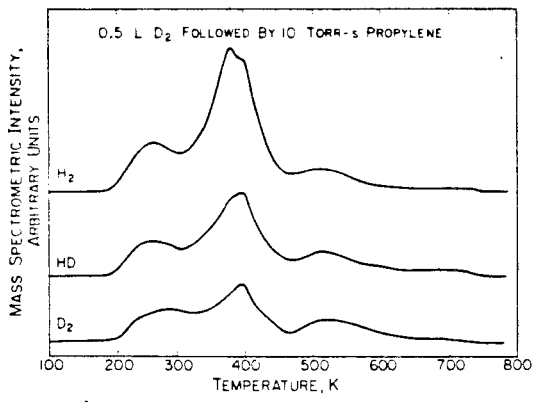

FIG. 8. Thermal desorption spectra of H_2, HD, and D_2 following exposure of the Ir(110)-(1×2) surface to 0.5 L of deuterium followed by 10 Torr s of propylene.

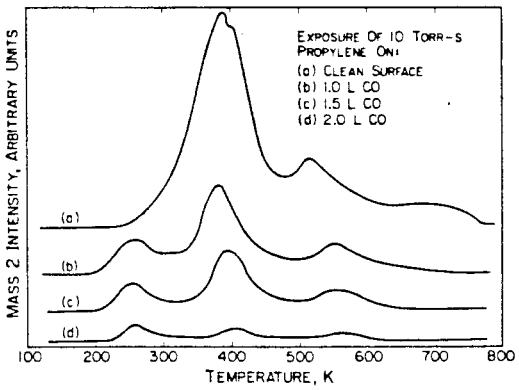

FIG. 9. Thermal desorption spectra of hydrogen following exposure of 10 Torr s of propylene to the clean and CO-precovered surfaces as shown.

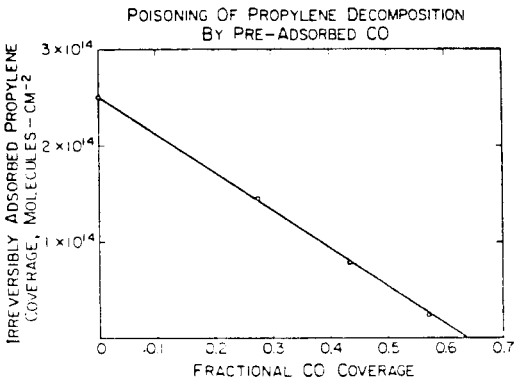

FIG. 10. Irreversibly adsorbed adlayer coverage as a function of precoverage of CO.

with increasing preexposure to CO and second, the presence of CO on the surface induces the desorption of hydrogen from the β_1' adstate. The latter has been observed previously for the coadsorption of hydrogen and CO on the clean surface, and for the exposure of other hydrocarbons on surfaces which were preexposed to CO.[3,15] The total saturation coverage of dissociatively adsorbed propylene decreases linearly in precoverage of CO, as shown in Fig. 10.

The postadsorption of CO on surfaces preexposed to propane at 100 K has been shown to cause two effects.[3] As with the postadsorption of hydrogen, a decrease in the amount of dissociatively adsorbed propane and an increase in the amount of molecularly adsorbed propane are observed. In addition, the postadsorption of CO can cause a shifting of hydrogen from the β_2' adstate to the β_1' adstate. The former is not observed for the postadsorption of CO on surfaces preexposed to cyclopropane and propylene. However, the shifting of hydrogen from the β_2' adstate to the β_1' adstate has been observed for both of these hydrocarbons as well. Thermal desorption spectra of hydrogen are shown in Fig. 11 after the postexposure of 2 L of CO on surfaces with preexposures of propylene of (a) 2.5, (b) 6 and (c) 10 Torr s. Figure 11(c) is identical to that which would be observed in the absence of the postexposure to CO. Corresponding thermal desorption spectra of CO show that almost no CO desorbs from the surface preexposed to 10 Torr s of propylene. Similar thermal desorption spectra of CO from surfaces with other preexposures to propylene indicate that the irreversibly adsorbed propylene poisons the postadsorption of CO. The thermal desorption spectra in Figs. 11(a) and 11(b) show the shifting of hydrogen from the β_2' adstate to the β_1' adstate. However, desorption of the α adstate occurs in the same temperature regime (along with some hydrogen which has not been shifted from the β_2' adstate) as in the absence of postadsorbed CO. This is a further indication that the α adstate is a reaction-limited as opposed to a desorption-limited adstate.

B. Adsorption on Ir(111)

Clearly, the β_2' adsites cause a characteristic dehydrogenation reaction to occur for a variety of hydrocarbons adsorbed on the Ir(110)-(1×2) surface. For comparison, the adsorption of hydrogen, propane, cyclopropane, and propylene has been investigated on the close-packed Ir(111) surface. The fourfold hollow sites of the Ir(110)-(1×2) surface, which are apparently related to the reactive β_2' adsite, are not present on the (111) surface, except possibly at defect and step sites. The LEED pattern of the clean crystal did not exhibit any spot splitting, which would be indicative of a regularly stepped surface. However, the kinetics of both adsorption and desorption of hydrogen indicate the presence of defects, the concentration of which is ~2.5%–5% of the concentration of surface sites.[16]

In order to quantify the coverages of dissociatively adsorbed hydrocarbons on the Ir(111) surface, it was necessary to measure the coverage–exposure relationship for hydrogen. The thermal desorption spectra resulting from the adsorption of hydrogen on the clean surface are shown in Fig. 12 for exposures ranging from 0.5 to 250 L. At saturation coverage, it is assumed that the number of adsorbed hydrogen atoms is equal to the number of exposed iridium atoms at

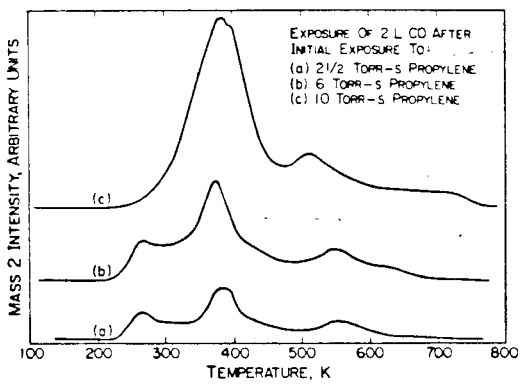

FIG. 11. Thermal desorption spectra of hydrogen after exposure of 2 L of CO to the Ir(110)-(1×2) surface preexposed to: (a) 2.5, (b) 6, (c) 10 Torr s of propylene.

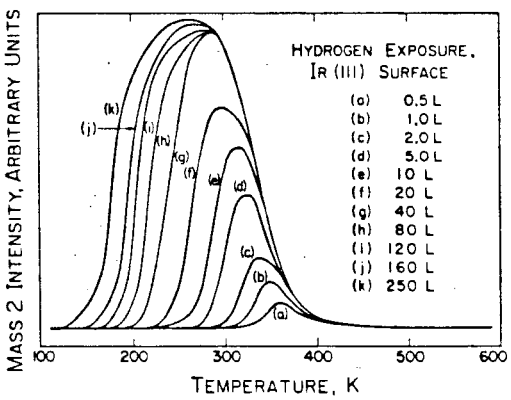

FIG. 12. Thermal desorption spectra of hydrogen as a function of exposure of hydrogen to the Ir(111) surface.

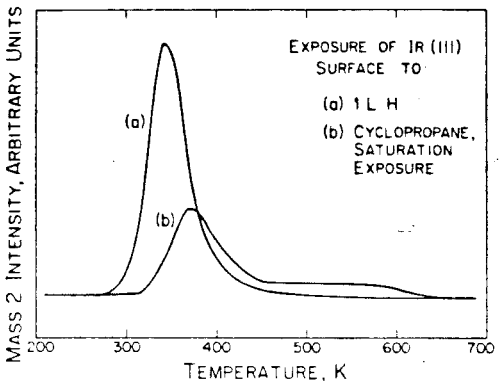

FIG. 13. Thermal desorption spectra of hydrogen resulting from exposure of the Ir(111) surface to: (a) 1.0 L of hydrogen. (b) 10 Torr s of cyclopropane (saturation).

the surface. If the adsorption of hydrogen on the Ir(111) surface is similar to that observed on the Pt(111) surface by Christmann and Ertl, then this estimate should be correct to within $\sim 10\%$.[17]

The dissociative adsorption of propane and cyclopropane on this surface was similar. In both cases, the thermal desorption spectra of hydrogen for saturation coverages of these alkanes were very similar and revealed that little hydrogen desorption occurred. In Fig. 13 thermal desorption spectra of hydrogen are shown for (a) 1 L exposure of hydrogen, and (b) saturation exposure of cyclopropane. Since the irreversible adsorption of one cyclopropane molecule results in the desorption of three hydrogen molecules, $\sim 1\times 10^{13}$ molecules cm^{-2} adsorb dissociatively. For propane, the corresponding value is less than 5×10^{12} molecules cm^{-2}. Both of these estimates are approximately a factor of 20 less than the similar values for dissociative adsorption on the Ir(110)-(1×2) surface,[1,3] and indicate that the reaction occurs at defect sites.

The dissociative adsorption of propylene on the Ir(111) surface resulted in considerably different thermal desorption

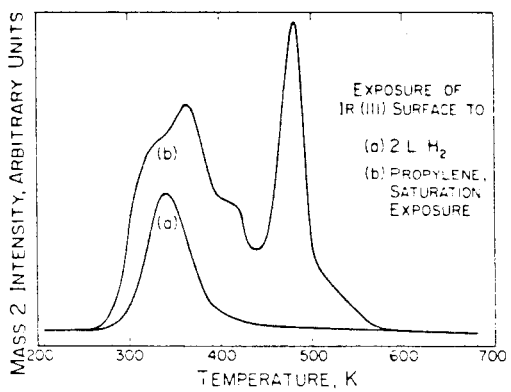

FIG. 14. Thermal desorption spectra of hydrogen resulting from exposure of the Ir(111) surface to: (a) 10 Torr s of propylene (saturation). (b) 2 L of hydrogen.

spectra of hydrogen than were observed for the alkanes. In Fig. 14 spectra are shown for (a) an exposure of 10 Torr s of propylene, which saturates the irreversibly adsorbed adlayer, and (b) an exposure of 2 L of hydrogen to the clean surface. No attempt has been made at a detailed interpretation of the dehydrogenation reactions associated with the propylene adlayer. The saturation coverage of the dissociatively adsorbed adlayer of propylene is estimated to be 3.9×10^{14} molecules cm^{-2}. It is apparent that the chemistry of dehydrogenation of hydrocarbons on the Ir(111) surface is very much a function of the particular molecule adsorbed.

IV. DISCUSSION

The five hydrocarbon molecules investigated are structurally similar as a group only in that each one has a three-carbon atom framework. Yet certain aspects of their chemistry on the Ir(110)-(1×2) surface are quite similar. All undergo dissociative adsorption to form surface hydrogen and stable hydrocarbon fragments. Dehydrogenation occurs preferentially at the β_2' adsite when it is vacant. In each case, the (relatively) stable γ fragments that are formed have a stoichiometry of approximately C_3H_2. Hydrocarbons with the same initial stoichiometry, i.e., cyclopropane and propylene, or propyne and allene, show very similar thermal desorption spectra of hydrogen for the same coverages. Sufficiently strong adsorbates poison the β_2' adsite, limiting the dehydrogenation reactivity of the surface.

It has been proposed previously that the hydrocarbon fragment corresponding to the γ adstate of hydrogen may be formed from the parent molecule by total dehydrogenation of the first and third carbon atoms leaving a bridging methylene group which is stable so long as carbon–carbon bonding is thermally stable.[3] Such an argument explains easily the stoichiometry of the fragments formed in the case of propane and cyclopropane. In the case of the other three hydrocarbons, hydrogen from the first and third carbon atoms migrates to the second carbon atom by 1,2 shifts. Such shifts are certainly facile, as has been indicated by the rapid hydrogen–deuterium exchange into the γ adstates. This would explain how such differing pairs of molecules as cyclopropane and propylene, and propyne and allene could have such similar low coverage thermal desorption spectra of hydrogen. In the former case, it would appear that at some temperature below ~ 450 K (probably already at 100 K) the cyclopropane ring opens, causing its fragment to be similar to that formed by propylene. Ring opening due to partial π-bond character of cyclopropane (as well as possibly ring strain) would explain why its dehydrogenation reaction cannot be inhibited by postadsorption of hydrogen or CO at 100 K, while the dehydrogenation reaction of the saturated hydrocarbons previously studied can be partially inhibited in this fashion up to 130 K.

The low temperature broadening of the β_2' adstate of propylene (or the α adstate), and the high temperature broadening of the β_2' adstates of propyne and allene which occurs after the β_2' adsites have been saturated have not been observed with the saturated hydrocarbons studied previously. These are the hydrocarbons that might be expected to

chemisorb strongly to the surface through reaction of their π bonds to form strong metal–carbon bonds. Recent work has shown that ethylene also shows a low temperature α state at high coverages, outside of the envelope of β_2 surface hydrogen.[18] Since these states develop only at higher coverages, it is possible that they would correspond to reversible adstates on surfaces which are less active toward dehydrogenation. Such an explanation for these α adstates would also explain the absence of the α adstate for cyclopropane, which is the only significant difference between the thermal desorption spectra of hydrogen for cyclopropane and propylene. These α adstates apparently are due to reaction-limited desorption, i.e., the hydrogen does not appear to be desorbing from β_1-like adsites. On Pt(111), Salmeron *et al.* observed that propylene has two reversible adstates: one at 140 K and one at 280 K.[8] On the Ir(110)-(1×2) surface only an adstate corresponding to the lower temperature one on the platinum surface is observed. Such a species presumably chemisorbs through its π bond to the surface, and on the Ir(110)-(1×2) surface dehydrogenation occurs as opposed to desorption. On the Pt(111) surface, fragments formed from acetylene have greater high temperature stability than fragments formed from ethylene.[8] Hence, the high temperature (rather than low temperature) dehydrogenation of the high coverage adstates of propyne and allene appears to be reasonable. The formation of these adstates accounts for most of the increase in the coverage of the dissociatively adsorbed adlayers for the unsaturated hydrocarbons as compared to the saturated hydrocarbons.

The temperatures of the intensity maxima of desorption of the molecular adlayers appear to correlate inversely with the saturation coverages of the corresponding dissociatively adsorbed adlayers. The indication is that these states still interact with the metal surface, and that this interaction weakens with increasing dissociative adlayer coverage due to some combination of site blocking and electronic effects. The molecular adstate of propane interacts strongly with the metallic substrate, and it is probably a part of the first adlayer. The molecular states of propylene, propyne, and allene interact much more weakly, and they appear to constitute a second adlayer. The molecular overlayer of cyclopropane apparently populates both first and second adlayers. This is consistent with the fact that the saturation coverage at 100 K of molecularly adsorbed cyclopropane is greater by over 50% than that of either propane or propylene.

The ability of H_2 and CO postadsorbed at 100 K on propane adlayers to limit dissociative propane chemisorption allows a threshold temperature of the dissociation reaction to be measured. The postadsorption of neither H_2 nor CO can inhibit the dissociative adsorption of cyclopropane and propylene at 100 K, and, presumably, this is true for propyne and allene as well, i.e., these hydrocarbons are dissociatively adsorbed at 100 K. The very low reaction threshold temperature for propane (130 K) would lead us to believe that a reaction threshold temperature of below 100 K for these less saturated hydrocarbons is not unreasonable. For cyclopropane, such a conclusion is in agreement with previous UPS results which show little or no indication of molecular cyclopropane until the dissociatively adsorbed overlayer is saturated.[1]

The relative poisoning ability of hydrogen toward the irreversible adsorption of cyclopropane and propylene apparently would indicate that the ability to form a strong surface bond without necessarily breaking a carbon–hydrogen bond is the crucial difference. Hence, cyclopropane acquires the character of a molecule containing a π bond, i.e., reactivity at 100 K and high coverage of the irreversible adlayer, only in the presence of vacant β_2' adsites. When these sites are poisoned, cyclopropane acts like a fully saturated hydrocarbon. Hence, the dissociative adsorption of cyclopropane is poisoned by the preadsorption of hydrogen, and cyclopropane does not show broadening of the β_2' adstate with increasing coverage of the dissociatively adsorbed overlayer.

Stronger poisons, such as surface carbon and CO, limit the dissociative adsorption of all five hydrocarbons. On the carbon-covered surface formed by the dehydrogenation of the dissociated adlayers, the relative decrease in the saturation coverage of the dissociatively adsorbed adlayer is the same as that for hydrogen adsorbed in the β_2 adstate. This shows directly the importance of the β_2' adsite for this dehydrogenation reaction. The shifting of hydrogen adsorbed in the β_2 adstate to the β_1 adstate by the coadsorption of CO made such a direct measurement difficult for this poison. However, it was demonstrated that the poisoning ability of CO toward this reaction was linear in its coverage.

The adsorption measurements on the Ir(111) surface indicate clearly the importance of the β_2' adsites for the dehydrogenation of propane and cyclopropane under our reaction conditions. The small extent of irreversible adsorption was certainly caused by defect sites on the surface. The reactivity of the unsaturated hydrocarbons was more clearly related to individual differences in molecular electronic and geometric structure than to the dominance of any surface adsite. Apparently the reactivity of saturated hydrocarbons with the Ir(110)-(1×2) surface is due to some combination of a geometric effect and an electronic effect induced by its particular surface geometry.

V. CONCLUSIONS

On the Ir(110)-(1×2) surface, all five hydrocarbons investigated exhibit irreversible adsorption initially, leading to the formation of surface fragments of approximate stoichiometry C_3H_2. This occurs in spite of the differences in their electronic and geometric structure. Upon saturation of the β_2' adsites, these structural differences are reflected in that the unsaturated hydrocarbons exhibit dissociatively adsorbed adstates which appear to be formed through the reaction of π electrons. All five hydrocarbons form molecularly adsorbed adstates at low temperatures. In all cases, surface carbon and CO were found to act as poisons to the β_2 adsite of hydrogen and toward its particular dehydrogenation reaction. The poisoning ability of hydrogen varied inversely with the π-bond character of the molecule. Similar studies on the Ir(111) surface demonstrated the importance of the β_2' adsite

on the Ir(110)-(1×2) surface, since reactivity on the close-packed surface varied with the structure of the hydrocarbon and was not dominated by any particular surface adsite.

[1]T. S. Wittrig, P. D. Szuromi, and W. H. Weinberg, J. Chem. Phys. **76**, 716 (1982).
[2]T. S. Wittrig, P. D. Szuromi, and W. H. Weinberg, Surf. Sci. **116**, 414 (1981).
[3]T. S. Wittrig, P. D. Szuromi, and W. H. Weinberg, Surf. Sci. **76**, 3305 (1982).
[4]C.-M. Chan, M. A. Van Hove, W. H. Weinberg, and E. D. Williams, Solid State Commun. **30**, 47 (1979); Surf. Sci. **91**, 440 (1980).
[5]T. E. Madey and J. T. Yates, Jr., Surf. Sci. **76**, 397 (1978).
[6]L. E. Firment and G. A. Somorjai, J. Chem. Phys. **66**, 2091 (1977).
[7]F. M. Hoffmann, T. E. Felter, P. A. Thiel, and W. H. Weinberg, Surf. Sci. **130**, 173 (1983); J. Vac. Sci. Technol. **18**, 651 (1981); T. E. Felter, F. M. Hoffmann, P. A. Thiel, and W. H. Weinberg, Surf. Sci. **130**, 163 (1983); F. M. Hoffmann, T. E. Felter, and W. H. Weinberg, J. Chem. Phys. **76**, 3799 (1982).
[8]M. Salmeron and G. A. Somorjai, J. Phys. Chem. **86**, 341 (1982).
[9]J. L. Taylor, D. E. Ibbotson, and W. H. Weinberg, J. Chem. Phys. **69**, 4298 (1978).
[10]D. E. Ibbotson, T. S. Wittrig, and W. H. Weinberg, Surf. Sci. **110**, 294 (1981).
[11]D. E. Ibbotson, T. S. Wittrig, and W. H. Weinberg, J. Chem. Phys. **72**, 4885 (1980).
[12]A. M. Baro and H. Ibach, J. Chem. Phys. **74**, 4194 (1981).
[13]J. A. Gates and L. L. Kesmodel, Surf. Sci. **124**, 68 (1983).
[14]P. M. George, N. R. Avery, W. H. Weinberg, and F. N. Tebbe, J. Am. Chem. Soc. **105**, 1393 (1983).
[15]D. E. Ibbotson, T. S. Wittrig, and W. H. Weinberg, Surf. Sci. **97**, 297 (1980).
[16]J. R. Engstrom and W. H. Weinberg (in preparation).
[17]K. Christmann and G. Ertl, Surf. Sci. **60**, 365 (1976).
[18]P. D. Szuromi and W. H. Weinberg (in preparation).

APPENDIX E

Adsorption and Reaction of *n*-Alkanes on the Pt(110)-(1x2) Surface

[The text of Appendix E consists of an article coauthored with P. D. Szuromi and W. H. Weinberg, which has appeared in *The Journal of Physical Chemistry* **89**, 2497 (1985).]

Reprinted from The Journal of Physical Chemistry, 1985, 89, 2497.
Copyright © 1985 by the American Chemical Society and reprinted by permission of the copyright owner.

Adsorption and Reaction of *n*-Alkanes on the Pt(110)-(1×2) Surface

P. D. Szuromi, J. R. Engstrom, and W. H. Weinberg*

Division of Chemistry and Chemical Engineering, California Institute of Technology, Pasadena, California 91125 *(Received: November 26, 1984)*

The interaction of ethane, propane, *n*-butane, and *n*-pentane with the reconstructed Pt(110)-(1×2) surface has been investigated, principally by mass spectrometry. Ethane and propane exhibit only weak molecular chemisorption, whereas low coverages of *n*-butane and *n*-pentane undergo dissociative adsorption at approximately 200 K to form surface hydrogen and hydrocarbon fragments. The surface site required for dissociation is similar to that for the adsorption of hydrogen at lower coverages, since dissociative adsorption is inhibited strongly by surface hydrogen. Similar activation of alkanes has been observed previously for the Ir(110)-(1×2) surface, but on the close-packed Pt(111) and Ir(111) surfaces dissociative adsorption of these alkanes is either not observed or occurs only at defect sites. Thus surface geometry exhibits a strong influence on C–H bond activation in alkanes.

Introduction

The interaction of saturated hydrocarbon molecules with the Pt(110)-(1×2) surface has been studied by thermal desorption mass spectrometry and low-energy electron diffraction (LEED). This work was motivated by previous results concerning the interaction of saturated hydrocarbons with the Ir(110)-(1×2) surface and the (111) surfaces of Ir and Pt.[1-6] On the Ir(110)-(1×2) surface all alkanes except methane adsorb dissociatively at low surface coverages and at temperatures below 130 K.[1-4] These reactions are limited by the availability of high coordination β'_2 adsites.[1] The activation of carbon–hydrogen bonds liberates hydrogen, which eventually saturates these sites. For the normal alkanes from C_2 through C_7 saturation coverages of the dissociatively adsorbed overlayers is on the order of 1×10^{14} molecule cm^{-2}. No evidence was found for hydrogenolysis products arising from reaction of the hydrocarbons with surface hydrogen. On the Ir(111) surface, similar dissociation reactions are observed only at defect sites.[2,3] Saturation coverages of the dissociatively adsorbed overlayer are at least twenty times less than the corresponding coverages on the (110)-(1×2) surface. Furthermore, the normal alkanes from ethane through octane exhibit no significant reactivity with the Pt(111) surface under ultrahigh vacuum conditions.[5,6] These results suggest that the availability of high coordination adsites is critical in lowering the activation barriers that must be overcome in cleaving carbon–hydrogen bonds in alkanes.

The results presented here concerning the interaction of alkanes with the (110)-(1×2) surface of platinum extend further the understanding of the effect of surface geometry and electronic structure on the activation of alkanes. Although the exchange of deuterium into benzene adsorbed on the Pt(110) surface has been observed,[7] to our knowledge the interaction of saturated hydrocarbons under ultrahigh vacuum conditions has not been investigated previously on this surface of platinum. The alkanes studied include ethane, propane, *n*-butane, and *n*-pentane. Neither

(1) W. H. Weinberg, *Surv. Prog. Chem.*, **10**, 1 (1983).
(2) P.D. Szuromi and W. H. Weinberg, *J. Vac. Sci. Technol.*, **A1**, 1219 (1983).
(3) P. D. Szuromi, J. R. Engstrom, and W. H. Weinberg, *J. Chem. Phys.*, **80**, 508 (1984).
(4) P. D. Szuromi and W. H. Weinberg, *Surf. Sci.*, **145**, 407 (1984).
(5) L. E. Firment and G. A. Somorjai, *J. Chem. Phys.*, **66**, 2901 (1977).
(6) M. Salmeron and G. A. Somorjai, *J. Phys. Chem.*, **86**, 341 (1982).
(7) M. Surman, S. R. Bare, P. Hofmann, and D. A. King, *Surf. Sci.*, **126**, 349 (1983).

0022-3654/85/2089-2497$01.50/0 © 1985 American Chemical Society

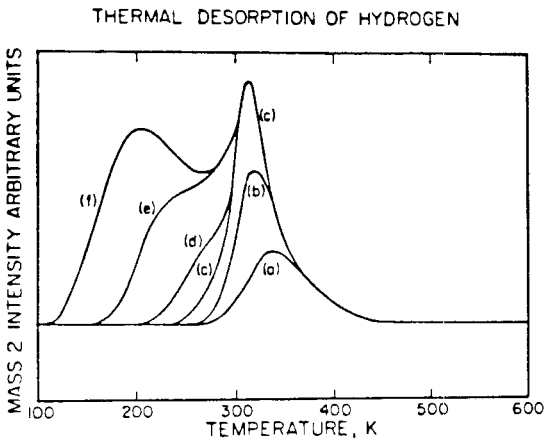

Figure 1. Thermal desorption spectra of hydrogen after exposures of H_2 of (a) 0.02 (b) 0.05 (c) 0.5, (d) 2.0 (e) 20, and (f) 50 langmuirs.

molecular nor dissociative adsorption of methane could be observed under our experimental conditions, namely surface temperatures above 100 K.

Experimental Procedures

The experiments were performed in an ion-pumped stainless steel bell jar which has been described in detail previously.[8] The base pressure of the bell jar was below 2×10^{-10} torr of reactive contaminants. The Pt(110) crystal was cut from a single crystal of platinum and was polished to within 1° of the (110) orientation by using standard metallographic techniques. The crystal was etched in aqua regia and cleaned in situ by argon ion sputtering at high temperatures (1200 K), high temperature annealing (1400 K) and heating in oxygen at 800 K and 5×10^{-7} torr. Auger electron spectroscopy was used to verify surface cleanliness. The determination of the presence of silicon by Auger spectroscopy is complicated by the overlap of its LMM transition at 92 eV with the platinum ONN transition. On Pt(111) both surface and subsurface silicon can be oxidized and the presence of silicon inferred from the oxygen transition of its oxide.[9] Silicon was present in our sample and was removed by several cycles of oxidation and argon ion bombardment. The formation of silicon oxide species was minimized subsequent to this treatment by cleaning the crystal of carbidic carbon with oxygen at 5×10^{-8} torr for 5 min at temperatures less than 600 K, followed by annealing to 1000 K to ensure desorption of surface oxygen.[10] The Auger electron spectrum of the clean surface is in good agreement with that published recently by Mundschau and Vanselow[11] for a surface from which impurities such as sulfur, phosphorus, and silicon have been removed. After cleaning and annealing, the (1×2) LEED pattern characteristic of the surface reconstruction of the clean surface could be observed. Streaking was observed at times in the fractional-order beams, indicating that some disorder was present across the close-packed rows. This has been observed in other investigations of the Pt(110)-(1×2) surface.[12] The missing row model of the surface reconstruction accounts for data obtained by Rutherford backscattering[12] and by helium atom diffraction,[13] and is the only model of the several that have been proposed which is in agreement with recent results from low energy alkali impact collision ion spectroscopy.[14]

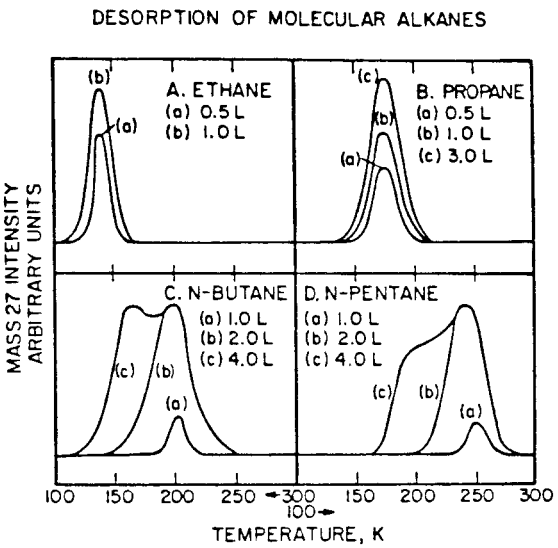

Figure 2. Thermal desorption spectra of molecularly adsorbed alkanes (monitoring mass 27) for adsorption of (A) ethane, (B) propane, (C) *n*-butane, and (D) *n*-pentane. Exposures are shown next to the corresponding spectra.

The adsorption temperature was 100 K for ethane and propane and 150 K for *n*-butane and *n*-pentane. The higher adsorption temperature for the latter two was employed to minimize the adsorption of hydrogen from the background, since these two alkanes adsorb dissociatively. Heating rates between 15 and 20 K/s were employed. The hydrocarbons used were purified cryogenically, and the purity was verified by mass spectrometry.

Results

Thermal Desorption of Hydrogen. A knowledge of the thermal desorption spectra of hydrogen adsorbed on the clean surface as a function of coverage is necessary to interpret the desorption spectra of hydrogen resulting from the dissociative adsorption of these saturated hydrocarbons. In Figure 1 the thermal desorption spectra are shown for exposures of hydrogen of (a) 0.02 (b) 0.05 (c) 0.5 (d) 2.0 (e) 20, and (f) 50 langmuir. In assigning the absolute surface coverage, we have used the value of Jackman et al.[12] from nuclear microanalysis, namely a saturation coverage of 1.1×10^{15} atoms cm^{-2} at 170 K. A study of the adsorption and desorption kinetics as a function of hydrogen coverage will be published separately.[15] These spectra are in good agreement with those published previously by Ferrer and Bonzel.[16] The state that desorbs above 300 K has a considerably higher probability of adsorption than does the state which desorbs at lower temperatures. We label these two adstates β_2 and β_1, respectively. The coverage–exposure relation suggests that there are two consecutive regimes obeying second-order adsorption kinetics which have different "initial" probabilities of adsorption, which we estimate to be unity and 5×10^{-3}, respectively. The saturation coverage of the β_2 adstate is approximately half that of the β_1 adstate, based on an extrapolation of the coverage–exposure curve. On the Ir(110)-(1×2) surface, the β_2 adstate, which has its desorption maximum at 400 K, exhibits first-order adsorption kinetics with an initial probability of adsorption of unity, while the lower temperature β_1 adstate exhibits second-order adsorption kinetics with a much lower "initial" probability of adsorption, namely 7×10^{-3}.[17] The β_2 adstate accounts for one-third of the adsorbed hydrogen. These differences were attributed to the differences

(8) J. L. Taylor, D. E. Ibbotson, and W. H. Weinberg, *J. Chem. Phys.* **69**, 4298 (1978).
(9) H. Niehus and G. Comsa, *Surf. Sci.*, **102**, 614 (1981).
(10) C. M. Comrie and R. M. Lambert, *J. Chem. Soc. Faraday Trans. 1*, **72**, 1659 (1976).
(11) M. Mundschau and R. Vanselow, *Phys. Rev. Lett.*, **53**, 1084 (1984).
(12) T. E. Jackman, J. A. Davies, D. P. Jackson, W. N. Unertl, and P. R. Norton, *Surf. Sci.*, **120**, 389 (1982).
(13) A. M. Lahee, W. Allison, R. F. Willis, and K. H. Rieder, *Surf. Sci.*, **126**, 654 (1983).
(14) H. Niehus, *Surf. Sci.*, **145**, 407 (1984).
(15) J. R. Engstrom, W. Tsai and W. H. Weinberg, manuscript in preparation.
(16) S. Ferrer and H. P. Bonzel, *Surf. Sci.*, **119**, 234 (1982).
(17) D. E. Ibbotson, T. S. Wittrig and W. H. Weinberg, *J. Chem. Phys.*, **80**, 4885 (1980).

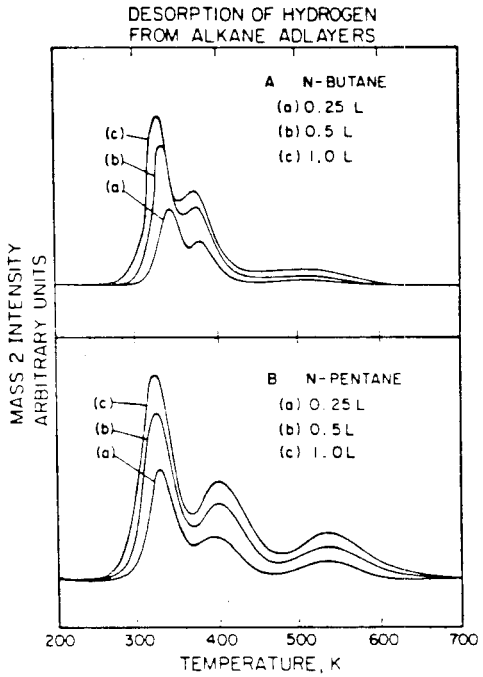

Figure 3. Thermal desorption spectra of hydrogen resulting from exposure to (A) *n*-butane and (B) *n*-pentane. Exposures are shown next to the corresponding spectra.

in coordination at the two adsites. Apparently the two desorption states on the Pt(110)-(1×2) surface arise also from desorption from two different sites.

Thermal Desorption of Hydrogen and Alkanes from Alkane Overlayers. The interaction of ethane, propane, *n*-butane, and *n*-pentane with the Pt(110)-(1×2) surface has been characterized by thermal desorption mass spectrometry. In all cases the only *hydrocarbon* that is observed to desorb is the parent alkane, i.e., no self-hydrogenolysis was observed. For ethane and propane *only* desorption of the molecularly adsorbed alkane is observed. As shown in Figure 2, A and B, this occurs at 140 and 175 K, respectively. For *n*-butane and *n*-pentane only the desorption of hydrogen is observed after such low exposures to the surface. The thermal desorption spectra of hydrogen are shown as a function of exposure in Figure 3A for *n*-butane and in Figure 3B for *n*-pentane. Both desorption-limited and reaction-limited evolution of hydrogen occurs. The hydrogen desorption peak near 320 K is due to desorption from the metal surface (cf. Figure 1), whereas the peaks at approximately 400 and 550 K are due to decomposition of hydrocarbon fragments adsorbed on the surface. The surface coverage of dissociatively adsorbed molecules at saturation, in units of 10^{13} molecules cm^{-2}, is 6.0 ± 0.6 for *n*-butane and 7.5 ± 0.8 for *n*-pentane, based on the hydrogen coverage data of Jackman et al.[12] The amount of surface hydrogen which results from a saturation coverage of *n*-butane is 55% of that required to saturate the β_2 adstate, while for *n*-pentane the corresponding value is 70%. The ratios of the areas of the peaks at 320, 400, and 550 K are estimated to be 5:3:2 for *n*-butane and 5:5:2 for *n*-pentane. Overlap of these desorption peaks introduces an error of at least 15% to these values. Molecular desorption of the parent hydrocarbon accompanies dissociative adsorption at higher exposures, as may be seen in Figure 2C for *n*-butane and in Figure 2D for *n*-pentane. At lower coverages desorption occurs at 210 and 245 K respectively, while at higher coverages a second desorption state is observed at 160 and 190 K. Desorption of multilayers should occur at the same temperatures as observed on the Ir(110)-(1×2) surface, at 110 and 140 K, respectively.[4] After the thermal desorption experiments, surface carbon is readily detectable by Auger spectroscopy. The fractional-order LEED

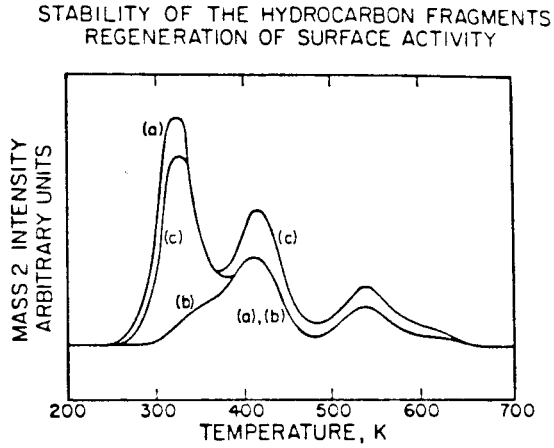

Figure 4. Thermal desorption spectra of hydrogen after exposure of (a) the clean surface to 1.0 langmuir of *n*-pentane; (b) the clean surface to 1.0 langmuir of pentane, annealing to 320 K for 30 s, and cooling to 150 K; and (c) the surface in experiment b to an additional 1.0 langmuir of *n*-pentane.

beams, which are characteristic of the surface reconstruction, do not appear to have changed in relative intensity compared to the clean surface.

Thermal Desorption from Annealed Alkane Overlayers. Several experiments were conducted to investigate the stability of the hydrocarbon fragments, the presence of which is evident from the reaction-limited desorption of hydrogen. If an adlayer of *n*-butane or *n*-pentane is annealed to 320 K for times on the order of 1 min, and then cooled to 150 K, a thermal desorption spectrum of the resulting surface reveals that no change in intensity occurs for the reaction-limited desorption of hydrogen. This is shown in Figure 4, in which the thermal desorption spectrum of hydrogen in (a) results from exposure of the clean surface to 1.0 langmuir of *n*-pentane, while that shown in (b) results from the same exposure of *n*-pentane annealed, as described above, for 30 s. Above 400 K the spectra are identical, indicating that the hydrocarbon fragments on the surface, which are manifest by the high temperature desorption states, are stable in the presence of the vacant surface sites at which hydrocarbon may be adsorbed.

The adsites which give rise to the thermal desorption peak of hydrogen at 320 K are apparently the sites responsible for dissociative adsorption of *n*-butane and *n*-pentane. The dissociative adsorption of these alkanes saturates upon exposure of 1.0 langmuir at 150 K. However, if these overlayers are annealed to 320 K, so that surface hydrogen desorbs, and are then cooled to 150 K and reexposed to the alkane, the intensity of the reaction-limited high temperature desorption of hydrogen increases. In Figure 4c the thermal desorption of hydrogen is shown which results from an exposure of 1.0 langmuir of *n*-pentane at 150 K, annealing the surface to 320 K for 30 s, cooling to 150 K, and then reexposing the surface to 1.0 langmuir of *n*-pentane. An increase in intensity of approximately 70% in the reaction-limited desorption of hydrogen at 400 and 550 K occurs. This indicates that the dissociative adsorption of alkanes requires the same site as that for the high-temperature desorption state of hydrogen on the clean surface.

A saturated overlayer of *n*-pentane annealed to 700 k retains no hydrogen, and results in the formation of surface carbon. This surface retains approximately 90% of its initial activity toward dissociative adsorption of *n*-pentane. In Figure 5a, the hydrogen thermal desorption spectrum is shown after an exposure of 1.0 langmuir of *n*-pentane to the clean surface, whereas in Figure 5b the corresponding spectrum is shown for an exposure of 1.0 langmuir of *n*-pentane to the surface which resulted after the measurement of Figure 5a. The shifting of the reaction-limited desorption states to higher temperatures is evidently caused by the presence of surface carbon. The LEED pattern observed after

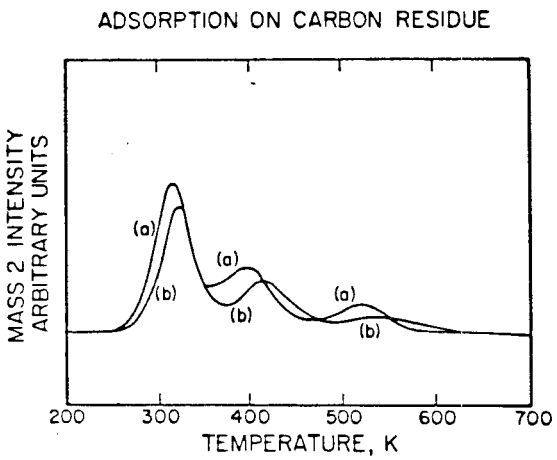

Figure 5. Thermal desorption spectra of hydrogen after exposure of (a) 1.0 langmuir of *n*-pentane and (b) 1.0 langmuir of *n*-pentane to the surface after the experiment in (a).

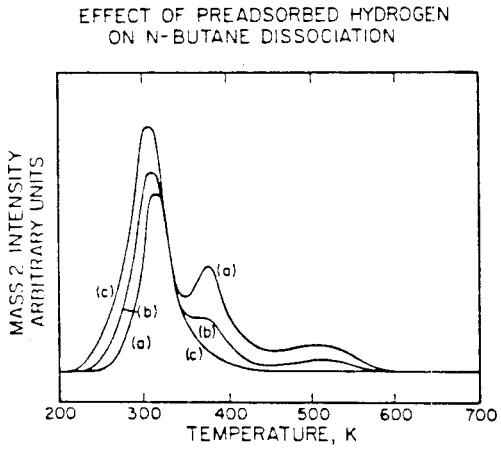

Figure 6. Thermal desorption spectra of hydrogen after exposure of 1.0 langmuir of *n*-butane to (a) the clean surface; (b) the surface in (a) exposed to 0.05 langmuir of hydrogen; and (c) the surface in (a) exposed to 0.5 langmuir of hydrogen.

this experiment possesses all the beams characteristic of the (1×2) reconstruction. After five cycles of exposure of 1.0 langmuir of *n*-pentane, annealing to 700 K, and cooling to 150 K, the saturation coverage of the dissociatively adsorbed *n*-pentane has decreased by 50%. The desorption temperature for low coverages of the molecularly adsorbed *n*-pentane shifts to approximately 200 K from 245 K. The fractional-order LEED beams are almost completely extinguished at this point, resulting in a (1×1) pattern which has high background intensity. Thus high carbon concentrations can remove the surface reconstruction. An ultimate reactivity of *n*-pentane of 4.0×10^{14} molecules cm^{-2} can be estimated from these experiments.

Coadsorption of Hydrogen and Alkanes. The strong dependence of dissociative adsorption of alkanes on the availability of the high-temperature hydrogen adsorption site on the Pt(110)-(1×2) surface suggests that preadsorption of hydrogen would inhibit activation of C–H bonds in alkanes by this surface. In Figure 6a the thermal desorption spectrum of hydrogen is shown for an exposure of 1.0 langmuir of *n*-butane to a surface previously exposed to (a) 0.02 langmuir of hydrogen (background exposure); (b) 0.05 langmuir of hydrogen; and (c) 0.5 langmuir of hydrogen. The reaction-limited desorption of hydrogen at 400 and 550 K is absent in spectrum c, indicating that no dissociative adsorption of *n*-butane occurs. Similar results have been obtained for *n*-

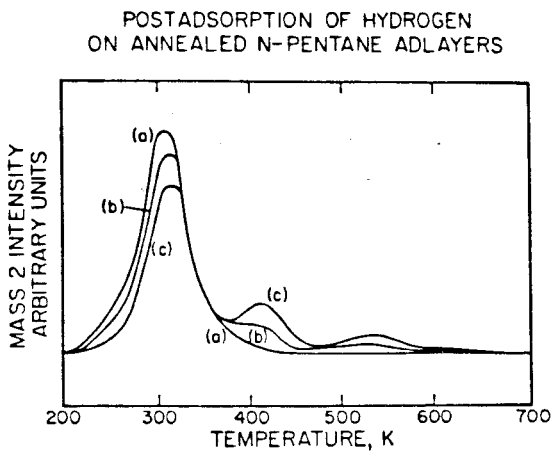

Figure 7. Thermal desorption spectra of hydrogen after the adsorption of 0.5 langmuir of hydrogen on a surface exposed previously to 1.0 langmuir of *n*-pentane which had been annealed for 30 s to (a) 150, (b) 180, and (c) 200 K.

pentane. This inhibition in dissociatively adsorbed alkanes is related linearly to the precoverage of hydrogen. The inhibition is complete after an exposure of only 0.5 langmuir of hydrogen, which corresponds to approximately one-third of the amount of hydrogen that can be adsorbed on the clean surface (cf. Figure 1). As adsorption of hydrogen from the background could not be avoided in our experiments due to the high adsorption probability of hydrogen at low coverages, the saturation coverages of *n*-butane and *n*-pentane quoted previously were obtained by linear extrapolation to zero hydrogen precoverage.

The effect of postadsorption of hydrogen on overlayers of *n*-butane and *n*-pentane depends on the thermal history of the alkane overlayer, due to the activated and irreversible nature of the dissociative adsorption of these alkanes. If either *n*-butane or *n*-pentane is adsorbed at 150 K and 0.5 langmuir of hydrogen is then exposed to the surface while it is still at 150 K, the dissociative adsorption of the alkane is inhibited completely. However, if the alkane overlayer is annealed to higher temperatures, the inhibition effect can be suppressed. In figure 7 thermal desorption spectra of hydrogen are shown for an exposure of 0.5 langmuir of hydrogen on a surface exposed previously to 1.0 langmuir of *n*-pentane which had been annealed for 30 s to (a) 150, (b) 180, and (c) 200 K. The desorption of hydrogen from the high-temperature states in spectrum c and the desorption from the molecular state are identical to that which results for exposure of the clean surface to 1.0 langmuir of *n*-pentane at 150 K, indicating that dissociation has gone to completion after 30 s at 200 K. The desorption of molecular *n*-pentane which occurs in experiment a is approximately equal to that for adsorption of 1.5 langmuir of *n*-pentane at 150 K, due to the complete inhibition of dissociation by surface hydrogen. The increase in the reaction-limited desorption of hydrogen and the decrease in desorption of the molecularly adsorbed alkanes with increasing annealing temperatures demonstrates that the dissociation of these alkanes is activated and will go to completion in under 1 min by approximately 200 K.

The coadsorption of deuterium was investigated to determine if exchange could occur between hydrogen in the hydrocarbon fragments and hydrogen adsorbed on the surface of the metal. If such exchange occurs, the use of deuterium labeling of these alkanes to reveal structural information in thermal desorption studies is complicated by mixing between states. In Figure 8 the thermal desorption spectra of masses 2 and 3 are shown for exposure of the surface to 0.02 langmuir of deuterium followed by 1.0 langmuir of *n*-pentane. Some coadsorption of background hydrogen occurs as well. The desorption of HD from the reaction-limited high-temperature desorption states proves that exchange of surface deuterium into the hydrocarbon fragments occurs. Such exchange is incomplete, however, since the relative

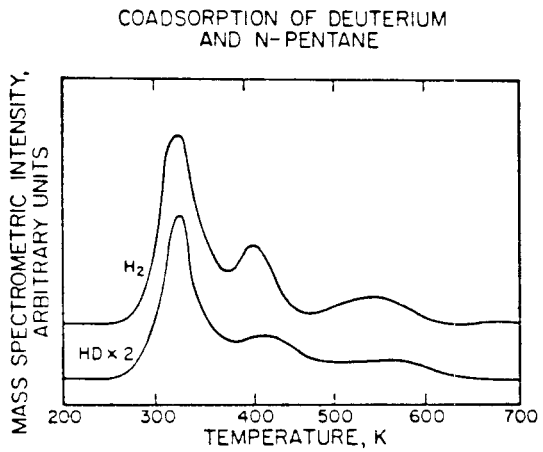

Figure 8. Thermal desorption spectra of masses 2 and 3 after exposure of the surface to 0.02 langmuir of deuterium followed by 1.0 langmuir of *n*-pentane.

intensity of the features at 400 and 550 K compared to that 320 K is approximately half as much in the HD spectrum compared to the H_2 spectrum. The partial exchange observed here is in qualitative agreement with the rate measured by Surman et al.[7] for the exchange of deuterium into benzene adsorbed on this surface.

Discussion

The dissociative adsorption of alkanes on the Pt(110)-(1×2) surface is an activated process, which at 200 K occurs at a sufficiently high rate that it competes effectively with desorption from the molecularly chemisorbed states of these alkanes. Thus the dissociative adsorption of methane, ethane, and propane could not be observed under our (low-pressure) experimental conditions, since desorption of the molecularly adsorbed state occurs below this temperature. For *n*-butane and *n*-pentane the higher desorption temperature of molecular chemisorption allows their dissociation to be observed. The surface site which is critical to the initial step of carbon–hydrogen bond activation appears to be the same one at which dissociatively adsorbed hydrogen (from molecular hydrogen) is bound and which has been defined as the β_2 adstate. The saturation of this site by hydrogen prevents dissociative adsorption of *n*-butane and *n*-pentane. This accounts for the following aspects of the dissociative adsorption of alkanes on this surface: (1) The dissociatively adsorbed overlayer saturates at an adsorption temperature of 150 K; (2) The surface is reactivated for further dissociative adsorption by the desorption of surface hydrogen; (3) Dissociative adsorption is inhibited both by the preadsorption of hydrogen into the β_2 adstate and by the postadsorption of hydrogen onto nondissociated alkane overlayers at low temperatures. The studies involving the postadsorption of hydrogen demonstrate further the existence of a kinetic barrier to dissociation which can be overcome near 200 K.

The activity of the Pt(110)-(1×2) surface toward dissociative adsorption of alkanes can be compared to that exhibited by the Ir(110)-(1×2) surface.[1-4] The kinetic barrier to dissociative adsorption is not so great on iridium, since on that surface the activation of carbon–hydroen bonds occurs readily near 130 K. Thus ethane and propane adsorb dissociatively on the Ir(110)-(1×2) surface under our experimental conditions.[1] Their desorption temperatures of 140 and 175 K on the platinum surface, which should be similar to the values on iridium if the dissociative adsorption did not occur, are in accord with such a temperature for overcoming the activation barrier. Molecular desorption of ethane and propane on the Ir(110)-(1×2) surface occurs at 120 and 155, K, respectively. The difference in kinetic barriers for dissociative chemisorption correlates with the estimated energetic differences in the two product states. Whereas the metal–hydrogen bond strengths are probably equal, the metal–carbon bonds formed on the iridium surface should be stronger than those formed on the platinum surface, since metal–carbon bond strengths for diatomic metal carbides are greater for iridium than for platinum [150 compared to 145 (±1) kcal/mol[18]].

The hydrocarbon fragments formed on the platinum surface, which are manifest as the reaction-limited thermal desorption states of hydrogen, have a higher hydrogen content than those formed on the iridium surface. The greater dehydrogenation activity of iridium is reflected not only in the higher desorption temperature of hydrogen from the clean surface, but also in the activation of ethane and propane by this surface. While a simple model involving metallacycles was proposed to explain fragment stoichiometries on the iridium surface,[1] it is apparent that such a model does not readily explain the stoichiometries observed on platinum. The higher desorption temperature for surface hydrogen on iridium also accounts for the complete exchange of surface deuterium into the hydrocarbon fragments formed on that surface, while on platinum such exchange occurs but is kinetically limited and incomplete. In both cases deuterium labeling of the hydrocarbon does not reveal structural information directly in thermal desorption mass spectrometry due to the exchange reaction.

The molecular desorption of these alkanes at low coverages occurs at temperatures approximately 30 K higher on the Pt-(110)-(1×2) compared to the same surface of iridium. At higher coverages the desorption temperatures of *n*-butane and *n*-pentane shift to values similar to those observed on iridium. Such a shift is also observed for adsorption onto the carbon residue. Since the coverages of dissociatively adsorbed alkanes are lower on the platinum surface, this suggests that the higher desorption temperatures represent desorption of the alkane from a metal surface site, while the lower desorption temperatures represent desorption from a site where surface carbon or hydrocarbon fragments screen the interaction between the alkane and the metal.

While high concentrations of surface carbon did not relax the reconstruction of the Ir(110)-(1×2) surface, the fractional-order LEED beams characteristic of the surface reconstruction are virtually extinguished under similar conditions for platinum. Stabilization of the unreconstructed Pt(110) surface by carbon has also been noted by Ferrer and Bonzel.[16] Relaxation of the surface reconstruction for the (110) surface of platinum, but not for iridium, occurs under certain conditions for the adsorption of CO and NO.[19,20]

Whereas activity toward dissociative adsorption on the Ir(110) surface is inhibited readily on the presence of surface carbon or hydrocarbon fragments which result from the adsorption of a saturation coverage of an alkane overlayer on the clean surface,[21] this is not observed on the Pt(110) surface. In this case approximately 1.5×10^{14} molecules cm^{-2} of *n*-pentane must adsorb dissociatively and dehydrogenate to surface carbon before an inhibition of 50% is observed. Several aspects of the relative reactivities may contribute to this, namely (1) the higher saturation coverages of the dissociatively adsorbed overlayers on the clean surface of iridium compared to platinum; (2) the inhibition of dissociative adsorption of alkanes due to the presence of surface hydrogen which adsorbs from the background; (3) the loss of the reconstruction of the platinum surface due to the presence of surface carbon, which generates a surface with twice as many high coordination adsites; and (4) the possibility that the surface carbon remaining on the platinum surface may enter the subsurface layer as the surface reconstruction relaxes, diminishing its effectiveness as an inhibitor. The coverage of carbon atoms estimated to inhibit fully the dissociation of alkanes on the Pt(110)-(1×2) surface, 2×10^{15} cm^{-2}, is approximately twice the coverage required on the same surface of iridium.[21]

(18) S. K. Gupta, B. M. Nappi, and K. A. Gingerich, *J. Phys. Chem.*, **85**, 971 (1981).
(19) J. L. Taylor, D. E. Ibbotson, and W. H. Weinberg, *J. Chem. Phys.*, **69**, 4298 (1978).
(20) D. E. Ibbotson, T. S. Wittrig, and W. H. Weinberg, *Surf. Sci.*, **110**, 294 (1981).
(21) T. S. Wittrig, P. D. Szuromi, and W. H. Weinberg, *J. Chem. Phys.*, **76**, 3305 (1982).

The activation of *n*-butane and *n*-pentane on the reconstructed Pt(110)-(1×2) surface contrasts sharply with the adsorption of these alkanes on the close-packed Pt(111) surface. No dissociative adsorption of alkanes (through *n*-octane) was observed under similar experimental conditions.[5] Similar results were observed for the adsorption of *n*-heptane on the corresponding Ir(111) surface, except for the observation of a small reactivity ($<1 \times 10^{13}$ molecule cm^{-2}) which could be associated with defect sites.[22] These results suggest that the activation barrier on these close-packed surfaces is greater than 16 to 17 kcal/mol compared to approximately 7 to 8 kcal/mol on the Ir(110)-(1×2) surface and 11 to 12 kcal/mol on the Pt(110)-(1×2) surface, assuming preexponential factors of 10^{12} to 10^{13}. Clearly the enhanced reactivity of alkanes on the (110)-(1×2) surfaces of iridium and platinum as compared to the close-packed surfaces is due to some combination of geometric and electronic effects induced by its particular surface geometry.

Conclusions

The interaction of ethane, propane, *n*-butane and *n*-pentane with the reconstructed Pt(110)-(1×2) surface has been investigated at low temperatures and pressures principally employing mass spectrometry. Ethane and propane exhibit only molecular chemisorption, whereas low coverages of *n*-butane and *n*-pentane undergo dissociative adsorption at approximately 200 K to form surface hydrogen and hydrocarbon fragments. The availability of unoccupied β_2 adsites of hydrogen is critical for the dissociative adsorption of these alkanes. Preadsorption of hydrogen into this adstate inhibits dissociation, and this inhibition is complete upon saturation of the β_2 adstate. Both postadsorption of hydrogen on *n*-butane and *n*-pentane overlayers and the absence of dissociative adsorption for ethane and propane indicate that the kinetic barrier to carbon–hydrogen bond activation is overcome at approximately 200 K. The surface carbon formed in these reactions can, at sufficiently high concentrations, cause the lifting of the surface reconstruction.

Similar activation of alkanes has been observed previously for the Ir(110)-(1×2) surface, but on this surface the activation barrier to dissociative adsorption corresponds to a surface temperature of 130 K. On the close-packed Pt(111) and Ir(111) surfaces, dissociative adsorption of these alkanes is either not observed or occurs only at defect sites in the low coverage limit. This confirms a strong influence of surface geometry on C–H bond activation in alkanes.

Acknowledgment. This research was supported by the National Science Foundation under Grant No. CHE-8206487.

Registry No. Pt, 7440-06-4; ethane, 74-84-0; propane, 74-98-6; *n*-butane, 106-97-8; *n*-pentane, 109-66-0.

(22) See ref 2 and 3, and unpublished results.